<u>PhD Thesis in Biomedical and Life Sciences</u>

By

MAHMOUD MOHAMED ELSAYED BAYOUMI

<u>Title</u>

Understanding the Replication Kinetics of Influenza A Viruses under Chicken N^6-methyladenosine (m6A) Epitranscriptomic Pressure

Under supervision of

<u>Prof. Muhammad Munir</u>

Division of Biomedical and Life Sciences, Lancaster University, Lancaster, United Kingdom

<u>Dr. Leonie Unterholzner</u>

Division of Biomedical and Life Sciences, Lancaster University, Lancaster, United Kingdom

April 2023

Declaration of originality

I declare that the content of this thesis is my own work and has not been submitted by

myself in substantially the same form for the award of a higher degree elsewhere. Any

sections of the thesis which have been published have been clearly identified.

Mahmoud M. E. Bayoumi

- **List of Contents**

- **List of Tables**

- **List of Figures**

Chapter 1: General Introduction

Chapter 2: Materials and Methods

Chapter 3: Structural Insights into Avian m6A Machinery and

Evolutionary Conservation of Potential m6A Sites Among IAVs

Chapter 4: Anti-Viral Potential of Chicken m6A Machinery Against Influenza A Viruses

Chapter 5: Mechanistic studies on chALKBH5 and chWTAP in regulating IAVs infection

Chapter 6: Generation of Different m6A-Mutant Influenza A Viruses and The Impact of m6A Marks on Virus Replication Kinetics

Chapter 7: Transcriptome-wide Host and Viral m6A Methylome

And chALKHB5 Interactome: Initial Observations and Future Prospects

- **<u>List of Abbreviations</u>**

A^O	Angstrom
µM	Micrometre
2OG	2-oxoglutarate analogue residue
3D	Three-dimensional
6mA	6-methyladenine
a.a.	Amino acid
ac^{4}C	N4-acetylcytidine
ActD	Actinomycin D
AGID	Agar gel immunodiffusion
AI	Avian influenza
AIV	Avian influenza virus
ALKBH5	alkylated DNA repair protein (AlkB) homologue 5.
ANOVA	One-way analysis of variance
APS	Ammonium persulphate
bp	Base pair
BSA	Bovine serum albumin
cDNA	Complementary deoxyribonucleic acid
CLSM	Confocal laser scanning microscopy
CMV	Cytomegalovirus
CPE	Cytopathic effect
cRNA	Complementary RNA
CRISPR	Clustered Regularly Interspaced Short Palindromic Repeats

DAPI	4',6-diamidino-2-phenylindole
dCas13s	Catalytically inactive CRISPR-Cas13 effectors
DMSO	Dimethyl sulphoxide
dNTPs	Deoxynucleotide triphosphates
E. coli	Escherichia Coli
EBV	Epstein - Barr Virus
ECE	Embryonated chicken eggs
EDTA	Ethylene diamine tetra acetic acid
ELISA	Enzyme-linked immune-sorbent assay
EM	Electron microscopy
ER	Endoplasmic reticulum
EV-71	Enterovirus-71
FAO	Food and agricultural organization
FFU	Foci-forming unit
FTO	Fat mass obesity-associated protein
GFP	Green fluorescent protein
HA	Haemagglutination assay
HA	Haemagglutinin protein
HA2	Haemagglutinin subunit 2
HBV	Hepatitis B virus
HCMV	Human cytomegalovirus
HCV	Hepatitis C virus
HI	Haemagglutination inhibition

HIV-1	Human immunodeficiency virus type-1
HMPV	Human metapneumovirus
hnRNPs	Heterogeneous nuclear ribonucleoproteins
HPAIVs	Highly pathogenicity avian influenza viruses
HSV-1	Herpes simplex virus type 1
IAVs	Influenza A viruses
IBVs	Influenza B viruses
ICVs	Influenza C viruses
IFA	Immunofluorescence assay
IGF2BPs	insulin-like growth factor 2 mRNA-binding proteins
IP	Immunoprecipitation assay
IRD	Influenza research database
KDa	Kilo Dalton
KO/KD/KI	Knock-out/Knock-down/Knock-in
KSHV	Kaposi's sarcoma-associated herpesvirus
lncRNA	Long non-coding RNA
LPAIVs	Low pathogenicity avian influenza viruses
M	Matrix Protein
m^1A	N1-methyladenosine
m^5C	5-methylcytidine
m^6A=m6A	N6-methyl-adenosine
m^6A_m	N6,2′-O-dimethyladenosine
MCMC	Bayesian Markov chain Monte Carlo

MDA5	Melanoma differentiation-associated protein 5
MeRIP-seq	Methylated RNA-immunoprecipitation sequencing
METTL14	Methyltransferase like-14
METTL3	Methyltransferase like-3
ML	Maximum likelihood
MLV	Murine leukaemia virus
MOI	Multiplicity of infection
mRNA	Messenger RNA
MS	Mass spectrometry assay
MSA	Multiple sequence alignments
MTD	Methyltransferase domain
MWs	molecular weights
NA	Neuraminidase
NDV	Newcastle disease virus
NEP	Nuclear export protein
NFDM	Non-fat dry milk
NFW	Nuclease free water
NLS	Nuclear localization sequence
nm	Nanometre
Nm	2′-O-methylation of the ribose sugar
NP	Nucleoprotein
NS	Non-structural
NS1	Non-structural-1

Nt	Nucleotides
ORF	Open reading frame
PA	Polymerase acidic
PAGE	Polyacrylamide gel electrophoresis
PA-m6A-seq	photo-crosslinking assisted m6A sequencing strategy
PAR-CLIP	Photoactivatable-ribonucleoside-enhanced crosslinking and immunoprecipitation
PB1	Polymerase basic 1
PB2	Polymerase basic 2
PBS	Phosphate buffered saline
PBST	Phosphate buffered saline-tween 20
PCR	Polymerase chain reaction
PDB	Protein database
PFU	Plaque forming unit
PRRs	Pathogen recognition receptors
PVDF	polyvinylidene fluoride
RBCs	Red blood corpuscles
RBM15	RNA-binding motif protein 15
RBPs	RNA binding proteins
RIP-qPCR	RNA-immunoprecipitation-qPCR
RLRs	RIG-I-like receptors
RNA	Ribonucleic acid
RNP	Ribonucleoprotein

rpm	Revolution per minute
rRNA	Ribosomal RNA
RSV	Respiratory syncytial virus
RT-qPCR	Reverse Transcription – quantitative Polymerase Chain Reaction
SAM	S-adenosyl-methionine
SARS-CoV-2	Severe Acute Respiratory Syndrome Coronavirus-2
SD	Standard deviation
SDS	Sodium dodecyl sulphate
SnRNA	Small nuclear ribonucleic acid
SOC	Super optimal culture
SPF	Specific pathogen-free
SV40	Simian Virus 40
TAE	Tris Acetate EDTA
TAP	Tris Acetate Phosphate
$TCID_{50}$	50% Tissue culture infective dose
TE	Tris-EDTA
TEMED	Tetramethylethylenediamine
TLRs	Toll-like receptors
TM	Transmembrane
TPCK	Tosyl phenylalanyl chloromethyl ketone
tRNA	Transfer RNA
µg	Microgram
µL	Microlitre

UV	Ultraviolet
VIRMA	Vir-like m6A methyltransferase-associated
vRNA	Viral RNA
VSV	Vesicular stomatitis virus
WHO	World health organization
WT	Wildtype
WTAP	Wilms tumour 1-associated protein
YTHDC1	YTH- domain-containing protein-1
YTHDF1	YTH- domain-family protein-1
ZC3H13	Zinc-finger CCCH-type containing-13
ZnF	Zinc finger containing domain
α-KG	Alpha-ketoglutaric acid

Acknowledgments

My sincerest thanks to Prof. Muhammad Munir for giving me the opportunity and privilege to study and work under his tutelage, supervision, endless donation, and unlimited support during every step that allowed me to finish the PhD work smoothly and effectively.

I would also like to thank my secondary supervisor Dr. Leonie Unterholzner for her support and guidance in supervisory meetings. Her valuable BLS lectures for PhD students helped me immensely in thesis writing.

Throughout my PhD studies, I have been lucky enough to work in Munir's lab with many brilliant individuals, including Manar Khalifa, Emily Clayton, Julianne Vilela, and Dr. Lucy Balderstone.

I would also like to express my gratitude and appreciation to staff members, technical staff, PhD students, and postdocs from other groups in the department for their technical support.

I want to thank my family in the UK and the rest in Egypt for everything they have done for me during my project.

Finally, I would like to thank the Egyptian Ministry of Higher Education and the British Council for funding my PhD grant.

Abstract

Influenza A viruses (IAVs) pose serious public health consequences, causing severe epidemics and occasional pandemics. Human IAV pandemics are associated with zoonotic spillover from animals to humans, especially from birds. Infection of IAV in chickens induces a range of transcriptional and epitranscriptional changes. Methylation at the N6-position of adenosines (m6A) is the most abundant chemical post-transcriptional modification deposited onto mRNA in eukaryotic species. The m6A regulates various RNA metabolic processes, including RNA structure, stability, protein translation, and splicing. Notably, the m6A has also been reported in viruses to play central regulatory roles in the viral lifecycle and host-pathogen interaction.

The m6A marks are installed onto mRNA by a complex group of methyltransferases (METTL3/14/WTAP complex), removed by a group of demethylases (ALKBH5 and FTO), and read by readers (YTHDF1-3, YTHDC1, and YTHDC2). The genetics and functions of m6A cellular machinery are well-characterized in humans; however, knowledge in animals, including birds, remained elusive.

This PhD project assessed the unique evolutionary patterns and genetic and structural alterations of chicken m6A machinery proteins compared to human orthologues. The conservation of m6A marks was also predicted in all IAV strains, and virus-specific m6A marks were highlighted and exploited to determine their roles in virus replication kinetics.

While IAV infection transcriptionally reduced m6A-associated genes, several m6A-associated proteins, including chALKBH5, downregulated replication of IAVs and

protein expression in a time-course manner. Mechanistic investigations revealed that middle and carboxy (C)-fragments were shown to be responsible for the antiviral effect of chALKBH5 against H9N2 and H1N1 influenza subtypes, whereas the nuclear localization signal located at C-fragment regulated the antiviral action of chALKBH5.

Using CRISPR/Cas13 editing technology, the chALKBH5 was tethered to a catalytically inactive variant, dCas13b, to remove m6A marks from IAV transcripts. Targeted demethylation of the individual or multiple m6A modifications in the haemagglutinin (HA) gene of IAV H9N2 downregulated viral replication and protein expression. An in-house generated reporter chALKBH5 cell line revealed that chALKBH5 mediated inhibition of IAV is via interaction with the viral NP protein, but not NS1. Notably, in contrast to human WTAP, chWTAP failed to interact with the chMETTL3/14 complex, suggesting a differing mechanism in m6A methylation in chicken.

Using reverse genetics of IAV, several m6A sites were added or removed from the HA gene of H9N2. The presence of m6A marks promotes IAV replication and protein expression, whereas demethylation has the opposite effect. Ultimately, using m6A-seq, the alteration in the m6A methylome in virus-infected DF1 chicken cell line was mapped and H9N2 m6A peaks were identified. Using mass spectrometry, the chALKBH5 interactome was determined. Finally, it was shown that chALKBH5 exerts a pan-antiviral function against various RNA viruses. Taken together, viral and host m6A were epitranscriptomically investigated, which will unravel an array of future studies to examine the potential of m6A to regulate IAVs transmission across multiple susceptible species.

Chapter 1

General Introduction

1.1. Influenza viruses

Influenza is an acute respiratory distress caused by influenza A virus belonging to the *Orthomyxoviridae* family. Influenza A viruses (IAVs) can infect many host species, including humans, birds, swine, equines, and sea mammals. Moreover, influenza B and C infect infrequently infect humans. Interestingly, influenza D has been confirmed to affect cattle, goats, and pigs only (Asha and Kumar, 2019; Long et al., 2019).

1.1.1. Short history of influenza viruses

In the sixteenth century, a rapid spread of catarrhal fever symptoms was reported in Great Britain. The old historical records indicated that it could be the first influenza epidemic in the modern era. Still, without a doubt, influenza probably occurred from antiquity, possibly the absence of definite characteristic signs like cholera, making it challenging to identify and record (Kilbourne, 1987). With the advancement of the human population and mass transportation (using animals), modern influenza pandemics started to emerge.

Many human outbreaks were coincidental with signs of cough among horses between the 1600s–1800s. Nonetheless, horse-to-human transmission has not been recorded (Kilbourne, 1987). Additionally, earlier reports involved other animals, including pigs, with human influenza in modern times (Scholtissek et al., 1985; Kilbourne, 2006). Notably, avian species were massively involved in human fatalities clearly started in Hong Kong in 1997 (H5N1) (Subbarao et al., 1998), in the Netherlands in 2003 (H7N7) (Fouchier et al., 2004), then H5N1 in Hong Kong re-emerged in 2003 (Peiris et al.,

2004). All these observations indicate the essential role of avian species in shaping the ecology of influenza viruses around the globe.

Tracing back the human sera indicated that influenza circulated in humans between 1889 and 1898 caused by the H2N2 subtype of IAV. Whereas between 1899 and 1917, influenza infection was driven by H3N8. Notably, H1N1 was the predominant cause between 1918 and 1957 (Rekart et al., 1982; Cox et al., 2007). However, among all subtypes of IAVs, only three were well-established in humans; H1N1, H2N2, and H3N2 (Cox et al., 2007).

Coming closer to the past century, four influenza pandemics have occurred, 'Spanish flu' was caused by H1N1 in 1918, 'Asian influenza' caused by H2N2 in 1957, 'Hong Kong influenza' by H3N2 in 1968, and the most recent pandemic was 'swine influenza' cause by H1N1 in 2009. Pandemics usually occur after the emergence of a novel influenza virus generally arises from animal sources such as avian species, as in 1918. Moreover, reassortment (interchange of viral segments) between avian and human strains was the leading cause of pandemics, as in 1957 and 1968, or reassortment in pigs (2009). The subsequent spread of these novel viruses to naïve human beings caused substantial morbidity and mortality (Cox and Subbarao, 2000).

The 'Spanish flu' (1918) was the most severe pandemic, which caused more than 50 million deaths around the globe (Biggerstaff et al., 2014). Notably, following pandemics, several descendants arise to replace or co-circulate in human populations with the pre-pandemic subtypes. Therefore, the descendants of the H1N1 pandemic swine influenza 2009 (H1N1pdm09) strains are co-circulating along with the predominant subtypes affecting humans (Paules and Subbarao, 2017).

1.1.2. Classifications and nomenclature

Influenza viruses are classified into genera (i.e., types) based on traditional serological reactions of their internal proteins, including nucleoprotein (NP) and matrix 1 (M1). That is typically performed by immunoprecipitation tests, including agar gel immunodiffusion test (AGID) (Swayne and Suarez, 2000). IAVs are further subtyped based on either serological reaction of the hemagglutinin (HA) and neuraminidase (NA) surface glycoproteins or the sequence analysis of HA and NA gene segments. The serologic subtyping of HA revealed 16 subtypes of HA (1–16) and 9 subtypes of NA (1–9). Most combinations of these 16 HA and 9 NA subtypes have been reported in domestic or wild birds comprising avian influenza viruses (AIVs), but distribution varies by year, geographic location, and host species (Fouchier et al., 2005). Recently, H17N10 and H18N11 viruses have also been isolated from central American bats (Tong et al., 2013).

Webster et al., (1992) recommended a system for the nomenclature of influenza viruses. The name should include the genus and species from which the virus was isolated. Followed by the location of the isolate, the number of the isolate, and the year of isolation. In the case of IAVs, the HA and NA subtypes should be included. For example, the first isolate of the H5N1 virus from chickens in Egypt, which was isolated in 2006, was named A/chicken/Egypt/1/2006 (H5N1) (Webster et al., 1992).

Albeit humans are prone to be infected with influenza A, B, and C viruses, two subtypes are predominant, co-circulating the H1N1 and H3N2, which are the primary causes of seasonal infections (Gatherer, 2009). Interestingly, several subtypes can occasionally

cross the species barrier to infect humans, including avian H5N1, H7N9, and H9N2, generating sporadic zoonotic infections (Mostafa et al., 2018).

Avian influenza viruses are further classified based on their pathogenicity into either highly pathogenicity (HPAIVs) or low pathogenicity (LPAIVs). Clinically, HPAIV strains are characterized by high morbidity and mortality of up to 100% of infected birds, whilst LPAIVs are characterized by a reduction in body weight in broilers and/or a slight drop in egg production in layers. Genetically, the molecular determinants of pathogenicity include the presence of multibasic amino acids (a.a.) in the cleavage site in the HA protein in HPAIVs (will be detailed later). The H5Nx and H7Nx strains are commonly highly pathogenic (Swayne and Suarez, 2000).

1.1.3. Influenza virus morphology

Influenza virus particles are pleomorphic with spherical or filamentous morphology or a mixture of both. Among clinical isolates that have undergone a limited number of passages in eggs or tissue culture, influenza viruses are more filamentous than spherical particles (**Figure 1.1A-D**). In contrast, extensively passaged laboratory strains consist primarily of spherical virions (80–120 nm in diameter). Despite their distinctive shape, the filamentous virions possess many of the serological, haemagglutinating, and enzymatic characteristics of the spherical particles (Bourmakina and García-Sastre, 2003).

The morphology of influenza virions seems primarily determined by the M protein (Bourmakina and García-Sastre, 2003). Although both the HA and NA likely play a role in virus morphology (Jin et al., 1997). Viral particles comprise a host-derived lipid

bilayer envelope in which the virus-encoded HA, NA, and M2 are embedded with an

inner shell of matrix (M1) protein. In the centre, the nucleocapsids of the viral genome

are located **(Figure 1.1E)** (Webster et al., 1992; Pleschka, 2013).
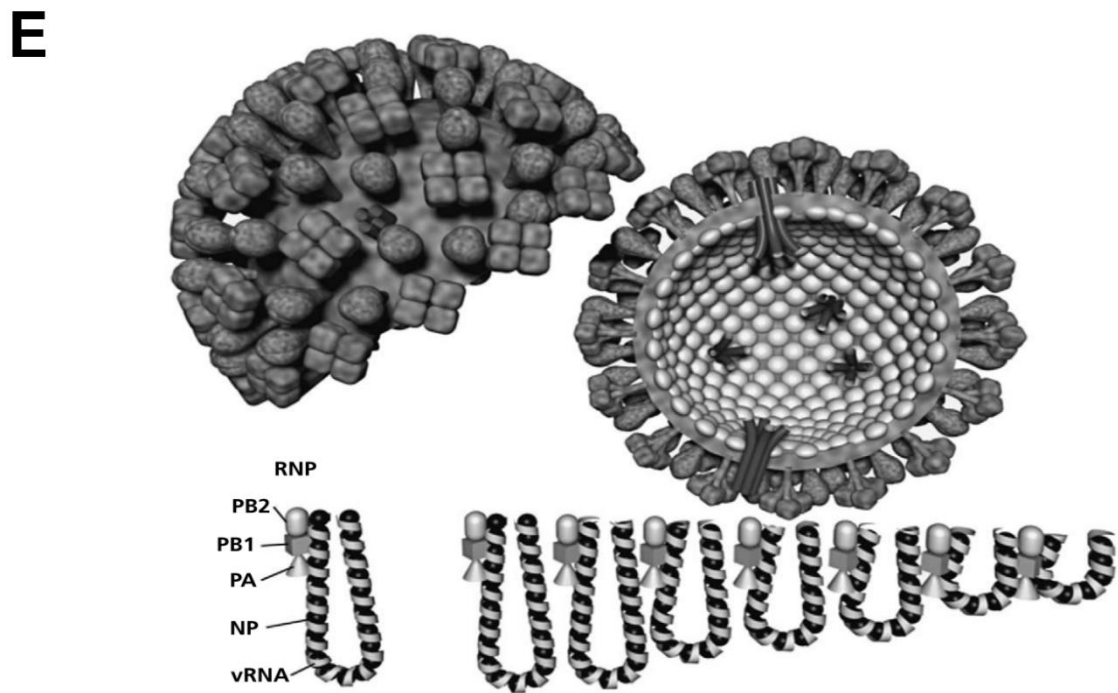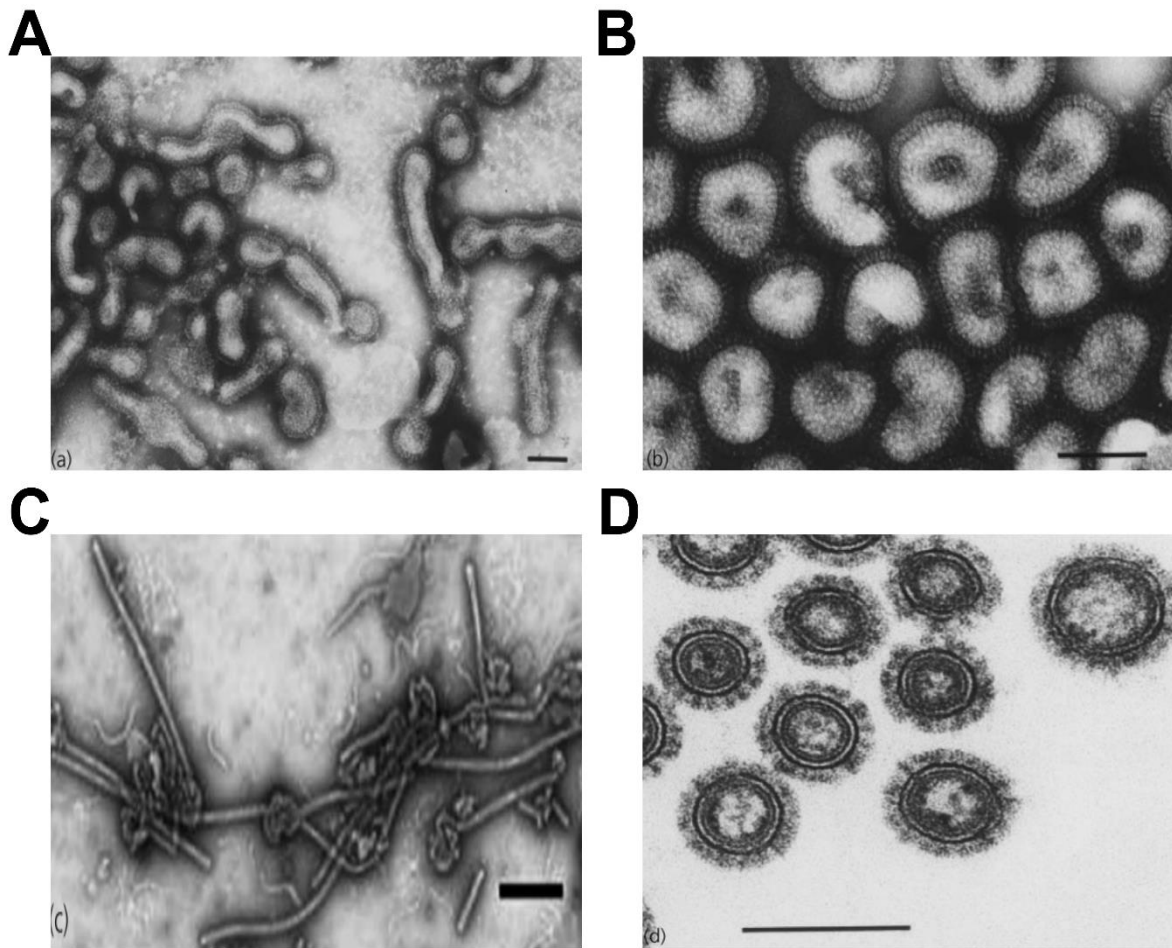
Figure 1.1: Morphology of influenza A viruses (IAVs). **(A-D)** Various morphology of influenza viruses, including filamentous, pleomorphic, and spherical-shaped virions. **(E)** Schematic of the IAV virion. The outer surface contains viral glycoproteins, hemagglutinin (HA), neuraminidase (NA), and the M2 protein ion channel. The virion contains the nucleoproteins associated with the vRNAs (vRNPs). The viral polymerases are associated with the RNPs. The figure is adapted from a previous publication (Cox et al., 2007).

1.1.4. Genome structure and protein functions of influenza A viruses

Influenza viruses are segmented viruses with negative polarity (i.e., vRNA cannot be translated into proteins). The segment numbers vary between genera with 8 segments in IAVs and influenza B viruses (IBVs) and 7 in influenza C viruses ICVs. The IBVs have the largest concatenated coding capacity (~14600 nucleotides), whereas IAVs and ICVs possess (~13600 nucleotides) and (~12900 nucleotides), respectively.

Notably, each viral segment has conserved nucleotides in the un-translated regions (UTRs); these sequences act as promoters in each viral RNA species **(Figure 1.2)** (Webster et al., 1992; Fodor et al., 1995; Neumann and Hobom, 1995). The genome of influenza A viruses (IAVs) encodes at least ten core proteins as follows:
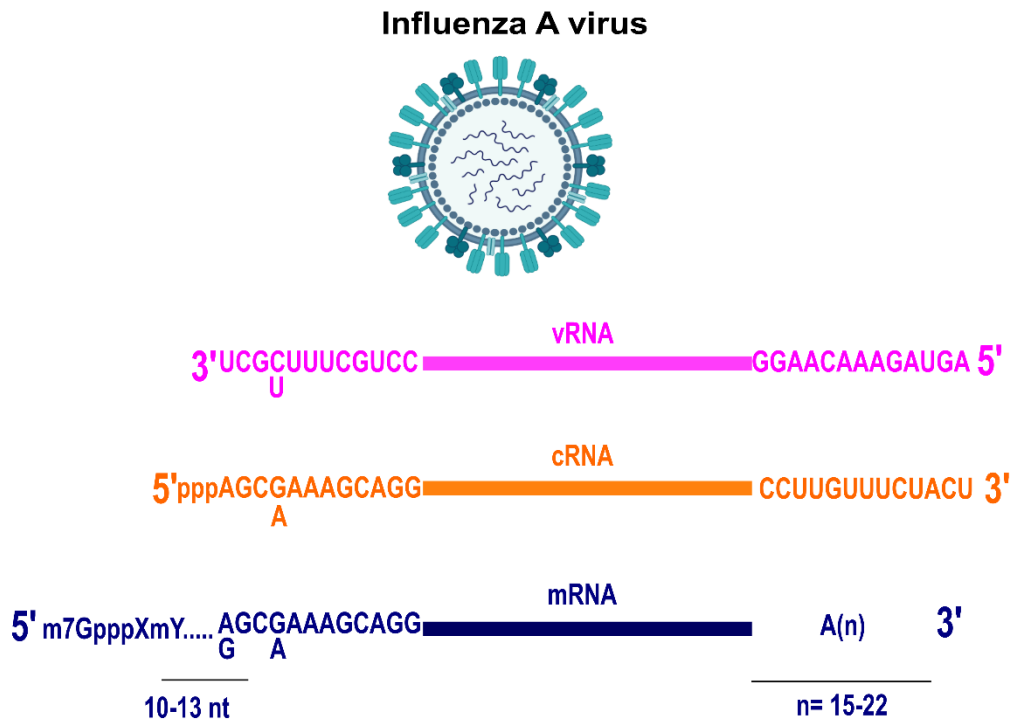
Figure 1.2: Schematic of the difference between various types of RNA species in IAVs lifecycle. The highly conserved 12/13 nucleotides in each strand are indicated.

1.1.4.1.   Segment 1-Basic Polymerase Protein 2 (PB2)

Segment 1 of the influenza A virus encodes one viral polymerase subunit, PB2. It is widely accepted that PB2, PB1, PA, and NP form a minimum set of proteins required for viral transcription and replication (Honda et al., 2002). The PB2 contains nuclear localization signals to direct transportation into the nucleus of infected cells for viral transcription and replication (Jones et al., 1986; Mukaigawa and Nayak, 1991).

PB2 is an essential protein for generating the cap structure for viral mRNAs. Influenza viral polymerase studies demonstrated that the PB2 subunit is a cap-binding protein

(Blaas et al., 1982). The analysis indicated that the cap-binding site is probably located near the carboxyl terminus (de la Luna et al., 1989). The studies also indicated that cell lines expressing PB1, PA, and NP, but not PB2, can synthesize transcription products lacking 5′ cap structures, showing that PB2 is a critical polymerase subunit for the cap-snatching process (Nakagawa et al., 1995; De Vlugt et al., 2018).

Several studies reported that PB2, PB1, and PA form a polymerase complex for viral transcription and replication. Immunoprecipitation assays on influenza viral polymerase demonstrated that PB2 is associated with the PB1 subunit. Analysis of deletion mutants of PB2 indicated that the amino terminus of this protein is a binding site for PB1 (Digard et al., 1989; Toyoda et al., 1996). Moreover, functional analysis of the PB2 protein has also shown that this polymerase subunit contains a novel binding site for the PB1 subunit and two regions for binding nucleoprotein (NP) with regulatory interaction potential (Poole et al., 2004).

PB2 is also suggested to be a significant determinant in controlling the pathogenicity of influenza A viruses. Using reverse genetics techniques, introducing a mutation at position 627 in the PB2 protein altered the virulence of H5N1/97 viruses in mice (Hatta et al., 2001).

1.1.4.2. Segment 2-Basic Polymerase Protein 1 (PB1)

The PB1 RNA polymerase subunit is encoded by segment 2. Several studies indicated that PB1 is the core viral RNA polymerase. Firstly, photochemical cross-linking assays demonstrated that the elongated RNA product and the viral RNA template cross-linked to PB1, suggesting that PB1 carries the site for RNA polymerization (Li et al., 1998).

Secondly, amino acid sequence comparison with other RNA polymerases showed that the PB1 contains the four conserved motifs of RNA-dependent RNA polymerases, and mutations in these motifs abolished the polymerase activity (Biswas and Nayak, 1994). Thirdly, nuclear extracts from cells expressing PB1 protein alone would transcribe vRNA templates (Kobayashi et al., 1996; Te Velthuis and Fodor, 2016).

Studies have also described the functional domains of PB1 involved in interaction with the other polymerase subunits. Immunoprecipitation studies of the influenza virus RNA polymerase suggested that PB1 contains independent binding sites for PB2 and PA. Further analysis indicated that deletion mutants of PB1 suggested that the amino- and carboxyl-termini of PB1 are binding sites for the PA and PB2 polymerase subunits, respectively. The nuclear localization signal of PB1 was also mapped to a region near the amino terminus. The PB1 subunit plays a vital role in assembling three polymerase protein subunits and the catalytic function of RNA polymerization (González et al., 1996). Notably, the activity of the PB1 is directed to transcriptase through binding with PB2 or replicase through binding with PA (Honda et al., 2002).

Some IAV PB1 genes have a second open reading frame (ORF) generating the so-called PB1-F2, a short (87–90 a.a.) influenza A virus protein discovered in 2001. After expression, it is rapidly degraded and is not required for viral replication in-ovo or in cultured cells (Chen et al., 2001). The PB1-F2 protein is recognized by the human immune system, resulting in both humoral and T-cell responses during infections with seasonal H3N2 or highly pathogenic H5N1 viruses. Expression of PB1-F2 has been shown to enhance viral pathogenicity in mouse models of influenza A virus infection (Zamarin et al., 2006).

1.1.4.3. Segment 3-Acidic Polymerase Protein (PA)

Segment 3 encodes the PA protein, the smallest subunit of the influenza RNA polymerase complex. Like the other influenza viral polymerase subunits, it contains nuclear localization signals required for transport into the nucleus. PA is known to be essential for viral transcription and replication (Huang et al., 1990) and mutations near the carboxyl terminus inhibit transcription by affecting the binding with PB1 (Zurcher et al., 1996).

It has been reported that a single amino acid mutation in the PA protein of the influenza virus RNA polymerase inhibits endonucleolytic cleavage of the capped RNAs and promotes the generation of defective interfering RNAs (Fodor et al., 2003; Dias et al., 2009). Furthermore, the PA is required for efficient nuclear accumulation of the PB1 subunit of the influenza A virus RNA polymerase complex (Fodor and Smith, 2004).

Furthermore, amino acid sequence comparison with other known proteins suggested that the PA has helicase and ATP-binding activities (de la Luna et al., 1989). Interestingly, PA is found to induce proteolysis in infected cells. Still, this property is not related to any known viral function, and the significance of these findings is yet to be determined. Functional analysis of PA deletion mutants identified the amino-terminal one-third of this protein as being responsible for the protease activity. When PA is expressed in cells without the other polymerase subunits, it induces general proteolysis of both viral and cellular co-expressed proteins. It has been demonstrated that PA is a phosphorylated protein. Thus, the biological functions of the PA protein might be regulated by a phosphorylation process (Sanz-Ezquerro et al., 1998).

1.1.4.4. Segment 4-Haemagglutinin (HA)

Segment 4 of IAV encodes HA protein. In viral particles, HA proteins associate as homotrimers. HA is primarily responsible for viral particles binding to sialic acid-containing receptors on the cell membrane. It also mediates the fusion of the viral and cellular membranes. It is essential to note that the HA glycoprotein is also the principal surface antigen of the influenza A virus and is a primary target for neutralizing antibodies (Cox et al., 2007; Ekiert and Wilson, 2012).

1.1.4.4.1. Three-dimensional (3D) structure

The first demonstration of the 3D structure of the HA molecule was performed for the ectodomain of the human H3N2 virus. The X-ray crystallographic structures have been determined for three different conformations, including the bromelain-cleaved soluble HA (BHA) of A/Aichi/2/68 (H3N2), which represents the conformation of cleaved HA, the uncleaved HA0 precursor, and fragments of low pH-treated BHA (Wiley et al., 1981; Bizebard et al., 1995; Chen et al., 1998).

Furthermore, the HA structures of the 1918 pandemic virus, H3 and H5 avian viruses, and H9 swine virus have been determined (Ha et al., 2001; Stevens et al., 2004). Structurally, the BHA is 13.5 nm long and 1.4–4 nm in triangular cross-section and contains all of the HA1 and the first 175 of the 221 amino acids of the HA2 subunit; it lacks only the hydrophobic membrane-anchoring peptide of HA2 (Brand and Skehel, 1972; Wiley et al., 1981).

The HA is folded into two structurally distinct domains, a globular head and a fibrous stalk. The globular head is entirely composed of HA1 residues and contains an eight-

stranded antiparallel β-sheet. This framework supports the receptor-binding site (RBS), surrounded by highly variable antigenic loop structures. The fibrous stalk region, more proximal to the viral membrane, consists of residues from both HA1 and HA2 (**Figure 1.3**). The cleavage site between HA1 and HA2 is in the middle of the stalk. The fibrous stem regions principally stabilize the trimeric structure rather than a loose association of the globular heads. HA0 and cleaved HA1 and HA2 are super-imposable except for the region spanning the cleavage site. In uncleaved HA, the cleavage site forms a prominent surface loop in the middle of the stalk. A cavity is located next to the cleavage site that is partially filled by the carboxyl terminus of HA1. Upon cleavage, the carboxyl terminus of HA1 becomes exposed on the trimer surface, indicating significant rearrangement and conformational change after cleavage of the HA0. The hydrophobic amino terminus of the HA2 (fusion peptide) becomes buried in the trimeric structure (Brand and Skehel, 1972; Wiley et al., 1981; Skehel and Wiley, 2000).

Figure 1.3: Structural arrangement of HA protein in various states. The upper diagram shows HA domains, The HA precursor (HA0) is cleaved into the sialic acid receptor binding domain (HA1) and stalk (HA2). All components in each domain are shown. Sequences of H1 in the cleavage site and fusion peptide are displayed in colour codes. The lower diagrams show the variation of HA monomer in the prefusion (native) form and active fusion form triggered by low pH. The colours indicated in the upper panel correspond to those in 3D structures. The figure is adapted from a previous report (Sriwilaijaroen and Suzuki, 2012).

1.1.4.4.2. Cleavage

In general, the HA0 is believed to be cleaved by trypsin-like proteases extracellularly. However, the presence of multiple basic amino acids within the cleavage site allows the protein to be cleaved by intracellular proteases, for example, furin, which are ubiquitously expressed in most tissues (Horimoto and Kawaoka, 1994; Webby et al., 2004). It is crucial to note that there is a significant link between HA cleavability and virulence which is now well understood in AIVs. In virulent H5 and H7 avian viruses, the HAs contain multiple basic amino acids at the cleavage site, cleaved intracellularly by endogenous proteases. In contrast, avirulent avian viruses and non-avian IAVs, except for H7N7 equine viruses, do not have multiple basic amino acids. The HAs lack a series of basic residues and are not subject to cleavage by such proteases. Thus, the tissue tropism of viruses may be determined by the availability of proteases responsible for the cleavage of different HAs, leading to differences in virulence (Kawaoka, 1991; Hatta et al., 2001).

Investigations revealed that two groups of proteases are responsible for HA cleavage. The first group includes enzymes recognizing a single arginine and able to cleave avirulent-type HAs, such as plasmin, blood-clotting factor X-like protease, tryptase Clara, and bacterial proteases. The second group, which remains to be identified in vivo, comprises ubiquitous intracellular subtilisin-related proteases, furin, and PC6, which cleave virulent type HAs with multiple basic residues at the cleavage site (Horimoto and Kawaoka, 1994; Cox et al., 2007).

It is essential to mention that in cell culture, the tosyl phenylalanyl chloromethyl ketone (TPCK)-treated trypsin was predominantly used. TPCK-trypsin cleaves HA0, as in the

case of lab-adapted H1N1 and H9N2, to promote multicycle infections for virus propagation on Madin-Darby canine kidney (MDCK; not DF1, which does not tolerate TPCK-trypsin), as will be described later in this project.

1.1.4.4.3. Fusion

The HA mediates the fusion of influenza A viruses to the endosomal membrane. In neutral pH, the fusion peptide, which forms a small part of the amino terminus of the HA2, located in the fibrous stem of the molecule (3.5 nm away from the viral membrane and, hence, 10 nm from the target endosomal membrane), and is well integrated into the subunit interface by a network of hydrogen bonds. The importance of the peptide in HA-mediated fusion is evident from the ability of mutations in this region to alter or abolish fusion activity (White, 1992). When the pH is about 5 (late endosomal pH), the tertiary structure of the HA is significantly altered. This change is critical for the fusion of the viral and endosomal membranes **(Figure 1.4)** (White and Wilson, 1987; White, 1992; Harrison, 2008).

The three-dimensional structure of the HA1 globular head remains unaltered mainly; however, HA2 undergoes significant refolding events in which the fusion peptide is relocated more than 100 Angstrom toward the target membrane (Wiley et al., 1981; Carr and Kim, 1993). The fusion process is initiated by low pH, which triggers a conformational change to expose the fusion peptide, which becomes inserted into the target membrane. Next, the outer leaflets of the membrane bilayer fuse (hemifusion), followed by the fusion of the inner monolayer. Further observations suggest that oligosaccharides in the stem stabilize HA in a conformation prone to undergo structural changes necessary for fusion. Moreover, the length of the HA cytoplasmic tail affects

fusion activity. The trans-membrane region of HA is essential in the fusion process, as glycosyl-phosphatidylinositol-anchored HA is impaired in its ability to form pores (Armstrong et al., 2000; Bentz and Mittal, 2003; Harrison, 2008).
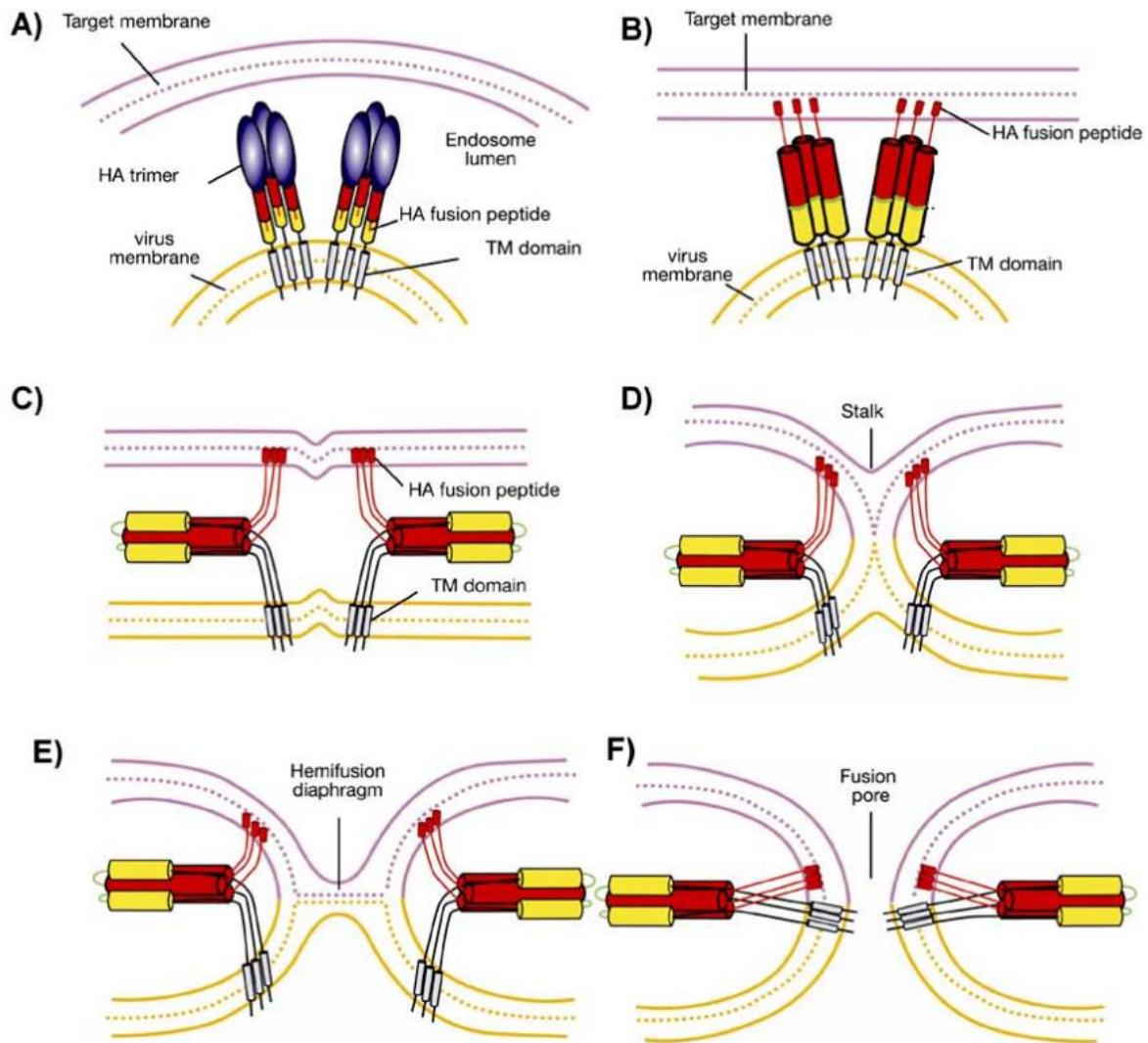
Figure 1.4: Schematic of HA-mediated influenza viral membrane fusion. **(A-F)** The sequential steps of HA viral membrane attached to the cell surface by the globular head (round). HA2 mediated the membrane fusion (stalk). The process is pH-dependent. The figure is adapted from a previous report (Cross et al., 2009).

1.1.4.4.4. Folding, intracellular transport, and assembly

The HA trimer is formed in the endoplasmic reticulum (ER) and is transferred to the cellular membrane via the Golgi apparatus (Skehel and Wiley, 2000). During HA synthesis in the ER, the HA interacts transiently with the BiP/GRP78 protein and calnexin before acquiring high mannose-type oligosaccharides and forming trimers, a prerequisite for transporting out of the ER (Doms et al., 1993). Through interaction with N-linked glycans in the HA, lectin chaperones such as calnexin and calreticulin regulate and facilitate HA folding. Cysteine residues in the ectodomain are essential for the efficient folding and stabilization of the final molecule. Disulphide bond formation occurs co-translationally. In the Golgi apparatus, the oligosaccharides of the HA are further processed to the complex type. In polarized cells, the final step of HA maturation is transporting to the apical cell surface (Roth et al., 1983; Doms et al., 1993).

It has been reported that HA is concentrated in lipid rafts. That are sphingomyelin and cholesterol-enriched microdomains in the cellular membrane (Takeda et al., 2003). These lipid rafts were believed to provide platforms for the assembly and budding of viruses, likely by increasing the local concentration of viral structural proteins. HA associates with rafts through its transmembrane domain; however, deletion of the HA cytoplasmic tail also affects raft association. Wild-type HA forms clusters at the surface of infected cells; in contrast, a mutant that lost the ability to associate with rafts was distributed randomly. A mutant virus containing the non-raft HA was characterized by reduced budding and fusion activity (Takeda et al., 2003).

1.1.4.4.5. Receptor binding

The sialylglycan receptors bound by the HA are usually linked to galactose (Gal) in an α2,6 or α2,3 configuration. In the case of the IAVs, which circulate across several mammalian species, the host glycan distribution and binding specificity of the viral HA largely determine the host range of the virus. The HA of avian IAVs usually displays a preference for α2,3 linked sialylglycans, whereas human IAVs preferentially bind α2,6 linked sialylglycans. The swine viruses have been reported to bind both α2,3 and α2,6 sialic acids but show a greater preference for the latter (**Figure 1.5**). For human-to-human transmission, the viral HA must efficiently bind to human cell surface receptors and possess the integral proteins that enable it to replicate efficiently in the cells of the human upper respiratory tract (Gambaryan et al., 1997; Skehel and Wiley, 2000).

Avian sialylglycan receptors can be found on non-ciliated cuboidal bronchiolar cells and alveolar type II cells in the lower respiratory tract, which might explain why direct human-to-human transmission by coughing or sneezing is inefficient, as the latter would necessitate the presence of avian-type receptors in the upper respiratory tract. Fortuitously, the restricted growth capabilities of H5N1 viruses in the human upper respiratory cells have thus far limited the pandemic potential of the virus. However, it has been reported that several mutations confer H5N1 direct transmission in mammals within regions of the receptor binding site (RBS), including Asn154Asp, Gln222Arg, and Ser223Asn of the HA. These mutations overlap with prominent antigenic positions (Yamada et al., 2006; Imai et al., 2012).
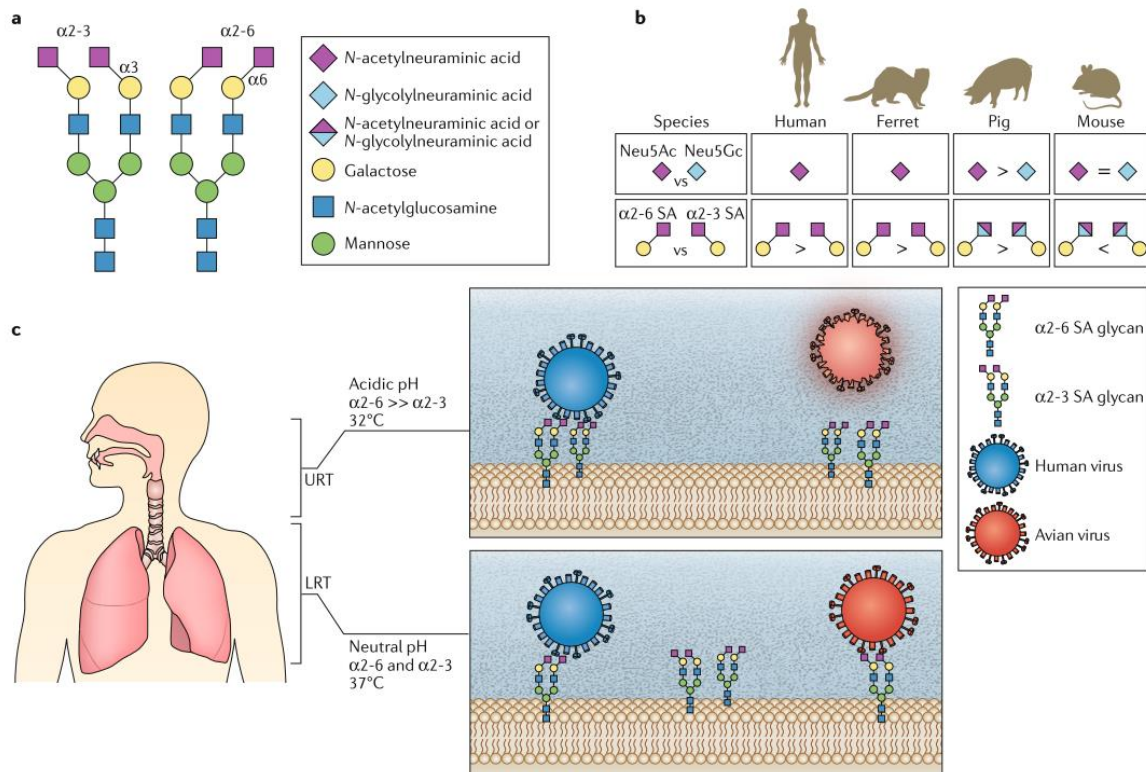
Figure 1.5: Receptor binding specificity drives viral host range. **(a)** Schematic of the sialylated receptors in a given host; component of each receptor is indicated. **(b)** Schematics of receptor distributions and the preferred receptor in different species are shown. **(c)** A diagram of the receptor distribution in the human airway determines the competent virus in each section. The figure is adapted from a previous report (Long et al., 2019).

1.1.4.5.   Segment 5-Nucleoprotein (NP)

Segment 5 encodes RNA binding protein, nucleoprotein (NP). The protein is 56 KDa phosphorylated basic protein and has a net positive charge at neutral pH (Kistner et al., 1989). Electron microscopy analysis revealed that each NP monomer has a banana-like elongated structure when expressed as an RNA-free single protein (Ruigrok and

Baudin, 1995; Ye et al., 2006). Very recently, the crystal structure of NP complexed with RNA substrate has been resolved (Tang et al., 2021). In agreement with previous electron microscopy results, interaction among the NP monomers occurs through a protein-flexible loop in the large bottom domain. Within the NP monomer, RNA binding has been proposed to occur in a channel between the two protein domains. (Martín-benito et al., 2001).

Moreover, NP has been suggested to encapsidate the viral RNA with a periodicity of one NP for each 20–24 bases of RNA (Albo et al., 1995). Furthermore, NP binds to vRNA via the ribose-phosphate backbone, leaving the bases exposed to solvation, ribonuclease digestion, and, most importantly, accessibility to the polymerase as a template for transcription (Baudin et al., 1994). NP interacts with PB1 and PB2 subunits in the viral RNA polymerase in forming the ribonucleoprotein (RNP) (Biswas et al., 1998). The NP was also thought to be the major switching factor determining whether genomic vRNA is transcribed into mRNA or used as a template to synthesize complementary RNA (cRNA) for genome replication (Skorko et al., 1991).

1.1.4.6. Segment 6-Neuraminidase (NA)

Segment 6 of influenza A virus encodes neuraminidase (NA). NA protein possesses enzymatic activity that is vital for the spread of the virus from host cells (Varghese et al., 1983). The protein size differs between NA subtypes and even within viruses from the same subtype. The three-dimensional structure of the NA revealed that the NA monomer consists of four domains: a short hydrophilic amino-terminal tail, a hydrophobic transmembrane domain, a stalk region, and a globular head that contains the enzymatic site for the protein (Varghese et al., 1983; Varghese and Colman, 1991).

The hydrophilic tail consists of 6 amino acids, MNPNQK, and is conserved in most type A influenza viruses, except for some swine-origin N1 proteins. The transmembrane domain sequence is highly variable between subtypes, but a hydrophobic stretch of hydrophobic amino acids is generally found between amino acids 8 and 37. The stalk region is also variable in sequence between subtypes but typically has 30 amino acid residues that were predicted to be hydrophilic; however, amino-acid deletions in the stalk region are common in poultry isolates. The NA protein in the virion forms a noncovalently bound homotetramer. However, the enzymatic activity is still present in individual units, even when the globular head is separated from the stalk and transmembrane regions of the protein (Matrosovich et al., 1999). The stalk appears to play a significant role in the budding function of the virus; viruses with stalk deletions have lower enzymatic activity, which, in severe cases, results in the aggregation of the virus on the cell surface, presumably affecting the efficient transmission of the virus. Influenza A viruses with stalk deletions are often associated with avian influenza of several NA subtypes isolated from poultry (Matrosovich et al., 1999).

1.1.4.7. Segment 7-Matrix Proteins (M1 and M2)
1.1.4.7.1. M1 Protein

The M1 protein forms a layer to separate the RNPs from the viral membrane. M1 also interacts with both the vRNA and protein components of RNP in the assembly and disassembly of influenza A viruses (Ruigrok et al., 2000). The M1 is reported to have several functions for the virus. It binds to RNA in a nonspecific sequence manner and inhibits viral transcription (Watanabe et al., 1996).

Additionally, M1 contains a nuclear localization signal and seems to regulate vRNP nuclear transport. When it binds to vRNP, it promotes vRNP nuclear export and inhibits vRNP nuclear import. Moreover, M1 is the primary determinant of virus budding and assembles into virus-like particles that are released into the medium; furthermore, M1 determines the morphology of influenza virions (Gómez-Puertas et al., 2000; Bourmakina and García-Sastre, 2003). Several studies demonstrated that the nuclear export of viral ribonucleoproteins is associated with the matrix protein. It has been proposed that the vRNA and M1 protein together promote the self-assembly of influenza virus NP into the typical quaternary helical structure of the vRNP. The interaction of NP with vRNAs and M1 in an environment devoid of other viral proteins may lead to the translocation of vRNP from the nucleus to the cytoplasm (Huang et al., 2001).

1.1.4.7.2. M2 Protein

The M2 is an integral membrane protein that exists as a disulphide-bonded homotetramer. The M2 tetramer has ion channel activity for pH regulation during viral infection (Pinto et al., 1992). In the endosome of infected cells, the ion channel activity of M2 allows acidification of the interior of the incoming viral particles. The acidification of the viral particle is believed to be essential for viral replication because it will enable incoming vRNP to dissociate from M1 proteins for nuclear import. Moreover, the ion channel activity of M2 is also reported to maintain a high pH in the Golgi vesicles to stabilize the native conformation of newly synthesized HA during the intracellular transport for viral assembly (Martin and Heleniust, 1991). Interestingly,

several reports have shown that universal vaccine candidates for influenza viruses can be developed by targeting the extracellular domain (M2e) (Neirynck et al., 1999).

1.1.4.8.   Segment 8-Nonstructural Proteins (NS1 and NS2)
1.1.4.8.1. NS1 Protein

The NS1 protein is the only non-structural protein of the influenza virus. It exists as an oligomer and accumulates mainly in the nucleus. The NS1 protein regulates cellular and viral protein expression by binding to different RNA molecules. In many in vitro studies, NS1 has been shown to bind to a wide range of RNA molecules, such as poly(A) containing cellular RNA, vRNA, vRNP, double-stranded RNA, small nuclear RNA (snRNA) (Qiu et al., 1995; Nemeroff et al., 1998).

It is also known to have inhibitory effects on splicing, cellular mRNA nuclear export, cellular mRNA polyadenylation by interacting with the cellular 3′ end processing machinery, and dsRNA protein kinase (PKR) activation. In contrast, the NS1 protein appears to enhance viral protein expression by stimulating the translation of viral mRNA (Chen et al., 1999; Hale et al., 2008).

However, an influenza virus lacking the NS1 gene was generated in interferon-deficient cells suggesting that the NS1 protein is not essential for the viral lifecycle in cell culture (Nemeroff et al., 1998). Notably, the NS1 protein of H5N1/97 was found to make the virus less susceptible to the antiviral effects of interferons and tumour necrosis factor-alpha (TNF-α). In addition, the NS1 of H5N1/97 was demonstrated to be a potent inducer of pro-inflammatory cytokines in human macrophages, suggesting the unusual

severity of human H5N1/97 disease might be due to the cytokine storm induced by the virus (Cheung et al., 2002).

1.1.4.8.2. NS2 Protein (NEP)

NS2 is a 14 kDa phosphorylated protein comprised of 121 amino acids that localize in the nucleus and cytoplasm of virus-infected cells. In early studies, it was believed that the NS2 protein was non-structural. However, further studies have indicated that low amounts of NS2 are incorporated into viral particles (Yasuda et al., 1993). Based on studies of NS2 mutants suggested that NS2 plays a role in promoting normal replication of the genomic RNAs. In addition, the carboxyl-terminal region of NS2 contains an M1 protein-binding site suggesting that NS2 might regulate and cooperate with the function of M1 (Yasuda et al., 1993). Based on the evidence that the NS2 protein contains a nuclear export signal and facilitates the vRNP export, multiple groups have proposed to rename this protein as NEP (viral nuclear export protein) (O'Neill et al., 1998; Neumann et al., 2000). A collective summary of the protein function of IAVs is listed in **Table 1.1**.

Table 1.1: Genome organization and functional proteins of IAVs.

Segment	vRNA(nt)	Viral protein(s)	Protein AA	Molecules/ Virion	Main Functions	References
1	2341	PB2	759	30-60	(1) Binding to cellular mRNA cap (2) Inhibits type I IFN induction via binding to mitochondrial antiviral signalling protein (MAVS)	(Iwai et al., 2010; Pleschka, 2013)
		PB2-S1	508	ND*	(1) Inhibition of RIG-I-mediated IFN signalling pathway (2) Interferes with polymerase activity via PB1 binding	(Yamayoshi et al., 2016)
2	2341	PB1	757	30-60	(1) Initiates viral mRNA transcription (2) Transcribes vRNA into cRNA for subsequent vRNA synthesis	(Bouvier and Palese, 2008; Iwai et al., 2010; Pleschka, 2013)
		PB1-F2	87-90	ND	(1) Regulates host IFN response (2) Promotes susceptibility to secondary bacterial infection (3) Induces apoptosis	(Zamarin et al., 2006; Varga et al., 2011)
		PB1-N40	718	ND	Sustains the balance between PB1 and PB1-F2 expression	(Tauber et al., 2012)
3	2233	PA	716	30-60	Cleaves the capped RNA structures for viral mRNA synthesis (endonuclease activity)	(Bouvier and Palese, 2008; Iwai et al., 2010)
		PA-X	252	ND	Regulates viral virulence and host response	(Gao et al., 2015)
		PA-N155	561	ND	modulate viral replication and pathogenicity	(Wang et al., 2018)
		PA-N182	534	ND		
4	1778	HA	566	500	(1) Receptor binding (2) Fuses viral and cell membranes (3) Main antigen	(Bouvier and Palese, 2008; Iwai et al., 2010)
5	1565	NP	498	1000	(1) vRNA binding and protection (2) component of vRNP complex (3) Imports vRNA to the nucleus	(Bouvier and Palese, 2008; Iwai et al., 2010; Pleschka, 2013)
6	1413	NA	454	100	(1) Releases virions (sialidase activity) (2) helps in penetration into the mucus barrier of the respiratory tract to infect the host cell	(Bouvier and Palese, 2008; Iwai et al., 2010)
7	1027	M1	252	3000	(1) Imports and export vRNPs (2) Viral assembly, budding, and virion morphology	(Bui et al., 2000; Iwai et al., 2010)
		M2	97	20-60	(1) Ion channel activity (2) Uncoating process	(Pinto et al., 1992; Bouvier and Palese, 2008; Iwai et al., 2010)
		M3	9	ND	ND	(Wise et al., 2012)
		M4	54	ND	ND	
		M42	99	ND	Complements M2	
8	890	NS1	230	ND	(1) Antagonizes antiviral IFN responses (2) Regulates viral mRNA splicing, translation, and export (3) Inhibits cellular mRNA translation	(Pleschka, 2013; Ayllon and García-Sastre, 2015; Mostafa et al., 2018)
		NEP	121	130-200	(1) Promotes vRNP nuclear export (2) Regulates vRNA replication	(Robb et al., 2009)
		NS3	187	0	ND	(Selman et al., 2012)

*ND: Non-determined.

1.1.5. Influenza A virus replication cycle and mechanisms of evolution

IAVs are enveloped with octameric single-stranded negative-sense RNA **(Figure 1.6a)**. NP surrounds each segment along with the heterotrimeric polymerase/transcriptase complex, PB1, PB2, and PA. Collectively known as viral ribonucleoproteins (vRNPs, **see section 1.1.4) (Figure 1.6b)**. The infection starts with the attachment of viral HA protein to sialic acid (SA) containing receptors on the cell surface (step 1). The entry of the virion is via endocytosis. The lower pH inside the endosome triggers conformational changes in HA **(see section 1.1.4.4.3)**. HA initiates the viral envelope fusion with the endosomal membrane (Benton et al., 2020). In parallel, acidic pH and a high K^+ entrance into virions through the ion channel M2 acidifies virions and induces dissociation of M1 from vRNPs, releasing the vRNPs into the cytoplasm (Martin and Heleniust, 1991; Dou et al., 2018).

Then, vRNPs are imported into the cell nucleus (step 2). After that, vRNAs are transcribed using the polymerase complex (step 3) (Engelhardt et al., 2005). The newly synthesized viral mRNAs are exported to cell cytoplasm for translation using cellular machinery (step 4). The newly formed polymerase complex proteins are then imported into the nucleus to initiate replication and further transcription (step 5). Newly synthesized vRNPs are exported to cell cytoplasm predominantly via M1 and the NEP **(see sections 1.1.4.7.1 and 1.1.4.8.2)** (Neumann et al., 2000) (step 6). vRNPs are transported to the cell surface for packaging, then vRNPs are assembled with the structural proteins, including HA, NA, M1, and M2 (step 7). Newly generated virions are formed via budding from the plasma membrane of host cells (step 8) **(Figure 1.6c)**.

There are two predominant methods for IAV evolution. (1) Antigenic drift (a minor change in genome composition) occurs due to the gradual accumulation of point mutations. Antigenic drift mainly leads to the emergence of new variants due to a lack of proof-reading activity of the polymerase complex (generating seasonal influenza). Mostly, point mutations are common in human influenza viruses compared with avian strains (Nelson and Holmes, 2007). (2) Antigenic shift (a major change in genome composition) occurs due to reassortments (interchange of viral segments) between different viruses during co-infection. Both methods are the primary cause of the influenza epidemic/pandemics so far. Significantly, reassortment was only documented to occur within the same genera strains (i.e., genus A, B, or C) but has not been reported between different genera (Urbaniak and Markowska-Daniel, 2014; Kim et al., 2018).
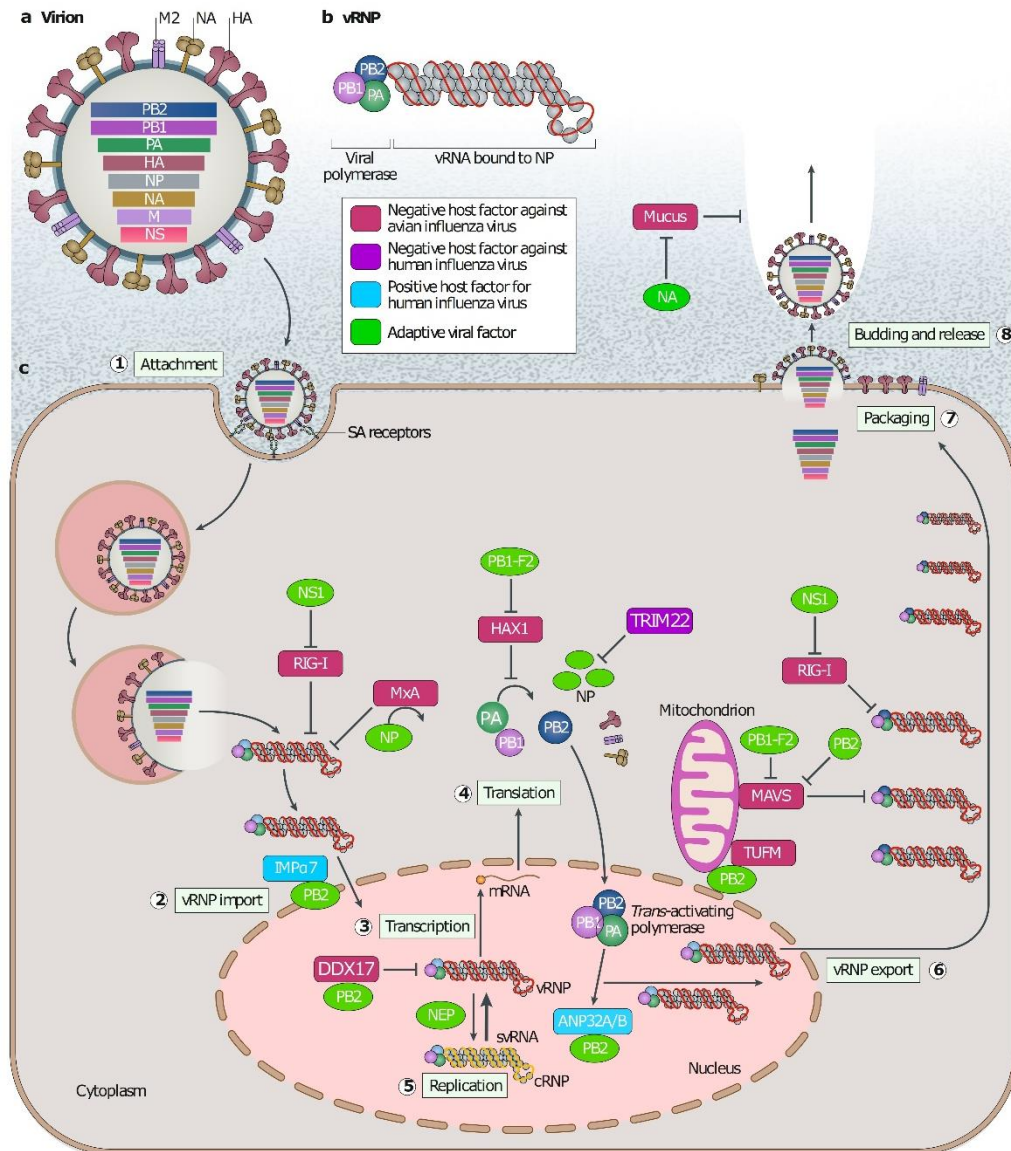
Figure 1.6: Influenza A virus replication cycle and viral determinants of replication. Schematic of IAV virion (a), vRNP polymerase complex (b), replication cycle (c). Antiviral factors against influenza viruses are represented by dark red and violet boxes. Light blue boxes represent the proviral elements of human influenza viruses. Green circles illustrate viral proteins. The figure was modified from a previous report (Long et al., 2019).

1.1.6. Transmission and clinical presentation of influenza viruses

The primary determinant of efficient spread in cases of pandemics was the cause of viral success in infecting naïve individuals. Three potential transmission methods were reported: aerosols, droplets, and contact inhalation. It has been confirmed that the release of infectious particles from an infected patient range from 0.1–100 µM, and the diameter in the particle size control the penetration capability to the respiratory tract. Significantly, the lower-sized particles (aerosols) can penetrate the lower respiratory tract, whilst the higher-sized particle settles in the upper respiratory tract (Killingley and Nguyen-Van-Tam, 2013).

Additionally, these particles might remain fully infectious for transmission for up to 3 hours (h), which varies according to the surrounding temperature and humidity. Furthermore, influenza virus infectiousness might withstand for up to 48 h on non-porous surfaces (Tellier, 2006). Interestingly, aerosol transmission is more effective in the virus transmission cycle than intentional intranasal inoculation. It has been verified that only 0.3 $TCID_{50}$ was required for aerosol transmission, whereas at least 127 $TCID_{50}$ were needed to induce intranasal inoculated infection in the ferret model. Thus, the WHO and CDC recommend using surgical masks to prevent the transmission cycle, mainly in healthcare settings (Paules and Subbarao, 2017).

Influenza has a short incubation period (1–2 days) with rapid onset of clinical signs that range from unnoticeable respiratory illness to fulminant signs that differ mainly according to viral characteristics and immunity of the infected individual. Increased body temperature is the most crucial feature (41°C). Additionally, headache, myalgia, and anorexia were noticed, accompanied by respiratory symptoms, including non-

productive cough, nasal discharge, and sore throat. Importantly, children usually exhibit higher clinical presentation than adults. Gastrointestinal symptoms in children are also common. Influenza viral pneumonia is usually uncommon compared with other clinical signs. However, influenza-associated pneumonia was identified in pandemics, which is characterized by diffuse bilateral infiltrates in chest images with negative bacterial culture (at the early stage of infection) (Cox and Subbarao, 1999; Paules and Subbarao, 2017). Notably, the Spanish flu pandemic reported bacterial pneumonia as a secondary infection (1918). Bacterial pneumonia usually starts as a biphasic illness with influenza signs occurring and then resolves. Two weeks later, fever with dyspnoea, productive cough, and lung consolidation on chest imaging occurs (Rothberg et al., 2008). In the 2009 pandemic, a large portion of fatalities was reported to be caused by secondary bacterial infections. *Streptococcus pneumoniae* and *Staphylococcus aureus* are the predominant causes of secondary bacterial pneumonia associated with influenza viruses. Myositis, myocarditis, and pericarditis are infrequently encountered in influenza viral infections (Gill et al., 2010; Paules and Subbarao, 2017).

1.1.7. Influenza-licensed therapeutics and approved vaccines

Four categories of influenza therapeutics have been approved; ion channel blockers, NA inhibitors, fusion inhibitors, and polymerase inhibitors. The ion channel inhibitors, including amantadine and rimantadine, are the predominant adamantane derivatives licensed to be used for IAVs. Owing to the accumulation of point mutations in M2 other categories of influenza therapeutics were proposed. Mostly, the circulating strains were found to be resistant to these ion channel blockers (Paules and Subbarao, 2017).

NA inhibitors, including oseltamivir (oral), zanamivir (intranasal), and peramivir (intravenous), were used successfully against influenza viruses in 2015- 2016 in Europe and the USA in the healthcare settings (Paules and Subbarao, 2017). However, resistance to NA inhibitors was also reported. Mutations gradually occurred in NA catalytic sites and deletion in the active site, rendering NA inhibitors non-efficient in the 2007-08 influenza season (Takashita et al., 2015). Notably, the predominant circulating strains after the 2009 pandemic were found to be susceptible to NA inhibitors. Overall, the circulating strains must be investigated to assess the available therapeutics. Interestingly, in Russia and Japan, fusion and polymerase inhibitors are recently licensed for seasonal and pandemic influenza viruses (Paules and Subbarao, 2017; Toots and Plemper, 2020).

The WHO approves seasonal vaccines utilizing the data of the circulating strains that are updated twice annually. The approved classes of influenza vaccines are inactivated, live attenuated, and recombinant HA. Vaccines usually include antigens of the predominant strains of H1N1, H3N2, and the dominant lineage of influenza B (trivalent) or both lineages of influenza B (quadrivalent) (Houser and Subbarao, 2015).

New approaches are still under research, including viral vectors, DNA-based vaccines, virus-like particles, and novel live-attenuated vaccines. Notably, novel adjuvants are also being investigated to enhance vaccine development and immunogenicity (Lambert and Fauci, 2010).

1.2.   RNA modifications regulate gene expression in eukaryotes and viruses

1.2.1. Chemical modifications in various RNA species

As early as the 1960s, with the emergence of the nucleotide sequencing era, the non-canonical nucleotides were noticed. Other than A, G, U, and C, the pseudouridine (Ψ) was reported in the first RNA sequencing of the tRNA isolated from yeast, frequently named the fifth nucleotide (Cohn, 1960; Holley et al., 1965). Later, it was identified that the long noncoding RNA species (lncRNA, including tRNA, rRNA, and spliceosomal RNA) carry massive diversity of modified nucleosides with crucial biological functions.

The transfer RNA (tRNA) was reported to bear the highest number of modified bases compared to other eukaryotic cell RNA species. Single tRNA molecule bear, on average, 13 modifications. That range from methylation of a ribose sugar to nucleobase and base isomerization. These modifications ensure proper folding and stability of tRNA molecules to achieve maximum decoding fidelity (Roundtree et al., 2017).

Similarly, the ribosomal RNA (rRNA) exhibited at least 200 modifications to confirm proper translation in eukaryotes. It is noteworthy that the ablation of pseudouridine or methylated ribose block rRNA biogenesis. The same results were also demonstrated with the RNA modifications on the spliceosomal RNA (Roundtree et al., 2017).

Vis-à-vis mRNA, the widely known modifications added post-transcriptionally to pre-mRNA are 5′ capping and poly(A) tail. These known modifications are responsible for transcript stability and translation initiation in eukaryotes. Interestingly, with the identifications of methylation to the 5′ cap in mRNA, several groups also reported

methylation of internal bases (Desrosiers et al., 1974; Perry and Kelley, 1974; Adams and Cory, 1975). Authors supposed these modifications have functional regulatory roles, as reported in the methylation marks added to the cellular histones and DNA. The most commonly identified marks are N6-methyladenosine (m^{6}A), N1-methyladenosine (m^{1}A), N6,2′-O-dimethyladenosine (m^{6}A$_m$), methylation to the ribose sugar in a given base (Nm), and 5-methylcytidine (m^{5}C). All chemical modifications installed to the mRNA are collectively referred to as the epitranscriptome **(Figure 1.7)** (Roundtree et al., 2017). In this project, the focus was only on the most common methylation mark, m6A, especially in the virus-related aspects.
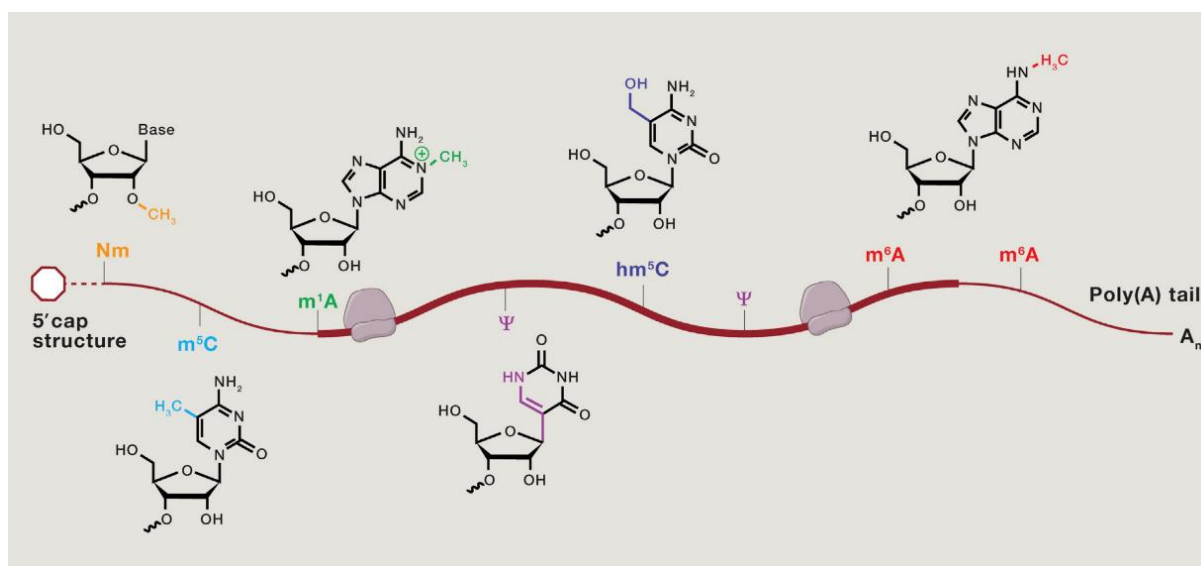
Figure 1.7: Schematic of the most common chemical modifications installed into mRNA in eukaryotes. The location of their distributions on given mRNA is also indicated. The figure is adapted from a previous report (Roundtree et al., 2017).

1.2.2. Methylation of various adenosine residues on mRNA

In the 1970s, methylated adenosines were detected in hepatoma cells (Desrosiers et al., 1974). After that, methylated adenosines were recorded in various organisms, including bacteria (Deng et al., 2015), yeast (Agarwala et al., 2012), plants (Yue et al., 2019), mice (Dominissini et al., 2012), and human (Meyer et al., 2012). The m6A has been reported to control various RNA metabolic functions, including translation, splicing, secondary structure, and stability (Li and Mason, 2014; Meyer and Jeffery, 2014). Moreover, m6A signatures are involved in various biological functions, including embryogenesis, mice fertility, and cellular differentiation, suggesting essential regulatory roles in cellular lifecycles (Niu et al., 2013; Zheng et al., 2013).

As mentioned earlier, the methylation of adenosine was noticed five decades ago. However, the methods utilized at this time were labelling cellular RNA followed by thin-layer chromatography techniques. These techniques usually provide an idea about the relative abundance of methylated residues. It has been reported that the m6A marks are located every 0.7–0.8 kb in the mRNA and 2–3 kb in the lncRNA (Lavi et al., 1977). Additionally, the labelling techniques followed by nucleic acid digestion displayed that the m6A marks were enriched predominantly in consensus sequence, the GA*C > AA*C sequences. A* denotes the methylatable adenosine (Wei and Moss, 1977).

However, the scientific community was reluctant to accept the m6A marks as biologically crucial in eukaryotes until recently. Two significant breakthroughs occur to make the m6A marks return back on track. Firstly, Jia et al., (2011) identified the first m6A demethylase enzyme. Indicating that the installation of the m6A marks has biological regulatory roles to be a reversibly dynamic process (Jia et al., 2011). In

follow-up research, the same group identified the second m6A demethylase, ALKBH5. Supporting the critical regulatory functions in eukaryotic cells, including proper metabolism and spermatogenesis (Zheng et al., 2013).

Secondly, at the same time, two independent groups developed a new high throughput sequencing method for the methylated RNA (m6A-seq or MeRIP-seq) to relatively identify the m6A topology in human mRNAs in different tissue in a transcriptome-wide approach (Dominissini et al., 2012; Meyer et al., 2012). Through these methods, the location and function of m6A in given mRNA could be feasible. Notably, the m6A-seq shows the m6A marks in a window of 100–200 nucleotides.

Very recently, more advances in epitranscriptome sequencing techniques have been available to achieve a near single nucleotide resolution, as will be described later in this study. Additionally, it has been reported that m6A methylome is relatively conserved between humans and mice (Dominissini et al., 2012). This finding also supports that the m6A marks have evolutionarily conserved functions among species.

Unlike m6A, the m1A installation blocks the interface of the Watson-Crick base-pairing model. Accordingly, create an evident structural alteration in the RNA secondary structure and protein binding. The m1A is less abundant in mRNA transcripts than the m6A and is reversed by ALKBH3. The m1A function is sought to promote efficient protein translation (Dominissini et al., 2016).

Additionally, the m6Am, which is located primarily in the first nucleotide after the m7G cap in the mRNA, is also noticed in the eukaryotic methylome to support RNA stability

against mRNA degradation (Mauer et al., 2017). However, more studies on these marks are still needed to understand their role in the various biological functions fully.

1.2.3. Regulation of m6A marks by m6A-associated machinery

As noted above, the m6A marks gained its wide reputation in regulating cellular function, as it is a dynamic regulation process. Installation of m6A marks is usually performed by m6A methyltransferase complex (m6A-writers). Then, others induce m6A reversal (m6A-demethylases or erasers). The third group is cellular RNA binding proteins interacting with the m6A marks to generate various functions, support RNA stability, and enhance translation and nuclear export (readers). All these groups are collectively named m6A machinery **(Figure 1.8)** (Meyer and Jaffrey, 2014, 2017; Roundtree et al., 2017; Jiang et al., 2021).
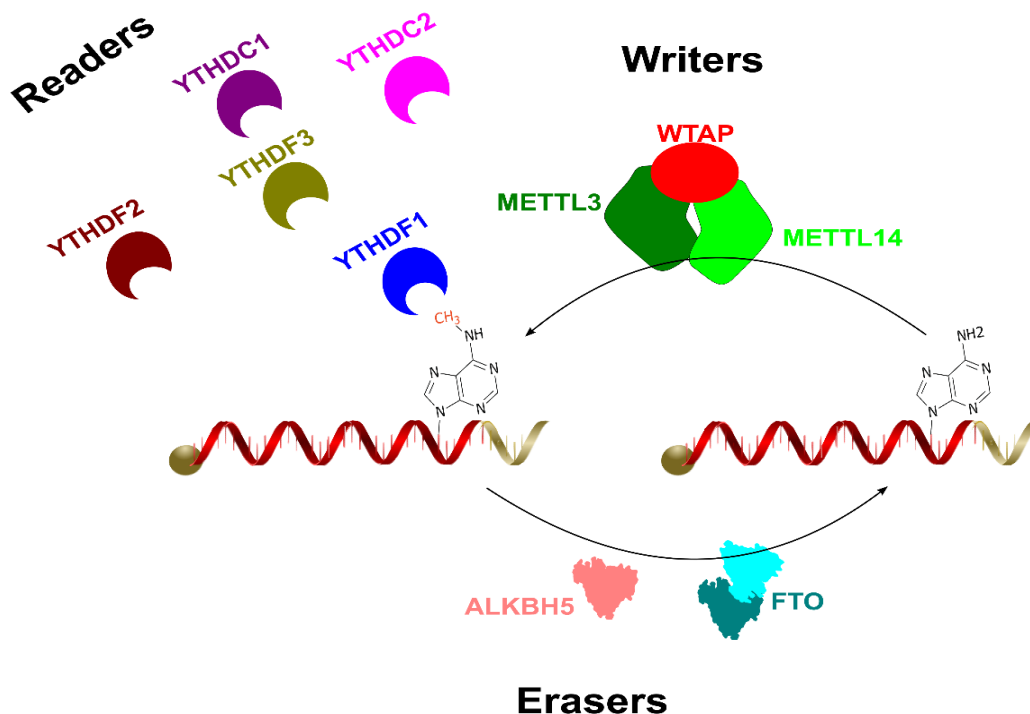
Figure 1.8: Schematic of m6A in mRNA and its m6A-related machinery. The m6A is installed on the pre-mRNA in the nucleus using m6A writers (methyltransferases). In turn, m6A erasers (demethylases) remove the m6A marks. Once methylated, one of the m6A-readers proteins interacts with m6A to induce specific biological function. Only the ten basic (bona fide) proteins in the m6A-machinery are shown.

A complex of proteins is shared in the m6A deposition on the candidate pre-mRNA. That is composed of an active unit named methyltransferase like-3 (METTL3), which is supported structurally by the METTL14 protein (Wang et al., 2016b, 2016a). Additionally, Wilms tumour 1-associated protein (WTAP) helps to target the whole complex to nuclear speckles for optimal methylation activity (Ping et al., 2014). It is worth mentioning that a long list of cofactors regulates the m6A methylation, including KIAA1429, RBM15, HAKAI, and ZC3H13. The structure and function of m6A-writers will be discussed in more detail in the corresponding chapters.

As a cellular dynamic process, the m6A marks are reversed using one of the two well-identified enzymes to demethylate mRNA. FTO and ALKBH5 belong to Alkb-homolgue family members to passively demethylate m6A-containing mRNA into adenosine. However, both differ in tissue distribution; FTO is mainly enriched in brain tissues, whereas ALKBH5 is predominantly enriched in the testes. Furthermore, ALKBH5 is expressed primarily in the nucleus, while FTO expression is expressed in both the nucleus and cytoplasm (Jia et al., 2011; Zheng et al., 2013; Meyer and Jaffrey, 2017). Additionally, both differ greatly in their substrate specificity. The ALKBH5

demethylates only the methylated adenosines. It was reviewed recently, FTO utilizes 3mU, m6A, m1A, and m6Am in various RNA species (Bayoumi and Munir, 2021c).

It is essential to mention that most of the chemical covalent bonds added to the cellular transcripts ultimately induce significant structural alterations. The change in the net charge, base-pairing potential (i.e., if the modifications are in the interface of the Watson-Crick model, including m1A), the overall RNA secondary structure, and protein binding are the most common alterations noticed with the presence of chemical modifications. Consequently, these changes will shape the outcome of gene expression in eukaryotes by modulating RNA stability, translation, and nuclear export through binding with the chemically modified RNA.

The m6A methylated RNA binds to various RNA-binding proteins; the most important are YTH- domain-containing proteins in the nucleus YTHDC1 or cytoplasm YTHDF1-3 and YTHDC2 (readers). The interacting reader protein exerts a specific function on the methylated transcripts that dictates the fate of RNA and cell biology. The nuclear YTHDC1 predominantly induces exon inclusion to mRNAs through recruitment for certain splicing factors (Xiao et al., 2016). Additionally, it has been reported that YTHDF1 promotes translation by enhancing ribosome loading and binding to initiation factors (Wang et al., 2015). In contrast, YTHDF2 regulates RNA metabolism via decreasing RNA stability and promoting RNA decay (Wang et al., 2014b; Du et al., 2016).

Interestingly, YTHDF3 demonstrated synergistic roles with YTHDF2 to promote RNA decay or interact with YTHDF1 to enhance protein translation, suggesting the cooperative manner of the cytoplasmic YTHDF 1-3 proteins to impact the biological

processes (Shi et al., 2017). YTHDC2 was reported to improve translation efficiency and promote normal spermatogenesis in mice (Hsu et al., 2017). However, in the following chapters, a long list of m6A machinery and their detailed structures will be described.

1.2.4. Role of epitranscriptomic modifications in regulating viral infection

While promoters and enhancers control eukaryotic gene expression, multiple chemical modifications installed on chromatin and RNAs can also dictate cellular biology. Therefore, given that identical twins might have the same genome, they could differ in their cellular gene expression and subsequent biological function and susceptibility to physiologic, metabolic, and pathological outcomes due to epigenetic and epitranscriptomic regulations.

Epigenetic gene regulations are a group of modifications that include histone remodelling, histone tail modifications, and DNA methylation. All these modifications trigger easier accessibility to genes prone to maximal expression than others at a particular moment (Tsai and Cullen, 2020). In contrast, epitranscriptomic gene regulation encompasses chemical modifications added to the RNA. In general, eukaryotic cells exploit the epigenetic and the epitranscriptomic chemical modifications on the cellular DNA and RNA, respectively, to control cellular differentiation and normal growth behaviours. Upon dysregulation, the affected tissues are prone to cancer and metabolic disorders (Meyer and Jaffrey, 2017; Roundtree et al., 2017; Huang et al., 2020).

Interestingly, viruses, like all organisms, utilize mRNA to express their proteins (depending on the cellular machinery) to support replication. However, viruses are continuously under the pressure of rapid RNA synthesis, protein expression, and replication to evade immune response before being competent in the virus-cell battle.

Recently, the association between epigenetic and epitranscriptomic control and the establishment of viral infection has begun to arise. Generally, eukaryotic cells can exploit the epigenetic forces as an antiviral response against a wide range of viruses. In turn, DNA viruses exploit cellular epigenetic silencing mechanisms to establish a latent infection cycle (Knipe et al., 2017).

Interestingly, viral RNA accepts this m6A decoration as well, suggesting that the viral RNA uses the epitranscriptomic marks to dictate the viral lifecycle (Kennedy et al., 2017; Baquero-Perez et al., 2021). Unlike epigenetic modifications, the study of the epitranscriptomic regulatory role in viral infection is still in its infancy. It is difficult to draw conclusions about its accurate impact on virus infection. Intriguingly, the m6A mark enhances viral gene expression and replication to certain viruses. In contrast, the same mark has the opposite effect on others (i.e., reduces viral gene expression and virion production).

As indicated earlier, viruses are under pressure to replicate rapidly. One of the mechanisms viruses can enhance replication and protein expression is through acquire/loss chemical modifications than the cellular mRNA counterparts. Scanty chemical modifications are currently known to regulate viral replication and gene expression, including the m6A, 5-methylcytidine (m^5C), N4-acetylcytidine (ac^4C), and 2′O-methylation of the ribose moiety of the ribonucleosides (refer to as Nm).

Fascinatingly, viruses accommodate 2-10 times m6A and m5C marks higher than their cellular counterparts. Similarly, the Nm is 10-30 times higher than cellular RNA (Courtney et al., 2017, 2019b, 2019a). All these increased levels of modified transcripts enhanced the viral replication and gene expression through either enhanced mRNA stability (m6A, ac4C) or mRNA translation (m6A, m5C) or evaded immune response (m6A, Nm). Notably, these previous findings only represent the levels in influenza and retroviral models, IAV, HIV-1, and MLV. Therefore, investigating more viruses would support the conclusion that RNA modifications are associated with more virus replication.

In contrast, other virus models oppose this hypothesis; various flaviviruses, including HCV and Zika virus, have been reported with significantly reduced virus replication associated with more m6A levels (Gokhale et al., 2016; Lichinchi et al., 2016b). It is arguably why highly evolving viruses could keep an evolutionary mark if it is indeed inhibitory. These discrepancies warrant more investigations in m6A virus-related fields.

1.2.5. Role of epitranscriptomic modifications in regulating the immune response to viral infection

Against viral infection, host innate immunity primarily depends on type 1 IFN response. The invading viral RNA is mainly recognized by cellular pathogen recognition receptors (PRRs), including RIG-I-like receptors (RLRs); retinoic acid-inducible gene-I (RIG-I; not present in chicken) and melanoma differentiation-associated protein 5 (MDA5), and toll-like receptors (TLRs) 3, 7 and 9. Viral stimulation triggers signals to express IFN-α and -β, which bind to the IFN alpha receptor (IFNAR), activating mainly the JAK-STAT pathway. Consequently, it stimulates the transcription of many IFN-

stimulated genes (ISGs) to promote competent antiviral responses (Ivashkiv and Donlin, 2014; Santhakumar et al., 2017).

Based on the above-mentioned impacts of epitranscriptomics in regulating various biological and pathological processes, it is unsurprising that m6A also regulates immune response against viral infection. It has been reported that m6A methylation of viral RNA mediates evasion from RIG-I recognition in various RNA and DNA models. In the human metapneumovirus (HPMV) model, m6A-deficient viruses promote conformational changes in the RIG-I to induce potent immune recognition (Lu et al., 2020). Furthermore, in hepatitis B and C viruses (HBV, HCV), depletion of METT3/14 (i.e., writers) decreases m6A levels on viral transcripts, leading to enhanced RIG-I recognition. YTHDFs protein has a protective effect by occupying m6A-containing RNA, hindering RIG-I recognitions (Kim et al., 2020c).

It has also been confirmed that the m6A negatively impacts the innate immune response. YTHDF2 and METTL3 depleted cells were associated with enhanced stability of IFNβ mRNA in an m6A-dependent manner. IFNβ mRNA carries m6A sites, which is highly stabilized in low m6A state condition. Accordingly, normal conditions facilitate virus replications by fast turnover of IFN mRNA (Winkler et al., 2019). Similarly, METTL14 depletion leads to enhanced IFNβ mRNA stability and expression, reducing human cytomegalovirus (HCMV) viral infection. In contrast, ALKBH5 has the opposite effect on viral replication (Rubio et al., 2018).

The YTHDF3 also displayed a negative regulatory role in an IFNβ mRNA-independent manner. YTHDF3 promotes the translation of a transcription repressor named forkhead box protein O3 (FOXO3) upon viral infection. That negatively regulates the expression

of ISGs. As a consequence, it promoted viral replication, including vesicular stomatitis virus (VSV), encephalomyocarditis virus (EMCV), and herpes simplex virus type 1 (HSV-1) (Zhang et al., 2019e). In contrast, YTHDF3 (as a model) negatively regulates various viral replication, including HIV-1, HBV, HCV, and Zika virus models, as will be fully described later in the study.

All this information significantly indicates the impact of m6A in various biological processes in eukaryotic cells, viral replication, innate immune modulation, and tumour progression/repression. Due to insufficient data availability, a final conclusion about the role of m6A cannot be inferred, especially in the viral lifecycle. Possibly future research could lead us to accurate conclusions. In this way, life-threatening viruses can be tackled not only genetically but also epitranscriptomically.

1.3. Project Aims and Objectives

The aim of the project was to provide novel information in the epitranscriptomic field that adds value to the existing data in the literature. The human m6A machinery is widely studied; however, studying the chicken m6A machinery could lead to better understanding of m6A regulatory roles, especially in influenza A viruses. The objectives of the individual chapters were as follows:

Chapter 3:

1. Use the available human m6A machinery structures to predict the variation among chicken orthologues, which could significantly impact functional differences.

2. Utilize the available epitranscriptomic data to depict a model of the m6A conservation pattern among all IAVs.

Chapter 4:

1. Functionally analyse/screen ten basic (bona fide) chicken m6A-associated proteins in different chicken cells.

2. Determine the most potent antiviral/proviral protein(s) and spot any biologically different protein(s) from the human counterparts.

3. Use two representative strains of IAVs, one already studied in the literature and a new one relevant to chicken m6A machinery and has zoonotic importance (i.e., H9N2).

4. Figure out the origin of the discrepancies usually noticed in the available investigations in viral m6A-related fields.

5. Determine the significant differences between human and chicken m6A machinery regulating influenza A viruses.

Chapter 5:

1. Investigate the mechanistic actions of some chicken m6A machinery that could reveal a potent antiviral/proviral role against IAVs.

2. Use traditional and state-of-art technologies to verify the m6A regulatory function of the protein of interest.

Chapter 6:

1. Determine the impact of m6A marks on viral replication kinetics by de novo synthesis of H9N2 viruses with various m6A-deficient levels.

2. Use various mutation strategies to create m6A-mutants other than those designed earlier in the literature.

Chapter 7:

1. Provide novel MeRIP-seq data to map and identify host and viral m6A methylome originating from chicken cells infected with the H9N2 for the first time.

2. To monitor/modulate the transcript-specific methylation state upon viral infection.

3. To map the cellular interactome of the m6A protein of interest expressed in chicken cells and infected with H9N2 using mass spectrometry. This could be exploited in the future to regulate viral infection by modulating the enriched interacting proteins.

Chapter 2

Materials and Methods

2.1. Materials

All chemicals, enzymes, antibodies, media, and instruments utilized in this study were used according to the manufacturer's recommendations.

2.1.1. Chemicals, consumables, and equipment

2.1.1.1. Chemicals

Chemical	Catalogue number	Manufacturer
Acetic acid	A6283	Sigma-Aldrich, St. Louis, USA
Acrylamide/Bis Solution (30%)	1610158	Bio-Rad, China
Agar-bacteriological Lennox L Agar	22700	Invitrogen, Life Technologies, USA
Agar-bacteriological Lennox L broth	12780	Invitrogen, Life Technologies, USA
Agarose-Low EEO	R1040	NBS-biologicals, Cambridge, UK
Ammonium persulfate (APS)	1610700	Bio-Rad, Japan
Ampicillin Na-Salt	A9518	Sigma-Aldrich, St. Louis, USA
Antibiotic-Antimycotic (100X)	15240062	Gibco, Life Technologies, UK

BSA (Albumin Bovine Fraction V)	05482	Sigma-Aldrich, St. Louis, USA
Calcium chloride dihydrate	C7982	Sigma-Aldrich, St. Louis, USA
Chloroform	C14960115	Fisher Scientific, UK
Coomassie Brilliant Blue G250	27815	Fluka, Switzerland
Crystal Violet	C0775	Sigma-Aldrich, St. Louis, USA
D (+) Sucrose	62248	Sigma-Aldrich, St. Louis, USA
DAPI	62247	Thermo Scientific, USA
Dimethyl sulfoxide (DMSO)	175462	Fisher Scientific, UK
Dulbecco's MEM (DMEM)	31966-021	Gibco, Life Technologies, UK
EDTA	324503	Millipore, USA
Ethanol	2107463	Fisher Scientific, UK
Foetal bovine serum	10500-64	Gibco, Life Technologies, UK
Glycerol	G5516	Sigma-Aldrich, St. Louis, USA
Glycine	G8898	Sigma-Aldrich, St. Louis, USA
HEPES buffer	15630080	Gibco, life technologies, UK
Hexadimethrine bromide (polybrene)	H9265	Sigma-Aldrich, St. Louis, USA
Invitrogen™ RediLoad™ Loading Buffer	750026	Fisher Scientific, UK
L-glutamine (200mM)	25030-081	Gibco, life technologies, UK
Magnesium chloride	M8266	Sigma-Aldrich, St. Louis, USA

MEM (10X)	21430-020	Gibco, life technologies, UK
Methanol	2196137	Fisher Scientific, UK
Methylene blue	M9140	Sigma-Aldrich, St. Louis, USA
NP40-50ml	85124	Thermo Scientific, USA
Nuclease free water	10977-035	Thermo Scientific, USA
NuPAGE (transfer buffer)	2270643	Novex, Life Technologies, USA
Opti-MEM	31985-070	Gibco, life technologies, UK
Paraformaldehyde	J19943-k2	Thermo Scientific, USA
Permeabilization buffer (10X)	00833356	Thermo Scientific, USA
Pierce Protease inhibitor tablet	A32963	Thermo Scientific, USA
Potassium chloride	P5405	Sigma-Aldrich, St. Louis, USA
Potassium phosphate dibasic	P0662	Sigma-Aldrich, St. Louis, USA
Protein G Sepharose® FF resin	PCG5182501	Generon, UK
Puromycin Dihydrochloride	A1113803	Gibco, China
SDS-sample buffer	1597380	Life Technologies, USA
SDS-solution 10%	1610416	Bio-Rad, USA
Skimmed milk powder	70166	Millipore, Switzerland
Sodium bicarbonate	S5761	Sigma-Aldrich, St. Louis, USA
Sodium chloride	S5886	Sigma-Aldrich, St. Louis, USA

Sodium dodecyl sulphate (SDS)	L3771	Sigma-Aldrich, St. Louis, USA
Sodium hydroxide	221465	Sigma-Aldrich, St. Louis, USA
Sodium phosphate dibasic	S5136	Sigma-Aldrich, St. Louis, USA
TEMED	1610801	Bio-Rad, USA
TPCK-treated trypsin	T1426	Sigma-Aldrich, St. Louis, USA
Tris-base	252859	Sigma-Aldrich, St. Louis, USA
Tris-EDTA 1X	BP2473	Fisher scientific, USA
Triton X-100	T8787	Sigma-Aldrich, St. Louis, USA
Trizma hydrochloride	RDD009	Sigma-Aldrich, St. Louis, USA
Trypsin 2.5%	15090-046	Gibco, Thermo Fisher, UK
Tween -20	P2287	Sigma-Aldrich, St. Louis, USA
VECTASHIELD antifade mounting buffer	ZH1108	Vector Laboratories, USA
Versene 1:5000 (1X)	15040-033	Gibco, Thermo Fisher, UK
β-mercaptoethanol	1610710	Bio-Rad, China

2.1.1.2. Consumables

Name	Feature	Manufacturer
0.45-, 0.2 um filter	E4780-1456	STAR LAB, UK
Amersham Hybond-N+ membrane	RPN203B	GE Healthcare, UK
Blotting papers	170396	Bio-Rad, USA
Cell culture flasks	25 ml, 75 ml	Corning, Mexico
Cell culture plates	6-, 24-, 96- well	Corning, Mexico
Cellvis plates	P24-1.5H-N	Sigma-Aldrich, USA
Conical centrifuge tubes	15 ml, 50 ml	Corning, Mexico
Embryonated chicken eggs	Day 0	TCS Biosciences, UK
Eppendorf tubes	1.5ml	Sarstedt, Germany
High-shell high-profile	96-well PCR plate	Bio-Rad, USA
Latex gloves	S, M, L	Fisher Scientific, Malaysia
Parafilm	13080	Star lab, Hamburg
PCR Tubes	0.2ml	Applied Biosystem, UK
Petri dishes for bacteria	100mm	Sarstedt, Germany
PVDF membrane	88518	Thermo Scientific, Ireland
qPCR-tube 0.1ml	8-tube strips	Bio-Rad, USA
Small animal blood	Chicken	TCS Biosciences, UK
Sterile pipette tips	10, 200, 1000 µl	STAR LAB, UK
Strippette	5, 10, 25 ml	Corning, Mexico

2.1.1.3. Equipment

Name	Manufacturer
Autoclave	Astell, UK
Bacterial incubator 37°C	SANYO, Switzerland
Balance	KERN EWJ, Sigma-Aldrich, USA
Cell culture CO_2 incubator	Panasonic, Japan
Centrifuge 5424 R	Eppendorf, Germany
Centrifuge Allegra X-30R	Beckman Coulter, UK
CFX96 Real-Time system	Bio-Rad, UK
ChemiDoc^{TM} MP imaging system	Bio-Rad, UK
Class 2 Microbiological Safety Cabinets	Contained Air Solution, BioMAT2, UK
CytoFLEX Flow Cytometer	Beckman Coulter, USA
Electrophoresis power supply	Power Ease 90w, life technologies, UK
End-over-end rotator	Stuart™ Sigma, USA
Fluorescence microscope	LSM880, Zeiss, Jena Germany
Freezer -20°C	Lab cold, UK
Freezer -80°C	PHCbi, IL, USA
Fridge	Lab cold, UK
Heat block	Thermo Scientific, USA
Ice maker	Scotsman, UK
Inverted cell culture microscope	Primovert, ZEISS, Jena, Germany

Magnetic stirrer	Stuart™ Sigma, UK
Milli-Q	IQ 7000, France
NanoDrop 2000 spectrophotometer	Thermo Scientific, USA
Optima L-100 XP ultracentrifuge	Beckman Coulter, UK
Orbital shaker	SANYO, Switzerland
pH-meter	Hanna Instruments, UK
Pipettes	Gilson, P10, 100, 1000
PTC-200 Peltier Thermal Cycler	Universal Resource Trading Ltd, UK
Rotor SW Ti-32	Beckman Coulter, UK
Roller mixer	Stuart™ Sigma, UK
Scipette multichannel	SciQuip Ltd, UK
SDS-PAGE system	Bio-Rad, UK
Shaking bacterial incubator	New Brunswick Scientific, USA
Shaking egg incubator	Ova-Easy advance, Brinsea, UK
Spectrolinker XL-1000	Spectro-UV, USA
Stripettor™ Ultra	Corning, Mexico
Trans- blot turbo membrane blotter	Bio-Rad, UK
UV transilluminator	Syngene, UK
Vortex	SLS, lab basics, UK
ZOE™ fluorescent cell imager	Bio-Rad, UK

2.1.1.4. Software

Software	Version	Company
BioEdit	7.2.5	Ibis Biosciences, Carlsbad, CA
Bowtie2	2.5.0	http://bowtie-bio.sourceforge.net/
CFX Manager™	3.1	Bio-Rad, UK
CytExpert	2.4	Beckman Coulter Inc.
FastQC	0.11.9	http://www.bioinformatics.babraham.ac.uk/projects/fastqc/
Geneious	9.1.4	Biomatters Ltd
Graphpad prism	8	GraphPad Software Inc. USA
HOMER	4.11	http://homer.ucsd.edu/homer/motif
ImageJ (FIJI)	1.52	NIH, Bethesda
IGV	2.3	Broad Institute, Boston, MA
MACS2	2.2.7.1	https://github.com/macs3-project/MACS/wiki/Install-macs2
Mascot	2.6.1	Matrix Science, UK
MegaAlign	3.18	DNAStar, Madison, WI, USA
Scaffold	5.2.1	Proteome Software Inc., USA
SnapGene®	3.2.1	GSL Biotech, Chicago, IL
trimmomatic	0.38	http://www.usadellab.org/cms/?page= trimmomatic
ZEN Microscopy	3.6	Carl Zeiss Imaging, Jena

2.1.1.5. Enzymes and markers

Enzyme/marker	Catalogue number	Manufacturer
BbsI-HF	R3539S	New England Biolabs, UK
EcoRI-HF	R3101S	New England Biolabs, UK
GeneRuler 1 kb Plus DNA Ladder	SM1331	Thermo Scientific, UK
KpnI-HF	R3142S	New England Biolabs, UK
NcoI	R0193S	New England Biolabs, UK
NheI-HF	R3131S	New England Biolabs, UK
Prestained Protein Ladder (10-180 kDa)	ab116027	Abcam, UK
Q5-high fidelity DNA polymerase	M0491S	New England Biolabs, UK
SacI-HF	R3156S	New England Biolabs, UK
SgrDI	ER2031	Thermo Scientific, UK
SmaI	ER0661	Thermo Scientific, UK
SpeI-HF	R3133S	New England Biolabs, UK
T4 DNA ligase	M0202	New England Biolabs, UK

2.1.1.6. Kits

Kit	Cat. No.	Manufacturer
Anti-FLAG® M2 Magnetic Beads	M8823	Sigma-Aldrich, St. Louis, USA
DNeasy blood & tissue kit	69504	QIAGEN, Germany
DreamTaq Green PCR Master Mix (2X)	K1081	Thermo Scientific, USA
Dynabeads mRNA purification kit	61006	Thermo Scientific, USA
EpiMark® N6-methyladenosine Enrichment kit	E1610S	NEB, UK
GeneJET Gel Extraction Kit	01237174	Thermo Fisher, Lithuania
LIVE/DEAD™ Fixable Violet Dead Cell Stain Kit	L34964	Thermo Fisher, USA
MAX Efficiency™ DH5α Competent Cells	18258012	Thermo Scientific, USA
Pierce™ ECL Western blotting substrate	32106	Thermo Scientific, USA
QIAamp® Viral RNA mini kit	52906	QIAGEN, Germany
QIAprep® Spin Miniprep kit	27106	QIAGEN, Germany
RNeasy® Mini Kit	74106	QIAGEN, Germany
RNA fragment reaction buffer	E6186A	NEB, UK
SuperScript IV Reverse Transcriptase	18090010	Thermo Scientific, USA

SuperScript™ III Platinum™ SYBR™ Green One-Step qRT-PCR Kit	11736059	Thermo Scientific, USA
TRIzol™ Reagent	15596026	Thermo Scientific, USA
TurboFect Transfection Reagent	R0531	Thermo Scientific, USA
ViaFect™ Transfection Reagent	E4981	Promega, UK

2.1.2. Primers

2.1.2.1. Primers for relative quantification of chicken m6A-associated genes

Gene	Name	Sequence (5′-3′)
chALKBH5	qchALKBH5-F	CGTCACGGTGCTCAGTGGAT
	qchALKBH5-R	CTGTTGCTTCCTGACAGGCG
chFTO	qchFTO-F	GCGTGGGACATAGAGACACCT
	qchFTO-R	ATGTTCCTCTTGAACAATCTGCCA
chMETTL3	qchMETTL3-F	TGGGTAAGTTCGCCGTGGTG
	qchMETTL3-R	CACGCGTTCGTAGCCCCAAA
chMETTL4	qchMETTL14-F	TGCTGCCCCAAGGTCATTTG
	qchMETTL14-R	ATGAGGCAGTGCTCCTTGGTT
chWTAP	qchWTAP-F	CCGAGAGAGCGGGCCTCC
	qchWTAP-R	TGCTTCACTAAGGCGAACCTTCT
chYTHDF1	qchYTHDF1-F	AGCGTTGACCCTCAGAGACC
	qchYTHDF1-R	TGACTGCCCAGAAAGGTAAGGT
chYTHDF2	qchYTHDF2-F	GCCAAGGCAACAAAGTGCAAAA
	qchYTHDF2-R	GCAGCCTCACCCAGAGAGTAG
chYTHDF3	qchYTHDF3-F	CACCAGCGTCGACCAGAGAC
	qchYTHDF3-R	GGGTCTGACATTGGTGGATAGC
chYTHDC1	qchYTHDC1-F	AAGCGAAGCCAGCGATTCTG
	qchYTHDC1-R	TCTCATGCTTCTTTTCTGAACCTGC

chYTHDC2	qchYTHDC2-F	CCTCAGGGCTTTCCAGGCAT
	qchYTHDC2-R	CAGCACCTCCTCTGGCTCTC
chRPL30	qchRPL30-F	GAGTCACCTGGGTCAATAA
	qchRPL30-R	CCAACAACTGTCCTGCTTT

2.1.2.2. Primers for relative quantification of chicken innate immune genes

Gene	Name	Sequence (5′-3′)
chMDA5	qchMDA5-F	GGACGACCACGATCTCTGTGT
	qchMDA5-R	CACCTGTCTGGTCTGCATGTTATC
chPKR	qchPKR-F	GCAGAAGTAAGAGTGAGGCAAATGA
	qchPKR-R	GCCACCTTTACCAATAGGCTCTAT
chSTING	qchSTING-F	GGTCCTACTACATCGGCTACCTGA
	qchSTING-R	GGCCTGAGCTTGTTGTCCTTATCT
chIFNα	qchIFNα-F	GACAGCCAACGCCAAGC
	qchIFNα-R	GTCGCTGCTGTCCAAGCATT
chIFNγ	qchIFNγ-F	GTGAAGAAGGTGAAAGATATCATGGA
	qchIFNγ-R	GCTTTGCGCTGGATTCTCA

2.1.2.3. Primers for relative quantification of H9N2-wt and different m6A-mutant viruses

Gene	Name	Sequence (5′-3′)
M gene	qH9N2-M- gene-F	AGATGAGTCTTCTAACCGAGGTCG
	qH9N2-M-gene-R	TGCAAAAACATCTTCAAGTCTCTG
HA gene	qH9N2-HA- gene-F	GACCAAATACAAGACGTATGG
	qH9N2-HA-gene-R	CCATTGCAAGTACAAGAGATGAGG

2.1.2.4. Primers for sequencing the entire HA gene of the different m6A-mutants

Gene	Name	Sequence (5′-3′)
HA gene	RG-Seq-H9-1-F	GCAAAAGCAGGGGAATTTCTTAACTAG
	RG-Seq-H9-1-R	CAATATACTTGGGGCAGGTCC
	RG-Seq-H9-2-F	CTCAGGAGAGAGCCATGG
	RG-Seq-H9-2-R	ACAAGGGTGTTTTTGCTAAC

2.1.2.5. Primers for cloning and sequencing of various chALKBH5 domains

Name	Sequence (5′-3′)
N-terminus-F	CCCGGAATTCGCCACCATGGCAGGCAGCGGATACAC
N-terminus-R	CCGGGGTACCGGTCCGAAGAAGTACTTGTTCC
M-terminus-F	CCCGGAATTCGCCACCATGAACAAGTACTTCTTCGG
M-terminus-R	CCGGGGTACCGGTGTCTTTCTCAGAATGATCACG
C-terminus-F	CCCGGAATTCGCCACCATGGTGATCATTCTGAGAAAGAC
C-terminus-R	CCGGGGTACCGGACAGTGTCTTCTCATTTTCAC
pCAGGS 5′	GCCTCTGCTAACCATGTTCATG
pCAGGS 3′	CCAACACACTATTGCAATGAAA

2.1.2.6. Primers for cloning and sequencing of various H9N2-NP domains

Name	Sequence (5′-3′)
N-terminus-F	GACTCCACCATGGCGTCTCAAGGCACCAAACG
N-terminus-R	TTTCTAGACTAGTCTTCAATTTCAACATTCCCAGG
M-terminus-F	GACTCCACCATGGGGGACGGGAAATGGGTGAGAGAG
M-terminus-R	TTTCTAGACTAGTCCTGTTGGTTGGTGTTTCCTCC
C-terminus-F	GACTCCACCATGGGGCCTGGGAATGTTGAAATTGAA
C-terminus-R	TTTCTAGACTAGTTCAATTGTCATATTCCTCTGC
pEF-LINK 5′	GTGTCGTGAAGAATTAGCTTGC
pEF-LINK 3′	GAAAGCGAGCTTAGTGATACTTG

2.1.2.7. Guide RNA and genome screening primers used to generate chALKBH5-KO-DF1 cell lines using CRISPR/Cas9

Name	Sequence (5′-3′)
ALK- Ex-2 F1	CACCGCGAAGCTCGCATTGACGATG
ALK- Ex-2 R1	AAACCATCGTCAATGCGAGCTTCGC
ALK- Ex-2 F2	CACCGAAAATACTTGTTCCGCAGCG
ALK-Ex-2 R2	AAACCGCTGCGGAACAAGTATTTTC
ALK-GS-F	CGGTTCGGAACACAGCGATTAC
ALK-GS-R	GATAGTCGTTGATCACGGCACTG

2.1.2.8. Guide RNA and genome screening primers used to generate chYTHDF2-KO-DF1 cell lines using CRISPR/Cas9

Name	Sequence (5′-3′)
F2-Ex1-F1	CACCGCAGCCCATCCTTCTGATGCA
F2-Ex1-R1	AAACTGCATCAGAAGGATGGGCTGC
F2-Ex1-F2	CACCGAAACGGGTCCGTGCATCAGA
F2-Ex1-R2	AAACTCTGATGCACGGACCCGTTTC
F2-GS-F	GCTGAACCTCAACCGTAGGAAGTCC
F2-GS-R	GTACTCACGGGGAGAGTTTGC

2.1.2.9. Primers for relative quantification of the strand-specific NP RNA of H9N2-wt and different m6A-mutant viruses

Name	Sequence (5′-3′)
vRNAtag_H9N2-RTF	GGCCGTCATGGTGGCGAAT taatgggcgaagaacaaggattgc
vRNAtag	GGCCGTCATGGTGGCGAAT
H9N2-vRNAPCRR	CTCAGGATGAGTGCAGACCGTGCC
cRNAtag_H9N2-RTR	GCTAGCTTCAGCTAGGCATC agtagaaacaagggtgttttcttc
cRNAtag	GCTAGCTTCAGCTAGGCATC
H9N2-cRNAPCRF	CGATCGTGCCTTCCTTTG
mRNAtag_H9N2-RTR	CCAGATCGTTCGAGTCGT tttttttttttttttttcttcaattgtc
mRNAtag	CCAGATCGTTCGAGTCGT
H9N2-mRNAPCRF	CGATCGTGCCTTCCTTTG

93

2.1.2.10. Primers for relative quantification of the strand-specific HA RNA of H9N2-wt and different m6A-mutant viruses

Name	Sequence (5′-3′)
vRNAtag_HA-RTF	GGCCGTCATGGTGGCGAAT ctcaggagagagccatgggag
vRNAtag	GGCCGTCATGGTGGCGAAT
vRNAtag_HA-PCRR	CCTTCTATGAATCCAGCTATGGCTC
cRNAtag-HA RTR	GCTAGCTTCAGCTAGGCATC agtagaaacaagggtgtttttgc
cRNAtag	GCTAGCTTCAGCTAGGCATC
H9N2 HA-cmRNAPCRF	GAAGGGGTTAAGCTTGAATCTG
mRNAtag-HA-RTR	CCAGATCGTTCGAGTCGT ttttttttttttttttgctaactatatacaa
mRNAtag	CCAGATCGTTCGAGTCGT
H9N2 HA-cmRNAPCRF	GAAGGGGTTAAGCTTGAATCTG

2.1.2.11. Primers for cloning chFTO in Psp.dCas13b-FLAG vector for targeted demethylation

Name	Sequence (5′-3′)
FTO-TD-F2	AGTCCCATCGATGGTACCAAGAGA AGAGCTGGCGAGAGAGAGAAGG
FTO-TD-R2	ATGCCGCTCGAGGCTAGCCACCAGG TTCTGCAGGTGCACGAT

2.1.2.12. Primers for cloning chALKBH5 with NLS2 mutation at C-terminus

Name	Sequence (5′-3′)
ALK-NLS2-F	TCGACGAGCACTTCAGCCC
ALK-NLS2-R	GGGCTGAAGTGCTCG

2.1.2.13. Guide RNA and genome screening primers were used to generate chALKBH5-mRuby3-reporter DF1 cell lines using CRISPR/Cas9

Name	Sequence (5′-3′)
ALK-Intron1-F	CACCGTTGCCCTCACGTTGTCCCCC
ALK-Intron1-R	AAACGGGGGACAACGTGAGGGCAAC
ALK-Intron4-F	CACCGATCCAGATGGTATCCGCACA
ALK-Intron4-R	AAACTGTGCGGATACCATCTGGATC
mRuby3- F	GTGTCCATGCCGTTGATCACCG
ALK-Exon2-R	GATAGTCGTTGATCACGGCACTG
ALK-Exon5-R	CACAGTCCTCCGTGTACTCGTAAGAC

2.1.2.14. Primers for MeRIP-RT-qPCR for the validation of m6A-seq analysis

Name	Sequence (5′-3′)
LY6E-m6A-F	CAAGTCTGGCCAGTCCATCTC
LY6E-m6A-F	CGGCATAGCTGGCTTTAACG
TNRC6A-m6A-F	GCATGGCCATCAATCACTGG
TNRC6A-m6A-R	GGCCCATTAATACTTCCATTGC
ZFC3H1-m6A-F	CTCTGTGGAAGAAAGTTTTGAGG
ZFC3H1-m6A-R	GCTCCTCTCAGCTGGAGTGG

2.1.2.15. crRNA-generating primers used for genome editing of H9N2 HA using CRISPR/Cas13b and sequencing verification primer.

Name	Sequence (5′-3′)
Site 1-F	CACCACAGTATCTGTGGAATTTGTTGACTGGTGG
Site 1-R	CAACCCACCAGTCAACAAATTCCACAGATACTGT
Site 2-F	CACCGAACATGATTTGCTTGTTCCATCGTGAGTC
Site 2-R	CAACGACTCACGATGGAACAAGCAAATCATGTTC
Site 3-F	CACCTTGAAGGTCCTATCTAAATTTTCTGTTGTT
Site 3-R	CAACAACAACAGAAAATTTAGATAGGACCTTCAA
Site 4-F	CACCTGATCATTTGAATGCTGGAAACCATACCAA
Site 4-R	CAACTTGGTATGGTTTCCAGCATTCAAATGATCA
Site 5-F	CACCGCCTGTTCATCTTGTCGATTATATTATTCA
Site 5-R	CAACTGAATAATATAATCGACAAGATGAACAGGC
Site 6-F	CACCGCCCTTTTAACCTTGTTATATAAATTGTTC
Site 6-R	CAACGAACAATTTATATAACAAGGTTAAAAGGGC
U6 Promoter- F	GAGGGCCTATTTCCCATGATT

2.1.3. Antibodies

Antibody	Cat. No	Dilution	Manufacturer
Alexa fluor goat anti-mouse IgG (488)	A11001	1:5000	Invitrogen, USA
Alexa fluor goat anti-mouse IgG (568)	A11004	1:5000	Invitrogen, USA
Alexa fluor goat anti-rabbit IgG (488)	A11008	1:5000	Invitrogen, USA
Alexa fluor goat anti-rabbit IgG (568)	A11011	1:5000	Invitrogen, USA
Goat polyclonal anti-rabbit IgG (HRP)	ab6721	1:2500	Abcam, UK
Goat polyclonal anti-mouse IgG (HRP)	ab6789	1:2500	Abcam, UK
Mouse monoclonal anti-HA-H9N2(IG10)	---	1:2500	Gift from Prof. Munir Iqbal
Mouse monoclonal anti-NP IAVs (HB-65)	---	1:2500	Gift from Prof. Munir Iqbal
Mouse monoclonal anti-HA tag	ab18181	1:2500	Abcam, UK
Mouse monoclonal anti-m6A	202-003	1:2500	Synaptic Systems, Germany

Mouse monoclonal anti-V5	ab27671	1:2500	Abcam, UK
Mouse monoclonal anti- α tubulin	ab7291	1:2500	Abcam, UK
Rabbit monoclonal anti-m6A	E1611A	1:250	EpiMark, NEB, UK
Rabbit polyclonal anti-m6A	ABE572	1:2500	Sigma, UK
Rabbit polyclonal anti-FLAG tag	F7425	1:2500	Sigma, UK
Rabbit polyclonal anti-HA tag	ab137838	1:2500	Abcam, UK
Rabbit polyclonal anti-V5	ab15828	1:2500	Abcam, UK

2.1.4. Solutions and buffers

Name	Purpose	Composition
Annealing buffer	gRNA	10mMTris, 1mM EDTA, 50mMNaCl
Blocking buffer	IFA blocking	5 % BSA in PBS
Blocking buffer	WB	5% skimmed milk powder in PBST
Coomassie stain	Protein gel stain	45% (v/v) ethanol, 10% (v/v) acetic acid, 0.25% (w/v) Coomassie Brilliant Blue G -250
Fixative	Cell fixation	4% paraformaldehyde (PFA) in PBS
Influenza infection media	Virus infection	DMEM, antibiotic-antimycotic 1x, 0.2% BSA, and 2 μg/ml TPCK Trypsin
Lysis buffer	WB/IP	10%NP-40, 1mM EDTA, 150mM NaCl, 20mM Tris-HCl (pH.7.4)
PBS	Washing and dilution	0.8% (w/v) NaCl, 0.02% (w/v) KCl, 0.02% (w/v) KH_2PO4, 0.135% (w/v), $Na_2HPO4 \cdot 2H_2O$
PBST	WB washing buffer	0.1% tween-20 in PBS
Permeabilization buffer	Permeabilization for IFA	0.1% Triton X100 in H_2O
Plaque media	Plaque assay	2xMEM, 1.6% Agarose, 0.2% BSA, antibiotic-antimycotic 2x, 2 μg/ml TPCK-Trypsin, 50mM HEPES

Separating gel solution	SDS-PAGE	10% (w/v) acrylamide/bisacrylamide stock solution, 0.1% (w/v) SDS, 375 mM Tris.HCl (pH 8.8), 0.05% (w/v) APS, 0.1% (v/v) TEMED
Stacking gel solution	SDS-PAGE	5% (w/v) acrylamide/bisacrylamide, 0.1% SDS, 125 mM Tris·HCl (pH 6.8), 0.075% (w/v) APS, 0.15% (v/v) TEMED
TAE (10x)	Gel electrophoresis	48.4 g of Tris base, 11.4 ml of glacial acetic acid (17.4 M), 3.7 g of EDTA, di-sodium salt in distilled water

2.2. Methods

2.2.1. In silico prediction and bioinformatic methods

2.2.1.1. Sequence data mining

To investigate the evolutionary variation of chicken m6A machinery, an in-silico analysis was performed to lay foundation for further functional characterization. Ten m6A-associated genes were investigated. Several species from class Aves were included in the analysis. Additionally, multiple species representing the key orders of class Mammalia were selected, including primates, ungulates, rodents, bats, insectivores, and carnivores. Representatives of reptiles, amphibians, and fish were also included in the analysis for comparison purposes. Amino acid sequences were retrieved in FASTA format from available public domains, including the Uniprot (www.uniprot.org) and the NCBI (www.ncbi.nlm.nih.gov) databases.

2.2.1.2. Evolutionary analysis for cross-species comparisons

Amino acid sequence alignments were performed using the Clustal W algorithm included in Lasergene software (DNAstar, USA). A multiple sequence alignment (MSA) was used to identify mutations in the studied genes, and the results were visualized using BioEdit (Hall, 1999). Various evolutionary algorithms were utilized to estimate the time of divergence along with the rate of evolution among different orthologues of a particular m6A-associated protein, including maximum likelihood (ML) analysis (Tamura et al., 2013) and Bayesian Markov chain Monte Carlo (MCMC) inference (BI) (Drummond et al., 2012). The phylogenetic ML trees were generated

using MEGA 7.0 software to predict the suitable statistical evolutionary model. One thousand bootstrap replicates were adopted to ensure the confidence of the final tree. Whereas for BI, the MrBayes algorithm was utilized to construct the phylograms using Jones-Taylor-Thornton (JTT) model using the gamma distribution and invariant sites (JTT + Γ4 + I). Ten runs plus an initial 25 percent burn-in were adopted for BI. Each run consisted of 2 files, with each containing 4×10^5 MCMC-sampled trees. The identity percentage and cross-species divergence were performed using the sequence demarcation tool (SDT) the amino acids were aligned with the MUSCLE algorithm (Muhire et al., 2014).

2.2.1.3. Protein modelling and molecular annotation

Ensembl genome browser (www.ensembl.org) was used to determine the location of m6A-associated genes in various analysed species. The m6A-associated genes were annotated to their matching chromosomes. After that, m6A-related gene locations were compared in only six species (orthologues); humans, mice, chickens, ducks, turkeys, and zebrafish. The two-dimensional structure prediction (2D) was performed by the PSIPRED web server (http://bioinf.cs.ucl.ac.uk/psipred/). The three-dimensional structure prediction (3D) was generated using PHYRE2 web-based server (Kelley and Sternberg, 2009) and confirmed with I-Tasser (Yang et al., 2015). Intensive models were adopted for the prediction. The predicted proteins of chicken and the well-characterized crystal structures of m6A-associated proteins in humans were visualized and annotated using PyMOL (v1.3 Schrodinger, LLC).

2.2.1.4. Determination of the reference viral HA for comparative analysis of DRACH signatures among IAVs

A comparative assessment was performed based on the public IAV epitranscriptome-wide profiling data (Courtney et al., 2017). The authors used two sequencing techniques to map the m6A sites across the H1N1-PR8 strain; a photo-crosslinking assisted m6A sequencing strategy (PA-m6A-seq) and Photoactivatable-ribonucleoside-enhanced crosslinking and immunoprecipitation (PAR-CLIP) (Hafner et al., 2010; Chen et al., 2015). Based on their m6A-PA-seq, 8/9 m6A sites were mapped across the HA mRNA/ vRNA, respectively. More interestingly, the authors adopted an elegant approach to validate the identified m6A sites functionally. They introduced mutations into most identified m6A sites. Consequently, they silently mutated the consensus sequences of m6A deposition 5′-RAC-3′ that coincident with the sequencing data. It is essential to mention that the adopted sequencing techniques at this time were not sensitive in mapping the m6A sites in a single-nucleotide-resolution (Courtney et al., 2017). In this project, the data of both the mRNA- and vRNA-HA were used as reference sequences for further comparative analysis to examine the conservation patterns of m6A sites among all HA subtypes of IAVs.

2.2.1.5. HA dataset collection of Influenza A viruses

Influenza Research Database (IRD) is the main public domain that contains all verified influenza HA sequences https://legacy.fludb.org/brc/home.spg?decorator=influenza; therefore, the IRD was used it to retrieve the needed sequences. The same domain provides the HA sequences in an organized format to utilize the data of each HA

separately. Similarly, specific settings to incorporate specific viruses within subtypes or specific host species were also adopted, as stated later. The H1N1 A/Puerto Rico/8/34/Mount Sinai (AF389118) was included as the reference strain in all performed comparative analyses.

2.2.1.6. Generation of consensus sequences for comparative analysis and identification of the conserved DRACH motifs

Multiple sequence alignments (MSA) were performed of the entire investigated HA subtype (i.e. H1–H18, separately) using the MUSCLE algorithm implemented in IRD (Squires et al., 2012). The computed and visualized MSA results and the generated consensus sequences were downloaded in FASTA format. Geneious software (v9.1.4) confirmed the alignment and the generated consensus sequences (Kearse et al., 2012). Moreover, Geneious can provide consensus sequences according to the required threshold frequency (TF) percentage and reveal the non-consistent bases as degenerate nucleotides. WebLogo software was used to determine the conserveness and diversity of all putative DRACH motifs (Crooks et al., 2004).

2.2.2. Molecular biology methods

2.2.2.1. Preparation of chemically competent *E. coli*

Preparation of chemically competent *E. coli* was carried out according to (Cohen et al., 1972) with some modifications. One vial of MAX Efficiency™ DH5α competent cells was thawed on ice, and the content was transferred into 10 ml of LB broth and incubated overnight at 37ºC in a shaking incubator (200 rpm). One millilitre of the overnight culture was added to a bottle containing 99 ml of LB broth and incubated at 37ºC with shaking (200 rpm) till the mid-log phase (about 3.5 h). The bottle was placed on ice, and the content was dispensed in 2 pre-chilled 50 ml tubes. After centrifugation at 5000 rpm for 5 min at 4ºC, the supernatants were discarded entirely, and each pellet was resuspended in 10 ml ice-cold 100 mM $MgCl_2$ buffer. The contents of both tubes were collected in one, and the tube was centrifuged at 5000 rpm for 5 min at 4ºC. The supernatant was discarded, and the pellet was resuspended in 30 ml ice-cold 100 mM $CaCl_2$. The tube was kept on ice for 20 min and then centrifuged at 3000 rpm for 5 min at 4ºC. The supernatant was discarded again, and the pellet was gently resuspended in 5 ml ice-cold 15% glycerol in 100 mM $CaCl_2$ solution medium. The competent cells were finally dispensed in 50 pre-cooled 1.5 ml microfuge tubes (100 µl each) and stored undisturbed at -80ºC till use for transforming competent *E. coli*.

2.2.2.2. Transforming competent *E. coli*

Chemically competent *E. coli* were transformed with existing plasmid DNA or freshly ligated new constructs. One vial of chemically competent *E. coli* was thawed on ice. The plasmid DNA (1–20ng) or ligation mixture (1–20 µl) was added to competent *E.*

coli in a circular manner. The vial was incubated on ice for 30 min. The competent *E. coli* were heat-shocked at 42°C for 45 seconds without shaking and immediately placed in ice for 5 min. Pre-warmed S.O.C medium (250 µl) was added to each vial. The vial was tightly capped and shaken horizontally (200 rpm) at 37°C for 1 hr. In the meantime, the agar plates of selective bacterial media were prepared for each transformation by dissolving LB agar in a microwave. After cooling to 55°C, ampicillin was added with a final concentration of 100 µg/ml. The agar was poured into bacteriological Petri dishes with a thickness of 3–5 mm and left to solidify.

Additionally, plates for bacterial cell viability and resistance were properly included in all experiments. A suitable volume of the transformation reaction (50 µl) was spread on each plate and was incubated overnight at 37°C. The development of circular white colonies on selective LB agar plates identifies bacterial growth. Separate well-defined bacterial colonies were picked and incubated in 1 ml LB broth containing 100 µg/ml ampicillin at 37°C overnight in a shaking incubator (200 rpm). A half millilitre of each bacterial culture was mixed with 0.5 ml of the preservation medium and stored at -80 °C for future use. The rest of the volume (i.e., 0.5 ml) was added to 4.5 ml of LB broth containing 100 µg/ml ampicillin and incubated overnight at 37°C with shaking (200 rpm) for plasmid purification.

2.2.2.3. Plasmid purification

The miniprep plasmid purification procedure was performed as the kit instruction manual recommended. The overnight bacterial culture was divided into a suitable number of microfuge tubes and centrifuged at 5000 rpm for 5 min. The bacterial pellets were resuspended in a 250 µl buffer P1 (containing RNase A) collected in one microfuge tube. Buffer P2 (250 µl) was added, and the tube was gently mixed by inverting 4-6 times till the mixture appeared clear but slightly viscous. Buffer N3 (350 µl) was added, and the tube was remixed by inversion 4–6 times till the solution appeared cloudy. After centrifugation at 13,000 rpm for 5 min, a compact white pellet was formed. The supernatant fluid (containing the plasmid DNA) was transferred to a spin column with a collection tube. The spin column was centrifuged at 13,000 rpm for 1 min, and the flow-through was discarded. The column was subjected to 2 washing steps using 500 µl PB buffer and 750 µl of PE buffer, respectively. The wash buffer was collected in the collection tube by centrifugation at 13,000 rpm for 1 min, and the flow-through was discarded. Another centrifugation at 13,000 rpm for 1 min was performed (with no buffer) to ensure complete dryness of the column. The column was finally placed in a new microfuge tube where 50 µl of the elution buffer (EB) was added at the centre of the column. The tube was kept standing for 5 min at RT and centrifuged again at 13,000 rpm for 1 min. After quantification, the eluted plasmid DNA was directly used in subcloning procedures or stored at -20ºC till use.

2.2.2.4. Restriction digestion of extracted plasmids

The procedure of restriction digestion of purified plasmids was performed as the enzyme instruction manual recommended. The typical restriction digestion reactions were prepared by mixing the following reagents in sterile 0.2 ml PCR tubes:

2.2.2.4.1. Restriction digestion mixture

Digestion mix	Amount
Plasmid	1-2 µg
rCutSmart buffer (10x)	2.5 µl
Restriction enzyme(s)*	1 µl/each
Nuclease free water	to 25 µl
Total	25 µl

*Restriction enzyme(s): differ according to experimental design, as will be specified later.

The tubes were spun down for 10–20 sec to remove drops in the lid and were incubated in a thermal cycler/incubator at 37ºC for 2 h, followed by heat inactivation of the enzyme(s) at 80ºC for 20 min. The digestion reaction products were run in 1% agarose gel along with a 1 Kbp DNA ladder.

2.2.2.5. Analysis of PCR/restriction digestion products by agarose gel electrophoresis

The procedure of agarose gel electrophoresis was performed as described before (Green and Sambrook, 2012). TAE buffer (1X) working solution was prepared by adding 5 ml of the 10X TAE buffer to 45 ml of autoclaved distilled water. Fifty (50) ml of 1% agarose solution was prepared by adding 0.5 gram of agarose powder to a glass bottle containing 50 ml of 1X TAE buffer. The powder was entirely dissolved by heating in a microwave oven for 1–2 min. The gel casting tray was assembled, and the comb was placed about 1 inch from one end of the tray in a vertical position so that the comb teeth were 2 mm above the tray's surface.

The agarose solution was left to cool in a water bath adjusted at 55ºC before (1X) gel red nucleic acid gel stain was added. The gel was poured into the gel casting tray and allowed to solidify for 20–30 min at RT. The comb was gently removed, leaving wells for sample loading. The casting tray was placed in an electrophoresis chamber and covered entirely with 1X TAE buffer. PCR, RT-PCR, and restriction digestion products (10 μl) were loaded in the preformed wells after mixing with loading dye. A similar volume of ready-to-use DNA ladder was dispensed in a separate well.

The electrophoresis chamber was covered, and the apparatus lid was connected to the power supply. Electrophoresis was performed at 100 volts for about 1 hr. The gel was removed from the electrophoresis chamber and was examined using short-wave UV light in a UV transilluminator (for cutting specific bands), and digital photos were kept/saved using the Chemidoc™ imaging system.

2.2.2.6. DNA extraction from agarose gel

Agarose gel electrophoresis was performed as described earlier **(Section 2.2.2.5.)**. Specific DNA bands of the expected molecular weight were excised from the agarose gel using a clean razor blade. The procedure of extraction of DNA from the gel was performed according to manufacturer instructions. Briefly, the gel slices were placed into a pre-weighed 1.5 ml tube. A 1:1 volume of binding buffer was added to the gel slice. The gel mixture was incubated at 50–60°C for 10 min until the gel slice was completely dissolved. Isopropanol (100 µl) was added to the thawed gel slice. The solubilized gel solution was transferred to the GeneJET purification column (800 µl). The column was centrifuged for 1 min at 13,000 rpm. The flow-through was discarded, and the column was placed back into the same collection tube. The column was subjected to 2 washing steps using 500 µl of washing buffer. The wash buffer was collected in the collection tube by centrifugation at 13,000 rpm for 1 min, and the flow-through was discarded. Another centrifugation at 13,000 rpm for 1 min was performed (with no buffer) to ensure complete dryness of the column. The column was finally placed in a new microfuge tube where 20–30 µl of the elution buffer (EB) was added at the centre of the column. The tube was let to stand for 5 min at RT and centrifuged again at 13,000 rpm for 1 min. After quantification, the eluted DNA was directly used in subcloning procedures or stored at -20ºC till use.

2.2.2.7. Ligation of linearized constructs

The procedure of ligating linearized constructs, linear plasmid(s), linear PCR products (insert), and annealed oligos was performed according to manufacturer instructions. The ligation mixture was prepared by mixing the following ingredients in a sterile PCR tube:

2.2.2.7.1. Ligation mixture

Ligation mixture	Amount
Purified linearized plasmid *	50 ng
Purified DNA insert	37.5 ng
T4 DNA ligase reaction buffer (10x)	2 µl
T4 DNA ligase enzyme	1 µl
Nuclease free water	to 20 µl
Total	20 µl

*Ligation mixture differs according to vector to insert length and desired ratio.

The tube was gently mixed and incubated at RT for 2 h or overnight at 4°C. The ligation mixture (1–20 µl) was used to transform chemically competent *E. coli* as described in **Section 2.2.2.2**. A suitable number of colonies were picked up and tested using colony PCR to test positive transformants.

2.2.2.8. Identification of bacterial transformants using colony PCR

The overnight cultures of bacterial colonies were individually transferred to microfuge tubes and were centrifuged at 5000 rpm for 5 min. The supernatant was removed entirely by pipetting, and the pellet was resuspended in 100 µl TE buffer and mixed

well by pipetting up and down. The tubes were incubated at 100°C in a heat block for 10 min and centrifuged at 10,000 rpm for 5 min. The DNA-containing supernatant was transferred to a new microfuge tube. For each colony, gene-specific primers were used in the green master as follows:

2.2.2.8.1. PCR reaction mixture

Reaction mixture	Amount
DreamTaq Green PCR Master Mix (2X)	12.5 µl
Forward primer	1 µl
Reverse primer	1 µl
DNA extract	1 µl
Nuclease free water	to 25 µl
Total	25µl

The tubes were spun down for 10–20 seconds to remove drops from inside of the lid and were placed in PTC-200 Peltier thermal cycler for amplification of the target sequences according to the following cycling protocols:

2.2.2.8.2. PCR reaction thermoprofile

Initial denaturation	94°C	10 min	1 cycle
Denaturation*	94	1 min	
Annealing*	52-72	30 seconds	40 cycles
Extension*	72	1 min/kb	
Final extension	72	10 min	1 cycle
Hold	4	∞	

*Repeated step

Agarose gel electrophoresis was used to visualize and analyse the PCR products, as described in **Section 2.2.2.5.** to identify positive transformants, which need further confirmation using sequencing.

2.2.2.9. Verification of PCR products/recombinant plasmids by sequencing

PCR products of interest and plasmid DNA extract of suspected positive colonies were further identified by sequencing. Twenty (20) µl aliquots of the plasmid DNA (100 ng/µl), or purified PCR products (10 ng/µl), and target-specific primers (3.2 pmol) were separated in 0.2 ml PCR tubes and sent for sequencing at source bioscience Ltd (Cambridge, UK). Sequence contigs were edited and assembled by BioEdit program version 7.2.5 (Ibis Biosciences, CA, USA) and analysed using the NCBI BLAST tool (http://blast.ncbi.nlm.nih.gov), Ensembl (mainly chicken genome), and SnapGene.

2.2.2.10. Amplification and purification of HA gene of the rescued m6A-mutants H9N2 viruses

Viral RNA extraction from each rescued m6A-mutant H9N2 (positive HA allantoic fluids) and the negative control allantoic fluid was performed according to the kit manufacturer's instructions. For each sample, lysis buffer AVL (560 µl) and carrier RNA (5.6 µl) were added to clear allantoic fluid (140 µl). The mixture was pulse-vortexed for 15 sec. The lysis mixture was incubated at RT for 10 min. After brief centrifugation to remove droplets from the inside lids, 560 µl of absolute ethanol was added to the mixture and mixed thoroughly by pulse-vortexing. The lysate was further incubated for 5 min at RT. The lysate was then pipetted into the QIAamp Mini column

with care to avoid wetting the rim. After centrifugation at 8000 rpm for 1 min, the collection tube was discarded, and the column was placed in a clean collection tube. The last step was repeated till the sample was fully loaded. Five hundred (500 µl) AW1 Buffer was added to the spin columns, followed by centrifugation at 8000 rpm for 1 min. The collection tube was changed again, and 500 µl of Buffer AW2 was added and centrifuged at 8000 rpm for 1 min. Another wash cycle with 500 µl of absolute ethanol was applied. The column was placed in a clean 2 ml collection tube and centrifuged at 14,000 rpm for 2 min to dry the membrane. Finally, the RNA was eluted by setting the column in a sterile 1.5 ml microfuge, and 45 µl Buffer AVE was added at the centre of the membrane. After incubation for 5 min at RT, the tubes were centrifuged at 14,000 rpm for 1 min. Elutes were quantified and ready for cDNA synthesis or stored at -80ºC till use.

2.2.2.11. First-strand synthesis (cDNA synthesis)

The viral RNA extract, target-specific primers, and SuperScript®VI first strand synthesis system components (dNTP mix, 5X first strand buffer, DTT, and RT enzyme) were thawed on ice and vortexed thoroughly for homogeneity. The cDNA synthesis mixture was prepared into a 0.2 ml thin-walled PCR tube for each sample. A typical 20 µl reaction included the following components in two steps:

2.2.2.11.1. cDNA reaction mixture (step 1)

Reaction mixture	Volume
Viral RNA extract	5 µl
Forward primer (10 µM each)	0.5 µl
Reverse primer (10 µM each)	0.5 µl
dNTP Mix (10 mM)	1 µl
Nuclease free water	to 13 µl
Total	13 µl

The mixture was incubated in a heat block at 65°C for 5 min. The tubes were transferred directly to the ice for 1 min at least. After brief centrifugation to spin down the contents, the following components were added to each tube:

2.2.2.11.2. cDNA reaction mixture (step 2)

Reaction mixture	Volume
First-strand Buffer (5x)	5 µl
DTT (0.1 M)	1 µl
SuperScript® IV RT enzyme	1 µl

The tube contents were mixed by pipetting gently and were incubated in a heat block at 53°C for 10 min. The reaction was inactivated by heating at 70°C for 15 min.

2.2.2.12. PCR amplification of genes and domains

The generation of blunt-end PCR products encoding viral HA gene fragments from different rescued m6A-mutant viruses, chicken m6A machinery (chFTO), or domains of chALKBH5 and viral NP was performed using Q5® High-Fidelity DNA Polymerase according to instructions of the kit's manufacturer. The template cDNA/plasmid, target-specific primers, and Q5 DNA polymerase kit components (High GC enhancer, 10x buffer, and enzyme) were thawed on ice and mixed thoroughly for homogeneity. A PCR mixture was prepared into a 0.2 ml thin-walled PCR tube. A typical 50 µl reaction included the following components:

2.2.2.12.1. Q5-High-fidelity PCR reaction mix

Reaction mixture	Volume
Q5 Amplification Buffer (5x)	10 µl
GC enhancer buffer (5x)	10 µl
dNTPs mixture (10 mM)	1 µl
Forward primer (10µM each)	2.5 µl
Reserve primer (10µM each)	2.5 µl
Q5 DNA Polymerase	0.5 µl
Template DNA (10pg-200ng)	1 µl
Nuclease free water	up to 50 µl
Total	50 µl

The tube contents were mixed thoroughly by pulse vertexing and spun down by brief centrifugation. The tubes were then placed in a thermal cycler for amplification of the target sequences according to the following thermo-cycling protocol:

2.2.2.12.2. Q5-High-fidelity PCR reaction thermoprofile

Initial denaturation	94°C	5 min	1 cycle
Denaturation*	94	15 sec	
Annealing*	58-68	30 sec	35 cycles
Extension*	68	1 min	
Final extension	68	5 min	1 cycle
Hold	4	∞	

*Repeated steps

After amplification, the PCR products were analysed for downstream applications, either for subcloning (chFTO, chALKBH5 domains, viral NP domains, etc.) or sequencing (viral HA gene fragments) as described earlier.

2.2.2.13. CRISPR-Cas9/13 genome editing technologies

2.2.2.13.1. CRISPR/Guide RNA annealing and vector cloning

In this study, CRISPR/Cas technology was utilized to drive genome editing in DNA using Cas9 and RNA using Cas13 (**Figure 2.1A**). Accordingly, guide RNA (gRNA) oligos (20 nt) specific to chicken- YTHDF2, and ALKBH5 genes were selected and designed to minimize the likelihood of off-target cleavage using the online Benchling tool. gRNA for chYTHDF2 and chALKBH5 were cloned in pSpCas9(BB)-2A-Puro (PX459) V2.0 (**Figure 2.1B**). The overhang (CACCG) was added to the 5′ end of the gRNA-forward specifying oligo sequence, and "AAAC" was added to the 5′ end of the

reverse complement of the gRNA-specifying oligo for cloning using the BbsI-HF®

restriction enzyme.

Whereas CRISPR RNA (crRNA) oligos (30 nt) were manually designed to target the

HA gene of H9N2 (UDL/08), crRNA was used for gene editing through targeted

demethylation. crRNA for the HA gene was cloned in the pC0043-PspCas13b crRNA

backbone **(Figure 2.1C)**. Similarly, overhang (CACCG) was added to the 5′ end of the

crRNA-forward specifying oligo sequence, and "CAAC" was added to the 5′ end of the

reverse complement of the crRNA-specifying oligo for cloning using the BbsI-HF®

restriction enzyme. The extra 'G' should be added to the 5′ end of the gRNA/crRNA

sequence just after the restriction enzyme overhang. This G was added to ensure

efficient initiation of the gRNA/crRNA transcription from the U6 promoter.
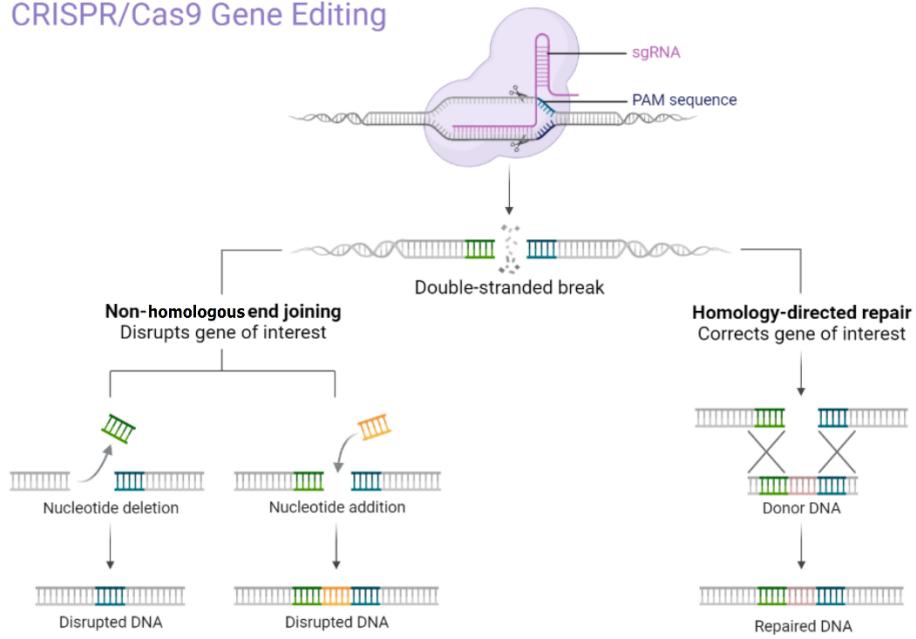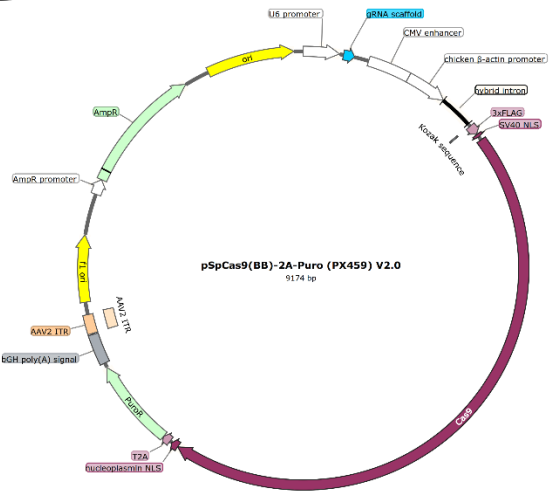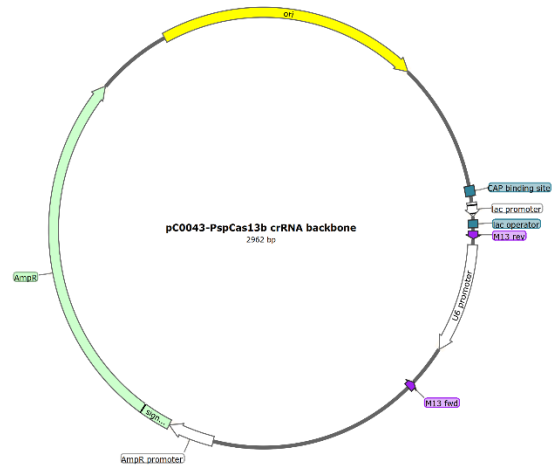
Figure 2.1: Schematic overview of CRISPR/Cas9 system. (**A**) and plasmids used for cloning sgRNA (**B**) and crRNA (**C**).

The oligos were resuspended in nuclease-free water to 100 µM stock solution. The oligos were annealed using an annealing buffer as follows:

2.2.2.13.1.1. gRNA/crRNA annealing mixture

Mix	Volume
Forward Oligo (100 µM)	2 µl
Reverse Oligo (100 µM)	2 µl
Annealing buffer*	2 µl
Nuclease free water	14 µl
Total	20 µl

*Annealing buffer: 10 mM Tris, 1 mM EDTA, 50 mM NaCl

The oligos were annealed at 95°C for 5 min and then cooled down to 37°C for 1 hr. The annealed oligos were diluted 1/50 for gRNA and 1/10 for crRNA for ligation.

2.2.2.13.1.2. CRISPR/Cas plasmids restriction mixture

Digestion Mix	Amount
Plasmid	1-2 µg
rCutSmart buffer (10x)	2.5 µl
BbsI-HF®	1 µl
Nuclease free water	to 25 µl
Total	25 µl

The plasmids (pSpCas9(BB)-2A-Puro (PX459) V2.0 for gRNA, pC0043-PspCas13b crRNA backbone (for crRNA) were digested overnight and heat-inactivated at 80ºC for 20 min before use. The concentration of purified linearized plasmid was measured by

nanodrop and used for ligation with the annealed oligo. The annealed oligos were cloned into linearized plasmids using a golden gate assembly with the following conditions:

2.2.2.13.1.3. CRISPR/Cas plasmids ligation mixture

Ligation Mix	Amount
Linearized plasmid DNA	0.1 µg
10x T4 DNA ligase buffer	2 µl
Diluted annealed Oligos	1 µl
T4 ligase	1 µl
Nuclease free water	to 20 µl
Total	20 µl

Ligation was performed at 16°C overnight. The total volume of the ligation reaction was transformed into DH5α competent cells **(Section 2.2.2.2.)**. Colonies were picked and analysed for successful cloning by colony PCR and sequencing using U6 promoter-specific primer **(Section 2.1.2.15.)**.

2.2.2.14. RNA extraction from virus-infected cells

The procedure of extraction of RNA from virus-infected cells was performed according to manufacturer instructions. The supernatant media (over virus-infected cells) was removed entirely (usually for plaque assay-based quantification of progeny viruses), and 350 µl of buffer RLT was added directly to the cells for lysis. The cell lysate was

centrifuged at maximum speed (12,000 rpm) for 3 min. The supernatant was carefully removed by pipetting and transferred to a new microfuge tube. An equivalent volume of 70% ethanol was added to the lysate and mixed well by pipetting (No centrifugation should be applied). Up to 700 μl of the mixture, including any precipitate, was dispensed in an RNeasy Mini spin column placed in a 2 ml collection tube. After centrifugation at 10,000 rpm for 15 sec, the follow-through was discarded, and 700 μl of Buffer RW1 was added to the spin column. The column was centrifuged again at 10,000 rpm for 15 sec, and the flow-through was discarded. Two wash cycles with 500 μl of Buffer RPE were performed as described before. Centrifugation in the second wash lasts for 2 min. The spin column was transferred to a new 2 ml collection tube and centrifuged at full speed for 1 min to dry the membrane. Finally, the column was placed in a sterile microfuge tube where 45 μl of RNase-free water was added directly onto the membrane. RNA was eluted by centrifugation at 10,000 rpm for 1 min.

2.2.2.15. Quantitative real-time RT-qPCR

Primer pairs for all tested genes designated for qPCR were designed to generate amplicons of 100–250 base pairs **(Section 2.1.2.)**. Primers were synthesized by Invitrogen by Life Technologies, UK. RT-qPCR was used to profile the expression level of chicken m6A-associated genes in DF1 cells. Additionally, RT-qPCR was used to quantify the fold-change in the expression of M, NP, and HA genes of AIV- H9N2 (or as stated) in m6A genes-transfected cells compared with mock-transfected using SuperScript™ III Platinum™ SYBR™ Green One-Step RT-qPCR Kit. The RT- qPCR mixture was prepared by combining the following reagents:

2.2.2.15.1. RT-qPCR mixture

RT-qPCR Reaction mixture	Volume
2X SYBR® Green Reaction Mix	12.5 µl
Forward primer (10µM each)	0.5 µl
Reserve primer (10µM each)	0.5 µl
$MgSO_4$ Enhancer	0.5 µl
SuperScript® III RT/Platinum® Taq Mix	0.5 µl
Template (1pg to 1µg total RNA)	<10 µl
Nuclease free water	up to 25 µl
Total	25µl

The qPCR tubes were spun down for 10–20 seconds to remove drops from inside of the lid and were placed in the CFX96 real-time PCR system for detection and amplification of the target sequences in real-time according to the following cycling protocol:

2.2.2.15.2. RT-qPCR thermoprofile

Reverse transcriptase step	50	15 min	1 cycle
Initial denaturation	95°C	5 min	1 cycle
Denaturation*	95	10 sec	40 cycles
Annealing-Extension*	60	30 sec	
Melt curve	65 to 95	increment 0.05 °C each 5 sec	
Hold	4	∞	

* Repeated steps

Relative mRNA expression for the viral and cellular innate immune gene (or as stated) was quantified compared to the chicken Ribosomal Protein L30 (chRPL30) gene, the reference/housekeeping loading control, as determined earlier (Yang et al., 2013). The fold change in relative viral/cellular expression levels was calculated using the following formula (Livak and Schmittgen, 2001)

Fold Change $= 2^{-\Delta\Delta Ct} = -(\Delta Ct$ of m6A-transfected$- \Delta Ct$ of mock-transfected lysates).

2.2.2.16. Methylated RNA-immunoprecipitation and sequencing (MeRIP-seq)

DF1 cells seeded in 6-well plates were infected with H9N2 UDL/08 (MOI=1.0) or left uninfected. At 24 h. post-infection, total RNA was extracted, as described in **section 2.2.2.14.** mRNA was enriched from total RNA using the Dynabeads mRNA purification kit. RNA was fragmented using the RNA Fragmentation Reagent (NEB) for 5 min and purified by ethanol precipitation. According to the manufacturer's recommendations, methylated RNA immunoprecipitation (MeRIP) was performed using an EpiMark® N6-methyladenosine Enrichment kit. Briefly, Protein G Dynabeads (25 µl) were washed three times in MeRIP reaction buffer (10 mM Tris-HCl, 150 mM NaCl, 0.1% NP-40, pH 7.4). The washed beads were incubated with 1 µl anti-m6A antibody for 2 h at 4°C with rotation. After washing with MeRIP reaction buffer three times, anti-m6A conjugated beads were incubated with RNA with rotation at 4°C overnight in 300 µl MeRIP reaction buffer with 1 µl RiboLock RNase inhibitor. Only 10% of each sample was kept and served as an input fraction. After washing the bead twice with 0.5 ml MeRIP reaction buffer, the beads were washed with low salt buffer (10 mM Tris-HCl, 50 mM NaCl, 0.1% NP-40: pH 7.4) and twice with high salt buffer (10 mM Tris-HCl,

500 mM NaCl, 0.1% NP-40: pH 7.4). The beads were washed once again with MeRIP reaction buffer. m6A-modified RNA was eluted in MeRIP reaction buffer containing 5mM m6A salt (Santa Cruz Biotechnology) for 30 min at 4°C with rotation. Elutes were concentrated by ethanol purification. RNA-seq libraries were prepared from eluate/MeRIP and 10% input mRNA (Dominissini et al., 2012; Gokhale et al., 2020).

The input and MeRIP mRNA fractions from virus-infected DF1 cells (three biological replicates) were subjected to MeRIP-seq libraries using Illumina's HiSeq 2000 sequencing system according to the manufacturer's instructions. Reads from input and MeRIP samples were quality-checked using fastqc (Version 0.11.9) (http://www.bioinformatics.babraham.ac.uk/projects/fastqc/). The quality-checked reads were trimmed to cut the terminal adapters, and low-quality reads using trimmomatic (Version 0.38) (Bolger et al., 2014). The trimmed reads were aligned to the chicken genome using the Bowtie2 aligner. The unaligned reads were aligned to the concatenated IAV H9N2-UDL transcriptome (Langmead and Salzberg, 2012). Then, m6A peak calling was performed to MeRIP over input using MACS2 utilizing the following flags: the effective genome size was 1.2e+9 (1.4e+4 for H9N2-UDL) -p 0.05 -nomodel -keep-dup auto -extsize 200 (extsize 100 with callsummit for H9N2) (Zhang et al., 2008). The Bed files of m6A peak clusters were visualized using the integrative genomics viewer (IGV) (Robinson et al., 2011). The enriched motifs in the m6A peak clusters were determined using the findMotifsGenome.pl script using the homer package (Version 4.11) (Heinz et al., 2010).

2.2.2.17. MeRIP-RT-qPCR

For MeRIP-RT-qPCR, RNA was extracted, and MeRIP-RT-qPCR was performed like MeRIP-seq **section 2.2.2.16** with modifications. No fragmentations are needed. Elutes were concentrated by ethanol precipitation. The input and the IP fractions were quantified using SuperScript™ III Platinum™ SYBR™ Green One-Step RT-qPCR Kit. The relative m6A level for each tested transcript was calculated as the percent of input and normalized to the respective IgG control. Fold change of enrichment was calculated graphed with an uninfected sample normalized to 1.

2.2.2.18. RNA-protein immunoprecipitation (RIP)-RT-qPCR (RIP-RT-qPCR)

RIP-RT-qPCR is usually performed to detect the potential interaction of RNA with ribonucleoprotein (RNP); here the aim was to determine whether m6A-erasers interact with HA transcripts. Therefore, the DF1 cells were transiently transfected for 24 h. with each in FLAG-tagged m6A-erasers, as will be described in **section 2.2.3.3**. DF1 cells were infected with H9N2 UDL (MOI=1.0) for an additional 24 h. Then, the transfected-infected DF1 cells were lysed for protein isolation (as will be described in **section 2.2.5.1**). The lysates were incubated with either anti-FLAG- or rabbit IgG antibody bound beads (as described in **section 2.2.2.16**). Only 10% of each sample was saved as an input fraction. After immunoprecipitation (IP), the IP and input fractions were lysed for RNA. The input and the IP fractions were quantified using SuperScript™ III Platinum™ SYBR™ Green One-Step RT-qPCR Kit. The relative mRNA HA level was calculated as the percent of input and graphed as fold enrichment calculated relative to IgG control (Imam et al., 2018).

2.2.2.19. Evaluating cellular mRNA stability using Actinomycin D

The stability of cellular transcripts within cells can be assessed and measured indirectly by analysing the mRNA half-life ($t_{1/2}$) following transcription inhibition using Actinomycin D (ActD). The stability of cellular transcripts was compared in DF1-wt and DF1-chALKBH5-KO cells. Accordingly, the two cell lines (i.e., wt and KO) were plated in 12-well cell culture plates. 24 h after plating, ActD (5 µg/ml) was added to the two DF1 cell lines. The samples were collected 0, 2, 4, and 8 h. post-ActD treatment. The cells were lysed for RNA isolation at the indicated time points and followed by RT-qPCR to the stated cellular mRNA. The quantification cycle (cq) values of each time point were compared with the cq values of time 0 (for normalization to calculate the relative abundance). The plots were graphed, and the mRNA decay rates were calculated using linear regression analysis (Dai et al., 2021).

2.2.3. Cell culture and microscopy

2.2.3.1. Cultivation and maintenance of mammalian cells

Chicken-origin DF1 cells (ATCC; CRL-12203), human HEK-293T (ATCC; CRL-11268), and canine MDCK (ATCC; CCL-34) cells were maintained in DMEM supplemented with 5% Foetal bovine serum (FBS) and antibiotic and antimycotic solution contains 10,000 units/ml of penicillin, 10,000 µg/ml of streptomycin, and 25 µg/ml of Gibco Amphotericin B. All cells were grown under cell culture conditions (5% CO_2, 37°C). The cells were routinely passaged every 3 days in T75 cell culture flasks once they reached confluency (almost 100%). The old growth media were removed, and cells were washed twice with PBS. For dissociation, the cells were treated with either trypsin only (DF1) or trypsin-versene (MDCK) for 5 min at 37°C. The cells were detached by gentle tapping on the sides of the vessels. Then, the cells were resuspended in growth media and transferred to centrifuge tubes. Notably, HEK-293T cells can easily be detached in PBS with gentle tapping. Cells were centrifuged at 1000 rpm for 5 min at RT. The supernatants were discarded, and the pellet was resuspended in an appropriate volume of growth media and seeded into suitable flasks/plates or used for continued culture (typically 1 vessel into 3–5).

2.2.3.2. Freezing and thawing of cells

Freezing of cells is usually used for long-term preservation; healthy and confluent cells were dissociated from cell culture flasks, resuspended in a growth medium, and pelleted at 1000 rpm for 5 min, as described earlier in the previous section. The cell pellets were

resuspended in ice-cold freezing media (10% DMSO in FBS). The cells were aliquoted in cryovials and cooled down immediately to -20°C for 1 hr, followed by -80°C overnight before permanent storage in liquid nitrogen.

The cells must be thawed quickly to obtain the best possible survival condition. Once the cryovials were removed from the freezer/liquid nitrogen tank, they were placed directly into a 37°C water bath and rotated until they were completely thawed. The cryovial contents were diluted in 10 ml growth media and centrifuged at 1000 rpm for 5 min. The pellet was resuspended in 15 ml growth media, transferred to cell culture vessels, and kept overnight at 37ºC in a CO_2 incubator. Then, after 24 h, attachment of the cells to the flask surface was checked. Cells can be washed twice with PBS to remove unattached cells and replaced with fresh growth media till confluency.

2.2.3.3. Transfection

Transfection of plasmid DNA was applied to DF1 and HEK-293T cells using the ViaFect and TurboFect transfection reagents, respectively, according to the manufacturer's instructions. DF1/HEK293T cells are usually seeded onto 6-, 12-, and 24-well plates to be 70–90% confluent on the transfection day. The cells were incubated at 37ºC in a CO_2 incubator. Four (4) µg plasmid DNA/well was used to transfect cells grown to 70–90% confluency in 12-well plates. Four (4) µg were added to 100 µl Opti-MEM or serum-free medium. Twelve (12) µl of transfection reagent (i.e., 1 µg DNA: 3 µl transfection reagent) were added to 100 µl Opti-MEM or serum-free medium. The

two tubes were incubated for 5 min at room temperature. After 5 min, the two tubes were combined and incubated for another 25 min at room temperature.

In the meantime, the old growth media over the cells was removed. Cells were washed with PBS, and 1 ml of growth media was added per each well of a 12-well plate. After incubation, the transfection mixture was added dropwise over the plate and rotated gently for a few min. The cells were kept in the CO_2 incubator for up to 48 h. according to the experimental design. The downstream applications, antibiotic selection, immunofluorescence, or analysis of cell lysates were performed as described in the respective sections.

2.2.3.4. Separation of single cell clone and generation of knock-out (KO) and knock-ins (KI) cell lines

2.2.3.4.1. Generation of KO cell line using limiting dilution approach

Single-cell clones (SCCs) of either chALKBH5 or chYTHDF2-KO cell lines were generated to test the antiviral activity of KO compared with DF1-wt cells. Firstly, an antibiotic kill curve was carried out to determine the optimal puromycin concentration (i.e., mammalian selective antibiotic). Confluent DF1 cells were cultured at various concentrations of puromycin (0–10 µg/ml). The optimal dose was determined as the puromycin's lowest concentration, killing 100% of non-transfected cells within 5–7 days. Two (2) µg/ml of puromycin was determined to be the optimal dose for DF1. Cells were seeded for 24 h before transfection in a 6-well plate to be 70–90% on the

day of transfection. Cells were transfected with recombinant Cas9 plasmids with either chALKBH5 or chYTHDF2 gene-specific gRNA using ViaFect.

Cells were incubated in growth media for 24 h before adding antibiotic selection media. The cells were left until the death of all non-transfected cell control with a change of antibiotic media every 48 h. Following antibiotic selection, single-cell clones were isolated in 96-well plates by a limited dilution approach.

Limited dilution is a common technique to isolate SCC and generate stable cell lines. Briefly, the antibiotic-resistant polyclonal cell populations were trypsinized and resuspended to 10,000 cells/ml. Antibiotic selection media (100 µl) was added to all wells of the 96-well plate except A1. Then, 200µl of the cell suspension was added to the A1 well and 2-fold serially diluted along column 1 from A1–H1 (first dilution series). An additional 100 µl medium was added to each well in column 1 (giving a final volume of cells and media of 200 µl/well). The second 2-fold serial dilution series was horizontally carried out throughout the entire plate from A1-A12, B1 to B12, and so on **(Figure 2.2)**. All wells were filled up to 200 µl by adding 100 µl medium to each well. The plate was placed in the incubator at 37°C. SCC should be visible by microscopy within 10–14 days. Wells with single clones are marked and carefully checked daily to ensure that it has only one clone with no other contaminating cells on the well edge. Once the single-cell clones are large enough, they are gently trypsinized from wells of a 96-well plate and transferred into a larger area (usually in a 24-well plate, then a 12-well plate for further propagation). Then, the cells were screened using PCR and sequence to detect and characterize the occurrence of frameshift mutation of the gene of interest in the target exon.
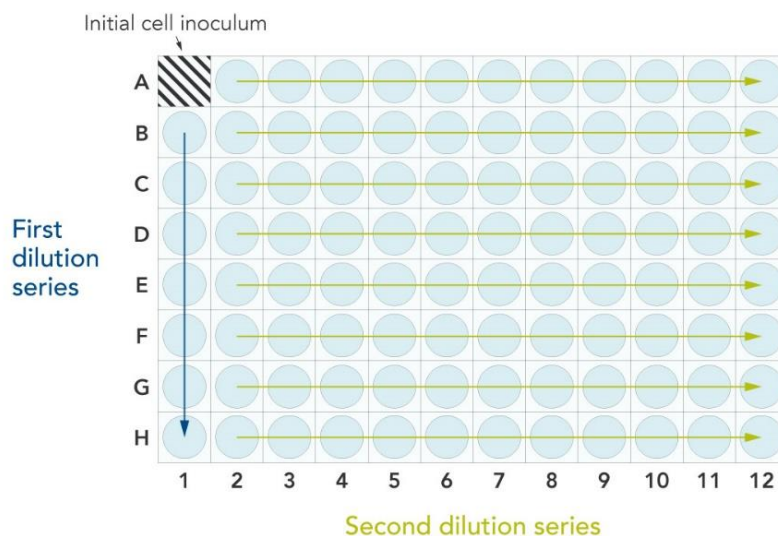
Figure 2.2: Plate setup for limited dilution method used to isolate single cell clones.

2.2.3.4.2. Generation of KI cell line using small cell culture cylinders

For generation of the KI cell line (mRuby3-chALKBH5-DF1), DF1 cells were co-transfected with (1) pUC57-Amp_CRISPIE donor vector containing mRuby3, (2) pX330 _CRISPIE plasmid encoding Cas9 and sgRNA to liberate mRuby3 from donor vector, (3) pSpCas9(BB)-2A-Puro (PX459) V2.0 vector encode Cas9 plasmid and gRNA target chALKBH5 intron 1 or 4 using ViaFect as described **in section 2.2.3.3**.

Transfected cells were incubated in growth media for 7 days. The media was changed over the DF1 cells every 2–3 days, depending on cell condition. After 7 days, the red cells are visible. The cells were split (1 well into 2) to let the red cells expand. Then, when good foci of red cells were noticed under a fluorescent microscope, cell culture cylinders were used to pick a single red clone. Each growing red clone was marked under the fluorescent microscope and picked up with small cell-culture cylinders. The

cylinders are made of glass and sealed to the cell culture plate with sterile silicone high vacuum grease to minimize possible leakage during the picking-up procedures. Cell culture plates need to be carefully examined under the fluorescent microscope, and once a well-isolated clone is identified, a circle is drawn around it with a marker pen.

Once a satisfactory number of clones were located, growth media were removed, and cells were washed with PBS. Then, using sterile forceps inside microbiological safety cabinet II, cloning cylinders were picked up and gently pressed into the sterile silicone grease to make the bottom sticky to the culture plate and avoid leakage. The cylinders were gently placed and pressed over the colony. This procedure must be very fast to prevent dying of the cell clones, and high care should be taken while placing the cylinders by avoiding contact of the grease with cells or sliding the cylinder across the colony. Then, 50 µl of trypsin was added to the cylinders, and the plate was incubated at 37°C for 3–5 min until cells became rounded and came off the dish bottom. The detached cells of every single clone were gently pipetted and transferred into an appropriate cell culture dish, usually each clone in each well of a 24-well plate with fresh growth medium. Then, the cells were screened using PCR and sequence to detect and characterize the correct integration of mRuby3 in the corresponding introns of chALKBH5.

2.2.3.5. Preparation of primary chicken embryo fibroblast (CEF)

Primary cell cultures are obtained directly from the animal tissues or organs. These cells have a short life span in the laboratory. At first, the eggs were candled to determine the embryo's presence, viability, and age. 9-days-old embryonated eggs were humanely killed by chilling on the fridge for a few hours to minimize bleeding. Then, inside the safety cabinet (containment level 3, CL3), the eggshells were surface sterilized with 70% ethanol. The eggshells above the air sacs were carefully removed, and shell membranes were also reflected. Then, the embryos were picked up by sterile forceps without piercing the yolk sac. The embryos were transferred into sterile Petri dishes, and the appendages and viscera were removed.

After that, the flesh was transferred into another sterile Petri dish containing DMEM and antibiotics. The flesh was washed three different times with sterile PBS. Then, the flesh was cut into fine pieces using sharp scissors. The minced flesh was placed into a sterile side-armed flask containing a magnetic bar and trypsin solution (0.25%). The cut pieces were stirred for 3–5 min using a magnet stirrer (trypsinization step).

The supernatant from the trypsinization step was poured into another receiving flask containing Foetal bovine serum and covered by a double layer of gauze to hold the cell clumps (anti-trypsinization step). The last step aimed to inactivate the trypsin to avoid its extensive action on cells. The trypsinization and anti-trypsinization steps were repeated 3–5 times to generate more singlet cells. The singlet cells were poured into centrifuge tubes and pelleted at 1500 rpm for 5 min. The pellet was resuspended in 5 ml growth medium. Then the cells were counted using a haemocytometer. The cells were plated at a suitable dilution and incubated till they reached the desired confluency.

2.2.3.6. Confocal fluorescence microscopy

The old growth media was removed from transfected or infected cells and the cells were rinsed twice with PBS. The cells were fixed for 1 hr. Then, the cells were washed once with PBS. The cells were treated with 0.1% Triton X100 in PBS for 10 min, and then cells were washed with PBS. The BSA 0.5% in PBS was used to block non-specific bindings for 1 hr the cells were probed with primary antibody diluted in PBS for 2 h. Then, cells were washed with PBS three times for 5 min each. Then, cells were incubated with species-specific secondary fluorescent conjugate in PBS for 1 hr. The cells were washed with PBS three times for 5 min each. The DAPI 1:10,000 in PBS was used to stain the nuclei for 5–10 min. The coverslips were mounted with an aqueous mounting medium (Vectashield antifade media). All steps were carried out at room temperature without allowing cells to dry at any stage. For live cell images, The Hoechst 1:10,000 in PBS was used to stain the nuclei for 5-10 min. The cellvis plates were transferred directly to the LSM880 confocal microscope for imaging in real-time under 37ºC and 5% CO_2 overnight.

2.2.3.7. Flow cytometry analysis of replication of the labelled viruses

A flow cytometry tool was used to determine the number of labeled virus-infected cells (infected, transduced). After 24 h of infections, cells were trypsinized according to **section 2.2.3.1**, pelleted, and washed once with PBS. The cells were centrifuged again at 3000 rpm for 5 min. The pellet was resuspended in live/dead marker according to the manufacturer's protocol for 30 min. The cells were washed and then fixed with 4%

paraformaldehyde for 30 min. Then, the cells were washed and resuspended in 1x permeabilization buffer for 15 min. Cells were washed and resuspended in 0.25% BSA for 30 min. The cells were washed and resuspended in 1x PBS before analysing cells by flow cytometry. Live and singlet cells were gated based on forward, and side scatters. Four-quadrant plots were generated using the untransduced and uninfected (RFP- and GFP-), transduced and uninfected (RFP + and GFP-), and untransduced-infected (RFP- and GFP+) cells. Analysis was carried out using CytExpert software, applying the same gating and analysis for all samples. However, in VSV-GFP and NDV-GFP models, virus-infected DF1 cells were gated in the FITC+ channel compared with negative cell control.

2.2.4. Virological methods

2.2.4.1. Generation of influenza H9N2 m6A-mutants with reverse genetics system

Wild-type H9N2 and m6A-mutants were rescued from cDNA using the 8-plasmid system (Hoffmann et al., 2000; Peacock et al., 2017). The plasmids were a gift from Prof Munir Iqbal, Pirbright Institute, UK. Briefly, HEK 293T cells were seeded into 6-well plates for 70–90% confluence in the next day. The growth media was replaced with Opti-MEM, and HEK293T cells were transfected with the 8-plasmid system (all share the identical 7 plasmids from gene PB2, PB1, PA, NP, NA, M, NS and differ in HA according to various m6A-mutation sites). Briefly, the transfection mixture was prepared by adding 8 µg DNA plasmids (i.e., 1 µg each) to 24 µl TurboFect transfection reagent diluted in 200 µl Opti-MEM and incubated at RT for 25 min, followed by dropwise addition of transfection mixture to the cells and incubation at 37°C and 5% CO_2 overnight.

In the meantime, MDCK cells were seeded for the next day. The old transfection mix was removed. The HEK293T cells were resuspended in 1x DMEM, antibiotic and antimycotic solution contains 10,000 units/ml of penicillin, 10,000 µg/ml of streptomycin, and 25 µg/ml of Gibco Amphotericin B, BSA 0.2%, and TPCK-trypsin (2 µg/ml). The resuspended cells were mixed with MDCK cells and were incubated for 2–3 days. The cell culture supernatants were transferred into centrifuge tubes and were centrifuged at 5000 rpm for 5 min. This clear supernatant was ready to be inoculated into embryonated eggs. All rescue trials and the rest of the virological methods were performed in containment level 3 laboratories (CL3).

2.2.4.2. Virus inoculation on embryonated-chicken-eggs (ECEs)

Before the development cell culture techniques in the 1940s, ECEs were the most suitable host for isolating many avian and some human viruses. Additionally, ECEs are considered a good host for virus propagation after virus rescue on mixed HEK/MDCK cells. Upon receiving day zero ECEs, the eggs were incubated for 9 days in a shaking egg incubator at 37ºC and 40–60% humidity. The eggs were monitored daily to remove the infertile or dead eggs by candling them over dark background. The site of the embryo and the top of the air sac were marked using a pencil before inoculation.

Inside the microbiological safety cabinet, the top of the eggs was surface sterilized using 70% ethanol. On the top of the eggshell, one tiny pore was generated using egg porer. The virus/potential cell culture supernatants were inoculated in the allantoic sac (100–200 µl) **(Figure 2.3)**. The top of the eggshell was sealed using medical plaster. Then, the eggs were incubated for up to 72 h at 37ºC and 40–60% humidity with daily observation. Then, the eggs were chilled overnight in the fridge to kill embryos and prevent haemorrhage. Eggs were gently opened from the top to harvest the allantoic fluids in labelled centrifuge tubes and were freezed at -80ºC till use for further confirmatory steps.
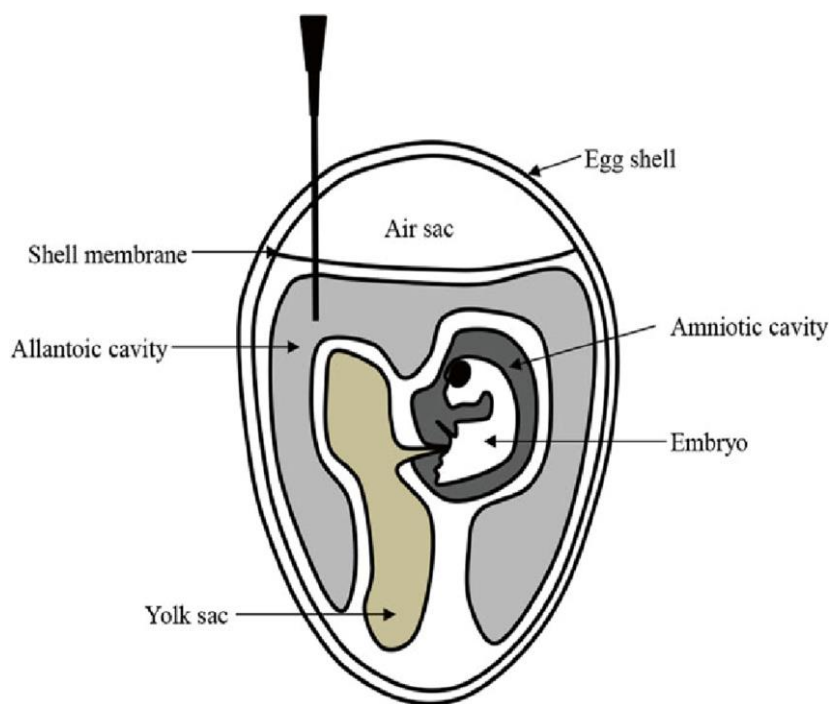
Figure 2.3: Intra-allantoic inoculation route in an anatomical structure of a 9-day-old embryonated chicken egg.

2.2.4.3. Haemagglutination assay (HA)

HA is the aggregation of red blood cells (RBCs) in suspension in the presence of haemagglutinating virus particles. The HA assay is mainly used for the identification and titration of haemagglutinating viruses. The whole chicken blood was shipped with an anti-coagulant. Upon receipt of blood, the whole blood was washed to separate the RBCs. Briefly, the whole blood was transferred to a centrifuge tube (15 ml). The blood was mixed gently by inversion and centrifuged at 2000 rpm for 10 min. The supernatant was decanted, usually containing plasma and some white blood cells. The bottom containing the packed RBCs was washed 3x with PBS and centrifuged until the supernatant became clear. RBCs (1%) in PBS were prepared from the original packed RBCs.

The viruses/allantoic fluids were thawed for testing. Fifty (50) µl PBS was dispensed into a 96 U-shaped well plate in the cabinet. Fifty (50) µl was added to the first well or the row for each viral sample. Then, two-fold serial dilution was applied through mixing by pipetting. Fifty (50) µl of 1% RBCs were added to all dilutions of tested samples. The plate was incubated at RT to read after 25–30 min. If haemagglutination occurs, this indicates a HA virus is present, as the virus particles suspend the RBCs. If the RBCs are pelleted, this indicates no HA virus is present. Positive control haemagglutinating virus, negative control mock-inoculated allantoic fluid, and RBCs control were included in all HA assays. Each sample was tested in duplicate.

2.2.4.4. Ultracentrifugation and virus purification

Different rescued m6A-mutant viruses were generated on ECEs. The harvested allantoic fluids were clarified by centrifugation at 5,000 xg for 30 min at 4°C. Influenza virus particles were pelleted down from cleared supernatants by ultracentrifugation at 100,000 xg for 2 h at 4°C over a sucrose cushion (30% sucrose in TNE buffer, 10 mM tris pH8.0, 1 mM EDTA, 100 mM NaCl) using an ultra-centrifuge and SW-32Ti rotor. Then, the virus pellet was resuspended in 500 µl 1x TNE buffer. The resuspended virus pellet was further purified through a 10–50% sucrose gradient. The sucrose gradient tube was centrifuged at 130,000 xg for 2 h at 4°C. The virus band was identified against a dark background, carefully collected, diluted in TNE buffer, and subjected to another ultracentrifugation cycle (130,000 xg for 2 h at 4°C). The supernatant was carefully poured off, and the virus pellet was finally resuspended in l ml of 1x TNE buffer.

2.2.4.5. Virus infection and propagation in cell culture

The appropriate cell density for infection is a 70–90% confluent monolayer. The growth media over DF1 or MDCK cells was decanted. The cells were washed twice with sterile PBS to remove remnants of dead cells. One (1.0) MOI of virus inoculum was added to infection media (1x DMEM, 1x antibiotic antimycotic solution, BSA 0.2%, HEPES buffer (50 mM). Two (2) ug/ml TPCK-treated trypsin was added to the media over the MDCK only in case of virus propagation on cells. It is important to note that in all antiviral assays tested using DF1 cells, no TPCK-trypsin was added (DF1 cells do not tolerate any TPCK-trypsin) to promote multicycle infection. The cell culture vessel or plate was kept for 2 h (adsorption time), with gentle tilting every 20 min to promote uniform virus distribution and to protect cells from dryness. After 2 h, the infection media were removed, and cells were washed twice using PBS to remove any unadsorbed virus. The vessels were incubated at 37°C for 24 h after infection or as indicated later.

In the case of virus propagation on MDCK, the vessel was usually incubated for 3–4 days till the appearance of CPE (cytopathic effect; usually cell rounding and death in IAV). Mock-infected cells were included as a control. The viruses were harvested in appropriate-sized centrifuge tubes. Cell culture fluid was centrifuged at 3000 rpm for 15 min, and the supernatant was collected and stored in a freezer at -80ºC.

2.2.4.6. Quantification of influenza viruses by plaque assay

The old growth media over MDCK in 6-well plates was removed, then the cells were washed twice with PBS. In the meantime, A ten-fold serial dilution was performed per each virus/cell culture supernatant in DMEM. The plates were shaken every 20 min. After 2 h, the plates were washed twice with PBS. Two (2) µg/ml TPCK-trypsin was added to a 2× influenza plaque medium. A 1:1 influenza plaque medium (2x MEM, 2x antibiotic antimycotic solution, L-glutamine (4 mM), BSA 0.2%, HEPES buffer (50 mM) was mixed with warm 1.6% agarose solution and immediately before solidification. A 3 ml of plaque medium was added per well and kept to solidify at room temperature (24–27°C). The plates were incubated at 37°C in a CO_2 incubator. After 72 h, one ml of 4% paraformaldehyde was added to each well to fix the MDCK cell monolayer and inactivate the virus for 1 hr. Then, the agarose plug was carefully removed from each well using a sterile spatula and disposing of the agar in a biological waste container. One (1) ml crystal violet solution of 0.2% was added to each well, and incubated for an additional 20 min at RT. Then, the crystal violet solution was removed, and the wells were washed with 1 to 2 ml water to rinse the excess stain solution. The plates were kept to dry at room temperature (24–27 °C) before counting plaques (**Figure 2.4**). Plaque count and diameter between different rescued m6A-mutant viruses were determined using ImageJ.
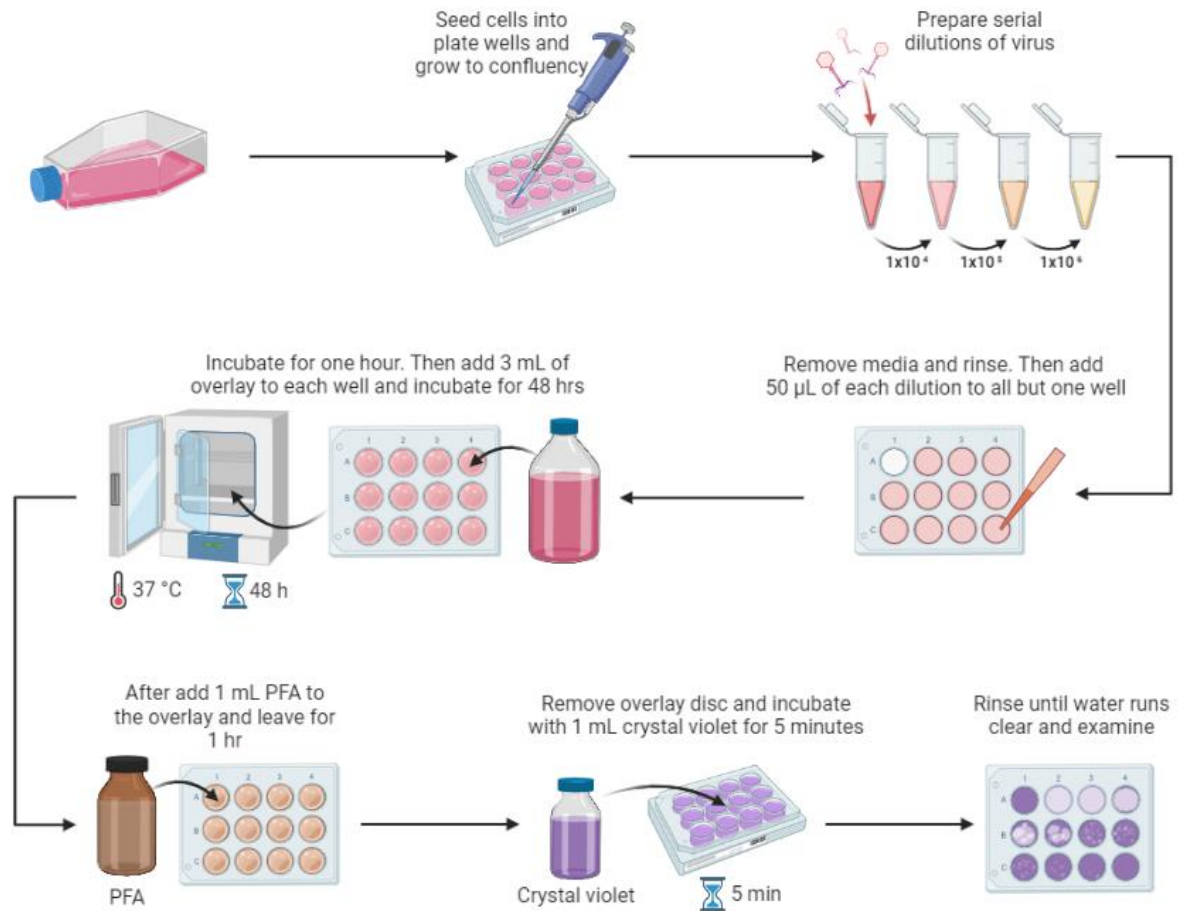
Figure 2.4: Schematic of steps involved in the plaque assay procedure.

2.2.4.7. Generation of lentiviruses expressing chicken m6A-related proteins

The cDNAs encoding chicken m6A-related genes were chemically synthesized and cloned into a bicistronic expression vector (pTRIP.CMV.IVSb.chicken m6A gene.ires.TagRFP), which was utilized for lentiviruses production (Schoggins et al., 2011; Santhakumar et al., 2018). HEK-293T cells were seeded in poly-lysine pre-coated plate with a seeding density of 5×10^5 per each well of 6-well plates. The cells were co-transfected with chicken m6A-related genes expressing proviral DNA (chYTHDF1-3, chYTHDC1, chALKBH5, chFTO, chMETTL3, chMETTL14, chWTAP), HIV-I gag-

pol, and VSV-G in a ratio of 1:0.8:0.2 using TurboFect (3 µl/1µg DNA; Thermo). Cell

supernatants were collected at 48, 72, and 96 h post-transfection and then cleared by

centrifugation (1500 rpm for 5 min). The supernatants were pooled and supplemented

with 4 µg/ml polybrene and 20 mM HEPES. All procedures were performed according

to manufacturer recommendations. CEF cells were transduced with MOI=1.0 of a

lentivirus-expressing specific m6A protein in DMEM media containing 5% FBS, 20

mM HEPES and 4 µg/ml polybrene. Transduction was facilitated by centrifugation

(1000g for 1 hr at 37°C), and cells were incubated at 37°C. Three days later, cells were

infected with the GFP-tagged H9N2 virus with a MOI=1.0, according to the infection

protocol described in **Section 2.2.4.5**.

2.2.5. Biochemical methods

2.2.5.1. SDS polyacrylamide gel electrophoresis (SDS-PAGE)

SDS-PAGE is a standard biochemical procedure used to separate proteins based on their molecular weight through stoichiometric binding to negatively charged sodium dodecyl sulphate (SDS). SDS evenly renders all protein molecules net negative charge, so when the voltage is applied, all the proteins migrate through gel pores toward the positive electrode.

2.2.5.1.1. Preparation of cell lysates

After 24–48 h post-transfection, the growth medium was discarded. The cell monolayer was washed twice with ice-cold PBS. Then, PBS was decanted. The cells were treated with ice-cold lysis buffer NP40 (completed with protease inhibitors cocktail;100 µl/well of 6-well plate). The cells were lysed on ice for 1 hr in a platform rocker in slow motion. Cells were scraped off and transferred to a 1.5 ml microfuge tube using a cell scraper. The cells were centrifuged at 15000 rpm for 15 min at 4ºC. The supernatant was transferred into a new Eppendorf (this stage clears the lysate from cell debris). The cell lysate was directly used in biochemical assays or stored at -20ºC till use. On the day of SDS-PAGE, the prepared cell lysate was thawed on ice and mixed with LDS sample buffer. The 4x LDS sample buffer was diluted to 2x using MilliQ H_2O in a microfuge and completed with 10% of β-mercaptoethanol. Fifteen (15) µl sample loading buffer was added to 15 µl cell lysate in a 1.5 ml Eppendorf tube. The lysates were boiled at 98ºC for 5 min and were ready to be loaded alongside a prestained protein ladder (5 µl) into the SDS-PAGE gel.

2.2.5.2.2. Preparation of stacking and resolving gels

The SDS-PAGE was performed as described before (Green and Sambrook, 2012) with some modifications. The larger rectangular glass plate mini-protein electrophoretic cell II (Bio-Rad) containing the already fixed spacers was laid down on a clean, dry surface. The smaller glass plate was placed on top of the spacers. The bottom of the two spacers and the two glass plates were all aligned together. The aligned two glass plates were assembled inside green gates, and all were assembled in the casting stand.

The system consists of two gels, a resolving gel in which proteins are resolved based on their molecular weights (MWs) and a stacking gel in which proteins are concentrated before entering the resolving gel. The constituents and percent of gels mainly used in the study were as follows:

2.2.5.2.2.1. SDS-PAGE gel composition:

Constituents	Resolving gel (10%)	Stacking gel (5%)
Distilled water	8 ml	4 ml
30% acrylamide/Bis	7 ml	1 ml
1.5M Tris-HCl pH 8.8	5 ml	-
0.5M Tris-HCl pH 6.8	-	0.75 ml
10% SDS	200 µl	60 µl
APS 10%	200 µl	60 µl
TEMED	8 µl	6 µl

The separating gel was freshly prepared and poured slowly between the two glass plates using a micro-pipettor till reaching the mark present on the gel casting stand at the level of nearly 2/3 of the larger glass plate length. The resolving (separating) gel was immediately overlaid with 0.1 ml isopropanol and was left for 45 min till the complete polymerization of the gel. The isopropanol overlay was removed and replaced with distilled water for washing. This process was repeated several times. The stacking gel was prepared and poured between the two glass plates to fill the space between the separating gel and the top of the short glass plate. A Teflon comb was directly inserted between the two glass plates without the insertion of gas bubbles. The gel was left for additional 30 min for complete polymerization before the comb was removed. The formed wells were washed with distilled water and SDS running buffer several times. The clamp assembly carrying the formed gel was removed from the gel casting stand and was fixed in the electrode assembly, which was subsequently laid in the buffer chamber and covered with SDS-running buffer 1x at a level halfway between the short and the large plates.

The run was applied at 70 volts for 30 min, then 100 volts for approximately 90 min (till the bromophenol blue stain became located 1 cm before the end of the gel). The electrode assembly was removed, and the plate sandwich was plugged out. The glass plate sandwich was disassembled, and the stacking gel was cut out. The separating gel was transferred to a Petri dish containing Coomassie brilliant blue stain solution and incubated for 1hr on a rocker platform. The stain was drained and replaced with destain solution with continuous agitation on the rocker platform for 30 min. De-staining step

was repeated several times until the gel became transparent and the bands appeared visible. A digital camera photographed the gel.

2.2.5.2. Characterization of the expressed protein using western blot assay

Western blot is usually used for specific detection of proteins after SDS-PAGE. The overexpressed proteins were separated in SDS-PAGE and transferred electrophoretically to the PVDF membrane according to the procedures described earlier (Towbin and Gordon, 1984) with some modifications of semidry blotting as follows:

The SDS-PAGE was typically performed as described in **Section 2.2.5.1**. The gel was not stained in Coomassie blue staining solution but was ready to transfer into PVDF membranes. The PVDF membrane requires activation by immersion for 2 min in methanol. The gels were equilibrated for 30 sec in a transfer buffer. The package was arranged as follows: one extra thick blot paper pre-wet in transfer buffer in the bottom, then the activated pre-wetted PVDF membrane, then carefully placed the gel on top of the membrane, and lastly placed, one extra-thick blot paper pre-wetted in transfer buffer on top of the gel with no air bubbles. Following the manufacturer's recommendation for semidry system sittings, the gels were removed carefully after trimming the membrane borders. The membranes were transferred into 50 ml tubes containing blocking buffer (5% non-fat dry milk powder in PBST) in a roller for 1 hr at RT. Then, the blocking powder was removed, and primary antibodies (in 5% non-fat dry milk powder in PBST) were added according to each antibody dilution. After adding the respective primary

antibody. The tubes were incubated at 4ºC overnight. Then, the membranes were washed 3 times for 5 min each with 5 ml PBST.

Similarly, the secondary antibodies were added in the appropriate dilution (in 5% non-fat dry milk powder in PBST) for 2 h at RT on a roller. The membranes were washed 3 times for 5 min each with 5 ml PBST. After washing, the membranes were kept in a plastic sheet for band development, and ECL substrate was prepared (take an equal amount of detection solution A and B (1ml each) in a tube and mixed well) was added to the membrane for imaging using a Gel Doc system.

2.2.5.3. Immunoprecipitation using ANTI-FLAG M2 magnetic beads and mass spectrometry

Immunoprecipitation is a biochemical method that enables the purification of a protein. An antibody for the protein of interest is incubated with a cell lysate. Specific antibodies are allowed to bind to the protein lysate in the solution. The antigen (protein of interest)/ antibody complex is then immunoprecipitated of the sample using beads **(Figure 2.5)**. Transfection and sample preparation, lysis, etc., were previously discussed in **sections 2.2.3.3. and 2.2.5.1.** Anti-FLAG M2 magnetic beads were used to pull out the chALKBH5 (protein of interest, or as stated later) with possible other cellular interactors. Anti-FLAG M2 magnetic beads were thoroughly resuspended by gentle inversion. Twenty (20 µl) resin per sample was transferred to a 1.5 ml tube. The beads were equilibrated by resuspension with 5 packed volumes with TBS (50 mM Tris HCl, 150 mM NaCl, pH 7.4), and beads were washed by rotation for 5 min in an end-over-

end rotor. Then, the tubes were placed in an appropriate magnetic separator to collect the beads. The supernatant was discarded. The washing step using 5 packed volumes was repeated twice. The protein lysates were transferred to the equilibrated beads and incubated in the rotator device overnight at 4°C with gentle mixing to capture the FLAG-tagged proteins (binding step). A 20 µl from each sample was kept as an unbound fraction. Once the binding step was complete, the magnet separator was applied to tubes containing magnetic beads to remove the supernatant. The beads were washed 3x with PBS to remove the non-specifically bound proteins. The washing step was performed with 20 packed gel volumes (~ 0.5ml) of TBS buffer. Fifty (50 µl) of sample loading dye was added to the immunoprecipitated samples for western blot, as previously discussed **in section 2.2.5.2**.

The enriched protein samples were identified using tandem mass spectrometry (MS/MS). The samples were sent to the University of Manchester BioMS Core Facility (RRID: SCR_020987). The Mascot (from Matrix Science, UK) was utilized for peptide identification, which was further analysed by Scaffold (from Proteome Software Inc., USA) to determine the statistically enriched peptides. The list of the enriched proteins included for protein-protein interaction (PPI) and pathway analysis are those had unique peptides identified only in the chALKBH5-transfected followed by H9N2 UDL-infected cells but not in both the empty- or chALKBH5-transfected cells (majority of listed proteins; ~75%). Moreover, the differentially expressed proteins recorded at least 2X fold higher or detected in an absolute difference of 5 unique peptides higher than empty- and chALKBH5-transfected cells are included in the list of enriched proteins.

This significantly enriched list of proteins was analysed using the STRING database by adding multiple protein settings. The cut-off value for the PPI interaction was set to 0.5. The full STRING network was utilized to show PPI. The line thickness indicates the strength of functional interactions.

Immunoprecipitation Principle
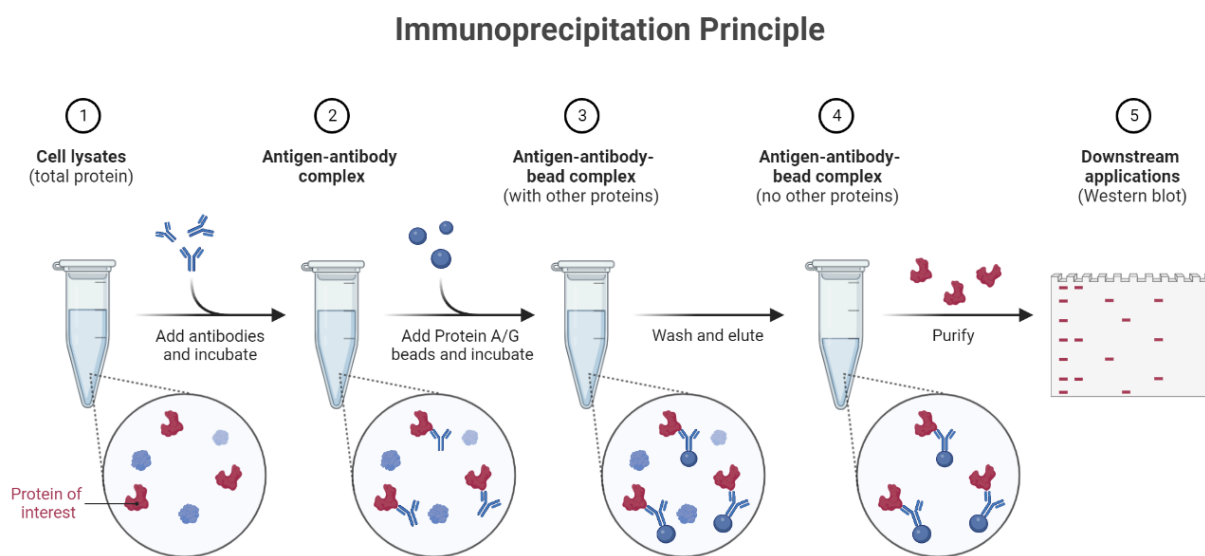
Figure 2.5: Schematic of immunoprecipitation assay.

2.2.5.4. m6A dot blot assay

The m6A dot-blot assay is one of the biochemical assays that provide rapid semi-quantitative assessments of m6A levels upon specific stimulation, including virus infection. The total RNA was extracted from mock- and virus-infected cells as described in **Section 2.2.2.14**. Total RNA was denatured at 95°C to disrupt secondary structures in a heat block for 3 min. RNAs were chilled on ice immediately after denaturation to prevent the re-formation of secondary structures of RNA. A drop of 5 μl of RNA (containing about 0.5 μg total RNA) was applied directly onto the Hybond-N+

membrane optimized for nucleic acid transfer and then cross-linked to the membrane in a Stratalinker 2400 UV crosslinker twice using the auto-crosslink mode (1200 microjoules [x100]; 25–50 sec). Then, the membranes were washed in 10 ml of wash buffer in a clean washing tray for 5 min at RT with gentle shaking to wash off the unbound RNA. The membrane was incubated in 10 ml of blocking buffer for 1 hr at RT with gentle shaking. Then, the membranes were probed with anti-m6A antibody (generated in mouse) in 10 ml dilution buffer overnight at 4°C with gentle shaking. Then, the membranes were washed three times for 5 min each in 10 ml of wash buffer with gentle shaking. The membranes were exposed to rabbit anti-mouse IgG-HRP in 10 ml dilution buffer for 2 h at RT with gentle shaking. Then, the membranes were washed three times for 5 min each in 10 ml of wash buffer with gentle shaking. The dots were developed by incubating the membrane with ECL Western Blotting Substrate (1:1 substrate A: B) for 2 min in darkness at room temperature. In the exact biological/technical replicates, the dotted membranes were stained with methylene blue for 20 min, then rinsed with distilled water, and photographed the dots. As dot blot analysis is a semi-quantitative approach, the signals from the dot blot images were quantified by ImageJ. The statistical analysis was performed on at least three biological replicates.

2.2.6. Statistical analysis:

The means were compared using the Student's t-test, where only two groups were involved. When multiple comparisons were required for a single factor (e.g., sm6A proteins' antiviral assays), experimental means were compared using a one-way analysis of variance (one-way ANOVA). mRNA stability and $t_{1/2}$ were performed on normalized values using linear regression analysis. p values were calculated with GraphPad prism 8. The data usually represents the average of three biological replicates with the standard deviation (SD). ns: non-significant; $p > 0.05$, $*p < 0.05$, $**p < 0.01$, $***p < 0.001$.

Chapter 3

Structural Insights into Avian

m6A Machinery

and

Evolutionary Conservation of

Potential m6A Sites Among

IAVs

3.1. Chapter Introduction

3.1.1. Structural and functional insights into m6A-methyltransferases

3.1.1.1. Identification of minimal unit of m6A-methyltransferase

Even though m6A marks were reported in the 1970s, the m6A methyltransferase complex was not identified until the 1990s. Rottman and colleagues (1994) were the first to identify the m6A-methyltransferases. The authors purified complex prototype components identified as methyltransferase unit A (MT-A) and MT-B; the isolated proteins varied in molecular weight between 30–800 kDa. Each unit can add a methyl group to adenosine independently. Notably, the MT-A unit comprises multiple subunits, one of which was identified to possess an S-adenosyl methionine (SAM; the methyl donor) binding site on a protein of 70 kDa, identified as MT-A70 (Bokar et al., 1994; Rottman et al., 1994). The MT-A70 was further renamed methyltransferase-like-3 (METTL3) (Gray et al., 2015).

The advancement of the epitranscriptomic field through m6A-seq data (Dominissini et al., 2012; Meyer et al., 2012) on one hand and understating that the m6A mark is dynamically reversed by m6A-demethylases; fat mass obesity-associated protein (FTO) and alkylated DNA repair protein (AlkB) homolog-5 (ALKBH5) (Jia et al., 2011; Zheng et al., 2013) on the other hand, inspired several groups to extend their study on the m6A machinery, including methyltransferase complex. In 2014, more than one group used METTL3 to identify the interacting partners using mass spectrometry (Liu et al., 2014; Ping et al., 2014; Schwartz et al., 2014b; Wang et al., 2014c).

All of these groups also used a bioinformatics analysis and identified that METTL14 shares 43% a.a. similarity to METTL3 and both contain methyltransferase domain (MTase or MTD, the potential active unit for methylation) (Bujnicki et al., 2002; Iyer et al., 2016). Therefore, authors initially supposed that METTL3 and METTL14 interact with each other, forming a stable complex, and induce methyltransferase activity (Liu et al., 2014; Ping et al., 2014; Schwartz et al., 2014b; Wang et al., 2014c).

It has been noticed that loss of the METTL3/14 complex is associated with perturbation of cell differentiation, spermatogenesis, and disease formation (Zhong et al., 2008; Hsu et al., 2017; Vu et al., 2017). Additionally, the loss of METTL3 and METTL14 negatively impacts cellular m6A levels (Liu et al., 2014; Wang et al., 2016b). Interestingly, the m6A writer complex is heavily involved in cellular homeostasis and cancer progression through m6A-dependent pathways (Barbieri et al., 2017; Knuckles et al., 2017; Choe et al., 2018). These findings indicate that the core methyltransferases are METTL3/14, and there is a need to identify structural insights into the m6A-methyltransferase complex.

In 2016, three groups independently revealed the crystallographic structure of METTL3 and METTL14, and it seems the groups had similar general conclusions, supporting each other (Śledź and Jinek, 2016; Wang et al., 2016b, 2016a). All these groups identified the structure of METTL3/14 MTDs in the presence of the SAM to identify the mechanistic action of METTL3/14 to transfer a methyl group into adenine base, as none were able to use RNA substrate instead. The METTL3/14 was purified and amenable for crystallization together. The METTL3/14 heterodimer complex resembles a flying butterfly. As described earlier, both have an MTD, and their MTDs are almost

identical. Each MTD has the basic structure of a Rossman-like fold, which is comprised

of 8 β sheets, 4 α helices, and 3_{10} helices. The Rossman-like fold is almost identical in

the two proteins; however, METTL3 harbours three additional loops, identified as gate

loop-1, -2, and interface loop **(Figure 3.1)** (Wang et al., 2016b).
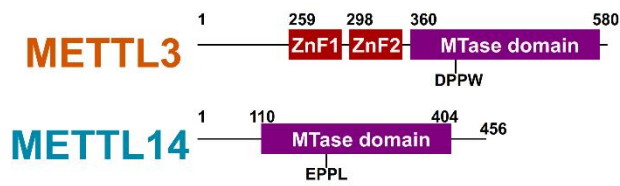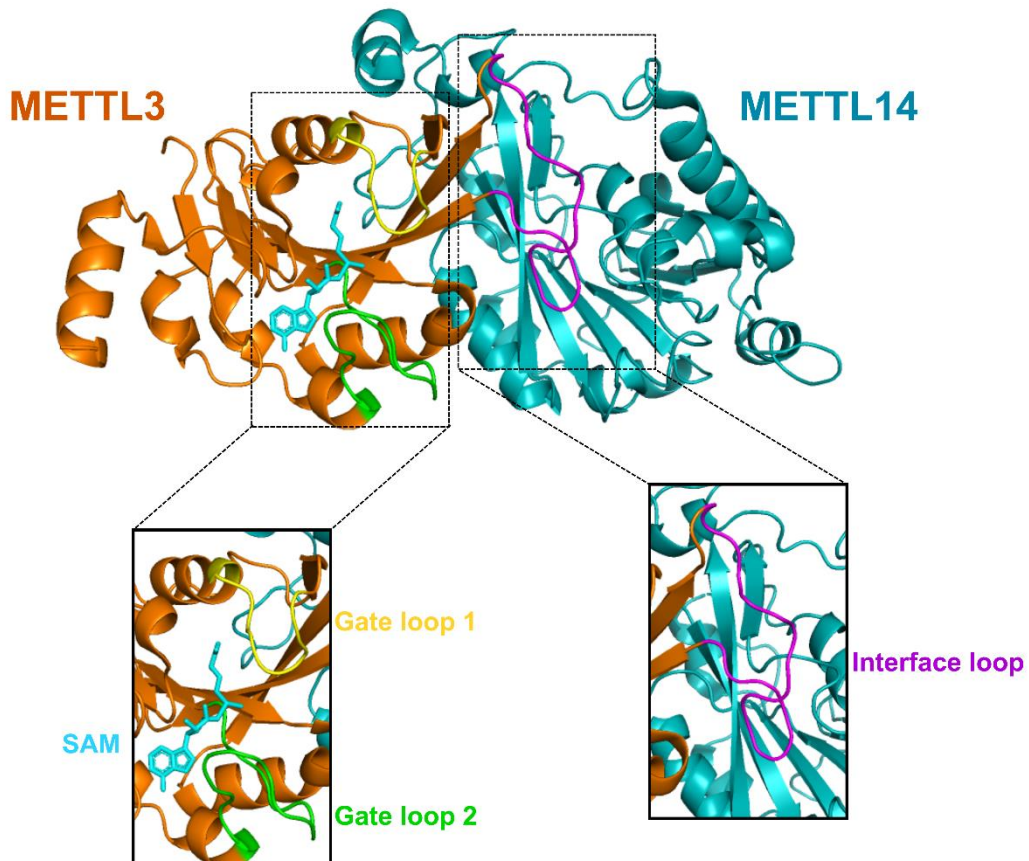
Figure 3.1: Structural insights into the core m6A-methyltransferase complex, the METTL3/14. **(A)** Schematic of the domain architecture of METTL3/14. ZnF; zink finger containing domain. MTase; methyltransferase domain. **(B)** The overall 3D structure of the SAM-bound heterodimer of METTL3(brown)/14(blue teal) (PDB ID: 5IL1) and close-up views of the gate loop 1 (yellow), gate loop 2 (green), and interface loop (magenta), SAM is also indicated by cyan residue.

Given that METTL3 and METTL14 have the same basic fold, but METTL3 possesses extra loops, indicating additional functions to METTL3. The SAM, the methyl donor in the methyltransferase activity, is located in the groove between gate loop-1 (395–410 amino acid residue) and gate loop-2 (507–515 amino acid residue; **Figure 3.1B**). Additionally, SAM is stabilized by critical residues in the groove, and targeted mutations of these residues abolish the methyltransferase activity (Wang et al., 2016b). It is essential to mention that the 395-DPPW-398 motif, which is the evolutionarily conserved motif for co-ordinating the adenine base to accept the CH_3 group, is very close to the SAM to support methyltransferase action. To conclude, gate loop-1 and -2 share in forming the catalytic grove for co-ordinating SAM **(Figure 3.1B)** (Wang et al., 2016b; Huang and Yin, 2018).

Moreover, the interface loop of METTL3 (462–479 amino acid residue; **Figure 3.1B)** and the N-terminal of METTL14 form another groove to accommodate the RNA substrate. Loss of the critical amino acids in this groove affects RNA substrate binding negatively, without affecting SAM binding ability **(Figure 3.1B)** (Śledź and Jinek,

2016; Wang et al., 2016b, 2016a). Together, gate loops are essential for methyltransferase activity and the interface loop is vital for RNA substrate binding.

It has been reported that only METTL3 could accommodate SAM (between gate loops). Although a vestigial groove was also located in METTL14, it was occluded to carry SAM (Śledź and Jinek, 2016). Therefore, the three groups independently tested the hypothesis that METTL14 works synergistically with METTL3 without having any catalytic activity. Notably, this finding opposes what was previously hypothesized, which was that METTL3 and METTL14 both had MTase activity (Śledź and Jinek, 2016; Wang et al., 2016b, 2016a).

Targeted mutational analysis of critical residues in the catalytic cages of METTL3 and METTL14 indicated that METTL3 only has catalytic activity. Additionally, SAM was not found in the ligand-binding pocket in the METTL14, which was too small to accommodate SAM. Interestingly, phylogenetic analysis and amino acid comparison indicated that DPPW (the catalytic cage residues) in METTL3 was almost conserved among all investigated species. However, EPPL, the homologue catalytic cage in METTL14, had lost its conservation in the studied species (Bujnicki et al., 2002; Iyer et al., 2016; Śledź and Jinek, 2016; Wang et al., 2016b, 2016a).

Importantly, the METTL3 alone was recorded as weak methyltransferase; however, binding with the METTL14 strongly supports activity by maintaining the proper architecture of the complex (Wang et al., 2016a, 2016b). As mentioned earlier, the groove made by the METTL14 and the interface loop of METTL3 support the RNA binding. RNA binding is also supported by two CCCH (zinc-finger) domains located in METTL3 (Śledź and Jinek, 2016; Wang et al., 2016a). The aforementioned data

indicate that METTL3 and METTL14 works co-operatively to form the minimal methyltransferase complex. METTL14 acts primarily as the RNA binding component and supports the integrity of the whole complex and METTL3 act as the bona fide methyltransferase enzyme.

3.1.1.2. Other factors in m6A-methyltransferase complex

Several co-factors help the core methyltransferase complex for optimal function, including the Wilms' tumour 1-associating protein (WTAP). WTAP guides the writer heterodimer complex (METTL3/14) to nuclear speckles (Ping et al., 2014; Schöller et al., 2018). Recently, Vir-like m6A methyltransferase-associated (VIRMA) factor was also found to bind to METTL3/14/WTAP and promotes m6A-modification preferentially in the 3′ UTR and near the stop codons (Yue et al., 2018).

Additionally, zinc-finger CCCH-type containing 13 (ZC3H13) is another newly identified co-factor that is a part of the writer complex and regulates RNA m6A methylation. The ZC3H13 predominantly promotes gathering the writer complex in the nucleus and regulates embryonic stem cell pluripotency in an m6A-dependent manner (Wen et al., 2018). RNA-binding motif protein 15 (RBM15) and its paralogue RBM15B are additional co-factors that promote optimal activity and specificity of m6A writers to particular coding and noncoding transcripts, including X-inactive specific transcript (XIST) (Patil et al., 2016). The ZCCHC4 was recently found to methylate 28S rRNA in humans and regulate translational aspects in carcinogenesis (Ma et al., 2019). Additionally, METTL16 was reported to methylate the methionine adenosyltransferase 2A mRNA (MAT2A), which is vital for embryonic development in the murine model (Doxtader et al., 2018; Mendel et al., 2018).

3.1.2. Structural and functional insights into m6A-demethylases

As a physiological dynamic process, the reversal of methylation is needed to alleviate the effects of the installed chemical modifications or dynamically reverse RNA alteration to perform an appropriate function in the cell lifecycle (Han et al., 2010; Bayoumi and Munir, 2021c). To date, only two m6A-erasers are well-characterized the FTO and ALKBH5. Albeit both erasers have m6A-demethylation activity, they differ in the demethylation process (Fu et al., 2013). ALKBH5 is predominantly located in the nucleus, whereas FTO can shuttle between the cytoplasm and nucleus.

Interestingly, both erasers are involved in various pathological processes. FTO and ALKBH5 predominantly have adverse outcomes on cancer progression. Moreover, both erasers possess multiple metabolic and physiological regulatory roles in the cell cycle. Intriguingly, FTO and/or ALKBH5 have distinct roles in viral infection that differ according to the virus, even in viruses that belong to the same family (Huang et al., 2020; Bayoumi and Munir, 2021c), which will be discussed in detail in the following chapter.

3.1.2.1. Enzymatic Biochemistry of m6A-erasers

Identifying various nucleobases exposed to demethylation is crucial for understanding their intracellular biological processes. The primary target substrate for ALKBH5 is ssRNA carrying m6A-marks. ALKBH5 induces demethylation by the α-ketoglutaric-dependent oxidase pathway (Aik et al., 2014; Feng et al., 2014). Moreover, ALKBH5 also targets rRNA to interact with dimethylated adenosine (m^6_2A) nucleobase (Ensfelder et al., 2018).

Compared to ALKBH5, FTO has been identified to interact and demethylate more substrates. The earliest studies indicate that the FTO demethylates 3-methylthymine (3mT) in single-stranded DNA (ssDNA) over double-stranded DNA. Moreover, FTO induces the demethylation of 3-methyluracil (3mU), especially on ssRNA (Gerken et al., 2007; Jia et al., 2008). The same group identified the m6A carried on ssRNA as the primary target for FTO (Jia et al., 2011; Wei et al., 2018; Zhang et al., 2019d); however, they noticed that FTO demethylates m6A marks in mRNA in both the cytoplasm and nucleus with different percent according to the cell line.

Additionally, FTO demethylates the di-methylated at N6 and 2′ -O-position (m^6A_m), the +1 position to 5′ cap in mRNA, on cytoplasmic mRNA. Furthermore, the authors also reported activity toward N1-methyladenosine (m^1A) in tRNA located in both the nucleus and cytoplasm to regulate protein translation (Liu et al., 2016; Wei et al., 2018). In addition, the FTO targets the m^6A and cap m^6A_m in small nuclear RNAs (snRNA) that control gene expression (Wei et al., 2018).

It is essential to mention that another report indicates that FTO primarily demethylates m^6A_m but not m6A to regulate RNA stability and translation (Mauer et al., 2017). This report opposes the most compelling pieces of evidence stating FTO substrates (Jia et al., 2011; Fu et al., 2013; Wei et al., 2018; Zhang et al., 2019d). It is worth mentioning that m^6A_m methyltransferase deficiency does not affect any vital intracellular processes (Akichika et al., 2019). In contrast, detrimental cellular alterations were reported in FTO/METTL3-deficient cells (Zhao et al., 2014a; Li et al., 2017). A recent study indicated that the phosphorylated CTD Interacting Factor-1 (PCIF-1) is an m^6A_m methyltransferase. The whole-transcriptome mapping findings also detected no

crosstalk between the m6A and m^6A_m. They noticed that the m^6A_m induces gene regulation mainly through affecting protein translation process (Sendinc et al., 2019). Markedly, another report emphasizes that PCIF-1 has no regulatory role in protein translation (Boulias et al., 2019). Regarding viral evidence, it was argued that the hepatitis C virus (HCV) was reported to carry m6A marks onto viral RNA and readily respond to the demethylation activity of FTO despite lacking the 5′ cap (Gokhale et al., 2016). The physiological substrates for m6A-erasers are shown in **Figure 3.2**.
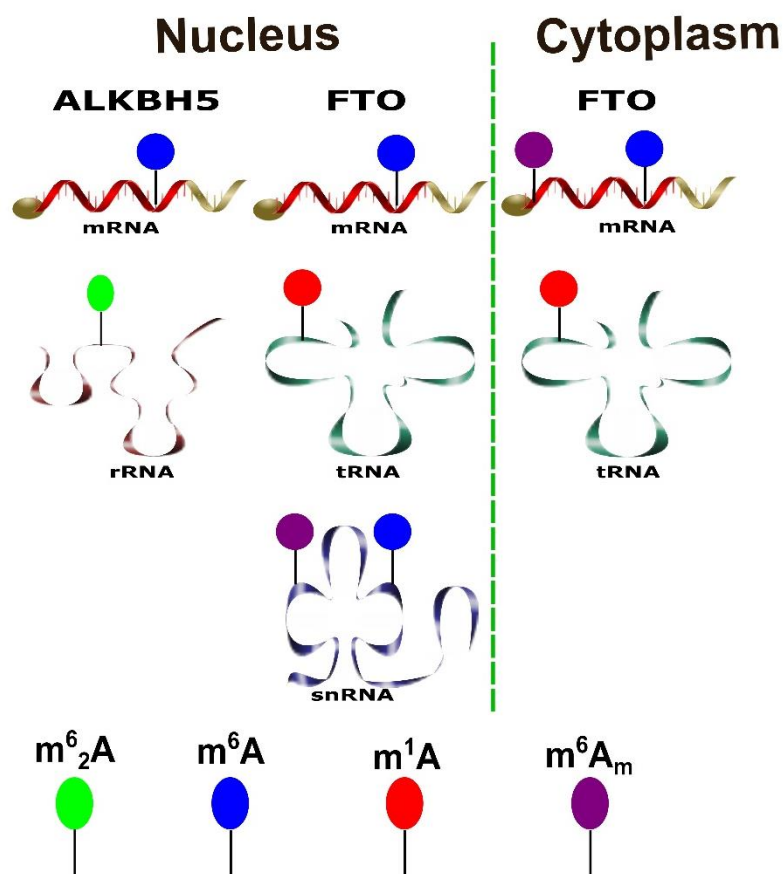
Figure 3.2: Schematic of m6A-eraser substrates in various forms of RNA. The cellular distribution of each eraser is indicated. The figure is adapted from our publication (Bayoumi and Munir, 2021c).

3.1.2.2. Structural insights into m6A erasers determine their substrate specificities

3.1.2.2.1. ALKBH5

The human ALKBH5 comprises a polypeptide chain of 394 amino acids (Zheng et al., 2013; Huang and Yin, 2018). However, it seems that performing a crystallographic analysis of the entire ALKBH5 was challenging; only the truncated version ALKBH5$_{66-292}$ was suitable for both active in vitro demethylation and crystallographic investigations. Accordingly, the amino and carboxyl termini were not crucial for ALKBH5 oxidative demethylation. The carboxyl terminus was reported to harbour multiple serine residues to mediate phosphorylation (Aik et al., 2014; Feng et al., 2014).

Similar to the ALKBH protein family, the ALKBH5 has the basic jelly-roll scaffold structure (double-stranded β-helix, DSβH, **Figure 3.3A**). The jelly-roll fold is comprised of 8 antiparallel β sheets in all investigated species (Jia et al., 2011; Aik et al., 2012, 2014; Bayoumi et al., 2020). In addition to the basic jelly-roll scaffold, the ALKBH5 has secondary amino acid motifs that support specific nucleotide recognition and impede the catalysis of double-stranded nucleic acid substrates. It is imperative to note that of all the ALKBH1-8 family members, ALKBH4 and ALKBH7 do not possess any secondary amino acid motifs; interestingly, they do not identify or catalyse RNA methylation but utilize protein substrates instead (Li et al., 2013; Wang et al., 2014a).

In 2014, more than one group independently revealed the crystallographic structure of truncated ALKBH5 (Aik et al., 2014; Feng et al., 2014; Xu et al., 2014a). All showed that the ALKBH5 has three secondary amino acid motifs. Motif-1 is very close to the active catalytic site in the centre. This motif provides more space to accommodate a

bulker substrate compared to ALKBH2. Further to crystallographic investigations, some residues are critical for ALKBH5 demethylation, including the actively coordinated residues (HxD…H). Moreover, K132 was reported to interact with the methylated adenosine, while R130 interacts with the phosphate backbone of the target methylated strand **(Figure 3.3A)**. Significantly, abrogating mutations to these key residues were associated with loss of ALKBH5 activity (Choudhary et al., 2009; Feng et al., 2014). The second motif promotes more elasticity to various RNA secondary structures than other ALKBH family members (Feng et al., 2014). Similarly, in motif-2, key residues are essential for substrate specificity through interacting with the methylated strand, including Q146, K147, and R148 **(Figure 3.3 A and C)**. Importantly, targeted mutations to these residues are also associated with a significant reduction of ALKBH5 activity (Yang et al., 2008; Han et al., 2010; Feng et al., 2014).

The third motif is crucial for selecting only single-stranded RNA as target substrates **(Figure 3.3A)**. Although motif-3 is located in other members of the ALKBH family, ALKBH5 flips to induce a stearic hindrance against the double-stranded nucleic acids through disulphide bond formation. Typically, the disulphide bonding connects between C230 and C267. Furthermore, the residue F234 in the motif-3 has also been identified to interact and direct the methylated adenosine toward the ALKBH5 catalytic site (McDonough et al., 2010; Aik et al., 2014; Feng et al., 2014). To conclude, identifying unique motifs and residues could be exploited to understand the substrate better and nucleotide-specificity for upcoming biomedical fundamental research and development of selective inhibitors, as recently reviewed (Bayoumi and Munir, 2021c).
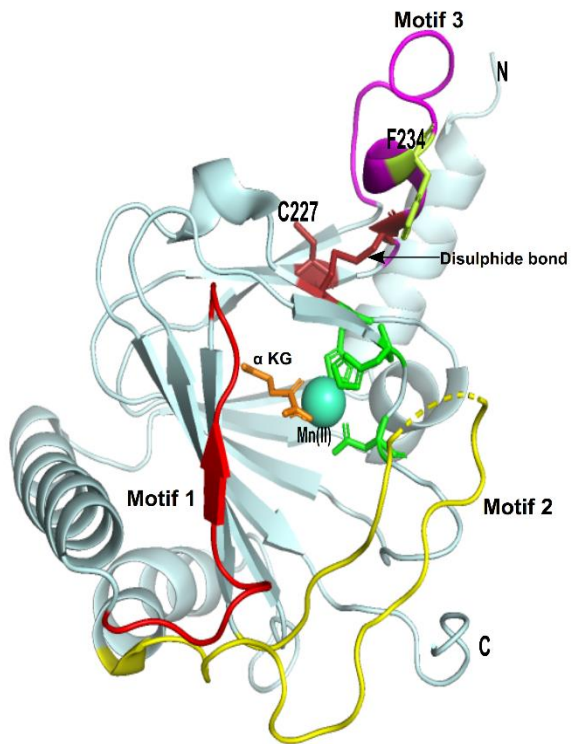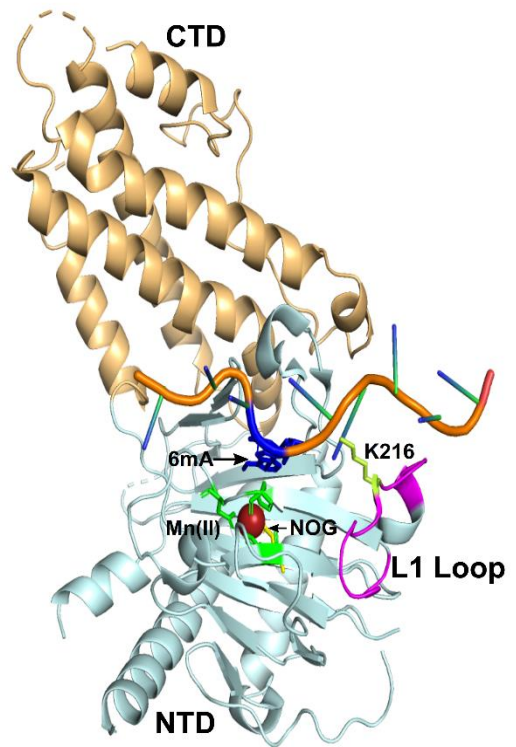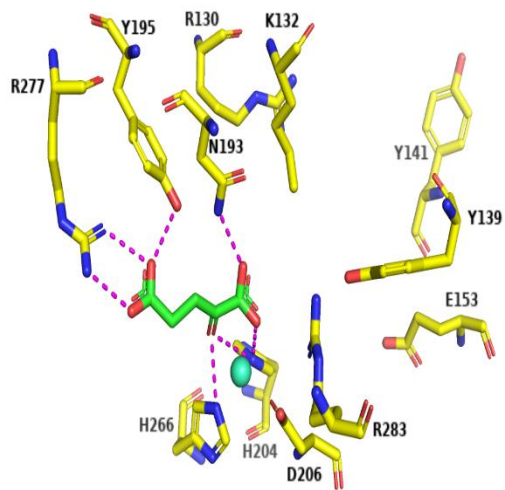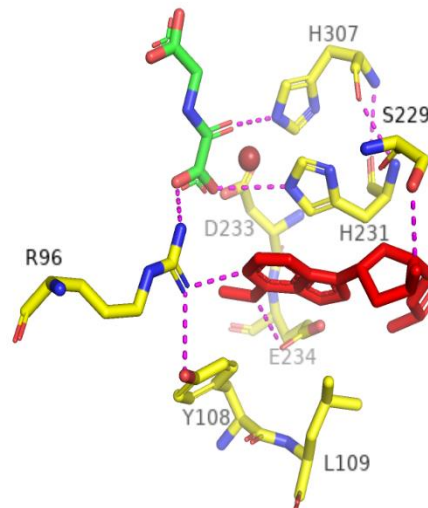
Figure 3.3: Structural insights into m6A-demethylases. **(A)** The overall 3D structure of human ALKBH5 (PDB ID: 4NRO), the jelly-roll fold, is depicted in cyan. The secondary structure motif 1-3 are labeled red, yellow, and magenta, respectively. The conserved HxD…H (that accommodate the methylated adenosine) residues are indicated by green colour. An orange residue indicates alpha-ketoglutaric acid (α-KG). The manganese atom is represented by a cyan circle. N: N-terminus, C: C-terminus. **(B)** The overall 3D structure of human FTO (PDB ID: 5ZMD). The long loop-1 (L1) is indicated by a magenta colour. 2-oxoglutarate (NOG) is shown by a yellow residue. A firebrick circle represents the manganese atom. 6-methyladenine substrate (6mA) is indicated by blue colour. CTD; C-terminal domain, NTD; N-terminal domain. **(C)** The active site of the ALKBH5 (PDB ID: 4NRO). Alpha-ketoglutaric acid residue (α-KG) is represented by green colour and attached by active site residues by magenta covalent bonds; a cyan circle indicates the manganese atom. **(D)** The active site of the FTO (PDB ID: 5ZMD). The 2-oxoglutarate analogue residue is represented by green colour. 6-methyladenine substrate (6mA) is indicated by red colour and attached by active site residues by magenta covalent bonds. A firebrick circle represents the manganese atom.

3.1.2.2.2. FTO

Like ALKBH5, FTO has the basic jelly-roll scaffold structure DSβH. However, FTO contains two major domains, the amino-terminal domain (NTD; 1–326) and the carboxyl-terminal domain (CTD; 327–498). The active demethylase site is buried in the NTD. Crystallographic investigation indicates that the first 31 amino acids are not essential for FTO demethylation activity. Additionally, The CTD is an evolutionarily

conserved domain to support NTD for demethylation (Han et al., 2010). Similar to the secondary motifs stated earlier in ALKBH5, FTO also has long loop 1(L1; residues 210–223), an evolutionary stretch to support impeding the double-stranded nucleic acid substrates and support nucleobase recognition and stabilization **(Figure 3.3B)** (Han et al., 2010; Feng et al., 2014; Zhang et al., 2019d).

As indicated earlier in the physiological substrates for m6A-erasers, the FTO surpasses ALKBH5 in the target nucleobases, including m6A, m6Am, m1A, 6mA, 3mT, and m3U. All these indicate that the FTO also possesses a bulker active site to accommodate various nucleobases (Han et al., 2010; Jia et al., 2011; Wei et al., 2018; Zhang et al., 2019d).

Crystallographic investigations indicated that two lysine residues are essential to accommodate the target in the catalytic site; K216 is located in the long loop-1, and K88 is located in the short loop (86-88). Inside the catalytic pocket, several residues are essential for stabilizing the target base, including I85, L109, Y108, V228, S229, W230, and H231. The methyl group in the nucleobase is precisely stabilized in the pocket by some residues, including Y106, L203, and R322 **(Figure 3.3D)**.

In the stabilized target strand in the active site, as indicated above, some critical residues are also essential to bind with the ribose ring, including A229. At the same time, R96 and E234 interact with the purine ring. Targeted mutation of these interacting residues abrogates FTO activity (Zhang et al., 2019d). it has been reported that mutation of critical residues homologue to the R96 in FTO, including Q112 in ALKBH2 and M61 in prototype bacterial AlkB protein reduce their enzymatic functions (Han et al., 2010), indicating conserved demethylation activity in AlkB family members.

Regarding substrate specificity, FTO primarily targets m6A and m^6A_m; it is important to note that m6A antibodies can cross-react and bind m^6A_m; the same adenosine base is shared between m^6A and m^6A_m. Therefore, the antibody-dependent method in the miCLIP single nucleotide resolution was reported to differentiate the two nucleotides based on their locations. The m^6A_m is usually located in the first position after the m7G-cap in the mRNA (Linder et al., 2015).

Functionally, in comparison to m6A, the m^6A_m marks were reported less frequently in the whole cell epitranscriptome, with at least one log lower frequency than m6A (Molinie et al., 2016; Wei et al., 2018; Zhang et al., 2019d). N6-methyl adenine is the preferred nucleobase, and 3mT is the least preferred for FTO. Compared to ALKBH5, FTO can accommodate larger 3D structures, including stem-loop and hairpin structures, due to the pincer-like structure formed by the long L1 loop and short loop (Zhang et al., 2019d).

Unlike m6A-writers and readers, m6A-erasers are flexible in their sequence requirements in target substrates. Moreover, m6A erasers can identify the methylated adenosine in similar sequences with the same consensus motif. Additionally, FTO is superior in functional activity to ALKBH5. Moreover, the sequels of m6A erasers could differ according to the structure of methylated RNA duplex or hairpin, indicating that the m6A is a conformational marker (Zou et al., 2016).

3.1.3. Structural and functional insights into m6A-readers

In the first m6A-methylome identified in 2012, m6A marks were read in the cytoplasm using particular RNA binding proteins (RBPs) through their YTH domain fold, later known as YTHDF2-3 (Dominissini et al., 2012). It is essential to mention that at least 174 evolutionary conserved proteins were identified in the eukaryotes that carry the YTH domain (Stoilov et al., 2002). Five YT521-B homology (YTH) domain-containing proteins are well-identified in mammals, including YTHDF1-3 and YTHDC1-2 **(Figure 3.4A)**. All these five members target methylated substrate mRNA and exert a specific function that affects their fates in a cell-type-independent manner (Dominissini et al., 2012; Edupuganti et al., 2017; Patil et al., 2017; Wojtas et al., 2017).

Several groups demonstrated the structure of YTH family proteins from different species (Li et al., 2014; Theler et al., 2014; Xu et al., 2014b, 2015). Structurally, the YTH domain belongs to the archaeosine transglycosylase-like and pseudouridine synthase superfamily (Zhang et al., 2010; Cerrudo et al., 2014; Luo and Tong, 2014). This YTH-domain is characterized by a sphere-like fold, with a core of 4–6 parallel β-sheets surrounded by 4–8 α-helixes (Xu et al., 2014b).

In the centre of the YTH domain, at least three conserved residues accommodate the methylated adenosine, comprising the aromatic cage. The m6A marks are usually recognized by these residues, including W411, W465, and W470 in YTHDF1, W432, W486, and W491 in YTHDF2, W377, W428, and L439 in YTHDC1 **(Figure 3.4B)** (Xu et al., 2014b; Huang and Yin, 2018). Like the m6A-methyltransferases and demethylases, critical residues adjacent to the aromatic cage of the reader proteins are crucial for the stability of the methylated RNA in the aromatic cage. Accordingly,

mutation of these residues would abolish binding to methylated adenosines (Li et al., 2014; Theler et al., 2014; Xu et al., 2014b, 2015).

Notably, substrate sequence preference for m6A readers is also noticed, such as m6A writers. YTHDC1 prefers guanosine (G) in the -1 position (i.e., the nucleotide prior to the methylated adenosine). Due to the hydrogen bonds between the Val 382 in the YTHDC1 and G in the GGm6AC. It was recorded that any base other than the (G) in the -1 position affects the binding efficiency of YTHDC1 negatively. Similarly, YTHDC1 prefers (G) and (C) in (-2) and (+1) positions, respectively, in the aromatic cage **(Figure 3.4)** (Xu et al., 2014b).

A
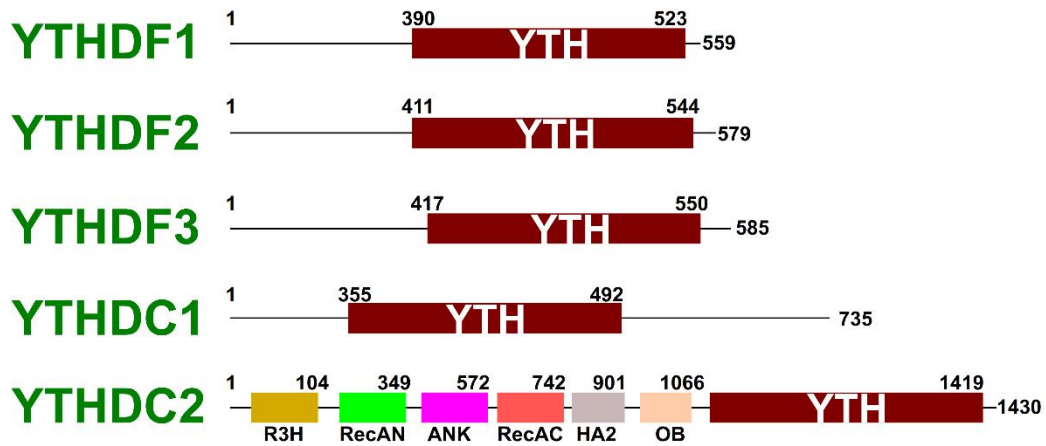
B
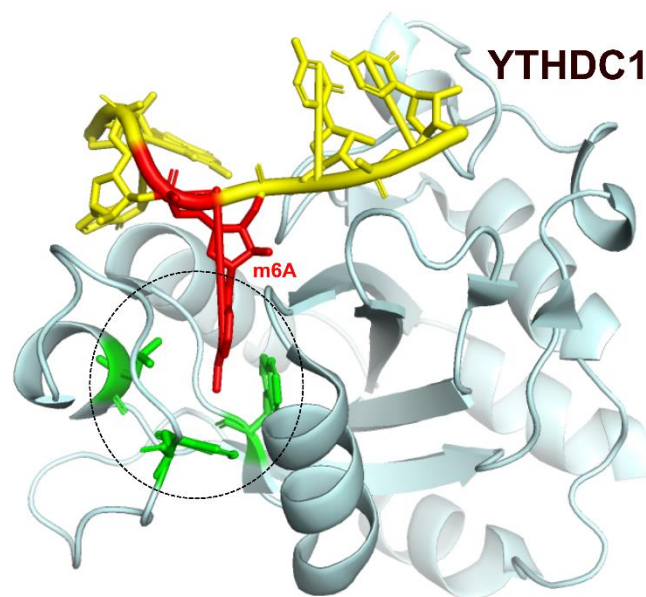
Figure 3.4: Structural insights into m6A-readers. **(A)** Schematic of domain architecture of the YTH-domain family in humans. YTH; YTH-domain fold. R3H; ATP-dependent helicase domain containing conserved arginine (R) and histidine (H) residues. RecA-N and C; helicase domain: conserved helicase N- and C-terminal domain. HA2; HA helicase associated domain. OB; oligonucleotide/oligosaccharide binding domain.

ANK; ankyrin repeat domain. **(B)** The overall 3D structure of the GGACU bounded YTHDC1 (PDB ID: 4R3I). m6A is indicated by red residue. The dotted circle determines the aromatic cage boundaries. The aromatic cage is marked by three green residues; W377, W428, and L439.

During the access of the methylated transcripts into the cytoplasm, the m6A-containing RNA is exposed to RNA-binding proteins, including YTHDF1-3 and YTHDC2. Each of these RNA-binding proteins exerts various functions on methylated RNA according to spatial and temporal contexts (Liao et al., 2018; Shi et al., 2019).

It has been confirmed that YTHDF2 predominantly regulates RNA metabolism via decreasing RNA stability, promoting RNA decay. YTHDF2 acts primarily by enhancing the binding of the target RNA to various processing bodies (i.e., RNA decay sites), thus regulating RNA lifetimes (Wang et al., 2014b). Other reports indicated that YTHDF2 recruits the deadenylase complex named C- C motif chemokine receptor 4 - negative on TATA-less (CCR4–NOT) to enhance RNA decay (Du et al., 2016).

Conversely, YTHDF1 was reported to promote protein translation upon binding to methylated mRNAs through enhancing ribosome loading and binding to initiation factors (Wang et al., 2015). Intriguingly, YTHDF3 was shown to play a synergistic role with YTHDF2 to promote RNA decay or interact with YTHDF1 to enhance protein translation, suggesting the cooperative manner of the cytoplasmic YTHDF1–3 proteins to impact the biological processes (Shi et al., 2017).

Similarly, nuclear YTHDC1 regulates RNA metabolism by promoting exon inclusion to mRNAs through recruitment for certain splicing factors (Xiao et al., 2016). YTHDC1, in co-operation with METTL16, also enhances mRNA stability (Shima et al., 2017). Furthermore, YTHDC2 was reported to improve translation efficiency and promote normal spermatogenesis in mice (Hsu et al., 2017).

Not only are the YTH domain-containing proteins responsible for RNA protein binding to methylated RNA, but newly recognized RNA-binding proteins were also identified to regulate intracellular biological processes. Various heterogeneous nuclear ribonucleoproteins (hnRNPs) were reported to affect the abundance of particular mRNA and promote alternative splicing (Liu et al., 2015).

In contrast to YTHDF2, the newly identified insulin-like growth factor 2 mRNA-binding proteins, including IGF2BP1/2/3, were confirmed to positively regulate RNA stability and protein translation, affecting gene expression outputs through binding to methylated RNA by K homology domains of the IGF2BPs (Huang et al., 2018). Additionally, G3BP1 and FMR1 proteins were found to regulate mRNA stability and translation in an m6A-regulated manner. Interestingly, these proteins work as RNA sequence- and cell-type-dependent m6A-readers (Edupuganti et al., 2017). More recently, the proline-rich coiled-coil 2 A (prrc2A), a newly identified reader, regulated oligodendrocyte functions in an m6A-dependent manner (Wu et al., 2019).

3.1.4. Evolutionary conservation of m6A sites among viruses

The first m6A-seq data revealed that the human m6A methylome is highly conserved with the mouse m6A methylome (Dominissini et al., 2012), indicating the m6A marks are evolutionarily conserved among species. Additionally, the m6A marks in the cellular methylome are enriched primarily on coding sequences, near-stop codons, and 3′ untranslated regions, which is also found conserved among species (Dominissini et al., 2012; Meyer et al., 2012; Ke et al., 2015). The installation of m6A marks is primarily added to the consensus sequence motif. The m6A sites were markedly reported to be enriched in some DRA*CH sequences, where A* represents the methylatable adenosine; D represents any nucleotide, but not C; H represents any nucleotide, but not G; R represents A and G) (Linder et al., 2015; Kim and Siddiqui, 2022).

Similar to the cellular transcripts, the viral m6A-seq analysis of the HIV-1 virus model indicates that various genotypes had conserved m6A sites, given the genome plasticity of HIV-1 (as ssRNA virus model), pointing out that the m6A is also conserved in viruses as well (Kennedy et al., 2016). The m6A conservation is also evident among viruses belonging to the *Flaviviridae* family (Gokhale et al., 2016; Lichinchi et al., 2016b).

Regarding influenza A viruses (IAVs), the virus model in the study here, m6A-seq analysis indicates that influenza carries 24 m6A sites in the entire transcriptome, eight located on the HA mRNA (Courtney et al., 2017). The latter study demonstrated the positive impact of m6A on influenza replication and gene expression. Upon removal of consensus sites preferred for m6A installation, the virus replication gene expression was significantly downregulated.

Potentially IAV replication could be inhibited by disturbing the m6A sites. However, identifying the m6A sites of each strain is not only technically challenging but also very costly. Moreover, viral m6A prediction software is unavailable due to insufficient knowledge about viral m6A methylome.

3.1.5. Chapter Aims

The aim of this chapter was to provide detailed evolutionary and structural analyses of chicken m6A machinery representative of avian species as a primary step to pave the way for studying epitrascriptomics in the veterinary field, and to investigate the conservation pattern of potential m6A sites among IAVs for future virus intervention. The objectives were to determine:

1. Synteny between the m6A-related genes in various orthologues.

2. Structural variations in chicken m6A-methyltransferases, m6A-demethylases, and m6A-readers.

3. Locations of DRACH motifs that coincide with the published m6A-seq data to be used for conservation analysis.

4. Conservation pattern of DRACH signatures among various IAVs subtypes, within subtypes, and the determinants of m6A sites among viruses.

3.2. Chapter Results

3.2.1. Variations in synteny among m6A-related genes

Six species were selected for chromosomal comparative collinearity investigations, compared to humans. The selected species were chosen to represent the evolutionary closely-related level species (i.e., Mammalia, represented by mice) that diverged approximately 40–80 million years (Waterston et al., 2002). Moreover, avian species was selected as intermediate-level species (i.e., Aves, represented by chickens, ducks, and turkeys) that diverged approximately 310 million years from humans (Hillier et al., 2004). Furthermore, a representative of a distantly-related level species (i.e., Osteichthyes, represented by zebrafish) diverged around 450 million years from an ancestor with humans was selected (Frazer et al., 2003).

Although all analysed m6A-related genes were identified in the existing Ensembl databases, some m6A-writer proteins were not annotated. METTL3 was uncharacterized in both the ducks and turkeys. Additionally, METTL14 was not annotated in turkeys so far. A common feature among the studied species was that the m6A-related genes were located in different chromosomes. Genes of m6A machinery were located either on autosomal chromosomes (in humans and zebrafish) or both autosomal and sex chromosomes as identified in avian species and mice **(Figure 3.5)**.

Compared to humans, YTHDF1, YTHDC1, and METTL14 were syntenic (shared the same chromosome number) in chickens, in chromosomes 20, 4, and 4, respectively. Conserved synteny was also observed in some genes between mice and humans (YTHDF3 and METTL3). However, the loss of conserved synteny was evident in other

orthologues, even among avian species. Except for YTHDC2, no synteny was observed in humans and zebrafish **(Figure 3.5)**. In conclusion, loss of conserved synteny was noticed among the investigated m6A-related orthologues.
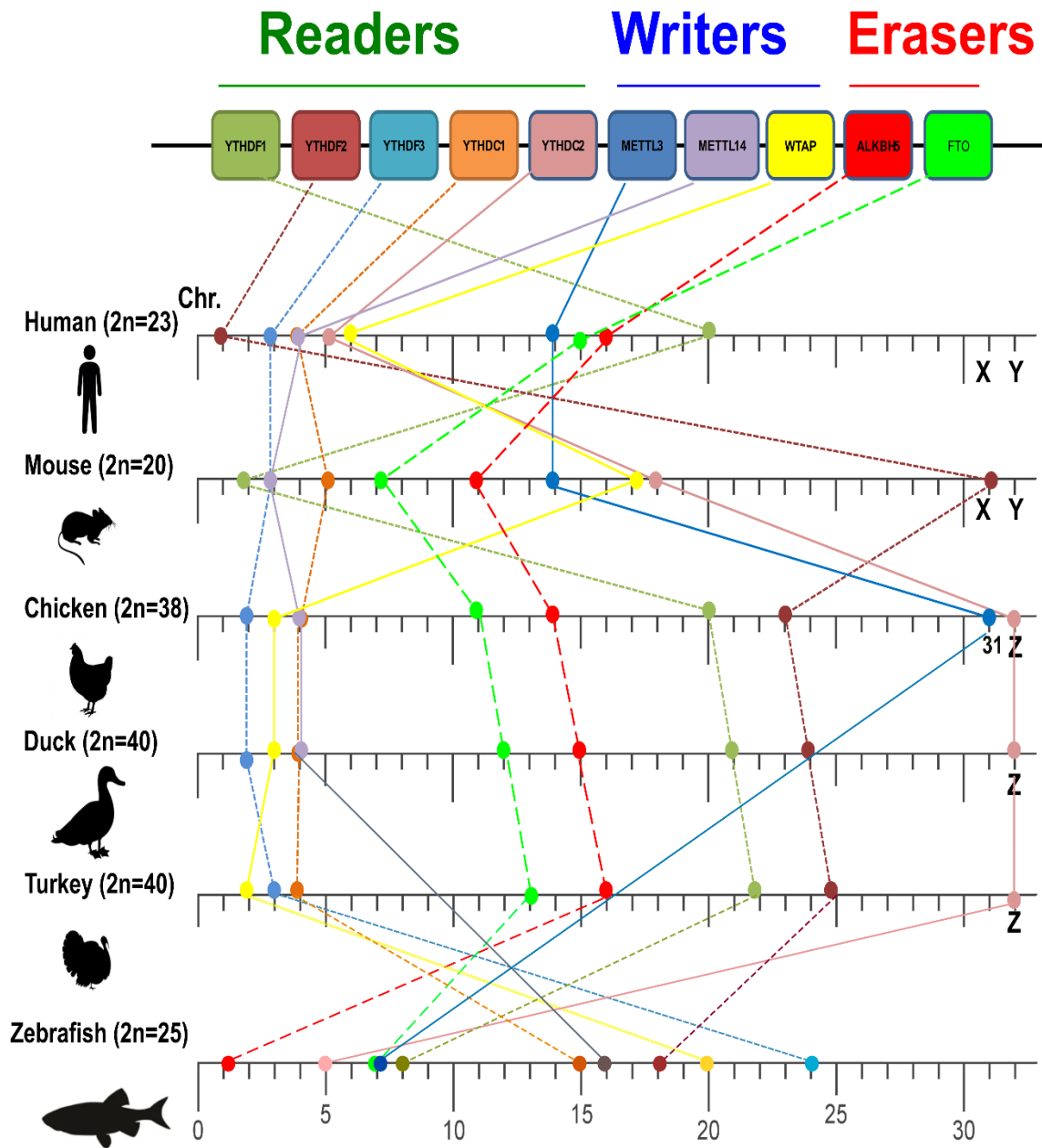
Figure 3.5: Variations in the synteny among m6A-related genes. Chromosome numbers, species, and the numbers of diploid chromosomes are indicated. The figure is adapted from our publication (Bayoumi et al., 2020).

3.2.2. Evolutionary variation in avian m6A-writers

Multiple orthologues representing various orders were analysed to study the genotypic evolutionary variation of avian m6A machinery, including mammals, amphibians, reptiles, and fish. As indicated earlier, the main components of m6A-methyltransferase complex METTL3 and METTL14 are not well characterized in all species. A truncated fragment was identified for METTL3 of turkeys. Interestingly, METTL3 was not identified well in wild birds (data not shown).

All phylograms of the m6A-methyltransferase complex were clustered in a distinct clade from the other orthologues **(Figure 3.6A)**. Additionally, compared with humans, the homology percent of the amino acids between chicken m6A writers differed greatly, showing the lowest percentage of identity in chicken METTL3 (82%) **(Figure 3.6B).** At the same time, the rest of the methyltransferase complex (METTL14 and WTAP) revealed similar phylograms, but higher amino acid homology was recorded (~90% identity).

Generally, the 3D structure of the m6A-writers complex resembles a butterfly, in which three main functional loops were identified in the METTL3 enzyme; gate loop-1, -2, and interface loop, as specified previously (Śledź and Jinek, 2016; Wang et al., 2016b; Huang and Yin, 2018). Compared to humans, no change in the amino acids of the main functional loops was detected in chickens. Moreover, no change in the leader helix (LH) was recorded; the LH was functionally validated as the stimulator for binding with the WTAP in humans (Schöller et al., 2018). However, multiple point mutations were observed in zinc finger-1 (ZnF-1), ZnF-2, and methyltransferase domain (MTD) **(Figure 3.6C)**.

181

Nonetheless, the gate loops revealed misfolding in the predicted structure **(Figure 3.7)**. Furthermore, point mutations were also detected throughout the MTD of METTL14 without affecting the conserved rudimentary catalytic EPPL motif, which is a homologue to the functional catalytic domain in METTL3. Similarly, chicken WTAP showed multiple mutations predominantly in the non-coiled-coil domain (C-terminus) compared to the human orthologue.
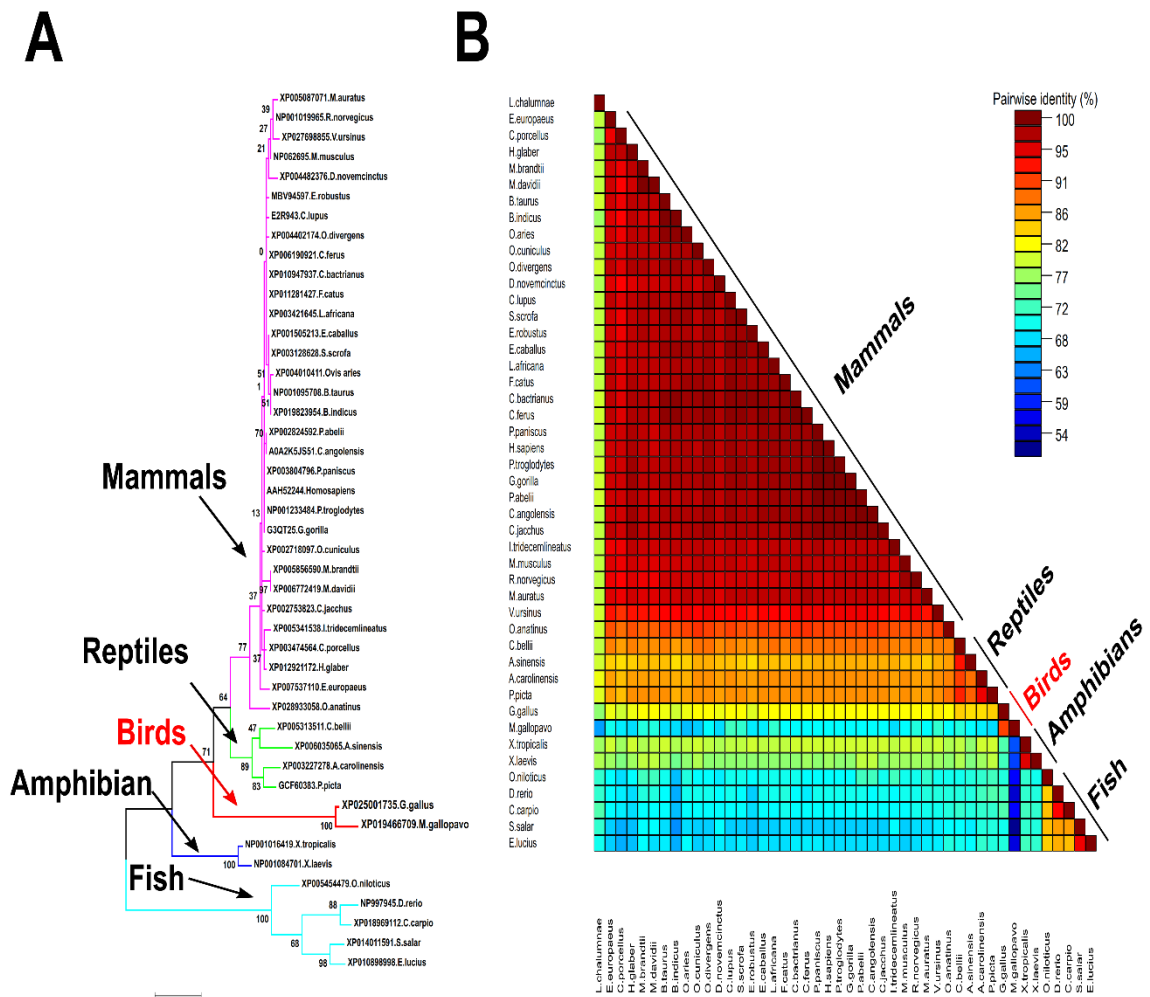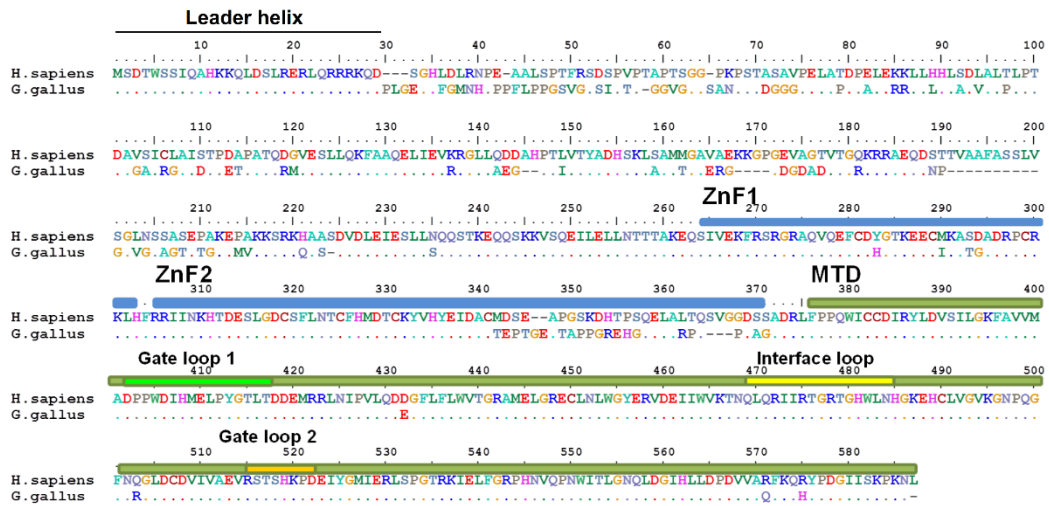
Figure 3.6: The evolutionary variations in avian m6A-writers. **(A)** Phylogram of the amino acid sequence alignment of the entire METTL3 among various species, the phylogram generated by MrBayes. The bootstrap values are illustrated on the left of each node. Error bar is also indicated. **(B)** Pairwise identity percent of the sequence alignment of the entire METTL3 among various species, the plot generated by the SDT program. The amino acids were aligned with the MUSCLE algorithm. The identity percentage is also shown in the coloured scale bar. **(C)** Sequence alignment of chicken and human METTL3 proteins. Identical letters are represented by dots, whereas point mutations are indicated by coloured letters. The figure is adapted from our publication (Bayoumi et al., 2020).
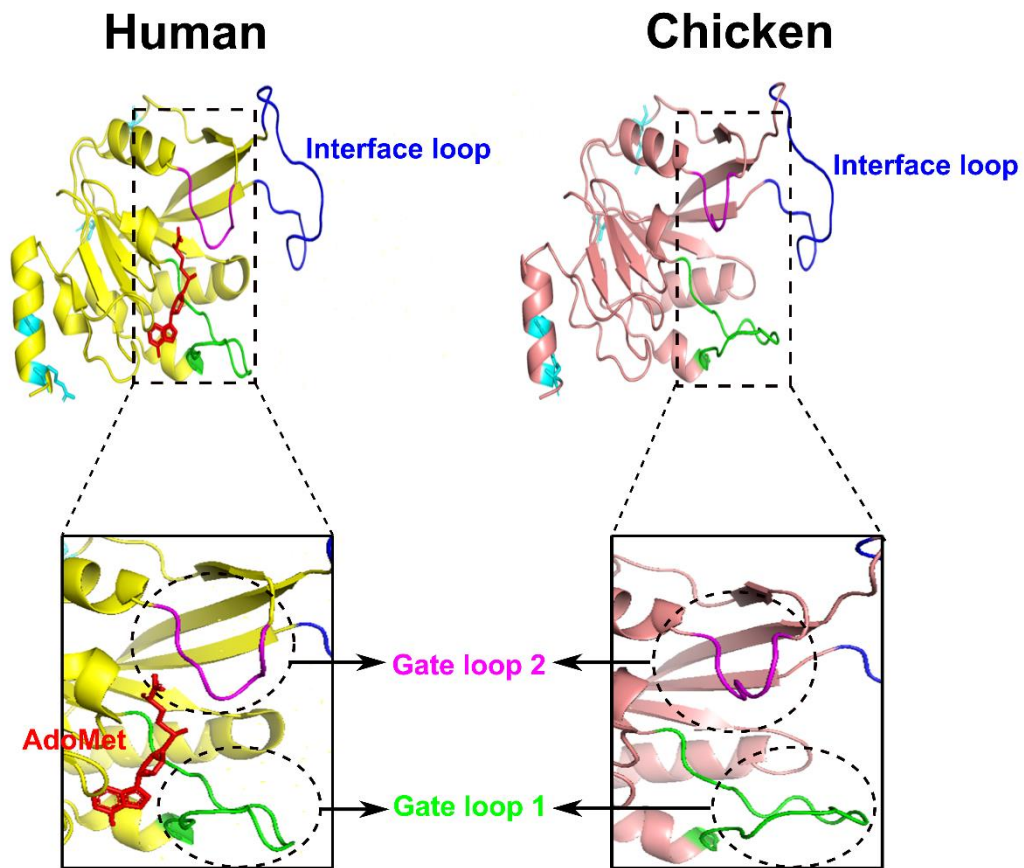
Figure 3.7: Structural comparison between human and chicken METTL3s. The methyltransferase domains of human METTL3 (PDB ID: 5IL1; left) and the predicted chicken domain (right) are illustrated. Cyan sticks represent point mutations. The prediction was performed using I-Tasser and Phyre2 and visualized and annotated using PyMoL. ZnF: Zinc finger, MTD: Methyltransferase domain. The figure is adapted from our publication (Bayoumi et al., 2020).

3.2.3. Evolutionary variation in avian m6A-erasers

Compared with human m6A machinery, the amino acid identity percentage was recorded as the lowest in avian FTO (55–64%), whereas avian ALKBH5s shared about 80% identity with human orthologues **(Figure 3.8A)**. Like, chicken writers, Bayesian inference (BI) phylograms grouped chicken m6A-demethylases into a distinct cluster with duck genes showing a higher divergence than chicken and turkey. Amphibians and fish were extensively distant in both phylograms **(Figure 3.8B)**.

Regarding multiple sequence alignment (MSA) of m6A-erasers, the Fe^{2+} co-ordinated residues (HxD.H) were conserved in almost all compared species, as indicated in FTO **(Figure 3.9A)**. Even though avian species have consistent, distinctive amino acid mutations, the critical amino acid residues that are supposed to reside in the catalytic domain were conserved with humans, including Ile 85, Tyr 108, Leu 109, Val 228, Ser 229, and Trp 230 **(Figure 3.9A)**.

Additionally, the characteristic long loop 1 of FTO (L1) in avian species revealed an E200Q mutation. Interestingly, a consistent Q86K mutation in avian species was also noticed in FTO; binding efficiency has been reported to be enhanced in human FTO that harbour this induced mutation (Zhang et al., 2019d). Moreover, the visible surface of FTO showed unique inserts of 8–11 amino acids between the α4- and α5-helices in avian species **(Figure 3.9A, B)**. Although FTO showed the lowest amino acid identity, the 3D prediction of avian demethylases showed a higher structural similarity with human FTO through synonymous structural mutations **(Figure 3.9C)**.
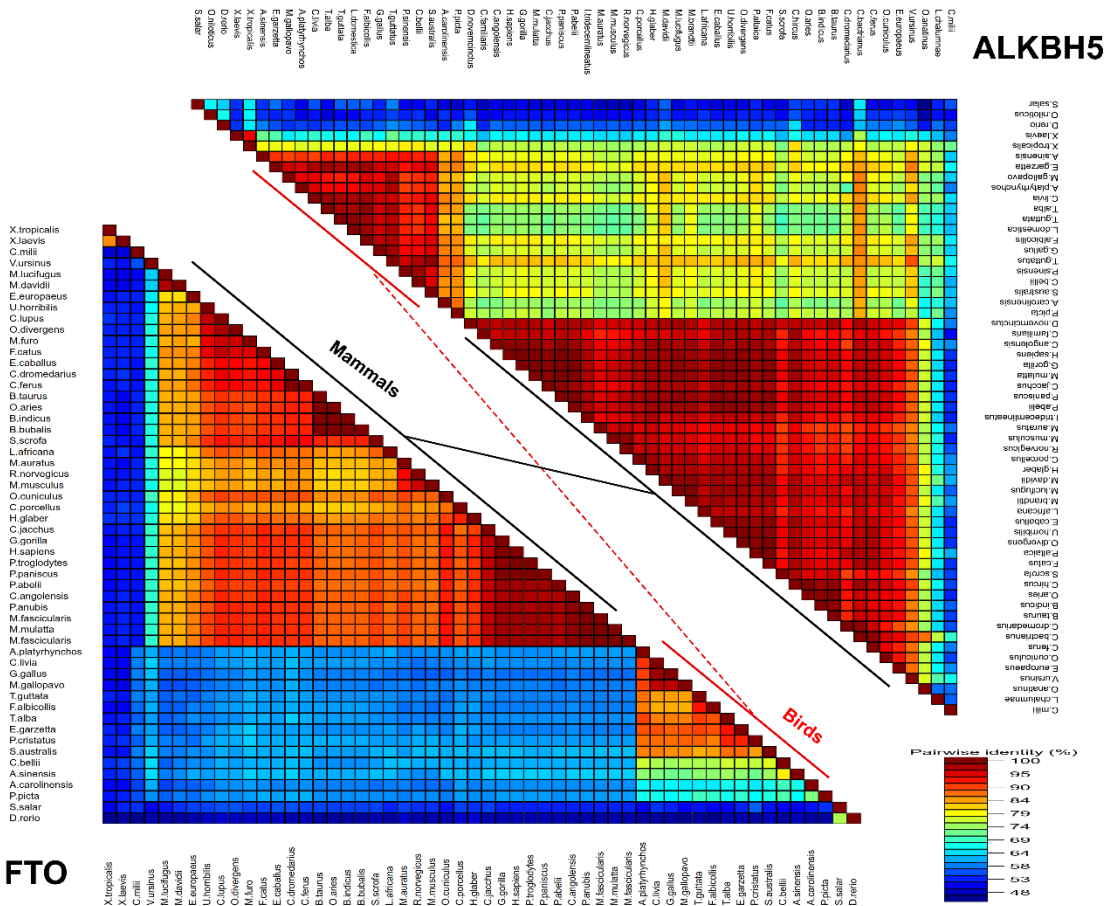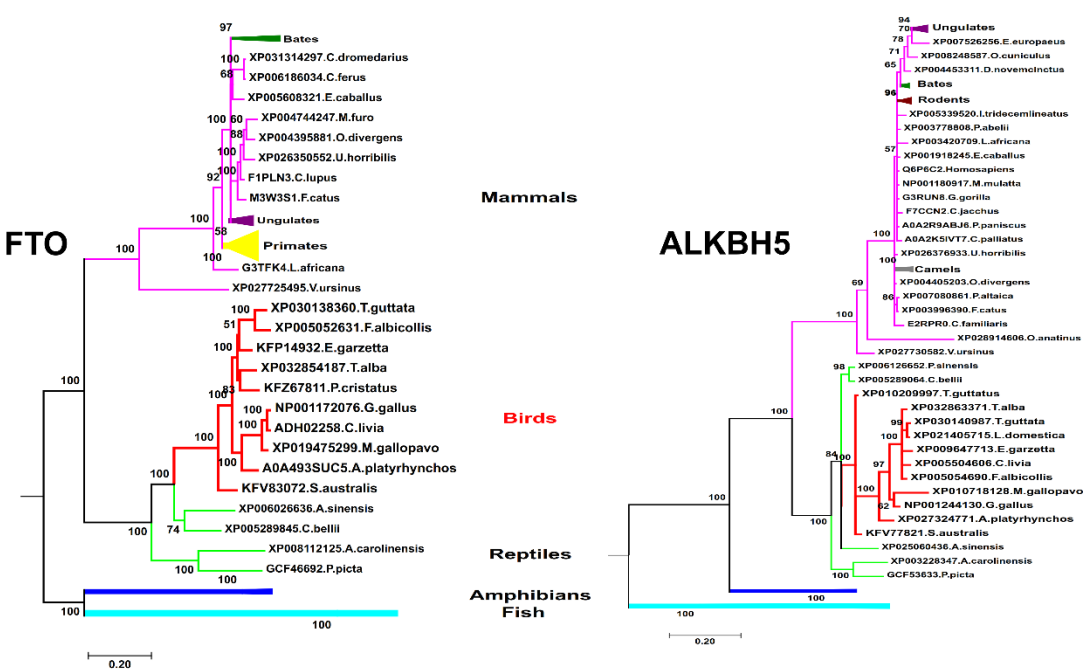
Figure 3.8: The evolutionary variations in avian m6A-erasers. **(A)** Pairwise identity percent of the sequence alignment of the entire m6A-erasers among various species, the plot is generated by the SDT program. The amino acids were aligned with the MUSCLE algorithm. The identity percentage is also indicated in the scale bars. **(B)** Phylograms of the amino acid sequence alignment of the entire m6A-erasers among multiple species. The phylograms are generated by the MrBayes program. The bootstrap values are illustrated on the left of each node. The figure is adapted from our publication (Bayoumi et al., 2020).
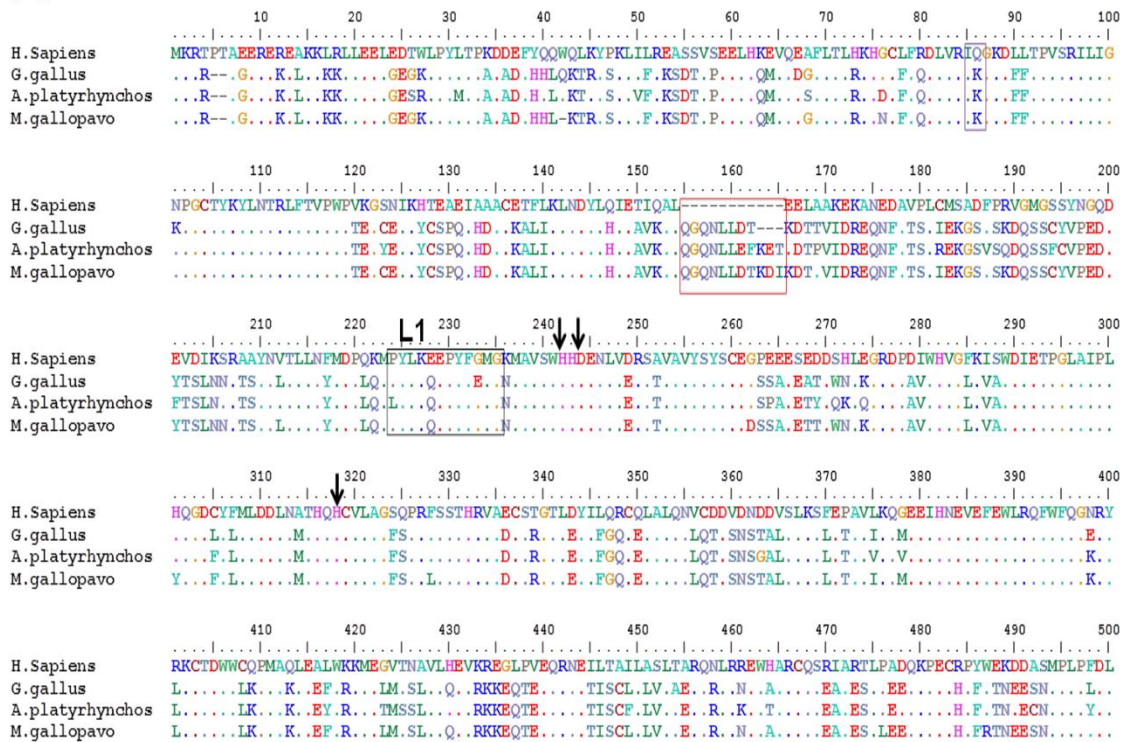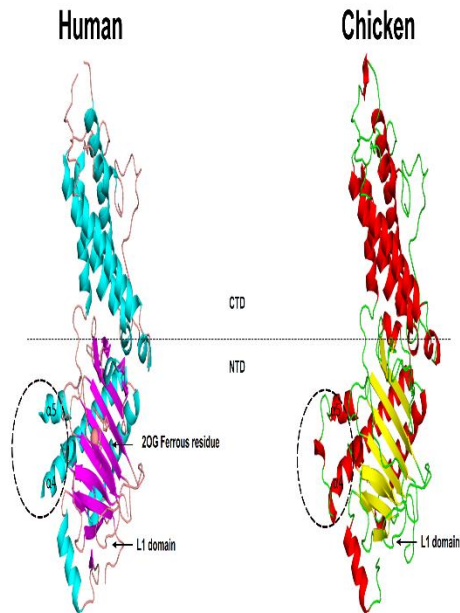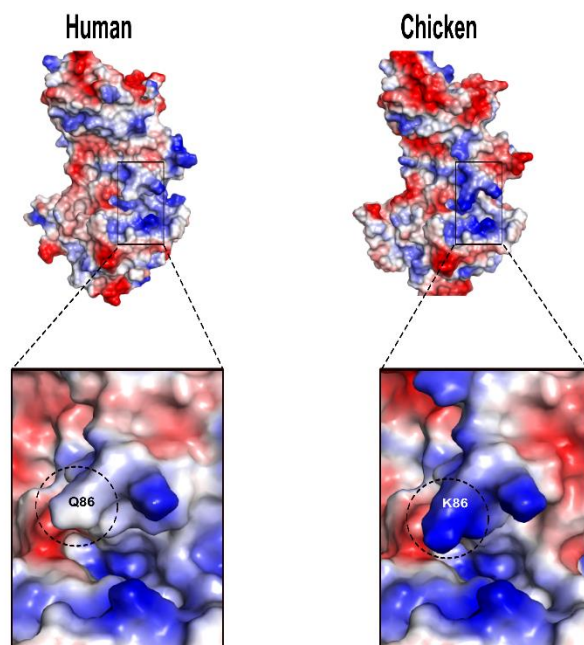
Figure 3.9: Structural alterations between human and chicken FTOs. **(A)** Sequence alignment of the entire FTO sequences between chicken and humans. The insertions, unique loop (L1), and Q86K mutation in avian proteins are represented by red, black, and blue boxes, respectively. **(B)** The entire 3D structure of human FTO (PDB ID: 3LFM) and the predicted chicken FTO are illustrated. The amino-terminal and carboxyl-terminal domains are indicated as NTD and CTD, respectively. The long loop 1 (L1) is also indicated. **(C)** The electrostatic surface illustrates the Q86K mutation, and the blue-to-red colours indicate basic-to-acid amino acids. The prediction was performed using I-Tasser and Phyre2 and visualized and annotated using PyMoL. The figure is adapted from our publication (Bayoumi et al., 2020).

3.2.4. Evolutionary variation in avian m6A-readers

Albeit the phylograms of the avian m6A-readers showed the same pattern as described in m6A-methyltransferases and demethylases, the avian YTHDF2 was grouped with mammalian orthologues. Amphibians were found to lack the YTHDF2 among the YTH-domain family **(Figure 3.10A)**. Among avian m6A machinery, the highest amino acid homology percentage was found in m6A-readers, except in YTHDC2, recording 85–96%. Percent identities of all species were represented in **(Figure 3.10B)**.

The amino acid multiple sequence alignment (MSA) showed several consistent point mutations reflecting the avian evolutionary pattern, with a higher degree of conservation in the YTH domain. In the YTH domain of YTHDF2, no mutations were recorded. Only one and three mutations were recorded in the YTH domains of YTHDF3 and YTHDF1, respectively (data not shown).

Regarding YTHDC1, Trp-377, Trp-428, and Leu-439 residues constitute the hydrophobic residues at which m6A residues were supposed to be buried and were also conserved in all investigated species (Liao et al., 2018). Moreover, Asn-363, Asn-367, and Ser-378 residues also jointly form H-bonding with the m6A base that was conserved in the avian species. Overall, all these conserved residues in the YTH domain propose a conserved strategy for m6A recognition in almost all eukaryotic species **(Figure 3.10C, D)**.

Uniquely, an insert of 45 residues was noticed in chicken YTHDC1, and a deletion of 14 residues was also found from all investigated avian species compared with humans **(Figure 3.10C, D)**. So far, no available published data on the entire YTHDC1 molecule

has been found to delineate the functions of these mutations. Only three consistent mutations were found in the avian YTHDC1-YTH domain **(Figure 3.10D)**. The predicted 3D structure of the avian YTH domain of YTHDC1 showed a similarity to the characterized human protein. However, the aromatic cage for m6A recognition was found wider in the chicken YTH- domain; however, the three detected mutations in the avian species did not disturb the predicted structure **(Figure 3.11)**.
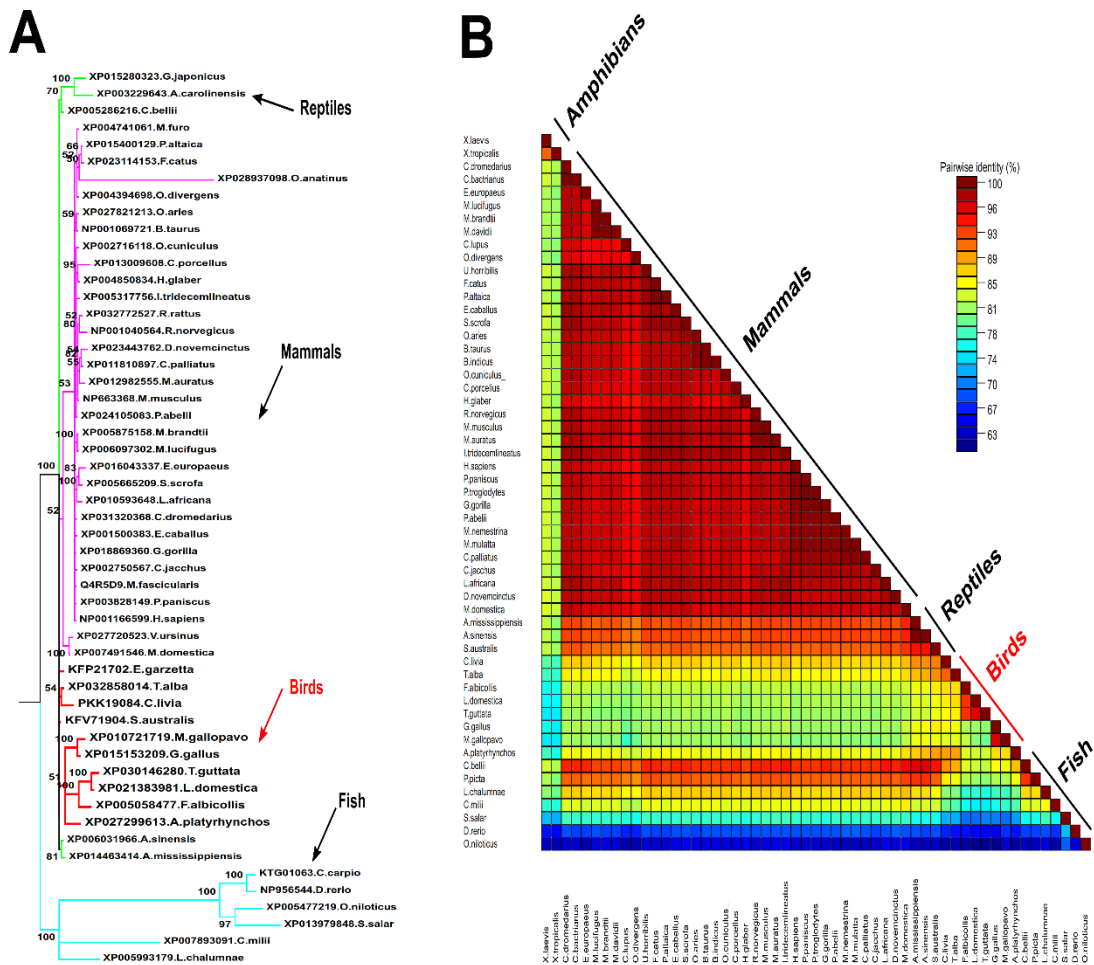
Figure 3.10: The evolutionary variations in avian m6A-readers. **(A)** The phylogram of the amino acid sequence alignment of the entire YTHDF2 protein among various species is the phylogram generated by MrBayes. The bootstrap and error bars are indicated. **(B)** Pairwise identity percent to the sequence alignment of the entire YTHDC2 protein among various species, the plot generated by the SDT program. The identity percentage is indicated in a scale bar. The amino acids were aligned with the MUSCLE algorithm. **(C)** Schematics of human and chicken YTHDC1 domain architectures, insertion, and deletions are shown. **(D)** Sequence alignment of some avian and human YTHDC1 proteins. The insertion and deletion in chicken amino acids are marked by blue and red rectangles.
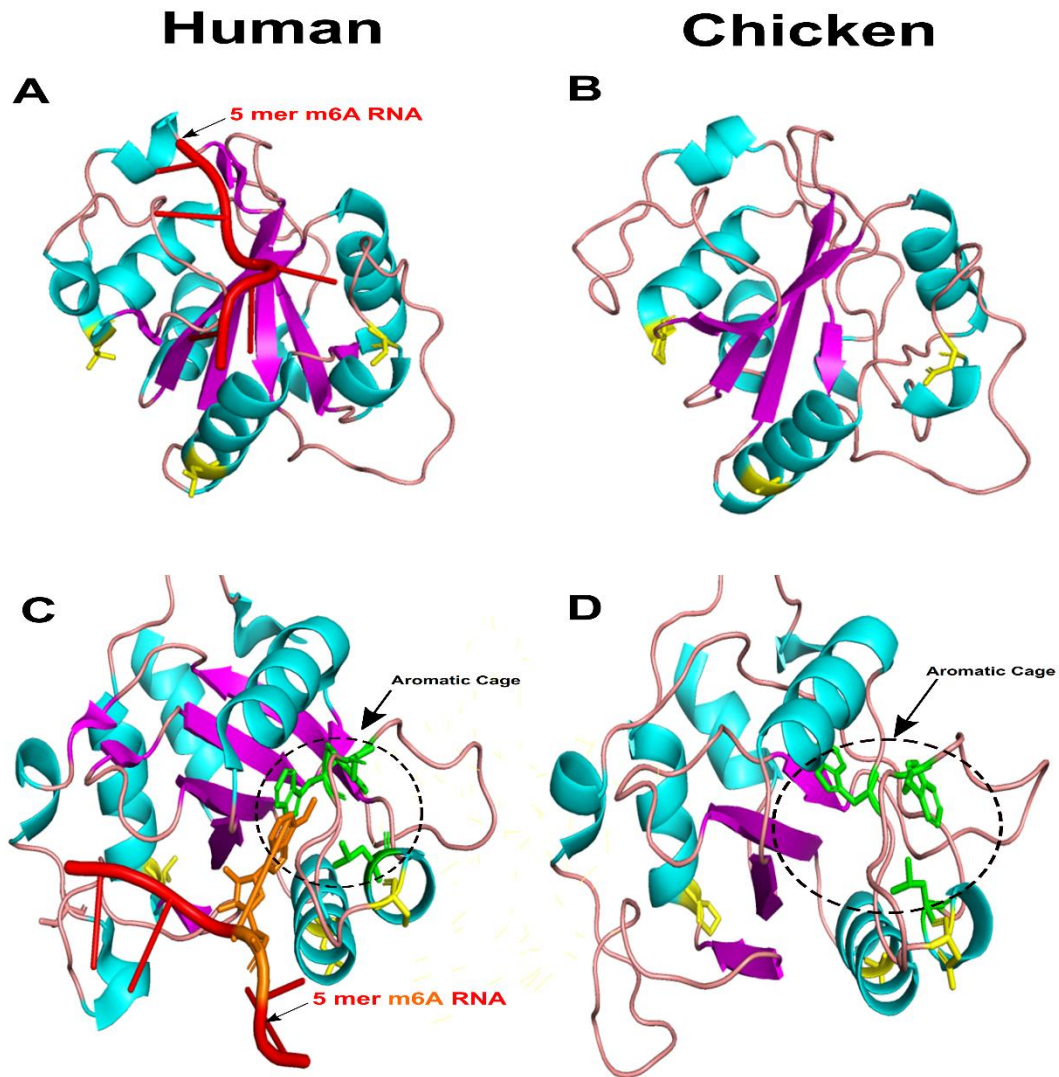
Figure 3.11: Structural comparison between human and chicken YTHDC1s. **(A and C)** The YTH- domains of human YTHDC1 (PDB ID: 4R3I). **(B and D)** The predicted chicken domain. Point mutations are represented by yellow sticks. The prediction was performed using I-Tasser and Phyre2 and visualized and annotated using PyMol. The hydrophobic aromatic cages are indicated by dotted circles. The figure is adapted from our publication (Bayoumi et al., 2020).

3.2.5. Identification of potential m6A-sites in the reference HA gene of IAVs

To identify common m6A sites among IAVs, a reference sequence with specified numbers and locations of m6A sites is essential. The epitranscriptome meta-data on IAV H1N1 was utilized (Courtney et al., 2017). In this study, authors identified nine and eight m6A-sites in vRNA and mRNA, respectively across the entire HA gene (**Figure 3.12**). The HA gene is the only gene that has publicly available epitranscriptome data. Thus, the main focus on investigating m6A sites among the entire HA gene in both mRNA and vRNA was adopted.

In this regard, the influenza research database was utilized to collect and compare HA sequences among IAVs. A total of 769,880 sequences were listed in the Influenza Research Database (IRD; as of September 15th, 2022) of which 96,449 sequences were listed as HA sequences. Among those HA sequences, 70,100 were identified as unique HA sequences. These unique sequences were used for the comparative analysis.

The eight m6A sites identified in mRNA of HA gene (the reference sequence A/Puerto Rico/8/34/Mount Sinai strain (accession number: AF389118)) were recognized and validated by synonymous mutations to 12 out of 14 (5'R<u>m6A</u>C3') sites (R=A or G) as sites were not mapped in a single nucleotide-based level. Similarly, the nine m6A sites identified on the vRNA of the HA gene were validated by silent mutations to 12 (5'R<u>m6A</u>C3') sites as well (Courtney et al., 2017).

In the publicly available data, the authors depend on the short Rm6AC sequences to mutate and validate m6A sites; however, the wider DRACH was adopted for the conservation analysis (D= any nucleotide but not C, H= any nucleotide but not G). Additionally, the 14 DRACH motifs were used for the study (the 12 RAC sites validated

in the H1N1 analysis + 2 sites corresponding to the metadata of the epitranscriptome of mRNA of HA) **(Figure 3.13A)**.

Three Rm6AC sites identified in the reference HA gene did not match the broader DRACH motifs, which indeed differ in D and H sites **(Figure 3.13A)**. The 14 DRACH motifs were distributed across the reference HA sequence. However, more than one motif was mapped in the middle and end of the HA gene **(Figure 3.13A)**. The 14 DRACH motifs exhibited various diversity and conserveness according to WebLogo analysis **(Figure 3.13B)**.

Like mRNA, 12 DRACH sites were utilized for further analysis of vRNA of the HA. These 12 DRACHs were coincident with the nine verified motifs in the epitranscriptome data **(Figure 3.13C and D)**. Overall, DRACH motifs could be more representative than the short Rm6AC motifs for the computational analysis of the potential m6A sites among HA genes.
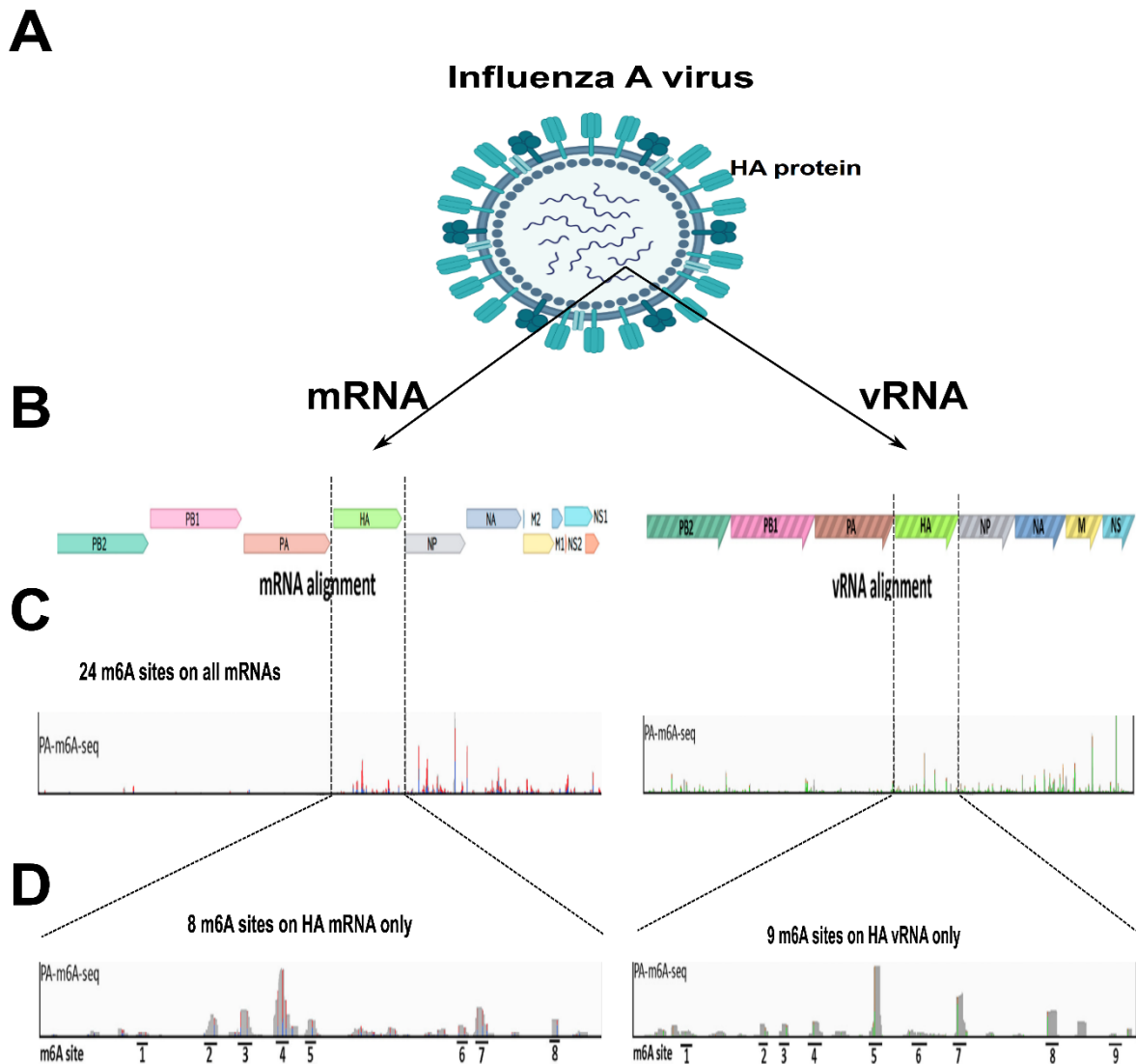
Figure 3.12: Rationale of the design of the conserved DRACH sites among influenza A viruses depending on the verified m6A sites. **(A)** The schematic of IAV contains eight segments, including HA. **(B)** Concatenated map of the IAVs transcripts. The vRNA and mRNA are indicated **(C)** Identification of 24 m6A sites on IAV H1N1 PR8 strain on +/- strands represented by PA-m6A-seq data. **(D)** An expanded view of the PA- m6A-seq data on HA mRNA/vRNA shows that the eight/nine m6A sites on the HA strand are indicated. C and D are adapted from a previous study (Courtney et al., 2017).
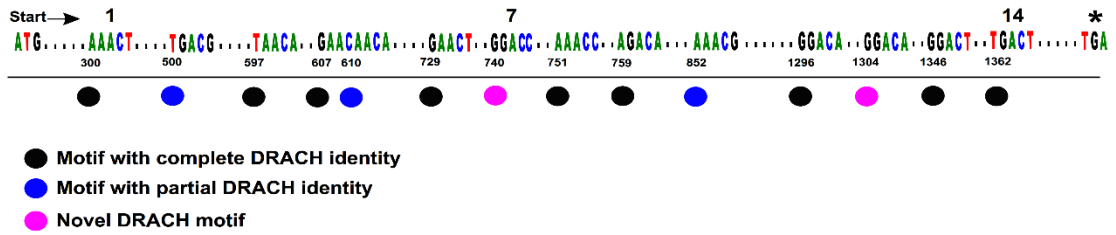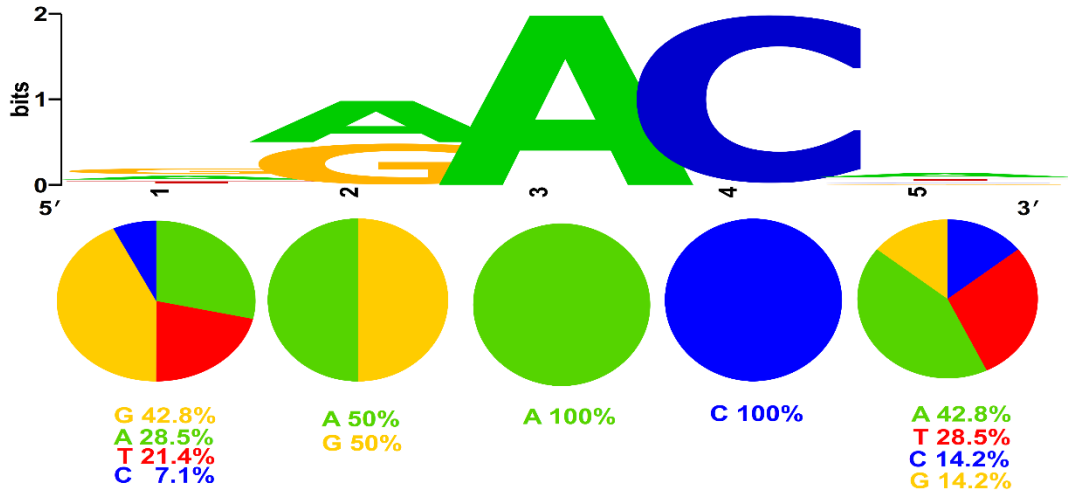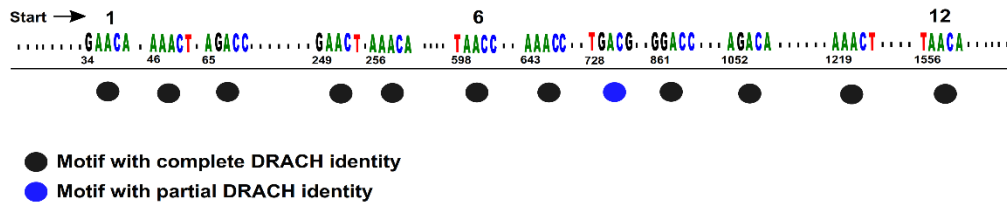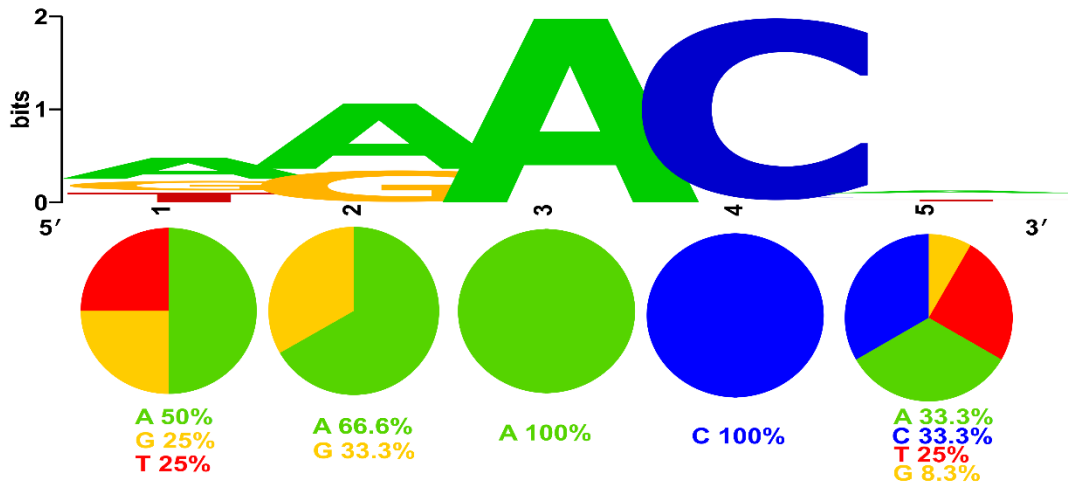
Figure 3.13: Locations, conserveness, and diversity of the identified DRACH motifs. Schematic representation of the potential motifs on the reference HA mRNA **(A, B)** and vRNA **(C, D)** that coincides with the m6A peaks identified in **(Figure 3.12)** (Courtney et al., 2017). Coloured circles indicate motifs containing the complete, partial, and novel DRACH. (**B, D**) WebLogo-based conserveness and diversity of nucleotides in the proposed DRACH motifs in HA mRNA (B) and vRNA (D). The height of each stack represents the sequence conservation. The relative frequency of each nucleotide is represented by the height of the letter in each stack. Coloured pie charts show the percent of each nucleotide in each position. The figure is adapted from our publication (Bayoumi and Munir, 2021a).

3.2.6. The pattern of DRACH conservation among the H1 subtype

To identify the conserved DRACH motifs among subtypes, a comparative analysis of each subtype against the reference HA strain A/Puerto Rico/8/34/Mount Sinai strain (accession number AF389118) was performed. In the study, investigating each subtype (i.e., H1, H2, H3…etc.) was adopted, then extended the investigation within the same subtype (i.e., H1N1, H1N2, H1N3, …etc.), then to investigate the affected species, location or years. Starting with the H1 subtype, which infects mainly humans and pigs, representing almost one-third of all HA sequences deposited on the IRD (approximately 36%). A total of 25,611 HA sequences were investigated.

The generated consensus sequence of the H1 subtype was found to harbour 40 typical DRACH sites on the entire HA. Six motifs were found to be highly conserved compared to the previously determined 14 DRACHs of interest, with a conservation percentage ranging between 85-99%, as listed in **(Table 3.1)**. In the comparative analysis of motifs, the full DRACHs was only considered. Although the 5th motif was detected in 85% of the sequences, a putative m6A site was not consider (data not shown). In conclusion, six DRACHs were conserved in H1 sequences, which grouped in the middle and end of the HA mRNA **(Table 3.1)**.

mRNA	Seq no.*	DRACH^	Motif1	Motif2	Motif3	Motif4	Motif5	Motif6	Motif7	Motif8	Motif9	Motif10	Motif11	Motif12	Motif13	Motif14
H1N1 PR8[1]	1	40	✓	✓	✓	✓	✓	✓	✓	✓	✓	✓	✓	✓	✓	✓
H1	25,576	40						✓95%	✓99%		✓90%		✓85%	✓99%	✓99%	
H2	618	36	✓65%			✓95%			✓99%		✓50%			✓99%	✓99%	✓50%
H3	23,286	42		✓90%					✓99%	✓90%	✓90%					✓85%
H4	1,646	51		✓65%		✓65%			✓99%	✓50%			✓65%			✓85%
H5	5,472	34							✓99%	✓75%				✓99%	✓99%	✓75%
H6	1,836	40			✓85%					✓75%				✓99%	✓99%	
H7	2,237	45						✓50%			✓50%		✓95%			✓50%
H8	168	48		✓95%								✓85%	✓50%		✓95%	✓65%
H9	6,408	43		✓99%						✓90%					✓99%	
H10	983	45							✓95%	✓50%			✓95%			
H11	781	38	✓50%			✓75%			✓95%	✓75%			✓90%		✓90%	
H12	337	46		✓90%		✓75%				✓85%			✓85%		✓95%	
H13	409	43													✓95%	
H14	35	44						✓100%								✓100%
H15	16	44											✓50%			
H16	217	41													✓99%	
H17	2	41											✓100%		✓100%	
H18	2	47				✓100%									✓100%	

Table 3.1: Summary of conserved DRACHs identified in IAVs HA mRNAs. * The total number of HA sequences identified on the influenza research database. [1] The reference strain is A/Puerto Rico/8/34/Mount Sinai, HA accession no. AF389118. ^The number of the typical DRACH motifs identified in the entire consensus sequence of each subtype. The table is adapted from our publication (Bayoumi and Munir, 2021a).

3.2.7. The pattern of DRACH conservation among H3, H5, and H9 subtypes

Similarly, the H3, H5, and H9 sequences were investigated to extend the conservation pattern analysis to other subtypes. These major IAV subtypes constitute approximately 50% of the sequences deposited in the influenza research database, as listed in **Table 3.1**. Additionally, these subtypes infect various animals, avian species, and humans around the globe. Regarding the conservation pattern of identified DRACHs in the H3 sequences, only five DRACHs were shared with the reference HA; 2, 7–9, and 14. The conservation percent detected ranges between 85% and 99%, as shown in **Table 3.1**. Concerning H5, 5 DRACHs out of the 14 were also conserved with the reference H1N1 PR8 strain. Additionally, the conserved motifs followed the same clustering pattern in the middle DRACH-7 and -8 and end of HA gene DRACHs 12-14 with a conservation percent range between 75-99% **(Table 3.1)**.

Unlike the H3 and H5 subtypes, the H9 subtype showed only three conserved DRACHs; at the start, middle, and end of the HA gene. However, all three share the highest conservation percentage (90–99%). To sum up, H3, H5, and H9 subtypes shared a considerable DRACH conservation compared with the reference HA. However, they varied in the clustering location of the conserved DRACHs, either in the middle of HA (H3), or end of HA (H5), or well separated across the reference HA (H9).

3.2.8. The pattern of DRACH conservation among the rest of the IAVs subtypes

The rest of the HA sequences were investigated to extend the comparative computational analysis among IAVs. These minor IAVs subtypes comprise approximately less than 13% of the sequences deposited on the influenza research database, as listed in **Table 3.1**. These subtypes infect mostly various avian species (H10–16) and bats H17 and H18. Each subtype was analysed with the reference PR8 HA strain. Unlike the significant HA-containing subtypes, these subtypes shared the lowest conserved DRACHs among IAVs.

Motif -11 was the most conserved in H7, and motifs-7 and -14 were the most conserved in H4. Importantly, motif-11 and -13 were still the most conserved among HA subtypes affecting avian species. Motif-13 was the highest conserved in the HA subtypes that were found to affect bats. Interestingly, some uncommon conserved DRACHs were noticed in these HA sequences; DRACH-1 in H11 and H2, DRACH-3 in H6, and DRACH-10 in H8 with varying degrees of conservation, as listed in **Table 3.1**. It is important to note that 3' end DRACHs were also conserved in avian and bat species. DRACHs-13, -11, and -7 were the highest among all investigated sequences (**Table 3.1**).

3.2.9. The pattern of DRACH conservation among different hosts and viruses within the subtypes

After investigating the conservation of DRACHs in each subtype compared to the reference HA sequence, the pattern of DRACH conservation among different hosts and certain viruses within the subtypes was further investigated. For this, essential viruses and subtypes of public health importance in terms of pathogenicity, further subtyping, geographic locations…etc were investigated. A detailed comparative analysis of H1N1 sequences was performed. H1N1 sequences constitute approximately 80% of the sequences deposited in the influenza research database within the H1 subtype. Thus, it is unsurprising that the prototype six DRACHs out of the 14 were still conserved in H1N1 sequences **(Table 3.2)**.

A comparison between pandemic and non-pandemic sequences was also performed to investigate the effect of DRACHs conservation on pathogenicity. No apparent variation was identified in the six conserved DRACHs among all affected countries. However, DRACH-8 was found as an extra-motif in half of non-pandemic sequences. Additionally, some variations were noticed between viruses within the H1 sequences. Swine H1N1 showed an extra DRACH-14 with a loss of DRACH-11 compared with human H1N1. H1N2 lost DRACH-9 in human and swine HA sequences. Interestingly, DRACHs-6, -7, -12, and -13 were the most conserved motifs regardless of virus, pathogenicity, species, and geographic distributions **(Table 3.2)**. Regarding sequences with the H2 subtype, human H2N2 lost DRACH-14, and mallard H2N2 lost DRACH-1. Moreover, human H3N2 sequences were unique in sharing DRACH-14 compared to avian and swine sequences **(Figure 3.14)**.

Most importantly, the zoonotic H5N1, H7N9, and H9N2 sequences that were isolated from humans were maintained the same conserved DRACHs of the prototype chicken viruses **(Figures 3.14 and 3.15)**. Overall, the identified DRACHs seemed to be virus-specific rather than species-, host-, pathogenicity-, and geographic distribution-specific.
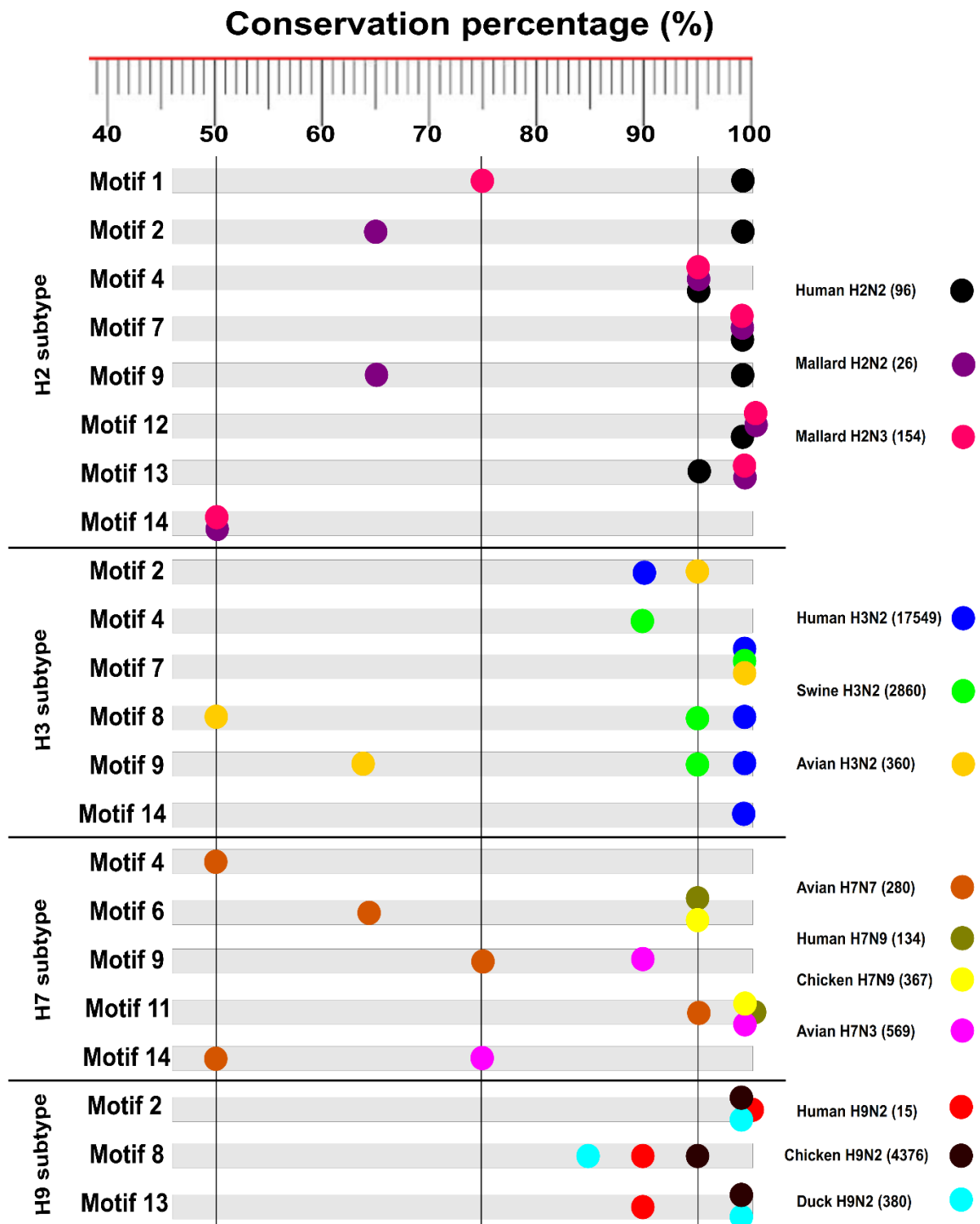
Figure 3.14: Summary of conserved DRACHs between key IAVs. Conserved motifs of mRNA, host species, virus, and the number of sequences deposited on IRD are indicated. The conservation percentage is displayed on the upper scale. The figure is adapted from our publication (Bayoumi and Munir, 2021a).
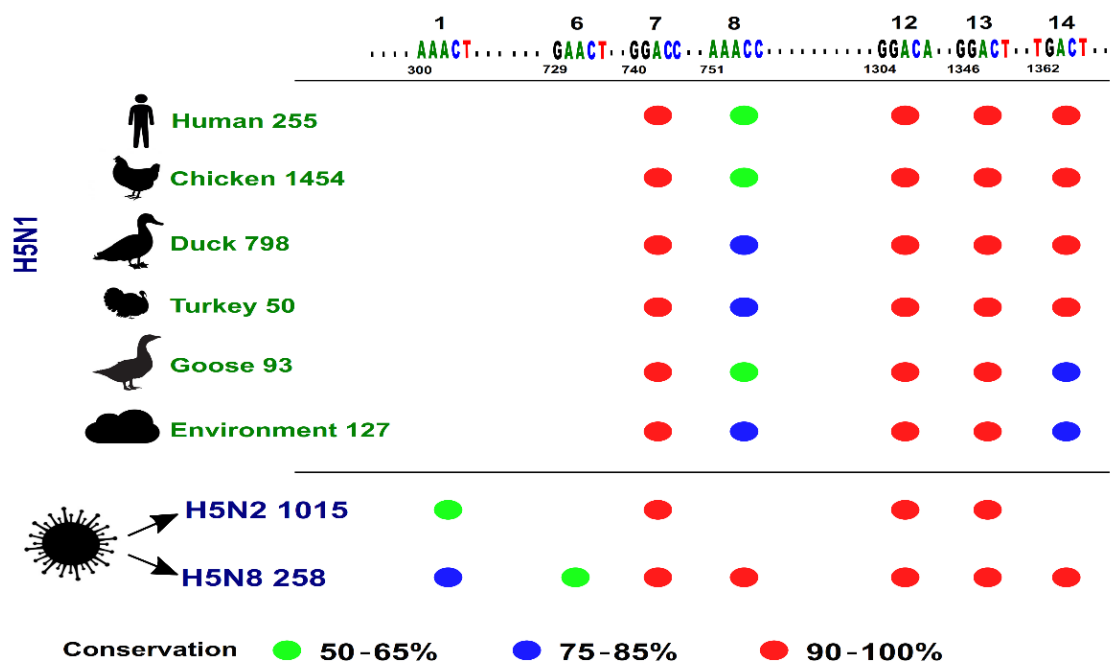
Figure 3.15: Summary of conserved DRACHs between mRNA of the H5 IAV. Conserved motifs on mRNA, host species, virus, and the number of sequences deposited on IRD are indicated. Coloured dots indicate the conservation percentage. The figure is adapted from our publication (Bayoumi and Munir, 2021a).

Table 3.2: Summary of conserved DRACHs among different species and viruses located on the mRNA of the H1 subtype. The table is adapted from our publication (Bayoumi and Munir, 2021a).

mRNA	Seq no.	Motif2	Motif6	Motif7	Motif8	Motif9	Motif11	Motif12	Motif13	Motif14
H1	25,576		√95%	√99%		√90%	√85%	√99%	√99%	
Human H1N1	16,471		√95%	√99%		√90%	√90%	√99%	√99%	
-Pandemic H1N1	10,993		√99%	√99%		√99%	√99%	√99%	√99%	
-Non-pandemic H1N1	5,490		√95%	√99%	√50%	√65%	√99%	√99%	√99%	
Swine H1N1	4,366		√50%	√95%		√95%		√99%	√99%	√65%
Human H1N2	43		√95%	√100%	√90%		√99%	√99%	√99%	
Swine H1N2	3,614	√50%	√90%	√95%	√65%		√75%	√99%	√99%	√65%

3.2.10. The pattern of DRACH conservation among IAVs HA vRNA

As a negative sense RNA virus, the conservation pattern of potential m6A sites on vRNA was also investigated. Nine m6A sites were previously determined across vRNA of the HA of the PR8 reference sequence (Courtney et al., 2017). The 9 m6A sites were coincident with 12 RACs, which were also functionally validated by synonymous mutations. Thus, the broader putative m6A site (the DRACH motifs) for further comparative analysis was adopted, as indicated earlier in mRNA.

Similarly, the putative motifs were distributed across the length of the vRNA of IAVs **(Figure 3.13C)**. Next, the twelve DRACHs among all HA subtypes as performed for the mRNA sequences was compared. It was apparent that motif-8 out of the 12 motifs did not match the broader DRACH, which was later found non-conserved among H1 sequences **(Table 3.3)**. Remarkably, DRACH numbers in the consensus sequence in vRNA in each subtype were found to be much lower than the mRNA (less than half the number of mRNA).

DRACH conservation was analysed per each subtype of IAV. Similar to mRNA, H1 and H3 sequences had the most conserved DRACHs. However, in H9 viruses, DRACH-5 was the sole conserved motif. Additionally, low-conserved DRACHs were found in the HA subtypes that infect wild avian species and bats. DRACHs-5, -7, and -11 were the most conserved motifs among the vRNA of IAVs, while DRACHs-2, -4, and -12 were the least conserved among IAVs **(Table 3.3)**.

After investigating the conservation of DRACHs in each subtype compared to the reference HA sequence, the pattern of DRACH conservation among different hosts and

certain viruses within the subtypes was investigated. H1N1 sequences showed maintenance of the 4 conserved DRACHs as identified in all H1 subtypes **(Table 3.3 and 3.4)**.

The pH1N1 was found to gain an extra DRACH-2 in vRNA (50%) of the analysed sequences. This observation was in contrast to what was seen in mRNA sequences. However, both share the same conserved 4 DRACH motifs **(Table 3.4)**. Additionally, compared to human sequences, swine H1N1 gained an extra DRACH-2. Four motifs were conserved regardless of viruses, pathogenicity, species, and geographic distributions **(Table 3.4)**. Overall, vRNA sequences showed a lower number of total and conserved DRACHs among IAVs **(Figure 3.16)**.
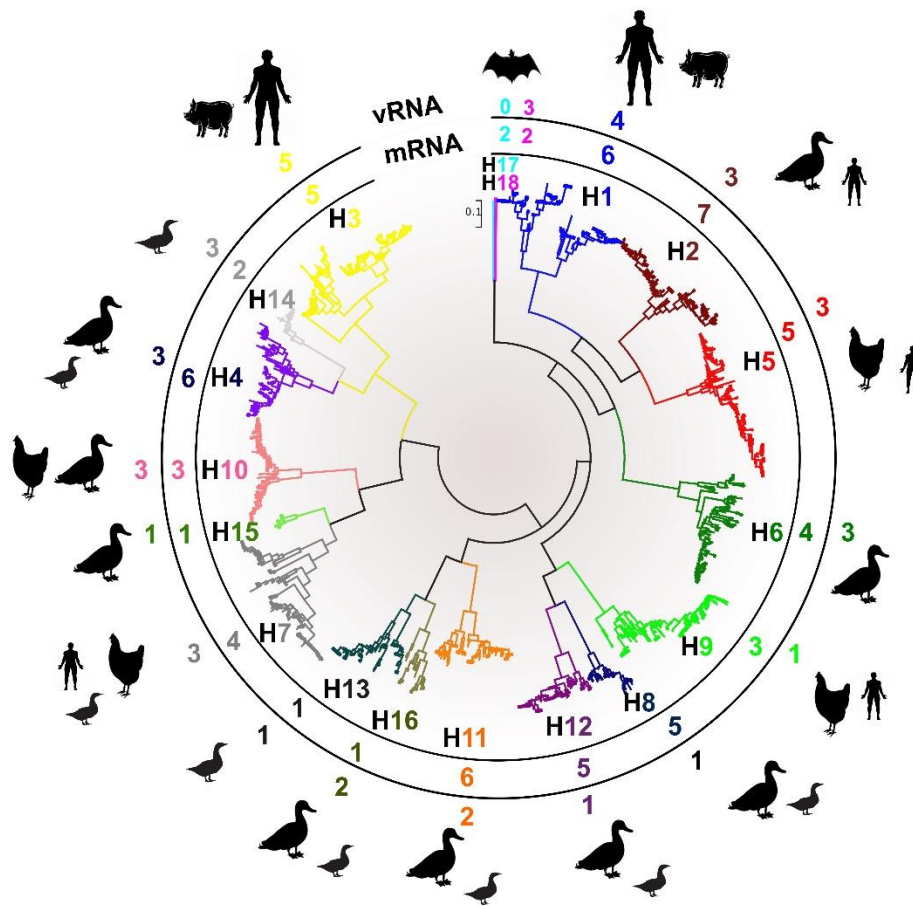
Figure 3.16: Summary of conserved DRACH motifs in all HA subtypes of IAVs. The HA subtyping system is represented by a maximum-likelihood phylogram in the centre representing sequences of each subtype. The numbers of conserved DRACH motifs to each HA subtype are indicated. The most susceptible species affecting each subtype are also shown. The figure is adapted from our publication (Bayoumi and Munir, 2021a).

vRNA	Seq no.*	DRACH^	Motif1	Motif2	Motif3	Motif4	Motif5	Motif6	Motif7	Motif8	Motif9	Motif10	Motif11	Motif12
H1N1 PR8[1]	1	27	✓	✓	✓	✓	✓	✓	✓	✓	✓	✓	✓	✓
H1	25,576	29			√95%			√90%				√95%		√90%
H2	618	26	√50%						√50%			√65%		
H3	23,286	25					√85%	√75%	√85%	√95%			√95%	
H4	1,646	26	√95%				√75%			√99%				
H5	5,472	27				√75%	√75%		√50%					
H6	1,836	23	√85%	√95%								√50%		
H7	2,237	26						√75%	√50%	√95%				
H8	168	26							√95%					
H9	6,408	26					√85%							
H10	983	19			√95%			√85%					√50%	
H11	781	42					√90%		√75%					
H12	337	25	√99%											
H13	409	24					√65%							
H14	35	19	√100%		√100%		√100%							
H15	16	21					√100%							
H16	217	26							√75%				√75%	
H17	2	17												
H18	2	17	√100%				√50%		√100%					

Table 3.3: Summary of conserved DRACHs identified in IAVs HA vRNAs. * The total number of HA sequences identified on the influenza research database. [1] The reference strain is A/Puerto Rico/8/34/Mount Sinai, HA accession no. AF389118. ^The number of the possible DRACH motifs identified in the consensus sequence per each subtype. The table is adapted from our publication (Bayoumi and Munir, 2021a).

Table 3.4: Summary of conserved DRACHs among different species and viruses located on the vRNA of the H1 subtype. The table is adapted from our publication (Bayoumi and Munir, 2021a).

vRNA	Seq no.	Motif1	Motif2	Motif3	Motif5	Motif6	Motif7	Motif8	Motif10	Motif11	Motif12
H1	25,576			✓95%		✓90%			✓95%		✓90%
Human H1N1	16,471			✓99%		✓99%			✓99%		✓99%
-Pandemic H1N1	10,993		✓50%	✓99%		✓99%			✓95%		✓99%
-Non-pandemic H1N1	5,490			✓99%		✓99%			✓99%		✓99%
Swine H1N1	4,366		✓75%	✓99%		✓85%			✓50%		✓95%
Human H1N2	43	✓95%		✓90%	✓90%	✓95%	✓95%	✓95%	✓99%	✓85%	✓99%
Swine H1N2	3,614	✓85%		✓95%		✓95%	✓75%	✓85%	✓95%	✓65%	✓95%

3.3. Chapter Discussion

Multiple avian species have recently joined the growing list of published complete genomes, including chicken. The chicken is the bridging model between the two evolutionary extreme species; humans and mice (i.e., evolutionary closely related species) from one side and fish (i.e., evolutionary distantly related species) from the other side. Thus, comparative genomics can be exploited to fill some gaps and uncover the evolutionary alterations compared with other species (Furlong, 2005).

Among thousands of avian species, chickens are fundamental models in most immunological and microbiological investigations. Chickens are usually used in investigative studies due to their biological and genetic characteristics and ease of handling. Furthermore, they play a crucial role in influenza A virus epidemiology and their potential to generate viruses can cross the species barrier generating pandemics (Vainio and Imhof, 1995; Horimoto and Kawaoka, 2001; Stewart et al., 2013). Therefore, unraveling some aspects of the chicken genome will add value to basic science. Here in this chapter, the first detailed evolutionary and structural analyses of chicken m6A machinery, a representative of avian species is provided, as a primary step to pave the way for studying epitranscriptomics in veterinary fields.

The chickens genome is only 40% of the size of the human genome size (Hillier et al., 2004). It should be noted that mapping genes in their chromosomes among other orthologues might discover syntenic loci, in which specific genes are allocated in a relatively similar order among the chromosomes of various orthologues. Albeit the genome of humans and chickens has been detected to possess a higher degree of synteny in long blocks (Hillier et al., 2004), 70% of m6A-associated genes studied here (7 out

of 10 genes) lost their synteny. Given that the entire chicken genome has more than 20,000 genes, thus only ten genes is considered a small number for generalization but might suggest further aspects of the potential evolutionary events in chicken genes. Interestingly, chicken YTHDF2 (chYTHDF2) showed a loss of synteny; however, it is in the same clade of phylogram as mammalian YTHDF2, unlike other m6A-associated machinery. This finding might point to shared common ancestral loci and functions other than mRNA metabolism. Additionally, the minor degree of synteny among avian orthologues could also be explained by the slight variation in their diploid number of chromosomes (2n = 38–40).

The m6A marks are installed primarily by METTL3, which is helped by METT14, WTAP, and potentially other co-factors. The active domain in the METTL3 is the methyltransferase domain (MTD). In gate loop-1, it was observed that the catalytic motif DPPW was conserved between humans and chickens in amino acid sequence alignments. The conservation highlights a similar methyl transfer mechanism from AdoMet (CH_3-donor) to the target adenosine residue of RNA (Wang et al., 2016b).

Nevertheless, several mutations were observed in the chicken METTL3 active sites and loops; the predicted structures of gate loop-1 and -2 were altered. Moreover, mutations in zinc finger domains (mostly ZnF2) were noticed in chickens, which could affect RNA substrate binding (Śledź and Jinek, 2016). Further structural analysis is required to confirm prediction accuracy and support the abovementioned notions. Considering that METTL14 acts as a scaffold to help METTL3 in humans, chicken METTL14 was compared with a human counterpart. Interestingly, the vestigial active site EPPL motif equivalent to DPPW of METTL3 was also maintained between both species, suggesting

that the chicken METT14 is highly likely to be a stearic helper of the active methyltransferase as well (Śledź and Jinek, 2016; Wang et al., 2016a).

Similarly, chicken WTAP possesses several mutations that do not include the coiled-coil domain (i.e., N-terminus), reflecting the conserved function among mammals and birds. The structure and function of WTAP in the chicken will be discussed in detail in this study. The C-terminal mutations require further investigation. No defined crystal structures are available to delineate the structural and functional importance. Intriguingly, most avian species lack a well-identified METTL3 protein in the current versions of databases that leaves an open question about their methyltransferase mechanism. Future research is required to underpin this process.

m6A-erasers are ferrous α-ketoglutaric-dependent dioxygenases, which are involved in nucleic acid metabolism. Only two enzymes are well characterized as m6A-erasers: ALKBH5 and FTO. Both share the same basic structure and function. However, FTO surpasses ALKBH5 in activity and the number of target substrates (Wei et al., 2018; Bayoumi and Munir, 2021c). The unique loop (L1; residues 213-224) is a critical feature that distinguish FTO from other ALKBH family members. The L1 loop is primarily responsible for hindering the binding to double-stranded nucleic acid substrates (Han et al., 2010). Chicken FTO shows a single amino acid mutation in L1 that is highly unlikely to affect the protein structure, as shown in the predicted form. Compared with the human counterpart, chicken FTO possesses lysine residue at position 86. A previous report confirmed that the induced mutation (K86Q) in human FTO has a higher binding affinity to the N6 methyl-adenine substrate (Zhang et al., 2019d), suggesting that chicken FTO has higher binding activity than human FTO. Conservation of critical

amino acids in chicken FTO active site proposes that the demethylation activity might remain constant compared with humans.

Furthermore, in chicken FTO, the noticed insertion suggests structural stability. Biochemical and structural studies are needed to confirm these findings. Conservation of iron-co-ordinated motifs in all investigated species supports the core function of the ALKBH5 family in both the evolutionary intermediate- and distantly-related species (data not shown).

Humans have five well-characterized readers belonging to the YTH-domain family. These YTH domains prefer guanosine (G) at (-1) position to m6A (i.e., the nucleotide before the methylated adenosine). Additionally, the conservation of Leu 380, Met 438, Val 382, and Asn 383 in chicken YTHDC1 highlights that the avian readers also prefers guanosine in a position preceding the methylated adenosine as in humans through hydrogen (H) bonding, and the presence of other residues are prone for stearic clash with the valine 382 (Xu et al., 2014b; Liao et al., 2018).

Like humans, the chicken YTH-domain proteins were found to possess a higher degree of similarity; some have complete identity with YTH-domain with humans (i.e., chYTHDF2), which signifies an additional function in the evolutionary process. Additionally, the few recorded mutations in chicken were found not to affect the conserved aromatic cage. Importantly, mutations at the aromatic cage were confirmed to abrogate the recognition function of readers to the target substrates (Li et al., 2014). Although the chicken YTH domain of YTHDC1 is similar to that in humans, the cage was found to be slightly wider than the human one. The effect of unique insertions and deletions could not be assessed due to the lack of availability of well-characterized

entire YTHDC1 and YTHDC2 structures. The availability of more crystal structures could help enrich our knowledge in studying m6A machinery in both chickens and humans, improving basic biomedical sciences and veterinary research.

The epitrascriptomic m6A marks are the most abundant chemical modifications deposited onto viral and cellular RNA. Additionally, these marks controls multiple aspects of cell biology and the fate of virus-cell interaction (Kennedy et al., 2017; Dang et al., 2019; Baquero-Perez et al., 2021). Furthermore, the m6A marks have been shown to be an evolutionarily conserved among vertebrates (Ke et al., 2015). Moreover, inhibiting m6A deposition has been reported with various detrimental effects on cells and hosts (Meyer and Jaffrey, 2014). A high degree of conservation between the m6A machinery among vertebrates was confirmed in this chapter, and published by (Bayoumi et al., 2020).

Earlier research reported the presence of m6A marks in influenza A viruses in the 1970s using biochemical and RNA labelling assays. These assays detected 24 m6A sites through the entire IAV genome, with eight marks in the HA gene (Krug et al., 1976; Narayan et al., 1987). Interestingly, after developing whole transcriptome and epitranscriptome data, the high-throughput sequencing data supported the previous influenza results. Eight/nine m6A sites were mapped in mRNA/vRNA of the HA gene of the PR8 strain of H1N1 (Courtney et al., 2017). The authors mapped the HA gene using photo-assisted-m^{6}A-sequence (PA-m^{6}A-seq) and photoactivatable-ribonucleoside-enhanced crosslinking and immunoprecipitation (PAR-CLIP). However, these approaches were not precise in determining m6A sites at single-nucleotide resolution (Courtney et al., 2017).

The cellular m6A sites are primarily deposited onto a particular motif sequence (DRACH, in which D= any nucleotide but C, R= A, and G, H= any nucleotide but G) (Dominissini et al., 2012; Meyer et al., 2012). Furthermore, single-nucleotide resolution assays reported that the m6A marks are prevalent in DRACH motifs (Linder et al., 2015). Additionally, several investigations functionally validated this motif for ablating m6A sites through synonymous mutations of both cellular and viral genes (Courtney et al., 2017; Imam et al., 2018; Xue et al., 2019). Therefore, the DRACH sequence to investigate the conservation pattern among IAVs was used. This broader motif could help narrow the window rather than the shorter RAC motif against the evolving nature of influenza viruses.

Courtney et al. (2017) have introduced 12 synonymous mutations to RAC sequences (out of 14), corresponding to the eight detected m6A peaks across mRNA of the HA sequence (Courtney et al., 2017). The m6A sites were ablated through these synonymous mutations, and the rescued viruses were attenuated in an animal model. The two other RACs have not been mutated easily without a change of the amino acid code (which is identified here as DRACH-7 and -12). Therefore, fourteen DRACHs were used for comparative analysis to determine the conservation pattern among IAVs. Notably, three mutated RACs did not follow the broader DRACHs. Interestingly, the comparative analysis listed these DRACHs as the lowest conserved among IAVs, suggesting these sites are doubtful real m6A sites.

Previous investigations confirmed that the cellular m6A methyltransferase stringently added m6A sites on highly conserved sequences (Wei and Moss, 1977; Zou et al., 2016). It is worth mentioning that the DRACH/RAC motifs number could not be the

same as the m6A sites as the mapped m6A peak could accommodate several adjacent DRACHs. It is challenging to accurately determine the specific m6A sites using non-single nucleotide resolution assays. The clustering of the m6A site is usually a characteristic feature in cellular transcripts (Linder et al., 2015).

Bioinformatic approaches were used to investigate the pattern of conservation of DRACHs (putative m6A sites) across the HA sequences of influenza A viruses. HA gene is the major glycoprotein and the highly variable genetic structure responsible for viral virulence (Naguib et al., 2015). Using the publicly available influenza research database allowed us to decipher the conservation pattern among unique 70,100 HA sequences (Squires et al., 2012). Confirming the presence of six conserved DRACHs among H1 sequences (36% of all HA sequences) suggests that these potential m6A sites are not strain-specific and possibly influenza-specific.

Moreover, the clustering pattern of the conserved DRACHs (usually in the middle and end of the HA gene) suggests a fundamental role in RNA folding, stability, and structure, as described in other RNA virus models (Kennedy et al., 2016, 2017). However, functional RNA analysis is still in need to support influenza data. Although some minor variations were noticed between viruses in the same subtype, four DRACHs were reported in all affected host species, isolation date, and location in vRNA and mRNA.

It was also evident that the genotypic variation of HA did not affect conservation patterns of specific DRACHs. According to HA subtyping phylograms, H1, H5, and H9 sequences are considered clade I, and H3 sequences belong to clade II (Valkenburg et

al., 2016). Although H3 sequences are not in the same clade, conserved DRACHs were noticed in both HA1 (DRACHs 7-9) and HA2 (DRACH-14).

In a trial to correlate influenza pathogenicity and m6A sites, the analysis showed that the highly pathogenic avian influenza viruses chicken-H5N1 and H5N8 have more conserved DRACHs than chicken H9N2 (low pathogenic influenza virus) (Smith and Donis, 2015; Abdelwhab et al., 2016; Yehia et al., 2018). However, in the mRNA analyses, the zoonotic viruses affecting humans that are of chicken origin (H5N1, H9N2, H7N9); the conserved DRACHs were the same. The same results were also noticed in the vRNA analysis (data not shown). Furthermore, pH1N1 sequences were noticed to carry less conserved DRACHs than non-pandemic sequences were noticed (Otte et al., 2016). Therefore, the association between the number of m6A sites and enhanced pathogenicity is doubtful. Moreover, conservation of the same DRACHs among various host species in the H5N1 subtype (i.e., human, turkey, chicken, goose, duck, and environmental isolates) was observed. To conclude, it seems that the putative m6A sites are primarily virus-specific rather than pathogenicity-, clade-, host species-, and geographic-specific. The same results were reported in Zika and HIV-1 virus models (Kennedy et al., 2016, 2017; Lichinchi et al., 2016b).

Although uncommon conserved DRACH sites (DRACH-1, -3, -10) were noticed in the HA subtypes that infect humans, avian species, and bats, the scanty number detected in those species could be the cause of this observation. However, among subtypes containing a low HA sequence number, the highest conserved DRACHs, motifs-13, -11, and 7, are still maintained. This result also supports that m6A sites are conserved regardless of the low pathogenicity in the affected species. Functional validation is still

needed. Considering the enormous number of HA sequences analysed in the study (70,100 HA sequences), the DRACHs having lowest conservation are DRACH-5 and -10. Interestingly, those RACs in PR8 lack the broader DRACH on mRNA sequences. The same finding was noticed in DRACH-8 in vRNA, suggesting DRACHs are more reliable for further synonymous mutation in influenza viruses.

Remarkably, the determined conserved DRACHs among the H1 subtype were also detected using publicly available cellular m6A prediction software SRAMP (Zhou et al., 2016). However, other predicted sites in SRAMP did not match the publicly available mapped sites on the PR8 strain (data not shown).

Several questions are still not addressed and are challenging to answer based on these bioinformatics data. Among these are the low number of conserved DRACHs in bats and some avian species. Nonetheless, all HA subtypes share almost similar total DRACHs on HA consensus sequences (36–47 DRACH sites). Moreover, the higher number of DRACHs in mRNA than vRNA remains in question. Possibly emphasizing the importance of m6A on the stability and translation of mRNA. Several investigations are in need as well to support this hypothesis. The following chapters will discuss this comparative analysis to decipher the link between the level of DRACHs and the replication kinetic and spread.

Chapter 4

Anti-Viral Potential of Chicken

m6A Machinery Against Influenza

A Viruses

4.1. Chapter Introduction

4.1.1. The interplay between the m6A modification and viral infection

Several decades ago, m6A marks were identified to be incorporated in viral RNAs. However, due to technological limitations, the topological and functional characteristics of epitranscriptomic m6A marks were not clearly defined in viral-host interaction (Lavi and Shatkin, 1975; Hashimoto and Green, 1976; Krug et al., 1976; Kane and Beemon, 1985; Narayan et al., 1987). In recent years, the ever-rising progress in epitranscriptome-wide sequencing technologies has been exploited to identify and relatively quantify m6A marks (Hafner et al., 2010; Meyer et al., 2012; Liu et al., 2013; Chen et al., 2015; Linder et al., 2015; Price et al., 2020). These technologies have been harnessed, unravelling aspects of the m6A marks in understanding host-pathogen interactions, as shown below. The outcomes are described in relation to the Baltimore system of virus classification, as follows:

4.1.2. Class I Viruses: Double-Stranded DNA

Unlike most RNA viruses, DNA viruses have full access to most m6A machinery. Additionally, viral transcripts expressed from DNA viruses bear m6A modifications. Notably, unique pro- or anti-viral role patterns for viral m6A modifications in regulating DNA replicating viruses were not clear, as described below:

4.1.2.1. The role of m6A in regulating viruses belonging to the *Herpesviridae* family

4.1.2.1.1. Herpes virus type 1 (HSV-1)

Herpesviruses have been reported to carry m6A marks since the 1970s (Moss et al., 1977). A systematic study confirmed that m6A positively regulates the HSV-1 lifecycle. Adding the chemical 3-deazaadenosine (DAA) reduces the SAM methyl donor and inhibits cellular m6A mark deposition, inhibiting virus replication more than 1000-fold (Feng et al., 2021). Accordingly, overexpression of METTL3 induces virus replication, whereas its knockdown inhibits viral replication. The opposite effect occurred when cells were transfected with m6A-erasers. Interestingly, depleting YTHDF3 significantly downregulates virus replication by 90%. Overall, all these findings clearly demonstrate that m6A regulates HSV-1 replication positively, and modulating m6A machinery could be an excellent antiviral strategy. However, the mechanistic actions of these findings have not yet been investigated (Feng et al., 2021).

4.1.2.1.2. Human cytomegalovirus (HCMV)

The m6A has been proposed to play a pivotal role in HCMV through a negative interferon (IFN) response mechanism. A significant reduction in HCMV titre was observed in m6A writer and reader knockout cells (Winkler et al., 2019). Interestingly, interferon β (IFNβ) mRNA was found to be m6A modified in METTL3- and YTHDF2-depleted cells and was highly stabilized. The same results were found upon introducing the UV-treated virus, suggesting a non-viral mechanism controlling the replication in knockout cells. Mechanistically, the m6A modifications are negative regulators of IFNs

by controlling the fast turnover of IFN mRNAs and thus enhancing viral proliferation (Winkler et al., 2019).

4.1.2.1.3. Kaposi's Sarcoma-Associated Herpesvirus (KSHV)

Like other herpesviruses, KSHV mRNA undergoes m6A modifications, and m6A-modified mRNAs increased markedly during stimulation for KSHV lytic replication. Moreover, inhibition of m6A marks on replication transcription activator (RTA; an essential switch protein during the transition to lytic infection) halts the KSHV lytic cycle (Ye et al., 2017). Additionally, FTO knockdown increased m6A levels and enhanced lytic gene expression, whereas knockdown of METTL3 had the opposite effects. This information indicated a proviral impact of m6A in the KSHV lytic cycle (Ye et al., 2017).

In the same cell line, primary effusion lymphoma (BCBL-1) cells, others noted that YTHDFs protein members had a positive role in the viral lytic cycle; more interestingly, authors identified the staphylococcal nuclease domain-containing protein 1 (SND1), a novel m6A-reader in KSHV lytic cycle. Structural analysis showed that the SND1 has an aromatic cage similar to the YTH domain identified in the YTHDFs and has a proviral effect in the KSHV lytic cycle (Baquero-Perez et al., 2019).

It has also been reported that the knockdown of YTHDF2 and METTL3 in renal carcinoma cell (iSLK) cells predominantly reduces viral gene expression and virion production. Intriguingly, the same report also showed that YTHDF2 and METTL3 depletion has the opposite effect on viral gene expression in TREx BCBL-1 cells.

Suggesting that m6A has a central role in regulating KSHV and functioned in a pro- and antiviral manner according to the investigated cell lines (Hesser et al., 2018).

Adding more layers of complexity in understanding the effect of m6A machinery in regulating KSHV, another investigation revealed that the knockdown of YTHDF2 increased viral gene expression. Mechanistically, the YTHDF2 facilitates viral transcript degradation, thus inhibiting the KSHV lytic life cycle in the iSLK cell line (Tan et al., 2018). Overall, all investigated studies revealed that the m6A modifications play critical roles in the KSHV life cycles; however, the functional role of YTHDF2 remains unclear, and the discrepancy needs to be fully addressed.

4.1.2.1.4. Epstein - Barr Virus (EBV)

The association between the functional role of m6A installed onto EBV transcripts and EBV lytic and latent cycles and EBV-associated cancers was also elucidated (Lang et al., 2019). It has been reported that METTL14 was markedly increased during EBV latency and reduced during the lytic infection. The study also investigated that EBNA3C, a viral-encoded oncoprotein activated METTL14 transcription, and directly interacted with METTL14, promoting its stability. In this way, EBNA3C exploits METTL14 to regulate tumour formation (Lang et al., 2019). Recently, it has been verified that YTHDF1 causes a significant downregulation of EBV replication (Xia et al., 2021a). YTHDF1 destabilized primary viral transcripts, including BZLF1 and BRLF1, by recruiting destabilizing components, suggesting the antiviral role of YTHDF1 in regulating EBV (Xia et al., 2021a).

4.1.2.2.   The role of m6A in regulating viruses belonging to the *Adenoviridae* family

The earliest report confirming m6A-bearing adenoviruses spans back to the 1970s (Hashimoto and Green, 1976). Owing to the complexity of the adenovirus genome and transcriptome, combined m6A-seq and direct RNA long-read nanopore sequencing were performed. The study verified that the adenovirus serotype 5 (Ad5) is also m6A modified. The authors showed that METTL3 positively regulates Ad5 replication. The rest of the m6A machinery had no effect on the virus replication. This report displayed that the depletion of METTL3 specifically impacts late viral mRNAs by reducing their splicing efficiency (Price et al., 2020).

4.1.2.3.   The role of m6A in regulating viruses belonging to the *polyomaviridae* family

Since the 1970s, the m6A marks were identified in Simian Virus 40 (SV40) transcripts. SV40 belongs to the *Polyomaviridae* family, which is characterized by tumour formation (Lavi and Shatkin, 1975; Canaani et al., 1979). However, the functional role of these marks was not clarified until recently with the advancement of high throughput m6A sequencing techniques. Tsai et al. (2018) have mapped 13 m6A sites in SV40 transcripts, where 2 were detected in the early and 11 were identified in the late transcripts (Tsai et al., 2018). Additionally, the authors determined that YTHDF2 and METTL3 selectively promote significant virus replication and gene expression. Loss-of-function experiments on YTHDF2 and METTL3 had the opposite effect. Furthermore, abrogative synonymous mutations to the mapped m6A sites in late viral

transcripts revealed inhibition of viral gene expression, suggesting that m6A has a positive regulatory role on SV40 (Tsai et al., 2018).

4.1.3.   Class II Viruses: Single-Stranded DNA

Although this class contains many viruses of significant importance, no data have been published so far on the impact of m6A on their replication.

4.1.4.   Class III Viruses: Double-Stranded RNA

4.1.4.1.   The role of m6A in regulating viruses belonging to the *Reoviridae* family

4.1.4.1.1. Rotavirus (RV)

A very recent study showed that the rotavirus (RV) substantially increased cellular m6A methylome and selectively downregulated ALKBH5. Through m6A-seq analysis, it has been noticed that the IFN regulatory factors 7 (IRF7) carries enrichment of m6A and thus modulates viral infection possibly through stable and sustained expression. Notably, METTL3-depleted mice showed an enhanced immune response to ensure rapid virus clearance through IRF7 upregulated pathway in an m6A-dependent manner. Interestingly, RV restored its antiviral activity after depleting IRF7 in the METTL3-deficient mice (Wang et al., 2022).

4.1.5.   Class IV Viruses: Single-Stranded RNA, Positive Sense

4.1.5.1.   The role of m6A in regulating viruses belonging to the *Picornaviridae* family

4.1.5.1.1. Enterovirus-71 (EV71)

Hao et al. (2019) reported that RNA undergoes m6A modifications using MeRIP-seq analysis that showed m6A sites primarily enriched at viral structural proteins (VPs),

including VP1 and VP3. Almost all components of the m6A cellular machinery were affected by EV71 infection, and almost all the nuclear m6A machinery translocated to the cytoplasm upon stimulation with this cytoplasmic-replicating virus (Hao et al., 2019). Moreover, METTL3/14 and YTHDF proteins played a proviral role in regulating EV71 in Vero cells, while FTO had a negative regulatory role. It was also observed that ALKBH5 fails to modulate the EV71 life cycle. Marked reduction in viral replication was also noticed when bona fide selected m6A sites located on viral genomes were ablated. Therefore, the m6A residues in EV71 mRNA played a positive role in viral replication (Hao et al., 2019). Interestingly, the same report confirmed that YTHDF proteins had an antiviral role in the RD cell line (Hao et al., 2019).

4.1.5.2.   The role of m6A in regulating viruses belonging to the *Flaviviridae* family

Gokhale et al. (2016) have also demonstrated that most *Flaviviridae* family members, including hepatitis C, Zika, yellow fever, West Nile, and dengue viruses, were edited by m6A marks and these were relatively conserved in the family. Intriguingly, they reported that m6A had a negative impact on hepatitis C virus (HCV) virus production. Knockdown of m6A methyltransferases increased virion production, while FTO, but not ALKBH5, had the opposite effect. Additionally, they reported the colocalization of YTHDFs with lipid droplet to regulate virion release negatively, indicating that m6A had a negative regulatory effect on the HCV lifecycle. To demonstrate the functional relevance of m6A directly impacting the HCV lifecycle, m6A-abrogating mutations in the virion genome increased virus production (Gokhale et al., 2016). Another independent study investigating the Zika virus model (ZIKV), confirmed that ZIKV RNA is m6A modified, and supported the negative regulatory role of YTHDFs and

methyltransferases on virus replication and protein expression (Lichinchi et al., 2016b). The rationale behind highly evolving viruses in maintaining the epitranscriptomic marks, if they are indeed inhibitory, needs further explanation.

It has been reported that stimulation of various members of the *Flaviviridae* family significantly increased cellular m6A methylome in an m6A-dependent manner. Some of the stimulated transcripts control *Flaviviridae* infection accordingly, either by regulating protein expression (i.e., RIOK3) or splicing (i.e., CIRBP) (Gokhale et al., 2020). Additionally, m6A modification to HCV pathogen-associated molecular patterns region was reported to reduce recognition by RIG-I, and YTHDFs protect methylated transcripts from cell innate immune sensing (Kim et al., 2020c). Overall, m6A controls the *Flaviviridae* infection cycle and the cellular methylome against innate immune response.

4.1.5.3. The role of m6A in regulating viruses belonging to the *Togaviridae* family
4.1.5.3.1. Chikungunya virus

In an elegant study, the 4-thiouracil (4sU)-labeled chikungunya virus was allowed to infect cells, and the pre-replicated viral genome and the interacting cellular proteins were identified by mass spectrometry. The chikungunya virus was determined to harbour m6A marks, and YTHDF1 was among the interacting RNA binding proteins (RBPs) and significantly downregulated virus replication. Investigating YTHDFs revealed various outcomes for the chikungunya virus, where YTHDF-1 and -3 restricted virus replication, and YTHDF2 promoted it. Other m6A machinery and the mechanistic effect of YTHDFs in regulating virus infection warrant further investigations (Kim et al., 2020a).

4.1.5.4. **The role of m6A in regulating viruses belonging to the *Coronaviridae* family**

4.1.5.4.1. Porcine epidemic diarrhoea virus (PEDV)

The m6A marks are readily expressed in the porcine epidemic diarrhoea virus (PEDV), which infects mainly young piglets (Chen et al., 2020). Interestingly, the m6A-seq analysis indicated 7 peaks located predominantly in the ORF1b, which encodes non-structural proteins. Functional analysis of m6A machinery in regulating PEDV revealed that writers METTL3/14 and readers YTHDF-1 and -2 have an inhibitory role, while FTO has the opposite effect (Chen et al., 2020). Intriguingly, the decoration of the m6A marks in the non-structural regions of the PEDV genome may contribute to the innate immune inhibitory function.

4.1.5.4.2. Severe Acute Respiratory Syndrome Coronavirus-2 (SARS-CoV-2)

Regarding the methylome of SARS-CoV-2, the causative agent responsible for the COVID-19 pandemic, m6A-seq and miCLIP combined technologies have been used to provide single nucleotide resolution data to show that SARS-CoV-2 bears 8 m6A sites. Moreover, METTL3/14 downregulated virus replication; in contrast, ALKBH5 upregulated the replication of SARS-CoV-2. Like PEDV, SARS-CoV-2 substantially improves m6A cellular methylome in Vero and Huh7 cells (Liu et al., 2021). Based on the previous data, it seems that the m6A epitranscriptomic marks negatively regulate coronaviruses.

Notably, another report using SARS-CoV-2 and HCoV-OC43 showed that METTL3 and YTHDF1-3 promote both virus replication in the VeroE6 cell line, and their

depletion suppresses viral infection (Burgess et al., 2021). Although the discrepancies are clearly noticed, the difference in the cell line could be the plausible cause, which makes judging the overall impact of m6A in coronavirus regulation challenging.

4.1.6. Class V Viruses: Single-Stranded RNA, Negative Sense

4.1.6.1. The role of m6A in regulating viruses belonging to the *Pneumoviridae* family

4.1.6.1.1. Respiratory syncytial virus (RSV)

RSV undergoes m6A modifications, and the major virus structural protein G has been noticed to contain m6A sites. Abrogative silent mutations to these m6A sites enriched on the G gene significantly reduced viral replication kinetics (Xue et al., 2019). Inhibition of the methyltransferase complex decreased gene expression and viral replication, whereas inhibiting the eraser enzymes had the opposite effect. Moreover, the YTHDF proteins had a positive regulatory role indicated by enhanced viral gene expression and virion production upon overexpression (Xue et al., 2019).

4.1.6.1.2. Human pneumovirus (HMPV)

The human pneumovirus (HMPV), another member of pneumoviruses, possesses m6A marks that positively regulate viral replication and gene expression in the same manner and functional relevance indicated in the RSV model (Lu et al., 2020). Interestingly, this model also illustrated that the m6A marks can be exploited to enable viruses to evade the innate immune response by escaping the innate immune sensors, including RIG-I (Lu et al., 2020).

4.1.6.2. **The role of m6A in regulating viruses belonging to the *Rhabdoviridae* family**

4.1.6.2.1. Vesicular stomatitis virus (VSV)

The m6A regulates VSV infection by disrupting innate antiviral immunity. Upon VSV infection, the nuclear DEAD-box-46 (DDX46) helicase recruits the ALKBH5, which demethylates the m6A marks from key immune modulators. Upon demethylation, these mRNAs of innate immune modulators remain sequestered in the nucleus, inhibit IFN, and promote replication. ALKBH5 knockdown induced IFN production and inhibited VSV replication (Zheng et al., 2017). Others have also reported that ALKBH5 knockdown strongly suppresses VSV replication. Mechanistically, ALKBH5 depletion induces high m6A on α-ketoglutarate dehydrogenase (OGDH) transcripts, negatively affecting their stability. Accordingly, the metabolite itaconate pathway required for viral replication will ultimately be inhibited (Liu et al., 2019).

A recent investigation supported that METTL3 reshapes the innate immune response to accelerate rapid clearance after VSV infection. Overexpressed METTL3 translocates to the cytoplasm, installing extra m6A marks on the VSV RNA. This negatively affects the dsRNA formation and dampens the immune response, hence upregulating VSV replication. Upon METTL3 depletion, reduced m6A levels enhanced type I IFN expression, ultimately inducing virus clearance (Qiu et al., 2021). Overall, m6A marks play a role in the VSV infection cycle by regulating the innate immune response.

4.1.6.3. The role of m6A in regulating viruses belonging to the *Orthomyxoviridae* family

4.1.6.3.1. Influenza A viruses (IAVs)

This section was transferred to the end of the introduction due to its direct relevance to this study.

4.1.7. Class VI Viruses: Single-Stranded RNA containing reverse transcriptase enzyme

4.1.7.1. The role of m6A in regulating viruses belongs to the *Retroviridae* family

4.1.7.1.1. Human immunodeficiency virus-1 (HIV-1)

All investigated epitranscriptomic studies also confirmed that m6A modifications control the HIV-1 lifecycle in various manners. It has been reported that HIV-1 RNA bears at least 14 m6A peaks in the coding and non-coding sequences. Additionally, the host m6A increased substantially upon viral stimulation, and these m6A marks enhanced virus production (Lichinchi et al., 2016a). The mechanistic investigation also indicated that m6A influences gene expression and the nuclear export of viral RNA. Furthermore, the METTL3/14 enhanced viral gene expression, while ALKBH5 had the opposite effect (Lichinchi et al., 2016a). Others reported the same conclusion; however, they mapped the m6A marks in the 3′ UTR only, and the YTHDFs recruited to viral RNA to promote viral gene expression in the CD4^{+} T and HEK-293T cell lines (Kennedy et al., 2016).

In contrast, it has also been shown that YTHDFs inhibited viral production in virus-producing cells by inhibiting the reverse transcriptase enzyme in the primary CD4^{+} T

cells (Tirumuru et al., 2016; Lu et al., 2018). A recent study also supports the antiviral role of YTHDF3 in regulating HIV-1 replication in the reverse transcription step. YTHDF3 was incorporated in the released virion capsid protein to inhibit the newly infected cells in this investigation. Accordingly, viral protease degraded the cellular encapsidated protein YTHDF3 to restore optimal infectivity (Jurczyszak et al., 2020).

The above-mentioned data revealed several discrepancies in the role of m6A in regulating HIV-1 replication. These variations may be attributed to different epitranscriptomic sequencing techniques or cell lines used in individual studies. Moreover, selective and individual investigation on m6A-related enzymes may yield misleading conclusions. Nevertheless, all confirmed that the m6A marks of HIV-1 RNA substantially impact various aspects of the virus life cycle.

4.1.7.1.2. Murine leukaemia virus (MLV)

Similar to HIV-1, m6A mRNA modifications have been verified in the MLV genome, including m6A and m5C. Surprisingly, authors noticed these RNA modifications are presented in higher magnitude than that mapped in the cellular counterparts in given transcripts. Moreover, upon overexpression of YTHDF2, the viral replication enhanced significantly, indicating the proviral role of m6A on MLV infection (Courtney et al., 2019a).

4.1.8.   Class VII Viruses: Double-Stranded DNA containing reverse transcriptase enzyme

4.1.8.1.   The role of m6A in regulating viruses belonging to the *Hepadnaviridae* family

4.1.8.1.1. Hepatitis B Virus (HBV)

Another salient example of the role of m6A in tumour-causing viruses is HBV. The m6A residues have been identified in HBV mRNAs and hepatic tissues collected from HBV patients (Imam et al., 2018). Loss-of-function studies revealed that m6A affects mRNA stability and regulates the pregenomic RNA (pgRNA) and reverse transcriptase (Imam et al., 2018). The m6A-seq analysis also revealed that the m6A marks are located within the epsilon stem-loop region. The m6A marks were mapped in both 5′ and 3′ ends of the pgRNA and the 3′ ends of viral transcripts. m6A mutational analysis confirmed that m6A located in the 5′ stem-loop of the pgRNA regulated efficient reverse transcription, while the m6A located in the 3′ stem-loop negatively affected the stability of all HBV mRNAs, indicating a dual regulatory role of m6A (Imam et al., 2018).

The same group also confirmed that mutational analysis in the m6A site in the 5′ stem-loop of the pgRNA affects RIG-I binding affinity to evade the innate immune system. RIG-I is a crucial member of innate immune sensors that detect mainly viral RNA. Recognizing non-self RNA triggers various proinflammatory cytokines and type I IFN to establish an antiviral response (Kim et al., 2020c; Lu et al., 2020).

4.1.9.   The role of m6A in regulating influenza A viruses

IAVs are nuclear-replicating RNA viruses that have been identified to carry m6A marks on their genome since the 1970s. This earlier report indicated through biochemical RNA labelling analysis that the influenza virus bears 24 m6A sites in the entire segmented genome (Krug et al., 1976). Later, another report indicated that the 24 m6A sites were unequally distributed among the genome of IAV. It has also been identified that the highest m6A marks were on HA and NA genes, whereas some genes, such as PB2 and NP segments, lack any m6A modifications (Narayan et al., 1987). Nonetheless, due to the lack of m6A topology information, the functional relevance of these marks on the viral RNA remained unclear till recently.

Using photo-assisted crosslinking m6A sequencing (PA-m6A-seq) combined with photoactivatable ribonucleoside-enhanced crosslinking and immunoprecipitation (PAR-CLIP) data revealed that H1N1 (A/Puerto Rico/8/34/Mount Sinai) bears 8/9 m6A sites on viral mRNA/vRNA, respectively (Courtney et al., 2017). They also verified that YTHDF2 and METTL3 significantly enhanced virus replication and gene expression; through this way, authors suggested the positive regulatory role of m6A in regulating IAVs. The potential m6A sites on the HA plus and minus strands were mapped. Using m6A-deficient viruses, it was revealed that the m6A dramatically reduced replication and protein expression in culture and showed reduced pathogenicity in vivo, confirming the positive regulatory role of m6A in the H1N1 infection.

Some epitranscriptomic studies revealed discrepancies in their conclusions, as stated earlier. Nevertheless, all investigations have confirmed that the m6A marks impact various aspects of the viral life cycle. Here in this project, a systematic analysis of the

role of chicken m6A machinery was envisaged in regulating various influenza A viruses. A summary of the m6A-related protein regulatory role in various viruses is listed in **Table 4.1**.

Table 4.1: Summary of the roles of m6A machinery in regulating viruses.

Class		Reference	Writers		Readers			Erasers	
			METTL3	METTL14	YTHDF1	YTHDF2	YTHDF3	ALKBH5	FTO
I	HSV-1	(Feng et al., 2021)	+*				+	-	
	HCMV	(Winkler et al., 2019)	+			+			
	KSHV	(Ye et al., 2017)	+						-
		(Hesser et al., 2018)	+/-			+/-			
		(Tan et al., 2018)				-			
		(Baquero-Perez et al., 2019)	+		+	+	+		-
	EBV	(Lang et al., 2019)		+					
		(Xia et al., 2021a)			-				
	Ad5	(Price et al., 2020)	+						
	SV40	(Tsai et al., 2018)	+			+			
III	RV	(Wang et al., 2022)	+						
IV	EV71	(Hao et al., 2019)	+	+	+/-	+/-	+/-		-
	HCV	(Gokhale et al., 2016)	-						+
	ZIKV	(Lichinchi et al., 2016b)	-		-	-	-		
	CV	(Kim et al., 2020a)			-	+	-		
	PEDV	(Chen et al., 2020)	-	-	-	-			+
	SARS-COV-2	(Liu et al., 2021)	-	-				+	
		(Burgess et al., 2021)	+		+	+	+		
	HCoV-OC43	(Burgess et al., 2021)	+		+	+	+		
V	RSV	(Xue et al., 2019)	+	+	+	+	+	-	-
	HMPV	(Lu et al., 2020)	+	+	+	+	+	-	-
	VSV	(Zheng et al., 2017)						+	
		(Liu et al., 2019)						+	
	IAV	(Qiu et al., 2021)	+						
		(Courtney et al., 2017)	+			+			
VI	HIV-1	(Lichinchi et al., 2016a)	+	+				-	
		(Kennedy et al., 2016)			+	+	+		
		(Tirumuru et al., 2016)			-	-	-		
		(Lu et al., 2018)			-	-	-		
		(Jurczyszak et al., 2020)				-			
	MLV	(Courtney et al., 2019a)				+			
VII	HBV	(Imam et al., 2018)	-	-		-	-	+	+

*(+) indicate a positive regulatory effect of the m6A-related protein on the infecting virus model. (-) indicate a negative regulatory effect of the m6A-related protein on the infecting virus model. (+/-) indicates that the impact differs in different cell models. The viruses in each class, according to Baltimore classification, are indicated.

4.1.10. Chapter Aims

Given the above-mentioned literature describing either the pro- or anti-viral activity of m6A machinery regulating virus infection, this chapter aimed to provide a comprehensive functional analysis of chicken m6A in regulating influenza A viruses. specifically, to:

1. Functionally validate the expression of m6A machinery in chicken cells.

2. Determine whether there is a variation in the expression pattern of chicken m6A machinery compared to human orthologues.

3. Determine whether viral infection alters the expression pattern of chicken m6A machinery.

4. Systematically categorize the chicken m6A machinery into either pro- or anti-viral factors.

5. Confirm the results using more than one technique and cell to minimize the possibility of future discrepancies.

6. Determine the most potent antiviral factor for further mechanistic downstream analysis.

7. Generate a knockout cell line to the most potent antiviral protein to confirm the functional relevance of that protein.

4.2.   Chapter Results

4.2.1. Chicken m6A regulatory proteins show diverse subcellular localization independent of influenza A virus H9N2 infection.

In order to understand the subcellular localization of ten m6A-associated proteins, the coding sequences of individual genes were chemically synthesized and cloned into the pCAGGS expression vector. The pCAGGS plasmids are controlled by CAG complex (i.e., chicken β-actin promoter and linked with the cytomegalovirus (CMV) enhancer) to support ectopic expression. Due to the lack of commercial antibodies and to enable a synchronized detection system, the m6A proteins were tagged with FLAG at the C-terminus. All chicken m6A proteins were expressed successfully in the chicken fibroblast (DF1) cell line, and the subcellular locations were validated using the immunofluorescence assay (IFA) using anti-FLAG antibodies **(Figure 4.1)**.

The chicken m6A-reader proteins, including chYTHDF1-3 and chYTHDC2 were expressed in the cytoplasm and chYTHDC1 in the nucleus, similar to human orthologues. Regarding m6A-demethylases, the chALKBH5 predominantly localized in the nucleus, whereas chFTO shuttled between the nucleus and cytoplasm **(Figure 4.1A)**. It has been reported that the human m6A-methyltransferase complex (METTL3, METTL14, and WTAP) co-localize with nuclear speckles (Ping et al., 2014). Though it was clearly noticed that chMETTL3 and chMETTL4 localized in the nucleus, chWTAP expressed in the cytoplasm **(Figure 4.1A)**.

Influenza A viruses replicate in the nucleus and undergo m6A modifications, then the structural proteins, including the haemagglutinin (HA), are transported to the cytoplasmic membranes for release (Skehel and Wiley, 2000; Pleschka, 2013). To

determine whether H9N2 alters the expression pattern of the chicken m6A machinery, especially the cytoplasmic m6A-related proteins. Transiently transfected DF1 were infected with IAV H9N2 UDL/08 strain (MOI=1.0) for 24 h. Staining of cells with monoclonal antibodies against the HA protein of H9N2 marks the virus-infected cells. Analysis of at least 500 cells showed no translocation of any of the m6A-associated proteins in subcellular compartments in the virus-infected cells **(Figure 4.1B)**.

Interestingly, chWTAP was also detected in the cytoplasm in the virus-stimulated cells **(Figure 4.1B)**. The specificity of the chicken m6A-machinery expression was also detected using western blot at the expected sizes **(Figure 4.1D)**. To sum up, chicken m6A-associated proteins were readily expressed in chicken cells and showed no alteration of their expression pattern upon stimulation with the H9N2 virus; however, in contrast to human WTAP, chWTAP exhibited cytoplasmic localization in both virus-infected and mock-infected cells.
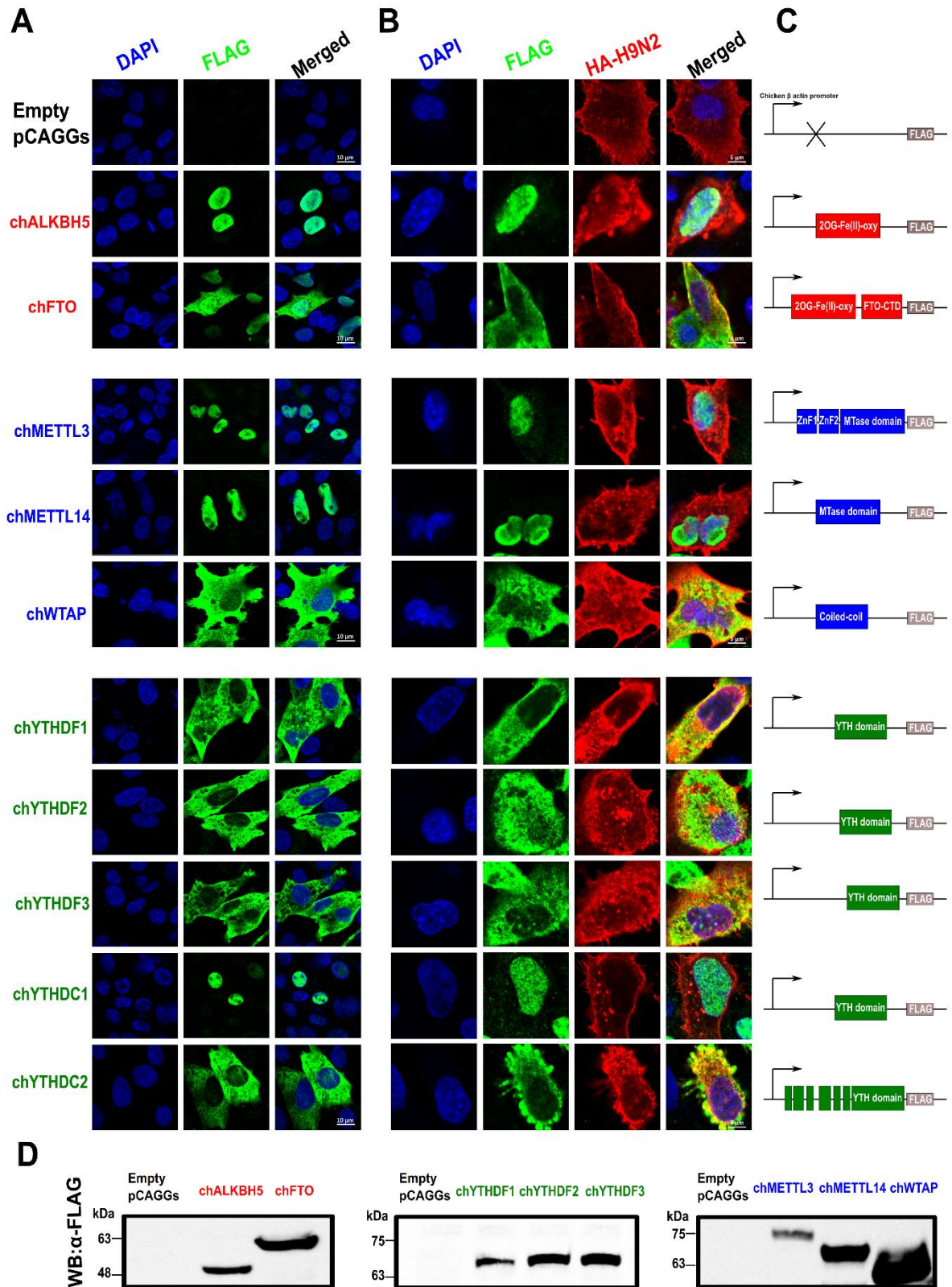
Figure 4.1: Influenza A virus (H9N2) infection does not alter the expression pattern of the chicken m6A machinery. **(A)** Ectopic expression of m6A-related proteins in chicken fibroblasts DF1 cells. The nucleus (blue) and m6A (green) were labeled with DAPI stain and anti-FLAG-specific antibodies, respectively. Scale bars are 10 µm. **(B)** Ectopic expression of m6A-related proteins in influenza-infected DF1 cells using H9N2 MOI=1.0. The nucleus (blue), m6A (green), and virus protein (red) were labeled with DAPI stain, anti-FLAG, and anti-viral HA-specific antibodies, respectively. Scale bars are 5 µm. **(C)** Schematics of specific domains for each of the m6A-related proteins and FLAG tag is indicated by a brown box in the 3' end. **(D)** Western blot-based validation of expression of m6A machinery in chicken. Empty pCAGGS plasmid transfected cells served as the negative control throughout the experiments.

4.2.2. Chicken m6A machinery downregulates the replication of influenza A viruses

To decipher which of the chicken m6A-associated machinery possesses proviral or antiviral effects against influenza A viruses (IAVs). The H1N1 virus (PR8 strain), a laboratory-adapted IAV, that has been studied earlier was used, to investigate the impact of only human METTL3 and YTHDF2 in A549 cells (Courtney et al., 2017). Additionally, the chicken-origin H9N2 virus (UDL/08 strain) was explored as a relevant strain to chicken m6A-related machinery and has zoonotic and public health importance.

The DF1 cells were transfected individually with the chicken m6A-associated proteins, followed by infection with either the H1N1 or H9N2. The cell supernatants were collected to quantify the progeny (released) virus titre using plaque assay. Except for chYTHDF1, all m6A-readers significantly inhibited H9N2 replication compared to mock-transfected control; chYTHDF2 has the most potent antiviral effect ($p<0.001$). Additionally, chALKBH5 exhibited a significant antiviral impact ($p<0.01$), whereas chFTO (the second m6A eraser) inhibited but not significantly the influenza A virus. Notably, the m6A-methyltransferases have failed to show either proviral or antiviral effects against H9N2 viral replication in three independent biological replicates **(Figure 4.2A, B)**.

Interestingly, both chYTHDF2 and chMETTL3 did not affect H1N1 replication in DF1 cells. In contrast, chYTHDF-1, -3, and chALKBH5 revealed a significant antiviral potential even against human IAV H1N1 **(Figure 4.2C, D)**. Collectively, these observations highlight the diversity of m6A-associated proteins against different strains

of IAV (H9N2 and H1N1). Owing to the profound antiviral effect of chALKBH5 against both viruses, the molecular mechanisms associated with the chALKBH5-mediated antiviral outcome were investigated.
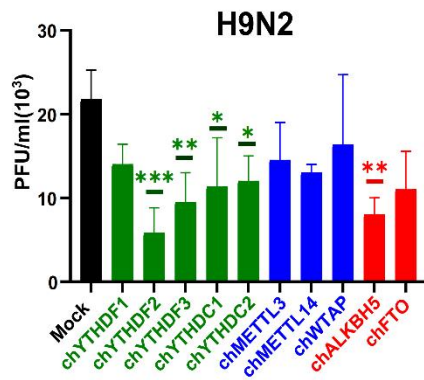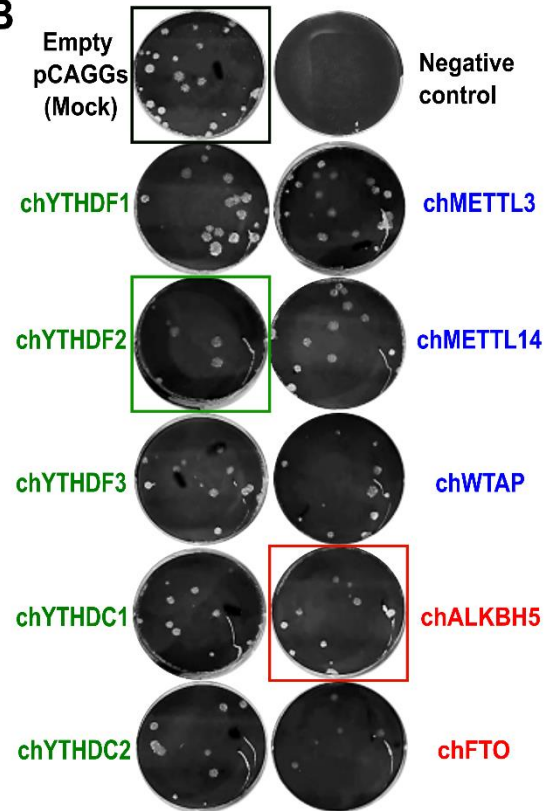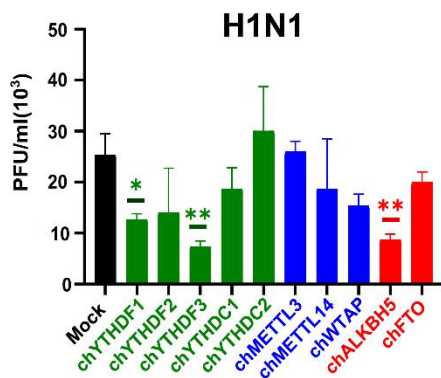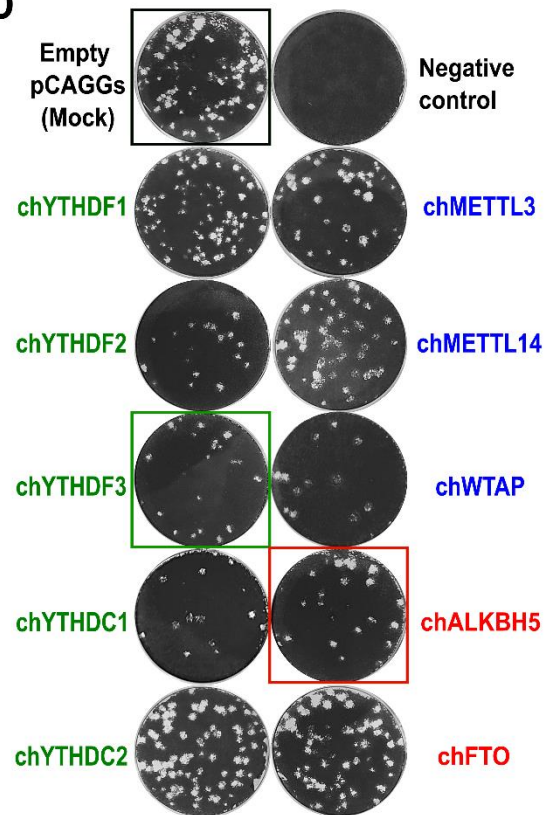
Figure 4.2: Chicken m6A machinery downregulates the replication of influenza A viruses. **(A)** Plaque assay-based quantification of the progeny viruses released from m6A-machinery transfected DF1 cells then infected with H9N2 UDL/08 (MOI=1.0). **(C)** Plaque assay-based quantification of the progeny viruses released from m6A-machinery transfected DF1 cells then infected with H1N1 PR8 (MOI=1.0). Empty plasmid transfected-infected cells served as a mock control. These data represent the average of three biological replicates with SD indicated. $*p < 0.05$, $**p < 0.01$, $***p < 0.001$ using one-way ANOVA. **(B, D)** Representative plaque counts of each transfected m6A-related protein then infected with either (B) H9N2 or (D) H1N1. The progeny viruses were quantified on MDCK cells and stained after 72 h post-infection (hpi); only countable plaque wells were shown. The most potent antiviral proteins were boxed compared to mock.

4.2.3. Chicken m6A machinery inhibits the viral protein expression and transcription of influenza A viruses.

Whether the effect of chicken m6A-associated machinery on IAV replication is at the viral protein expression or the gene transcription levels was investigated. The transfected and infected DF1 cells (as described above) were lysed to investigate viral protein expression. In cells infected with H9N2, viral gene expression was determined using monoclonal antibodies to the viral HA protein. Complementary to the plaque assay-based quantitative analysis, chicken m6A-machinery reduced the expression of both HA1 and HA0 subunits of H9N2, and the antiviral effect was especially noted for both chicken readers and erasers **(Figure 4.3A)**. In H1N1, viral gene expression was determined using monoclonal antibodies against the NP protein. Interestingly, NP expression was the lowest in the chALKBH5 and chYTHDF3-transfected cells amongst all investigated m6A-associated proteins (similar to plaque counts) **(Figure 4.3B)**. These results highlight that the antiviral impact of chicken m6A-associated proteins is attributed to the protein expression level.

The level of viral protein expression can be directly affected by the level of the viral transcript. The m6A-gene transfected and IAV-infected cells were also lysed to quantify viral gene transcription. Relative mRNA expression for the M gene of H9N2 was quantified using the chicken Ribosomal Protein L30 (chRPL30) gene, the chicken reference gene, as determined earlier (Yang et al., 2013). Notably, compared to mock-transfected control, all chicken m6A-associated proteins significantly downregulated M gene expression ($p<0.001$) of H9N2 **(Figure 3C)**.

Next, whether H9N2 infection affected the expression of chicken m6A machinery was assessed. Toward this end, using RT-qPCR, H9N2 UDL/08-infected DF1 cells were analysed for the expression of m6A-associated genes. It was found that H9N2 downregulates all chicken m6A-associated machinery except chYTHDF2 and chYTHDC1 **(Figure 4.3D)**. Taken together, chicken m6A-related proteins antagonize the IAV replication by downregulating viral gene transcription and, subsequently, viral protein expression in H9N2-infected cells. In response, IAV downregulated chicken m6A-associated genes.
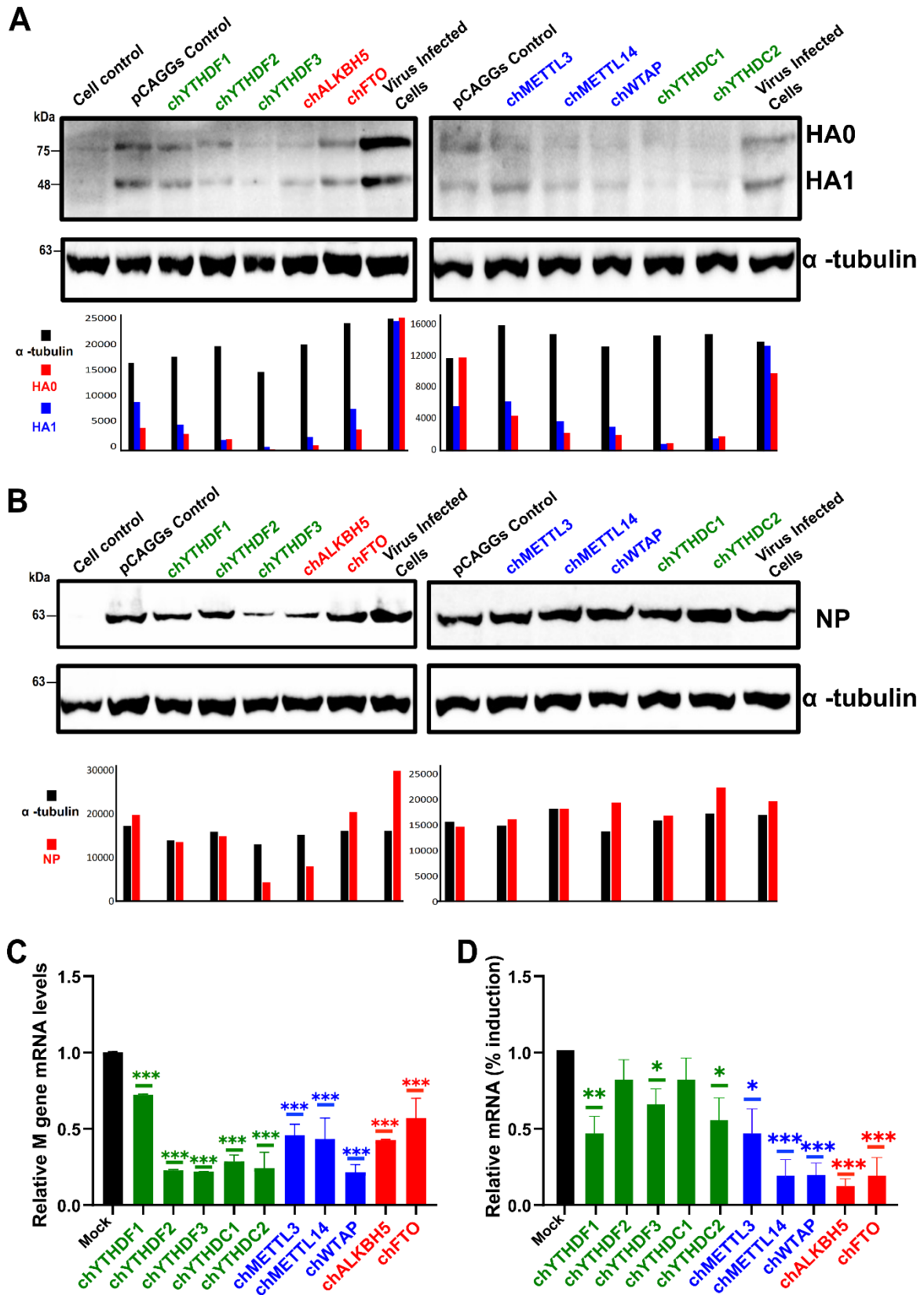
Figure 4.3: Chicken m6A machinery inhibits protein expression and viral transcription of influenza A virus. **(A)** Immunoblot-based analysis of DF1 cells was transfected with the designated chicken m6A-machinery then infected with IAV H9N2-UDL/08 (MOI=1.0). IAV H9N2 protein expression was determined using viral HA protein represented by HA0 and HA1 expression as indicated. **(B)** Immunoblot-based analysis of DF1 cells transfected with the designated chicken m6A-machinery then infected with IAV H1N1-PR8 (MOI=1.0). IAV H1N1 protein expression was determined using viral NP protein. α-tubulin was utilized as the loading control. ImageJ was used to determine the quantification of the band intensities for HA, NP, and values were graphed as column bars. A representative western blot of each virus is shown. **(C)** RT-qPCR-based analysis to determine the expression levels of M gene mRNA of IAV H9N2. DF1 transfected with designated m6A machinery normalized with empty vector control to 1.0 using the chRPL30 as a chicken cellular housekeeping loading control. **(D)** RT-qPCR was performed to determine the levels of chicken m6A-gene expression upon stimulation with IAV H9N2 for 24 h, compared with a mock-infected sample. These data represent the average of three biological replicates with SD indicated. $*p < 0.05$, $**p < 0.01$, $***p < 0.001$ using one-way ANOVA.

4.2.4. Lentiviral-mediated expression of chicken m6A genes downregulates influenza A virus (H9N2) replication in a primary chicken cell

Several discrepancies have been reported previously on the role of m6A machinery against viruses, including HIV-1, which is attributed to be cancer cell-line dependent (Kennedy et al., 2016; Tirumuru et al., 2016). To confirm the antiviral potential of m6A proteins in an ectopic expression system, these functions were investigated in a primary chicken cell using a lentiviral-based system.

For this purpose, fresh chicken embryo fibroblast (CEF) cells were prepared and transduced with lentiviral particles bicistronically expressing red fluorescent protein (RFP) and m6A protein. Additionally, to enable a compatible viral quantification based on flow cytometry, a recombinant IAV that expresses green fluorescent protein (GFP) fused with the NS1 gene of the H9N2 virus was generated **(Figure 4.4A, B)**. This system allowed gating cells based on RFP as a surrogate for the m6A protein expression (transduced, red) and virus-infected cells (infected, green) using flow cytometric-based analysis **(Figure 4.4C)**.

After 72 h post-transduction of freshly prepared CEF cells, the cells were infected with the H9N2-GFP at an MOI of 1.0. After an additional 24 h, CEF cells were fixed, sorted, and gated using flow cytometry. As expected, the majority of chicken m6A-related proteins downregulated H9N2-GFP-expressing cells, as shown in **Figure 4.4D**.

Notably, chALKBH5 significantly inhibited the IAV H9N2, as was noted in all antiviral assays for both H9N2 and H1N1. In order to confirm and compare the antiviral potential of chALKBH5, chIFIT5 was used which has been verified earlier as an antiviral protein

against influenza viruses by our group (Santhakumar et al., 2018). Empty vector-transfected cells were used as a negative control and chIFIT5-expressing cells as a positive control, it was observed that the chALKBH5-expressing cells significantly downregulated the expression of H9N2-GFP ($p < 0.001$; **Figure 4.4E)**. To sum up, chicken m6A-related proteins exhibit antiviral activity against IAVs, and chALKBH5 was the most potent among all investigated proteins using diverse antiviral screening approaches. Therefore, chALKBH5 was taken forward for molecular and downstream mechanistic analysis against H9N2.
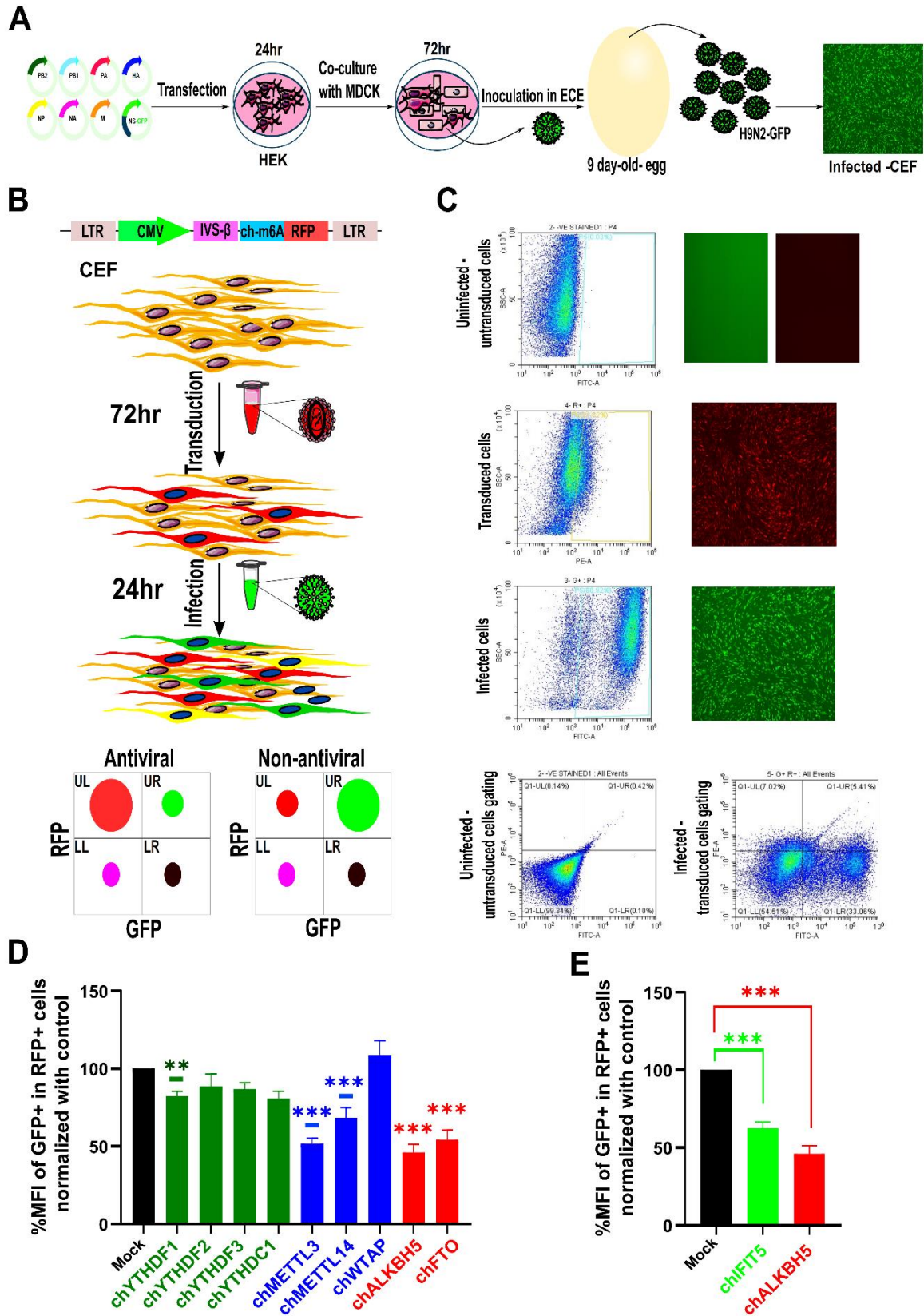
Figure 4.4: Lentiviral expressed chicken m6A machinery downregulates influenza A virus (H9N2) replication in a primary cell model. **(A)** Schematic of generation of H9N2-GFP virus. Eight plasmid systems were utilized containing NS1-GFP. The eight-plasmid system was transfected into HEK-293T cells. Then, HEK cells were co-cultured with MDCK before inoculation into embryonated chicken eggs (9 days). **(B)** Lentiviral vectors bicistronically expressing the chicken m6A-protein fused with RFP marker gene were transduced into CEF cells for 72 h (Empty-RFP plasmid used as control). These gene-expressing cell populations were further infected with H9N2-GFP for 24 h before flow cytometry analysis. Transduced and infected cells were gated into four quadrants accordingly to transduced only (RFP+, GFP-), infected only (RFP-, GFP+), infected-transduced cells (RFP+, GFP+), untransduced-uninfected cells (RFP-, GFP-). Low GFP levels in the transduced cells demonstrated the antiviral activity of a given protein (low green in the total red). **(C)** Representative images of controls, transduction, infection, and gating were indicated for both fluorescent microscopy and flow cytometry. **(D)** The cumulative mean fluorescent intensity (MFI) of three independent replicates normalized with empty-RFP lentivirus control. **(E)** MFI of three independent replicates of lentiviruses expressing chALKBH5, which normalized with empty lentivirus as a negative control and lentivirus expressing-chIFIT5 as a positive antiviral control. These data represent the average of three biological replicates with SD indicated. $*p < 0.05$, $**p < 0.01$, $***p < 0.001$ using one-way ANOVA.

4.2.5. chALKBH5 downregulates influenza A virus (H9N2) in a time-lapse manner and is significantly enhanced by the chYTHDF2 combination.

To determine whether chALKBH5 inhibits IAV H9N2 only after 24 h (as tested before) or in a time-course manner. A one-step growth curve was performed. DF1 cells were transfected with chALKBH5 or mock-transfected and then infected with the H9N2 UDL/08 strain (MOI=1.0). For plaque counts, virus-containing supernatants were collected at 4-, 8-, 12-, 24-, and 48- hours post-infection (hpi), and for IAV M gene mRNA expression analysis, RNA from virus-infected cells was extracted. Virus titre increased until its highest level at 24 h post-infection, and thereafter a slight decline at 48 h was noticed. The chALKBH5 inhibits virus replication ($p<0.05$) and gene transcription ($p<0.001$) at all indicated time points, as shown in **Figure 4.5A-C**.

A previous report indicated that human YTHDF2 has a potent proviral effect against H1N1 (Courtney et al., 2017). However, the findings clearly revealed that chYTHDF2 has a potent antiviral consequence **(Figures 4.2-4.4)**. Another experimental design was adopted to confirm that chYTHDF2 possesses antiviral activity in chicken. DF1 cells were co-transfected with either chALKBH5 and chYTHDF2 or chALKBH5 alone (concentrations were normalized with empty vectors). The antiviral assays (plaque counts and RT-qPCR) revealed significant downregulation of IAV in chYTHDF2 and chALKBH5 transfected cells ($p<0.001$) **(Figure 4.5D-F)**. This finding confirmed that chYTHDF2 synergizes the antiviral action of chALKBH5 against IAV. Collectively, chALKBH5 inhibited H9N2 in a time-dependent manner, chYTHDF2 enhanced the antiviral activity of the chALKBH5, and chYTHDF2 individually carried antiviral potential against IAV in chicken cells.
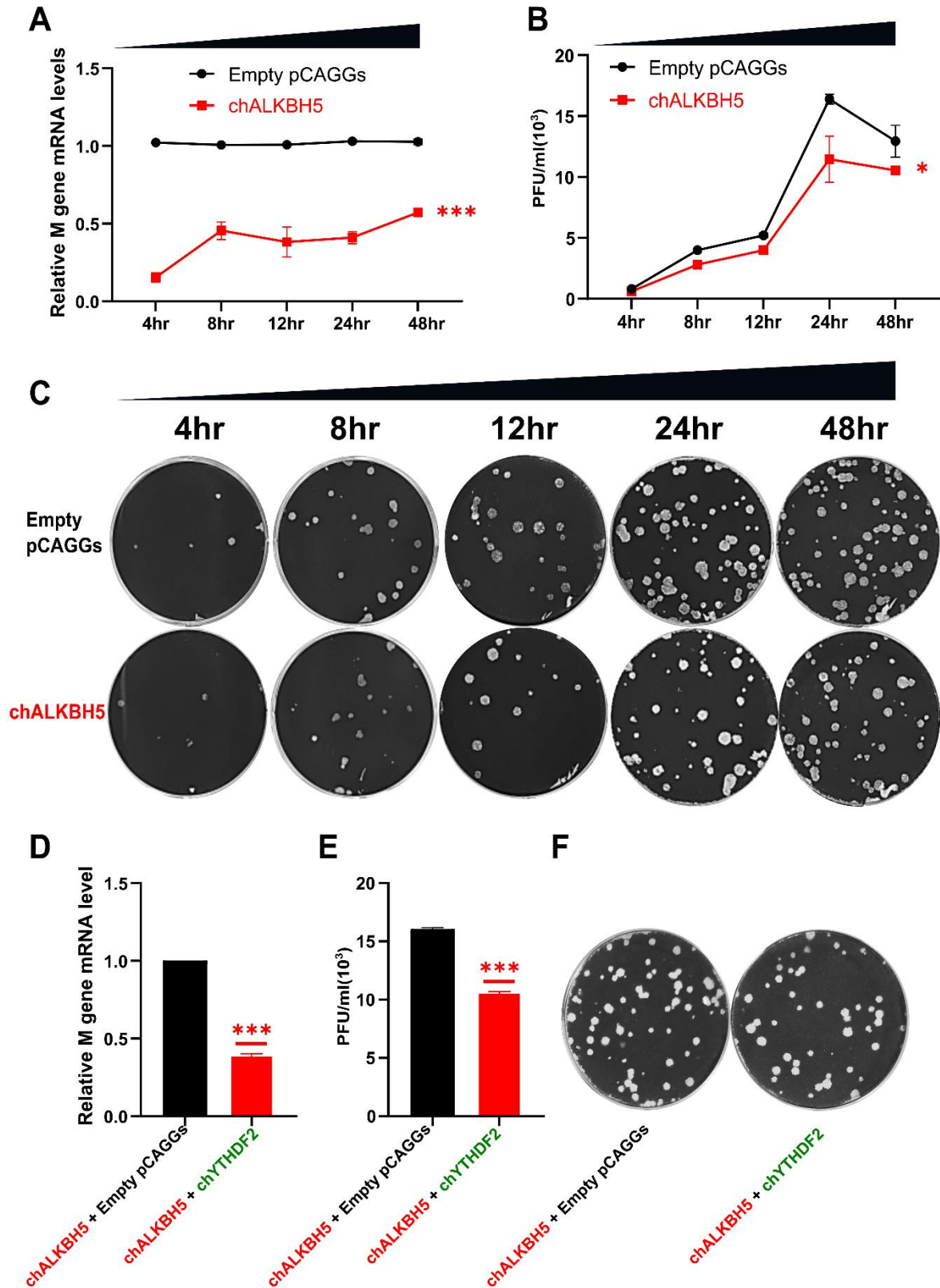
Figure 4.5: chALKBH5 downregulates influenza A virus (H9N2) in a time-lapse manner and is significantly enhanced by the chYTHDF2 combination. **(A)** RT-qPCR was performed to determine the levels of the IAV H9N2 M mRNA after transfection with either empty vector or chALKBH5, then infected with H9N2 UDL/08 (MOI=1.0) at the indicated time points post-infection. DF1 transfected with chALKBH5 normalized with empty vector control to 1.0 in each time-point using the chRPL30 as a chicken housekeeping control. **(B)** Plaque assay-based quantifications of the progeny viruses from the empty transfected-infected cells (mock) and chALKBH5-transfected-infected DF1 cells. The progeny viruses were quantified on MDCK cells post-infection at the indicated time points. **(C)** Representative plaque counts of each transfected empty/chALKBH5 protein and then infected with H9N2. The released viruses were quantified using plaque assay on MDCK cells after 72 h. Only countable plaque wells are shown. **(D)** RT-qPCR was performed to determine the levels of the IAV H9N2 M mRNA after transfection with either empty vector+chALKBH5 or chYTHDF2+chALKBH5 then infected with H9N2 (MOI=1.0). **(E)** Plaque assay-based quantification of the progeny viruses from the empty plasmid+chALKBH5 transfected-infected cells and chALKBH5+chYTHDF2-transfected-infected DF1 cells. The progeny viruses were quantified on MDCK cells. **(F)** Representative plaque counts per transfected m6A-related protein are indicated and then infected with H9N2. The progeny viruses were quantified using plaque assay on MDCK cells after 72 h. Only countable plaque wells are shown. These data represent the average of three biological replicates with SD indicated. $*p < 0.05$, $**p < 0.01$, $***p < 0.001$ using Student's t-test.

4.2.6. Influenza A virus (H9N2) replication is non-significant in chALKBH5-KO compared to wild-type DF1 cells.

It was shown that chicken m6A machinery mainly possesses antiviral potential, and none of the m6A proteins showed a proviral effect against IAV. Additionally, through overexpression analysis, chALKBH5 appeared as the most potent antiviral protein against IAVs. Therefore, a chALKBH5-knockout (KO) cell lines were generated to demonstrate the impact of chALKBH5 against IAV in chALKBH5-depleted cells. To this aim, DF1 cells were transfected with vectors expressing Cas9 endonuclease and sgRNA to target the coding sequence of chALKBH5, as shown in **Figure 4.6A, B**. Through the limiting dilution technique, the chALKBH5-KO cell lines were generated. Owing to the lack of chALKBH5-specific antibodies, chALKBH5-KO-cells were validated using single-cell clones (SSC) sequencing. Two SSC expressing only frame-shift mutations in the target exon 2 (clone 1 carried 8nt deletion and clone 2 carried 76nt deletion) were used, as shown in **Figure 4.6C-E**.

DF1-wt and DF1-chALKBH5-KO were infected with H9N2, and viral quantification was performed using plaque assay (progeny virus released in the supernatant) and RT-qPCR (RNA from virus-infected cells). Both antiviral assays showed enhanced but non-significant ($p > 0.05$) virus replication **(Figure 4.7A, C)**. However, in complementation experiments, supplementing the chALKBH5 KO-cell line with ectopic expression of chALKBH5 restored the antiviral action of chALKBH5 using the same antiviral assays **(Figure 4.7B, D)**. Overall, the chALKBH5 KO cell lines supported the virus replication non-significantly compared to DF1-wt cells; however, overexpression of chALKBH5 in the KO cells reversed the antiviral action.
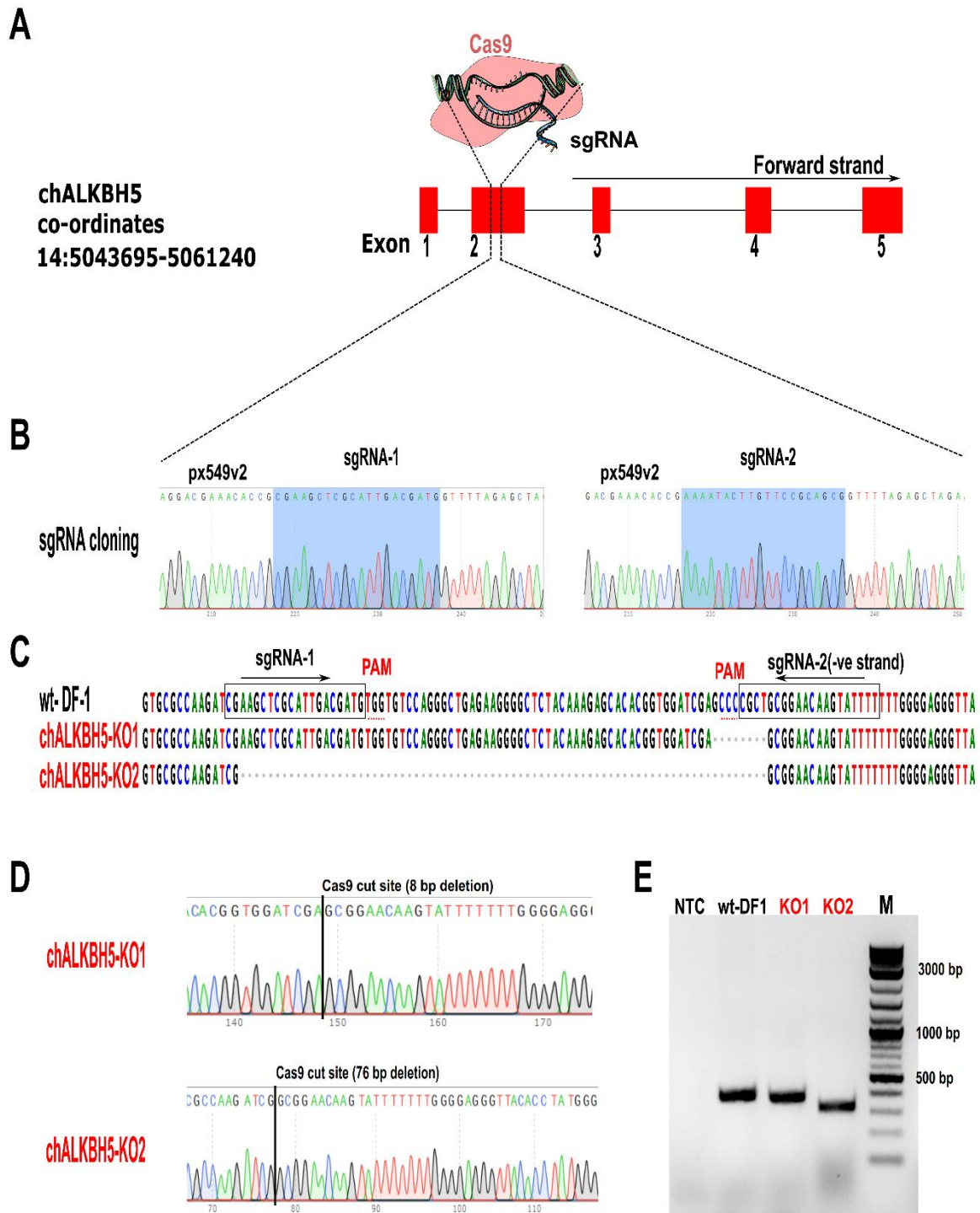
Figure 4.6: Generating DF1-chALKBH5 KO cell lines. (**A**) Schematic of chALKBH5 loci in the chicken genome, number of exons, and target exon are shown. (**B**) Sequence confirmation of cloning of two sgRNAs targeting exon 2 of chALKBH5. (**C**) Schematic diagram showing the location of sgRNA in exon 2 of chALKBH5 and sequence

alignment with the two KO-cell clones. **(D)** Sequence confirmation of KO cell lines at the target exon. The cut site and the numbers of deleted nucleotides are indicated. **(E)** Gel electrophoresis image showing the variation between KO-cell clones compared with DF-1 wt.
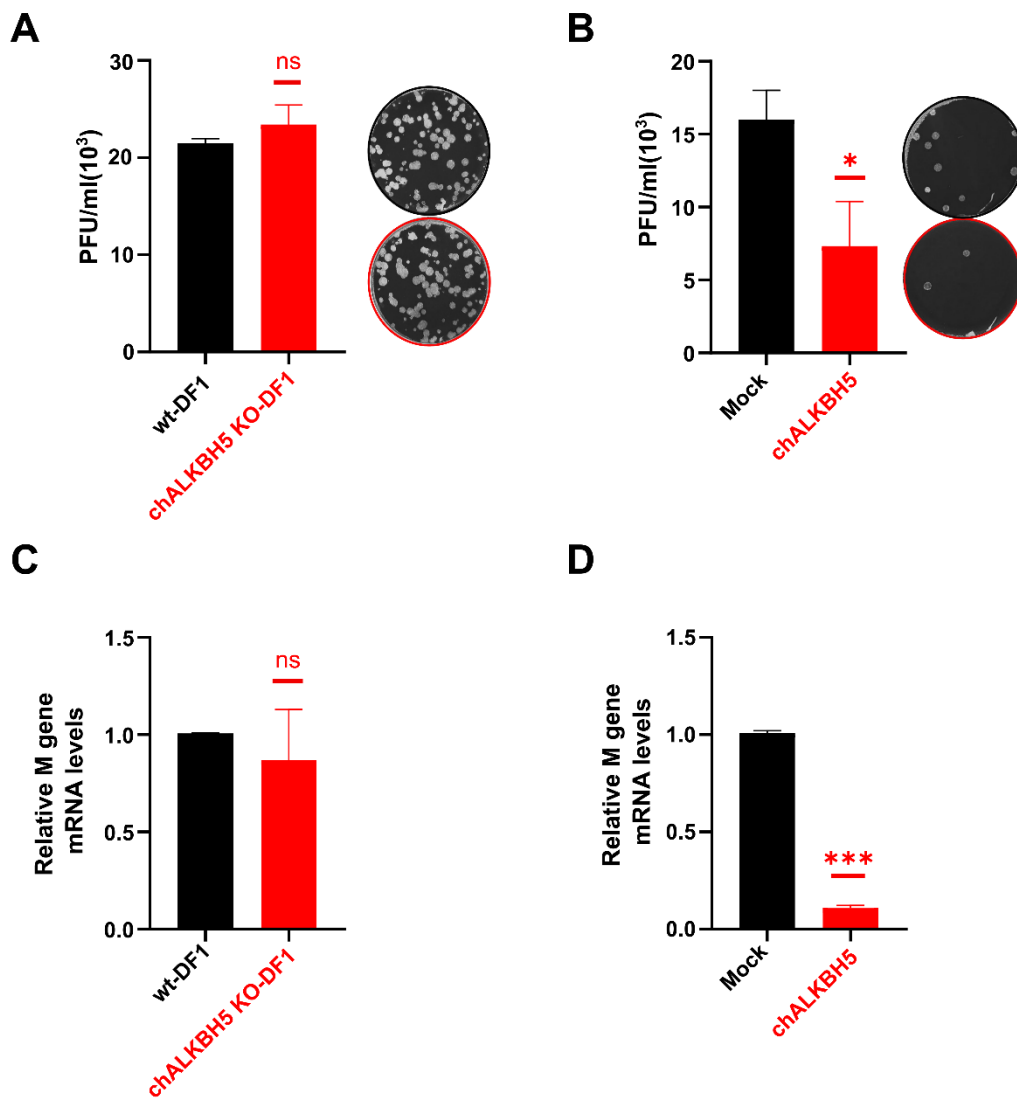
Figure 4.7: Influenza A virus (H9N2) replication is not significantly different in chALKBH5-KO compared to wild-type DF1 cells. **(A)** Plaque counts of egressing (progeny) viruses after infecting either DF1-wt or chALKBH5-KO cell lines with H9N2 UDL/08 (MOI=1.0) for 24 h. **(B)** Plaque counts of progeny viruses after transfecting KO cell lines with chALKBH5 (empty vector transfected as mock), then infecting with H9N2 UDL/08 (MOI=1.0) for 24 h. **(A and B)** The progeny viruses were quantified using plaque assay on MDCK cells after 72 h. Representative plaque counts of each condition are shown. Only wells containing representable and countable plaques are

shown. **(C, D)** RT-qPCR was performed to determine the levels of the IAV H9N2 M

mRNA from virus-infected cells as indicated in the A and B sections. These data

represent the average of three biological replicates with SD indicated. ns: non-

significant p>0.05, *p < 0.05, ***p < 0.001 using Student's t-test.

4.2.7. Influenza A virus (H9N2) replication is non-significant in chYTHDF2-KO compared to wild-type DF1 cells.

Based on the previous results (plaque counts, viral RNA transcription, and protein expression), the chYTHDF2 has an antiviral role against the H9N2 UDL/08 strain. Therefore, chYTHDF2-knockout (KO) chicken cell lines were generated to support the previous ectopic expression analysis. To this aim, DF1 cells were transfected with vectors expressing Cas9 endonuclease and sgRNA to target the coding sequence of chYTHDF2, as indicated in **Figure 4.8A, B**. Through the limiting dilution technique; two KO cell lines were generated. The chYTHDF2 KO cells were also validated using single-cell clones (SSC) sequencing expressing frame-shift mutation in the target exon 1. Two SSCs were selected and used, including clone 1 (-7nt, deletion) and clone 2 (+1nt, insertion), as shown in **Figure 4.8C-E**.

Both DF1-wt and chYTHDF2-KO cells were infected with H9N2 for 24 hrs and using plaque assay (virus supernatant), and RT-qPCR (RNA from virus-infected cells) showed non-significant support for the virus replication (**Figure 4.9A, C**). However, the complementation experiment by transfecting KO cell lines with chYTHDF2 restored the antiviral action of chYTHDF2 using the same antiviral assays (**Figure 4.9B, D**). To conclude, the generated KO cell lines revealed a non-significant virus replication compared to DF1-wt cells, and overexpression of chYTHDF2 restored the antiviral action in chYTHDF2 KO cells.
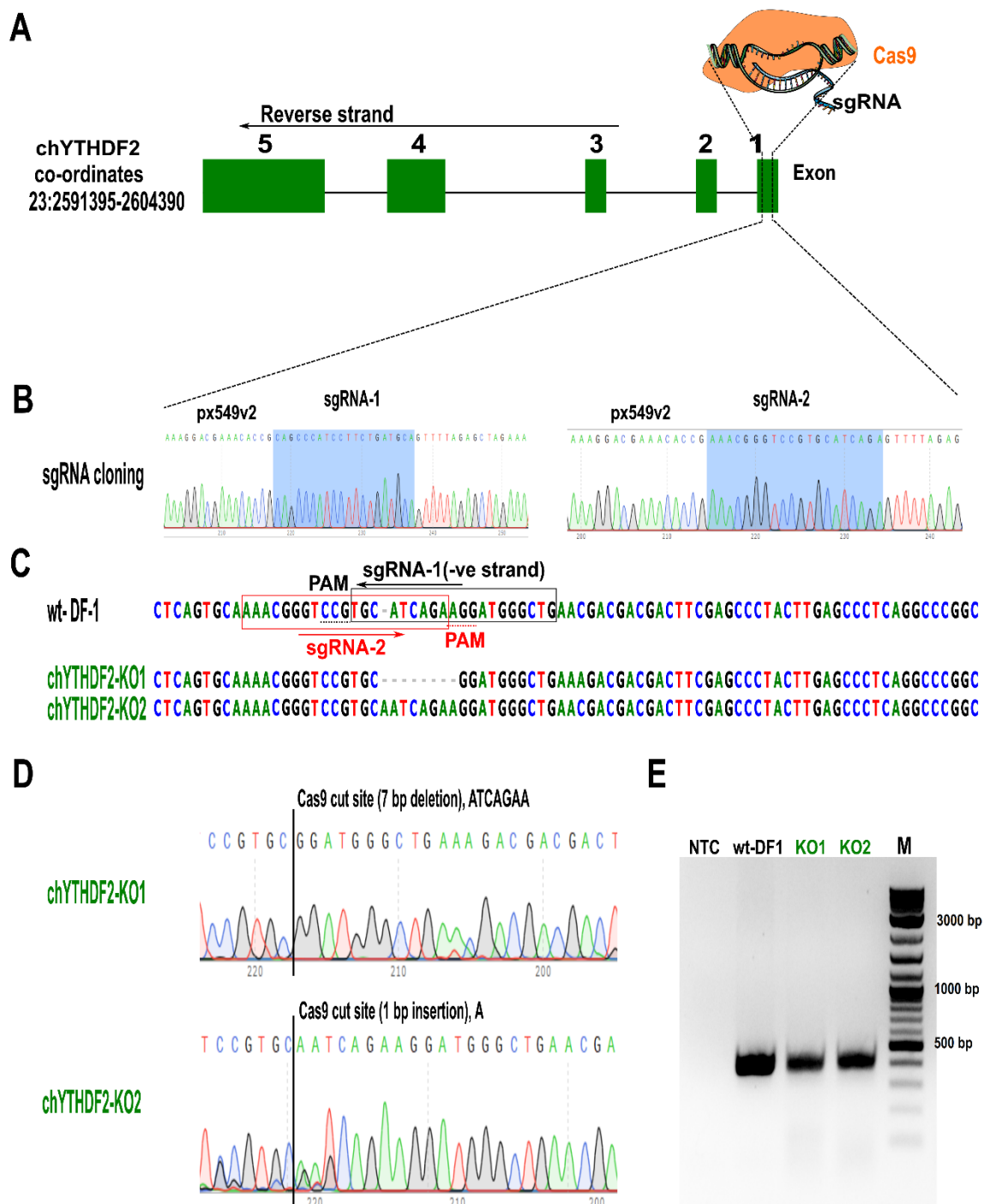
Figure 4.8: Generating DF1- chYTHDF2 KO cell lines. **(A)** A schematic diagram of chYTHDF2 loci in the chicken genome, number of exons, and target exon are shown. **(B)** Sequence confirmation of cloning of two sgRNA targeting exon 1 of chYTDHF2. **(C)** Schematic diagram showing the location of sgRNA in exon 1 of chYTHDF2 and

sequence alignment with the two KO cell clones. **(D)** Sequence confirmation of KO cell lines at the target exon. The cut site and the numbers of deleted/inserted nucleotides are indicated. **(E)** Gel electrophoresis image showing the variation between KO-cell clones compared with DF-1 wt.
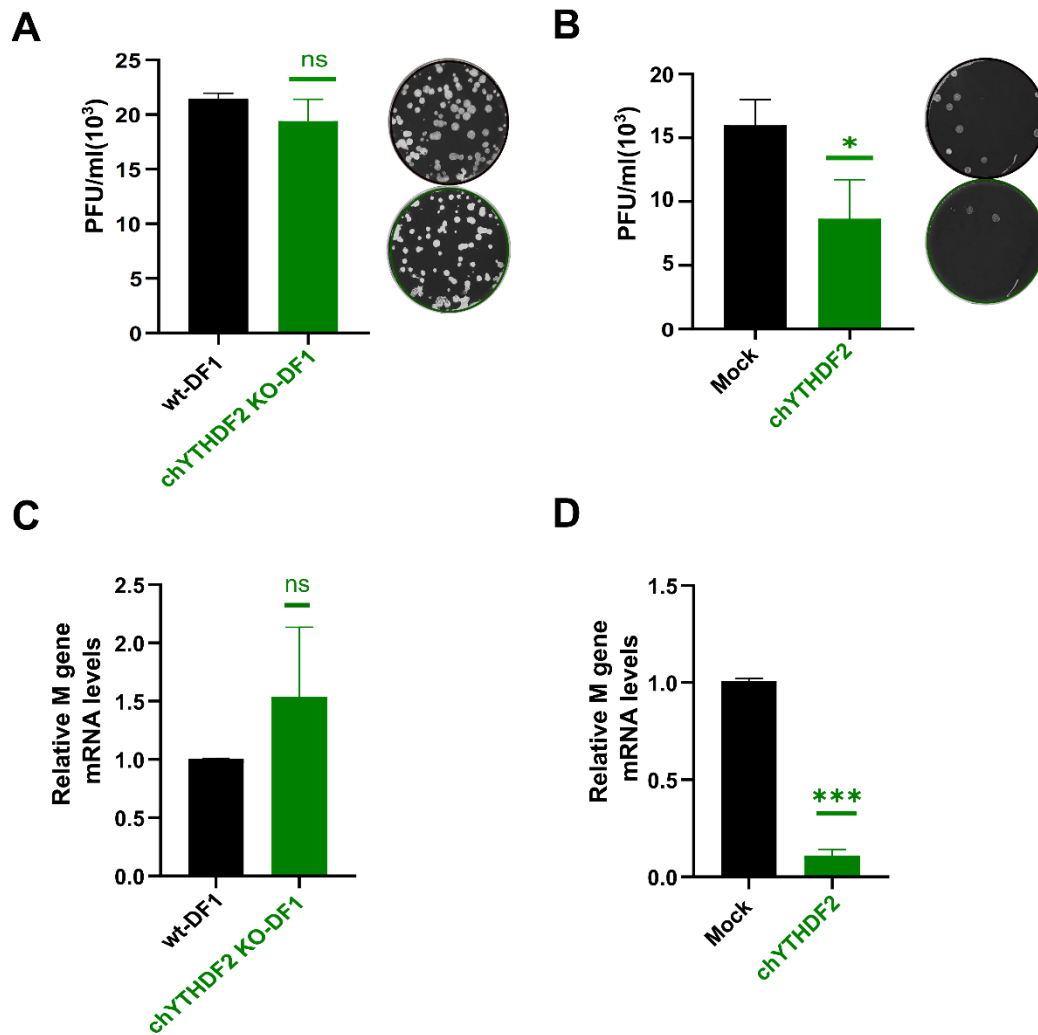
Figure 4.9: Influenza A virus (H9N2) replicated is not significantly different in chYTHDF2-KO compared to wild-type DF1 cells. **(A)** Plaque counts of progeny viruses after infecting DF1-wt or chYTHDF2-KO-cell lines with H9N2 UDL/08 (MOI=1.0) for 24 h. **(B)** Plaque counts of progeny viruses after transfecting KO cell lines with chYTHDF2 (empty vector transfected as mock), then infected with H9N2 UDL/08 (MOI=1.0) for 24 h. **(A and B)**. Representative plaque counts of each condition are shown. The released viruses were quantified using plaque assay on MDCK cells after 72 h. Only wells containing countable plaques are shown. **(C, D)** RT-qPCR was performed to determine the levels of the IAV H9N2 M mRNA from virus-infected cells

as indicated in (A, B). These data represent the average of three biological replicates with SD indicated. ns: non-significant $p > 0.05$, $*p < 0.05$, $***p < 0.001$ using Student's t-test.

4.3.   Chapter Discussion

Investigating the pro- or anti-viral effect of chicken m6A-associated machinery is deemed essential for exploring chickens. It has been reported that the m6A-related proteins have different proviral or antiviral outcomes according to the investigated virus in a cell-type-dependent manner. Therefore, deciphering which chicken m6A-associated proteins are proviral or antiviral was addressed. It was demonstrated that the chicken m6A-machinery negatively modulated influenza virus replication.

Chicken m6A machinery has not been investigated against any virus. Therefore, the first step was to validate the expression of chicken m6A-machinery in chicken cell models after demonstrating their evolutionary variations. Accordingly, ten cDNA coding sequences were fused with the FLAG tagged-containing vectors, each encoding chicken m6A-related proteins (the five prototype m6A-binding proteins, chYTHDF1-3, chYTHDC1-2, and three m6A-methyltransferases chMETTL3/14/WTAP, and the two well-known m6A-demethylases (chALKBH5, chFTO)). Tags were utilized in this study as specific antibodies to the endogenous chicken m6A-machinery were unavailable.

The expression of each of the ten proteins of interest in DF1 cells clearly indicated that m6A-interacting proteins are functional in chickens, as demonstrated by immunofluorescence (IFA) and western blot analysis. chYTHDC-1 and -2 were not detected in western blot analysis but were readily detected in IFA. Swapping chYTHDC1-2 from FLAG-tagged to HA-tagged vectors was also performed. However, YTHDC1-2-HA tagged proteins were also detected using IFA, but not in western blot (data not shown). As mentioned earlier, the presence of specific antibodies against the

endogenous m6A-related protein of chicken would solve this issue. Fortunately, neither YTHDC-1 nor -2 exhibited any outstanding findings/alterations (regarding IAVs) that negatively affected the downstream applications to influence the flow of the study.

Further to the expression pattern of m6A-related enzymes and proteins, only chicken WTAP (chWTAP) was notably different to the human orthologue. A huge body of work reported WTAP expression in the nucleus to target human METTL3/14 to localize into nuclear speckles for the m6A-methyltransferase activity, either ectopically expressed or detected by specific antibodies in humans (Ping et al., 2014; Schöller et al., 2018). However, chWTAP was exclusively noticed in the cytoplasm, even after stimulation with IAVs. This finding suggests that chWTAP does not interact and/or is not a part of the m6A-methyltransferase complex in the chicken. It has been reported that the N terminal coiled-coil domain contains the nuclear localization signal in the human counterpart (Schöller et al., 2018). Changes were only noted in C-terminus (Bayoumi et al., 2020). A functional analysis of this finding will be discussed in the following chapter.

However, upon stimulation with H9N2 for 24 h, no change in the expression pattern of m6A-machinery was detected, indicating that the time-lapse analysis is dispensable. However, specific antibodies to chicken m6A machinery will be beneficial to enrich our understanding for future investigations.

Given the functional expression of chicken m6A-machinery, deciphering which of these proteins has a proviral or antiviral potential is the next question to be answered. Two IAV strains were investigated, a prototype and laboratory-adapted human H1N1 PR8

strain and H9N2 UDL/08 strain that infects humans and chickens (zoonotic potential) as a relevant homologous infection model in chicken cells.

In this study, viral replication kinetics were confirmed in at least two different assays to minimize future discrepancies and ensure a given result. Plaque assay, typical in all investigated analyses (the gold standard for quantification of influenza A viruses) and either relative protein expression or mRNA transcription analysis of viral proteins/genes normalized with reference chicken-specific controls. Flow cytometry-based analysis was also utilized using labeled versions of the investigated virus.

It was clear from plaque assay-based virus counts that most chicken m6A machinery inhibited H9N2, including chYTHDF2, which was reported earlier to potentiate H1N1 virus replication (Courtney et al., 2017). Moreover, chYTHDF2 has a non-significant effect on replication kinetics against H1N1. In contrast, chYTHDF-1 and -3 exhibited a potent antiviral effect. Despite the same virus being investigated, the cell differs; A549 (human) versus DF1 cells (chicken). As discussed earlier, no detectable mutations were recorded in the functional YTH domain of YTHDF2 between humans and chickens, suggesting cell-specific variation affects the outcomes of virus replication (Bayoumi et al., 2020). Cell-type variation effect was also recorded with KSHV, SARS-CoV-2, and HIV-1 viruses; interestingly, all discussed the impact of YTHDF2 (Kennedy et al., 2016; Tirumuru et al., 2016; Hesser et al., 2018). Notably, the effect of chALKBH5 in human cell lines was not investigated in this study, as the constructs used in the study were codon optimized to work optimally in chicken cells. Thus, the investigation of human cell lines would potentially biased.

Viral protein expression analysis supports the viral quantification assay. Expression analysis of the H9N2 HA showed that all H9N2 was inhibited in chicken m6A-machinery transfected cells showed inhibition of H9N2. However, only chYTHDF-1, -3, and chALKBH5 inhibited NP expression of the H1N1. Furthermore, a significant reduction in viral gene transcription was clearly identified in the H9N2 investigations.

Despite the same cells (i.e., DF1) and constructs being utilized to investigate two IAVs, some variations among the potential antiviral proteins were noticed. The chYTHDF2 was a specific antiviral for H9N2, whereas chYTHDF-1 and -3 were for H1N1. Variations in replication kinetics of the H1N1 human virus inside the chicken cell line could potentially rationalize this difference. The interaction between IAVs and chicken m6A machinery may reveal additional insights. Notably, no proviral protein was noted among all investigated m6A proteins. All m6A machinery tends to inhibit H9N2 gene transcription and virus replication. In turn, H9N2 downregulated all m6A-machinery gene expression, highlighting complex virus-host interaction at the m6A interface.

Building from function analysis on the cell line, a primary chicken cell for antiviral analysis was also utilized to avoid future discrepancies originating from investigated primary cells and their derived cell line (Kennedy et al., 2016; Tirumuru et al., 2016). Although plaque assay-based quantification is the most suitable technique, the progeny (released) virus may be generated from both transfected-infected or infected-only cells, making the quantification biased if the transfection efficiency was not optimal (around 50% in DF1). Using empty plasmid as transfection control removes the possibility of false antiviral impacts.

Using flow cytometry-based analysis, only gating GFP+ cells (infected) from the RFP+ cells (transduced) was performed, and this approach has offered more accurate determinations of either proviral or antiviral effects. Conversely, using a recombinant virus expressing an extra GFP protein would affect replication kinetics compared with H9N2-wt. Furthermore, transduction would vary from one protein to another, even within the same family member, as previously reported in YTHDF family members (Courtney et al., 2017).

The antiviral actions of chALKBH5 remained evident in all tested assays against H9N2 and H1N1. Moreover, investigating another well-known antiviral protein in chicken was deemed essential as a positive control. Therefore, the antiviral action of chIFIT5 and chALKBH5 in CEF cells was investigated, and both were found to downregulate H9N2-GFP significantly (Santhakumar et al., 2018). Although the investigated assays did not show identical results, none of the assays indicated a proviral action of any protein. Moreover, all these findings matched the antiviral potential of chALKBH5.

Investigating IAV H9N2 replication in time-lapse after transient overexpression with chALKBH5 clearly demonstrated that chALKBH5 inhibited replication at all time points (4-48 h). These finding altogether point to the fact that chALKBH5 possibly exhibits antiviral functions through direct interaction with either viral transcript(s) or protein(s) to inhibit all virus replication stages. These possibilities will be discussed in detail in the next chapter. Notably, the highest virus titre tested after infection was 24 hr, either mock or chALKBH5 transfected (when infected with MOI=1.0). Virus replication was reduced after 48 hpi (DF1 cells at 48 hpi almost deteriorated, data not

shown). Therefore, in all investigated antiviral assays, MOI=1.0 for 24 h was used to suit optimal cell- and transfection-efficacy conditions.

Investigating chYTHDF2 in this chapter was essential to confirm its antiviral effect in chicken cells. A previous study reported that human orthologue has a potent proviral role against the H1N1 PR8 virus in A549 cells transduced with lentiviruses expressing YTHDF2 (Courtney et al., 2017). However, this finding opposes that chYTHDF2 has antiviral potential against H9N2, and only chYTHDF-1 and -3 (alongside chALKBH5) have an antiviral role against H1N1 in chicken cells. As indicated in **Chapter 3**, no single mutation was noticed in the functional C-terminus YTH- domain between human and chicken YTHDF2, in contrast, the mutations were only recorded in the N-terminus (Bayoumi et al., 2020). It is evident that host variation is the cause of the difference by a yet unidentified mechanism. Moreover, to confirm chYTHDF2 antiviral potential, co-transfection with chALKBH5 enhanced the antiviral activity. This information ensures that the proviral and antiviral role of m6A-associated proteins is possibly cell/host specific.

Generating KO cells was confirmed after validating the presence of frameshift mutations in the coding sequences. The antiviral activity of a given protein in the KO cells is usually reported as higher or no change in virus replication, as described in the literature and listed in **Table 4.1**. Surprisingly, both KO cell lines showed no significance change in non-significant virus replication compared with wild-type cells. However, overexpression of either chALKBH5 or chYTHDF2 in the corresponding KO cells restored antiviral potential. There are several possibilities for the lack of significant differences in IAV replication in KO cell lines. Firstly, both candidates carry ubiquitous

and essential roles in the cell cycle as RNA binding protein (chYTHDF2) or m6A-demethylase (chALKBH5). It is plausible that the absence of chALKBH5 or chYTHDF2 is compensated by other m6A readers or eraser proteins in the KO cell line (i.e., functional redundancy), which requires the deletion of multiple genes simultaneously. Secondly, the KO cells potentially express higher innate immune genes that restrict enhanced virus replication, which will be defined in detail in the next chapter. Altogether, the array of findings supports the antiviral action of chALKBH5 and chYTHDF2 candidates against H9N2.

Chapter 5

Mechanistic studies on chALKBH5

and chWTAP in regulating IAVs

infection

5.1. Chapter Introduction

5.1.1. Mechanistic actions of ALKBH5 and FTO in regulating various biological processes

5.1.1.1. Biological functions of the m6A-erasers

5.1.1.1.1. Pathological regulatory aspects of m6A-erasers

The m6A-demethylases are extensively involved in the development of various cancers. ALKBH5 plays a vital role in regulating breast cancer development through hypoxia-inducible factor in an ALKBH5-dependent pathway. Mechanistically, ALKBH5 was reported to demethylate m6A marks from NANOG, which is one of the chief regulatory factors in promoting pluripotency. The m6A removal from NANOG supports mRNA stability and protein expression, aggravating breast cancer (Zhang et al., 2016a). After that, it was verified that the knockdown of ALKBH5 from breast cancer cell lines suppressed breast-to-lung metastasis in mice (Zhang et al., 2016b).

Overexpression of FTO was also correlated with breast cancer development. FTO demethylates 3′ UTR BNIP3 mRNA, a pro-apoptotic protein belonging to the Bcl-2 tumour suppressor family. The FTO demethylation activity promotes BNIP3 degradation to support breast cancer proliferation and metastasis (Niu et al., 2019). It appears that both ALKBH5 and FTO stimulate breast cancers through methylation reversal of the target transcripts (Deng et al., 2018a; Mauer and Jaffrey, 2018; Rajecka et al., 2019; Melstrom and Chen, 2020).

Similar to the action in breast cancers, ALKBH5 promotes lung adenocarcinoma and malignant brain tumour glioblastoma, through demethylation of Forkhead box M1

mRNA (FOXM1), a primary tumour inducer. ALKBH5 increases transcript stability and protein expression (Dixit et al., 2017; Zhang et al., 2017; Chao et al., 2020; Malacrida et al., 2020).

ALKBH5 contributed significantly to physiological osteogenesis (Yu et al., 2020). However, ALKBH5 mediates osteosarcoma by removing the m6A marks from plasmacytoma variant translocation 1 (PVT1), which is a tumorigenic noncoding RNA. Consequently, the stability of PVT1 is significantly increased to support osteosarcoma in animal models (Int et al., 2020). Similarly, ALKBH5 promotes gastric cancer by regulating a long noncoding RNA nuclear paraspeckle assembly transcript 1 (NEAT1) (Zhang et al., 2019b; Zhu et al., 2020). ALKBH5 was also identified to modulate ovarian cancers and induce Bcl-2 transcript stability via demethylation (Zhu et al., 2019). ALKBH5 also controls testicular germ cell type II cancers in males; however, the mechanism was not fully identified (Nettersheim et al., 2019).

FTO has been reported to modulate melanoma, and single-nucleotide polymorphisms in FTO have been associated with a high risk of melanoma (Iles et al., 2013; Deng et al., 2018b). Moreover, FTO targets anti-melanoma gene transcripts, including PD-1, C-X-CR-4, and SOX10 by demethylation (Yang et al., 2019b; Melstrom and Chen, 2020; Zhao et al., 2020b). The most studied tumorigenic role of FTO was in acute myeloid leukaemia. FTO demethylates m6A marks of both ASB2 and RARA mRNAs decreasing stability, hence leukemogenesis (Li et al., 2017; Huang et al., 2019; Weng et al., 2019; Zhao et al., 2020b).

Unlike all mentioned regulatory roles of m6A-erasers in promoting tumorigenic, ALKBH5 expression downregulates pancreatic cancers. By demethylation, ALKBH5

targets KCNK15-AS1, a long non-coding RNA, to inhibit pancreatic cancer metastasis (He et al., 2018). Likewise, ALKBH5 targets integrin alpha-6 (ITGA6) mRNA to inhibit bladder cancers (Jin et al., 2019). To summarize, the m6A-erasers demethylate specific mRNA and long noncoding RNA to induce or inhibit carcinogenesis.

5.1.1.1.2. Physiological and metabolic regulatory roles of m6A-erasers

ALKBH5 was also reported to play a negative role in placenta development during pregnancy through its adverse action on trophoblast invasion, promoting recurrent miscarriage. ALKBH5 reduces the half-life of cysteine-rich angiogenic inducer-61 (CYR61) mRNA. The CYR61 involved in cell differentiation, migration, and normal embryogenesis (Li et al., 2019).

Expression levels of m6A-erasers were correlated with impaired fertility. FTO was reported to regulate m6A levels in pre-mature ovarian insufficiency, mediating infertility (Ding et al., 2018). Likewise, ALKBH5 deficiency in male mice impaired their fertility due to a global increase in m6A levels. Uncontrolled m6A levels ultimately harm the meiotic metaphase stage of spermatocytes (Zheng et al., 2013). This finding was explained later, ALKBH5-ensured proper production of longer 3′ UTR transcripts with correct splicing through an m6A-dependent manner (Tang et al., 2017). Furthermore, ALKBH5 regulates adipogenesis and myogenesis by modulating differentiation markers such as CEBPb and myogenin (Choi et al., 2019). FTO also caused differentiation of the neuronal stem cells in adult mice (Cao et al., 2019).

The m6A-erasers also regulate some metabolic processes, inducing autophagy, an evolutionarily conserved degradation pathway in the cell. ALKBH5 positively regulates the m6A levels on the chief regulator in autophagy, the transcription factor EB mRNA (TFEB) (Song et al., 2019). Additionally, FTO was commonly studied in obesity-related research. Single-nucleotide polymorphisms (SNPs) primarily located in intron-1 of FTO were linked with obesity in humans (Zhao et al., 2014b). It has been suggested that the FTO gene is under the control of nearby associated genes, including IRX3, to be the primary regulator in obesity (Smemo et al., 2014; Zhou et al., 2017; Deng et al., 2018b; Mauer and Jaffrey, 2018). Various pathological and physiological regulatory roles of m6A-demethylases are summarized in **Table 5.1**.

Table 5.1. Various regulatory aspects of m6A-erasers

m6A demethylase	Regulatory Aspect	Tissue Involved	Regulatory Gene(s)	References
ALKBH5	**Cancer Type**	Breast Cancer	NANOG	(Zhang et al., 2016a, 2016b)
		Glioblastoma	FOXM1	(Dixit et al., 2017; Zhang et al., 2017; Malacrida et al., 2020)
		Lung Adenocarcinoma	FOXM1	(Chao et al., 2020)
		Pancreatic Cancer	CNK15-AS1 WIF- 1	(He et al., 2018) (Tang et al., 2020)
		Bladder Cancer	ITGA6	(Jin et al., 2019)
		Oral Squamous Cell Carcinoma	FOXM1 / NANOG	(Shriwas et al., 2020)
		Osteosarcoma	PVT1	(Int et al., 2020)
		Gastric Cancer	EAT1	(Zhang et al., 2019b; Zhu et al., 2020)
		Colon Cancer		(Yang et al., 2019a)
		Ovarian Cancer	Bcl2	(Zhu et al., 2019)
		Male Germ Cell Tumour		(Nettersheim et al., 2019)
	Metabolic Disorder	Male Infertility	Correct spliced / longer transcripts	(Tang et al., 2017)
		Autophagy (ischaemic heart disease)	FEB	(Song et al., 2019)
	Differentiation	Placenta	CYR61	(Li et al., 2019)
		Adipogenesis	CEBPb	(Choi et al., 2019)
		Myogenesis	Myogenin	(Choi et al., 2019)
FTO	**Cancer Type**	Breast Cancer	NIP3	(Niu et al., 2019)
		Melanoma	PD-1 CXCR4 SOX10	(Yang et al., 2019b; Melstrom and Chen, 2020; Zhao et al., 2020b)
		Acute Myeloid Leukaemia	ASB2 and RARA	(Li et al., 2017; Huang et al., 2019; Weng et al., 2019; Zhao et al., 2020b)
		Gastric Cancer		(Xu et al., 2017; Zhang et al., 2019a)
	Metabolic Disorder	Obesity	FTO gene Intron1 IRX3	(Zhao et al., 2014b) (Smemo et al., 2014)
	Differentiation	Premature Ovarian Insufficiency Neuronal Stem Cells		(Ding et al., 2018) (Cao et al., 2019)

5.1.1.1.3. Viral regulatory roles of m6A-erasers

As mentioned earlier, all studied viral RNAs accept m6A marks, which dictate the viral lifecycle and outcome of the virus-host battle (Dang et al., 2019). Likewise, m6A-demethylases promote carcinogenesis in an m6A-dependent manner in cellular transcripts (**Section 5.1.1.1.1**), ALKBH5 and FTO direct oncogenic viruses to induce tumorigenesis by acting on viral RNA (Imam et al., 2018; Tan et al., 2018; Tsai et al., 2018; Lang et al., 2019). METLL3, METTL 14, and FTO mediate regulatory functions on hepatitis B viruses (HBV). They collectively regulate viral gene expression and reverse transcription to modulate the fate of HBV in liver disease pathogenesis and tumour formation (Imam et al., 2018). Additionally, epitranscriptome sequencing data revealed that m6A promotes late and lytic transition; m6A-erasers are vital regulators in KSHV infection and KSHV-induced oncogenesis (Ye et al., 2017; Hesser et al., 2018; Tan et al., 2018). Similarly, ALKBH5 regulates EBV latent protein EBNA3C to enhance tumorigenesis via an m6A-dependent pathway in Epstein-Barr virus (EBV) (Lang et al., 2019). All current findings indicate that m6A-erasers have adverse regulatory roles in oncogenic viruses promoting carcinogenesis.

As indicated in **Chapter 4,** the m6A demethylases have unclear selective roles in the lifecycles of various viruses. ALKBH5 was involved in the regulatory functions of HIV-1 and VSV (Lichinchi et al., 2016a; Tirumuru et al., 2016; Liu et al., 2019). In contrast, FTO selectively modulates viral infection of HCV (Gokhale et al., 2016) and enterovirus-71 (Hao et al., 2019). Both demethylases have regulatory functions in Zika and respiratory syncytial viruses (Lichinchi et al., 2016b; Xue et al., 2019).

To summarize, the m6A demethylases usually display various regulatory functions in cellular contexts. The main mechanistic action is typically the demethylation of their selective targets. Upon demethylation, m6A-erasers enhance/inhibit mRNA transcripts' expression and stability of mRNA transcripts. However, which demethylases affect which transcript/virus remains unclear. Therefore, developing specific inhibitors for m6A-demethylases is an ambitious target to alleviate many cancers and viral diseases, as reviewed earlier (Bayoumi and Munir, 2021c). In this chapter, a trial to comprehensively decipher the mechanistic action(s) of chALKBH5 and chFTO in regulating IAVs was performed.

5.1.2. Genome editing technologies in the biological- and virus-related fields.

5.1.2.1. Introduction to CRISPR/Cas13 effectors

Bacteriophage usually infects bacteria and archaea. Consequently, prokaryotes developed an adaptive immune system to fend off invading phage; the Clustered Regularly Interspaced Short Palindromic Repeats (CRISPR)–CRISPR-associated (Cas; CRISPR–Cas) systems (Makarova et al., 2006). The CRISPR/Cas system is comprised mainly of nuclease(s) and CRISPR array. The array is composed of spacers and repetitive sequences. The spacers are usually short sequences derived from invading viruses to stimulate further degradation. At the same time, the direct repeats are the regulatory elements in that battle (Jansen et al., 2002; Yosef et al., 2012; Vercoe et al., 2013).

Developing immunity in prokaryotes usually occurs in three stages. In the first adaptation stage, random sequences (i.e., spacers) derived from viruses are incorporated into genomic sequences by prokaryotic Cas1 and Cas2 proteins and repetitive sequences inserted in between (spacer acquisition) (Boyaval et al., 2007). In the second maturation stage, the integrated arrays are transcribed into precursor CRISPR-RNA (pre-crRNA), which is further processed to generate developed crRNAs comprised of the spacers and repeat sequences (Deltcheva et al., 2011; Jinek et al., 2012). In the third stage, the developed crRNA joins the nuclease to scan for a complementary seed sequence (Semenova et al., 2011). In the subsequent viral invasion, Cas effector(s) exert their nuclease activity to degrade the viral nucleic acid **(Figure 5.1)** (Wiedenheft et al., 2011; Van Der Oost et al., 2014; Marraffini, 2015).
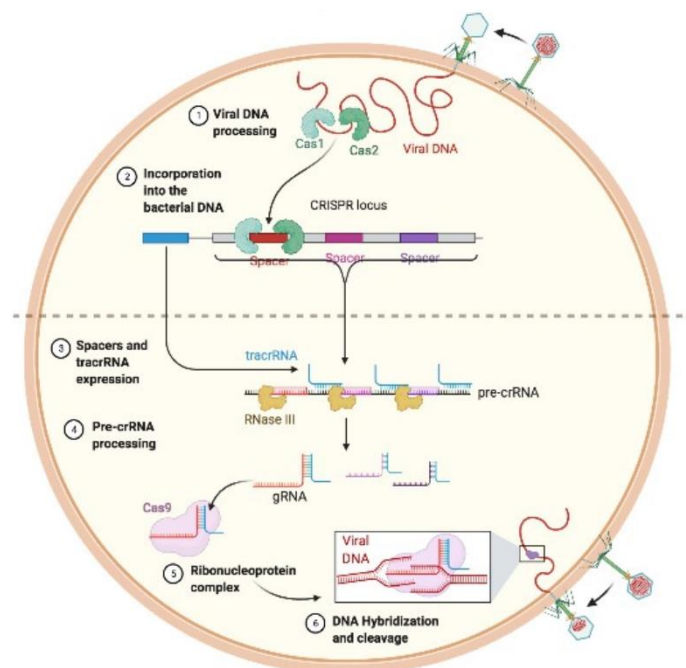

Figure 5.1: Schematic of the adaptive immune system of *Streptococcus pyogenes* against viral phage. Bacteriophage start with the initial invasion of the bacteria; Cas1 and Cas2 process and integrate viral sequences into bacterial DNA in the CRISPR locus

(spacer acquisition, 1 and 2). The CRISPR array is transcribed and processed into mature crRNA (maturation, 3 and 4). Finally, the ribonucleotide complex (Cas protein and guide RNA) hybridizes with the complementary sequence of viral DNA and induces cleavage of invading viral genome (interference phase, 5 and 6) in case of re-infection.

CRISPR-Cas systems are categorized into two main classes; class I, in which the effectors are composed of multiple protein subunits. In contrast, class II has a single multidomain Cas protein. Moreover, CRISPR/Cas systems can be divided into types based on spacer acquisition components (i.e., Cas1 and Cas2); type I–VI. Class I include types I, III, and IV, whereas Class II has types II, V, and VI **(Figure 5.2)** (Makarova et al., 2018, 2020).
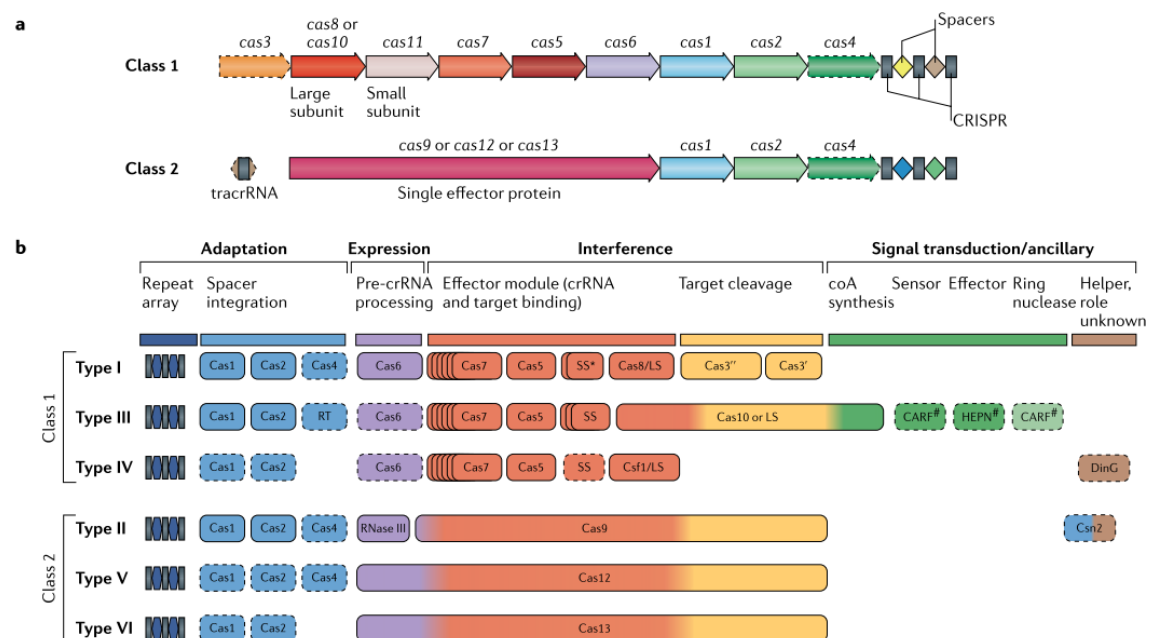

Figure 5.2: Schematic of CRISPR-Cas systems categorization and organization. **(a)** The genetic organization of class 1 is mainly composed of multi-Cas proteins along

with crRNA to a target sequence and induce bonding and nuclease activity. Class 2 is primarily composed of multi-domain single-effector Cas protein. **(b)** The illustration indicates the functional modules of CRISPR-Cas systems in another categorization of CRISPR/Cas systems according to types I-VI. The genetic, structural, and functional organizations of the CRISPR/Cas types are indicated. The figure is adapted from a previous report (Makarova et al., 2020).

Owing to their higher specificity and limited off-target effects, CRISPR/Cas systems attained a good reputation in molecular biological techniques, including viral RNA interferences and viral diagnostics (Brezgin et al., 2019; Banan, 2020). The most studied model in the CRISPR/Cas system was the CRISPR/Cas9, which targets dsDNA, revolutionizes our understanding in multiple biological fields, and regulates both genome and epigenome (Soppe and Lebbink, 2017; Banan, 2020).

On the other hand, endonuclease Cas 13 variants have recently been validated to harness RNA in biotechnology and molecular biology to disturb cellular transcripts and modulate and edit the transcriptome **(Figure 5.3)** (Abudayyeh et al., 2016; East-Seletsky et al., 2016).

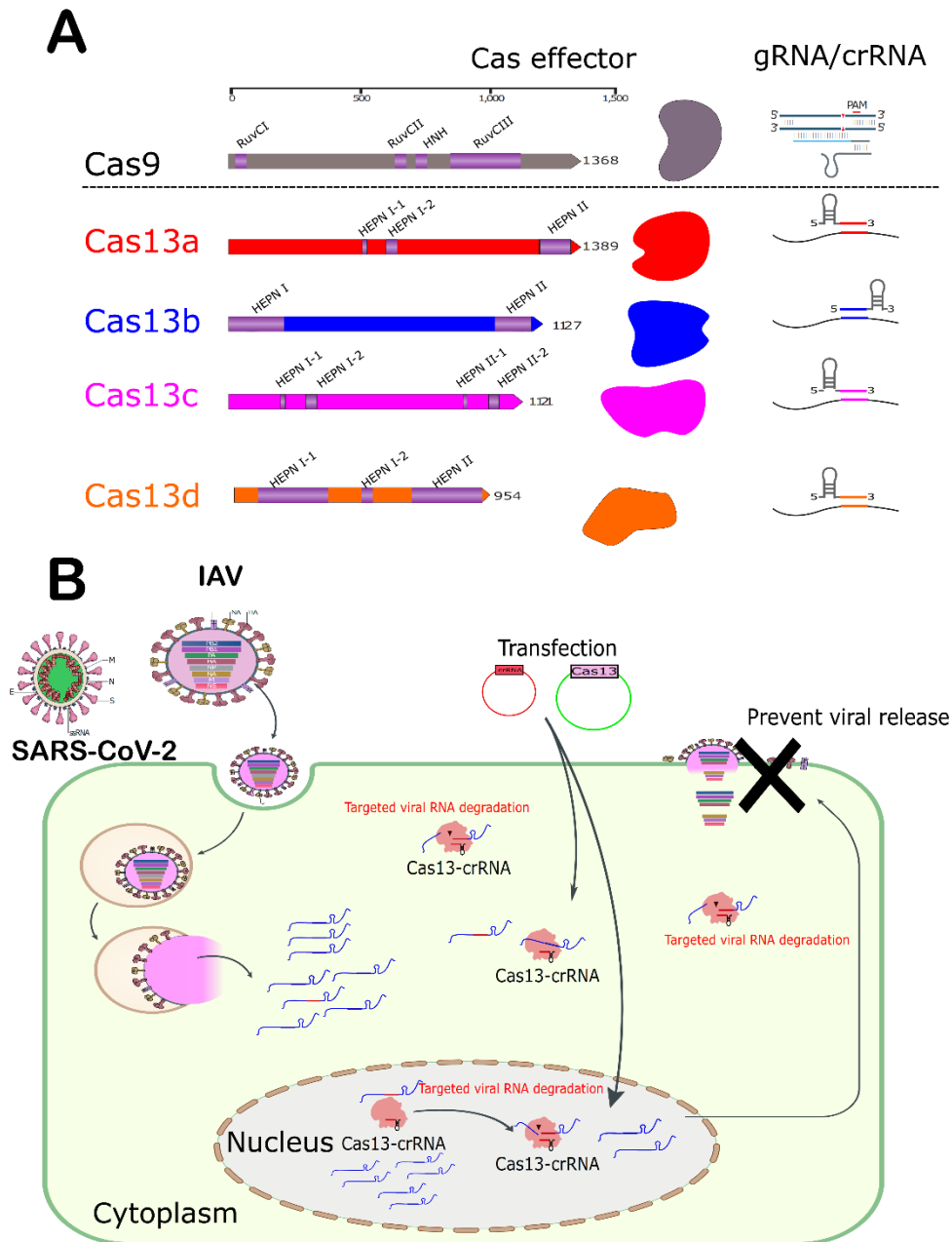**Figure 5.3:** Domain architectures of various CRISPR/Cas effectors and RNA-mediated degradation of Cas13 effectors. **(A)** Schematic of the architecture of class II CRISPR/Cas nucleases (multidomain single effector protein). The approximate length of each protein is indicated at the top scale. Schematic of gRNA and crRNAs of the Cas9 and Cas13s, respectively, are also shown. **(B)** Schematic of the mechanistic action

of RNA-mediated interference of Cas13 nucleases in a cell model for viral degradation. The figure is adapted from our publication (Bayoumi and Munir, 2021b).

5.1.2.2. CRISPR-Cas13 as a novel viral transcriptome-degradation and diagnostic platform

Viruses threaten all life forms, including humans, plants, and animals worldwide (Nomaguchi and Adachi, 2017; Woolhouse and Brierley, 2018). RNA viruses usually emerge with potential pandemic threats, including influenza, Zika, Ebola viruses, and, very recently, SARS-CoV-2 (Woolhouse and Brierley, 2018; Wu et al., 2020; Zhou et al., 2020). RNA viruses are responsible for at least 200 human diseases and contribute to 6% of human deaths worldwide (Lozano et al., 2012; Woolhouse et al., 2012; Woolhouse and Brierley, 2018). With all these facts, human viral diseases are only confronted by nine approved antivirals and fifteen licensed vaccines (De Clercq and Li, 2016).

These insufficient numbers of antiviral and chemotherapeutics are caused by either viral-adapted genetic shift and drift or antibody-dependent enhancement and other immune-mediated diseases. Additionally, generating ideal vaccines and broad antivirals could take decades, along with high costs, complicating the notion (Bai et al., 2012; Irwin et al., 2016; Kamath, 2016). All these challenges indicate an urgent need to develop a new strategy for combating viral diseases with high specificity, sensitivity, economics, and broad viral activity. Nowadays, Cas13 effectors and rationally designed crRNA(s) could target intracellular RNA for viral interference **(Figure 5.3B)**.

Regarding CRISPR/Cas13 diagnostics, the above-mentioned adaptive immune system in prokaryotes provided an exceptional advantage for diagnosis in vitro. Upon degrading the viral sequence, the Cas13 promiscuously degrades adjacent non-target RNA, which is referred to as collateral activity, an earlier step for programmed cell death (Abudayyeh et al., 2016). This collateral activity was leveraged to degrade a synthetic-labeled non-target RNA (reporter) in vitro **(Figure 5.4)**. Successful examples of using CRISPR/Cas13-mediated RNA interference are summarized in **Table 5.2**.
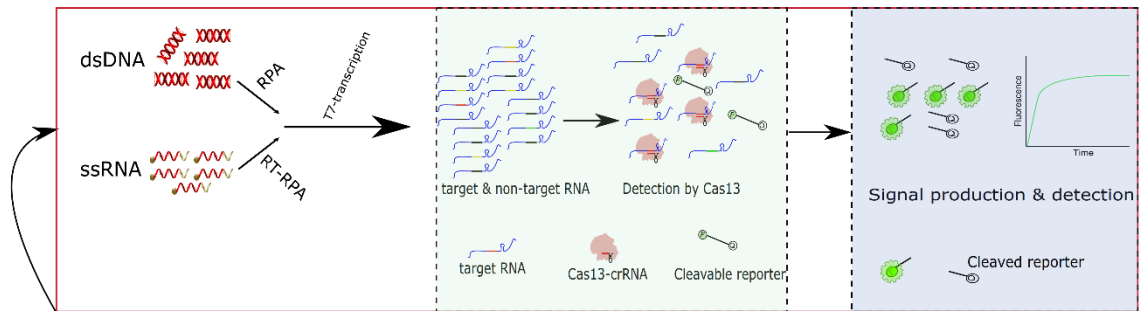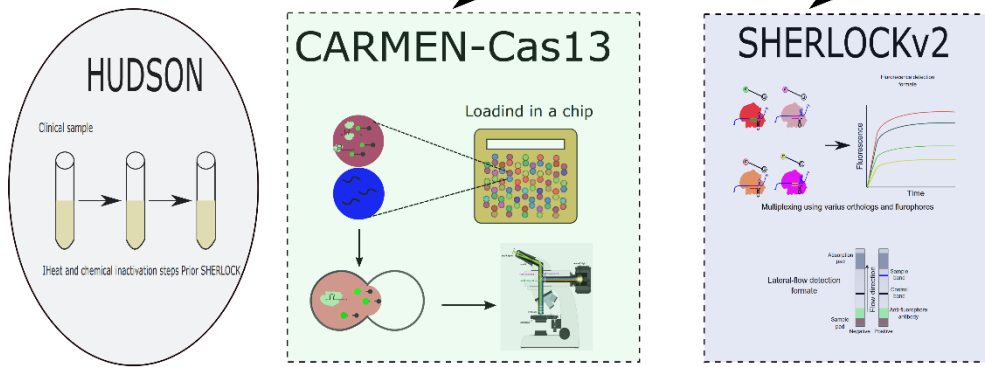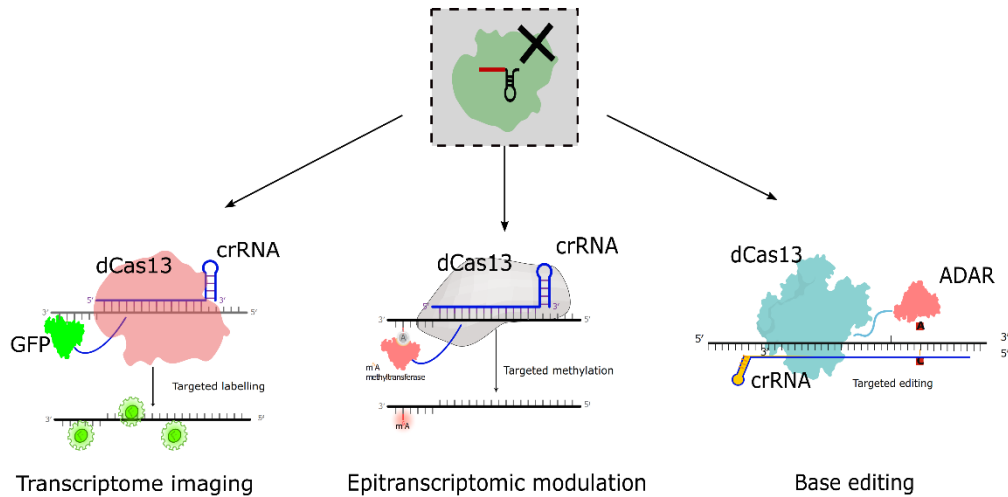
Figure 5.4: Schematic of CRISPR/Cas13-mediated diagnostics and catalytically inactive Cas13s effectors in virus-related fields. **(A)** Schematic of Specific High-Sensitivity Enzymatic Reporter UnLOCKing (SHERLOCK). RPA; recombinase polymerase amplification. **(B)** Schematic of the modifications to the SHERLOCK assay. CARMEN; combinatorial arrayed reactions for multiplexed evaluation of nucleic acids. Emulsions are added to the chip for detection, usually using fluorescence-based microscopy. HUDSON; heating unpurified diagnostic samples to obliterate nucleases, the HUDSON is ideally executed prior to the prototype SHERLOCK assay. SHERLOCKv2 differs from the prototype in using a combination of multiple Cas13s effectors indicated by various colour-coded proteins. SHERLOCKv2 differs in readout format using later-flow strips. (C) Schematics of the catalytically inactive (dead) Ca13s fusion applications for base-editing, imaging, and epigenetic modulation. The figure is adapted from our publication (Bayoumi and Munir, 2021b).

Table 5.2. Summary of the applications of Cas13 effectors in viral RNA-mediated degradation and CRISPR-based diagnostics

Application	Viruses	Cas13 orthologues	References
RNA-degradation			
	Turnip mosaic virus (TuMV)	*Lsh*Cas13a	(Aman et al., 2018a) (Aman et al., 2018b)
	Turnip mosaic virus (TuMV) tobacco mosaic virus (TMV)-RNA- based overexpression (TRBO-G)	*Lwa*Cas13a *Psp*Cas13b CasRx	(Mahas et al., 2019)
	Potato virus Y (PVY)	*Lsh*Cas13a	(Zhan et al., 2019)
	Southern rice black-streaked dwarf virus (SRBSDV)	*Lsh*Cas13a	(Zhang et al., 2019c)
	Influenza A virus (IAV) Respiratory syncytial virus model (RSV)	*Lbu*Cas13a	(Bawage et al., 2018)
	Lymphocytic choriomeningitis (LCMV) Vesicular stomatitis virus (VSV) IAV.	*Lwa*Cas13a *Psp*Cas13b	(Freije et al., 2019)
	severe acute respiratory syndrome coronavirus 2 (SARS-CoV-2) IAV	CasRx	(Abbott et al., 2020)
	SARS-CoV-2 IAV	*Lbu*Cas13a	(Blanchard et al., 2021)
	Hepatitis C Virus HCV	*Lsh*Cas13a	(Ashraf et al., 2021)
	Porcine reproductive and respiratory syndrome virus (PRRSV)	*Psp*Cas13b	(Cui et al., 2020)
CRISPR-based diagnosis			
	ZIKA and Dengue RNA (SHERLOCK)	*Lwa*Cas13a	(Gootenberg et al., 2017)
	ZIKA and Dengue RNA (SHERLOCKv2)	*Lwa*Cas13a, *Cca*Cas13b, *Lba*Cas13a, *Psm*Cas13b	(Gootenberg et al., 2018)
	Flaviviruses (HUDSON-SHERLOCK)	*Lwa*Cas13a	(Myhrvold et al., 2018)
	All 169 human-associated viruses, Including IAV, SARS-CoV-2, HIV (CRISPR-Cas13 with CARMEN)	*Lwa*Cas13a	(Ackerman et al., 2020)
	Ebola virus (EBV) and Lassa virus (SHERLOCK-HUDSON)	*Lwa*Cas13a	(Barnes et al., 2020)(Qin et al., 2019)

5.1.2.3. Using the catalytically inactive/dead CRISPR-Cas13 effectors (dCas13s) for better understanding virus-host interaction

It has been reported that the Cas13 module can be harnessed to induce RNA base editing by fusing a catalytically inactive Cas13 with the adenosine deaminase acting on RNA type 2 (ADAR2) (Cox et al., 2017). This strategy yielded high binding specificity, efficiency, and unnoticeable off-target effect for editing adenosine-to-inosine (A-to-I) in cellular transcripts. This approach was named RNA Editing for Programmable A to I Replacement (REPAIR; **Figure 5.4C)** (Cox et al., 2017). Through this strategy, various genetic disorders would be solved shortly in the mRNA levels instead of using exogenous proteins usually associated with aberrant outcomes and enhanced immunogenicity (Qu et al., 2019). Additionally, this system is validated in various mammalian and yeast cells (Cox et al., 2017; Jing et al., 2018; Qu et al., 2019).

After that, RNA-guided dCas13s effectors have been harnessed in intracellular RNA regulatory processes, including blocking cellular transcript RNA-protein binding sites (Yao et al., 2019). Very recently, dCas13s have been fused successfully with multiple splicing factors to alter exon exclusion and inclusion in the cellular transcriptome (Du et al., 2020; Leclair et al., 2020).

These achievements inspired various groups to utilize the Cas13-based RNA editing approach to induce epitranscriptome modifications to cellular transcripts. Several efforts have been made to fuse dCas13 effectors with different m6A-related proteins, including METTL3 and ALKBH5, inducing targeted methylation and demethylation of specific cellular transcripts, respectively **(Figure 5.5)** (Li et al., 2020; Wilson et al., 2020; Zhao et al., 2020a; Xia et al., 2021b).
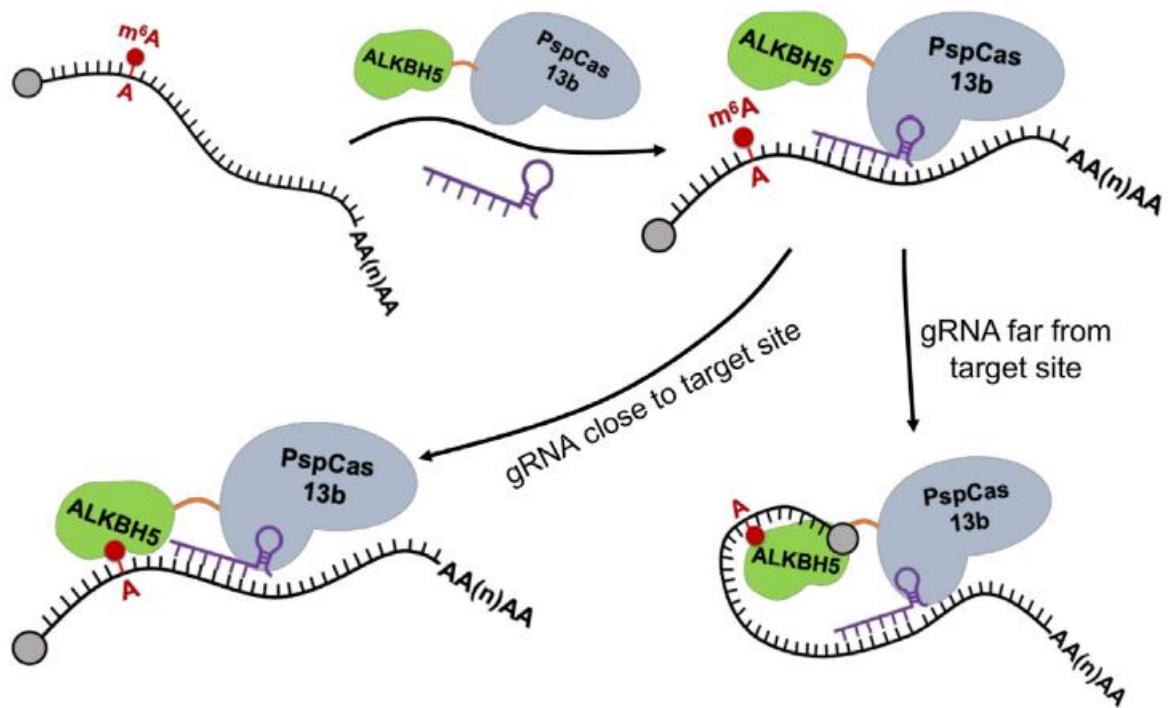
Figure 5.5: Schematic of ALKBH5 targeted demethylation to a given cellular transcript. The figure is adapted from a previous study (Li et al., 2020).

Further to the finding that chALKBH5 downregulated influenza viral infection, thinking to be the first proof-of-evidence to implement a genome editing strategy to modulate viral replication is an ambitious target, through inducing targeted/programmable demethylation by fusing chALKBH5 with dCas13b. In this manner, chALKBH5 would bind to target viral transcript (HA mRNA) and induce m6A-demethylation, inhibiting viral replication and gene expression.

5.1.3. Endogenous labelling of cellular proteins, a viable method for dissecting the location and function of proteins in real-time

Conventional immunolabelling techniques for visualizing cellular proteins are usually incompatible with live imaging. Real-time visualization of a given protein is crucial to delineate its mechanistic actions in the cellular processes through tagging with a fluorescent protein. However, fluorescent protein tagging by overexpression has fallen short in this regard due to uncontrollable off-target effects and misleading results compared to the endogenous version. Therefore, knock-ins of fluorescent-tagged proteins endogenously could be a viable solution (He and Huang, 2018).

Until recently, the endogenous labelling of cellular proteins could not be achieved without very complex schemes (Fortin et al., 2014) or even associated with global expression of the fluorescent protein with poor contrast to be used for *in vivo* models (Herzog et al., 2011). With the era of CRISPR-based techniques, genome editing technologies have revolutionized our understanding of many biological processes (Cong et al., 2013; Heidenreich and Zhang, 2016; Doudna, 2020). Through CRISPR-based techniques, multiple reporter cell lines and animal models were generated via knock-ins of fluorescent-tagged proteins into endogenous targets (Suzuki et al., 2016; Uemura et al., 2016; Gao et al., 2019; Artegiani et al., 2020); however, the majority of the research is focused in the neuroscience field.

As previously discussed in the gene editing technology section, the knock-ins are usually achieved by sgRNA-guided Cas protein (commonly the Cas9) to induce double-strand breaks (DSBs). Following the breaks, the cellular machinery starts its endogenous DNA repair machinery to cut sites primarily by two mechanisms, either

insertion or deletion (non-homologous end joining, NHEJ) or replacement of donor

DNA if available at cut and repair site (homology-directed repair, HDR; **Figure 5.6)**

(Doudna, 2020).
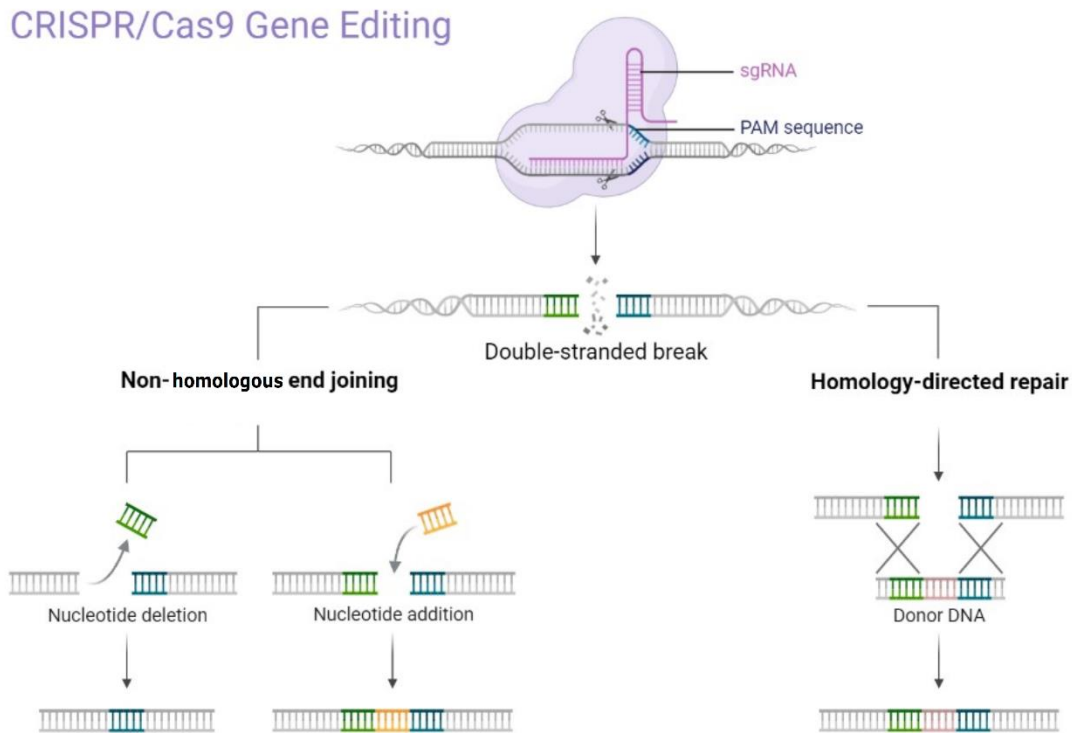
Figure 5.6: CRISPR/Cas9 genome editing toolbox. CRISPR/Cas9 protein induces a

double-strand breaks into a genome sequence targeted by sgRNA. The cut sites are

usually repaired through insertion or deletion into the cut site (NHEJ, left). If a donor

sequence is available can be replaced instead through homology-directed repair (HDR,

right).

Knock-ins of the fluorescent protein into a genomic sequence are usually achieved

through insertion into the coding sequence of the protein of interest using NHEJ or

HDR. These methods are typically hampered by poor insertion and expression rates due to the possibility of shifting the coding sequence of the protein due to the uncontrolled integration event into target exonic sequences (Suzuki et al., 2016; Uemura et al., 2016; Roberts et al., 2017; Gao et al., 2019; Artegiani et al., 2020).

Very recently, Zhong et al. (2021) have established a robust method to illuminate neuronal cells using NHEJ by targeting intronic sequences of the gene of interest (Zhong et al., 2021). The authors used donor molecules containing the coding sequence of fluorescent proteins flanked by intronic, splice acceptor, and splice donor sequences. Once incorporated into the intron of the cellular protein of interest, the fluorescent protein will be integrated into the target protein after splicing out the introns (including any possible insertion/deletion (INDELs) events due to integration), making the resultant mRNA error-free. The technique was named CRISPR-mediated insertion of exon (CRISPIE; **Figure 5.7)** (Zhong et al., 2021).
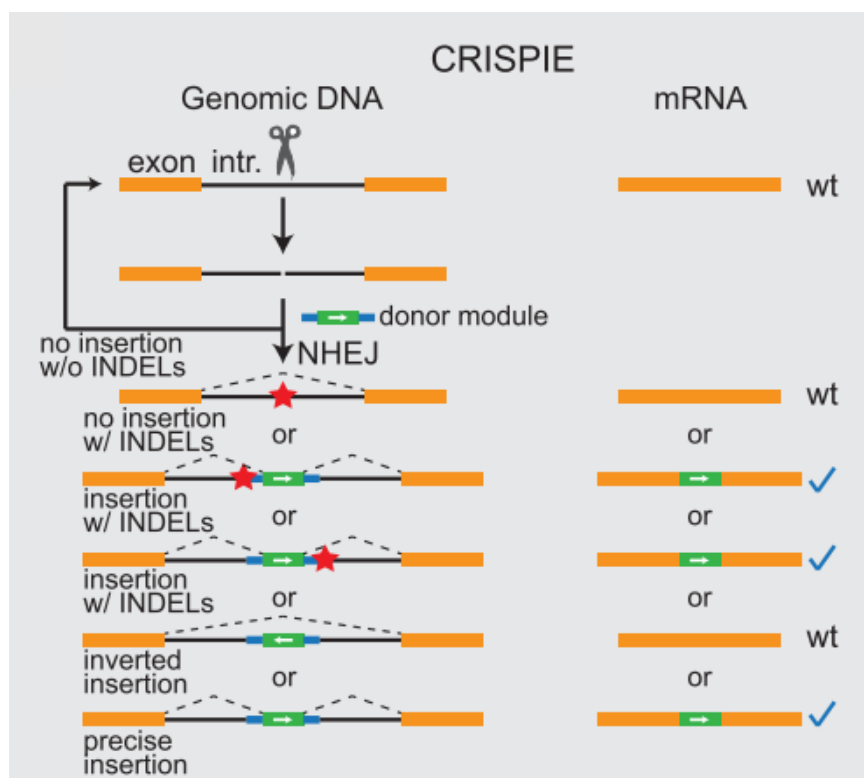
Figure 5.7: Schematic of CRISPR-mediated insertion of exon strategy (CRISPIE) to visualize target cellular protein. The CRISPR/Cas9 guided by sgRNA induces double-strand breaks into the introns of interest, generating insertion and deletions (INDELs, represented by red stars). The donor module contains the fluorescent protein, intron, splice donor, and acceptor sequences inserted into the generated breaks. Creating either wild-type or inserted fluorescent protein in the mRNA of interest is error-free. The endogenous exons/introns are indicated by orange boxes and black lines, respectively. Green boxes and blue lines indicate the donor module. The figure is adapted and modified from a previous investigation (Zhong et al., 2021).

Rather than only using this strategy for the neuroscience field, Visualizing the chALKBH5 in real-time (by generating a reporter chALKBH5 DF1 cell line) could be amenable in virus-related aspects. To confirm the nuclear expression of chALKBH5. Using the live imaging tool in virus-related research and provide a mechanistic tool for better understanding virus replication kinetics in real-time.

5.1.4. m6A methyltransferase complex in human

The m6A methyltransferase complex is comprised of multiple proteins, including METTL3, METTL14, WTAP, RBM15/RBM15B, KIAA1429, ZC3H13, HAKAI, that trigger methyl group transfer to generate N6-methyladenosine (m6A) (Huang and Yin, 2018). However, the predominant and most crucial protein for methyltransferase activity is METTL3 (the active subunit). METTL3 tightly binds to the catalytically inactive subunit METTL14, which serves as an RNA binding scaffold indicated by the crystal structure. METTL3/14 belongs to the methyltransferases family and contains an MT-A70 domain, later named methyltransferase domain, MTD) (Śledź and Jinek, 2016; Wang et al., 2016b, 2017b).

This heterodimer is guided by Wilms' tumour 1-associated protein (WTAP), which is linked with the splicing process in the cells, to target them to the nuclear speckles. The absence of these essential components negatively affects RNA methylation (Horiuchi et al., 2013; Liu et al., 2014; Ping et al., 2014).

Mapping of interaction surfaces of METTL3/14 and WTAP indicates that METTL3/14 interact via their methyltransferase domains. At the same time, METTL3 binds (with its short leader sequence in the far N-terminus) with the N-terminal (coiled-coil) domain of WTAP in humans **(Figure 5.8)** (Schöller et al., 2018). The latter study also confirmed nuclear expression of the ectopic METTL3/14 and WTAP in HEK-293T cells (Schöller et al., 2018), which is identical to what has been reported in the endogenous METTL3/14 and WTAP in HeLa cells (Ping et al., 2014). Moreover, it is important to mention that neither RNA nor m6A modifications are essential for METTL3/14/WTAP formation (Ping et al., 2014).

Precise identification of the nuclear localization sequences of METTL3 and WTAP was also verified in humans (Schöller et al., 2018). All these findings indicate that human METTL3/14 and WTAP interact with each other in a complex in the nucleus. However, this chapter will show that the above-mentioned facts are not identical to chicken methyltransferase machinery, including the cytoplasmic expression of chWTAP, which does not interact with the METTL3/14 complex.
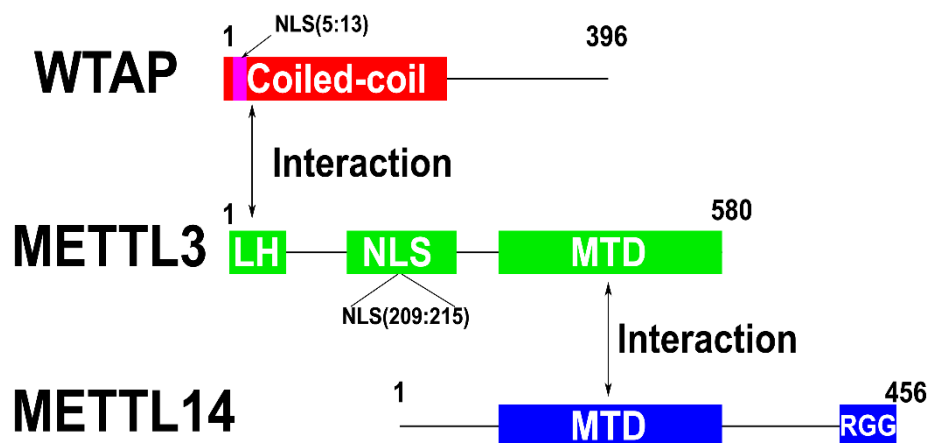
Figure 5.8: Schematic of the interaction surfaces between METTL3, METTL14, and WTAP in humans. The characteristic domain(s) and nuclear localization sequence (NLS) locations in each protein are shown. MTD: Methyltransferase domain, LH: leader helix. RGG: C-terminal RGG repeats in METTL14.

5.1.5. Chapter Aims

In the previous chapter, it was demonstrated that chALKBH5 has a potent antiviral activity. Additionally, it was noticed that chWTAP is expressed in the cytoplasm, differing from what was demonstrated for WTAP in humans. Therefore, in this chapter, the aim was to determine the mechanistic action of chALKBH5 in inhibiting influenza A viruses and determine whether chWTAP is a part of chicken m6A-methyltransferase complex. The objectives were to:

1. Determine the rationale behind the DF1 chALKBH5-KO cell line having a non-significant increase in progeny viruses after infection compared to DF1-wt.

2. Identify the functional domain(s) responsible for the antiviral activity of chALKBH5.

3. Functionally annotate the NLS sequence of chALKBH5.

4. Determine whether chALKBH5 promotes target demethylation of viral transcripts as a potential cause of antiviral activity by fusing chALKBH5 with dCas13b, compared with the chFTO.

5. Determine any possible interactions of chALKBH5 with viral proteins using an in-house generated reporter chALKBH5-DF1 cell line.

6. Determine whether the chWTAP is indeed a part of the m6A writer complex in chicken.

5.2. Chapter Results

5.2.1. DF1-chALKBH5 KO cells showed enhanced innate immune responses and mRNA stability

In the previous chapter, it was confirmed that chALKBH5 has antiviral activity against IAVs, however, the generated chALKBH5-KO chicken cells exhibited similar levels of virus replication to DF1-wt cells. To test the hypothesis that the absence of chALKBH5 could potentiate innate immune response, DF1-chALKBH5 KO and DF1-wt cells were infected with IAV H9N2 with an MOI of 1.0 for 24 hpi. Total RNA was isolated for RT-qPCR to quantify key innate immune genes, including chMDA5, chPKR, chSTING, and chIFNγ.

Interestingly, all investigated innate immune genes were significantly higher in KO than DF1-wt cells, as shown in **Figure 5.9A**. As expected, no significant expression of viral HA gene expression was noticed, as reported earlier for the M gene **(Figure 5.9B)**. Investigating cells only without infection reproduced the same findings **(Figure 5.9C)**. Collectively, chALKBH5-KO cells exhibited enhanced innate immune response that makes no differences in virus replication in KO cells compared to wild-type cells.

The ALKBH5 and FTO are m6A-demethylases. Therefore, generating chALKBH5-KO cells possibly has enhanced levels of m6A compared with the wild-type. To this end, total RNA was extracted from both DF1-chALKBH5 KO cells, and DF1-wt and m6A-dot blot assay was performed. Equal amounts of RNA were dotted into the nylon membrane and probed using anti-m6A antibodies. Interestingly, the KO cells exhibited a significant increase in m6A levels ($p < 0.01$) **(Figure 5.9D)**.

To investigate cellular mRNA stability, actinomycin D (ActD) was used to induce transcription inhibition of cellular mRNA. The chALKBH5-KO and wt cells were incubated with 5 µg/ml ActD at the indicated time points. RNA was extracted, and the fold change of the remaining mRNA was quantified. The mRNA stability testing revealed that chYTHDF3 and chWTAP had significantly enhanced stability ($p < 0.05$) with an increase in half-life ($t_{1/2}$), as indicated **(Figure 5.9E)**. To sum up, DF1-chALKBH5 KO cells showed an enhanced innate immune response by impeding RNA degradation, hence, exhibiting similar viral replication compared to DF1-wt.
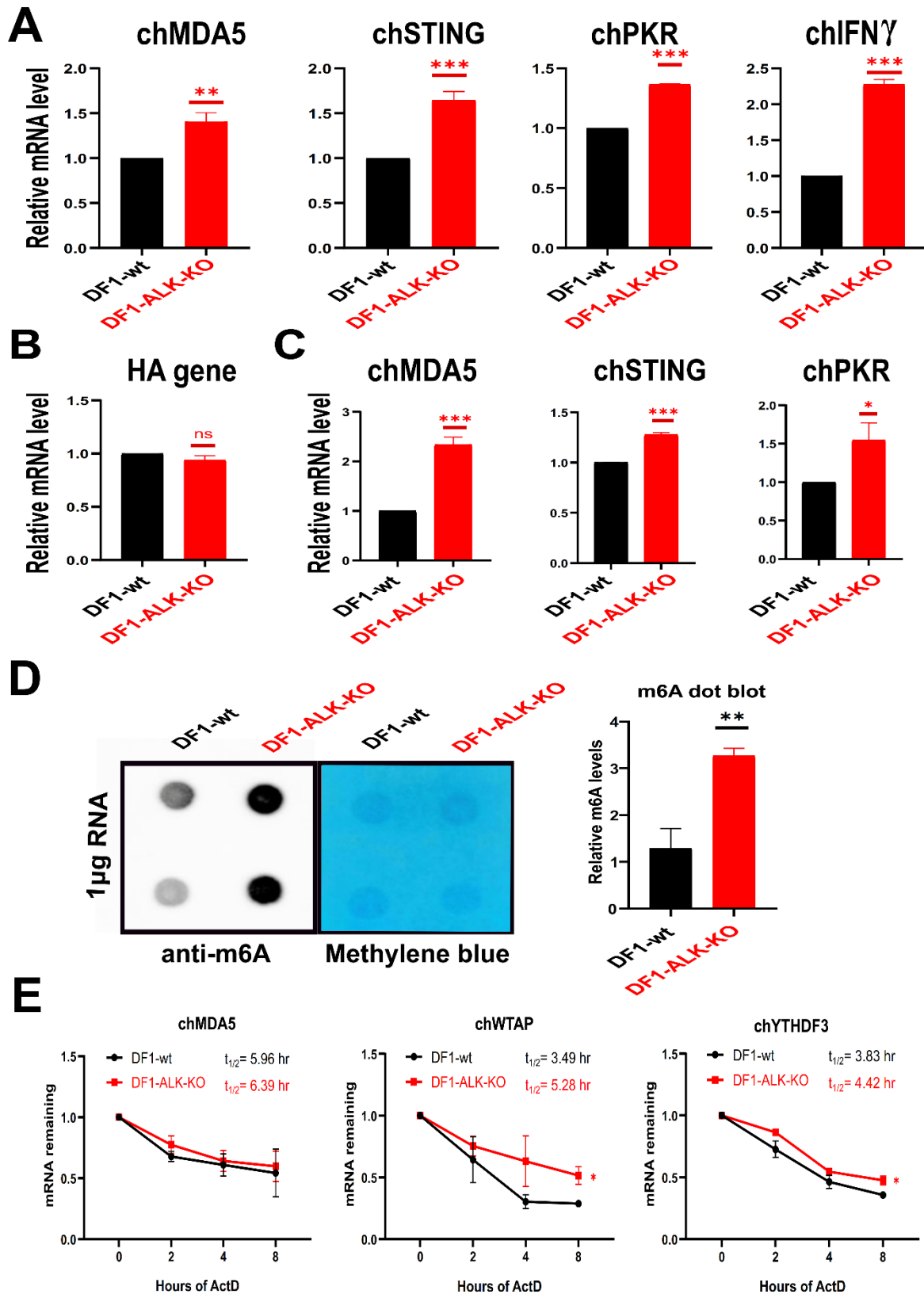
Figure 5.9: DF1-chALKBH5 KO cells showed an enhanced innate immune response and mRNA stability. **(A)** RT-qPCR was performed to determine the expression levels of key innate immune genes, 24 hpi with H9N2-UDL (MOI=1.0) in both chALKBH5-KO and DF1-wt cells. **(B)** RT-qPCR was performed to determine the IAV H9N2 HA mRNA levels at 24 hpi with H9N2-UDL (MOI=1.0) in both chALKBH5-KO and DF1-wt cells. **(C)** RT-qPCR was performed to determine the expression levels of key innate immune genes in uninfected DF1-wt cells and chALKBH5-KO cells. (A-C) the relative RNA levels were normalized to the chRPL30 housekeeping gene, and the DF1-wt values normalized to 1.0. **(D)** m6A-dot blot assay to relatively quantifies m6A levels between uninfected DF1-wt cells and chALKBH5-KO cells. Only two biological replicates are shown. The identical replicates were stained with methylene blue as the loading control. The relative quantity of the m6A level is represented by column bars. **(E)** RT-qPCR analysis of the remaining RNA in both chALKBH5-KO and DF1-wt. RNA was harvested at 0, 2, 4, and 8 h post actinomycin D treatment, and the relative levels of remaining transcripts were analysed by linear regression analysis. These data represent the average of three biological replicates with SD indicated. ns: non-significant; $p > 0.05$, $*p < 0.05$, $**p < 0.01$, $***p < 0.001$ using Student's t-test.

5.2.2. Chicken ALKBH5 middle (M) and carboxyl (C) fragments are responsible for the antiviral activity against influenza A viruses

To determine which part/domain(s) are responsible for the influenza antiviral activity. The ALKBH5 contains at least one identified functional domain, 2OG-(Fe)II-oxy (Aik et al., 2014; Feng et al., 2014). Therefore, chALKBH5 was expressed as three fragments; N-fragment represents the upstream sequence of the functional domain, M-fragment represents the active domain, and C-fragment represents the sequences downstream of the functional domain **(Figure 5.10A, B)**. Accordingly, primers that amplify each domain were designed without affecting the coding frame of chALKBH5 and maintaining the FLAG-tag in the 3′ end to facilitate further labelling. Using the PCR cloning strategy, three domains were generated and confirmed using PCR, restriction digestion, and sequencing **(Figure 5.10C, D)**.

The expression of three protein fragments was also verified using immunofluorescence analysis. Interestingly, chALKBH5 N-fragment was only seen diffuse expression in the cytoplasm, however, it has been predicted that the N-fragment possesses the nuclear localization sequence (NLS) of ALKBH5 in humans (Aik et al., 2014). Similarly, M-fragment was determined to be expressed as perinuclear dots. Markedly, C-terminal was detected solely in the nucleus (similar to the apo chALKBH5-wt) **(Figure 5.10E)**.

Which fragment(s) still exhibited antiviral potential after transfecting and infecting DF1 cells with IAVs was tested. Plaque counts and relative viral protein expression were utilized to determine the antiviral activity. It was clearly noticed that overexpression of M- and C-fragments significantly reduced in plaque counts for H9N2 (along with chALKBH5-wt) compared to empty plasmid (mock-transfected) ($p < 0.001$). Moreover,

expression of HA0 was reduced (~50%) and HA1 (~30%) in M- and C-termini overexpression **(Figure 5.11A, B)**. Similarly, the H1N1 virus model demonstrated the same findings in plaque counts and reduced NP expression in those domains **(Figure 5.11C, D)**. To conclude, M- and C-fragments but not the N-fragments are responsible for antiviral activity in chALKBH5, and C-terminus possibly carries the nuclear localization sequence.

A
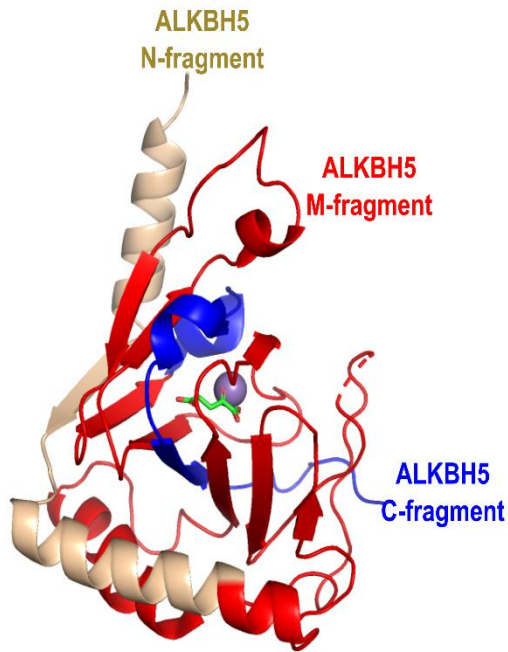
B
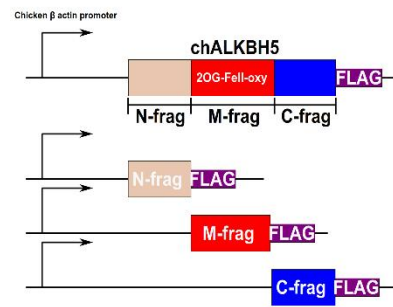
C
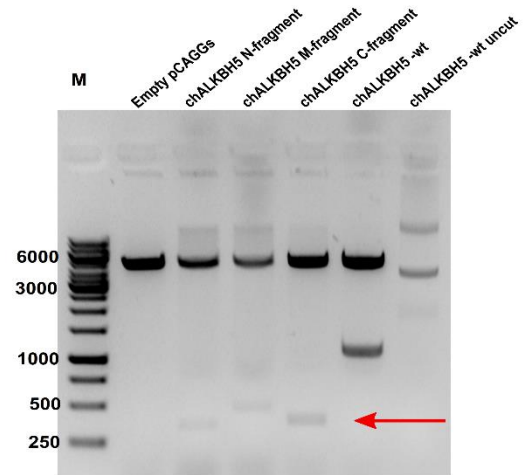
D
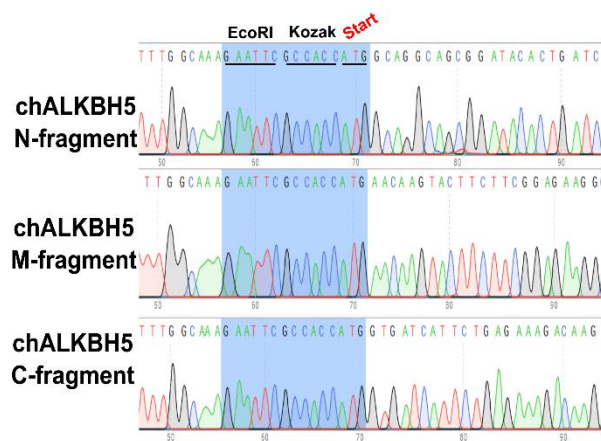
E
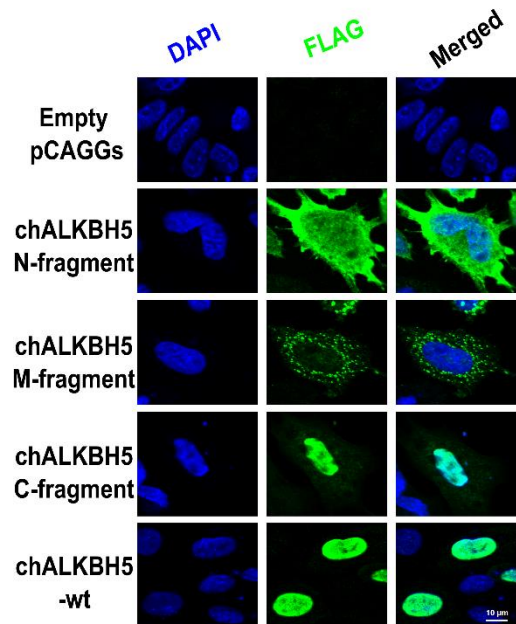
Figure 5.10: Cloning and expression of various chALKBH5 domains. **(A)** Overall three-dimensional structure of human ALKBH5 (PDB ID: 4NRO). The N-, M-, and C-fragments are represented by light brown, red, and blue colours, respectively. A green residue illustrates alpha-ketoglutaric acid (α-KG), and a violet circle represents the manganese atom. **(B)** Schematic illustration of chALKBH5 domains. The chALKBH5-wt and each terminus are indicated. The FLAG tag is marked by a violet box at the 3′ end of each terminus and wild-type protein. **(C)** Confirmation of successful cloning of all termini using restriction digestion. Restriction digestion was performed using EcoRI and KpnI restriction enzymes (i.e., the restriction sites flanking each terminus). Empty and chALKBH5-wt vectors served as control. A red arrow indicates restriction-digested chALKBH5 fragments. An uncut vector is displayed as digestion control. **(D)** Confirmation of successful cloning and orientation of all fragments using Sanger sequencing. EcoRI, Kozak sequence, and translation start sites are indicated by blue shading. **(E)** Confirmation of expression of chALKBH5 termini using confocal microscopy on chicken DF1-transfected cells. The nucleus (blue) and chALKBH5-termini (green) were labeled with DAPI or FLAG-specific antibodies, respectively. Empty plasmid and chALKBH5-wt transfected controls are also indicated. Scale bars are 10 µm.
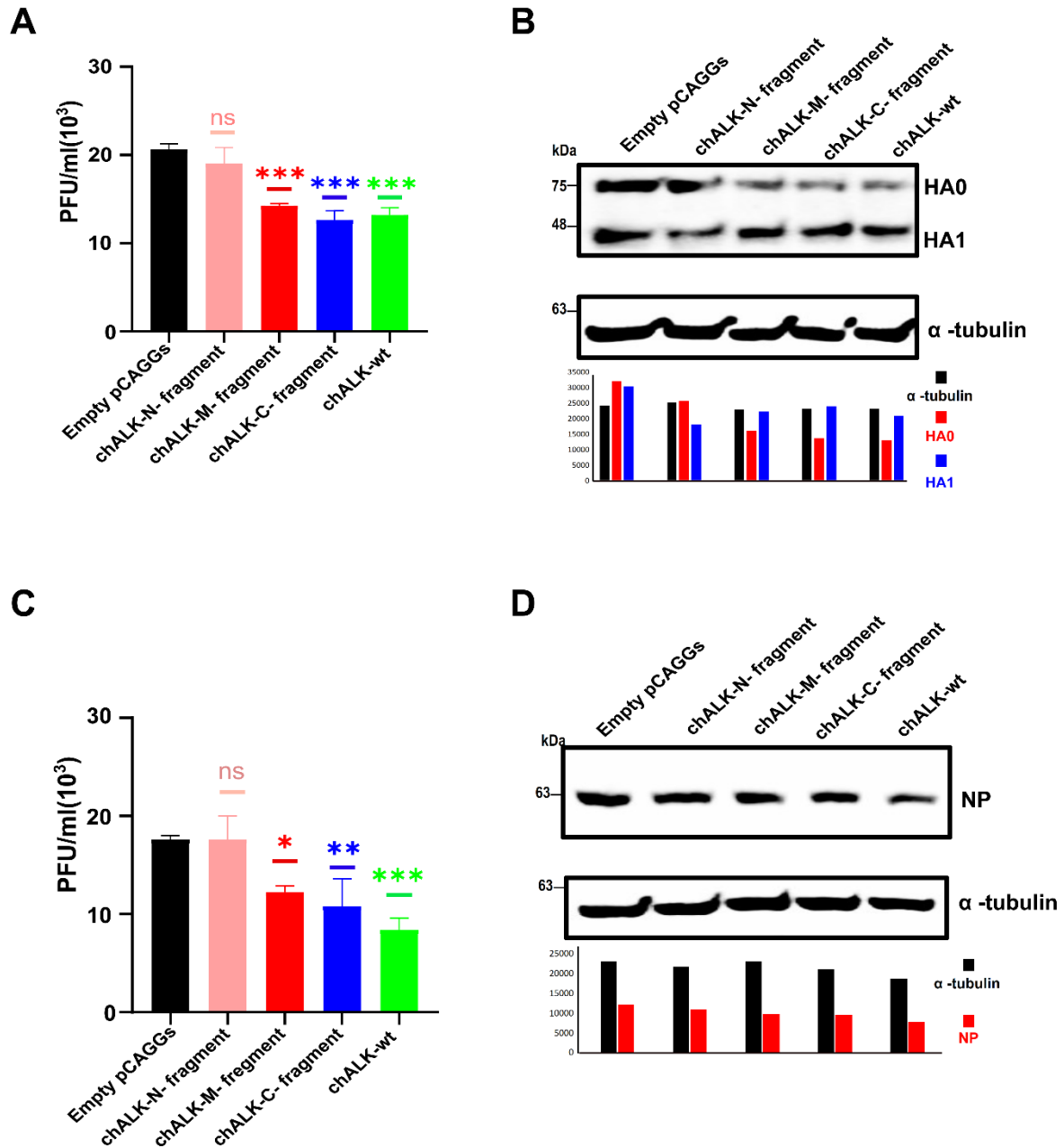
Figure 5.11: The middle (M) and carboxyl (C)-fragments of chALKBH5 are responsible for the antiviral activity against IAVs. **(A and C)** Plaque assay-based quantification of the progeny viruses from various chALKBH5-termini transfected-infected DF1 cells, empty plasmid and chALKBH5-wt transfected and infected cells served as antiviral controls. The released viruses were quantified using plaque assay on MDCK cells; (A) infected with H9N2 UDL/08 (MOI=1.0), (C) infected with H1N1

PR8 (MOI=1.0). These data represent the average of three biological replicates with SD indicated. *p < 0.05, **p < 0.01, ***p < 0.001 using one-way ANOVA. **(B, D)** Viral protein expression analysis on DF1 cell lysates that were transfected with the designated chALKBH5 termini, then infected with (MOI=1.0) of either IAV-H9N2-UDL/08 (B) or IAV-H1N1-PR8 (D). HA-protein expression (H9N2) or NP-protein expression (H1N1) is determined by western blot at 24 hpi. A representative western blot of each virus is shown. The α-tubulin was used as the loading control. ImageJ was used to determine the quantification of the band intensities for HA, NP, and α-tubulin, and values are graphed as column bars.

5.2.3. The nuclear localization signal of chALKBH5 is located in the C-terminus

It has been shown that the nuclear localization (NLS) is predicted in the N-fragment of human ALKBH5 (Aik et al., 2014). Interestingly, the fragmentation analysis of chALKBH5 termini demonstrated that C-terminus possibly has the NLS in chALKBH5. In contrast, the N-fragments is solely expressed in the cytoplasm, which abolishes the earlier prediction, as shown earlier **(Figure 5.10E)**.

To this aim, in-silico prediction was performed using the most common NLS prediction software; NucPred, cNLSMapper, seqNLS, and NLStradamus (Lisitsyna et al., 2017). Although most prediction software indicated an NLS is located in the N-terminus, by reducing the threshold values, two locations were mapped in C-terminus **(Figure 5.12A)**. Therefore, it was decided to design and chemically synthesize a chALKBH5-NLS-1 construct, and the design of the chALKBH5-NLS-1, in turn, was further modified to generate another chALKBH5-NLS-2 construct (via restriction digestion) with mutations targeting the two predicted sites at C-terminus, as indicated in **Figure 5.12A**.

The chALKBH5-NLS-1 construct was synthesized, where the predicted site of 300-PKRSHRKA-307 was replaced with alanine residues (300-AAAAAAA-307) **(Figure 5.12B)**. Additionally, a unique restriction site (SgrDI) was introduced at the 5′ of the second predicted site without altering amino acid codes to facilitate further subcloning. This way, the second predicted site can be excised to generate chALKBH5-NLS-2. Restriction digestion, using SgrDI and SmaI (which is genuine in the pCAGGS plasmids), was performed and replaced by a very short oligo

(CGAGCACTTCAGCCC) to support the correct frame and ligation (i.e., SgrDI and SmaI have no compatible ends) **(Figure 5.12C)**.

The three forms of chALKBH5 (i.e., wt, NLS-1, and NLS-2) were transfected into DF1 cells to determine sub-cellular localization. After three independent replicates of the immunofluorescence analyses, the chALKBH5-wt was found in the nucleus (more than 95%), as expected. However, the shuttling between nuclear and cytoplasmic expression was clearly reported (~50%) in chALKBH5-NLS-1. Interestingly, the chALKBH5-NLS-2 showed that the ratio of cytoplasmic to nuclear versions was increased (more than 70%); notably, more cells were expressed solely in the cytoplasm **(Figure 5.12D)**. To conclude, the NLS sequence of chALKBH5 is confirmed in the C-terminus.
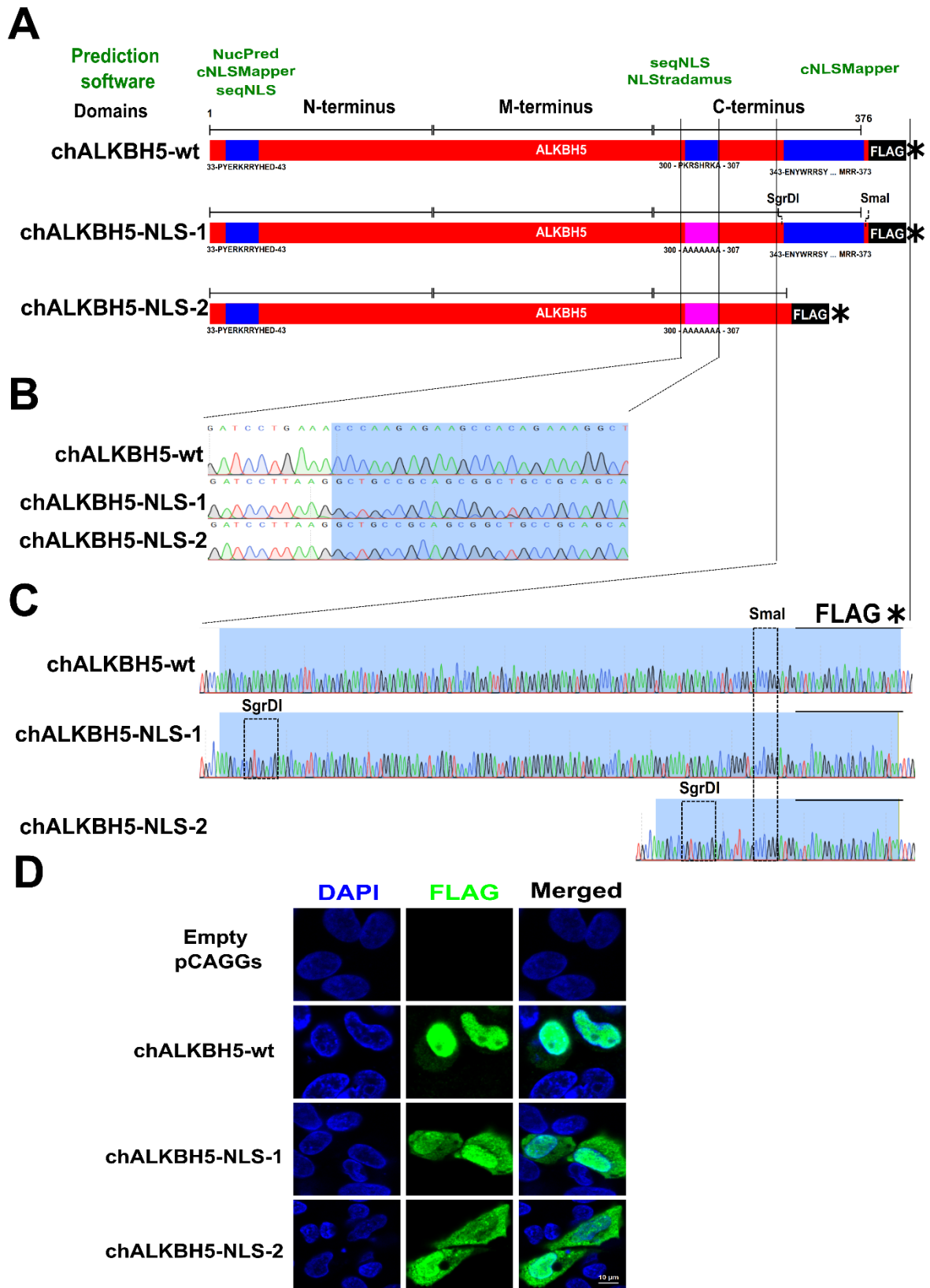
Figure 5.12: The nuclear localization signal of chALKBH5 is located in C-terminus. **(A)** Schematic diagrams of each chALKBH5 construct; wt, NLS-1, and NLS-2. Blue boxes indicate the predicted NLS sequences. The prediction software is indicated by green colour above each expected site. Magenta colours in NLS mutants indicate the mutated alanine residues. **(B and C)** Sequence confirmation of the induced mutations in the C-terminus of each predicted NLS site. Restriction sites are indicated by dotted-black boxes. **(D)** Confocal microscopy images of each expressed chALKBH5 form. The nucleus (blue) and chALKBH5 forms (green) were labeled with DAPI or FLAG-specific antibodies, respectively. Empty plasmid and chALKBH5-wt controls are also indicated. Scale bars are 10 µm.

5.2.4. chALKBH5 downregulated IAV H9N2 replication through programmable demethylation by fusion with dCas13b

After the antiviral fragments regulating IAVs were identified, the mechanistic action of chALKBH5 against IAVs, which had not been elucidated earlier was also investigated. As discussed above, one of the main functions of ALKBH5 in regulating cell RNA metabolism is to demethylate single-stranded RNA transcripts. Loss of m6A marks from mRNA of HA of the influenza virus was reported to inhibit virus replication in culture and reduce pathogenicity in vivo (Courtney et al., 2017).

To investigate whether chALKBH5 could bind to HA mRNA in vitro, a preliminary step to ensure that chALKBH5 could interact to demethylate viral transcripts in culture. Therefore, RNA-protein immunoprecipitation (RIP) was performed. The chALKBH5-FLAG vector was transiently transfected in DF1 cells and then infected with H9N2. Cells were lysed and pulled down with anti-FLAG or IgG (i.e., control) antibodies. Using RIP-RT-qPCR, HA mRNA was significantly enriched in FLAG-tagged lysates (p <0.05) relative to control IgG antibodies **(Figure 5.13A)**.

This finding supports that chALKBH5 binds to viral mRNA; however, it does not validate actual demethylation activity. To confirm the demethylation of chALKBH5 toward the m6A marks on the HA gene of H9N2, programmable demethylation was performed using Cas13 genome editing technologies (Cas13b) **(Figure 5.13B)**. The chALKBH5 was fused to a dead (inactive) version of Cas13b (dCas13b) to disrupt the RNA cleavage potential but retain the tethering impact guided by the site-specific crRNAs. Using crRNAs, the dCas13b-chALKBH5 fused chimera was tethered to bind to the HA of H9N2, hence initiating demethylation.

The dCas13b-chALKBH5 construct, tagged with FLAG, was chemically synthesized. Initially, an NLS was incorporated at the 5′ end of the dCas13b effector to mediate nuclear expression. The NLS sequence was flanked with two restriction sites on each end to facilitate NLS removal and generation of a second cytoplasmic version (**Figure 5.13C**). Both nuclear and cytoplasmic versions of dCas13b-chALKBH5 were readily expressed, and as expected, the expressed protein was detected in the nucleus and cytoplasm, respectively (**Figure 5.13C**).

Six crRNAs targeting highly enriched DRACH motifs in the HA mRNA were designed and cloned in the crRNA vector backbone (**see Figure 5.15**). DF1 cells were transfected with 6 crRNAs complementary to HA mRNA/cRNA along with either cytoplasmic or nuclear versions of dCas13b-chALKBH5. Non-target crRNA was utilized as a control (scrambled crRNAs). 24 h after transfection, cells were infected with H9N2 UDL/08 (MOI=1.0). The antiviral potential was determined using plaque counts and HA protein expression analysis. Interestingly, only the nuclear version of dCas13b-chALKBH5 exhibited a significant reduction in viral replication (p <0.01) and HA protein expression (~30%) (**Figure 5.13D and 5.14**).

The crRNAs were designed to target six locations in the HA plus strands. Two crRNAs were designed in the 5′ end, two in the middle, and two in the 3′ end (**Figure 5.15**), based on the analysis of DRACHs conservation in **Chapter 3**. Next, to determine whether target crRNAs and locations control the antiviral activity of nuclear-dCas13b-ALKBH5. Accordingly, the DF1 cells were transfected with two crRNAs each. Notably, crRNAs targeting both 5′ and 3′ ends of HA mRNA were found to possess potent antiviral activity compared with middle crRNA, expressed as reduced titre s of

the progeny viruses ($p < 0.05$) and HA mRNA ($p < 0.01$; **Figure 5.16A, B**). It is essential to note that the relative M gene mRNA level was not affected ($p > 0.05$). This observation indicated clearly that the designed crRNAs specifically targeted HA to exhibit programmable demethylation of HA but not the M gene **(Figure 5.16C)**. Overall, chALKBH5 interaction with the HA mRNA gene was confirmed to downregulate HA through targeted demethylation, hence, reduce viral replication and gene expression.

A

chALKBH5

IP

IgG   FLAG   Input

kDa

48 — FLAG

63 — α-tubulin

chALKBH5

B

dCas13b   crRNA

m⁶A eraser
(ALKBH5 & FTO)

A(n)AA

Targeted demethylation

dCas13b   crRNA

A(n)AA

HA mRNA

HA mRNA

C

Nuclear   NLS   Psp dCas13b   chALKBH5

Cytoplasmic   Psp dCas13b   chALKBH5

NLS

DAPI   FLAG   Merged

Empty
pCAGGs

Nuclear dCas13b
-chALKBH5

Cytoplasmic
dCas13b -chALKBH5

10 μm

D

Cy-dC13b-chALK+scramble
Cy-dC13b-chALK+HA guides
Nu-dC13b-chALK+scramble
Nu-dC13b-chALK+HA guides

kDa

75 — HA0

48 — HA1

63 — α-tubulin

α-tubulin
HA0
HA1

322

Figure 5.13: Chicken ALKBH5 inhibits IAV H9N2 protein expression through programmable demethylation. **(A)** RNA-immunoprecipitation (RIP)-RT-qPCR. Cell lysates were subjected to IP with an anti-FLAG antibody or IgG as a control. RT-qPCR analysis of HA mRNA was quantified as a percent of input and presented as fold enrichment relative to IgG control. Immunoblot analysis of chALKBH5-FLAG in the input and IP is also indicated. These data represent the average of three biological replicates with SD indicated. *$p < 0.05$ using unpaired Student's t-test. **(B)** Schematic of programmable demethylation using dCas13b. the chicken m6A-erasers (ALKBH5, FTO) are tethered to dCas13b and targeted to HA mRNA/cRNA using crRNA to facilitate programmable demethylation of m6A to A. **(C)** Schematic of nuclear and cytoplasmic versions of dCas13b-chALKBH5 and confocal microscopy images of each expressed Cas13b-chALKBH5 in DF1 cells. The nucleus (blue) and dCas13b-chALKBH5 versions (green) were labeled with DAPI or FLAG-specific antibodies, respectively. Negative empty plasmid control is also indicated. Scale bars are 10 µm. **(D)** Immunoblot analysis of DF1 cell lysates transfected with the designated dCas13b-chALKBH5 and HA-specific crRNA or scramble crRNA, then infected with H9N2-UDL/08 (MOI=1.0). HA-protein expression is determined by western blot at 24 hpi. α-tubulin was used as the loading control. ImageJ was used to quantify the band intensities for HA (HA0 and HA1) and α-tubulin, and values are graphed as column bars. A representative western blot of each dCas13b version is shown. Cy: cytoplasmic version, Nu: nuclear version, dC13b: deadCas13b, chALK: chALKBH5, scramble: scramble crRNA, HA guides: HA mRNA-specific crRNAs.

Figure 5.14: Chicken ALKBH5 downregulated H9N2 virus replication through programmable demethylation when fused with dCas13b. **(A and B)** Plaque assay-based quantification. The viral titres of progeny viruses from DF1 cells that were transfected with the designated dCas13b-chALKBH5, cytoplasmic (A) and nuclear (B), and either HA-specific crRNA or scramble crRNA, then infected with H9N2-UDL/08 (MOI=1). The released viruses were quantified using plaque assay on MDCK cells. These data represent the average of three biological replicates with SD indicated. ns= non-significant $p > 0.05$, $**p < 0.01$ using unpaired Student's t-test. Cy: cytoplasmic version, Nu: nuclear version, dC13b: deadCas13b, chALK: chALKBH5, scramble: scramble crRNA, HA guides: HA mRNA-specific crRNAs.

A

HA plus strand

B

crRNA.1

dCas13b-ALKBH5

C

5' NCR- HA   **Start**

3' NCR- HA
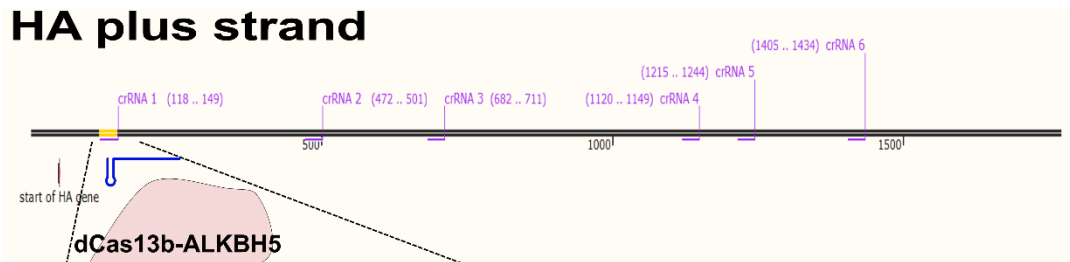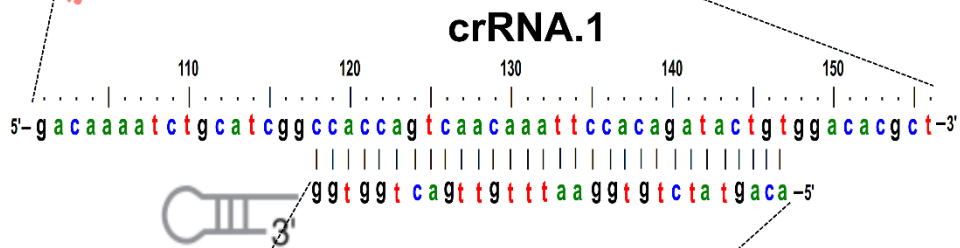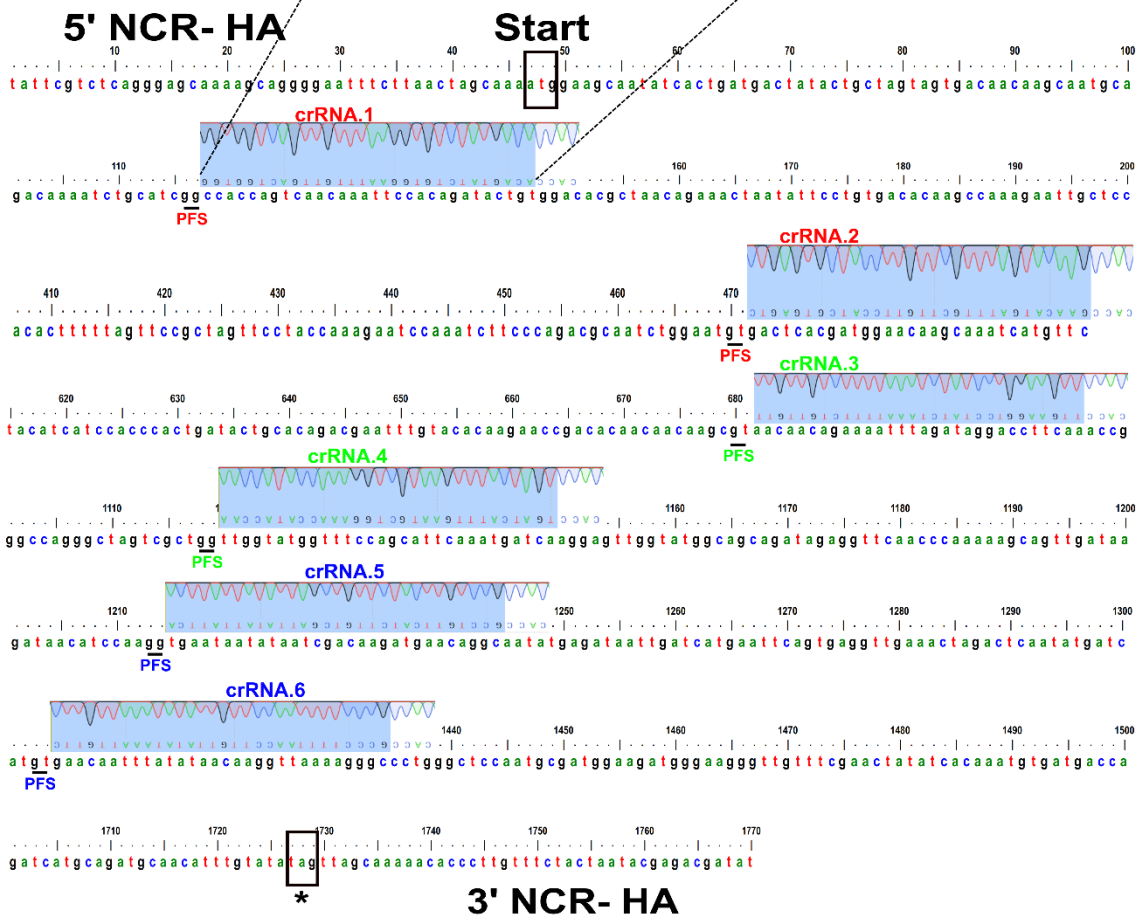
Figure 5.15: Schematic of design of crRNAs on the HA mRNA/cRNA strands. **(A)** Schematic of the entire HA mRNA/cRNA and crRNAs target. **(B)** An enlarged view of the HA sequence and the complementary spacer of crRNA.1, as an example. **(C)** Distribution of all 6 crRNAs and their locations on HA plus strands. The sequence confirmations of spacers are indicated in an inverted manner to show the complementarity with the plus strands. crRNA1+2 is indicated by red colour, crRNA3+4 is indicated by green colour, and crRNA5+6 is denoted by blue colour. Start and stop codons are shown on HA plus strands by black boxes. PFS; protospacer flanking sequence, the PAM homologue of Cas13b is indicated by underlines (GK, K= G/T). NCR; non-coding region.
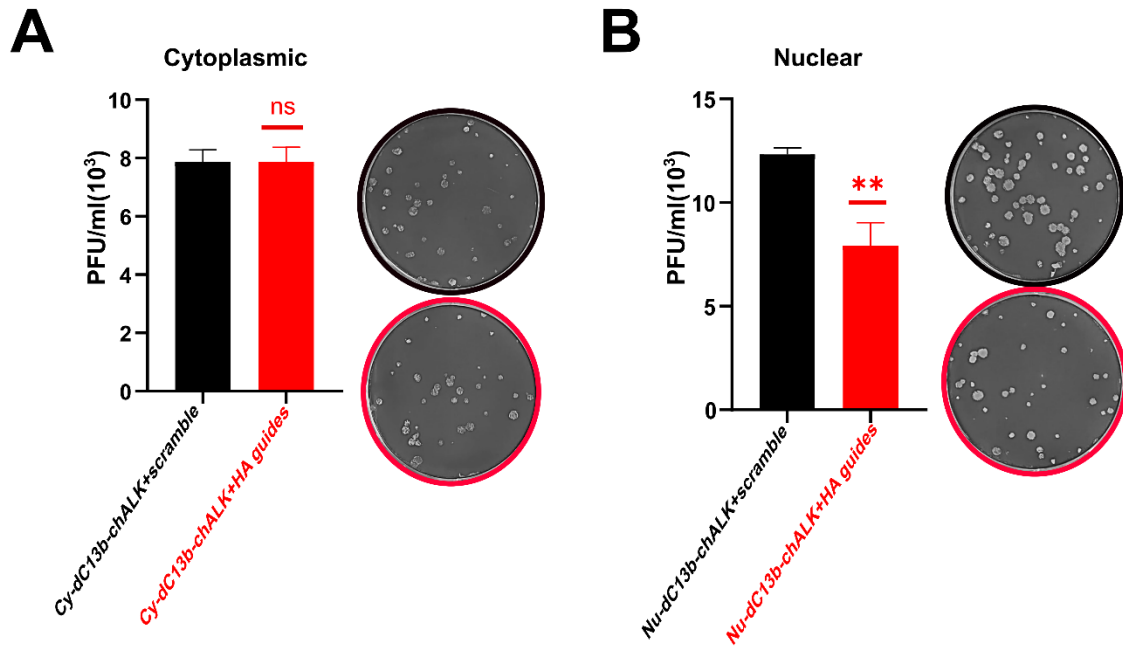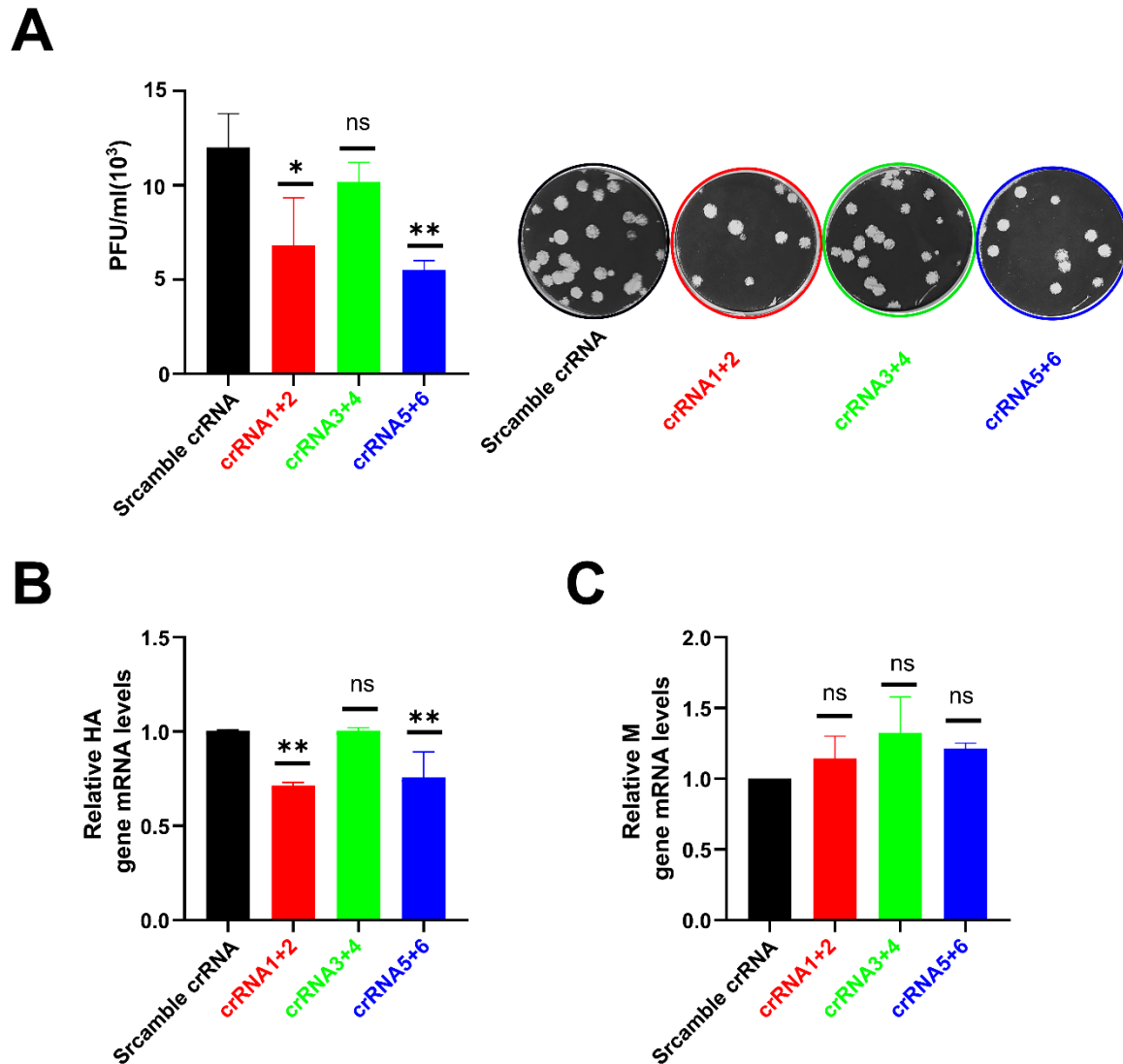
Figure 5.16: Chicken ALKBH5 downregulated H9N2 virus replication through programmable demethylation fusion with dCas13b at target-specific locations. **(A)** Plaque assay-based quantifications. The viral titre of released viruses from DF1 cells that were transfected with the designated Nuclear (Nu) dCas13b-chALKBH5 and HA crRNA or scramble crRNA, then infected with IAV-H9N2-UDL/08 (MOI=1.0). The released viruses were quantified using plaque assay on MDCK cells. A representative countable well per each designated crRNA is indicated. **(B)** RT-qPCR was performed to determine HA gene mRNA expression levels at 24 hpi; DF1 cells were transfected by Nu-dCas13b-chALKBH5 and designated crRNAs, then infected with (H9N2,

MOI=1.0). **(C)** RT-qPCR was performed to determine M gene mRNA expression levels at 24 hpi; DF1 cells were transfected by Nu-dCas13b-chALKBH5 and designated crRNAs, then infected with (H9N2, MOI=1.0). (B and C) DF1 transfected with designated crRNA normalized with scramble crRNA control to 1.0 using the chRPL30 as a chicken cellular housekeeping loading control. These data represent the average of three biological replicates with SD indicated. ns: non-significant $p > 0.05$, *$p < 0.05$, **$p < 0.01$ using the one-way ANOVA.

5.2.5. Chicken FTO does not regulate IAV H9N2 through programmable demethylation

Similar to ALKBH5, the FTO acts as m6A demethylase to cellular and viral RNA. Further to above mentioned antiviral assays, chFTO was not an antiviral against both H9N2 and H1N1. Moreover, chFTO did not affect viral protein expression **(Chapter 4, section 4.2.2, 4.2.3)**. Enforced chFTO to induce programmable demethylation was adopted to regulate influenza virus (H9N2), as chALKBH5 displayed. Like chALKBH5, chFTO-FLAG was transfected into DF1 cells and then infected with H9N2 (MOI=1.0). RIP-RT-qPCR analysis of RNA isolated from immunoprecipitated cell lysates displayed that only HA mRNA was significantly enriched in FLAG-tagged lysate compared with IgG control (p<0.01; **Figure 5.17A**).

The previously synthesized nuclear (nu-) construct nu-dCas13b-ALKBH5 was also designed with sets of restriction enzymes to replace chALKBH5 with any other m6A-related protein. In this regard, primers that amplify chFTO to be cloned into the nu-dCas13b vector were designed. The chFTO was cloned and confirmed using restriction digestion and sequencing. As expected, similar to the nu-dCas13b-chALKBH5, the nu-dCas13b-chFTO expression was readily observed in the nucleus **(Figure 5.17B, C)**. In comparison to chALKBH5 tethered construct, the chFTO-tethered construct exhibited reduced but non-significant antiviral activity when investigated with all six crRNAs targeting HA mRNA **(Figure 5.18)**. Overall, the chFTO could bind to HA in vitro but does not regulate influenza virus replication through programmable demethylation.
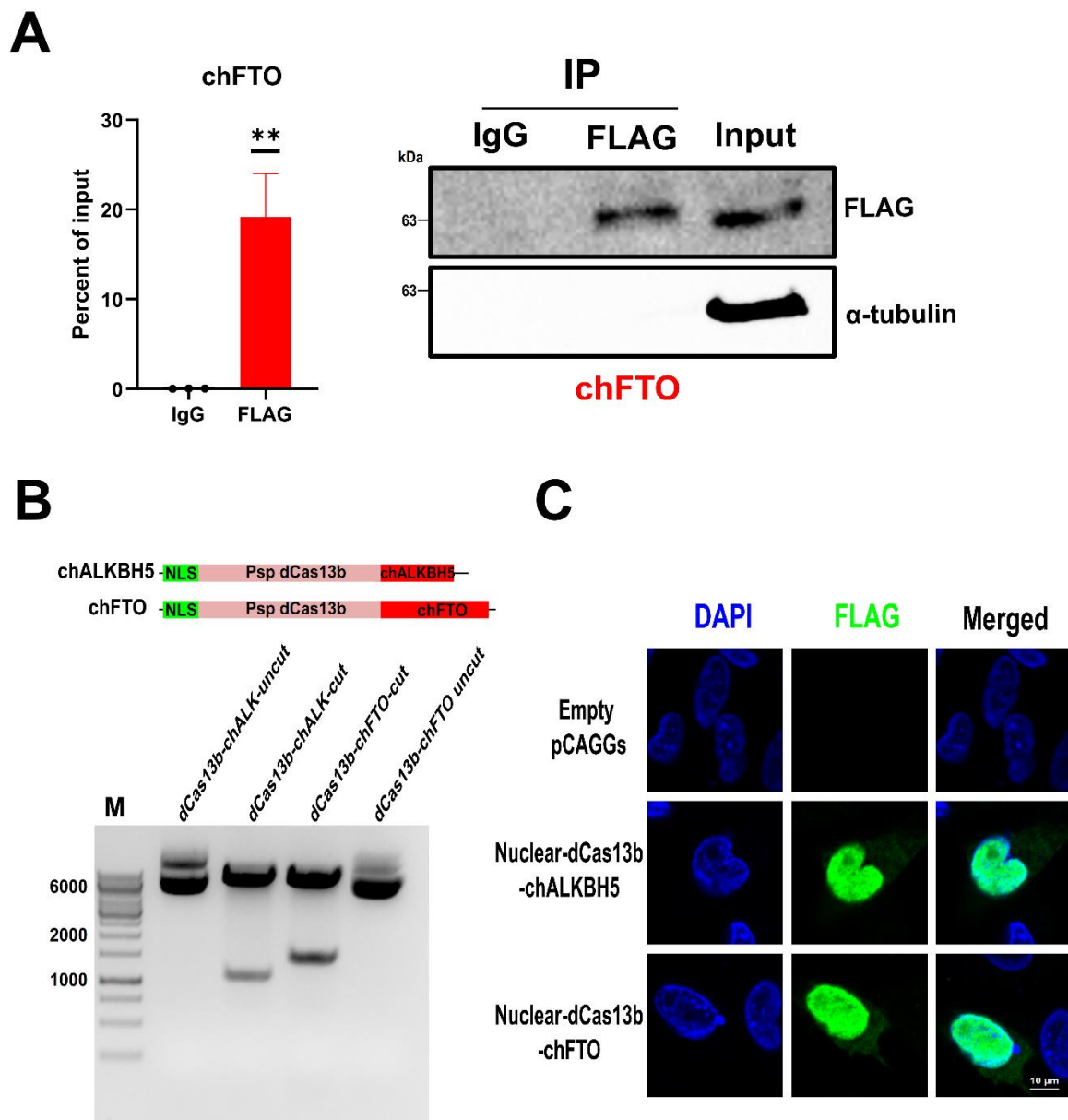
Figure 5.17: Cloning and expression of chFTO-dCas13b to mediate targeted demethylation. **(A)** RNA-immunoprecipitation (RIP)-RT-qPCR. Cell lysates transfected with chFTO and infected with H9N2 were subjected to IP with anti-Flag antibody or IgG as a negative control. RT-qPCR analysis of HA mRNA was quantified as a percent of input and presented as fold enrichment relative to IgG control. Immunoblot analysis of chFTO-FLAG in the input and IP is also indicated. These data

represent the average of three biological replicates with SD indicated. **$p < 0.01$ using unpaired Student's t-test. **(B)** Schematic of nuclear versions of dCas13b-chALKBH5 and -chFTO. Confirmation of successful cloning of nu-dCas13b-chFTO using restriction digestion. Restriction digestion was performed using KpnI and NheI enzymes (the restriction sites flanking each eraser). Uncut vectors are indicated as restriction-digestion control. **(C)** Confocal microscopy images of each expressed dCas13b-tethered. The nucleus (blue) and dCas13b-chALKBH5/chFTO versions (green) were labelled with DAPI or FLAG-specific antibodies, respectively. Empty plasmid-transfected cells are also indicated. Scale bars are 10 µm.
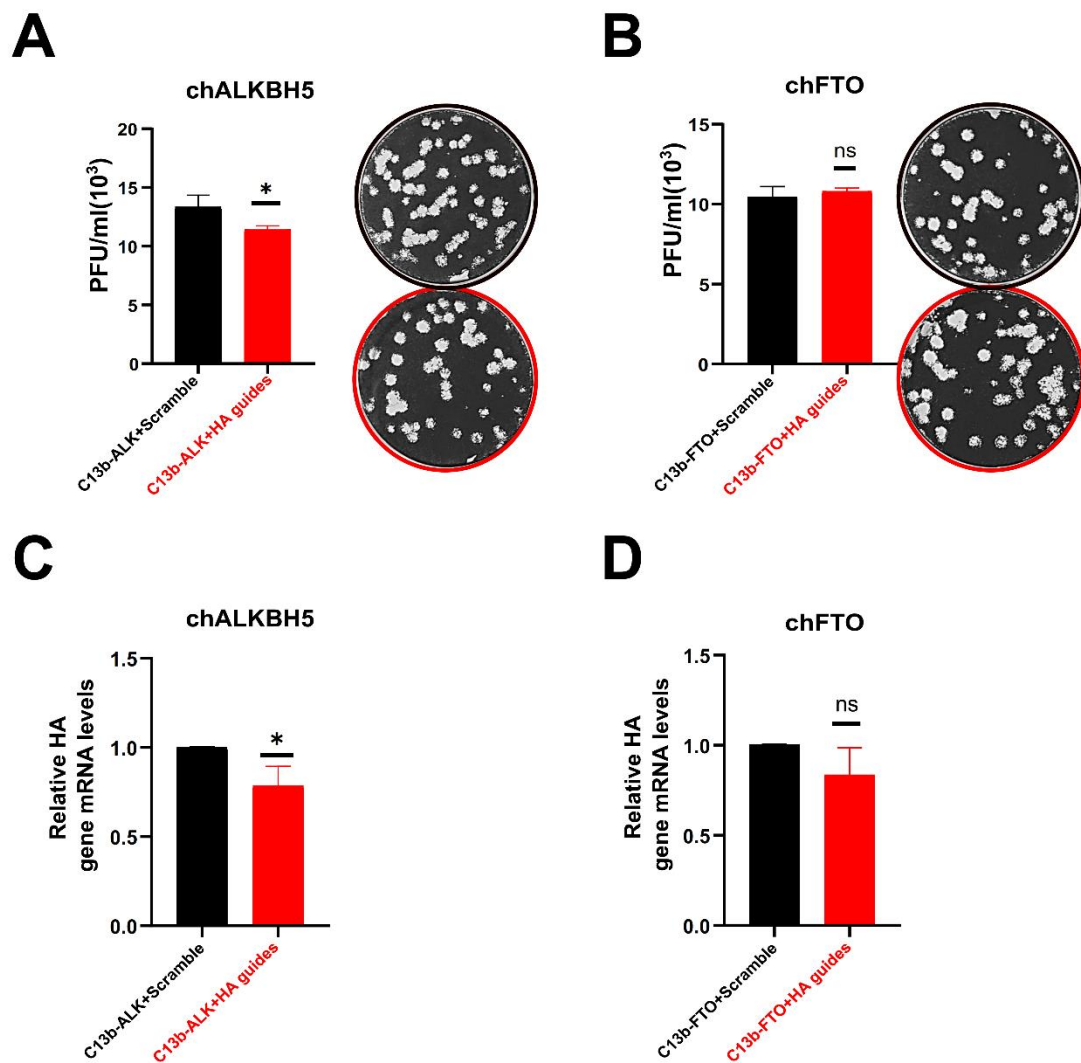
Figure 5.18: Chicken FTO does not inhibit the H9N2 virus replication through programmable demethylation. **(A and B)** Plaque assay-based quantification. The progeny viral titres from DF1 cells that were transfected with the designated tethered eraser and crRNAs were then infected with IAV H9N2-UDL/08 (MOI=1.0). The released viruses were quantified using plaque assay on MDCK cells. A representative countable well per each designated experiment is indicated. These data represent the average of three biological replicates with SD indicated. ns: non-significant; $p > 0.05$, *$p < 0.05$ using unpaired Student's t-test. **(C and D)** RT-qPCR was performed to

determine HA gene mRNA expression levels at 24 hpi; DF1 cells were transfected by designated tethered erasers and crRNAs, then infected with (H9N2, MOI=1.0). DF1 transfected with designated crRNA normalized with scramble crRNA control to 1.0 using the chRPL30 as a chicken cellular housekeeping loading control. These data represent the average of three biological replicates with SD indicated. ns: non-significant p>0.05, *p < 0.05 using unpaired Student's t-test. C13b: dead-inactive Cas13b, chALK: chALKBH5, scramble: scramble crRNA, HA guides: HA mRNA-specific crRNAs.

5.2.6. chALKBH5 downregulates IAV H9N2 through interaction with viral NP protein, but not NS1

The above-mentioned antiviral potential of chALKBH5 against both H9N2 and H1N1 IAVs possibly indicates that chALKBH5 interacts with viral protein(s) to suppress viral infection in a time-dependent manner, as shown in **Chapter 4, section 4.2.5**. To test whether chALKBH5 would interact with influenza viral proteins, endogenous chALKBH5 was labelled by generating a reporter DF1 cell. To track chALKBH5 in a time-lapse manner, characterize endogenous expression, and investigate the interaction with viral proteins.

Very recently, the endogenous labelling of some cytoskeletal proteins of neuronal cells, including actin, has been reported through CRISPR-mediated insertion of exon (Zhong et al., 2021), as indicated in **Section 5.1.3**. Similarly, mRuby3 (red) was utilized as a donor exon to be inserted in either intron-1 (first intron) or -4 (last intron) of the chALKBH5 gene through sgRNAs and Cas9 **(Figure 5.19 A, B)**. DF1 cells co-transfected with (1) fluorescent donor exon (i.e., mRuby3) and (2) a plasmid that expresses Cas9 and sgRNA to cut and liberate mRuby3 from the fluorescent donor, and (3) a plasmid that expresses Cas9 and sgRNAs target introns of chALKBH5 **(Figure 5.19 A-C)**.

The mRuby3 was endogenously labeled into chALKBH5 both in intron-1 and -4. The reporter cells were confirmed using PCR and sequencing using primers that target mRuby3 and exon 2 or 5, respectively, as indicated in **Figure 5.19 D-F**. Using live imaging under confocal microscopy, the endogenously labelled chALKBH5-mRuby3 was predominantly expressed in the nucleus, as expected **(Figure 5.20)**. It is important

to mention that the picked KI cell clones (using cell culture cylinders) were not pure clones to display the difference between CRISPIEd and DF-1-wt in the same fields, as indicated in **Figure 5.20**. The chALKBH5-mRuby3 reporter cells were infected with H9N2-, NDV-, and VSV-GFP models (MOI=1.0). After 6 hpi, the cells were transferred to confocal microscopy for live imaging for additional 12 hpi (i.e., 6 to 18 hpi).

Under H9N2-GFP infection, live imaging of reporter cells at 6 hpi revealed the start of GFP expression (note, NS1-GFP plasmid was utilized for virion production). It was clear that the cells that are infected in the non-labeled DF1 express higher GFP (**Figure 5.21B**). Moreover, reporter cells infected with the H9N2-GFP virus could interact with chALKBH5-mRuby3, as expressed by mixed yellow colour in time-lapse as indicated in **Figure 5.21B (white arrow)**; however, this was not ubiquitous, as shown in **Figure 5.21B (yellow arrow)**. Uninfected reporter cells served as the negative control (**Figure 5.21A**). Interestingly, in NDV-GFP infection, most non-reporter cells were infected cells (no yellow colour was noticed, **Figure 5.22A**). Notably, VSV-GFP showed almost 100% infection at the end of the time-lapse, with nearly complete cell lysis (**Figure 5.22B**).

Next, to verify which viral protein could be the target for chALKBH5 interaction, DF1 cells were co-transfected with chALKBH5-FLAG and V5-NP (directly cloned from H9N2 UDL/08 strain using PCR). Viral NP was initially chosen due to its intranuclear expression and polymerase complex-supportive role in the nucleus, as is the expression of chALKBH5. Immunofluorescence analysis (IFA) demonstrated that NP is usually expressed in both cytoplasm and nucleus. The expression of chALKBH5 was only

noticed in the nucleus, as expected. Co-transfection showed the co-localization of both proteins in the nucleus (**Figure 5.22A**).

Additionally, an immunoprecipitation assay (IP) was performed using anti-FLAG antibodies to map the possible interaction between chALKBH5 and viral NP. Interestingly, the V5-NP was enriched in the chALKBH5-expressed cells (**Figure 5.23B**). These findings indicate that chALKBH5 interacts with the NP through IP and IFA.

A similar investigation of the possible interaction of chALKBH5 and NS1 protein was performed (the NS1 was directly cloned from H9N2 UDL/08 strain using PCR). IFA indicated both cytoplasmic and nuclear expression of the NS1. However, in the IP, NS1 was not enriched in the eluted fraction; in contrast, NS1 was noticed only in the unbound fraction (**Figure 5.23C, D**), suggesting only weak/transient interactions were noticed in the live images.

Influenza NP has two main domains (body and head) interacting with polymerase proteins (Ye et al., 2006). In a trial to extend the investigation, primers spanning different domains were designed to amplify the fragments and were cloned in the parental vectors in fusion with the V5 tag to determine the functional domain for interaction with chALKBH5. These were named as N-, M-, C- NP termini. These domains were confirmed using cloning, sequencing, and expression analysis (**Figure 5.24A-C**). It was clearly noticed that none of the expressed domains were localized in the nucleus, all solely expressed in the cytoplasm (**Figure 5.24D**).

Next, immunoprecipitation was performed using all generated domains (along with NP-wt). Notably, NP-wt clearly interacted with chALKBH5, as expected; however, none of the generated fragments were enriched with chALKBH5 (**Figure 5.24E**). Taken together, chALKBH5 downregulated influenza virus replication through interaction with viral NP and not with NS1.

A

B

chALKBH5
co-ordinates
14:5043695-5061240

C

px549v2   sgRNA-intron1

px549v2   sgRNA-intron4

sgRNA cloning

D

ALKBH5 N-terminus Intron 1

ALKBH5 N-terminus Intron 4

E

CRISPIEd-DF1
Intron1   DF1-wt

1000

F

CRISPIEd-DF1
Intron4   DF1-wt

500
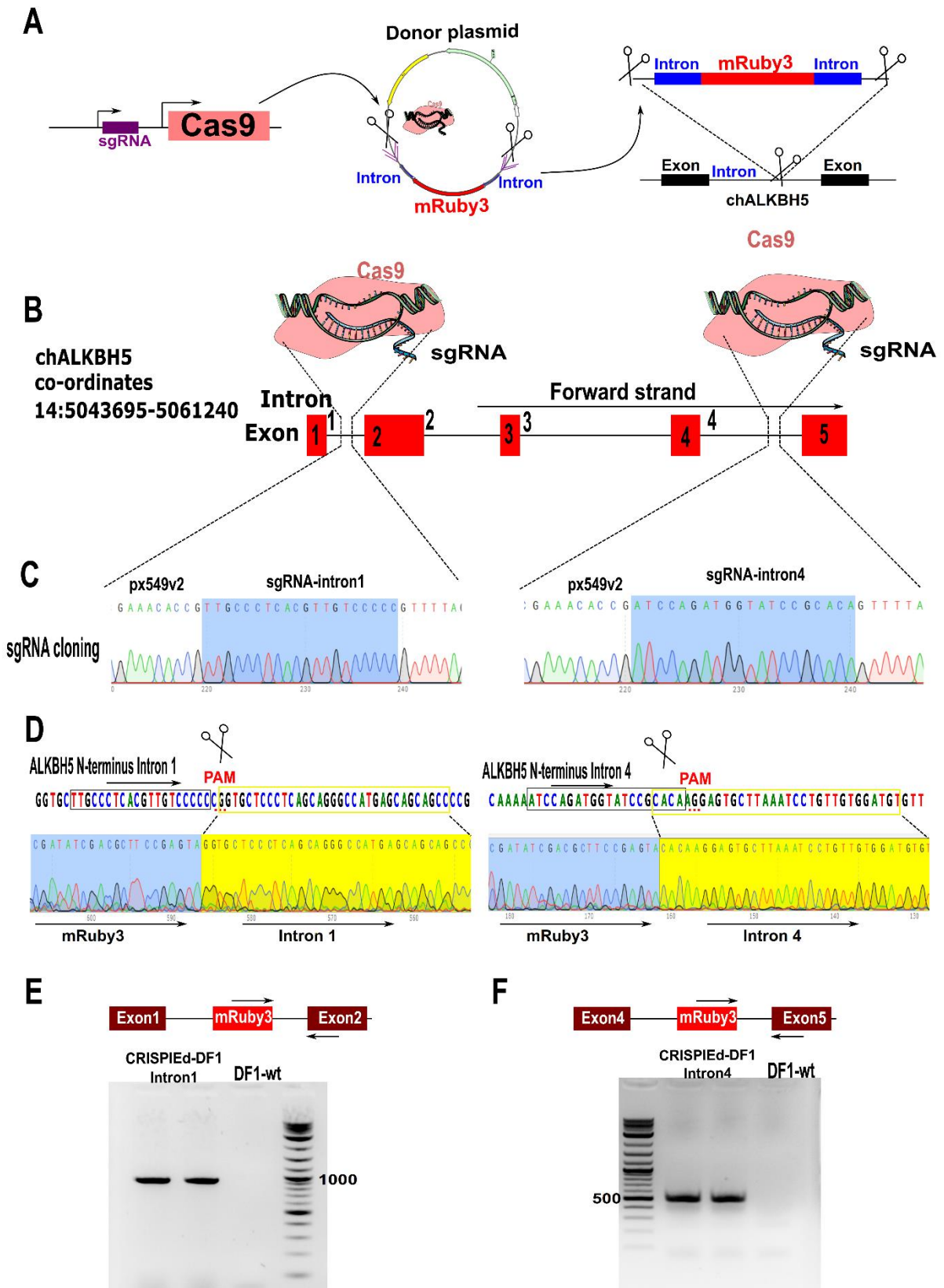
Figure 5.19: Generation of chALKBH5-mRuby3 reporter DF1 cells. **(A)** Schematic diagram of single guide Cas9 (sgRNA/SpCas9) plasmid, the donor plasmid, and schematic of the targeted intron of chALKBH5 showing the sgRNA targeting site and orientation. **(B)** A schematic diagram of chALKBH5 loci in the chicken genome, number of exons and introns, and target introns are shown. **(C)** Sequence confirmation of cloning of two sgRNA targeting introns of chALKBH5. **(D)** Schematic diagram and sequence confirmation showing the location of sgRNA in target introns of chALKBH5 with the label DF1 cells. The cut site and fusion with mRuby3 sequences are indicated. **(E and F)** Gel electrophoresis images showing the positive integration of labelled mRuby3-cell clones compared with DF-1 wt.
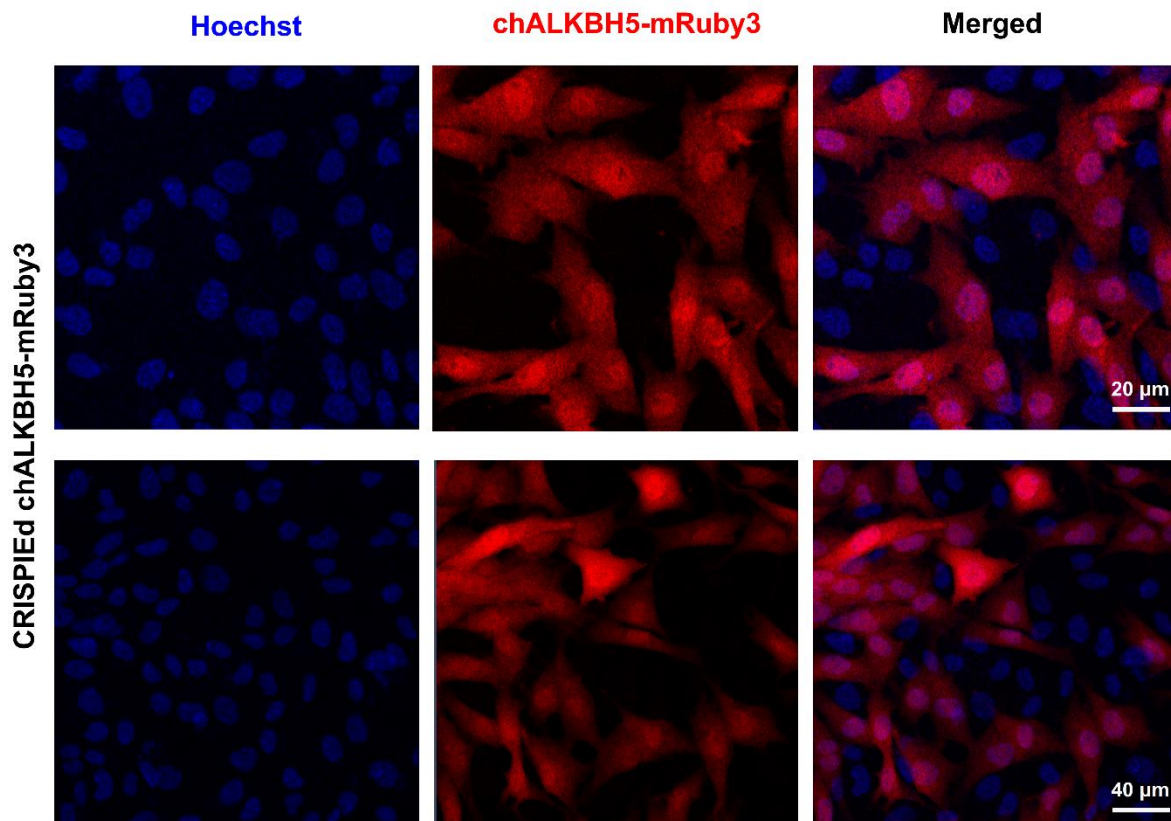
Figure 5.20: Generation of chicken DF1 cells with endogenously labeled chALKBH5-mRuby3. Two representative live images of DF1 cells confirmed the endogenous labelling with mRuby3 targeting chALKBH5. The endogenous labelling was performed using CRISPR-mediated insertion of exon (CRISPIE; CRISPIEd-chALKBH5-mRuby3). Live cells imaged in 24-well glass bottom Cellvis plates using confocal microscopy. Nuclei are stained with Hoechst. Integrated cells expressed mRuby3, whereas non-integrated wt-DF1 in between is shown by blue nuclei only (i.e., both are shown in the same field). CRISPIEd cells are labeled with the integrated mRuby3, as explained in **Figure 5.19**. Scale bars are also indicated.
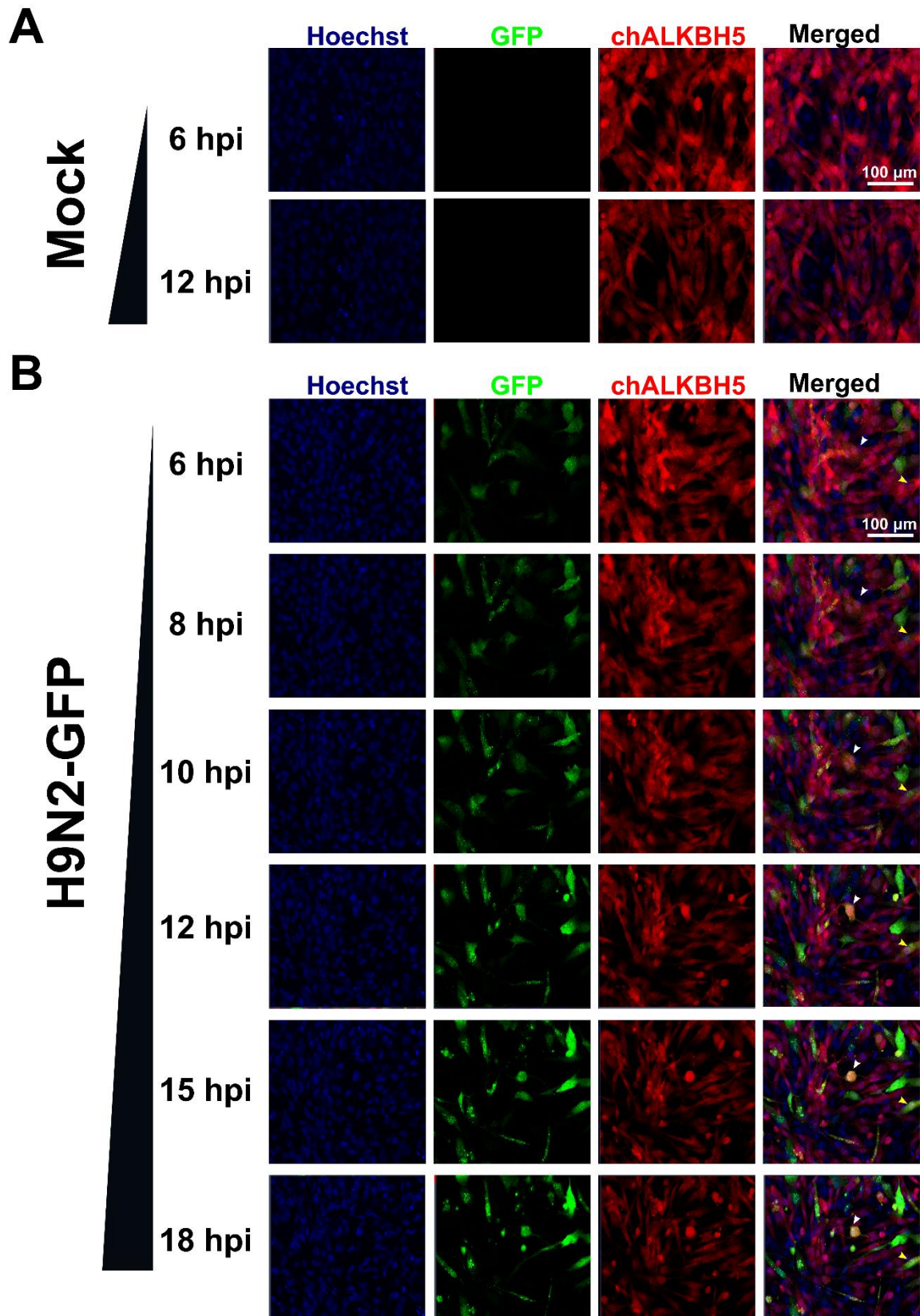
Figure 5.21: H9N2-GFP infection of the endogenously labeled chALKBH5-mRuby3 cells in a time-lapse manner. **(A)** Representative live images of the endogenously labeled uninfected DF1 cells (only two times are shown). **(B)** Representative live images of endogenously labeled DF1 cells infected with H9N2-GFP (MOI=1.0) in a time-lapse manner as indicated. The endogenous labelling was performed using CRISPR-mediated insertion of exon (CRISPIE; CRISPIEd-chALKBH5-mRuby3). Live cells imaged in 24-well glass bottom Cellvis plates using confocal microscopy. Nuclei are stained using Hoechst. Scale bars are 100 µm. CRISPIEd cells are labeled with the integrated mRuby3, as indicated in Figure 5.19.
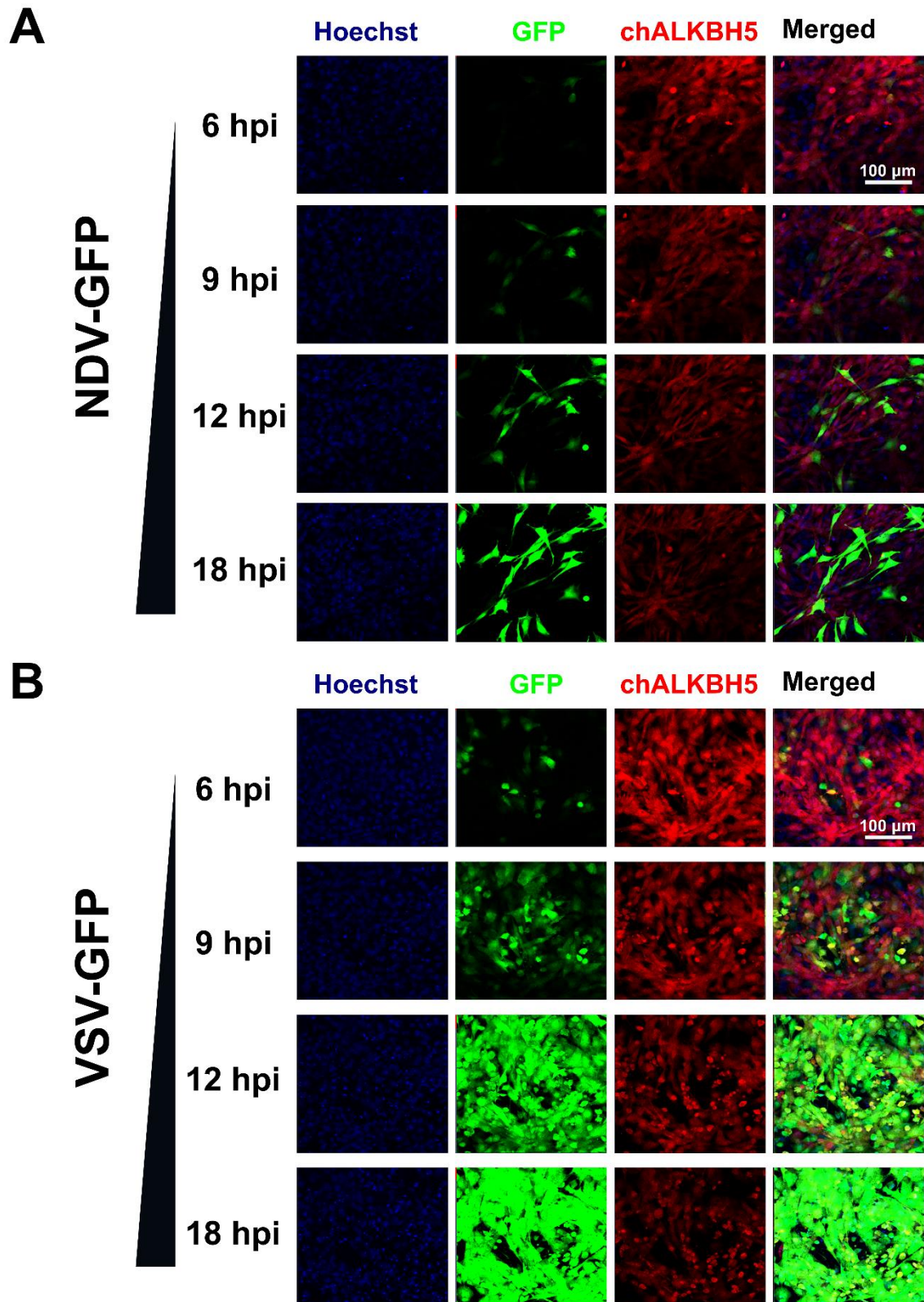
Figure 5.22: NDV-GFP and VSV-GFP infection of the endogenously labeled chALKBH5-mRuby3 in a time-lapse manner. **(A)** Representative live images of endogenously labeled DF1 cells infected with NDV-GFP (MOI=1.0) in a time-lapse manner as indicated. **(B)** Representative live images of endogenously labeled DF1 cells infected with VSV-GFP (MOI=1) in a time-lapse manner as indicated. The endogenous labelling was performed using CRISPR-mediated insertion of exon (CRISPIE; CRISPIEd-chALKBH5-mRuby3). Live cells imaged in 24-well glass bottom Cellvis plates using confocal microscopy. Scale bars are 100 µm. Nuclei are stained with Hoechst. CRISPIEd cells are labeled with the integrated mRuby3, as indicated in Figure 5.19.
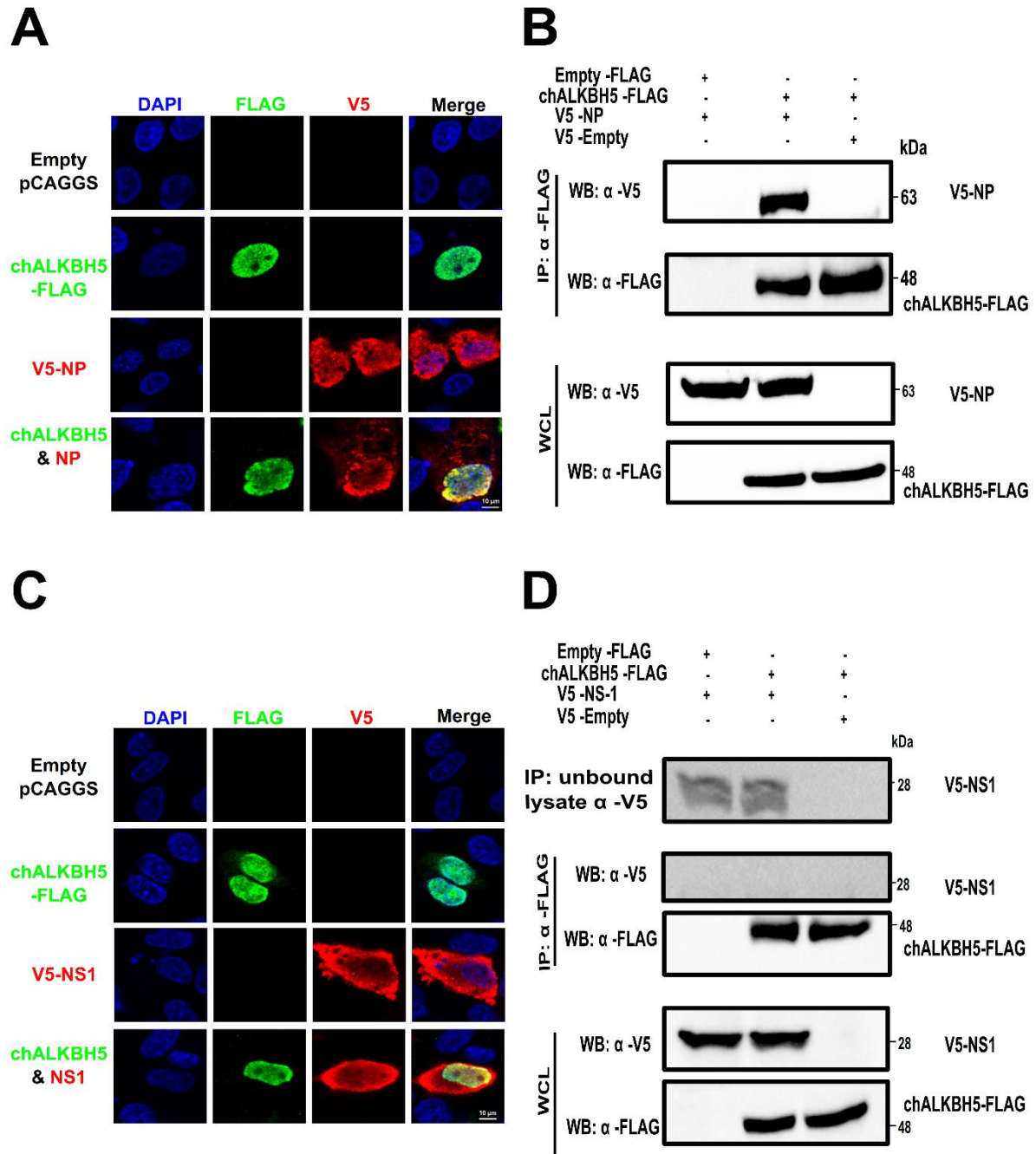
Figure 5.23: chALKBH5 interacts with the IAV NP protein but not the NS1. (**A and C**) Confocal microscopy of chicken DF1-transfected cells as indicated. The nucleus (blue), ALKBH5 (green), NP, and NS1 (red) were labeled with DAPI, or FLAG-, or V5- specific antibodies, respectively. Empty plasmid-transfected cells are served as a negative control. Scale bars are 10 μm. (**B and D**) Immunoprecipitation assay of

chALKBH5-FLAG with V5-NP (B) and V5-NS1 (D). Whole-cell lysates (WCL) and

immunoprecipitated fractions (IP) are indicated and the unbound fraction is also shown

(D). Control cells that were co-transfected with empty plasmids were properly included.

A representative western blot is shown.
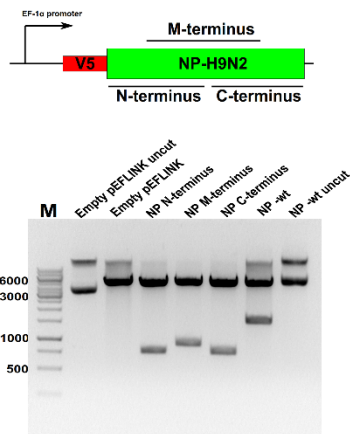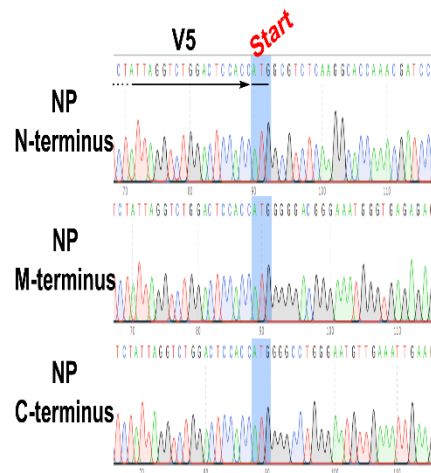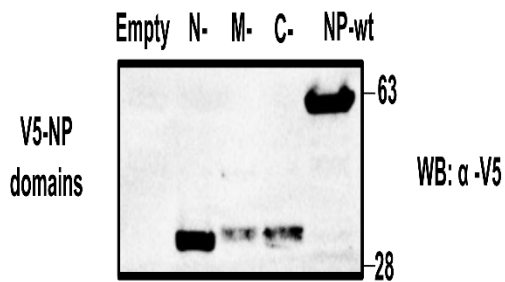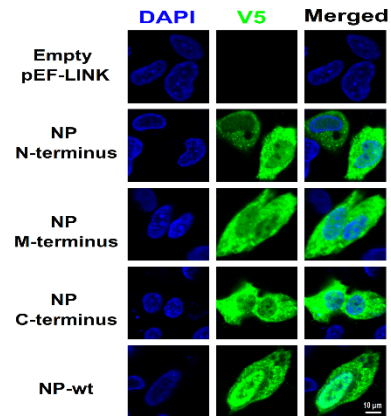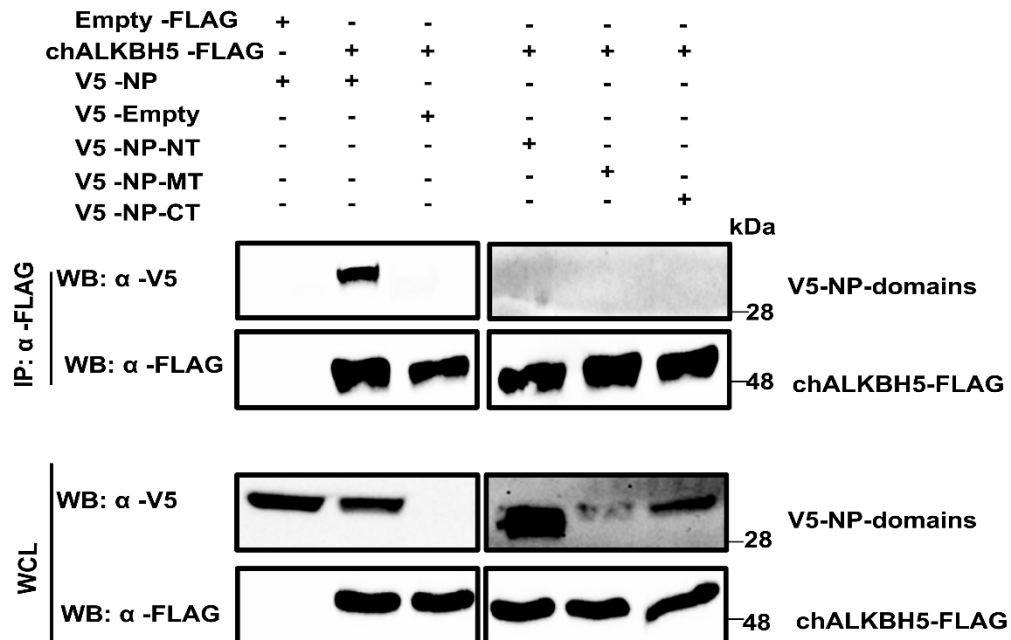
Figure 5.24: Cloning and expression of various domains of NP protein of IAV H9N2. **(A)** Schematic representation of viral H9N2 NP domains that were fragmented. Confirmation of successful cloning of all termini using restriction digestion. Restriction digestion was performed using NcoI and SpeI-HF (the restriction sites flanking each domain). Empty pEF-LINK and NP-wt plasmids served as controls. Uncut vectors are also indicated as a control of restriction digestion. **(B)** Confirmation of successful cloning and orientation of all domains was made using sequencing. The end of the V5-tag and translation start sequences are indicated by an arrow and blue shading, respectively. **(C)** Confirmation of expression of various viral NP domains using Western blotting, empty, and NP-wt transfected lysates served as controls. **(D)** Validation of expression of NP domains using confocal microscopy on chicken DF1-transfected cells. The nucleus (blue) and NP domains (green) were labeled with DAPI or V5-specific antibodies, respectively. Empty and NP-wt plasmid transfected cells are also shown. Scale bars are 10 µm. **(E)** Immunoprecipitation assay of chALKBH5-FLAG with NP-wt and various NP domains. Whole cell lysate (WCL) and Immunoprecipitated fraction (IP) are also indicated. A representative western blot is shown.

5.2.7. chWTAP does not interact with chMETTL3/14 methyltransferase complex

WTAP is the chief cofactor in humans that targets METTL3/14 to the nuclear speckles for active m6A methylation. Additionally, the interaction between WTAP and METTL3 has been verified in both immunoprecipitation assay and immunofluorescence assay (Ping et al., 2014; Schöller et al., 2018). However, our earlier investigation of chicken machinery indicated that chWTAP-FLAG was expressed solely in the cytoplasm. In order to understand the sub-cellular location, the chWTAP was swapped into the pCAGGS-HA backbone to replace the FLAG tag with the HA tag. As was the case with chWTAP-FLAG, the chWTAP-HA was readily expressed in the cytoplasm of DF1 cells, thus excluding a tag effect (**Figure 5.25B**).

The nuclear localization sequence (NLS) of WTAP has been verified in humans, which is located in the N-terminus (coiled-coil domain). Interestingly, no mutation was observed in the chWTAP, compared to human WTAP (**Figure 5.25A**). To analyse whether the investigated construct differs significantly from other chWTAP isoforms in the latest chicken genome release. Two main isoforms were identified; chWTAP-X1 representing our earlier investigated chWTAP and chWTAP-X2, which was 17 amino acids shorter than X1 (**Figure 5.25A**). To exclude the effect of the identified insert in the X1 isoform, another construct was designed and synthesized to match chWTAP-X2. Similar to chWTAP-X1, chWTAP-X2 was also expressed predominantly in the cytoplasm. It seems chWTAP is expressed in the cytoplasm through an unknown inherent mechanism in the chicken proteome.

Furthermore, as indicated earlier, the stimulation of chicken cells with IAVs does not alter the expression pattern of chWTAP (**Chapter 4, section 4.2.1**). To investigate any

possible alteration in expression upon co-transfecting chWTAP with the main methyltransferase complex (i.e., chMETTL3/14). All sets (chMETT3/14 and chWTAP) were cloned in both HA and FLAG-tagged vectors was performed to allow further labelling for downstream analysis. Using IFA, it was evident that chWTAP does not interact with chMETTL3/14. However, chMETTL3 successfully colocalizes with chMETTL14 in the nuclei (**Figure 5.25C**).

Next, the possibility of interaction in vitro was also investigated using an IP assay. For this purpose, DF1 cells were co-transfected with the chMETTL3-FLAG, chMETTL14-HA, and chWTAP-HA. The different sizes of the bands were used to detect each HA-tagged protein (i.e., chMETTL14-HA and chWTAP-HA). IP assay using the anti-FLAG antibodies indicated clearly that chMETTL3-FLAG immunoprecipitated the chMETTL14-HA. In contrast, compared with the input fraction, only weak interaction was noticed with chWTAP in the immunoprecipitated fraction. Investigating the other fractions of the immunoprecipitations indicates clearly that most chWTAP-HA was detected in the unbound fraction (**Figure 5.25D**). Interestingly, chMETTL14-HA was not detected in the unbound fraction. To conclude, chWTAP does not interact with chMETTL3/14 complex in the applied assays in culture and barely interacts with chMETTL3 using an in vitro assay.
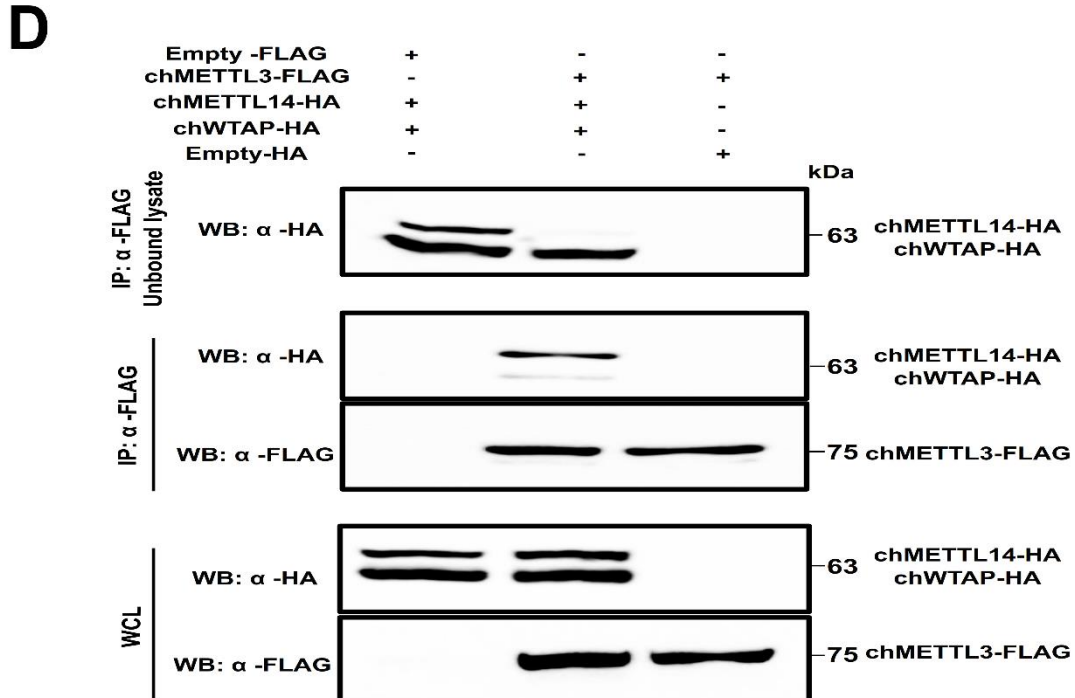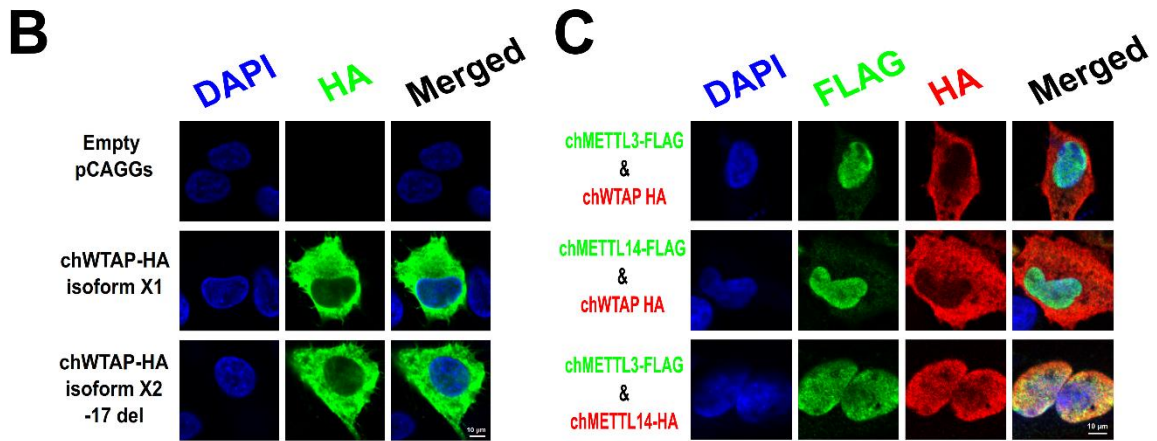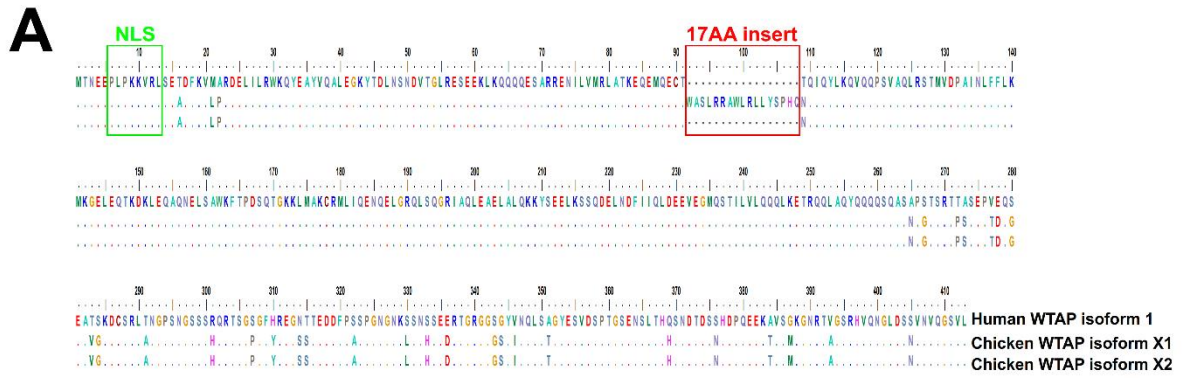
Figure 5.25: The chWTAP does not interact with the chMETTL3/14 complex. **(A)** Sequence alignment of the full-length of chicken and human WTAP amino acid sequences. The insertion of 17 a.a. in the chWTAPX1 isoform and nuclear localization sequence are indicated by red, and green boxes, respectively. Identical amino acid is indicated by coloured dots, and the variation is shown by coloured letters. **(B)** Confocal microscopy image on chicken DF1-transfected cells as indicated. The nucleus (blue) and HA (green) were labelled with a DAPI stain and HA-specific antibodies, respectively. DF1 cells transfected with an empty plasmid served as a negative control. Scale bars are 10 µm. **(C)** Confocal microscopy image of chicken DF1 co-transfected cells as indicated. The nucleus (blue) and FLAG (green) /HA (red) were labelled with DAPI stain or FLAG/HA-specific antibodies, respectively. Scale bars are 10 µm. **(D)** Immunoprecipitation assay of chMETTL3-FLAG with chWTAP-HA and chMETTL14-HA. Whole cell lysate (WCL)-, the immunoprecipitated fraction (IP)-, and unbound fractions are indicated. A representative western blot is shown.

5.3. Chapter Discussion

The ALKBH5 was reported to carry either pro-viral or anti-viral activity according to the investigated viral model. However, ALKBH5 was not investigated earlier in regulating H1N1 (Courtney et al., 2017). Therefore, it was crucial to examine the mechanistic effect of chALKBH5 for downregulating IAVs. In this chapter, two mechanisms of chALKBH5-mediated inhibition of influenza infection were verified and the functional domains responsible for antiviral activity were elucidated.

Overexpression of chALKBH5 downregulated replication of IAV and inhibited viral protein expression. Therefore, generating KO cell lines was expected to results in higher virus replication, as reported in ALKBH5 knockdown in various virus infection models (Xue et al., 2019; Lu et al., 2020). The DF1 chALKBH5-KO cells, however, showed no significant difference in virus replication compared with DF1-wt cells.

Two hypotheses could explain this observation; the first is that presence of chFTO (m6A-demethylase) induced m6A-related functional redundancy. The second possibility is that an enhanced innate immune response in the KO cells to impede enhanced virus replication. The chALKBH5 usually demethylates m6A marks, and its loss is expected to increase the cellular m6A methylome. Compared to uninfected DF1-wt cells, the chALKBH5 KO cell line exhibited a marked increase in the m6A signal in the m6A-dot blot assay, indicating that the chFTO did not replace chALKBH5 to restore cellular m6A homeostasis. This finding supports the specificity of chALKBH5 and chFTO to their substrates, as reviewed recently (Bayoumi and Munir, 2021c).

Enhanced innate immune responses associated with KO of any m6A-machinery in humans were previously reported (Zheng et al., 2017; Winkler et al., 2019). Interestingly, more than one adaptor for innate immune genes was upregulated in the chALKBH5 KO-infected cells. Intriguingly, testing the innate immune response in the uninfected cells also showed an enhanced innate immune response compared with the wild-type DF1 cells.

Moreover, the enhanced m6A levels in KO cells also suggest an increase in mRNA stability and/or protein expression, which has verified by an increase in the half-life of various cellular mRNA, including innate immune modulators. It is important to mention that chSTING and chPKR were readily expressed at 0–8 h post-ActD treatment in the KO cells; however, are not expressed beyond 2 h post-ActD treatment in the DF1-wt (data not shown). This finding clearly indicates that the m6A levels in the investigated mRNA molecules impede their turnover and support stability. The effect of the enhanced RNA stability on the protein expression levels in the KO cells; however, was not investigated. Notably, type 1 IFN response was noticed to be enhanced in ALKBH5 knockdown in humans (Zheng et al., 2017). Additionally, YTHDF2 KO cells expressed enhanced IFN response, as indicated elsewhere (Lu et al., 2021); therefore, it is likely that the same effect in chYTHDF2-KO cells to results in the lack of increased virus replication, compared to DF1-wt.

The ALKBH5 protein has 394 amino acids and a critical 2OG-active domain located in the middle of the protein. This functional domain is already well characterized using crystallographic analysis. However, the N- and C- fragments were not thoroughly investigated previously. Three domains were fragmented; upstream to the active

domain (N-fragment), the active domain M-fragment, which is expected to exert the antiviral effect, and the fragment downstream of the functional domain (C-terminus). Interestingly, M- and C-termini were involved in inhibiting H1N1 and H9N2 replication and protein expression, however, the N-terminus failed to interfere in the replication of IAV.

The N-terminus was notably and exclusively expressed in the cytoplasm. Interestingly, the NLS prediction sites for human and chicken ALKBH5 were the same in the N-terminus. Therefore, the cytoplasmic expression of the N-terminus is in conflict with this prediction. In contrast, the expression of the C-terminus was solely observed in the nucleus (similar to the chALKBH5-wt). The chALKBH5 sequence was analysed to determine NLS location using more than one prediction tool. The predicted site in the N-terminus was ignored, and by reducing prediction thresholds, two predicted sites were revealed in the C-terminus.

Mutating these two sites in the C-terminus increased the cytoplasmic expression of chALKBH5, especially in mutating the two sites together. However, solely cytoplasmic expression was not seen indicating that other factors controlling nuclear localization are not entirely determined for the chicken proteome, which warrants future investigation. Interestingly, the NLS of chWTAP (that will be discussed later) augments this hypothesis.

The chALKBH5-wt expression in the nucleus where IAV replication occurs supports a possible interaction, hence, downregulation. Notably, localization of N-terminus in cytoplasm supports this notion accordingly. The M-fragment, which encodes the active domain and shows perinuclear expression and the C-terminus, which is expressed in the

nucleus maintained the antiviral state against IAV. These findings indicate a possible link between the nuclear expression of chALKBH5 and its derivatives (i.e., domains/fragments) and influenza virus inhibition.

All these preliminary data indicate potential interaction of chALKBH5 with viral protein and/or viral RNAs. IAV was reported to contain a total of 24 m6A marks across the genome, and one-third of m6A marks are located only on the HA gene. Loss of the m6A mark from HA downregulated influenza replication and protein expression (Krug et al., 1976; Narayan et al., 1987; Courtney et al., 2017). It was hypothesized that chALKBH5 downregulated influenza virus replication through demethylating m6A marks from influenza segments, including HA. The RNA-immunoprecipitation assay (RIP) using chALKBH5-FLAG confirmed significant enrichment of HA mRNA using strand-specific primers. The finding indicates possible binding in vitro, however, the RIP assay finding does not necessarily indicate the actual functional/demethylation activity (Wheeler et al., 2018).

The most recent gene editing technologies have enriched our understanding of RNA protein interaction by tethering the protein of interest with the inactive Cas13 variant, especially in the cellular epigenomic field (Li et al., 2020; Wilson et al., 2020; Zhao et al., 2020a; Xia et al., 2021b). The inactive (dead) variant of Cas13 (dCas13) enables targeted binding but does not support the collateral activity of Cas13, as reviewed earlier (Bayoumi and Munir, 2021b). Therefore, the chALKBH5 was fused with dCas13b and targeted to HA mRNA guided by various crRNAs.

In this way, programmable demethylation was achieved, and virus replication was downregulated using only the nuclear version of the construct. Our previous data

indicated that the chALKBH5-wt was solely expressed in the nucleus and possibly demethylates m6A of HA in culture *in cis*; keep in mind that IAV replicates in the nucleus. This possibility was further supported by the cytoplasmic expression of the dCa13b-chALKBH5 chimera that failed to regulate the virus replication. Similarly, the N-terminus of chALKBH5 has the same cytoplasmic location, which supports the notion.

As per our manoeuvre in studying the conservation pattern described in **Chapter 3** and our previous report (Bayoumi and Munir, 2021a), the H9 subtype has three conserved DRACH motifs (i.e., DRACH- 2, -8, and -13). Therefore, crRNAs were designed to target these potential m6A sites. The crRNAs that targeted both the 5′ and 3′ end of the HA gene was confirmed to downregulate virus replication. It is important to note that the crRNA only targeted specifically HA mRNA but no other segments of the IAV (i.e., M gene).

It was observed earlier that chFTO does not regulate the replication of IAV and viral expression of H9N2. tether chFTO to dCas13b was an alternative assay that could enforce to downregulate IAV. In this manner, the selectivity of HA mRNA was also verified for chFTO. Despite this, chFTO-FLAG in RIP also showed enrichment for HA mRNA. Nevertheless, the virus replication was not affected. m6A machinery was noticed to bind to methylated and non-methylated mRNA (Gokhale et al., 2016; Edupuganti et al., 2017). Secondary RNA structures are possibly involved in this process for substrate specificity (Bayoumi and Munir, 2021c).

It was next hypothesized potential interaction with either NS1 and/or NP. The NS1 is the predominant innate immune-modulatory protein in IAV infection. Therefore,

interacting with chALKBH5 to suppress viral infection is possible (Hale et al., 2008). On the other hand, NP is a widely expressed protein and interacts with viral RNA throughout its lifecycle. The chALKBH5 binding with NP would downregulate IAV replication in a time-course manner.

Very recently, endogenous label of cytoskeletal proteins of neuronal cells, including actin, has been reported through CRISPR-mediated insertion of exon (Zhong et al., 2021). The authors inserted some fluorescent proteins between the introns of the genes of interest. In this way, INDELs that are possibly generated at insertion junctions would be spliced out, creating nearly error free in the mRNA levels (Zhong et al., 2021). Similarly, mRuby3 was used as a donor exon to be inserted in either intron-1 or -4 of the chALKBH5 gene of DF1 cells. To generate reporter DF1 cells with endogenously labelled chALKBH5 protein. This approach makes interaction of chALKBH5 with GFP-tagged viruses feasible and facilitate the study of viral replication kinetics in a real-time and time-lapse manner using a live imaging system. The live imaging also confirmed the predominant nuclear expression of endogenous chALKBH5 seen in the ectopic expression. The generated reporter cells indicated potential interaction with one or more viral proteins in the nucleus. The H9N2-NS1-GFP virus was investigated in labeled cells. The interaction between labelled protein NS1-GFP and chALKBH5-mRuby3 was weak to support potential interaction, which was further verified by the immunoprecipitation assay (IP) assays between NS1 and chALKBH5.

In contrast, H9N2 NP was enriched in the chALKBH5-FLAG immunoprecipitated fraction. The immunofluorescence assay confirmed this finding, indicating possible interaction in vitro. All these findings support various antiviral regulatory effects of

chALKBH5, demethylating m6A marks on HA and/or binding with NP proteins in the virus-infected cells.

In an effort to identify the potential NP domain that interacts with chALKBH5, NP was divided into three fragments. NP consists mainly of two known domains; body and head. The NP interacts with polymerase protein using the body domain (Ye et al., 2006). Thus, chALKBH5 could interact and impede the binding. Unlike chALKBH5, NP protein has a non-continuous structure (Ye et al., 2006). That makes proper 3D expression of each fragment challenging. Although all domains were readily expressed, none were expressed in the nucleus. Therefore, the domain mapping remained unidentified and need further fragmentations analysis.

The WTAP protein is the main co-factor that supports the nuclear localization of methyltransferase complex to nuclear speckles (Ping et al., 2014; Schöller et al., 2018). However, chWTAP was noticed to be exclusively expressed in the cytoplasm. Furthermore, chWTAP expression was not affected by viral infection. Interestingly, the mapped and validated NLS sequence of human WTAP was identical to the sequence chWTAP, which makes answering the cytoplasmic expression of chWTAP challenging. Testing various visualization tags or shorter isoforms did not identify cause of this unexpected expression in the cytoplasm.

Therefore, it was hypothesized that chWTAP is not a co-factor in the methyltransferase complex in chicken. Co-transfections between chMETTL14/3/WTAP and the immunofluorescence assay confirmed that chMETTL3 interacts readily with chMETTL14 in the nucleus but does not interact with chWTAP. Furthermore, the

immunoprecipitation assay also confirmed binding of chMETTL3 and chMETTL14 binding but not chWTAP, which is primarily detected in the unbound fraction.

In human m6A machinery, WTAP interacts with the leader sequence of METTL3 (the 28 aa in the N-terminus of METTL3). This leader sequence was also identical with chMETTL3, which makes weak interaction possible in only the IP assay. All these findings support that chWTAP does not interact with the chMETTL14/3 complex and may not be part of the methyltransferase complex in chicken.

Chapter 6

Generation of Different m6A-Mutant

Influenza A Viruses

and

The Impact of m6A Marks on Virus

Replication Kinetics

6.1. Chapter Introduction

6.1.1. Generating m6A-deficient viruses is crucial for studying the impact of m6A marks on virus replication kinetics

The m6A is the most prevalent internal chemical modification installed onto mRNAs in eukaryotes. The m6A marks are also commonplace on almost all studied viruses so far; highlighting their major regulatory roles in the viral lifecycle and fate of virus-cell interactions (Tsai and Cullen, 2020; Baquero-Perez et al., 2021). However, to directly demonstrate that m6A marks positively or negatively regulate virus replication, generating m6A-deficient mutant virus(s) is essential.

It has been reported that respiratory syncytial virus (RSV) bears multiple m6A peak clusters on both genomic RNA (vRNA; negative sense RNA) and antigenomic strands (i.e., mRNA/cRNA) (Xue et al., 2019). Moreover, most of the m6A-sites were located in the G gene, the major surface glycoprotein responsible for attachment to the cell. To demonstrate that these m6A marks exert a direct role in virus replication and pathogenicity, authors generated m6A-deficient viruses. Interestingly, the rescued mutants with low m6A marks on G mRNA were confirmed to have reduced replication kinetics in culture and cotton rats (Xue et al., 2019).

In follow-up research, the same group generated other m6A-deficient RSVs by removing potential m6A sites from the G gene on the antigenome strands (mRNA/cRNA, +G), the genome strand (vRNA, -G), and a mix of both (+/-G). All recombinant RSV mutant viruses exhibited markedly reduced replication kinetics compared with rescued wild-type RSV (Xue et al., 2021). These results indicate that

m6A directly impacts RSV viral replication, and the rescue of mutant viruses augments these findings. Similar results were also obtained in studying human metapneumovirus (HMPV) (Lu et al., 2020). In a trial to demonstrate the biological role of viral m6A on replication, the *de novo* synthesis of HMPV with the abrogation of m6A sites from viral transcripts was also attenuated in culture and animal models (Lu et al., 2020).

Mapping m6A sites on simian virus 40 (SV40) transcripts was also performed. Ablation of the m6A sites from late viral transcripts resulted a significant reduction in replication and virus spread (Tsai et al., 2018). The same group mapped the m6A marks on the murine leukaemia virus (MLV), followed by silent mutational abrogation of the m6A sites. They noticed significant attenuation of MLV-variants in culture. Altogether, these findings suggest a positive impact of presence of m6A on viral replication (Courtney et al., 2019a). On the other hand, others suggested that the presence of m6A marks negatively impacts the viral replication of HCV in which generating mutant viruses expressing low m6A marks significantly increased viral production (Gokhale et al., 2016).

Vis-à-vis influenza A viruses, Courtney et al. (2017) have described the direct impact of the m6A marks on influenza A virus replication in culture and an animal model. The PA-m6A-seq data revealed that H1N1 carries 8/9 m6A sites on mRNA/vRNA, respectively, of the HA gene. Several point mutations were introduced to change the 5′-RAC-3′ sites (the potential m6A sites) without affecting the amino acid codes. In this way, two m6A-deficient mutants were generated (+/-Mut; m6A sites on mRNA/vRNA of HA were removed). The authors revealed that these mutants had significantly reduced replication and pathogenicity compared with the H1N1 PR8 wild-type

(Courtney et al., 2017). However, all these studies were conducted in humans/mice using human influenza A viruses.

6.1.2. Reverse genetics systems for generating IAVs

The generation of wild-type and mutant viruses using cloned cDNA sequences is referred to as reverse genetics (RG). This approach allows to design and introduce deliberate mutations into the rescued/recovered virus. RG-based viruses, including influenza, have been commonly used in molecular virology laboratories worldwide. RG-based influenza viruses made outstanding achievements in basic and applied research by making the characterization of newly emerging viruses convenient. Moreover, RG-based viruses are the most common methods for generating influenza vaccine candidates.

Many viruses, belonging to different families, have been generated using RG-based system, including rabies virus, bovine respiratory syncytial virus, parainfluenza type 3, and rinderpest (Schnell et al., 1994; Baron and Barrett, 1997; Durbin et al., 1997; Buchholz et al., 1999). Moreover, the generation of recombinant Bunyaviruses, a negative sense three-segmented model, was also created (Bridgen and Elliott, 1996). Despite the first trials to implement the RG system for influenza viruses, which started in the 1980s (Beaton and Krug, 1986), several technical limitations originating from the unique replication strategy caused the RG-based system for influenza viruses to lag behind.

Influenza A viruses are negative-sense single-stranded RNA with eight segments. The negative polarity means that vRNA cannot initiate replication or transcription.

Consequently, eight cDNAs containing the authentic vRNA plus at least four cDNA encoding the minimal RNA transcription complex for IAVs (i.e., PB1, PB2, PA, and NP) are required as an artificial supply to generate a recombinant influenza A virus.

6.1.2.1. Helper virus-dependent methods for *de novo* synthesis of IAVs

Two main techniques were adopted to generate IAVs; helper virus-dependent and helper virus-independent methods, which were reviewed comprehensively elsewhere (Neumann and Kawaoka, 2001; Engelhardt, 2013; Neumann, 2021). In brief, in the helper virus-dependent methods, the vRNA of interest was synthesized in-vitro and admixed with a purified transcription complex. The cDNA sequence of the vRNA the gene segment of interest is cloned into a plasmid under the control of polymerase I (PolI) promoter and terminator. This ribonucleoprotein complex (vRNP) was transfected into cells infected by a helper virus to provide the rest of the seven vRNPs **(Figure 6.1)**.

The resultants are a mixture of wt (parental/helper virus) and the new recombinant virus incorporating the vRNA of interest (Luytjes et al., 1989). Therefore, rigorous selection methods are essential for isolating the recombinant virus from the parental helper. Several selection strategies were adopted, including selection based on temperature sensitivity, neutralizing antibodies, host range specificity, and drug resistance (Enami et al., 1990; Enami and Palese, 1991; Horimoto and Kawaoka, 1994).
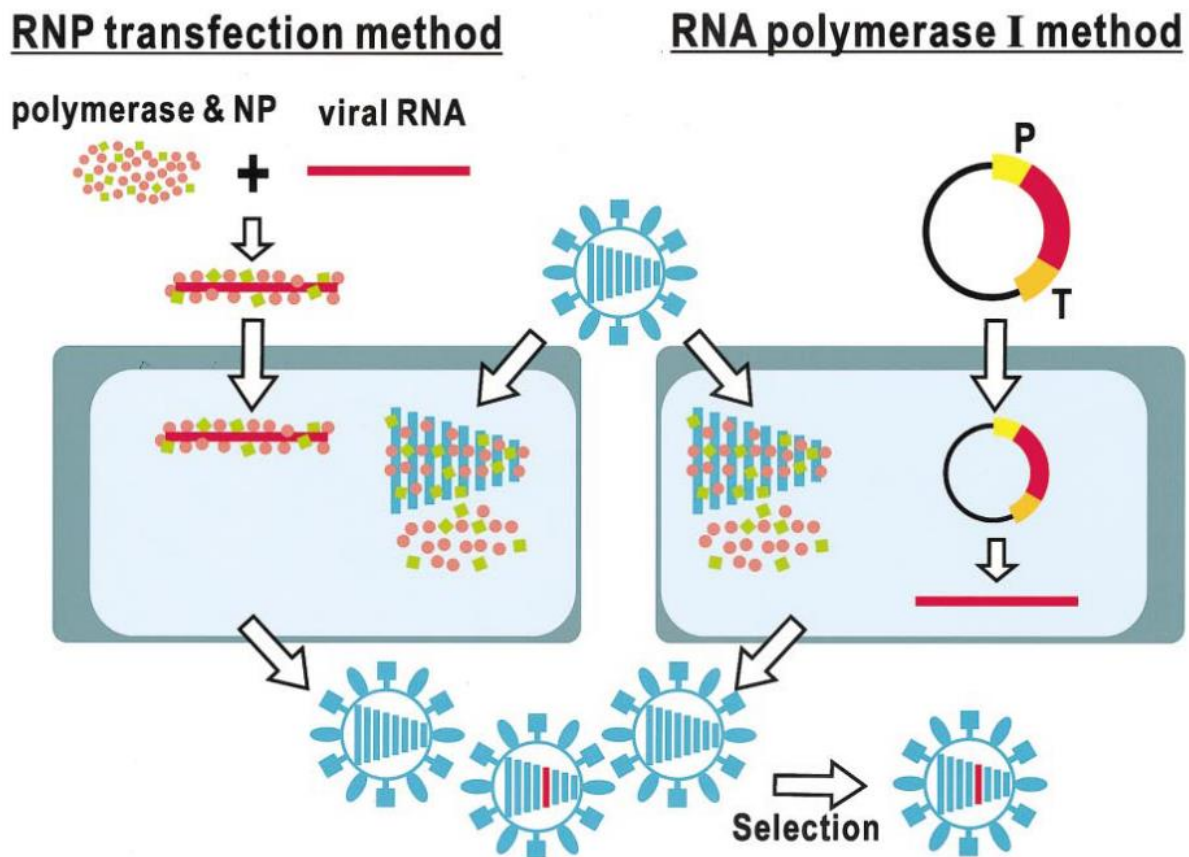
Figure 6.1: Schematic of reverse genetics system using helper virus-dependent methods for generating IAVs. The vRNA is chemically synthesized and mixed with the purified transcription complex PB1, PB2, PA, and NP in the RNP transfection method. Then, the vRNP is introduced into cells. In the RNA polymerase I method, a plasmid encoding the vRNA of interest flanked by RNA polymerase I promoter (P) and terminator (T) is transfected into cells. In both ways, the cells are infected with the helper influenza virus to provide the remaining seven segments. Then, a robust selection procedure is applied to remove the background helper virus. The figure is modified from a previous report (Neumann and Kawaoka, 2001).

6.1.2.2. Helper virus-independent methods for *de novo* synthesis of IAVs

Notably, the helper virus-dependent methods were inefficient for generating recombinant viruses because they worked only for one vRNA and specific viruses with selection methods available. Therefore, the generation of recombinant influenza from entirely cloned cDNA has emerged. Two groups independently generated IAVs using the cloned cDNAs under the effect of PolI promoter sequence (Fodor et al., 1999; Neumann et al., 1999). This system cloned the eight authentic vRNAs into plasmids flanked with human PolI promotor and murine polymerase terminator sequences. Additional 4-9 expression plasmids were provided to express viral proteins to provide a "kick-start" of viral replication **(Figure 6.2)**.
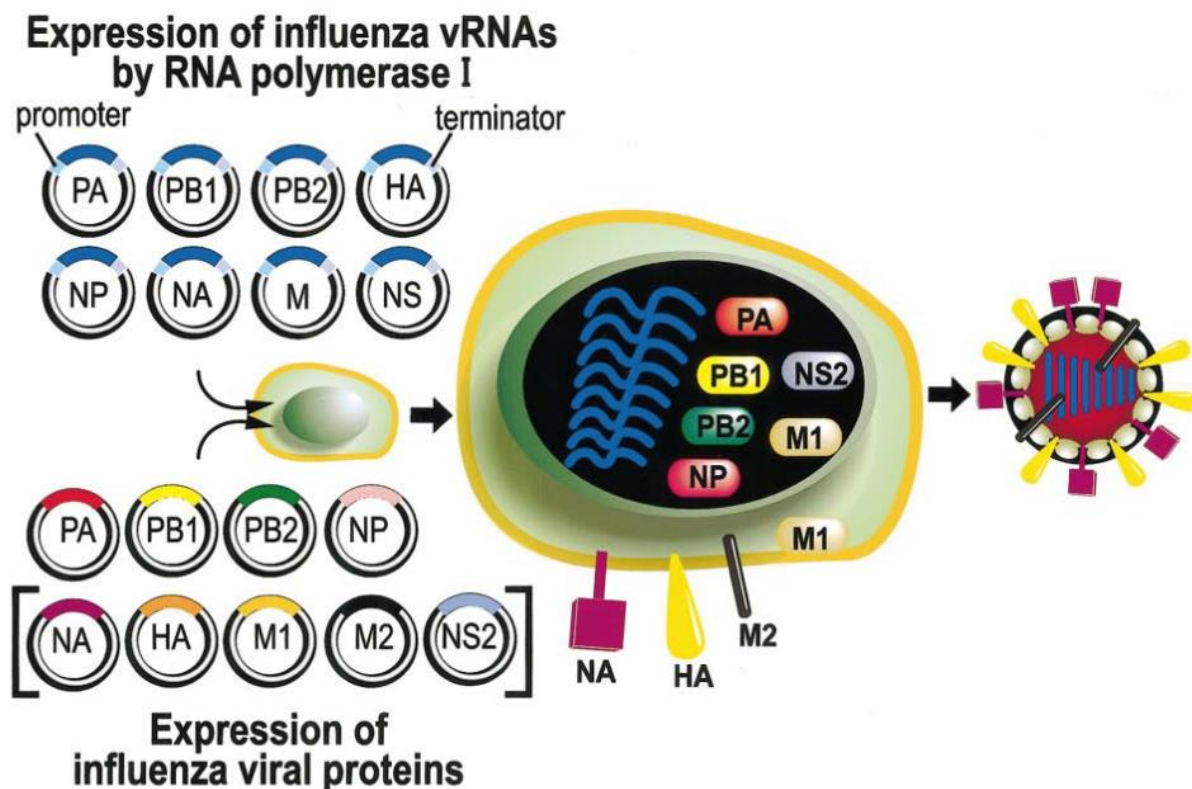
Figure 6.2: Schematic of generating IAVs using entirely cloned cDNAs. The vRNA sequences were flanked by the PolI promoter and terminator sequences. Additional 4-9

expression plasmids are co-transfected into cells to facilitate the expression of viral proteins that provide the minimal transcription unit for starting transcription. The figure is adapted and modified from a previous report (Neumann and Kawaoka, 2001).

Hoffman et al. (2000) have developed a bi-directional transcription system of *de novo* synthesis of IAV using a total of 8 plasmids. In this system, the vRNAs were cloned and flanked by the polI transcription system described above in the negative direction (to support vRNA production). This transcription unit was further flanked by another polII promoter and polyadenylation sequence in the positive direction (to support viral protein production) in one cassette per each segment (Hoffmann et al., 2000) **(Figure 6.3)**.
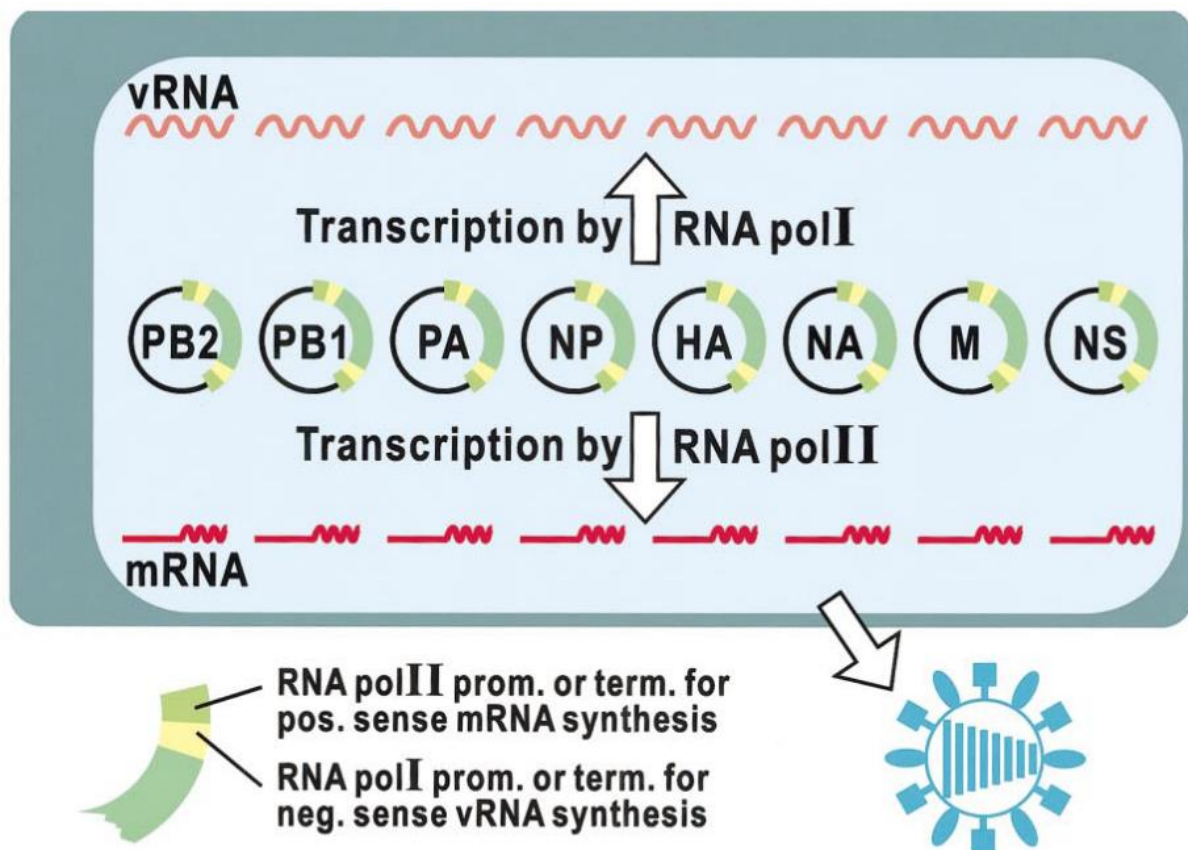
Figure 6.3: Schematic of *de novo* synthesis of IAVs using the bidirectional polymerase I/II-dependent system. The viral RNA is encoded under the control of polI promotor and terminator sequences in the negative orientation. Then, this transcription unit is further flanked by polII promotor and polyadenylation sequences for viral protein production. The figure is adapted and modified from a previous report (Neumann and Kawaoka, 2001).

Despite using either the polI or polI/II system for *de novo* synthesis of IAVs worldwide two decades ago, some modifications were also introduced to minimize the number of plasmids used for transfection (Zhang et al., 2009; Chen et al., 2014; Zhang and Curtiss, 2015). In this project, the eight-plasmid system was used for its convenience in generating many avian influenza viruses, including the H9N2-UDL/08, the strain of interest in this study (Peacock et al., 2016, 2017).

6.1.3. Chapter Aims

Given the reports mentioned earlier, the generation of m6A-deficient mutant viruses for studying virus replication was essential. To determine the impact of m6A marks on an avian influenza virus replication was performed with the introduction of synonymous mutations, some of them differ from designed generated earlier. The objectives were to:

1. Generate various H9N2 m6A-modified mutant viruses according to the topology of the mapped m6A sites.

2. Characterize different rescued viruses and validate their competence in replication.

3. Test the genetic and phenotypic stability of m6A-mutant viruses through passaging in eggs and on cell culture.

4. Investigate the impact of these m6A-targeted mutations on H9N2 virus replication and protein expression.

5. Test whether these mutant viruses are indeed m6A-deficient.

6. Investigate whether these mutations selectively affect the targeted strand/segment or other non-targets.

7. Determine the molecular determinants of reduced replication of the m6A-mutant viruses.

6.2. Chapter Results

6.2.1. Concept and design of H9N2 m6A-mutant viruses

The genome of IAVs is eight-segmented, negative-sense, and single-stranded RNA. The fourth segment encodes the HA protein, the major glycoprotein that mediates virus binding and entry to cells. Additionally, HA is responsible for the remarkable genetic plasticity with the highest mutation rate to be responsible for seasonal epidemics (Webster et al., 1992; Cox et al., 2007). Notably, viral epitranscriptome sequencing of the H1N1 PR8 strain mapped 8/9 m6A marks on the HA mRNA/vRNA, respectively (Courtney et al., 2017). Synonymous mutations of RAC sites that correspond to the m6A peaks located on vRNA or mRNA were generated, resulting in reduced virus replication and protein expression **(Figure 6.4)** (Courtney et al., 2017).

Our previous findings indicate that chALKBH5 induces the demethylation of m6A marks selectively from HA mRNA resulting in reduced virus replication **(Chapter 5, Section 5.2.4.)**. These data suggests that m6A marks on HA of H9N2 also have a proviral effect that is possibly unique among IAVs, and its removal negatively affects virus replication. Consequently, to verify the impact of m6A marks on H9N2 replication, m6A-mutant H9N2 viruses were generated.

To address this issue, ubiquitous synonymous mutations that disturb any possible DRACH site selectively were introduced into the HA mRNA sequence, which coincides with all potential m6A peaks mapped on the HA mRNA of H9N2 UDL using MeRIP-seq (will be discussed in the next chapter). In this regard, 27 DRACH sites were mutated without affecting the amino acid code to produce an m6A-mutant virus (m6A$^-$27) **(Figure 6.5)**.

Another m6A-mutant was rationally designed with ubiquitous synonymous mutations to add 29 DRACH sites into the HA mRNA sequence without affecting the amino acid code (m6A$^+$29) **(Figure 6.5)**.

It is important to note that recovering m6A$^-$27 and m6A$^+$29 mutants is challenging as they carry many mutations that could be structurally incompatible. Therefore, another rescue control m6A-mutant was designed to introduce only six mutations in DRACH sites without affecting the amino acid codes; some DRACHs are coincident with the potential m6A sites mapped on H9N2 UDL (m6A$^-$6). To conclude, three m6A-mutants were rationally designed for further rescuing to target the H9N2-UDL HA mRNA strand to investigate the impact of m6A on virus replication kinetics and protein expression.
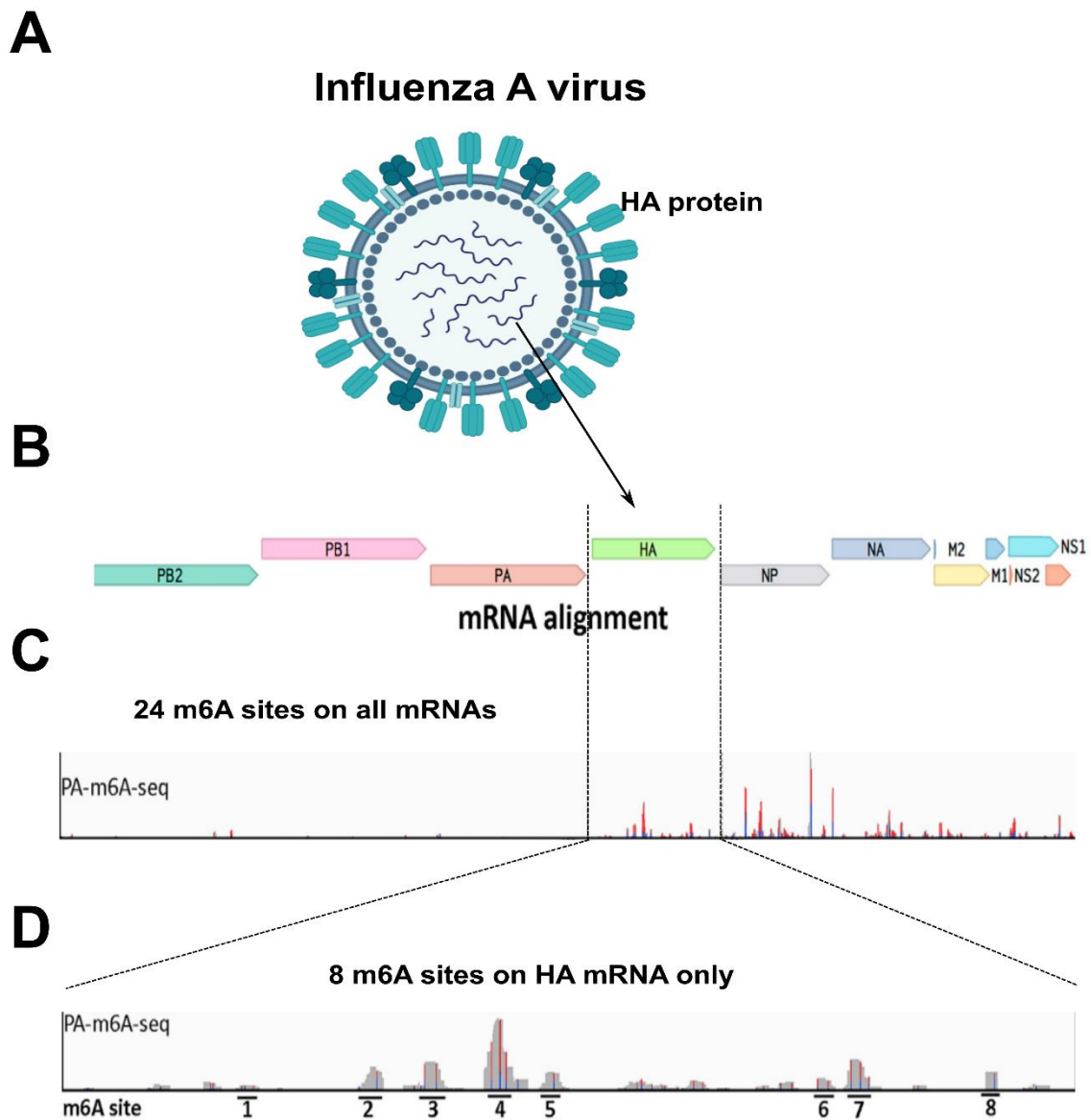
Figure 6.4: Rationale for designing m6A-mutant IAVs on HA plus strand. (**A**) Schematic illustration of IAV contains eight segments, including HA. (**B**) Concatenated map of IAV transcripts. (**C**) Identification of 24 m6A sites on IAV H1N1 PR8 strain on plus-sense strands represented by PA-m6A-seq data. (**D**) An expanded view of the PA-m6A-seq data on HA mRNA shows eight m6A sites on the HA plus-strand. C and D are adapted and modified from a previous study (Courtney et al., 2017).
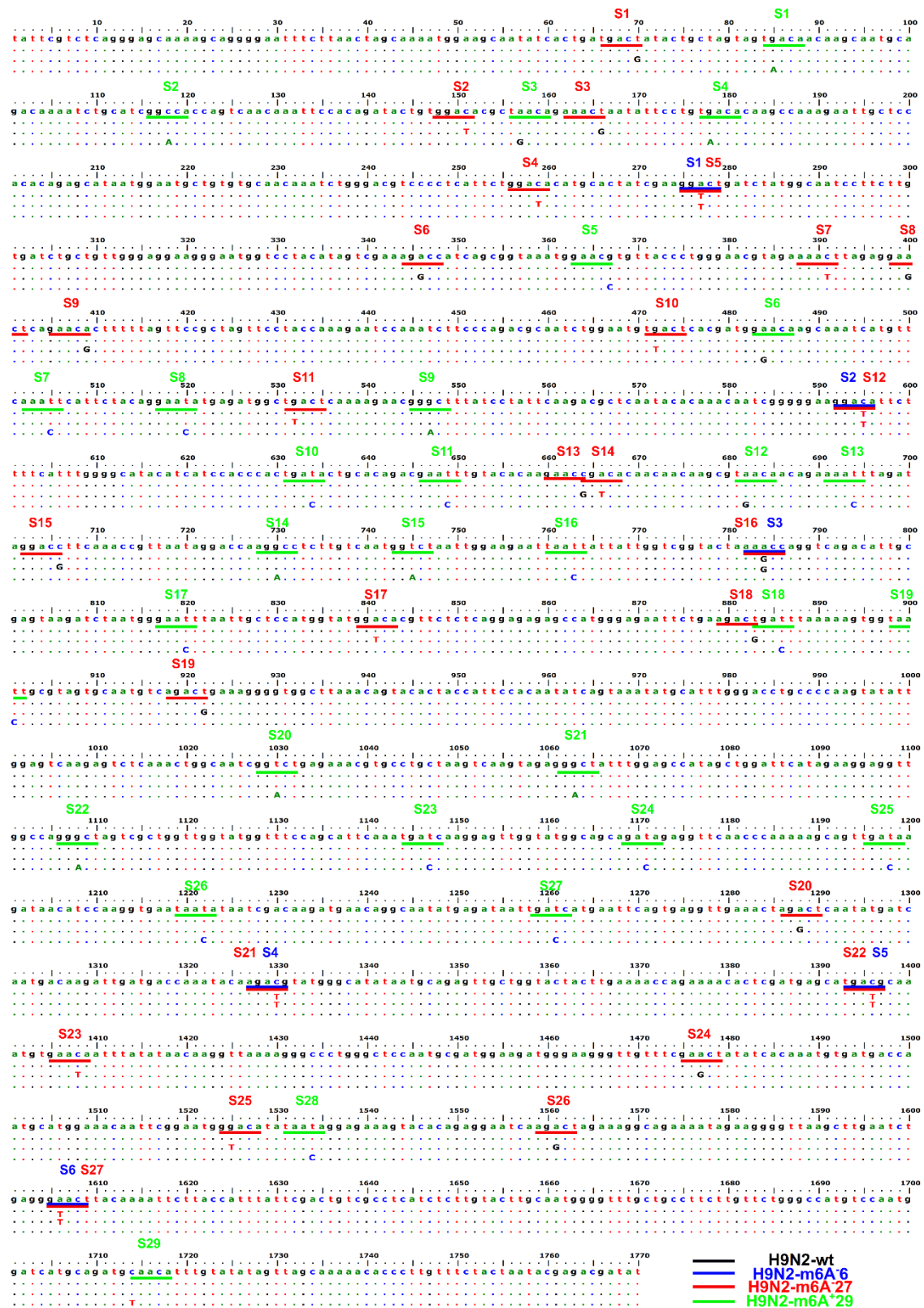
Figure 6.5: Schematic of synonymous mutations introduced to generate three H9N2-UDL m6A-mutants. The point mutations were introduced into the HA plus strand of the H9N2 UDL to ablate 6 and 27 or add an extra 29 consensus 5'-DRACH-3' (potential m6A sites). The first H9N2-UDL HA wt mRNA sequence is indicated by coloured letters. The second sequence is H9N2-UDL HA m6A⁻6 (i.e., m6A⁻6). The identically aligned nucleotides are shown as dots, whereas the introduced 6-point mutations are indicated by coloured letters to generate the m6A⁻6 mutant virus (blue). The third sequence is H9N2-UDL HA m6A⁻27 (i.e., m6A⁻27). The identically aligned nucleotides are shown as dots; only the introduced 27-point mutations are indicated by coloured letters to generate the m6A⁻27 mutant virus to remove potential m6A sites (red). The fourth sequence is H9N2-UDL HA m6A⁺29 (i.e., m6A⁺29). The identically aligned nucleotides are shown as dots, and only the introduced 29-point mutations are indicated by coloured letters to generate the m6A⁺29 mutant virus that possibly develops extra m6A sites (green).

6.2.2. Rescuing and characterization of three IAV H9N2 m6A-mutant viruses

As described earlier, IAV rescue using the 8-plasmid RG-based system was initially developed two decades ago (Hoffmann et al., 2000). It was later modified to generate H9N2-UDL strains (Peacock et al., 2016, 2017). The designed HA mutant constructs were chemically synthesized and cloned into pHW2000 plasmid (the bidirectional plasmid). Briefly, the eight plasmids were transfected into HEK-293T cells and then co-cultured with MDCK. After 48–72 h, the cell culture supernatants were inoculated into 9-day embryonated-chicken eggs **(Figure 6.6A)**. After an additional 72 h, the allantoic fluid harvests were investigated for positive hemagglutination activity (HA). The H9N2 UDL/08 wild-type was rescued as a positive control using the HA-wt sequence (this control virus will later be named UDL-wt). Transfecting 7-plasmids (without PB1) was used as a negative control. All harvested allantoic fluids showed a lattice shape formation confirming HA activity (except the negative control) **(Figure 6.6B)**.

Viral RNA was extracted from a representative positive allantoic fluid for each m6A-mutant. HA-gene-specific primers were designed for sequencing the entire H9N2 HA segments of the rescued m6A-mutant viruses. In addition to HA positivity, the sequence confirmed the recovery of three m6A-mutant viruses of interest (m6A$^-$6, $^-$27, and $^+$29). Representative sequences are shown for each of the mutants **(Figure 6.7)**.

The 4 rescued viruses (i.e., UDL-wt, m6A$^-$6, $^-$27, and $^+$29) were propagated, purified, and concentrated using ultracentrifugation. Then the purified viruses were quantified using plaque assay. An equal endpoint titre (i.e., equal plaque count) is essential to investigate the comparable replication kinetics of rescued viruses. To this end, the

quantity per virus was diluted to achieve equivalent plaque-forming units (PFU) **(Figure 6.6C)**. Notably, the plaque diameters of m6A-27 viruses were smaller than other m6A-mutants and UDL-wt viruses even after propagation for nine passages **(Figure 6.6D)**. To conclude, three H9N2-UDL m6A-mutants and UDL-wt viruses were rescued, characterized, and equal endpoint titres were generated.
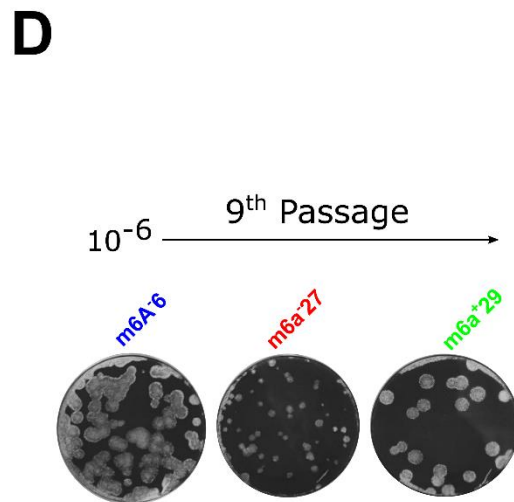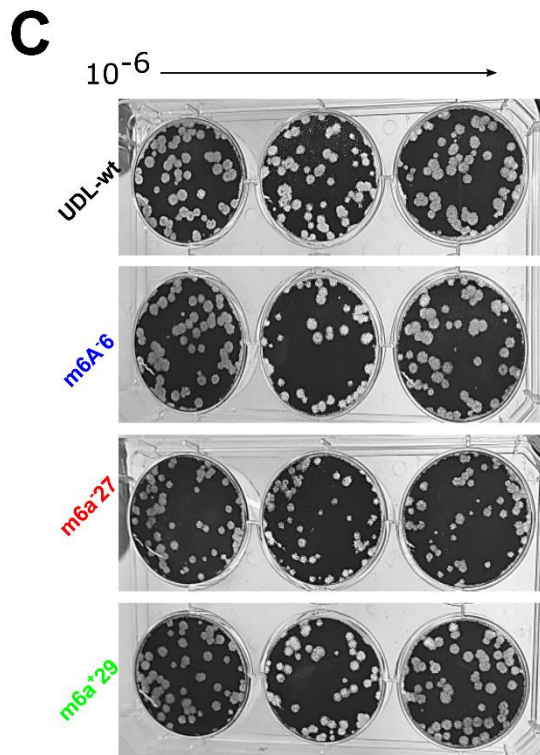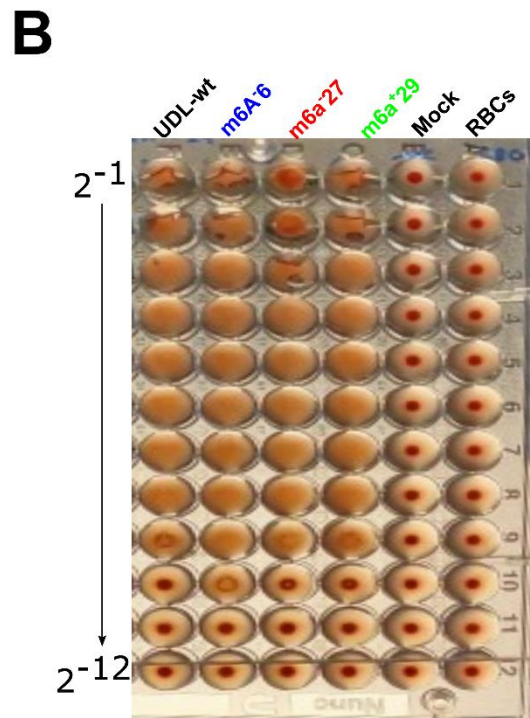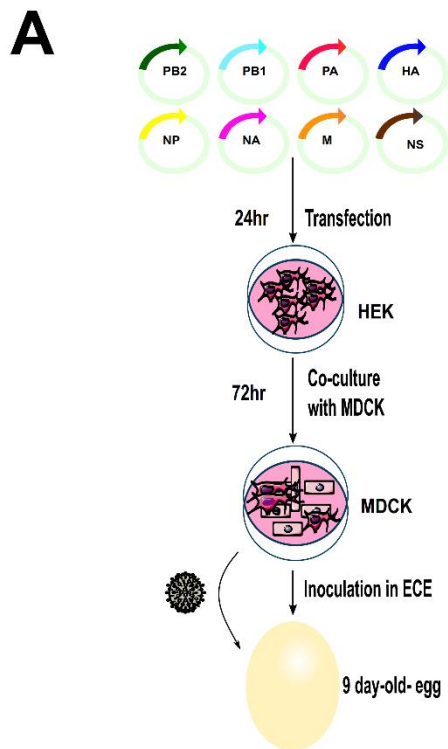
Figure 6.6: Rescuing and characterization of three IAV H9N2 m6A-mutant viruses. **(A)** Schematic of generation of IAV-H9N2 m6A-mutant viruses. The eight-plasmid system was utilized. Plasmids were transfected in HEK-293T cells. Then, HEK cells were co-cultured with MDCK before inoculation into embryonated chicken eggs (9 days old). **(B)** Hemagglutination assay for rapid testing of rescuing a potential HA virus. The positive results exhibited a lattice-shaped formation, and the negative results displayed a button-shaped formation. Negative control allantoic fluids and red blood cells (RBC) controls are indicated. **(C)** Plaque assay-based quantifications confirmed the generation of equal endpoint titres for investigating the viral replication kinetics. The 10^{-6} dilutions only are shown for three technical replicates for each studied virus. **(D)** Plaque assay of the rescued m6A-mutant viruses after nine passages, confirming viral replication competence and phenotypic spreading properties. Only 10^{-6} dilution is shown for each of the m6A-mutants. All shown plaque assays were propagated on MDCK for 72 h, and only the countable wells of interest are considered.
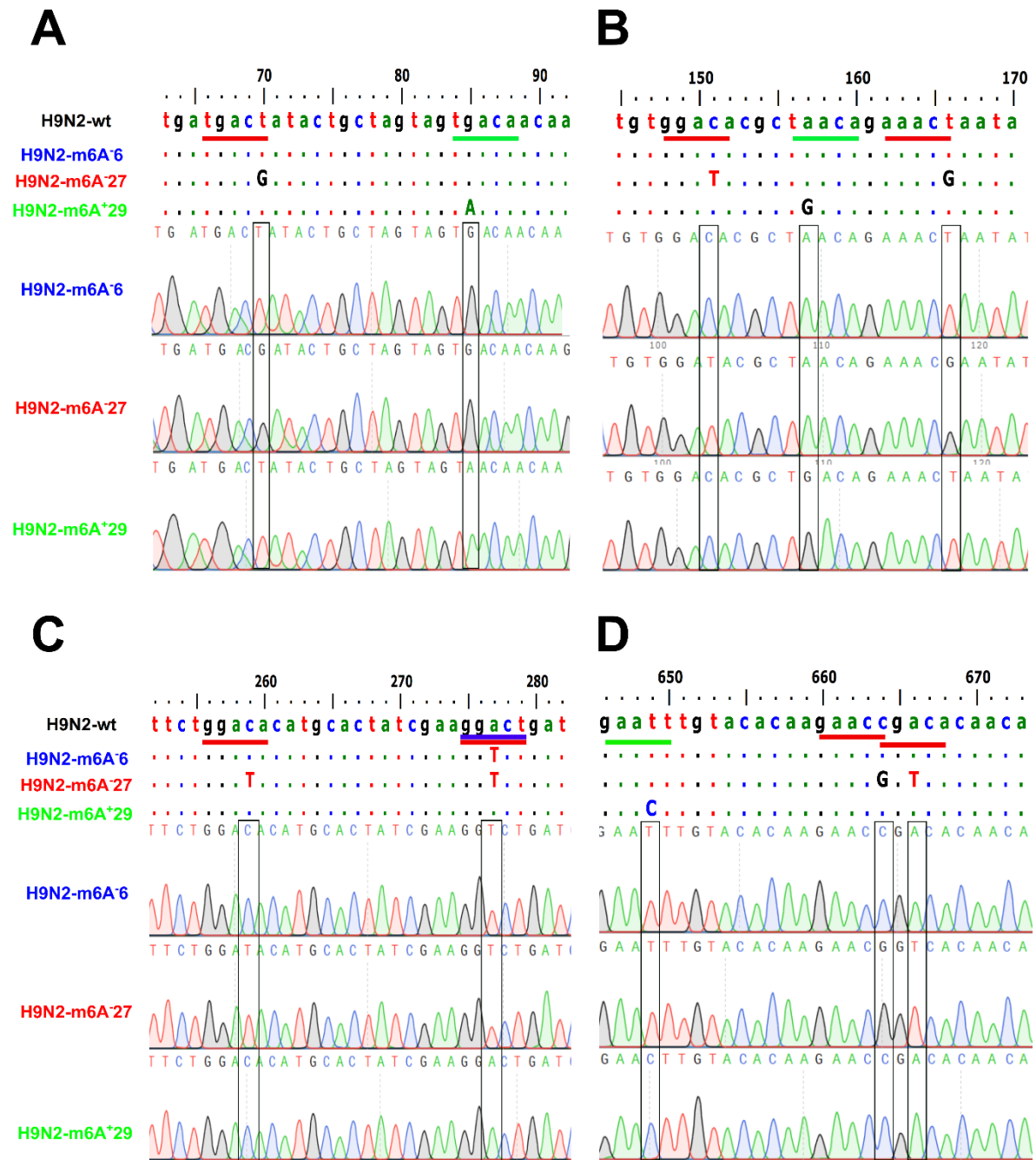
Figure 6.7: Sequence confirmation of three rescued IAV-H9N2 m6A-mutant viruses. **(A-D)** Representative HA plus strand sequences confirming correct rescuing of m6A-mutant of interest. The exact sequence location is presented for all three mutants to demonstrate differences. The identically aligned nucleotides are shown as dots; only the targeted mutations are indicated by coloured letters.

6.2.3. The m6A-mutant viruses are fully stable for at least nine passages

To investigate whether the DRACH sites incorporated or removed from the rescued m6A-mutant viruses affect genomic stability and phenotypic spreading properties, the three m6A-mutant viruses were passaged nine passages in both eggs (twice) and MDCK (once) in each propagation round of three (**Figure 6.8A**). The HA gene from both passages 1 and 9 was sequenced. Interestingly, the three m6A-variants exhibited no mutations in the HA sequences between passages 1 and 9. Sequencing confirmed the m6A modifications **(Figure 6.8B-D)**. Interestingly, m6A⁻27 demonstrated smaller plaque diameters than m6A⁻6 and m6A⁺29 **(Figure 6.6D)**, as demonstrated earlier in the first passage. Overall, the rescued m6A-modified viruses were genetically stable for at least nine passages and preserve the virus propagation and spreading capacity criteria.
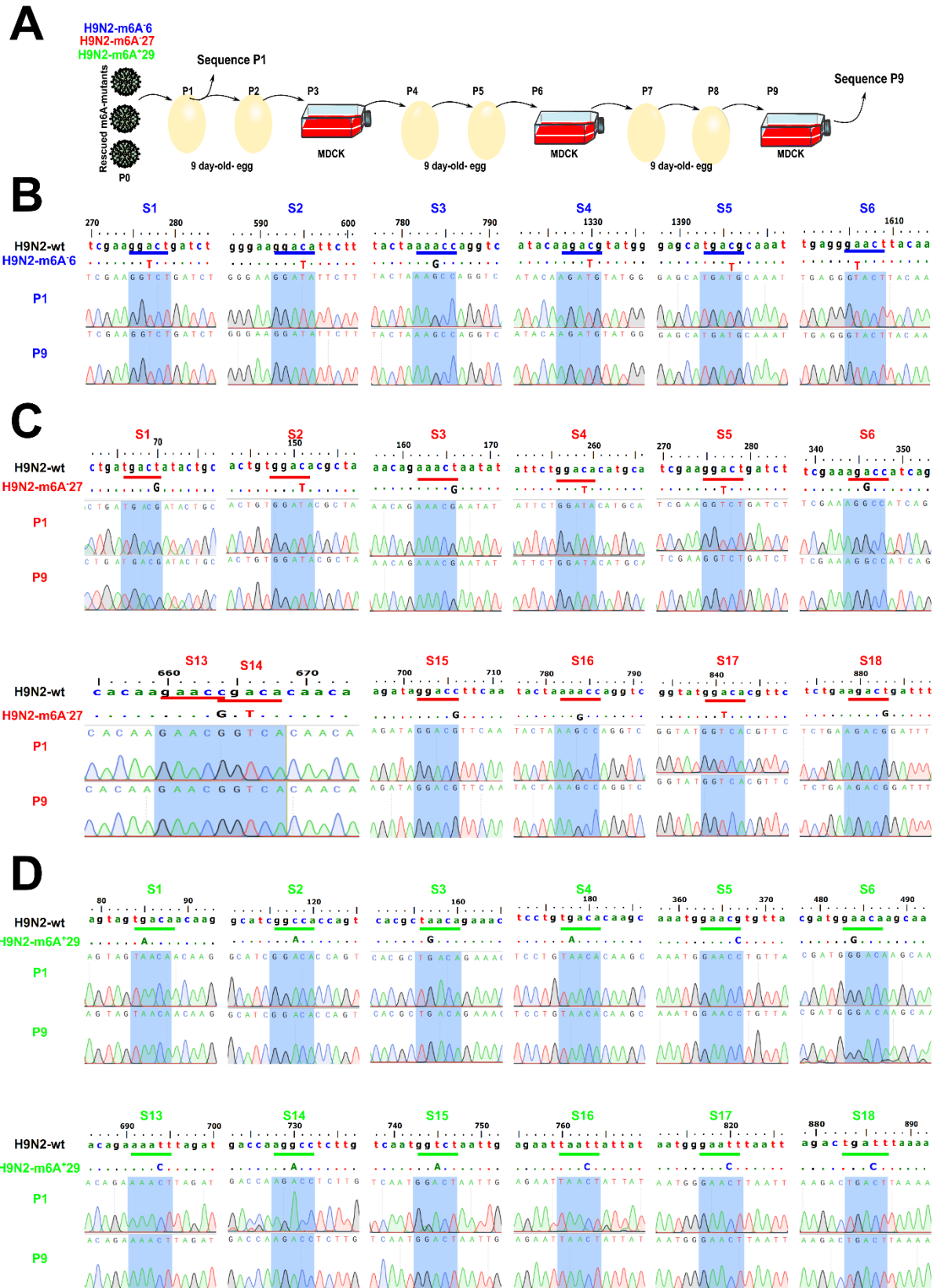
Figure 6.8: The m6A-mutant viruses were genetically stable for at least nine consecutive passages. **(A)** Schematic of the sequence confirmation of rescued viruses after passaging on both eggs and MDCK. **(B)** The six sequence locations confirm a stable m6A$^-$6 mutant for at least nine passages. The exact sequence location is presented in passages 1 (P1) and (P9) to demonstrate no genetic differences. The DRACH sequence is shaded in blue colour. **(C)** A representative of twelve sequence locations confirms a stable m6A$^-$27 mutant virus for at least nine passages. The exact sequence location is demonstrated in P1 and P9 to reveal identity. The DRACH sequence is shaded in blue colour. **(D)** A representative of twelve sequence locations confirms a stable m6A$^+$29 mutant virus for at least nine passages twice in egg and once on MDCK for each round of three. The exact sequence location is presented in P1 and P9 to demonstrate identity. The DRACH sequence is shaded in blue colour.

6.2.4. Disturbing m6A sites of the HA gene of IAV H9N2 selectively inhibit viral replication and gene expression.

After introducing the aforementioned synonymous mutations in the HA gene to disturb DRACH signatures, the impacts of these mutations on virus replication were investigated. DF1 cells were infected with an MOI of 1.0 of each m6A-mutant virus. After 24 h, the progeny viruses were collected for quantification, and virus-infected cells were split into two parts. One part was kept for RNA extraction and the other for viral protein expression. Infecting DF1 cells with the rescued H9N2 UDL-wt served as the control.

Compared to UDL-wt, the viral titres using plaque counts of the m6A$^-$6 mutant were non-significant (p >0.05). In contrast, plaque counts of m6A$^-$27 were significantly reduced (p <0.001); Interestingly, m6A$^+$29, which is designed to carry more m6A sites, was also considerably reduced (p <0.001; **Figure 6.9A**). As previously revealed in propagation experiments, the virus cell-to-cell spread in culture was affected with a significant (p <0.001) ~2-fold reduction in plaque areas of the m6A$^-$27 infected cells when compared to UDL-wt **(Figure 6.9B)**.

Regarding protein analysis, the HA protein expression was markedly reduced in both m6A$^-$27 and m6A$^+$29 but not in the m6A$^-$6. Protein expression clearly showed inhibition of ~40–50% in HA0 in m6A$^-$27 and m6A$^+$29 infected cells. Similar findings were also noticed in HA1 protein expression, as indicated in **Figure 6.9C**.

The relative HA mRNA level was significantly reduced in the m6A$^-$27 and m6A$^+$29 (p <0.001). However, the relative M mRNA level was non-significant among m6A-mutant

viruses compared to UDL-wt (p >0.05), indicating that the modification of m6A levels specifically affected HA viral transcripts **(Figure 6.9D and E)**. Taken together, significant reduction or addition of m6A marks in the HA gene selectively inhibits viral replication and gene expression and reducing m6A marks affects viral spreading capacity.
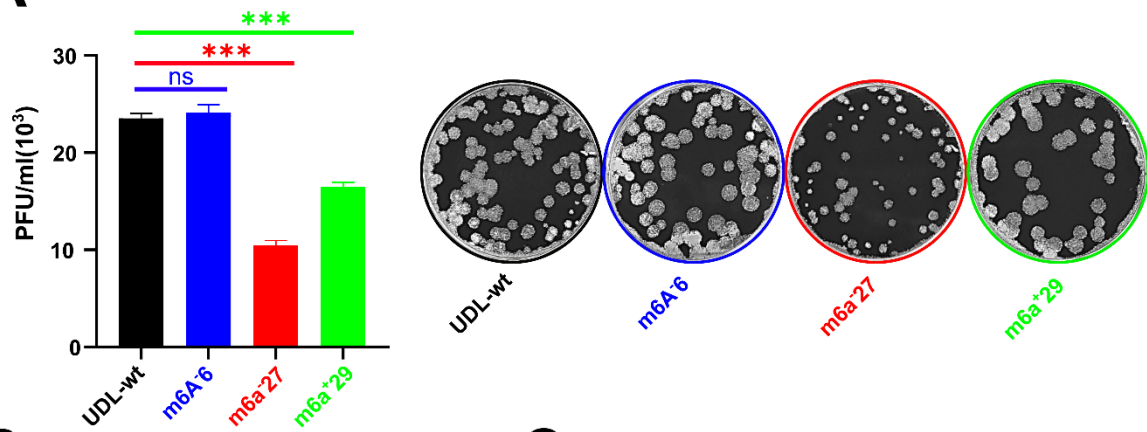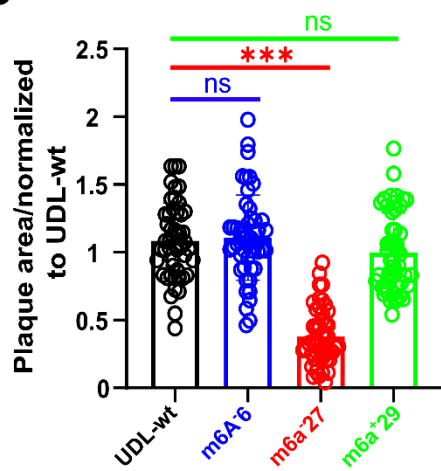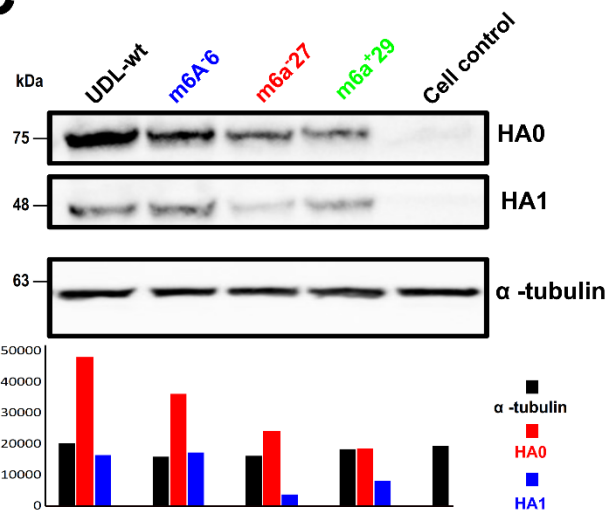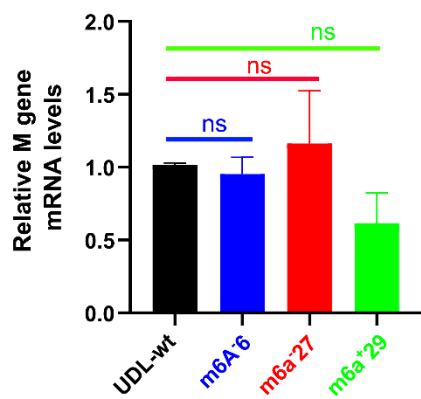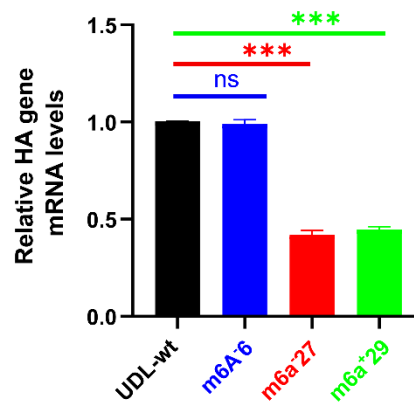
Figure 6.9: Disturbing m6A sites carried on the HA plus-strand of IAV H9N2 selectively inhibit viral replication and gene expression. **(A)** Plaque assay-based quantification of the progeny viral titre s from various m6A-rescued mutant viruses-infected DF1 cells. Viral titre s from IAV UDL-wt were used as a control (all tested viruses infected the DF1 cells at a MOI=1.0). 24 hpi, the released viruses were quantified using plaque assay on MDCK cells. The countable well for each virus is shown. **(B)** Virus spread capacity in culture for each m6A-rescued mutant virus as indicated, compared to control UDL-wt (related to figure 6.9A). Viral spread in culture is expressed as viral plaque area. A total of 50 plaques were measured, representing three independent experiments. Plaque areas were measured from scanned images using ImageJ and calibrated to the area of a 6-well plate. **(C)** Immunoblot analysis of viral protein expression of each rescued virus. DF1 cells were infected with the different m6A-mutant viruses as indicated or UDL-wt (all tested viruses infected the DF1 cells at a MOI=1.0). The HA0 and HA1 protein expression is determined by Western blot at 24 hpi. α-tubulin was used as the loading control. ImageJ was used to quantify the band intensities for HA0, HA1, and α-tubulin, and values are graphed as column bars. A representative Western blot analysis is shown. **(D and E)** RT-qPCR analysis of the expression levels of M/HA mRNA at 24 hpi with the designated mutant viruses on DF1 cells (MOI=1.0). The relative RNA levels were normalized to the chRPL30 reference gene, and the DF1-wt infected with UDL-wt values normalized to 1.0. All these data represent the average of three biological replicates with SD indicated. ns: nonsignificant $p > 0.05$, $*p < 0.05$, $**p < 0.01$, $***p < 0.001$ using one-way ANOVA.

6.2.5. Modifying m6A sites negatively affects vRNA, cRNA, and mRNA species of the HA gene but not the innate immune response

In an effort to investigate whether the m6A-mutated viruses were indeed hypomethylated (i.e., carry low levels of m6A in the released virions), the purified and concentrated virions were lysed for RNA extraction after the preparation of equal endpoints **(Figure 6.10A)**. Then, an equal amount of RNA extracted from 6×10^{10} PFU/sample was cross-linked to a nylon membrane to perform a viral m6A-dot blot assay using anti-m6A antibodies. However, it seems that the extracted quantity or propagated viruses were insufficient to be detected using the designated assay (had low viral sensitivity; **Figure 6.10B)**. Alternatively, another assay was adopted to detect downregulation in viral RNA (i.e., vRNA) of m6A-mutant viruses.

Influenza A viruses carry negative-sense vRNA strands. Once they enter the cells and start the replication cycle, positive single-stranded messenger RNAs (mRNAs) are generated to translate viral proteins. The vRNAs are also exploited to create a positive copy of complementary RNA (cRNA) for further viral replications (Kawakami et al., 2011). To investigate which strand is affected m6A marks were selectively altered on the plus strand of HA. To this aim, the strand-specific primers approach for influenza A viruses described earlier was used (Kawakami et al., 2011). For relative quantification of all HA RNA species in virus-infected cells (i.e., c/m/vRNA levels), the NP segment was used for normalization, which does not undergo splicing. Accordingly, the NP c/m/vRNA levels served as a normalizing control **(Figure 6.10C)**.

Interestingly in vRNA and mRNA levels, the relative HA RNAs were significantly reduced in both m6A$^-$27 (p <0.05) and m6A$^+$29 (p <0.001) compared to the UDL-wt

control, and only cRNA levels were reduced considerably in m6A$^+$29 in comparison to UDL-wt **(Figure 6.10D)**. The m6A$^-$6 RNA levels were non-significant compared with UDL-wt. This finding points to the fact that the vRNA is also downregulated even though only plus strand was disturbed, possibly affected by reduced m6A levels.

Next, whether the enhanced innate immune response negatively affects virus replication kinetics in the m6A-mutant viruses was investigated. To this aim, key innate immune genes expression was quantified for comparison among m6A-mutant viruses and UDL-wt, including chPKR, chMDA, chSTING, and chIFNα. Notably, none of the investigated genes were significantly regulated (p >0.05) **(Figure 6.11)**. It seems that disturbing m6A marks on viral HA affect all RNA species; however, the innate immune response remained unaffected.

A

10⁻⁸

UDL-wt   m6A⁻6   m6a27   m6a⁺29

B

6*10¹⁰PFU

UDL-wt   m6A⁻6   m6a27   m6a⁺29

Load

m6A

MB

C

Influenza A virus

NP
HA

HA / NP of UDL

vRNA
3'   5'

cRNA
5'   3'

mRNA
5'   AAAAA 3'

RT   qPCR

D

vRNA

Relative HA mRNA level

ns   *   ***

UDL-wt   m6A⁻6   m6a27   m6a⁺29

cRNA

Relative HA mRNA level

ns   ns   ***

UDL-wt   m6A⁻6   m6a27   m6a⁺29

mRNA

Relative HA mRNA level

ns   **   ***

UDL-wt   m6A⁻6   m6a27   m6a⁺29
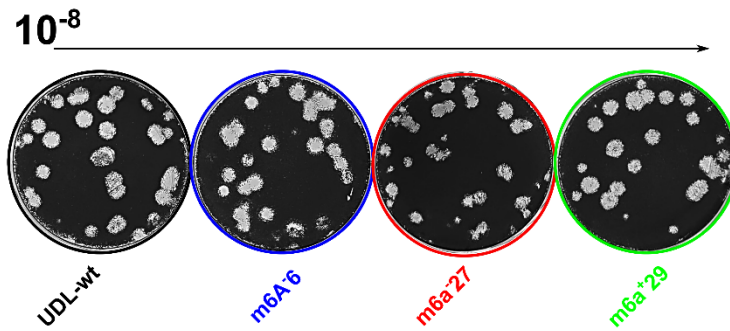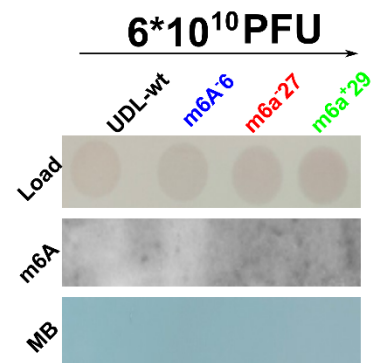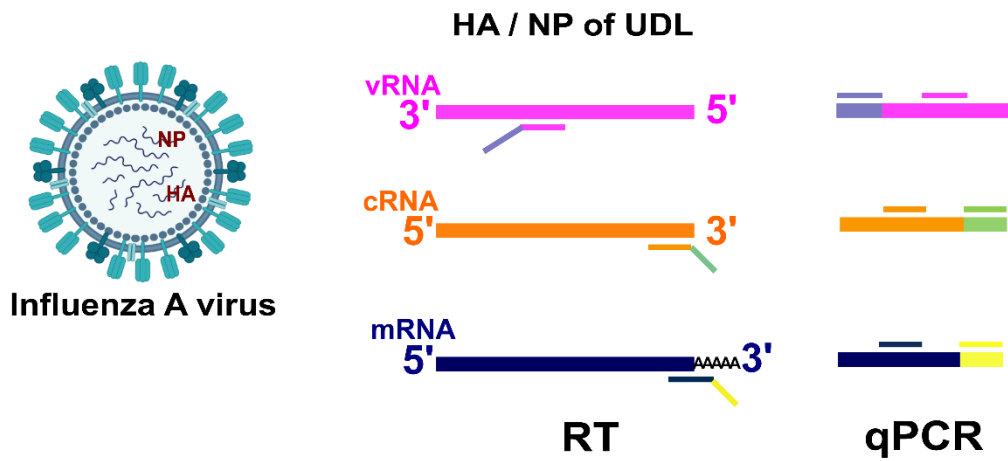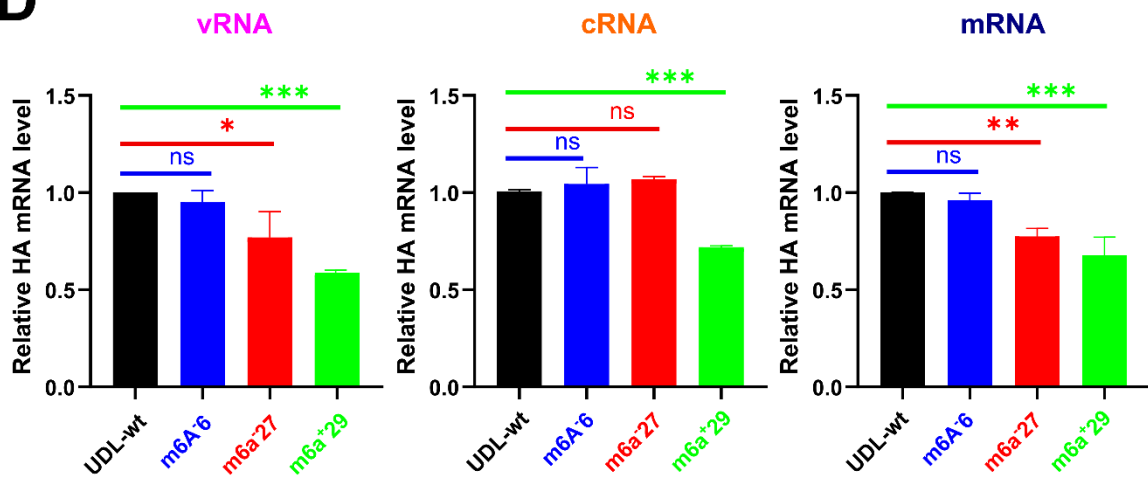
Figure 6.10: Disturbing m6A sites carried on the HA plus-strand of IAV H9N2 negatively affect vRNA, cRNA, and mRNA HA transcripts in virus-infected cells. **(A)** Plaque assay-based quantification confirms the equal endpoint titre after purification and concentration. The viral m6A-dot blot assay was used on the extracted released viral RNA (for detecting m6A levels on total vRNA). The 10^{-8} dilution is indicated per each virus. **(B)** A representative trial of viral m6A-dot blot assay. A total of 6×10^{10} PFU of each virus was used to extract viral RNA. The RNA dots on the nylon membrane are shown. The same membrane was probed with anti-m6A antibodies and stained with methylene blue (MB). **(C)** Schematic of experimental design for relative quantification of strand-specific RNA of IAV. **(D)** RT-qPCR analysis to determine the levels of expression of vRNA, mRNA, and cRNA at 24 hpi with the designated mutant viruses on DF1 cells (MOI=1.0). The H9N2 UDL-wt served as a control virus, and NP RNA levels served as a control for normalization. All these data represent the average of three biological replicates with SD indicated. ns: nonsignificant $p > 0.05$, $*p < 0.05$, $**p < 0.01$, $***p < 0.001$ using one-way ANOVA.
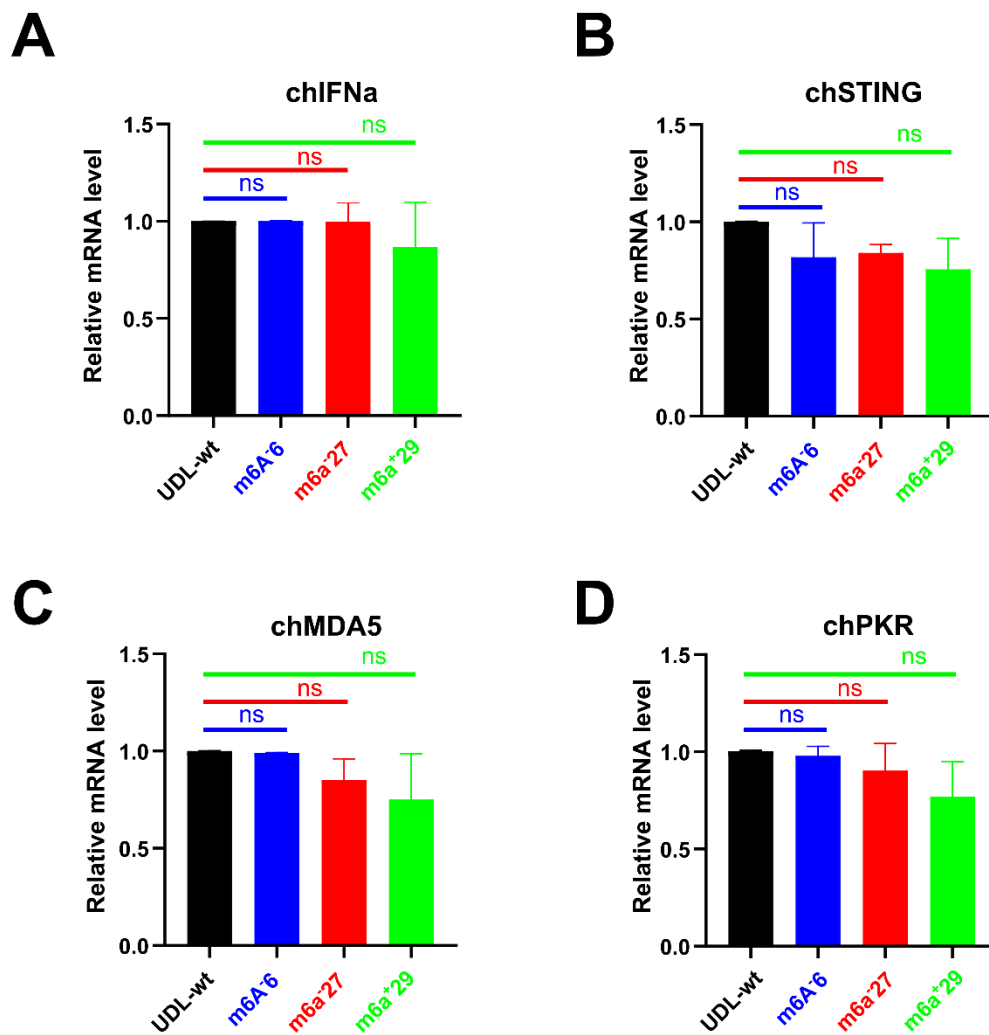
Figure 6.11: Disturbing m6A sites do not affect cellular innate immune response. **(A-D)** RT-qPCR analysis to determine the expression levels of innate immune genes at 24 hpi with the designated mutant viruses on DF1 cells (MOI=1.0). (A-D) The relative RNA levels were normalized to the chRPL30 housekeeping gene, and the DF1-wt infected with UDL-wt values normalized to 1.0. All these data represent the average of three biological replicates with SD indicated. ns: non-significant $p > 0.05$ using one-way ANOVA.

6.3. Chapter Discussion

The m6A mark on influenza viruses was identified five decades ago. Conventional biochemical analysis showed that influenza mRNA incorporates a total of 24 m6A marks across the genome (Krug et al., 1976). Later, reports clarified that the m6A marks have an unequal distribution among various transcripts (Narayan et al., 1987). However, the biological function of m6A marks in virus replication, and gene expression remains largely unknown. The recent PA-m6A-seq analysis confirmed the earlier findings that H1N1 PR8 is m6A-modified and enhanced virus replication and gene expression (Courtney et al., 2017). It is essential to note that not all viruses exhibit the positive regulatory role of the m6A. It has been shown that m6A has an inhibitory effect on some of the RNA viruses, including hepatitis C virus (HCV) and ZIKA virus (ZKV) (Gokhale et al., 2016; Lichinchi et al., 2016b). It remains to be determined why RNA viruses, which can mutate rapidly, could keep post-transcriptional marks if they are inhibitory *in cis*.

To demonstrate the direct role of m6A in regulating a given virus, rescuing mutant viruses is a tool to test the impact on virus replication and gene expression (Courtney et al., 2017; Tsai et al., 2018; Xue et al., 2019; Lu et al., 2020). It has been reported that human influenza m6A-deficient mutant viruses H1N1 carrying lower m6A by abrogating twelve RAC sites corresponding to 8 m6A peaks on HA mRNA could negatively affect virus replication (Courtney et al., 2017), indicating this technique is beneficial for studying m6A on influenza viruses.

m6A-deficient viruses according to the topology of the m6A sites mapped across the H9N2 UDL model were generated. The m6A marks are usually installed at specific

sites determined as the DRACH sequences (Linder et al., 2015; Bayoumi and Munir, 2021a). Therefore, performing ubiquitous mutations to remove any possible DRACH sites coincidentally with the mapped m6A peaks without affecting the amino acid codes would be a valid strategy. Through this manoeuvre, the potential m6A marks would be minimal. In this regard, the m6A$^-$27 mutant virus was recovered. Additionally, another variant was rescued, the m6A$^-$6, to carry relatively few mutated DRACH sites (i.e., -6 sites, compared with m6A$^-$27) and to be a control of rescuing the m6A-mutant avian influenza virus. In contrast, another m6A-mutant carrying additional DRACH sites (m6A$^+$29) was generated that could facilitate the incorporation of extra m6A marks.

The three viruses were successfully rescued, indicating that the introduced point mutations were not detrimental to the *de novo* synthesis of m6A-mutant viruses. Based on our knowledge, m6A$^-$27 and m6A$^+$29 mutant viruses are the highest number of mutations incorporated for RG-based generation of m6A-deficient viruses (Courtney et al., 2017; Tsai et al., 2018; Xue et al., 2019; Lu et al., 2020). This is why m6A$^-$6 mutant virus was generated to act as a control for rescuing virus. The absence of amino acid changes among rescued viruses was the possible cause of the successful virus recovery.

Interestingly, viral replicative fitness and genomic stability were not affected by either adding (m6A$^+$29) or abrogating (m6A$^-$27) m6A marks through consequent passaging. No mutations were evident even after nine passages in both embryonated eggs and cultured cells. Preserving the amino acid codes of HA among generated mutants is the leading cause of this stability. Furthermore, maintaining cell-to-cell spread by mutant viruses in the culture (expressed as a plaque area compared to the UDL-wt control) indicates that all the modifications are not lethal or detrimental in the long run.

However, this requires the propagation of the viruses for additional passages and sequence verifications. Notably, reduced plaque sizes were noticed before and after passaging the m6A$^-$27 mutant viruses. These findings benefit the rationale of influenza vaccine production (Hegde, 2015). Studies delineating the molecular mechanisms conferring the reduced cell-to-cell spread in m6A-27 were not performed.

The six mutations introduced to the DRACH sites in the m6A-6 mutant were insufficient to show a striking difference in the virus replication and protein expression. It is possible that these individually mutated sites are not actual m6A sites under the identified m6A peak, or the difference was unnoticeable compared to the wild-type virus. It is also important to mention that the introduction of silent mutations in viral mRNA transcripts does not necessarily prevent m6A addition in SV40. Silent mutations of the 20 DRACH consensus sequences coincided with 11 m6A-mapped peaks in late transcripts performed in SV40. Three peaks were entirely lost in the mutant virus, and the rest had either reduced m6A levels or were unaffected (Tsai et al., 2018). However, the m6A$^-$6 was a reasonable control for rescuing the viruses with more mutations.

Removing 12 RAC sites of the HA segment of H1N1-PR8 has been reported to be associated with reduced virus replication and HA expression (Courtney et al., 2017). Similar findings were noticed in the m6A$^-$27 mutant; however, this mutant was attenuated to exhibit additional reduced viral spread capacity (expressed as smaller plaque areas, normalized with control). These findings confirmed that removing DRACH sites coincided with the mapped m6A sites, functionally resulting in attenuated viral replication. Furthermore, the results suggest that m6A marks positively impacted H9N2-UDL virus replication and protein expression. Interestingly, this finding also

suggests that this editing event is virus-specific, as reported for m6A conservation among IAVs, as indicated in **Chapter 3** and mentioned in (Bayoumi and Munir, 2021a).

Based on the reduction of viral replication and gene expression in the hypomethylated virus m6A$^-$27, the generation of m6A-mutant viruses with higher DRACH sites potentially reflects into higher m6A sites. This way, significantly high viral titres could be achieved in cell culture for massive vaccine production instead of embryonated eggs (Hegde, 2015). However, it appears that enforcing viruses to incorporate more m6A modification would be detrimental. The rescued m6A$^+$29 mutant had low virus replication and protein expression. Although viral cell-to-cell spread in the culture was not affected.

Despite maintaining the original DRACH sequences, the generated extra DRACHs reduced the replication kinetics of the m6A$^+$29 mutant virus. Possibly the excessively generated DRACHs affected RNA stability negatively; however, this notion warrants further research by including fewer extra DRACHs (i.e., not +29). Additionally, these findings point out that m6A methyltransferases cannot easily be camouflaged by the number of DRACH sites in given transcripts, as indicated earlier (Wei and Moss, 1977; Zou et al., 2016).

Due to the absence of specific antibodies against various viral H9N2 proteins, the relative RNA levels demonstrated that the viral replication and protein expression selectively affected the disturbed segment (i.e., HA, but not the M gene). This result was also noticed in tethering dCas13b-chALKBH5 to deliberately demethylate HA in virus-infected cells. Notably, this finding was similar to what has been verified in the H1N1 model (Courtney et al., 2017). In contrast, RSV-mutants exhibited alteration of

other non-mutated transcripts (Xue et al., 2019). Possibly the difference in replication strategy and the segmented nature of the IAV genome are responsible for this notion.

To test the direct role of disturbing m6A sites on the HA plus strand on the progeny-released virus (HA negative strand). The rescued viruses were propagated in embryonated eggs, and the harvested allantoic fluids were clarified and concentrated for generating relatively high virus titres (6×10^{10} PFU/mutant virus). However, viral m6A-dot blot assay on the extracted vRNAs was not productive. It seems either the tested titre or the assay used was insufficient to confirm that m6A-mutant viruses are indeed hypomethylated. However, this assay would be inaccurate as the m6A is distributed in other segments, and determining relative expression would be challenging. no literature described the viral m6A detection using m6A dot blot (Krug et al., 1976; Narayan et al., 1987; Courtney et al., 2017).

To test this hypothesis, an alternative approach was adopted. Primers was designed that quantify various levels of RNA species (i.e., v/c/mRNA) as described earlier (Kawakami et al., 2011). Relative quantification was performed using the NP RNAs as normalizing controls because no modifications were introduced in the NP gene. Additionally, the NP is not known to be spliced (M and NS segments are well-known to be spliced in IAVs). Strand-specific quantifications indicated that (+) mRNA and (-) vRNA strands were significantly reduced in both m6A$^-$27 and m6A$^+$29 mutants. This finding suggests that disturbing plus strand reflects on other RNA species, as verified earlier (Xue et al., 2019) and points to the mechanism by which the m6A-mutant viruses were downregulated. Downregulating vRNA/mRNA synthesis in the virus-infected cells is reflected in the reduced viral titre/protein expression of the progeny viruses,

respectively. It may also suggest that the m6A$^-$27 and m6A$^+$29 could be hypomethylated (expressed as reduced vRNA synthesis potentially due to low m6A levels *in cis*).

Although (+) cRNA strand synthesis was not significantly reduced in the m6A-mutants except m6A$^+$29, the cRNA, in general, is relatively low in viral replication kinetics in influenza viruses with around 1–2 logs lower in RNA copy number/cells compared to vRNA and mRNA (Kawakami et al., 2011). Compared to the UDL-wt, downregulation of vRNA and mRNA in m6A$^-$27 and m6A$^+$29, but not in the m6A$^-$6, confirmed reduced viral replication (low vRNA) and inhibited viral HA expression (low mRNA) in those viruses.

An enhanced immune response could also be incriminated in the mechanism of the downregulation of viral replication in m6A-deficient viruses (i.e., m6A$^-$27 and m6A$^+$29); however, this was not observed when testing the expression of chicken innate immune genes. This finding was also reported in the m6A-deficient H1N1-PR8 (Courtney et al., 2017). The packaged vRNAs in their nucleocapsids (NP and polymerase complex) possibly provide partial protection against RNA sensors (Weber et al., 2015). It remains possible that exposing cells to unpackaged m6A-deficient vRNAs might reveal a different result.

Although the YTHDF2 findings in regulating IAV-PR8 in humans and chYTHDF2 findings in regulating IAV-UDL in chickens differed, a positive impact of m6A in enhancing influenza A virus replication and gene expression was in an agreement (Courtney et al., 2017). This outcome indicates no discrepancies in the m6A research, and the variation usually comes from investigated cell lines/host species. Additionally, m6A marks are virus-specific, but m6A machinery is host specific.

The previous literature on the viral m6A methylome of the influenza virus indicates that the m6A could regulate virus replication without affecting protein expression or RNA splicing (Courtney et al., 2017). Therefore, compiling all findings together could point out that the reduced replication in both m6A-deficient viruses had reduced various levels of RNA species synthesis even in the mutant incorporated with more DRACHs sites (i.e., m6A^{+}29). This finding is plausible due to the disturbance of viral RNA stability. Enforcing RNA to accommodate higher or lower m6A marks has a detrimental effect on virus replication expressed by selectively lower RNA synthesis and protein expression of the affected segment, supporting this hypothesis. Interestingly, m6A has been reported to destabilize RNAs and affect their turnover in the cytoplasm (Ke et al., 2017).

Overall, the direct effect of m6A on H9N2-UDL replication was demonstrated and provided several mechanistic insights underlining the compromised growth in the m6A-deficient viruses. However, the data presented so far do not comprehensively confirm the molecular determinants behind the reduced replication in m6A-deficient viruses, especially m6A^{+}29, which need further work.

Chapter 7

Transcriptome-wide Host and Viral

m6A Methylome

and

chALKHB5 Interactome: Initial

Observations and Future Prospects

7.1. Chapter Introduction

7.1.1. Methods of detecting m6A modifications in transcriptome-wide format

The RNA modifications, including the m6A, play a significant role in post-transcriptional regulation of host gene expression in eukaryotes. Today, at least 150 RNA modifications have been identified across the whole cellular transcriptome (Roundtree et al., 2017). However, the biological functions of these chemical modifications cannot be easily investigated without identifying their topology in transcriptome-wide formats. Moreover, determining the relative abundance under certain stimuli could be amenable (Zhao et al., 2016; Helm and Motorin, 2017; Roundtree et al., 2017).

7.1.1.1. Reverse transcriptase (RT)-dependent approaches for detection of RNA modifications

Owing to the variations in the chemical structure of modified bases on RNA that could be incompatible with the Watson-Crick base pairing model, the modified bases have different signatures when treated with RT-enzymes. When confronted with RT, the m1A lead to either mutation on the modified site or induce abortive elongation. Hence coverage drop in the sequence reads, making detection easier (RT-arrest model). Whereas the majority of the modifications that are not in the interface of the Watson-Crick base pairing model behave silently, including m6A, m5C, and pseudouridine (Ψ) (RT-silent models; **Figure 7.1A**) (Ryvkin et al., 2013; Helm and Motorin, 2017).

To overcome the RT-silent mode of some RNA modifications, several groups utilized chemical modifications to enhance the RT signature to achieve a substantial coverage

drop or, more interestingly, to change the desired modifications drastically to exhibit RT-arrest mode.

Pseudouridine (Ψ) is a salient example. Upon treating the Ψ containing RNA with N-cyclohexyl-N´-(2-morpholinoethyl) carbodiimide methyl- p-toluenesulfonate (CMCT), leads to change into RT-arrest mode, making detection by the high-throughput sequencing more accessible (Schwartz et al., 2014a). The m5C was harnessed in the same way when treated with bisulfite treatments **(Figure 7.1B)** (Schaefer, 2015).
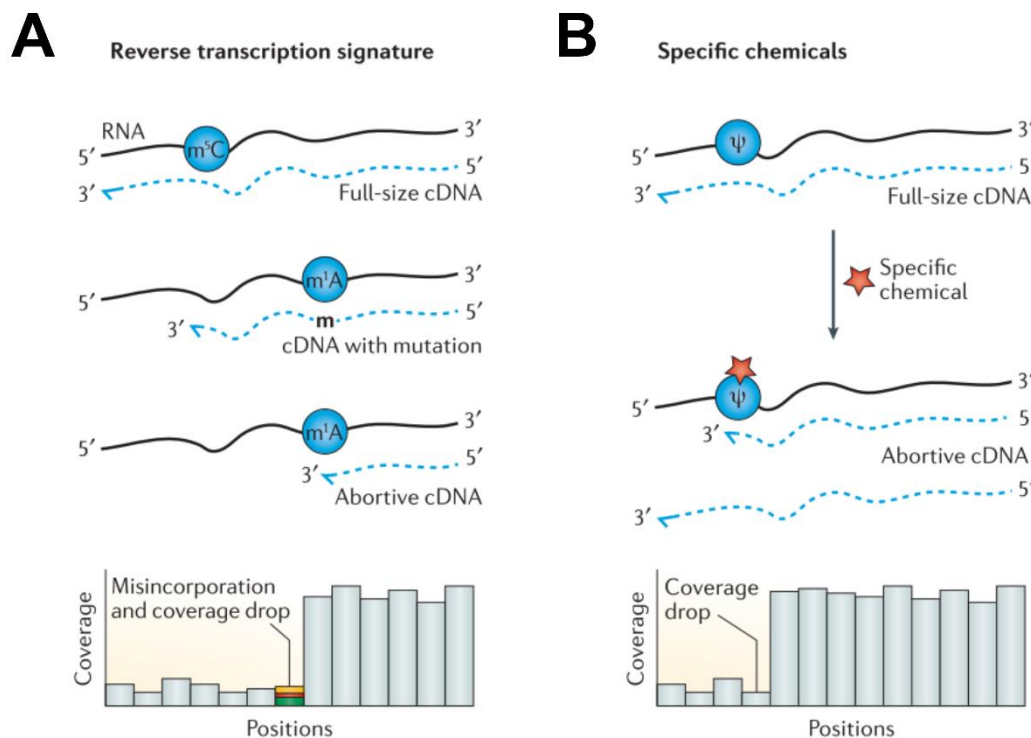
Figure 7.1: Detection of some RNA-modified nucleotide using reverse transcription (RT)-dependent techniques. **(A)** Schematic of different signature modes of chemical modifications in response to RT. Some are silent modes (m5C), and others respond by either mutations or abortive elongation of cDNA (m1A). **(B)** Induction of abortive

cDNA elongation using specific chemical treatment (pseudouridine, Ψ). The figure is modified from a previous report (Helm and Motorin, 2017).

7.1.1.2. Antibody-dependent approaches for m6A detection

The m6A marks, as noted above, do not behave like the RT-arrest mode, as the m6A is not located in the Watson-Crick interface model. This finding made detecting m6A marks lag behind other RNA modifications until 2012. The mRNA usually constitutes less than 10% of the total RNA; accordingly, the m6A-modified mRNA should be clarified from the heavily contaminated methylated RNA species (i.e., m6A is also noted in the non-coding RNA). Therefore, enrichment to the poly(A) species is a prerequisite for accurately identifying methylated mRNA. Poly(A) RNA enrichment, along with the presence of highly purified anti-m6A antibodies, facilitated the mapping of m6A-modification in transcriptome-wide format **(Figure 7.2A)** (Dominissini et al., 2012; Meyer et al., 2012).

The approach was later named m6A-seq or methylated RNA immunoprecipitation-sequencing (MeRIP-seq). In this approach, the purified mRNA is further fragmented to ~100 nucleotides before exposing to the anti-m6A antibodies to only enrich the methylated fragments. Later, through the same approach, with various modification-specific antibodies, different mRNA methylations were also identified, including m1A (Dominissini et al., 2016; Li et al., 2016a) and m5C (Mishima et al., 2015).

Notably, two issues should be considered in this approach. The first is the purity of used anti-m6A antibodies. It has been reported that 30-60% of m6A peaks are reproducible

using various anti-m6A antibodies with different purifications, even within the same cell line (Linder et al., 2015; Helm and Motorin, 2017; Baquero-Perez et al., 2021). The second is the m6A detection window. The mRNA fragments are around 100 nucleotides, making accurate identification of the methylated adenosines challenging. Generally, the identified enrichment is named as m6A peaks/peak clusters, not m6A sites, and m6A peaks possibly have more than one m6A site underneath. The DRACH (the predominant consensus site for m6A deposition) motif is highly encoded and distributed in both cellular and viral transcripts (Linder et al., 2015; Bayoumi and Munir, 2021a).

7.1.1.3. Enhancement of m6A modifications detection using UV-cross linking approaches to cognate nucleotides

In the prototype MeRIP-seq, anti-m6A antibodies are bound to methylated adenosine residues non-covalently, which makes stringent washing steps detrimental. Therefore, UV-crosslinking with a specified wavelength makes covalent interactions with nearby nucleotides to the target methylated adenosines. This approach would narrow the window of m6A peaks.

In the photo-crosslinking-assisted m6A sequencing (PA-m6A-seq), before RNA-immunoprecipitation (MeRIP), the cells are treated with 4-thiouridine (s^4U). During MeRIP, the anti-m6A antibody binds non-covalently to methylated adenosines, and through UV-crosslinking (+UV365), the antibody binds covalently to the nearby s^4U. After protein digestion, the s^4U (read as C in the RT step), in turn, leaves the RT signature as described earlier. Through sequencing, the methylated bases can be

predicted in nearby T-to-C mutations in a shorter window (20–30 nucleotides; **Figure 7.2B**) (Chen et al., 2015; Courtney et al., 2017).

Recently, a shorter window has been verified using the same approach to achieve a near single nucleotide resolution (Linder et al., 2015). The MeRIP assay can be combined with individual nucleotide resolution crosslinking and immunoprecipitation (iCLIP) results into m6A-iCLIP (miCLIP). The anti-m6A antibody binds non-covalently to target methylated adenosines and a covalently nearby cytidine (C). However, this approach uses a shorter wavelength (+UV254) and specific and highly purified anti-m6A antibodies. After protein digestion, the short fragments that remain attached covalently to the RNA lead to either misincorporation errors (usually C-to-T transition) or cDNA truncations **(Figure 7.2C)** (Linder et al., 2015).
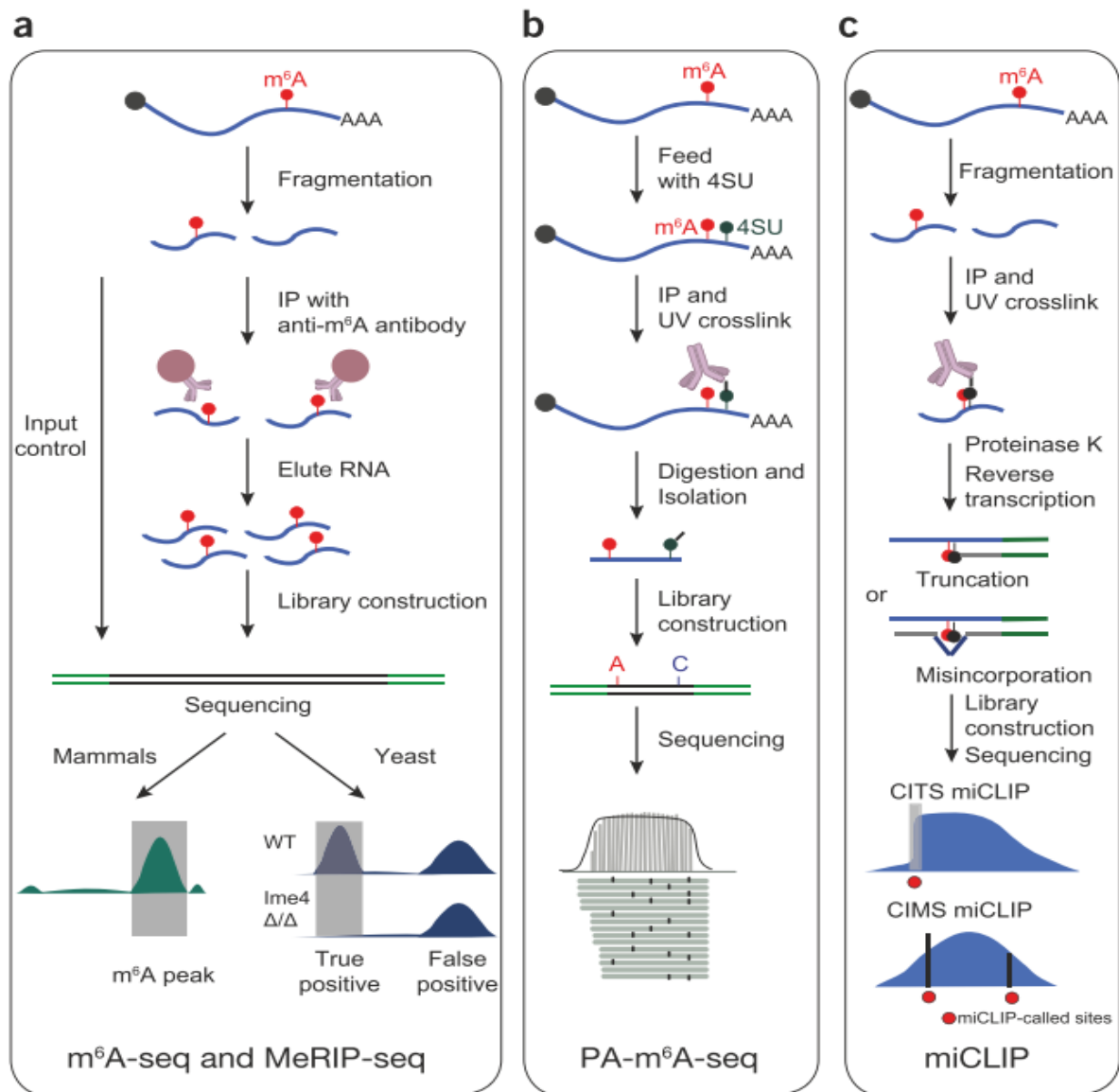
Figure 7.2: Schematics of epitranscriptome-wide m6A sequencing methods. **(a)** MeRIP-seq dependent on m6A-RNA enrichment using specific antibodies. **(b)** PA-m6A-seq combines both MeRIP and UV-crosslinking with the nearby 4ˢU. **(c)** miCLIP-seq combines both MeRIP and UV-crosslinking with the nearby cytidine. The figure is modified from a previous report (Li et al., 2016b).

7.1.1.4. Novel antibody-independent approaches for m6A detection

Although the above-described methods of m6A detection techniques are the most common in the last ten years, a massive surge in m6A-sequencing techniques has recently been noticed in the last 2–3 years. Differing from the antibody enrichment methods, the meCLICK-seq utilizes click chemistry labelling to m6A-modified bases by small molecules. That induced further degradation downstream to modified bases and compared with non-modified samples. Even though meCLICK-seq offers a good idea about the m6A relative abundance in epitranscriptome-wide format, it does not provide an idea about its topology in the genome (Mikutis et al., 2020).

To overcome this drawback, the m6A-related machinery has been used to easily target m6A bases to drive stable modification to support further detection. DART-seq (deamination adjacent to RNA modification targets) was used to label the (C) adjacent to m6A. The cytidine deaminase (APOBEC1) fusion to the m6A-binding YTH domain to induce C-to-U mutations can be read easily by the standard RNA-seq methods (Meyer, 2019). A similar approach has also been applied where FTO was used instead, termed the FTO-assisted chemical labelling method (the m6A-SEAL-seq). FTO induces stable chemical modification to the m6A bases to be detected easily in deep sequencing (Wang et al., 2020).

Similar to the transcriptomic-wide format, others also utilized nanopore sequencing for epitranscriptome detection. In this method, the proteins with nanopores are embedded in the membrane. The RNA moves towards nanopores by adjusted ionic currents. Therefore, based on the chemical property of the passing nucleotides, it induces alteration in the intensity that differs according to the modified bases. Ultimately, these

provide good information on the specificity of the base in long read sequencing format. This approach benefited epitranscriptomic profiling of SARS-CoV-2 and other viruses (Viehweger et al., 2019; Kim et al., 2020b; Price et al., 2020; Xu and Seki, 2020).

7.1.2. Affinity purification coupled with mass spectrometry (AP-MS) for elucidating protein-protein interactions

Proteins are the higher-order structural molecules responsible for participating in numerous protein-protein interactions (PPI) intracellularly. PPIs are crucial for elucidating various aspects of the cell cycle, including transcription and translation. It has been estimated that the human proteome is involved in ~650,000 PPI (interaction process, interactome). As anticipated, this large number in human interactome is higher than what has been reported in *Drosophila melanogaster* and *Caenorhabditis elegans* (Stumpf et al., 2008).

Several approaches have been described and applied to elucidate PPIs. For example, is the yeast two-hybrid assay, a prototype assay that involves mainly two proteins (or parts of proteins), bait and prey. If they interact and assemble, they exert successful enzymatic activity or gene expression, hence validating their interaction (Titeca et al., 2019).

In contrast, AP-MS is the commonly used high-throughput method to identify PPIs (and the interest here in the study). In this approach, the precleared lysates are incubated with antibody-conjugated beads. The antibody is usually monoclonal-specific to the bait protein. This step is followed by washing to minimize the non-specific interactors.

Then, the protein-protein complexes are eluted from the antibody-conjugated beads. Ultimately, the complex is identified by MS **(Figure 7.3A)**. Using various baits-pray from the verified and previously identified complex, it could infer specific protein networks in a given cellular process (Low et al., 2021).

Importantly, in some instances, endogenous bait proteins of interest lack the monoclonal antibodies to purify prey or investigate new species. Therefore, tagged versions of the protein are used to overcome this issue, which is introduced transiently or stably to cells of interest **(Figure 7.3B)**. The most common tags are FLAG, myc, strep, and His; however, a long list is reported elsewhere (Vandemoortele et al., 2019). It is essential to mention that the higher sensitivity of MS is associated with lists of non-specific proteins, as one of the significant challenges in the approach. Accordingly, empty controls are essential to eliminate the non-specific backgrounds. Additionally, using highly purified antibodies, stringent washing steps, and more than one tag in the baits could help to minimize the false positive interacting proteins.

Vis-à-vis in virological fields, AP-MS benefited SARS-CoV-2 research in the first few months after the emergence of COVID-19. Tagged viral proteins (strep-tag) were used to purify human interactors from HEK-293T cell lysates. More than 300 bona fide interactors have been verified for further drug repurposing. In a follow-up approach, other tagged viral baits from SARS-CoV-1 and MERS-CoV were used to conclude the common interactors to develop pan-corona therapeutics and establish protein networks for further understanding disease mechanisms (Gordon et al., 2020a, 2020b).

Currently, there are other variants of MS, including proximity-based labelling coupled to mass spectrometry (PDB-MS), cross-linking mass spectrometry (XL-MS), and

co-Fractionation coupled to mass spectrometry (coFrac-MS) which are not essential to describe in this study and reviewed elsewhere (Titeca et al., 2019; Low et al., 2021).
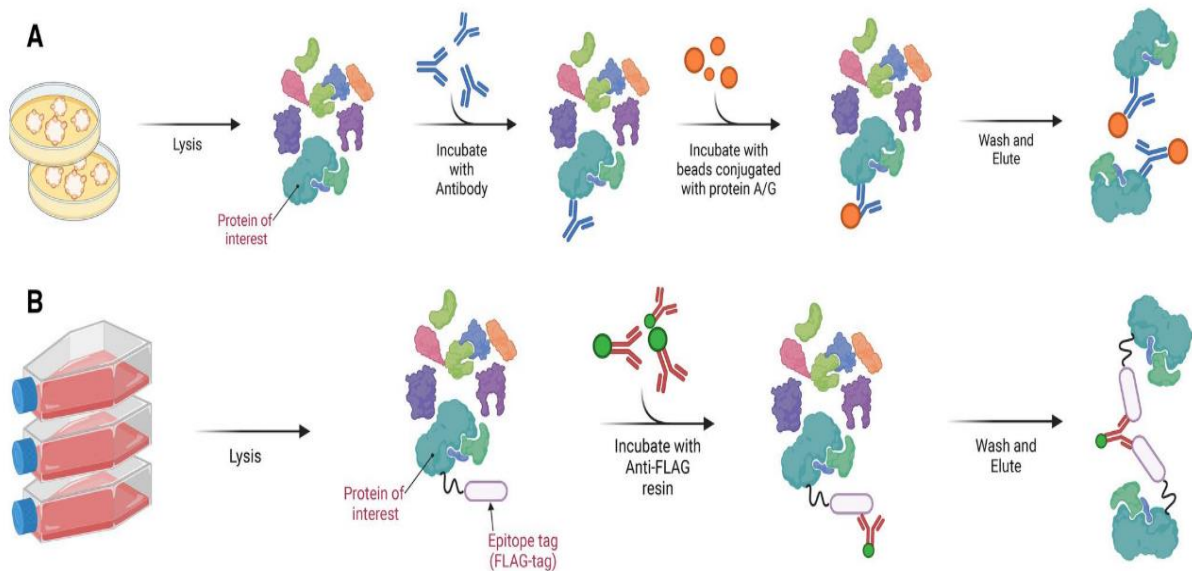
Figure 7.3: Schematics of affinity purification coupled with mass spectrometry (AP-MS). **(A)** The cell lysate containing the bait protein of interest is incubated with monoclonal specific antibodies, purified with beads, and subjected to MS analysis. **(B)** The cell lysate is incubated with expressed tagged bait protein and purified using the anti-epitope tag antibodies (FLAG-tagged version is shown). The purified complex is subjected to MS analysis. The figure is adapted from a previous report (Low et al., 2021).

7.1.3. Chapter Aims

The m6A methylation state can be upregulated upon stimulation with various viruses, including SARS-CoV-2 and HCV (Gokhale et al., 2020; Liu et al., 2021). The aim in this chapter was to determine the impact of influenza virus replication on chicken m6A methylome and mapping host and viral m6A marks across the transcriptome of H9N2 UDL-infected chicken cells to resolve the cellular interactome using chALKBH5 as bait protein in uninfected and infected cell models. These data would provide a piece of information that could be exploited later for a better understanding of the mechanism of influenza virus replication and for developing antiviral therapeutics. Ultimately, the aim is to determine whether the chALKBH5 is potent against influenza viruses or other viruses that have different replication strategies, as follows:

1. Determine the impact of influenza virus replication on cellular m6A methylome.

2. Map the m6A locations across the chicken transcriptome in H9N2 virus-infected cells using MeRIP-seq data to identify specific-cellular methylation states.

3. Map the m6A peaks across the transcriptome of H9N2.

4. Map the chALKBH5 cellular interactome in the presence of virus infection.

5. Demonstrate the antiviral potential of chALKBH5 against other viruses.

7.2. Chapter Results

7.2.1. Influenza A viruses enhance cellular m6A methylome

DF1 cells were stimulated with two IAVs (H9N2 or H1N1, MOI=1) for 24 hpi, followed by staining the cells with anti-m6A antibodies. Using confocal microscopy and maintaining the imaging parameters, cells stimulated with IAVs exhibited higher m6A signals than unstimulated cells. Furthermore, staining cells with anti-NP antibodies against H9N2-UDL and H1N1-PR8 strains also demonstrated high m6A expression, primarily from virus-infected cells **(Figure 7.4A)**.

To relatively quantify the m6A levels in stimulated and unstimulated cells, the m6A-dot blot assay was performed. Equal amounts of RNA were cross-linked and probed with anti-m6A antibodies. The intensity of the m6A signals was compared between infected and uninfected cells. Similar to immunofluorescence, RNA from cells stimulated with IAVs demonstrated a significant increase in m6A level using various RNA quantities, indicating that virus-infected cells are associated with enhanced m6A levels **(Figure 7.4B)**.

To determine the impact of influenza virus infection on the specific cellular transcript methylation states, m6A-seq (MeRIP-seq) was performed. The DF1 cells were infected with H9N2-UDL (MOI=1.0) for 24 h. Then, the infected cells were lysed for RNA extraction, mRNA enrichment, fragmentation, and immunoprecipitation with anti-m6A antibodies. The input and immunoprecipitated (MeRIP) fractions were subjected to MeRIP-seq and analysis **(Figure 7.5A)**, as reported earlier (Dominissini et al., 2012; Meyer et al., 2012).

Interestingly, the immunoprecipitated fraction enriched m6A peak clusters to encounter 4362 peaks compared to the input fraction. The DRACH motif was significantly enriched across the peaks identified in the virus-infected cells with a preference for GAC>AAC in the short RAC motif (p-value = 1e-133, percentage of the target = 50.05%; **Figure 7.5 B)**.

To verify the m6A-seq data, key genes were confirmed using MeRIP-RT-qPCR. The chRPL30, the housekeeping gene in chicken, revealed no m6A peaks in both input and MeRIP fractions, served as control and showed non-significant enrichments between H9N2-infected and mock-infected DF1 cells (**Figure 7.5C)**. Interestingly, others that displayed m6A peak cluster(s) in MeRIP-seq results were significantly enriched in MeRIP-RT-qPCR; the most significant was chLY6E (essential gene involved in virus entry and fusion steps), as shown in **Figure 7.5D and Figure 7.6**.
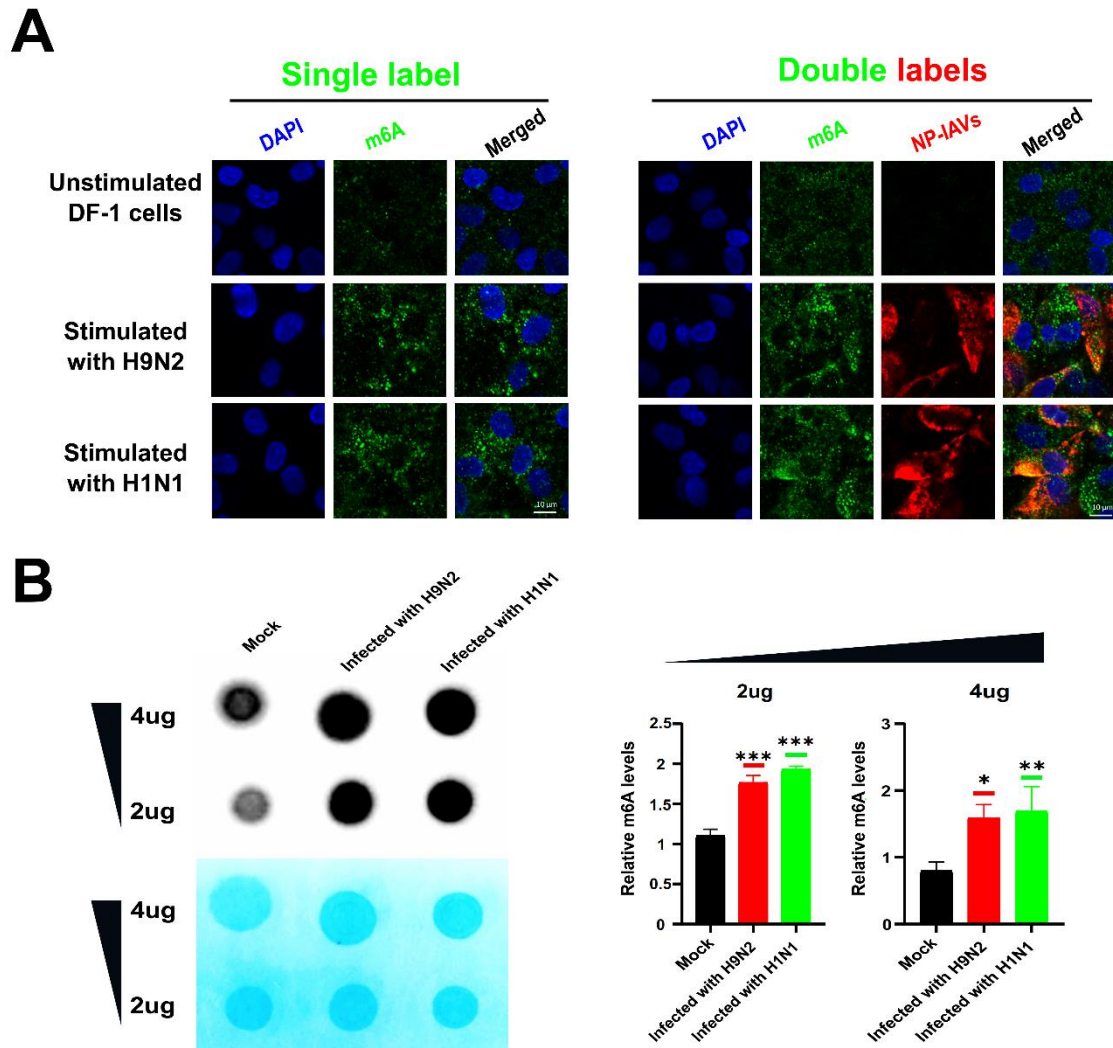
Figure 7.4: Influenza A viruses enhance cellular m6A methylome. **(A)** Confocal images of DF1 cells stimulated with different IAVs (MOI=1.0), the uninfected cells served as control. Imaging parameters were maintained in all figures. Cells either stained with anti-m6A antibodies (single label) or double stained with anti-NP (red) and anti-m6A antibodies (green; double labels). Nuclei were stained with DAPI. Scale bars are 10 µm. **(B)** The m6A-dot blot assay. RNA from infected and uninfected cells was dotted and crosslinked to the nylon membrane. The membrane was probed with anti-m6A antibodies. Equal RNA concentrations are indicated by methylene blue staining. Dot intensity signals were analysed using ImageJ and controlled with dots from uninfected

RNA signals. All these data represent the average of three biological replicates with SD

indicated. *$p < 0.05$, **$p < 0.01$, ***$p < 0.001$ using one-way ANOVA.

A
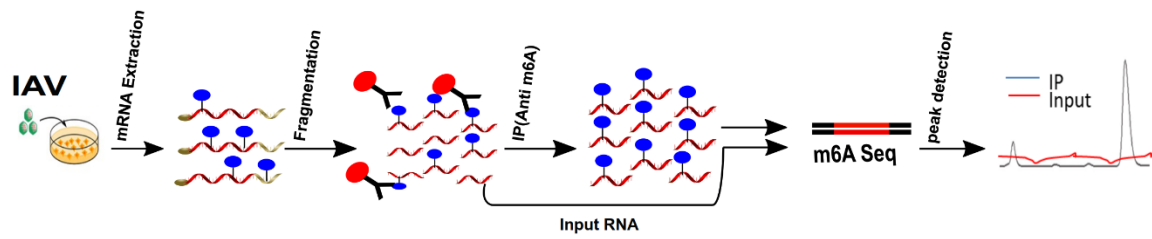
B

p-val=1e-133
% of targets =50.05%

C

chRPL30

Chr2

D

chYTHDF1

Chr20
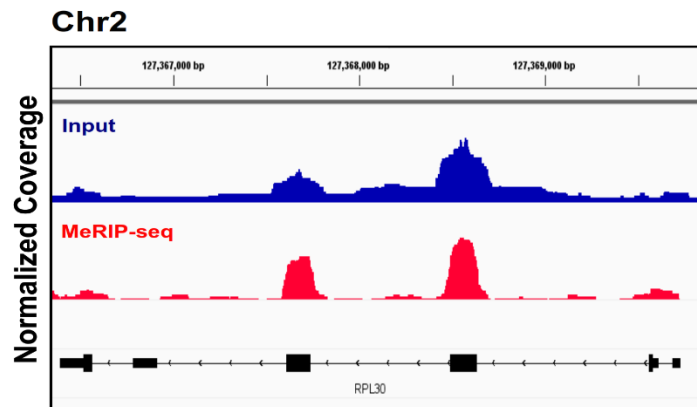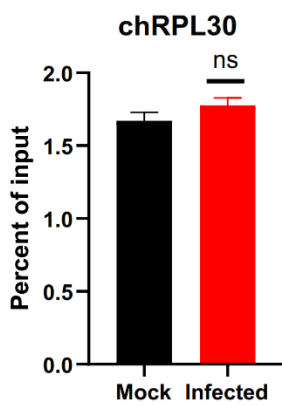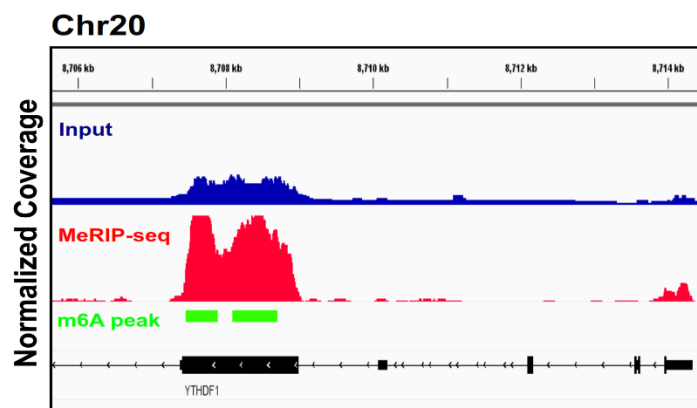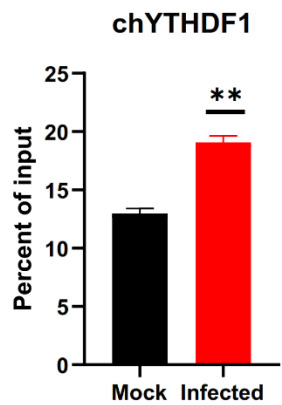
Figure 7.5: Influenza H9N2 infection alters m6A modification of specific cellular transcripts. **(A)** Schematic of the MeRIP-seq protocol. DF1-infected cells (H9N2-UDL, MOI=1.0, 24 hpi) were lysed for mRNA extraction, then fragmented and incubated with m6A-antibodies. Input and immunoprecipitated samples (MeRIP) RNA fractions were sequenced to identify m6A-containing fragments. The experiment was performed in triplicate. **(B)** Markedly enriched motifs located in the m6A identified peaks using HOMER analysis. The significance and the percentage of targets are indicated. **(C, D)** Representative of MeRIP-RT-qPCR analysis of relative m6A levels of key transcripts with infection-altered m6A modification. DF1-infected cells (H9N2, MOI=1.0, 24 hpi; Left). chRPL30 served as controls (does not have m6A peaks). RT-qPCR analysis of a given transcript was quantified as a percent of input and presented as fold enrichment relative to IgG control in both infected and uninfected samples. All these data represent the average of three biological replicates with SD indicated. $*p < 0.05$, $**p < 0.01$, $***p < 0.001$ using unpaired Student's t-test. The input and IP (MeRIP) reads were aligned to the reference genome using Bowtie2. The m6A peak clusters were called by MACS2 (indicated as green boxes under an enriched MeRIP peak). Dark blue and red tracks indicate normalized read coverage of input and MeRIP, respectively. A black annotation track indicates each designated gene in the chicken genome (Right). Chromosome numbers and genomic locations are also indicated. All above indicated tracks in the designated genes were visualized using the IGV browser.

Figure 7.6: Influenza H9N2 infection modulates m6A modification of specific cellular transcripts. **(A-D)** Representative of MeRIP-RT-qPCR analysis of relative m6A levels of key transcripts with infection-altered m6A modification. DF1-infected cells (H9N2, MOI=1.0, 24 hpi; Left). RT-qPCR analysis of a given transcript was quantified as a percent of input and presented as fold enrichment relative to IgG control. All these data represent the average of three biological replicates with SD indicated. $*p < 0.05$, $**p < 0.01$, $***p < 0.001$ using unpaired Student's t-test. The input and IP (MeRIP) reads were aligned to the reference genome using Bowtie2. The m6A peak clusters were called by MACS2 (indicated as green boxes under an enriched MeRIP peak). Dark blue and red tracks indicate normalized read coverage of input and MeRIP, respectively. A black annotation track indicates each designated gene in the chicken genome (Right). Chromosome numbers and genomic locations are also indicated. All above indicated tracks in the designated genes were visualized using the IGV browser.

7.2.2. Influenza A virus H9N2 mRNAs undergo m6A modifications

Chicken ALKBH5 data presented in this study clearly demonstrate that m6A addition strongly enhances IAV replication and its removal by either in-vivo targeted demethylation using dCas13b-chALKBH5 **(Chapter 5)** or through the rescue of m6A-deficient viruses **(Chapter 6)**. Herein, to precisely identify and map the m6A sites across the entire IAV H9N2 mRNA transcriptome. IAV mRNAs have been determined to be m6A modified mainly in DRACH sites (Krug et al., 1976; Narayan et al., 1987; Courtney et al., 2017; Bayoumi and Munir, 2021a).

Toward this end, H9N2 virus-infected cells (as already explained in the previous section) were lysed, mRNA enriched, fragmented, and subjected to m6A-antibodies for immunoprecipitation (MeRIP) followed by high-throughput sequencing (MeRIP-seq). The input/MeRIP reads were aligned to the cRNA of the H9N2-UDL strain. Three biological replicates of normalized read coverage followed by m6A peak calling indicated that 17 peak clusters were identified across the entire transcriptome **(Figure 7.7A)**. The m6A peaks were unequal between IAV segments; some showed no enrichment of any m6A peaks, including PB1, PB2, and M genes. Interestingly, PA (part of the polymerase subunit) has the highest m6A peak-containing segment (6 peaks). HA gene of the H9N2-UDL strain encounters only 3 m6A peaks, primarily at the 3′ end. As discussed in the previous chapter, the silent mutations were designed to coincide with the m6A peaks, primarily for the m6A$^-$6 and m6A$^-$27 deficient mutants, as indicated in **Figure 7.7B**. To conclude, the viral mRNAs isolated from chicken H9N2-infected cells are m6A-methylated with unequal distribution across the transcriptome.
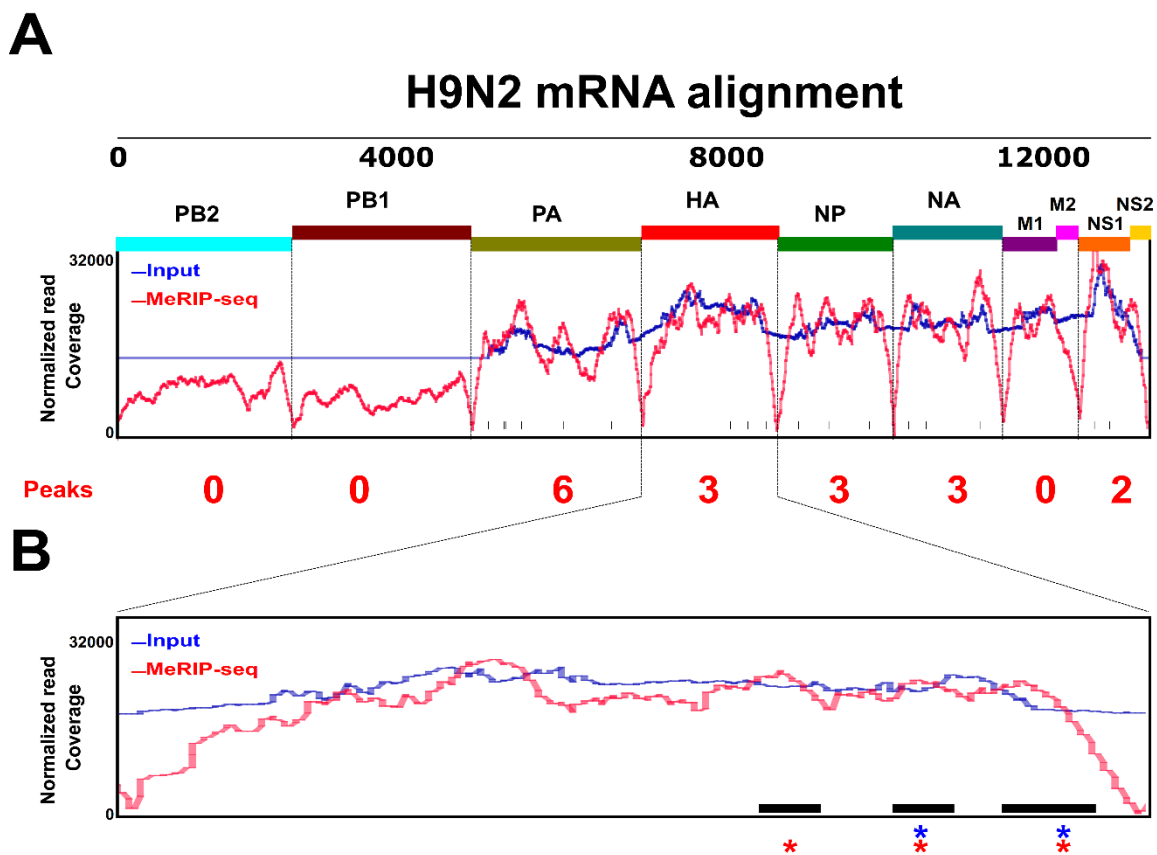
Figure 7.7: Topology of m6A peaks identified on influenza A virus H9N2 mRNA. (A) Mapping the m6A sites throughout the entire IAV H9N2 transcriptome using MeRIP-seq. DF1 cells infected by H9N2-UDL (MOI=1.0) for 24 h were utilized for analysis. Dark blue and red lines indicate normalized read coverage of input and MeRIP, respectively. The input and IP (MeRIP) reads were aligned to reference viral strain using Bowtie2. The m6A peak clusters were called by MACS2, which is shown as black lines under the enriched MeRIP peaks. Consistent m6A peaks are displayed for each segment by red numbers. (B) An enlarged view shows m6A peaks in the HA segment of the H9N2-UDL genome. The ablated DRACH sites that coincide with m6A peaks in the m6A$^-$6 and m6A$^-$27 mutants **(Chapter 6)** are indicated by blue and red asterisks, respectively. All above-indicated tracks/lines in the designated genes were visualized using the IGV browser.

7.2.3. The chALKBH5 enriched various metabolic and protein regulatory pathways in H9N2 virus-infected cells

As reported in the introduction, affinity purification coupled with mass spectrometry (AP-MS) is the most commonly used technique to identify protein-protein interactor(s) (PPIs) using protein bait with its specific antibodies. chALKBH5 was verified to be the most potent antiviral protein in the investigated chicken m6A machinery. Moreover, potential mechanisms of chALKBH5 in regulating IAVs was revealed. AP-MS was used to unveil some mechanistic actions of chALKBH5 indirectly by interacting with critical cellular proteome that could be used for future antiviral therapeutics (**Figure 7.8A**).

To this end, chALKBH5-FLAG was transiently overexpressed in DF1 cells, then cells infected with H9N2-UDL. Empty/chALKBH5-only transfected cell lysates served as a control to eliminate the non-specific interactors. The pull-down assay was verified (**Figure 7.8B, C**), followed by mass spectrometric analysis. The MS analysis revealed a list of 151 significant enriched proteins in the chALKBH5-transfected UDL-infected lysates compared to empty- and chALKBH5-transfected lysates. The PPI network interaction was highly significant ($p<10^{-16}$), as indicated in **Figure 7.9**.

Search Tool for Retrieval of Interacting Genes/Proteins (STRING) analysis revealed that chALKBH5 bait enriched various regulatory pathways in H9N2-virus-infected cells. Most importantly, the carbohydrate and amino acid metabolic processes followed by protein folding and translation regulatory pathways were significantly enriched in the list of PPIs. Gene ontology (biological processes) enriched multiple pathways, including the Krebs cycle (i.e., the primary source of energy inside the cells), protein

folding, translation, regulation of protein translation, mRNA metabolic processes, nucleocytoplasmic transport, and peptide metabolic process **(Figure 7.9)**.

Gene ontology (functional process) also enriched several pathways, including isocitrate dehydrogenase activity and RNA binding. The whole list is included in **Table 7.1**. The KEGG pathways described many regulatory aspects, including proteasome, glycolysis, ribosome, RNA transport, and salmonella infection enrichment processes **(Table 7.2)**.

A
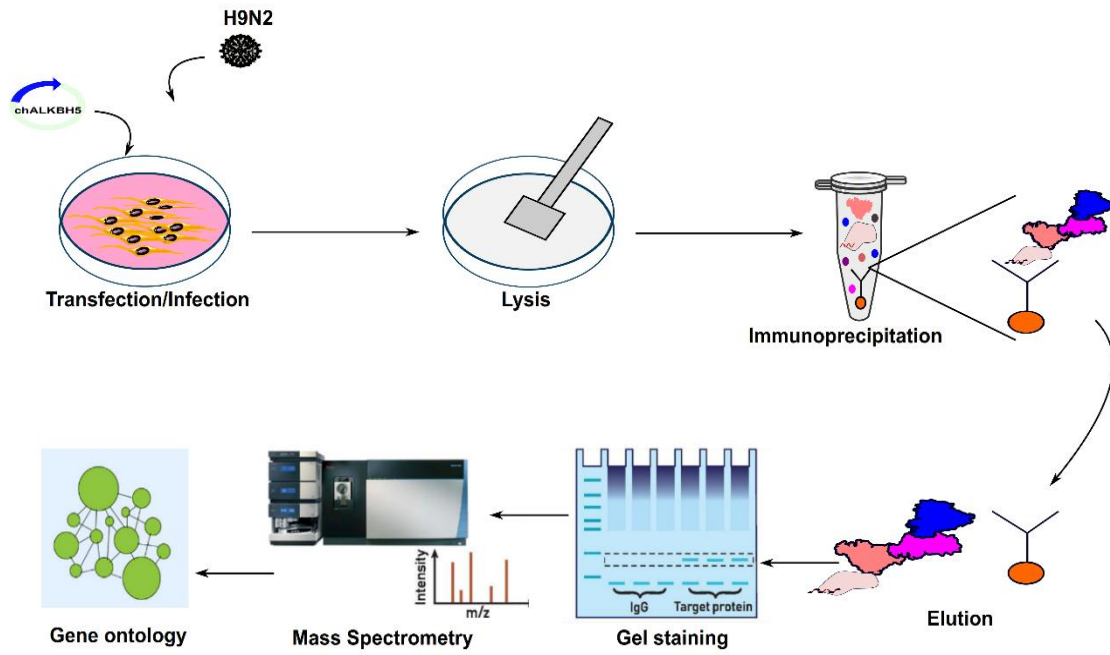
B
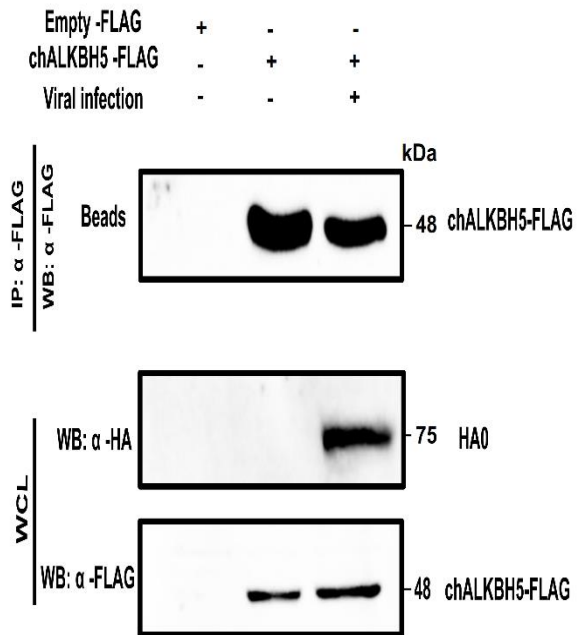
C
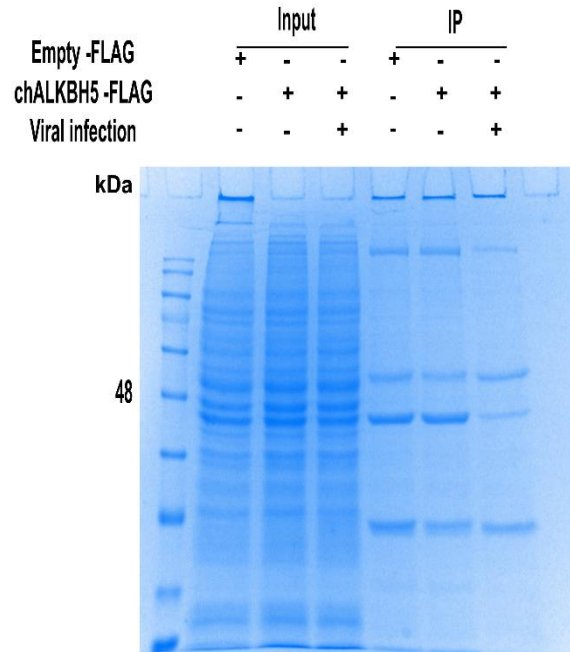
Figure 7.8: Pull-down and MS using chALKBH5 as a bait protein. **(A)** Schematics of pull-down and mass-spectrometry analysis. **(B)** Western blot analysis confirming successful pull-down assay of DF1 cells transfected with chALKBH5 and infected with H9N2 as indicated. The whole cell lysate (WCL, input)/IP fractions are shown. Empty transfected cells served as control. **(C)** Coomassie stained protein gel confirming pull-down assay of DF1 cells transfected with chALKBH5 and infected with H9N2 as indicated. Input/IP lysates are shown. Empty transfected cells served as control.
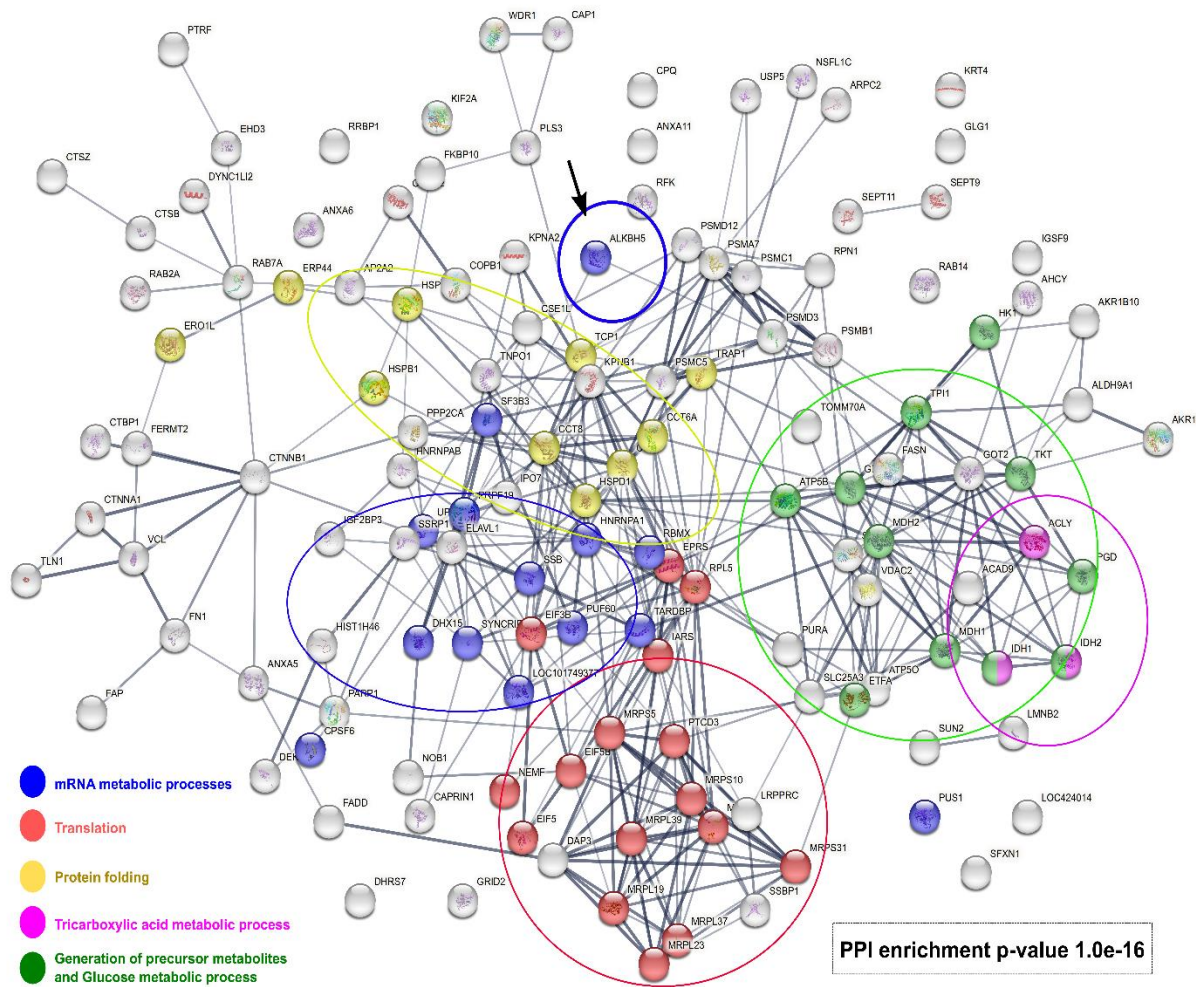
Figure 7.9: Protein-protein interaction analysis using chALKBH5 as a bait protein. A STRING protein-protein interaction analysis of all proteins significantly enriched in the chALKBH5-transfected H9N2 UDL-infected lysates was identified using Mass spectrometry. Different coloured circles indicate various gene ontology (biological processes) enrichment pathways, as indicated on the list on the lower left panel. The statistical significance of these protein-protein interactions is also shown on the lower right panel. The enriched list is normalized by two controls, empty- and chALKBH5-transfected only cells. chALKBH5 indicated by a black arrow.

Table 7.1: Summary of the key gene ontology (GO, molecular function) enrichment analysis of the list of significantly enriched proteins in the chALKBH5-transfected H9N2-UDL infected cell lysates.

term ID	term description	observed gene count	background gene count	strength	false discovery rate
GO:0004450	Isocitrate dehydrogenase activity	2	2	2.06	0.0492
GO:0048027	mRNA 5-UTR binding	3	12	1.46	0.0324
GO:0008536	Ran GTPase binding	4	35	1.12	0.0404
GO:0003730	mRNA 3-UTR binding	5	53	1.03	0.0248
GO:0016616	Oxidoreductase activity,	9	107	0.99	0.0005
GO:0051082	Unfolded protein binding	6	75	0.96	0.018
GO:0003735	Structural constituent of ribosome	9	134	0.89	0.0013
GO:0016853	Isomerase activity	7	132	0.78	0.0284
GO:0003729	mRNA binding	9	205	0.7	0.0234
GO:0005198	Structural molecule activity	16	469	0.59	0.0013
GO:0003723	RNA binding	32	963	0.58	1.62E-07

Table 7.2: Summary of key KEGG pathway enrichment analysis of the list of significantly enriched proteins in the chALKBH5-transfected H9N2-UDL infected cell lysates.

term ID	term description	observed gene count	background gene count	strength	false discovery rate
gga01210	2-Oxocarboxylic acid metabolism	3	13	1.42	0.009
gga00020	Citrate cycle (TCA cycle)	5	26	1.34	0.00052
gga03050	Proteasome	5	34	1.23	0.0011
gga00030	Pentose phosphate pathway	3	24	1.16	0.0291
gga00010	Glycolysis / Gluconeogenesis	5	48	1.08	0.0038
gga01200	Carbon metabolism	10	98	1.07	5.14E-06
gga00051	Fructose and mannose metabolism	3	31	1.05	0.0467
gga00620	Pyruvate metabolism	3	31	1.05	0.0467
gga01230	Biosynthesis of amino acids	5	57	1	0.0064
gga03010	Ribosome	6	101	0.83	0.009
gga04210	Apoptosis	5	103	0.75	0.0404
gga03013	RNA transport	5	113	0.71	0.0467
gga05132	Salmonella infection	7	177	0.66	0.0225

7.2.4. chALKBH5 downregulates various RNA viruses

It was confirmed that chALKBH5 downregulates IAVs. Additionally, it was demonstrated more than one mechanism of antiviral action. Therefore, chALKBH5 was hypothesized to have a pan-antiviral function through identified or unidentified mechanisms. To investigate the effect of chALKBH5 against other viruses. NDV (lentogenic pathotype) and VSV viruses were utilized in this regard. NDV and VSV viruses are good models for veterinary importance as such IAVs. Additionally, VSV is a model that represents another replication strategy with an independent multicycle infection that differs from NDV and H9N2.

DF1 cells were transfected with chALKBH5 for 24 h. Then, the NDV-GFP or VSV-GFP viruses infect DF1 cells for an additional 24 h (MOI=1.0). The cell culture supernatants were used for viral quantification. At the same time, virus-infected cells (green-labeled) were analysed by flow cytometry. Empty plasmid transfected-infected cells served as control. Interestingly, chALKBH5 transfected cells significantly reduced GFP+ cells in both models ($p < 0.01$) **(Figure 7.10A, B)**.

Furthermore, the VSV-GFP-released viruses were quantified using plaque assay and exhibited reduced virus titre in chALKBH5 transfected DF1 cells ($p < 0.01$). Similarly, The NDV-GFP was markedly reduced ($p < 0.05$) when quantified by plaque assay, expressed as foci-forming units **(Figure 7.10C, D)**. Overall, it seems that chALKBH5 has broad antiviral activity against different virus families and various replication strategies.
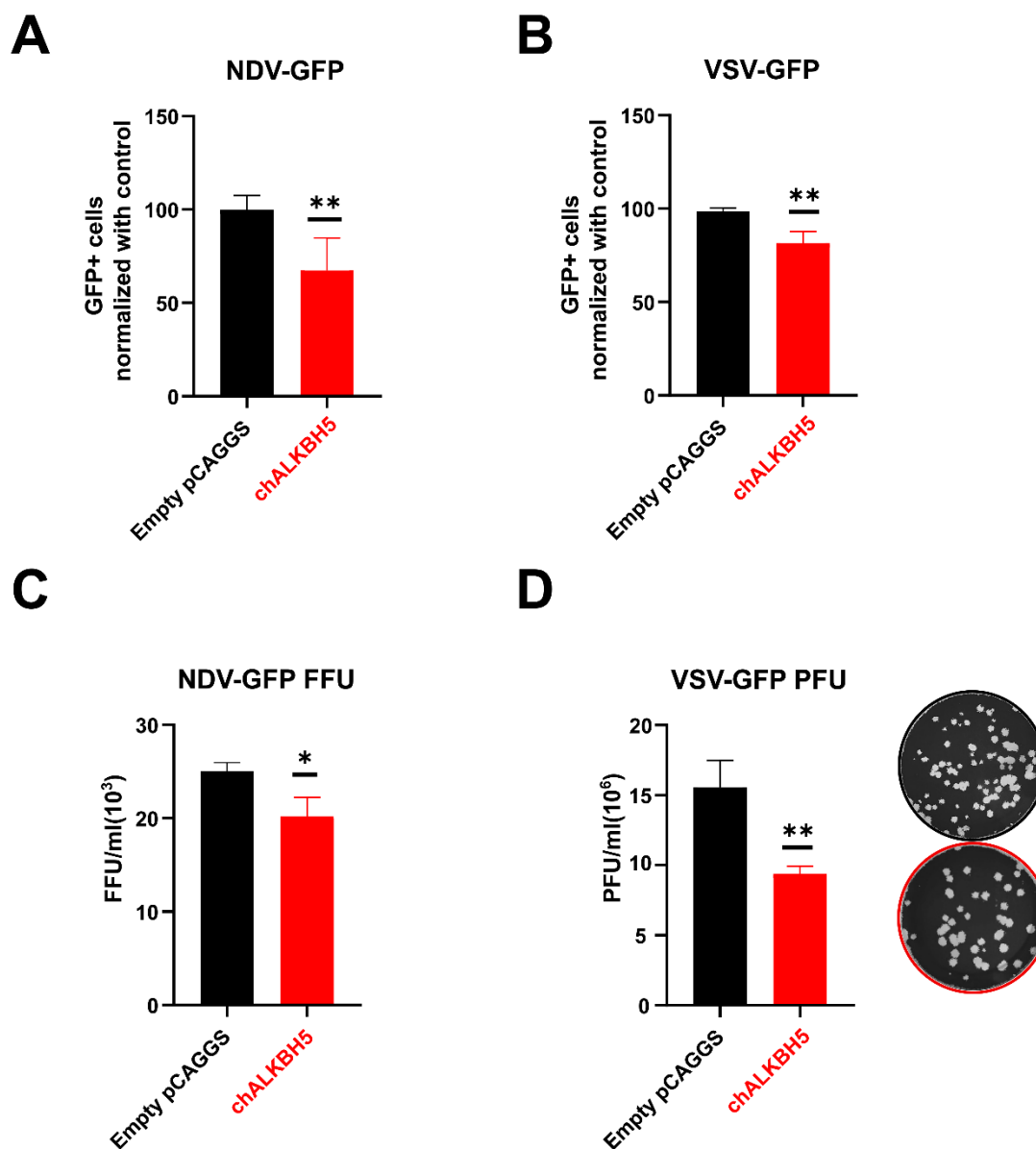
Figure 7.10: chALKBH5 downregulates various RNA viruses. **(A and B)** Flow cytometry-based analysis of GFP+ (infected) cells. DF1 cells were transfected with chALKBH5 or empty plasmid and infected with NDV-GFP (A) or VSV-GFP (B) for 24 h (MOI=1.0). **(C and D)** Plaque assay-based quantification. Viral titres from cell culture supernatants transfected and infected cells were utilized, as described for A and B. Viral titres determined on MDCK and expressed as plaque forming unit (VSV-GFP) or foci forming using (FFU) NDV-GFP. Representative images for countable wells are

indicated. All these data represent the average of three biological replicates with SD indicated. $*p < 0.05$, $**p < 0.01$ using unpaired Student's t-test.

7.3.   Chapter Discussion

In this chapter, more open questions were addressed pointing to future research directions. It has been reported that the cellular m6A methylome greatly enhanced and affected the topology of almost all investigated viruses in a manner that supports competent viral replication. KSHV infection triggers massive alterations in the pathways that regulate oncogenic and epithelial-mesenchymal transition in the latent cycle or modulate viral lytic replication (lytic cycle) (Tan et al., 2017). In the HCV model, viral infection altered innate immune and endoplasmic reticulum (ER) stress response pathways (Gokhale et al., 2020). SARS-CoV-2 enriched the membrane trafficking and apoptotic signalling pathway (Liu et al., 2021) and immune-related pathways in the Zika virus model (Lichinchi et al., 2016b).

Infected cells with IAVs revealed an enhanced cellular m6A methylome. Using IFA, when cells were treated and imaged using the exact parameters of laser power and gain between stimulated and unstimulated cells, displayed an idea of the m6A methylation state in cultured cells. Interestingly, this effect was also evident in the m6A-dot blot assay. The m6A methylation state was significantly upregulated in two influenza virus models (H1N1 and H9N2) in various RNA concentrations. This observation indicates IAV-mediated enhancement to chicken m6A methylome. Whether this increase in m6A methylation originates from the highly replicating virus, cellular-specific transcripts, or both cannot be easily concluded using an m6A-dot blot assay. Accordingly, MeRIP-seq analysis points out that the upregulation could originate from both (cellular and viral). At least 4362 m6A peaks were observed uniquely in the immunoprecipitated methylated RNA, which is smaller than what has been identified earlier in humans (i.e.,

12000 m6A sites) (Dominissini et al., 2012). Possibly the small genome size of chickens compared to humans is the potential cause (40% compared to the human genome) (Hillier et al., 2004).

Regarding viral methylation, as reported earlier in the H1N1 model, viral replicating RNA (i.e., mRNA) gains 24 m6A marks in the viral lifecycle (Courtney et al., 2017). This indicates that the increased m6A methylation is a combination of both viral and cellular methylome. Notably, the impact of viral methylation on the m6A-dot blot signal was minimal compared to the cellular part, as demonstrated in **Chapter 6, section 6.2.5** (this finding will be discussed in more detail in the general discussion chapter).

The MeRIP-seq data from virus-infected cells confirmed that the IAV H9N2-UDL is indeed m6A-methylated. It has been reported earlier that the IAV mRNA undergoes m6A modifications with unequal distribution between different segments. Moreover, HA had the highest m6A site-containing gene (8 m6A sites) (Krug et al., 1976; Narayan et al., 1987; Courtney et al., 2017). Although the MeRIP-seq revealed unequal m6A distribution across segments, HA mRNA bears only 3 m6A peaks. More interestingly, PA had the most m6A peaks (i.e., 6 peaks).

It is important to note that all previous reports mapped the m6A sites across human H1N1 isolates; WSN strain using the biochemical identification method (Krug et al., 1976; Narayan et al., 1987) and the PR8 strain using PA-m6A-seq method (Courtney et al., 2017). It seems that the unequal distribution of m6A differs among IAV subtypes. Notably, the previously described DRACH signature analysis indicated that H1N1 bear at least 6 conserved DRACH motifs, while H9N2 bears only 3 DRACH motifs

(Bayoumi and Munir, 2021a). All these in silico and MeRIP-seq data together support the notion that the m6A mark is virus-dependent.

It is essential to mention that the m6A peak/cluster does not necessarily reflect the presence of one m6A site using MeRIP-seq. As described in the previous chapter for various rescued m6A mutant viruses, the m6A$^-$6 mutant virus was designed to target DRACH sites coincident with some m6A clusters identified in the HA segment. Possibly this is why this mutant did not reveal significant attenuation in culture compared to the wild-type virus. These data indicate that the selected DRACH motifs under the m6A peak were not indeed m6A sites due to more than one DRACH motif under the same m6A peak, as noted in other viral models (Xue et al., 2019; Lu et al., 2020). Additionally, the mutated m6A sites were possibly insufficient to exhibit significant attenuation. In contrast, the rescued m6A$^-$27 mutant targeted all possible DRACH motifs under mapped m6A peaks, hence, inhibited viral replication significantly.

Although the PA showed more enrichment of m6A peaks than the HA mRNA isolated from H9N2 virus-infected cells, the m6A clusters were mapped on HA mRNA in this study. For two reasons; firstly, to prove the hypothesis that m6A positively regulates IAVs utilizing the same gene model reported earlier for the H1N1 PR8 strain (Courtney et al., 2017). Secondly, to confirm the earlier results of the programmed demethylation of HA mRNA using dCas13b-chALKBH5. Notably, crRNAs designed in the 3′ end (coincident with mapped m6A peaks) were significant in downregulating viral replication and gene expression. However, mutating m6A sites located in the PA gene warrant future investigations.

MeRIP-seq analysis also showed that the broad DRACH motif was significantly enriched under the m6A peaks. Interestingly, GAC was enriched as a shorter RAC motif than the AAC in cellular m6A-enriched motifs, suggesting host preferences. Furthermore, cellular m6A methylome (MeRIP-seq) indicated enrichment of key cellular transcripts, including m6A machinery genes, influenza viral regulatory genes, and innate immune genes, further verified by MeRIP-RT-qPCR. However, MeRIP-seq data from mock-infected chicken samples would reveal more in the future and help identify various regulatory pathways in viral-infected states.

The mass spectrometry data suggested multiple pathways in the significantly enriched protein list mapped in the chALKBH5 transfected H9N2 infected lysates, which can be grouped into two main categories: protein- and metabolic-related pathways. The protein-related pathways affect protein or RNA binding/metabolism. It is essential to mention that this is not surprising as chALKBH5 can affect RNA metabolism (possibly through demethylation of the RNA targets, as verified in this project).

Moreover, human m6A-related proteins were also confirmed to modulate metabolic-related pathways indirectly in an m6A-dependent manner to regulate viral infection. It has been reported earlier that ALKBH5 demethylates α-ketoglutarate dehydrogenase (OGDH) mRNA and affects its stability by YTHDF2, in turn, upregulates the metabolite itaconate to support viral replication. In contrast, ALKBH5-depleted cells inhibit viral replication (Liu et al., 2019).

Notably, none of the m6A machinery investigated in this study was enriched in the chALKBH5 transfected UDL-infected lysate (i.e., YTHDF effectors were not enriched). However, members of hnRNPs and IGF2BPs (i.e., other m6A-binding

proteins) were observed, possibly modulating protein translation pathways to limit viral infections in a cell-type-dependent manner (Alarcón et al., 2015; Huang et al., 2018).

On the other hand, the cellular metabolic-related pathways regulating viral infection were verified to enrich or deplete specific intermediate metabolites to enhance or limit viral infection, usually in an innate immune-independent manner (Wang et al., 2017a). However, testing the metabolomic profile was not addressed in this study.

Given the abovementioned findings, chALKBH5 potently downregulates both H9N2 and H1N1. Additionally, chALKBH5 was demonstrated regulates IAVs by inducing the demethylation of viral transcripts and binding to viral NP protein. The chALKBH5 also downregulates other viruses, including NDV and VSV. The provided MS data could also involve indirect protein interactors in either protein/RNA or metabolic-related pathways.

This outcome indicates that chALKBH5 could be a pan-antiviral factor. However, the underlying mechanism warrants further investigation soon. NDV and VSV models were used for their veterinary importance and the difference in the replication strategy compared with IAVs. Additionally, both differ significantly in genome structure (NDV and VSV are non-segmented RNA).

Regarding localization, both viruses replicate in the cytoplasm, whereas chALKBH5 was readily expressed in the nucleus. This fact indicates that chALKBH5 demethylation of viral transcripts in the nucleus and/or NP interaction (as influenza viruses) is unlikely unless it translocates in the cytoplasm; however, this hypothesis was not investigated.

Like H9N2 and lab-adapted H1N1, NDV-lentogenic pathotype replicates on DF1 cells in a single infection cycle without TPCK-trypsin (all do not carry multiple basic amino acids to support intracellular cleavage, as indicated in **section 1.1.4.4.2**). That means the progeny viruses are generated only from the initially infected cells. It is essential to mention that the chicken DF1 cells cannot tolerate any of the TPCK in the infection cycles (data not shown). Therefore, the VSV model was utilized to demonstrate the effect of chALKBH5 in a multicycle infecting virus model. These findings indicate that chALKBH5 is possibly a pan-antiviral protein through a yet-to-be-identified mechanism and warrants future research based on the provided proteome-wide data.

Chapter 8

General Discussion

8.1. Summary of the results

In this study, the impact of the m6A marks on IAVs replication kinetics were demonstrate and genetic and functional differences between chicken and well-studied human m6A machinery were reported. Starting with in silico prediction data, the uniqueness of chicken was displayed by loss of gene synteny and clustering in distinct clades in phylograms in most m6A-related proteins compared with humans, reflecting the avian evolutionary pattern. Although low amino acid sequence differed between in chickens and humans, the predicted proteins were maintained through synonymous structural mutations, suggesting the same function in the chicken, in general. Furthermore, the highly conserved DRACH motifs (the potential m6A sites) was identified among all IAV HA sequences using comparative genetic studies. This data would be beneficial for generating m6A-deficient viruses with reduced replication kinetics. The analysis also indicated that the m6A-sites are virus-specific rather than pathogenicity, clade, host species, and geographic-specific (**Chapter 3**).

The expression of ten basic components of the m6A machinery in chickens was also verified which showed the same expression pattern with human orthologues, except chWTAP. This expression pattern was maintained with H9N2 viral infection. It was demonstrated that most chicken m6A machinery downregulated IAV infection; in turn, infection with IAVs inhibited chicken m6A-associated gene expression. Additionally, through a combination of various antiviral assays, it was seen that the chALKBH5 was the most potent antiviral protein, even in a time-course manner. It was also identified that the chYTHDF2 has an antiviral potential in chicken, which differs from the known proviral role in human m6A machinery regulating the H1N1 model. Moreover, the

combination between chYTHDF2 and chALKBH5 demonstrated augmented antiviral outcomes, exhibiting that the functional variations in m6A machinery studies are host-specific, and this possibly is the rationale behind the discrepancy in viral m6A research **(Chapter 4)**.

Next, mechanistic studies of chALKBH5 for downregulating IAVs were identified. The middle- and carboxyl portions were identified responsible for antiviral function, and the NLS is located in the C-terminus to regulate IAV replication. The interaction of chALKBH5 with HA mRNA was identified and the demethylation activity of chALKBH5 were confirmed to target viral transcripts by programmed demethylation through tethering the chALKBH5 with a dead version of Cas13b (i.e., dCa13b-chALKBH5). Moreover, using a combination of IFA and IP assays, chALKBH5 was shown to interact with viral NP to reduce H9N2 virus replication. With the same assays, it was also demonstrated clearly that the chWTAP does not interact with the chMETTL3/14 and likely does not share in m6A methylation as the case in humans, exhibiting unique functional characteristics of chicken machinery **(Chapter 5)**.

Next, the RG-based system of IAV was utilized to generate m6A-mutant viruses. Various mutants were made by ablating m6A sites which coincide with the MeRIP-seq data of H9N2-infected cells. It was clearly verified that m6A-deficient viruses are genetically stable with reduced viral replication kinetics and slow spreading capacity to be attenuated in culture. This indicated the positive regulatory role in IAV replication and confirmed in silico studies that the m6A marks are virus-specific and m6A-machinery is host-specific **(Chapter 6)**.

Next, it was verified that infection of IAVs significantly enhanced cellular m6A methylome. Moreover, MeRIP-seq analysis was used to identify that infection affects specific cellular transcript methylation states. The same assay was used to determine the m6A peaks across the H9N2 transcriptome. Using mass spectrometry data, the cellular interactome of chALKBH5 was mapped in virus-infected cells, which showed that the metabolic and protein regulatory pathways were significantly enriched. Ultimately, it was also shown that the chALKBH5 could be a pan-antiviral protein by inhibiting the replication of various RNA viruses, including VSV and NDV. Suggesting additional mechanisms for the antiviral outcomes of chALKBH5 (**Chapter 7**).

8.2. The mystery of avian/chicken m6A-writer complex

Despite avian species displaying unique evolutionary machinery, as demonstrated in **Chapter 3, section 3.2.2.,** some lack a well-defined m6A-methyltransferase complex (i.e., METTL3/14), including ducks, turkeys, and predominantly wild birds. This finding leaves open questions about their m6A methylation mechanism. This could be attributed to poor genomic annotation in less studied avian species, and possibly proper annotations could define their methylation machinery correctly. The minimal known functional unit for the m6A-methyltransferase complex was investigated (i.e., chMETTL3/14/WTAP). However, as indicated in **Chapter 3, section 3.1.1**., additional writers have been identified, which could be the central functional unit in avian writers or even unidentified so far. This finding may also explain the rationale behind the lack of proviral activity in three investigated chicken writers.

Furthermore, in this investigation, chWTAP was expressed in the cytoplasm of chicken cells, even in IAV stimulated cells, which is different to the human orthologue **(Chapter**

4, section 4.2.1). Moreover, co-transfection of cells with chMETTL3/14 did not stimulate a change in the chWTAP expression pattern. Weak interaction in vitro was barely noticed, as indicated in **Chapter 5, section 5.2.7**. Notably, identical nuclear localization sequence (NLS) between human (functionally validated earlier) and chicken WTAP warrants future investigation on the exclusive cytoplasmic expression of chWTAP. It appears that the nuclear localization signals in chickens need further investigation.

8.3. Impact of in silico prediction on the functional relevance in m6A-related fields

More interestingly, chALKBH5 has the same observation; the predicted NLS in chicken ALKBH5 was noticed in the N-terminus; however, the prediction and mutational analysis indicated that the C-terminus harbours the NLS. Moreover, the induced mutations in the C-terminus were insufficient to completely shift chALKBH5 in the cytoplasm, as shown in **Chapter 5, section 5.2.3,** suggesting that other unknown factors control NLS in the chicken.

Adopted in silico prediction software for testing structural alterations, crystal structures of chicken m6A machinery could enrich the understanding of mRNA modifications in avian species. Nevertheless, the predicted structures benefit us in understanding the functional relevance of some proteins. The altered gate loops predicted in chMETTL3 could be one of the possible causes of the lack of the proviral effects of writers in chicken machinery, as indicated in **Chapter 3, section 3.2.2**.

the observation also suggests that chFTO binds to HA mRNA but does not affect its demethylation **Chapter 5, section 5.2.5**. Interestingly, the in-silico prediction analysis indicates that chFTO harbour residue (K86) which may explain the enhanced RNA binding activity, as noted in **Chapter 3, section 3.2.2,** and could be responsible for non-specific binding to methylated viral RNA.

Moreover, our approach for determining m6A conservation analysis indicated that DRACH sequences mapped in the mRNA are at least two logs higher than what was found in the vRNA **Chapter 3, section 3.2.10**, indicating a possible m6A role in viral protein expression. Notably, the rescued m6A-mutant viruses (removed from HA mRNA) verified a significant reduction in protein expression by at least half compared to UDL-wt **Chapter 6, section 6.2.4.** Altogether, in silico prediction possibly point out functional relevance and thus need to be carefully addressed.

8.4. Difference between chALKBH5 and chFTO

As indicated throughout the project, m6A demethylases have unclear selective roles in various stages of virus lifecycles. The ALKBH5 has been involved in the regulatory functions of HIV-1 and VSV infection models (Lichinchi et al., 2016a; Tirumuru et al., 2016; Liu et al., 2019). In contrast, FTO selectively modulates viral infection of HCV and EV-71 (Gokhale et al., 2016; Hao et al., 2019). Both demethylases have regulatory functions in the Zika and respiratory syncytial viruses (Lichinchi et al., 2016b; Xue et al., 2019). Regarding IAVs, human FTO and ALKBH5 have not been investigated so far.

In chicken, chFTO has a minimal role in regulating both H1N1 and H9N2; however, chALKBH5 significantly downregulated both. Collected findings indicated clearly that RNA specificity is the leading cause of their selectivity. In contrast to chALKBH5, enforcing chFTO to induce targeted demethylation to HA mRNA was not productive (Bayoumi and Munir, 2021c).

8.5. chALKBH5 expression pattern regulates influenza viral infections

The chALKBH5, the most potent antiviral factor investigated in the study, played critical roles in regulating IAVs replication and is associated with its nuclear expression. It has been verified that M- and C- fragments of chALKBH5 demonstrated potent anti-H1N1 and H9N2 activity, expressed perinuclear or exclusively nuclear, respectively. Moreover, when chALKBH5 fused with dCas13b was expressed in the nucleus, it had potent antiviral activity (targeted demethylation); however, the cytoplasmic version failed to inhibit IAV infection. Moreover, owing to the nuclear expression of NP of IAV, the chALKBH5 inhibited IAV replication by binding to NP in the nucleus, as demonstrated in **Chapter 5, section 5.2.6**.

However, the potent antiviral activity of the chALKBH5 against investigated cytoplasmic viruses (NDV and VSV) clearly indicated that chALKBH5 has an additional unidentified mechanism (**Chapter 7, section 7.2.3**). Possibly the unveiled protein interactome with the chALKBH5 may solve this mechanism.

8.6. Combining more than one approach unravels more aspects of viral epitranscriptomics, hence minimizing the discrepancy

The literature indicates a potential discrepancy in the results even though some studies used the same virus model, cell line, and sequencing technology. Herein, the previously investigated virus model (i.e., H1N1) was used and showed that the origin of the discrepancy comes clearly from using a different cell line (chicken DF1) than that was investigated earlier (human A549). However, the impact of the m6A on influenza replication remains the same even using other virus models and cells, indicating that the m6A-machinery effect is host-specific, and the m6A impact is virus-specific **(Chapters 4 and 6)**.

Nevertheless, using more than one technique to demonstrate the actual activity is deemed essential to minimize literature discrepancies, especially in viral epitranscriptomic fields. Therefore, the antiviral action in both DF1 (cell line) and CEF (primary cells) was confirmed to avoid discrepancies originating from the cell line and its primary origin noticed earlier in the HIV-1 model **(Chapter 4, section 4.2.4)** (Kennedy et al., 2016; Tirumuru et al., 2016).

Moreover, using more than one approach to test the functionality is crucial. Although chALKBH5 and chFTO demonstrate potential HA mRNA binding, chALKBH5 only exhibited targeted demethylation to HA mRNA **(Chapter 5, sections 5.2.4 and 5.2.5)**.

Furthermore, for the determination of the relative quantity of m6A level in total RNA in IAV-stimulated and unstimulated DF1 cells and KO cells, m6A-dot blot assay was used. However, the m6A-dot blot on purified vRNA was not productive; this finding

indicates both the m6A-blot could be unsuitable for vRNA m6A determination and the increased level of m6A in infected cells originating predominantly from the cellular transcripts (**Chapters 4, 6, and 7**). Using m6A-dot blot assay for vRNA only could give misleading results in the literature about the assay, hence the chance of discrepancy.

Most interestingly, combining different approaches, including IFA and IP assay, appeared crucial to demonstrate the functional activity of a given m6A-associating protein. Despite displaying a possible/weak interaction of NS1 protein with chALKBH5 in both live imaging and in IFA, the IP assay clearly confirm lack of this interaction NS1 is observed only in the unbound fraction of lysates. In contrast, NP clearly interacts with chALKBH5 in both IFA and IP (**Chapter 5, section 5.2.6**).

8.7. Future work

At the end of this study, a piece of information was summarized to add value to the viral epitranscriptomic fields in more than one aspect. However, some parts need further investigation, including the molecular determinants behind the reduced viral replication in m6A-deficient viruses with extra DRACH motif (m6A$^+$29). Possibly reducing the number of extra DRACHs could give more interesting findings. Moreover, the impact of m6A-deficient vRNAs in regulating innate immune sensing in chickens warrants further investigation. Additionally, molecular determinants on how chALKBH5 exhibits its pan-antiviral activity against various RNA viruses need further work. The above-mentioned proteome-wide data could figure out this issue shortly. Ultimately, using single nucleotide resolution techniques to determine chicken m6A methylome could enrich our understanding of infection-related pathways and used better to understand IAV transmission.

Chapter 9

References

References:

Abbott, T. R., Dhamdhere, G., Liu, Y., Lin, X., Goudy, L., Zeng, L., et al. (2020). Development of CRISPR as an Antiviral Strategy to Combat SARS-CoV-2 and Influenza. *Cell* 181, 865-876.e12. doi:10.1016/j.cell.2020.04.020.

Abdelwhab, E. M., Hassan, M. K., Abdel-Moneim, A. S., Naguib, M. M., Mostafa, A., Hussein, I. T. M., et al. (2016). Introduction and enzootic of A/H5N1 in Egypt: Virus evolution, pathogenicity and vaccine efficacy ten years on. *Infect. Genet. Evol.* 40, 80–90. doi:10.1016/j.meegid.2016.02.023.

Abudayyeh, O. O., Gootenberg, J. S., Konermann, S., Joung, J., Slaymaker, I. M., Cox, D. B. T., et al. (2016). C2c2 is a single-component programmable RNA-guided RNA-targeting CRISPR effector. *Science (80-.).* 353. doi:10.1126/science.aaf5573.

Ackerman, C. M., Myhrvold, C., Thakku, S. G., Freije, C. A., Metsky, H. C., Yang, D. K., et al. (2020). Massively multiplexed nucleic acid detection with Cas13. *Nature* 582, 277–282. doi:10.1038/s41586-020-2279-8.

Adams, J. M., and Cory, S. (1975). Modified nucleosides and bizarre 5′-termini in mouse myeloma mRNA. *Nature* 255, 28–33. doi:10.1038/255028a0.

Agarwala, S. D., Blitzblau, H. G., Hochwagen, A., and Fink, G. R. (2012). RNA methylation by the MIS complex regulates a cell fate decision in yeast. *PLoS Genet.* 8, 1–13. doi:10.1371/journal.pgen.1002732.

Aik, W. S., McDonough, M. A., Thalhammer, A., Chowdhury, R., and Schofield, C. J.

(2012). Role of the jelly-roll fold in substrate binding by 2-oxoglutarate oxygenases. *Curr. Opin. Struct. Biol.* 22, 691–700. doi:10.1016/j.sbi.2012.10.001.

Aik, W., Scotti, J. S., Choi, H., Gong, L., Demetriades, M., Schofield, C. J., et al. (2014). Structure of human RNA N6-methyladenine demethylase ALKBH5 provides insights into its mechanisms of nucleic acid recognition and demethylation. *Nucleic Acids Res.* 42, 4741–4754. doi:10.1093/nar/gku085.

Akichika, S., Hirano, S., Shichino, Y., Suzuki, T., Nishimasu, H., Ishitani, R., et al. (2019). Cap-specific terminal N 6 -methylation of RNA by an RNA polymerase II–associated methyltransferase. *Science (80-.).* 363, 1–13. doi:10.1126/science.aav0080.

Alarcón, C. R., Goodarzi, H., Lee, H., Liu, X., Tavazoie, S., and Tavazoie, S. F. (2015). HNRNPA2B1 Is a Mediator of m6A-Dependent Nuclear RNA Processing Events. *Cell* 162, 1299–1308. doi:10.1016/j.cell.2015.08.011.

Albo, C., Valencia, A., and Microbiologı, C. N. De (1995). Identification of an RNA Binding Region within the N-Terminal Third of the Influenza A Virus Nucleoprotein. *J. Virol.* 69, 3799–3806.

Aman, R., Ali, Z., Butt, H., Mahas, A., Aljedaani, F., Khan, M. Z., et al. (2018a). RNA virus interference via CRISPR/Cas13a system in plants. *Genome Biol.* 19, 1–9. doi:10.1186/s13059-017-1381-1.

Aman, R., Mahas, A., Butt, H., Ali, Z., Aljedaani, F., and Mahfouz, M. (2018b). Engineering RNA virus interference via the CRISPR/Cas13 machinery in

arabidopsis. *Viruses* 10. doi:10.3390/v10120732.

Armstrong, R. T., Kushnir, A. S., and White, J. M. (2000). The transmembrane

domain of influenza hemagglutinin exhibits a stringent length requirement to

support the hemifusion to fusion transition. *J. Cell Biol.* 151, 425–437.

doi:10.1083/jcb.151.2.425.

Artegiani, B., Hendriks, D., Beumer, J., Kok, R., Zheng, X., Joore, I., et al. (2020).

Fast and efficient generation of knock-in human organoids using homology-

independent CRISPR–Cas9 precision genome editing. *Nat. Cell Biol.* 22, 321–

331. doi:10.1038/s41556-020-0472-5.

Asha, K., and Kumar, B. (2019). Emerging influenza D virus threat: What we know so

far! *J. Clin. Med.* 8. doi:10.3390/jcm8020192.

Ashraf, M. U., Salman, H. M., Khalid, M. F., Khan, M. H. F., Anwar, S., Afzal, S., et

al. (2021). CRISPR-Cas13a mediated targeting of hepatitis C virus internal-

ribosomal entry site (IRES) as an effective antiviral strategy. *Biomed.*

Pharmacother. 136, 111239. doi:10.1016/j.biopha.2021.111239.

Ayllon, J., and García-Sastre, A. (2015). The NS1 Protein: A Multitasking Virulence

Factor. *Curr. Top. Microbiol. Immunol.* 386, 73–107. doi:10.1007/82.

Bai, S., Jorga, K., Xin, Y., Jin, D., Zheng, Y., Damico-Beyer, L. A., et al. (2012). A

guide to rational dosing of monoclonal antibodies. *Clin. Pharmacokinet.* 51, 119–

135. doi:10.2165/11596370-000000000-00000.

Banan, M. (2020). Recent advances in CRISPR/Cas9-mediated knock-ins in

mammalian cells. *J. Biotechnol.* 308, 1–9. doi:10.1016/j.jbiotec.2019.11.010.

Baquero-Perez, B., Agne, A., Carr, I., and Whitehouse, A. (2019). The Tudor SND1 protein is a m6A RNA reader essential for KSHV replication. *Elife* 5, 1–39. doi:10.1128/AAC.00162-09.

Baquero-Perez, B., Geers, D., and Díez, J. (2021). From A to m6A: The emerging viral epitranscriptome. *Viruses* 13. doi:10.3390/v13061049.

Barbieri, I., Tzelepis, K., Pandolfini, L., Shi, J., Millán-Zambrano, G., Robson, S. C., et al. (2017). Promoter-bound METTL3 maintains myeloid leukaemia by m6A-dependent translation control. *Nature* 552, 126–131. doi:10.1038/nature24678.

Barnes, K. G., Lachenauer, A. E., Nitido, A., Siddiqui, S., Gross, R., Beitzel, B., et al. (2020). Deployable CRISPR-Cas13a diagnostic tools to detect and report Ebola and Lassa virus cases in real-time. *Nat. Commun.* 11. doi:10.1038/s41467-020-17994-9.

Baron, M. D., and Barrett, T. (1997). Rescue of rinderpest virus from cloned cDNA. *J. Virol.* 71, 1265–1271. doi:10.1128/jvi.71.2.1265-1271.1997.

Baudin, F., Bach, C., Cusack, S., and Ruigrok, R. W. H. (1994). Structure of influenza virus RNP . 1 . Influenza virus nucleoprotein melts secondary structure in panhandle RNA and exposes the bases to the solvent. *EMBO J.* 13, 3158–3165. doi:10.1002/j.1460-2075.1994.tb06614.x.

Bawage, S., Tiwari, P., and Santangelo, P. (2018). Synthetic mRNA expressed Cas13a mitigates RNA virus infections. *bioRxiv*, 370460. doi:10.1101/370460.

Bayoumi, M., and Munir, M. (2021a). Evolutionary conservation of the DRACH

   signatures of potential N6 - methyladenosine (m6A) sites among influenza A

   viruses. *Sci. Rep.* 11, 1–12. doi:10.1038/s41598-021-84007-0.

Bayoumi, M., and Munir, M. (2021b). Potential Use of CRISPR / Cas13 Machinery in

   Understanding Virus – Host Interaction. *Front. Microbiol.* 12, 1–13.

   doi:10.3389/fmicb.2021.743580.

Bayoumi, M., and Munir, M. (2021c). Structural Insights Into m6A-Erasers : A Step

   Toward Understanding Molecule Specificity and Potential Antiviral Targeting.

   Front. Cell Dev. Biol. 8, 1–14. doi:10.3389/fcell.2020.587108.

Bayoumi, M., Rohaim, M. A., and Munir, M. (2020). Structural and Virus Regulatory

   Insights Into Avian N6-Methyladenosine (m6A) Machinery. *Front. Cell Dev.

   Biol.* 8, 543. doi:10.3389/fcell.2020.00543.

Beaton, A. R., and Krug, R. M. (1986). Transcription antitermination during influenza

   viral template RNA synthesis requires the nucleocapsid protein and the absence

   of a 5' capped end. *Proc. Natl. Acad. Sci. U. S. A.* 83, 6282–6286.

   doi:10.1073/pnas.83.17.6282.

Benton, D. J., Gamblin, S. J., Rosenthal, P. B., and Skehel, J. J. (2020). Structural

   transitions in influenza haemagglutinin at membrane fusion pH. *Nature* 583, 150–

   153. doi:10.1038/s41586-020-2333-6.

Bentz, J., and Mittal, A. (2003). Architecture of the influenza hemagglutinin

   membrane fusion site. *Biochim. Biophys. Acta - Biomembr.* 1614, 24–35.

   doi:10.1016/S0005-2736(03)00160-3.

Biggerstaff, M., Cauchemez, S., Reed, C., Gambhir, M., and Finelli, L. (2014). Estimates of the reproduction number for seasonal, pandemic, and zoonotic influenza: A systematic review of the literature. *BMC Infect. Dis.* 14, 1–20. doi:10.1186/1471-2334-14-480.

Biswas, S. K., Boutz, P. L., and Nayak, D. P. (1998). Influenza Virus Nucleoprotein Interacts with Influenza Virus Polymerase Proteins. *J. Virol.* 72, 5493–5501.

Biswas, S. K., and Nayak, D. P. (1994). Mutational analysis of the conserved motifs of influenza A virus polymerase basic protein 1. *J. Virol.* 68, 1819–1826. doi:10.1128/jvi.68.3.1819-1826.1994.

Bizebard, T., Gigant, B., Rigolet, P., Rasmussen, B., Diat, O., Böseckei, P., et al. (1995). Structure of influenza virus haemagglutinin complexed with a neutralizing antibody. *Nature* 376, 92–94. doi:10.1038/376092a0.

Blaas, D., Patzelt, E., and Kuechler, E. (1982). Identification of the cap binding protein of influenza virus. *Nucleic Acids Res.* 10, 4803–4812.

Blanchard, E. L., Vanover, D., Bawage, S. S., Tiwari, P. M., Rotolo, L., Beyersdorf, J., et al. (2021). Treatment of influenza and SARS-CoV-2 infections via mRNA-encoded Cas13a in rodents. *Nat. Biotechnol.* doi:10.1038/s41587-021-00822-w.

Bokar, J. A., Rath-Shambaugh, M. E., Ludwiczak, R., Narayan, P., and Rottman, F. (1994). Characterization and partial purification of mRNA N6-adenosine methyltransferase from HeLa cell nuclei. Internal mRNA methylation requires a multisubunit complex. *J. Biol. Chem.* 269, 17697–17704. doi:10.1016/s0021-9258(17)32497-3.

Bolger, A. M., Lohse, M., and Usadel, B. (2014). Trimmomatic: A flexible trimmer for Illumina sequence data. *Bioinformatics* 30, 2114–2120. doi:10.1093/bioinformatics/btu170.

Boulias, K., Toczydłowska-Socha, D., Hawley, B. R., Liberman, N., Takashima, K., Zaccara, S., et al. (2019). Identification of the m6Am Methyltransferase PCIF1 Reveals the Location and Functions of m6Am in the Transcriptome. *Mol. Cell* 75, 631-643.e8. doi:10.1016/j.molcel.2019.06.006.

Bourmakina, S. V., and García-Sastre, A. (2003). Reverse genetics studies on the filamentous morphology of influenza A virus. *J. Gen. Virol.* 84, 517–527. doi:10.1099/vir.0.18803-0.

Bouvier, N. M., and Palese, P. (2008). The biology of influenza viruses. *Vaccine* 26, 49–53. doi:10.1016/j.vaccine.2008.07.039.

Boyaval, P., Moineau, S., Romero, D. a, and Horvath, P. (2007). CRISPR Provides Acquired Resistance Against Viruses in Prokaryotes. *Science (80-.).* 315, 1709–1712.

Brand, C. M., and Skehel, J. J. (1972). Crystalline Antigen from the Influenza Virus Envelope. *Nat. new Biol.* 238, 145–147. doi:10.1038/239137a0.

Brezgin, S., Kostyusheva, A., Kostyushev, D., and Chulanov, V. (2019). Dead cas systems: Types, principles, and applications. *Int. J. Mol. Sci.* 20, 1–26. doi:10.3390/ijms20236041.

Bridgen, A., and Elliott, R. M. (1996). Rescue of a segmented negative-strand RNA

virus entirely from cloned complementary DNAs. *Proc. Natl. Acad. Sci. U. S. A.*
93, 15400–15404. doi:10.1073/pnas.93.26.15400.

Buchholz, U. J., Finke, S., and Conzelmann, K.-K. (1999). Generation of Bovine
Respiratory Syncytial Virus (BRSV) from cDNA: BRSV NS2 Is Not Essential
for Virus Replication in Tissue Culture, and the Human RSV Leader Region Acts
as a Functional BRSV Genome Promoter. *J. Virol.* 73, 251–259.
doi:10.1128/jvi.73.1.251-259.1999.

Bui, M., Wills, E. G., Helenius, A., and Whittaker, G. R. (2000). Role of the Influenza
Virus M1 Protein in Nuclear Export of Viral Ribonucleoproteins. *J. Virol.* 74,
1781–1786. doi:10.1128/jvi.74.4.1781-1786.2000.

Bujnicki, J. M., Feder, M., Radlinska, M., and Blumenthal, R. M. (2002). Structure
prediction and phylogenetic analysis of a functionally diverse family of proteins
homologous to the MT-A70 subunit of the human mRNA:m6A
methyltransferase. *J. Mol. Evol.* 55, 431–444. doi:10.1007/s00239-002-2339-8.

Burgess, H. M., Depledge, D. P., Thompson, L., Srinivas, K. P., Grande, R. C., Vink,
E. I., et al. (2021). Targeting the m6A RNA modification pathway blocks SARS-
CoV-2 and HCoV-OC43 replication. *Genes Dev.* 35, 1005–1019.
doi:10.1101/GAD.348320.121.

Canaani, D., Kahana, C., Lavi, S., and Groner, Y. (1979). Identification and mapping
of N6-methyladenosine containing sequences in Simian Virus 40 RNA. *Nucleic
Acids Res.* 6, 2879–2899.

Cao, Y., Zhuang, Y., Chen, J., Xu, W., Shou, Y., Huang, X., et al. (2019). Dynamic

effects of Fto in regulating the proliferation and differentiation of adult neural stem cells of mice. *Hum. Mol. Genet.*

Carr, C. M., and Kim, P. S. (1993). A spring-loaded mechanism for the conformational change of influenza hemagglutinin. *Cell* 73, 823–832. doi:10.1016/0092-8674(93)90260-W.

Cerrudo, C. S., Ghiringhelli, P. D., and Gomez, D. E. (2014). Protein universe containing a PUA RNA-binding domain. *FEBS J.* 281, 74–87.

Chao, Y., Shang, J., and Ji, W. (2020). ALKBH5-m6A-FOXM1 signaling axis promotes proliferation and invasion of lung adenocarcinoma cells under intermittent hypoxia. *Biochem. Biophys. Res. Commun.* 521, 499–506. doi:10.1016/j.bbrc.2019.10.145.

Chen, H., Angel, M., Li, W., Finch, C., Gonzalez, A. S., Sutton, T., et al. (2014). All-in-One Bacmids: an Efficient Reverse Genetics Strategy for Influenza A Virus Vaccines. *J. Virol.* 88, 10013–10025. doi:10.1128/jvi.01468-14.

Chen, J., Jin, L., Wang, Z., Wang, L., Chen, Q., Cui, Y., et al. (2020). N6-methyladenosine regulates PEDV replication and host gene expression. *Virology* 548, 59–72. doi:10.1016/j.virol.2020.06.008.

Chen, J., Lee, K. H., Steinhauer, D. A., Stevens, D. J., Skehel, J. J., and Wiley, D. C. (1998). Structure of the hemagglutinin precursor cleavage site, a determinant of influenza pathogenicity and the origin of the labile conformation. *Cell* 95, 409–417. doi:10.1016/S0092-8674(00)81771-7.

Chen, K., Lu, Z., Wang, X., Fu, Y., Luo, G. Z., Liu, N., et al. (2015). High-resolution N6-methyladenosine (m6A) map using photo-crosslinking-assisted m6A sequencing. *Angew. Chemie - Int. Ed.* 54, 1587–1590. doi:10.1002/anie.201410647.

Chen, W., Calvo, P. A., Malide, D., Gibbs, J., Schubert, U., Bacik, I., et al. (2001). A novel influenza A virus mitochondrial protein that induces cell death. *Nat. Med.* 7, 1306–1312. doi:10.1038/nm1201-1306.

Chen, Z., Li, Y., and M.Krug, R. (1999). Influenza A virus NS1 protein targets poly(A)-binding protein II of the cellular 3'-end processing machinery. *EMBO J.* 18, 2273–2283.

Cheung, C. Y., Poon, L. L. M., Lau, A. S., Luk, W., Lau, Y. L., Shortridge, K. F., et al. (2002). Induction of proinflammatory cytokines in human macrophages by influenza A (H5N1) viruses: A mechanism for the unusual severity of human disease? *Lancet* 360, 1831–1837. doi:10.1016/S0140-6736(02)11772-7.

Choe, J., Lin, S., Zhang, W., Liu, Q., Wang, L., Ramirez-Moya, J., et al. (2018). mRNA circularization by METTL3–eIF3h enhances translation and promotes oncogenesis. *Nature* 561, 556–560. doi:10.1038/s41586-018-0538-8.

Choi, S. Y., Choi, M. J., Cho, M. Y., and Park, Y. J. (2019). Alkbh5, a RNA Demethylase, Is Involved in Fine-tuning of Cell Differentiation (FS11-07-19). *Curr. Dev. Nutr.* 3, 7051274. doi:10.1093/cdn/nzz037.fs11-07-19.

Choudhary, C., Kumar, C., Gnad, F., Nielsen, M. L., Rehman, M., Walther, T. C., et al. (2009). Lysine acetylation targets protein complexes and co-regulates major

cellular functions. *Science (80-.).* 325, 834–840. doi:10.1126/science.1175371.

Cohen, S. N., Chang, A. C., and Hsu, L. (1972). Nonchromosomal antibiotic resistance in bacteria: genetic transformation of Escherichia coli by R-factor DNA. *Proc. Natl. Acad. Sci. U. S. A.* 69, 2110–2114. doi:10.1073/pnas.69.8.2110.

Cohn, W. E. (1960). Pseudouridine, a carbon-carbon linked ribonucleoside in ribonucleic acids: isolation, structure, and chemical characteristics. *J. Biol. Chem.* 235, 1488–1498. doi:10.1016/s0021-9258(18)69432-3.

Cong, L., Ran, F. A., Cox, D., Lin, S., Barretto, R., Hsu, P. D., et al. (2013). Multiplex Genome Engineering Using CRISPR/Cas Systems. *Science* 339, 819–823. doi:10.1126/science.1231143.Multiplex.

Courtney, D. G., Chalem, A., Bogerd, H. P., Law, B. A., Kennedy, E. M., Holley, C. L., et al. (2019a). Extensive epitranscriptomic methylation of A and C residues on murine leukemia virus transcripts enhances viral gene expression. *MBio* 10. doi:10.1128/mBio.01209-19.

Courtney, D. G., Kennedy, E. M., Dumm, R. E., Bogerd, H. P., Tsai, K., Heaton, N. S., et al. (2017). Epitranscriptomic Enhancement of Influenza A Virus Gene Expression and Replication. *Cell Host Microbe* 22, 377-386.e5. doi:10.1016/j.chom.2017.08.004.

Courtney, D. G., Tsai, K., Bogerd, H. P., Kennedy, E. M., Law, B. A., Emery, A., et al. (2019b). Epitranscriptomic Addition of m5C to HIV-1 Transcripts Regulates Viral Gene Expression. *Cell Host Microbe* 26, 217-227.e6. doi:10.1016/j.chom.2019.07.005.

Cox, D. B. T., Gootenberg, J. S., Abudayyeh, O. O., Franklin, B., Kellner, M. J., Joung, J., et al. (2017). RNA editing with CRISPR-Cas13. *Science (80-.).* 358, 1019–1027. doi:10.1126/science.aaq0180.

Cox, N. J., Neumann, G., Donis, R. O., and Kawaoka, Y. (2007). Orthomyxoviruses: Influenza. *Med. Microbiol. Eighteenth Ed.*, 634–698. doi:10.1016/B978-0-7020-4089-4.00064-0.

Cox, N. J., and Subbarao, K. (1999). Influenza. *Lancet* 354, 1277–1282. doi:10.1016/S0140-6736(99)01241-6.

Cox, N. J., and Subbarao, K. (2000). Global epidemiology of influenza: past and present. *Annu. Rev. Med.* 51, 407–421.

Crooks, G., Hon, G., Chandonia, J., and Brenner, S. (2004). WebLogo: a sequence logo generator. *Genome Res* 14, 1188–1190. doi:10.1101/gr.849004.1.

Cross, K., Langley, W., Russell, R., Skehel, J., and Steinhauer, D. (2009). Composition and Functions of the Influenza Fusion Peptide. *Protein Pept. Lett.* 16, 766–778. doi:10.2174/092986609788681715.

Cui, J., Techakriengkrai, N., Nedumpun, T., and Suradhat, S. (2020). Abrogation of PRRSV infectivity by CRISPR-Cas13b-mediated viral RNA cleavage in mammalian cells. *Sci. Rep.* 10, 9617. doi:10.1038/s41598-020-66775-3.

Dai, D. L., Li, X., Wang, L., Xie, C., Jin, Y., Zeng, M. S., et al. (2021). Identification of an N6-methyladenosine-mediated positive feedback loop that promotes Epstein-Barr virus infection. *J. Biol. Chem.* 296, 100547.

doi:10.1016/j.jbc.2021.100547.

Dang, W., Xie, Y., Cao, P., Xin, S., Wang, J., Li, S., et al. (2019). N6-Methyladenosine and Viral Infection. *Front. Microbiol.* 10, 1–12. doi:10.3389/fmicb.2019.00417.

De Clercq, E., and Li, G. (2016). Approved antiviral drugs over the past 50 years. *Clin. Microbiol. Rev.* 29, 695–747. doi:10.1128/CMR.00102-15.

de la Luna, S., Martínez, C., and Ortín, J. (1989). Molecular cloning and sequencing of influenza virus A/Victoria/3/75 polymerase genes: sequence evolution and prediction of possible functional domains. *Virus Res.* 13, 143–155. doi:10.1016/0168-1702(89)90012-9.

De Vlugt, C., Sikora, D., and Pelchat, M. (2018). Insight into influenza: A virus cap-snatching. *Viruses* 10. doi:10.3390/v10110641.

Deltcheva, E., Chylinski, K., Sharma, C. M., Gonzales, K., Chao, Y., Pirzada, Z. A., et al. (2011). CRISPR RNA maturation by trans-encoded small RNA and host factor RNase III. *Nature* 471, 602–607. doi:10.1038/nature09886.

Deng, X., Chen, K., Luo, G. Z., Weng, X., Ji, Q., Zhou, T., et al. (2015). Widespread occurrence of N6-methyladenosine in bacterial mRNA. *Nucleic Acids Res.* 43, 6557–6567. doi:10.1093/nar/gkv596.

Deng, X., Su, R., Feng, X., Wei, M., and Chen, J. (2018a). Role of N 6 -methyladenosine modification in cancer. *Curr. Opin. Genet. Dev.* 48, 1–7. doi:10.1016/j.gde.2017.10.005.

Deng, X., Su, R., Stanford, S., and Chen, J. (2018b). Critical Enzymatic Functions of FTO in Obesity and Cancer. *Front. Endocrinol. (Lausanne).* 9, 1–7. doi:10.3389/fendo.2018.00396.

Desrosiers, R., Friderici, K., and Rottman, F. (1974). Identification of methylated nucleosides in messenger RNA from Novikoff hepatoma cells. *Proc. Natl. Acad. Sci. U. S. A.* 71, 3971–3975. doi:10.1073/pnas.71.10.3971.

Dias, A., Bouvier, D., Crépin, T., McCarthy, A. A., Hart, D. J., Baudin, F., et al. (2009). The cap-snatching endonuclease of influenza virus polymerase resides in the PA subunit. *Nature* 458, 914–918. doi:10.1038/nature07745.

Digard, P., Blok, V. C., and Inglis, S. C. (1989). Complex Formation between Influenza Virus Polymerase Proteins Expressed in Xenopus Oocytes. *Virology* 171, 162–169.

Ding, C., Zou, Q., Ding, J., Ling, M., Wang, W., Li, H., et al. (2018). Increased N6-methyladenosine causes infertility is associated with FTO expression. *J. Cell. Physiol.* 233, 7055–7066. doi:10.1002/jcp.26507.

Dixit, D., Xie, Q., Rich, J. N., and Zhao, J. C. (2017). Messenger RNA Methylation Regulates Glioblastoma Tumorigenesis. *Cancer Cell* 31, 474–475. doi:10.1016/j.ccell.2017.03.010.

Dominissini, D., Moshitch-Moshkovitz, S., Schwartz, S., Salmon-Divon, M., Ungar, L., Osenberg, S., et al. (2012). Topology of the human and mouse m6A RNA methylomes revealed by m6A-seq. *Nature* 485, 201–206. doi:10.1038/nature11112.

Dominissini, D., Nachtergaele, S., Moshitch-Moshkovitz, S., Peer, E., Kol, N., Ben-Haim, M. S., et al. (2016). The dynamic N1 -methyladenosine methylome in eukaryotic messenger RNA. *Nature* 530, 441–446. doi:10.1038/nature16998.

Doms, R. W., Lamb, R. A., Rose, J. K., and Helenius, A. (1993). Folding and assembly of viral membrane proteins. *Virology* 193, 545–562. doi:10.1006/viro.1993.1164.

Dou, D., Revol, R., Östbye, H., Wang, H., and Daniels, R. (2018). Influenza A virus cell entry, replication, virion assembly and movement. *Front. Immunol.* 9, 1–17. doi:10.3389/fimmu.2018.01581.

Doudna, J. A. (2020). The promise and challenge of therapeutic genome editing. *Nature* 578, 229–236. doi:10.1038/s41586-020-1978-5.

Doxtader, K. A., Wang, P., Scarborough, A. M., Seo, D., Conrad, N. K., and Nam, Y. (2018). Structural Basis for Regulation of METTL16, an S-Adenosylmethionine Homeostasis Factor. *Mol. Cell* 71, 1001-1011.e4. doi:10.1016/j.molcel.2018.07.025.

Drummond, A. J., Suchard, M. A., Xie, D., and Rambaut, A. (2012). Bayesian phylogenetics with BEAUti and the BEAST 1.7. *Mol. Biol. Evol.* 29, 1969–1973. doi:10.1093/molbev/mss075.

Du, H., Zhao, Y., He, J., Zhang, Y., Xi, H., Liu, M., et al. (2016). YTHDF2 destabilizes m 6 A-containing RNA through direct recruitment of the CCR4-NOT deadenylase complex. *Nat. Commun.* 7. doi:10.1038/ncomms12626.

Du, M., Jillette, N., Zhu, J. J., Li, S., and Cheng, A. W. (2020). CRISPR artificial splicing factors. *Nat. Commun.* 11, 1–11. doi:10.1038/s41467-020-16806-4.

Durbin, A. P., Hall, S. L., Siew, J. W., Whitehead, S. S., Collins, P. L., and Murphy, B. R. (1997). Recovery of infectious human parainfluenza virus type 3 from cDNA. *Virology* 235, 323–332. doi:10.1006/viro.1997.8697.

East-Seletsky, A., O'Connell, M. R., Knight, S. C., Burstein, D., Cate, J. H. D., Tjian, R., et al. (2016). Two distinct RNase activities of CRISPR-C2c2 enable guide-RNA processing and RNA detection. *Nature* 538, 270–273. doi:10.1038/nature19802.

Edupuganti, R. R., Geiger, S., Lindeboom, R. G. H., Shi, H., Hsu, P. J., Lu, Z., et al. (2017). N6-methyladenosine (m6A) recruits and repels proteins to regulate mRNA homeostasis. *Nat. Struct. Mol. Biol.* 24, 870–878. doi:10.1038/nsmb.3462.

Ekiert, D. C., and Wilson, I. A. (2012). Broadly neutralizing antibodies against influenza virus and prospects for universal therapies. *Curr. Opin. Virol.* 2, 134–141. doi:10.1016/j.coviro.2012.02.005.

Enami, M., Luytjes, W., Krystal, M., and Palese, P. (1990). Introduction of site-specific mutations into the genome of influenza virus. *Proc. Natl. Acad. Sci. U. S. A.* 87, 3802–3805. doi:10.1073/pnas.87.10.3802.

Enami, M., and Palese, P. (1991). High-efficiency formation of influenza virus transfectants. *J. Virol.* 65, 2711–2713. doi:10.1128/jvi.65.5.2711-2713.1991.

Engelhardt, O. G. (2013). Many ways to make an influenza virus - review of influenza virus reverse genetics methods. *Influenza Other Respi. Viruses* 7, 249–256. doi:10.1111/j.1750-2659.2012.00392.x.

Engelhardt, O. G., Smith, M., and Fodor, E. (2005). Association of the Influenza A Virus RNA-Dependent RNA Polymerase with Cellular RNA Polymerase II. *J. Virol.* 79, 5812–5818. doi:10.1128/jvi.79.9.5812-5818.2005.

Ensfelder, T. T., Kurz, M. Q., Iwan, K., Geiger, S., Matheisl, S., Müller, M., et al. (2018). ALKBH5-induced demethylation of mono- and dimethylated adenosine. *Chem. Commun.* 54, 8591–8593. doi:10.1039/c8cc03980a.

Feng, C., Liu, Y., Wang, G., Deng, Z., Zhang, Q., Wu, W., et al. (2014). Crystal structures of the human RNA demethylase alkbh5 reveal basis for substrate recognition. *J. Biol. Chem.* 289, 11571–11583. doi:10.1074/jbc.M113.546168.

Feng, Z., Zhou, F., Tan, M., Wang, T., Chen, Y., Xu, W., et al. (2021). Targeting m6A modification inhibits herpes virus 1 infection. *Genes Dis.* doi:10.1016/j.gendis.2021.02.004.

Fodor, E., Devenish, L., Engelhardt, O. G., Palese, P., Brownlee, G. G., and García-Sastre, A. (1999). Rescue of Influenza A Virus from Recombinant DNA. *J. Virol.* 73, 9679–9682. doi:10.1128/jvi.73.11.9679-9682.1999.

Fodor, E., Mingay, L. J., Crow, M., Deng, T., and Brownlee, G. G. (2003). A Single Amino Acid Mutation in the PA Subunit of the Influenza Virus RNA Polymerase Promotes the Generation of Defective Interfering RNAs. *J. Virol.* 77, 5017–5020. doi:10.1128/jvi.77.8.5017-5020.2003.

Fodor, E., Pritlove, D. C., and Brownlee, G. G. (1995). Characterization of the RNA-fork model of virion RNA in the initiation of transcription in influenza A virus. *J. Virol.* 69, 4012–4019. doi:10.1128/jvi.69.7.4012-4019.1995.

Fodor, E., and Smith, M. (2004). The PA Subunit Is Required for Efficient Nuclear Accumulation of the PB1 Subunit of the Influenza A Virus RNA Polymerase Complex. *J. Virol.* 78, 9144–9153. doi:10.1128/jvi.78.17.9144-9153.2004.

Fortin, D. A., Tillo, S. E., Yang, G., Rah, J. C., Melander, J. B., Bai, S., et al. (2014). Live imaging of endogenous PSD-95 using ENABLED: A conditional strategy to fluorescently label endogenous proteins. *J. Neurosci.* 34, 16698–16712. doi:10.1523/JNEUROSCI.3888-14.2014.

Fouchier, R. A. M., Munster, V., Wallensten, A., Bestebroer, T. M., Herfst, S., Smith, D., et al. (2005). Characterization of a Novel Influenza A Virus Hemagglutinin Subtype (H16) Obtained from Black-Headed Gulls. *J. Virol.* 79, 2814–2822. doi:10.1128/jvi.79.5.2814-2822.2005.

Fouchier, R. A. M., Schneeberger, P. M., Rozendaal, F. W., Broekman, J. M., Kemink, S. A. G., Munstert, V., et al. (2004). Avian influenza A virus (H7N7) associated with human conjunctivitis and a fatal case of acute respiratory distress syndrome. *Proc. Natl. Acad. Sci. U. S. A.* 101, 1356–1361. doi:10.1073/pnas.0308352100.

Frazer, K. A., Elnitski, L., Church, D. M., Dubchak, I., and Hardison, R. C. (2003). Cross-species sequence comparisons: a review of methods and available resources. *Genome Res.* 13, 1–12. doi:10.1101/gr.222003.

Freije, C. A., Myhrvold, C., Boehm, C. K., Lin, A. E., Welch, N. L., Carter, A., et al. (2019). Programmable Inhibition and Detection of RNA Viruses Using Cas13. *Mol. Cell* 76, 1–12. doi:10.1016/J.MOLCEL.2019.09.013.

Fu, Y., Jia, G., Pang, X., Wang, R. N., Wang, X., Li, C. J., et al. (2013). FTO-mediated formation of N6-hydroxymethyladenosine and N 6-formyladenosine in mammalian RNA. *Nat. Commun.* 4, 2–9. doi:10.1038/ncomms2822.

Furlong, R. F. (2005). Insights into vertebrate evolution from the chicken genome sequence. *Genome Biol.* 6, 2–4. doi:10.1186/gb-2005-6-2-207.

Gambaryan, A. S., Tuzikov, A. B., Piskarev, V. E., Yamnikova, S. S., Lvov, D. K., Robertson, J. S., et al. (1997). Specification of receptor-binding phenotypes of influenza virus isolates from different hosts using synthetic sialylglycopolymers: Non-egg-adapted human H1 and H3 influenza A and influenza B viruses share a common high binding affinity for 6'-sialyl(N-ace. *Virology* 232, 345–350. doi:10.1006/viro.1997.8572.

Gao, H., Sun, Y., Hu, J., Qi, L., Wang, J., Xiong, X., et al. (2015). The contribution of PA-X to the virulence of pandemic 2009 H1N1 and highly pathogenic H5N1 avian influenza viruses. *Sci. Rep.* 5, 1–11. doi:10.1038/srep08262.

Gao, Y., Hisey, E., Bradshaw, T. W. A., Erata, E., Brown, W. E., Courtland, J. L., et al. (2019). Plug-and-Play Protein Modification Using Homology-Independent Universal Genome Engineering. *Neuron* 103, 583-597.e8. doi:10.1016/j.neuron.2019.05.047.

Gatherer, D. (2009). The 2009 H1N1 influenza outbreak in its historical context. *J.*

Clin. Virol. 45, 174–178. doi:10.1016/j.jcv.2009.06.004.

Gerken, T., Girard, C. A., Tung, Y. C. L., Webby, C. J., Saudek, V., Hewitson, K. S., et al. (2007). The obesity-associated FTO gene encodes a 2-oxoglutarate-dependent nucleic acid demethylase. *Science (80-.).* 318, 1469–1472. doi:10.1126/science.1151710.

Gill, J. R., Sheng, Z., Ely, S. F., Jr, D. G. G., and Beasley, M. B. (2010). Pulmonary Pathologic Findings of Fatal 2009 Pandemic. *Arch. Pathol. Lab. Med.* 134, 235–243. Available at: http://www.ncbi.nlm.nih.gov/pmc/articles/PMC2819217/.

Gokhale, N. S., McIntyre, A. B. R., Mattocks, M. D., Holley, C. L., Lazear, H. M., Mason, C. E., et al. (2020). Altered m6A Modification of Specific Cellular Transcripts Affects Flaviviridae Infection. *Mol. Cell* 77, 542-555.e8. doi:10.1016/j.molcel.2019.11.007.

Gokhale, N. S., McIntyre, A. B. R., McFadden, M. J., Roder, A. E., Kennedy, E. M., Gandara, J. A., et al. (2016). N6-Methyladenosine in Flaviviridae Viral RNA Genomes Regulates Infection. *Cell Host Microbe* 20, 654–665. doi:10.1016/j.chom.2016.09.015.

Gómez-Puertas, P., Albo, C., Pérez-Pastrana, E., Vivo, A., and Portela, A. (2000). Influenza Virus Matrix Protein Is the Major Driving Force in Virus Budding. *J. Virol.* 74, 11538–11547. doi:10.1128/jvi.74.24.11538-11547.2000.

González, S., Zürcher, T., and Ortín, J. (1996). Identification of two separate domains in the influenza virus PB1 protein involved in the interaction with the PB2 and PA subunits: A model for the viral RNA polymerase structure. *Nucleic Acids Res.*

24, 4456–4463. doi:10.1093/nar/24.22.4456.

Gootenberg, J. S., Abudayyeh, O. O., Kellner, M. J., Joung, J., Collins, J. J., and

Zhang, F. (2018). Multiplexed and portable nucleic acid detection platform with

Cas13, Cas12a and Csm6. *Science (80-.).* 360, 439–444.

doi:10.1126/science.aaq0179.

Gootenberg, J. S., Abudayyeh, O. O., Lee, J. W., Essletzbichler, P., Dy, A. J., Joung,

J., et al. (2017). Nucleic acid detection with CRISPR-Cas13a/C2c2. *Science (80-.

).* 356, 438–442. doi:10.1126/science.aam9321.

Gordon, D. E., Hiatt, J., Bouhaddou, M., Rezelj, V. V., Ulferts, S., Braberg, H., et al.

(2020a). Comparative host-coronavirus protein interaction networks reveal pan-

viral disease mechanisms. *Science (80-.).* 370. doi:10.1126/science.abe9403.

Gordon, D. E., Jang, G. M., Bouhaddou, M., Xu, J., Obernier, K., White, K. M., et al.

(2020b). A SARS-CoV-2 protein interaction map reveals targets for drug

repurposing. *Nature*. doi:10.1038/s41586-020-2286-9.

Gray, K. A., Yates, B., Seal, R. L., Wright, M. W., and Bruford, E. A. (2015).

Genenames.org: The HGNC resources in 2015. *Nucleic Acids Res.* 43, D1079–

D1085. doi:10.1093/nar/gku1071.

Green, M. R., and Sambrook, J. (2012). *Molecular Cloning: A Laboratory Manual,

4th Edition*. doi:10.3724/SP.J.1141.2012.01075.

Ha, Y., Stevens, D. J., Skehel, J. J., and Wiley, D. C. (2001). X-ray structures of H5

avian and H9 swine influenza virus hemagglutinins bound to avian and human

receptor analogs. *Proc. Natl. Acad. Sci. U. S. A.* 98, 11181–11186. doi:10.1073/pnas.201401198.

Hafner, M., Landthaler, M., Burger, L., Khorshid, M., Hausser, J., Berninger, P., et al. (2010). Transcriptome-wide Identification of RNA-Binding Protein and MicroRNA Target Sites by PAR-CLIP. *Cell* 141, 129–141. doi:10.1016/j.cell.2010.03.009.

Hale, B. G., Randall, R. E., Ortin, J., and Jackson, D. (2008). The multifunctional NS1 protein of influenza A viruses. *J. Gen. Virol.* 89, 2359–2376. doi:10.1099/vir.0.2008/004606-0.

Hall, T. A. (1999). BioEdit: a user-friendly biological sequence alignment editor and analysis program for Windows 95/98/NT. *Nucleic Acids Symp. Ser.* 41, 95–98. doi:citeulike-article-id:691774.

Han, Z., Niu, T., Chang, J., Lei, X., Zhao, M., Wang, Q., et al. (2010). Crystal structure of the FTO protein reveals basis for its substrate specificity. *Nature* 464, 1205–1209. doi:10.1038/nature08921.

Hao, H., Hao, S., Chen, H., Chen, Z., Zhang, Y., Wang, J., et al. (2019). N6-methyladenosine modification and METTL3 modulate enterovirus 71 replication. *Nucleic Acids Res.* 47, 362–374. doi:10.1093/nar/gky1007.

Harrison, S. C. (2008). Viral membrane fusion. *Nat. Struct. Mol. Biol.* 15, 690–698. doi:10.1038/nsmb.1456.

Hashimoto, S. I., and Green, M. (1976). Multiple methylated cap sequences in

adenovirus type 2 early mRNA. *J. Virol.* 20, 425–435. doi:10.1128/jvi.20.2.425-435.1976.

Hatta, H., Gao, P., Halfmann, P., and Kawaoka, Y. (2001). Molecular basis for high virulence of Hong Kong H5N1 influenza a viruses. *Science (80-.).* 293, 1840–1842. doi:10.1126/science.1062882.

He, M., and Huang, Z. J. (2018). Genetic approaches to access cell types in mammalian nervous systems. *Curr. Opin. Neurobiol.* 50, 109–118. doi:10.1016/j.conb.2018.02.003.

He, Y., Hu, H., Wang, Y., Yuan, H., Lu, Z., Wu, P., et al. (2018). ALKBH5 Inhibits Pancreatic Cancer Motility by Decreasing Long Non-Coding RNA KCNK15-AS1 Methylation. *Cell. Physiol. Biochem.* 48, 838–846. doi:10.1159/000491915.

Hegde, N. R. (2015). Cell culture-based influenza vaccines: A necessary and indispensable investment for the future. *Hum. Vaccines Immunother.* 11, 1223–1234. doi:10.1080/21645515.2015.1016666.

Heidenreich, M., and Zhang, F. (2016). Applications of CRISPR-Cas systems in neuroscience. *Nat. Rev. Neurosci.* 17, 36–44. doi:10.1038/nrn.2015.2.

Heinz, S., Benner, C., Spann, N., Bertolino, E., Lin, Y. C., Laslo, P., et al. (2010). Simple Combinations of Lineage-Determining Transcription Factors Prime cis-Regulatory Elements Required for Macrophage and B Cell Identities. *Mol. Cell* 38, 576–589. doi:10.1016/j.molcel.2010.05.004.

Helm, M., and Motorin, Y. (2017). Detecting RNA modifications in the

epitranscriptome: Predict and validate. *Nat. Rev. Genet.* 18, 275–291. doi:10.1038/nrg.2016.169.

Herzog, E., Nadrigny, F., Silm, K., Biesemann, C., Helling, I., Bersot, T., et al. (2011). In vivo imaging of intersynaptic vesicle exchange using VGLUT1 Venus knock-in mice. *J. Neurosci.* 31, 15544–15559. doi:10.1523/JNEUROSCI.2073-11.2011.

Hesser, C. R., Karijolich, J., Dominissini, D., He, C., and Glaunsinger, B. A. (2018). N6-methyladenosine modification and the YTHDF2 reader protein play cell type specific roles in lytic viral gene expression during Kaposi's sarcoma-associated herpesvirus infection. *PLoS Pathog.* 14, 1–23. doi:10.1371/journal.ppat.1006995.

Hillier, L. W., Miller, W., Birney, E., Warren, W., Hardison, R. C., Ponting, C. P., et al. (2004). Sequence and comparative analysis of the chicken genome provide unique perspectives on vertebrate evolution. *Nature* 432, 695–716. doi:10.1038/nature03154.

Hoffmann, E., Neumann, G., Kawaoka, Y., Hobom, G., and Webster, R. G. (2000). A DNA transfection system for generation of influenza A virus from eight plasmids. *Proc. Natl. Acad. Sci. U. S. A.* 97, 6108–6113. doi:10.1073/pnas.100133697.

Holley, R. W., Everett, G. A., Madison, J. T., and Zamir, A. (1965). Nucleotide Sequences in the Yeast Alanine Transfer Ribonucleic Acid. *J. Biol. Chem.* 240, 2122–2128. doi:10.1016/s0021-9258(18)97435-1.

Honda, A., Mizumoto, K., and Ishihama, A. (2002). Minimum molecular architectures for transcription and replication of the influenza virus. *Proc. Natl. Acad. Sci. U.*

S. A. 99, 13166–13171. doi:10.1073/pnas.152456799.

Horimoto, T., and Kawaoka, Y. (1994). Reverse genetics provides direct evidence for a correlation of hemagglutinin cleavability and virulence of an avian influenza A virus. *J. Virol.* 68, 3120–3128. doi:10.1128/jvi.68.5.3120-3128.1994.

Horimoto, T., and Kawaoka, Y. (2001). Pandemic threat posed by avian influenza A viruses. *Clin. Microbiol. Rev.* 14, 129–149. doi:10.1128/CMR.14.1.129-149.2001.

Horiuchi, K., Kawamura, T., Iwanari, H., Ohashi, R., Naito, M., Kodama, T., et al. (2013). Identification of Wilms' tumor 1-associating protein complex and its role in alternative splicing and the cell cycle. *J. Biol. Chem.* 288, 33292–33302. doi:10.1074/jbc.M113.500397.

Houser, K., and Subbarao, K. (2015). Influenza vaccines: Challenges and solutions. *Cell Host Microbe* 17, 295–300. doi:10.1016/j.chom.2015.02.012.

Hsu, P. J., Zhu, Y., Ma, H., Guo, Y., Shi, X., Liu, Y., et al. (2017). Ythdc2 is an N6 - methyladenosine binding protein that regulates mammalian spermatogenesis. *Cell Res.* 27, 1115–1127. doi:10.1038/cr.2017.99.

Huang, H., Weng, H., and Chen, J. (2020). m6A Modification in Coding and Non-coding RNAs: Roles and Therapeutic Implications in Cancer. *Cancer Cell* 37, 270–288. doi:10.1016/j.ccell.2020.02.004.

Huang, H., Weng, H., Sun, W., Qin, X., Shi, H., Wu, H., et al. (2018). Recognition of RNA N 6 -methyladenosine by IGF2BP proteins enhances mRNA stability and

translation. *Nat. Cell Biol.* 20, 285–295. doi:10.1038/s41556-018-0045-z.

Huang, J., and Yin, P. (2018). Structural Insights into N6-methyladenosine (m6A) Modification in the Transcriptome. *Genomics, Proteomics Bioinforma.* 16, 85–98. doi:10.1016/j.gpb.2018.03.001.

Huang, T. S., Palese, P., and Krystal, M. (1990). Determination of influenza virus proteins required for genome replication. *J. Virol.* 64, 5669–5673. doi:10.1128/jvi.64.11.5669-5673.1990.

Huang, X., Liu, T., Muller, J., Levandowski, R. A., and Ye, Z. (2001). Effect of influenza virus matrix protein and viral RNA on ribonucleoprotein formation and nuclear export. *Virology* 287, 405–416. doi:10.1006/viro.2001.1067.

Huang, Y., Su, R., Sheng, Y., Dong, L., Dong, Z., Xu, H., et al. (2019). Small-molecule targeting of oncogenic FTO demethylase in acute myeloid leukemia. *Cancer Cell* 35, 677–691. doi:10.1016/j.ccell.2019.03.006.Small-molecule.

Iles, M. M., Law, M. H., Stacey, S. N., Han, J., Fang, S., Pfeiffer, R., et al. (2013). A variant in FTO shows association with melanoma risk not due to BMI. *Nat. Genet.* 45, 428–432. doi:10.1038/ng.2571.

Imai, M., Watanabe, T., Hatta, M., Das, S. C., Ozawa, M., Shinya, K., et al. (2012). Experimental adaptation of an influenza H5 HA confers respiratory droplet transmission to a reassortant H5 HA/H1N1 virus in ferrets. *Nature* 486, 420–428. doi:10.1038/nature10831.

Imam, H., Khan, M., Gokhale, N. S., McIntyre, A. B. R., Kim, G. W., Jang, J. Y., et

al. (2018). N6-methyladenosine modification of hepatitis b virus RNA differentially regulates the viral life cycle. *Proc. Natl. Acad. Sci. U. S. A.* 115, 8829–8834. doi:10.1073/pnas.1808319115.

Int, C., Chen, S., Zhou, L., and Wang, Y. (2020). ALKBH5 - mediated - m 6 A demethylation of lncRNA PVT1 plays an oncogenic role in osteosarcoma. *Cancer Cell Int.*, 1–10. doi:10.1186/s12935-020-1105-6.

Irwin, K. K., Renzette, N., Kowalik, T. F., and Jensen, J. D. (2016). Antiviral drug resistance as an adaptive process. *Virus Evol.* 2, 1–10. doi:10.1093/ve/vew014.

Ivashkiv, L. B., and Donlin, L. T. (2014). Regulation of type i interferon responses. *Nat. Rev. Immunol.* 14, 36–49. doi:10.1038/nri3581.

Iwai, A., Shiozaki, T., Kawai, T., Akira, S., Kawaoka, Y., Takada, A., et al. (2010). Influenza A virus polymerase inhibits type I interferon induction by binding to interferon β promoter stimulator 1. *J. Biol. Chem.* 285, 32064–32074. doi:10.1074/jbc.M110.112458.

Iyer, L. M., Zhang, D., and Aravind, L. (2016). Adenine methylation in eukaryotes: Apprehending the complex evolutionary history and functional potential of an epigenetic modification. *BioEssays* 38, 27–40. doi:10.1002/bies.201500104.

Jansen, R., Van Embden, J. D. A., Gaastra, W., and Schouls, L. M. (2002). Identification of genes that are associated with DNA repeats in prokaryotes. *Mol. Microbiol.* 43, 1565–1575. doi:10.1046/j.1365-2958.2002.02839.x.

Jia, G., Fu, Y., Zhao, X., Dai, Q., Zheng, G., Yang, Y., et al. (2011). N6-

Methyladenosine in nuclear RNA is a major substrate of the obesity-associated FTO. *Nat. Chem. Biol.* 7, 885–887. doi:10.1038/nchembio.687.

Jia, G., Yang, C. G., Yang, S., Jian, X., Yi, C., Zhou, Z., et al. (2008). Oxidative demethylation of 3-methylthymine and 3-methyluracil in single-stranded DNA and RNA by mouse and human FTO. *FEBS Lett.* 582, 3313–3319. doi:10.1016/j.febslet.2008.08.019.

Jiang, X., Liu, B., Nie, Z., Duan, L., Xiong, Q., Jin, Z., et al. (2021). The role of m6A modification in the biological functions and diseases. *Signal Transduct. Target. Ther.* 6. doi:10.1038/s41392-020-00450-x.

Jin, H., Leser, G. P., Zhang, J., and Lamb, R. A. (1997). Influenza virus hemagglutinin and neuraminidase cytoplasmic tails control particle shape. *EMBO J.* 16, 1236–1247. doi:10.1093/emboj/16.6.1236.

Jin, H., Ying, X., Que, B., Wang, X., Chao, Y., Zhang, H., et al. (2019). N6-methyladenosine modification of ITGA6 mRNA promotes the development and progression of bladder cancer. *EBioMedicine* 47, 195–207. doi:10.1016/j.ebiom.2019.07.068.

Jinek, M., Chylinski, K., Fonfara, I., Hauer, M., Doudna, J. A., and Charpentier, E. (2012). A Programmable Dual-RNA – Guided DNA Endonuclease in Adaptive Bacterial Immunity. 337, 816–822.

Jing, X., Xie, B., Chen, L., Zhang, N., Jiang, Y., Qin, H., et al. (2018). Implementation of the CRISPR-Cas13a system in fission yeast and its repurposing for precise RNA editing. *Nucleic Acids Res.* 46, e90–e90.

doi:10.1093/nar/gky433.

Jones, I. M., Reay, P. A., and Philpott, K. L. (1986). Nuclear location of all three influenza polymerase proteins and a nuclear signal in polymerase PB2. *EMBO J.* 5, 2371–2376. doi:10.1002/j.1460-2075.1986.tb04506.x.

Jurczyszak, D., Zhang, W., Terry, S. N., Kehrer, T., Bermúdez González, M. C., McGregor, E., et al. (2020). HIV protease cleaves the antiviral m6A reader protein YTHDF3 in the viral particle. *PLoS Pathog.* 16. doi:10.1371/journal.ppat.1008305.

Kamath, A. V. (2016). Translational pharmacokinetics and pharmacodynamics of monoclonal antibodies. *Drug Discov. Today Technol.* 21–22, 75–83. doi:10.1016/j.ddtec.2016.09.004.

Kane, S. E., and Beemon, K. (1985). Precise localization of m6A in Rous sarcoma virus RNA reveals clustering of methylation sites: implications for RNA processing. *Mol. Cell. Biol.* 5, 2298–2306. doi:10.1128/mcb.5.9.2298.

Kawakami, E., Watanabe, T., Fujii, K., Goto, H., Watanabe, S., Noda, T., et al. (2011). Strand-specific real-time RT-PCR for distinguishing influenza vRNA, cRNA, and mRNA. *J. Virol. Methods* 173, 1–6. doi:10.1016/j.jviromet.2010.12.014.

Kawaoka, Y. (1991). Equine H7N7 influenza A viruses are highly pathogenic in mice without adaptation: potential use as an animal model. *J. Virol.* 65, 3891–3894. doi:10.1128/jvi.65.7.3891-3894.1991.

Ke, S., Alemu, E. A., Mertens, C., Gantman, E. C., Fak, J. J., Mele, A., et al. (2015). A majority of m6A residues are in the last exons, allowing the potential for 3′ UTR regulation. *Genes Dev.* 29, 2037–2053. doi:10.1101/gad.269415.115.

Ke, S., Pandya-Jones, A., Saito, Y., Fak, J. J., Vågbø, C. B., Geula, S., et al. (2017). m6A mRNA modifications are deposited in nascent pre-mRNA and are not required for splicing but do specify cytoplasmic turnover. *Genes Dev.* 31, 990–1006. doi:10.1101/gad.301036.117.

Kearse, M., Moir, R., Wilson, A., Stones-Havas, S., Cheung, M., Sturrock, S., et al. (2012). Geneious Basic: An integrated and extendable desktop software platform for the organization and analysis of sequence data. *Bioinformatics* 28, 1647–1649. doi:10.1093/bioinformatics/bts199.

Kelley, L. A., and Sternberg, M. J. E. (2009). Protein structure prediction on the web: A case study using the phyre server. *Nat. Protoc.* 4, 363–373. doi:10.1038/nprot.2009.2.

Kennedy, E. M., Bogerd, H. P., Kornepati, A. V. R., Kang, D., Ghoshal, D., Marshall, J. B., et al. (2016). Posttranscriptional m6A Editing of HIV-1 mRNAs Enhances Viral Gene Expression. *Cell Host Microbe* 19, 675–685. doi:10.1016/j.chom.2016.04.002.

Kennedy, E. M., Courtney, D. G., Tsai, K., and Cullen, B. R. (2017). Viral Epitranscriptomics. *J. Virol.* 91. doi:10.1128/jvi.02263-16.

Kilbourne, E. D. (1987). *History of influenza*. doi:10.1007/978-3-540-75855-6_12.

Kilbourne, E. D. (2006). Influenza pandemics of the 20th century. *Emerg. Infect. Dis.* 12, 9–14. doi:10.3201/eid1201.051254.

Killingley, B., and Nguyen-Van-Tam, J. (2013). Routes of influenza transmission. *Influenza Other Respi. Viruses* 7, 42–51. doi:10.1111/irv.12080.

Kim, B., Arcos, S., Rothamel, K., Jian, J., Rose, K. L., McDonald, W. H., et al. (2020a). Discovery of Widespread Host Protein Interactions with the Pre-replicated Genome of CHIKV Using VIR-CLASP. *Mol. Cell* 78, 624-640.e7. doi:10.1016/j.molcel.2020.04.013.

Kim, D., Lee, J. Y., Yang, J. S., Kim, J. W., Kim, V. N., and Chang, H. (2020b). The Architecture of SARS-CoV-2 Transcriptome. *Cell* 181, 914-921.e10. doi:10.1016/j.cell.2020.04.011.

Kim, G.-W., and Siddiqui, A. (2022). Hepatitis B Virus X Protein Expression Is Tightly Regulated by N6-Methyladenosine Modification of Its mRNA. *J. Virol.* 96. doi:10.1128/jvi.01655-21.

Kim, G. W., Imam, H., Khan, M., and Siddiqui, A. (2020c). N6-Methyladenosine modification of hepatitis B and C viral RNAs attenuates host innate immunity via RIG-I signaling. *J. Biol. Chem.* 295, 13123–13133. doi:10.1074/jbc.ra120.014260.

Kim, H., Webster, R. G., and Webby, R. J. (2018). Influenza Virus: Dealing with a Drifting and Shifting Pathogen. *Viral Immunol.* 31, 174–183. doi:10.1089/vim.2017.0141.

Kistner, O., Muller, K., and Scholtissek, C. (1989). Differential Phosphorylation of the Nucleoprotein of Influenza A Viruses. *J. Gen. Virol.* 70, 2421–2431.

Knipe, D. M., Raja, P., and Lee, J. (2017). Viral gene products actively promote latent infection by epigenetic silencing mechanisms. *Curr. Opin. Virol.* 23, 68–74. doi:10.1016/j.coviro.2017.03.010.

Knuckles, P., Carl, S. H., Musheev, M., Niehrs, C., Wenger, A., and Bühler, M. (2017). RNA fate determination through cotranscriptional adenosine methylation and microprocessor binding. *Nat. Struct. Mol. Biol.* 24, 561–569. doi:10.1038/nsmb.3419.

Kobayashi, M., Toyoda, T., and Ishihama, A. (1996). Influenza virus PB1 protein is the minimal and essential subunit of RNA polymerase. *Arch. Virol.* 141, 525–539.

Krug, R. M., Morgan, M. A., and Shatkin, A. J. (1976). Influenza viral mRNA contains internal N6-methyladenosine and 5'-terminal 7-methylguanosine in cap structures. *J. Virol.* 20, 45–53. Available at: http://www.pubmedcentral.nih.gov/articlerender.fcgi?artid=354964&tool=pmcentrez&rendertype=abstract.

Lambert, L. C., and Fauci, A. S. (2010). Influenza vaccines for the future. *N. Engl. J. Med.* 363, 2036–2044. doi:10.4161/hv.9023.

Lang, F., Singh, R. K., Pei, Y., Zhang, S., Sun, K., and Robertson, E. S. (2019). EBV epitranscriptome reprogramming by METTL14 is critical for viral-associated tumorigenesis. *PLoS Pathog.* 15, e1007796. doi:10.1371/journal.ppat.1007796.

Langmead, B., and Salzberg, S. L. (2012). Fast gapped-read alignment with Bowtie 2. *Nat. Methods* 9, 357–359. doi:10.1038/nmeth.1923.

Lavi, S., and Shatkin, A. J. (1975). Methylated simian virus 40 specific RNA from nuclei and cytoplasm of infected BSC 1 cells. *Proc. Natl. Acad. Sci. U. S. A.* 72, 2012–2016. doi:10.1073/pnas.72.6.2012.

Lavi, U., Fernandez-MuHoz, R., and James E.Darnell, J. (1977). Content of N-6 methyl adenylic acid in heterogeneous nuclear and messenger RNA of He La cells. *Nucleic Acids Res.* 4, 71–84.

Leclair, N. K., Brugiolo, M., Urbanski, L., Lawson, S. C., Thakar, K., Yurieva, M., et al. (2020). Poison Exon Splicing Regulates a Coordinated Network of SR Protein Expression during Differentiation and Tumorigenesis. *Mol. Cell* 80, 648-665.e9. doi:10.1016/j.molcel.2020.10.019.

Li, F., Zhao, D., Wu, J., and Shi, Y. (2014). Structure of the YTH domain of human YTHDF2 in complex with an m6A mononucleotide reveals an aromatic cage for m6A recognition. *Cell Res.* 24, 1490–1492. doi:10.1038/cr.2014.153.

Li, J., Chen, Z., Chen, F., Xie, G., Ling, Y., Peng, Y., et al. (2020). Targeted mRNA demethylation using an engineered dCas13b-ALKBH5 fusion protein. *Nucleic Acids Res.* 48, 5684–5694. doi:10.1093/nar/gkaa269.

Li, M. L., Ramirez, B. C., and Krug, R. M. (1998). RNA-dependent activation of primer RNA production by influenza virus polymerase: Different regions of the same protein subunit constitute the two required RNA-binding sites. *EMBO J.* 17, 5844–5852. doi:10.1093/emboj/17.19.5844.

Li, M. M., Nilsen, A., Shi, Y., Fusser, M., Ding, Y. H., Fu, Y., et al. (2013). ALKBH4-dependent demethylation of actin regulates actomyosin dynamics. *Nat. Commun.* 4. doi:10.1038/ncomms2863.

Li, S., and Mason, C. E. (2014). The Pivotal Regulatory Landscape of RNA Modifications. *Annu. Rev. Genomics Hum. Genet.* 15, 127–150. doi:10.1146/annurev-genom-090413-025405.

Li, X. C., Jin, F., Wang, B. Y., Yin, X. J., Hong, W., and Tian, F. J. (2019). The m6A demethylase ALKBH5 controls trophoblast invasion at the maternal-Foetal interface by regulating the stability of CYR61 mRNA. *Theranostics* 9, 3853–3865. doi:10.7150/thno.31868.

Li, X., Xiong, X., Wang, K., Wang, L., Shu, X., Ma, S., et al. (2016a). Transcriptome-wide mapping reveals reversible and dynamic N1-methyladenosine methylome. *Nat. Chem. Biol.* 12, 311–316. doi:10.1038/nchembio.2040.

Li, X., Xiong, X., and Yi, C. (2016b). Epitranscriptome sequencing technologies: Decoding RNA modifications. *Nat. Methods* 14, 23–31. doi:10.1038/nmeth.4110.

Li, Z., Weng, H., Su, R., Weng, X., Zuo, Z., Li, C., et al. (2017). FTO Plays an Oncogenic Role in Acute Myeloid Leukemia as a N6-Methyladenosine RNA Demethylase. *Cancer Cell* 31, 127–141. doi:10.1016/j.ccell.2016.11.017.

Liao, S., Sun, H., and Xu, C. (2018). YTH Domain: A Family of N6-methyladenosine (m6A) Readers. *Genomics, Proteomics Bioinforma.* 16, 99–107. doi:10.1016/j.gpb.2018.04.002.

Lichinchi, G., Gao, S., Saletore, Y., Gonzalez, G. M., Bansal, V., Wang, Y., et al. (2016a). Dynamics of the human and viral m(6)A RNA methylomes during HIV-1 infection of T cells. *Nat. Microbiol.* 1, 16011. doi:10.1038/nmicrobiol.2016.11.

Lichinchi, G., Zhao, B. S., Wu, Y., Lu, Z., Qin, Y., He, C., et al. (2016b). Dynamics of Human and Viral RNA Methylation during Zika Virus Infection. *Cell Host Microbe* 20, 666–673. doi:10.1016/j.chom.2016.10.002.

Linder, B., Grozhik, A. V., Olarerin-George, A. O., Meydan, C., Mason, C. E., and Jaffrey, S. R. (2015). Single-nucleotide-resolution mapping of m6A and m6Am throughout the transcriptome. *Nat. Methods* 12, 767–772. doi:10.1038/nmeth.3453.

Lisitsyna, O. M., Seplyarskiy, V. B., and Sheval, E. V. (2017). Comparative analysis of nuclear localization signal (NLS) prediction methods. *Biopolym. Cell* 33, 147–154. doi:10.7124/bc.00094C.

Liu, F., Clark, W., Luo, G., Wang, X., Fu, Y., Wei, J., et al. (2016). ALKBH1-Mediated tRNA Demethylation Regulates Translation. *Cell* 167, 816-828.e16. doi:10.1016/j.cell.2016.09.038.

Liu, J., Xu, Y. P., Li, K., Ye, Q., Zhou, H. Y., Sun, H., et al. (2021). The m6A methylome of SARS-CoV-2 in host cells. *Cell Res.* 31, 404–414. doi:10.1038/s41422-020-00465-7.

Liu, J., Yue, Y., Han, D., Wang, X., Fu, Y., Zhang, L., et al. (2014). A METTL3-METTL14 complex mediates mammalian nuclear RNA N6-adenosine methylation. *Nat. Chem. Biol.* 10, 93–95. doi:10.1038/nchembio.1432.

Liu, N., Dai, Q., Zheng, G., He, C., Parisien, M., and Pan, T. (2015). N6 - methyladenosine-dependent RNA structural switches regulate RNA-protein interactions. *Nature* 518, 560–564. doi:10.1038/nature14234.

Liu, N., Parisien, M., Dai, Q., Zheng, G., He, C., and Pan, T. (2013). Probing N6-methyladenosine RNA modification status at single nucleotide resolution in mRNA and long noncoding RNA. *RNA* 19, 1848–1856. doi:10.1261/rna.041178.113.4.

Liu, Y., You, Y., Lu, Z., Yang, J., Li, P., Liu, L., et al. (2019). N6-methyladenosine RNA modification–mediated cellular metabolism rewiring inhibits viral replication. *Science (80-.).* 365, 1171–1176. doi:10.1126/science.aax4468.

Livak, K. J., and Schmittgen, T. D. (2001). Analysis of relative gene expression data using real-time quantitative PCR and the 2-ΔΔCT method. *Methods* 25, 402–408. doi:10.1006/meth.2001.1262.

Long, J. S., Mistry, B., Haslam, S. M., and Barclay, W. S. (2019). Host and viral determinants of influenza A virus species specificity. *Nat. Rev. Microbiol.* 17, 67–81. doi:10.1038/s41579-018-0115-z.

Low, T. Y., Syafruddin, S. E., Mohtar, M. A., Vellaichamy, A., A Rahman, N. S., Pung, Y. F., et al. (2021). Recent progress in mass spectrometry-based strategies for elucidating protein–protein interactions. *Cell. Mol. Life Sci.* 78, 5325–5339. doi:10.1007/s00018-021-03856-0.

Lozano, R., Naghavi, M., Foreman, K., Lim, S., Shibuya, K., Aboyans, V., et al. (2012). Global and regional mortality from 235 causes of death for 20 age groups

in 1990 and 2010: A systematic analysis for the Global Burden of Disease Study 2010. *Lancet* 380, 2095–2128. doi:10.1016/S0140-6736(12)61728-0.

Lu, M., Xue, M., Wang, H., Kairis, E. L., Ahmad, S., Wei, J., et al. (2021). Nonsegmented Negative-Sense RNA Viruses Utilize N6 -Methyladenosine (m6 A) as a Common Strategy To Evade Host Innate Immunity. *J. Virol.* 95, 1–21.

Lu, M., Zhang, Z., Xue, M., Zhao, B. S., Harder, O., Li, A., et al. (2020). N 6- methyladenosine modification enables viral RNA to escape recognition by RNA sensor RIG-I. *Nat. Microbiol.* 5, 584–598. doi:10.1038/s41564-019-0653-9.

Lu, W., Tirumuru, N., Gelais, C. S., Koneru, P. C., Liu, C., Kvaratskhelia, M., et al. (2018). N 6 -Methyladenosine– binding proteins suppress HIV-1 infectivity and viral production. *J. Biol. Chem.* 293, 12992–13005. doi:10.1074/jbc.RA118.004215.

Luo, S., and Tong, L. (2014). Molecular basis for the recognition of methylated adenines in RNA by the eukaryotic YTH domain. *Proc. Natl. Acad. Sci. U. S. A.* 111, 13834–13839. doi:10.1073/pnas.1412742111.

Luytjes, W., Krystal, M., Enami, M., Parvin, J. D., and Palese, P. (1989). Amplification, expression, and packaging of a foreign gene by influenza virus. *Cell* 59, 1107–1113. doi:10.1016/0092-8674(89)90766-6.

Ma, H., Wang, X., Cai, J., Dai, Q., Natchiar, S. K., Lv, R., et al. (2019). N 6- Methyladenosine methyltransferase ZCCHC4 mediates ribosomal RNA methylation. *Nat. Chem. Biol.* 15, 88–94. doi:10.1038/s41589-018-0184-3.

Mahas, A., Aman, R., and Mahfouz, M. (2019). CRISPR-Cas13d mediates robust RNA virus interference in plants. *Genome Biol.* 20, 1–16. doi:10.1186/s13059-019-1881-2.

Makarova, K. S., Grishin, N. V., Shabalina, S. A., Wolf, Y. I., and Koonin, E. V. (2006). A putative RNA-interference-based immune system in prokaryotes: Computational analysis of the predicted enzymatic machinery, functional analogies with eukaryotic RNAi, and hypothetical mechanisms of action. *Biol. Direct* 1, 1–26. doi:10.1186/1745-6150-1-7.

Makarova, K. S., Wolf, Y. I., Iranzo, J., Shmakov, S. A., Alkhnbashi, O. S., Brouns, S. J. J., et al. (2020). Evolutionary classification of CRISPR–Cas systems: a burst of class 2 and derived variants. *Nat. Rev. Microbiol.* 18, 67–83. doi:10.1038/s41579-019-0299-x.

Makarova, K. S., Wolf, Y. I., and Koonin, E. V. (2018). Classification and Nomenclature of CRISPR-Cas Systems: Where from Here? *Cris. J.* 1, 325–336. doi:10.1089/crispr.2018.0033.

Malacrida, A., Rivara, M., Di Domizio, A., Cislaghi, G., Miloso, M., Zuliani, V., et al. (2020). 3D proteome-wide scale screening and activity evaluation of a new ALKBH5 inhibitor in U87 glioblastoma cell line. *Bioorganic Med. Chem.* 28, 115300. doi:10.1016/j.bmc.2019.115300.

Marraffini, L. A. (2015). CRISPR-Cas immunity in prokaryotes. *Nature* 526, 55–61. doi:10.1038/nature15386.

Martín-benito, J., Area, E., Ortega, J., Llorca, O., Valpuesta, J. M., Carrascosa, J. L.,

et al. (2001). Three-dimensional reconstruction of a recombinant influenza virus ribonucleoprotein particle. *EMBO Rep.* 2, 313–317.

Martin, K., and Heleniust, A. (1991). Nuclear transport of influenza virus ribonucleoproteins: The viral matrix protein (M1) promotes export and inhibits import. *Cell* 67, 117–130. doi:10.1016/0092-8674(91)90576-K.

Matrosovich, M., Zhou, N., Kawaoka, Y., and Webster, R. (1999). The Surface Glycoproteins of H5 Influenza Viruses Isolated from Humans, Chickens, and Wild Aquatic Birds Have Distinguishable Properties. *J. Virol.* 73, 1146–1155. doi:10.1128/jvi.73.2.1146-1155.1999.

Mauer, J., and Jaffrey, S. R. (2018). FTO, m 6 A m , and the hypothesis of reversible epitranscriptomic mRNA modifications. *FEBS Lett.* 592, 2012–2022. doi:10.1002/1873-3468.13092.

Mauer, J., Luo, X., Blanjoie, A., Jiao, X., Grozhik, A. V., Patil, D. P., et al. (2017). Reversible methylation of m6 Am in the 5′ cap controls mRNA stability. *Nature* 541, 371–375. doi:10.1038/nature21022.

McDonough, M. A., Loenarz, C., Chowdhury, R., Clifton, I. J., and Schofield, C. J. (2010). Structural studies on human 2-oxoglutarate dependent oxygenases. *Curr. Opin. Struct. Biol.* 20, 659–672. doi:10.1016/j.sbi.2010.08.006.

Melstrom, L., and Chen, J. (2020). RNA N 6 -methyladenosine modi fication in solid tumors : new therapeutic frontiers. *Cancer Gene Ther.*, 18–22. doi:10.1038/s41417-020-0160-4.

Mendel, M., Chen, K. M., Homolka, D., Gos, P., Pandey, R. R., McCarthy, A. A., et al. (2018). Methylation of Structured RNA by the m6A Writer METTL16 Is Essential for Mouse Embryonic Development. *Mol. Cell* 71, 986-1000.e11. doi:10.1016/j.molcel.2018.08.004.

Meyer, K. D. (2019). DART-seq: an antibody-free method for global m6A detection. *Nat. Methods* 16, 1275–1280. doi:10.1038/s41592-019-0570-0.

Meyer, K. D., and Jaffrey, S. R. (2014). The dynamic epitranscriptome: N6-methyladenosine and gene expression control. *Nat. Rev. Mol. Cell Biol.* 15, 313–326. doi:10.1038/nrm3785.

Meyer, K. D., and Jaffrey, S. R. (2017). Rethinking m 6 A Readers, Writers, and Erasers . *Annu. Rev. Cell Dev. Biol.* 33, 319–342. doi:10.1146/annurev-cellbio-100616-060758.

Meyer, K. D., and Jeffery, S. R. (2014). The dynamic epitranscriptome: N6 -methyladenosine and gene expression control. *Nat Rev Mol Cell Biol.* 15, 313–326. doi:10.1038/nrm3785.The.

Meyer, K. D., Saletore, Y., Zumbo, P., Elemento, O., Mason, C. E., and Jaffrey, S. R. (2012). Comprehensive analysis of mRNA methylation reveals enrichment in 3′ UTRs and near stop codons. *Cell* 149, 1635–1646. doi:10.1016/j.cell.2012.05.003.

Mikutis, S., Gu, M., Sendinc, E., Hazemi, M. E., Kiely-Collins, H., Aspris, D., et al. (2020). MeCLICK-Seq, a Substrate-Hijacking and RNA Degradation Strategy for the Study of RNA Methylation. *ACS Cent. Sci.* 6, 2196–2208.

doi:10.1021/acscentsci.0c01094.

Mishima, E., Jinno, D., Akiyama, Y., Itoh, K., Nankumo, S., Shima, H., et al. (2015). Immuno-northern blotting: Detection of RNA modifications by using antibodies against modified nucleosides. *PLoS One* 10, 1–17. doi:10.1371/journal.pone.0143756.

Molinie, B., Wang, J., Lim, K. S., Hillebrand, R., Lu, Z. X., Van Wittenberghe, N., et al. (2016). M6 A-LAIC-seq reveals the census and complexity of the m6 A epitranscriptome. *Nat. Methods* 13, 692–698. doi:10.1038/nmeth.3898.

Moss, B., Gershowitz, A., Stringer, J. R., Holland, L. E., and Wagner, E. K. (1977). 5'-Terminal and internal methylated nucleosides in herpes simplex virus type 1 mRNA. *J. Virol.* 23, 234–239. doi:10.1128/jvi.23.2.234-239.1977.

Mostafa, A., Abdelwhab, E. M., Mettenleiter, T. C., and Pleschka, S. (2018). Zoonotic potential of influenza A viruses: A comprehensive overview. *Viruses* 10, 1–38. doi:10.3390/v10090497.

Muhire, B. M., Varsani, A., and Martin, D. P. (2014). SDT: A virus classification tool based on pairwise sequence alignment and identity calculation. *PLoS One* 9. doi:10.1371/journal.pone.0108277.

Mukaigawa, J., and Nayak, D. P. (1991). Two signals mediate nuclear localization of influenza virus (A/WSN/33) polymerase basic protein 2. *J. Virol.* 65, 245–253. doi:10.1128/jvi.65.1.245-253.1991.

Myhrvold, C., Freije, C. A., Gootenberg, J. S., Abudayyeh, O. O., Metsky, H. C.,

Durbin, A. F., et al. (2018). Field-deployable viral diagnostics using CRISPR-Cas13. *Science (80-.).* 360, 444–448. doi:10.1126/science.aas8836.

Naguib, M. M., Arafa, A. S. A., El-Kady, M. F., Selim, A. A., Gunalan, V., Maurer-Stroh, S., et al. (2015). Evolutionary trajectories and diagnostic challenges of potentially zoonotic avian influenza viruses H5N1 and H9N2 co-circulating in Egypt. *Infect. Genet. Evol.* 34, 278–291. doi:10.1016/j.meegid.2015.06.004.

Nakagawa, Y., Kimura, N., Toyoda, T., Mizumoto, K., Ishihama, A., Oda, K., et al. (1995). The RNA polymerase PB2 subunit is not required for replication of the influenza virus genome but is involved in capped mRNA synthesis. *J. Virol.* 69, 728–733. doi:10.1128/jvi.69.2.728-733.1995.

Narayan, P., Ayers, D. F., Rottman, F. M., Maroney, P. A., and Nilsen, T. W. (1987). Unequal distribution of N6-methyladenosine in influenza virus mRNAs. *Mol. Cell. Biol.* 7, 1572–1575. doi:10.1128/mcb.7.4.1572-1575.1987.

Neirynck, S., Deroo, T., Saelens, X., Vanlandschoot, P., Jou, W. M., and Fiers, W. (1999). A universal influenza A vaccine based on the extracellular domain of the M2 protein. *Nat. Med.* 5, 1157–1163. doi:10.1038/13484.

Nelson, M. I., and Holmes, E. C. (2007). The evolution of epidemic influenza. *Nat. Rev. Genet.* 8, 196–205. doi:10.1038/nrg2053.

Nemeroff, M. E., Barabino, S. M. L., Li, Y., Keller, W., and Krug, R. M. (1998). Influenza virus NS1 protein interacts with the cellular 30 kDa subunit of CPSF and inhibits 3′ end formation of cellular pre-mRNAs. *Mol. Cell* 1, 991–1000. doi:10.1016/S1097-2765(00)80099-4.

Nettersheim, D., Berger, D., Jostes, S., Kristiansen, G., Lochnit, G., and Schorle, H. (2019). N6-Methyladenosine detected in RNA of testicular germ cell tumors is controlled by METTL3, ALKBH5, YTHDC1/F1/F2, and HNRNPC as writers, erasers, and readers. *Andrology* 7, 498–506. doi:10.1111/andr.12612.

Neumann, G. (2021). Influenza reverse genetics-historical perspective. *Cold Spring Harb. Perspect. Med.* 11, 1–9. doi:10.1101/cshperspect.a038547.

Neumann, G., and Hobom, G. (1995). Mutational analysis of influenza virus promoter elements in vivo. *J. Gen. Virol.* 76, 1709–1717. doi:10.1099/0022-1317-76-7-1709.

Neumann, G., Hughes, M. T., and Kawaoka, Y. (2000). Influenza A virus NS2 protein mediates vRNP nuclear export through NES-independent interaction with hCRM1. *EMBO J.* 19, 6751–6758. doi:10.1093/emboj/19.24.6751.

Neumann, G., and Kawaoka, Y. (2001). Reverse genetics of influenza virus. *Virology* 287, 243–250. doi:10.1006/viro.2001.1008.

Neumann, G., Watanabe, T., Ito, H., Watanabe, S., Goto, H., Gao, P., et al. (1999). Generation of influenza A viruses entirely from cloned cDNAs. *PNAS* 96, 9345–9350.

Niu, Y., Lin, Z., Wan, A., Chen, H., Liang, H., Sun, L., et al. (2019). RNA N6-methyladenosine demethylase FTO promotes breast tumor progression through inhibiting BNIP3. *Mol. Cancer* 18, 1–16. doi:10.1186/s12943-019-1004-4.

Niu, Y., Zhao, X., Wu, Y. S., Li, M. M., Wang, X. J., and Yang, Y. G. (2013). N6-

methyl-adenosine (m6A) in RNA: An Old Modification with A Novel Epigenetic Function. *Genomics, Proteomics Bioinforma.* 11, 8–17. doi:10.1016/j.gpb.2012.12.002.

Nomaguchi, M., and Adachi, A. (2017). Editorial: Highly mutable animal RNA viruses: Adaptation and evolution. *Front. Microbiol.* 8. doi:10.3389/fmicb.2017.01785.

O'Neill, R. E., Talon, J., and Palese, P. (1998). The influenza virus NEP (NS2 protein) mediates the nuclear export of viral ribonucleoproteins. *EMBO J.* 17, 288–296. doi:10.1093/emboj/17.1.288.

Otte, A., Marriott, A. C., Dreier, C., Dove, B., Mooren, K., Klingen, T. R., et al. (2016). Evolution of 2009 H1N1 influenza viruses during the pandemic correlates with increased viral pathogenicity and transmissibility in the ferret model. *Sci. Rep.* 6, 1–10. doi:10.1038/srep28583.

Patil, D. P., Chen, C. K., Pickering, B. F., Chow, A., Jackson, C., Guttman, M., et al. (2016). M6 A RNA methylation promotes XIST-mediated transcriptional repression. *Nature* 537, 369–373. doi:10.1038/nature19342.

Patil, D. P., Pickering, B. F., and Jaffrey, S. R. (2017). Reading m6A in the Transcriptome: M6A-Binding Proteins. *Trends Cell Biol.*, 1–15. doi:10.1016/j.tcb.2017.10.001.

Paules, C., and Subbarao, K. (2017). Influenza. *Lancet* 390, 697–708. doi:10.1016/S0140-6736(17)30129-0.

Peacock, T. P., Benton, D. J., James, J., Sadeyen, J.-R., Chang, P., Sealy, J. E., et al. (2017). Immune Escape Variants of H9N2 Influenza Viruses Containing Deletions at the Hemagglutinin Receptor Binding Site Retain Fitness In Vivo and Display Enhanced Zoonotic Characteristics . *J. Virol.* 91. doi:10.1128/jvi.00218-17.

Peacock, T., Reddy, K., James, J., Adamiak, B., Barclay, W., Shelton, H., et al. (2016). Antigenic mapping of an H9N2 avian influenza virus reveals two discrete antigenic sites and a novel mechanism of immune escape. *Sci. Rep.* 6, 1–12. doi:10.1038/srep18745.

Peiris, J. S. M., Yu, W. C., Leung, C. W., Cheung, C. Y., Ng, W. F., Nicholls, J. M., et al. (2004). Re-emergence of fatal human influenza a subtype H5N1 disease. *Lancet* 363, 617–619. doi:10.1097/01.idc.0000130890.12611.f3.

Perry, F. P., and Kelley, D. E. (1974). Existence of Methylated in Mouse L Cells. *Cell* I.

Ping, X. L., Sun, B. F., Wang, L., Xiao, W., Yang, X., Wang, W. J., et al. (2014). Mammalian WTAP is a regulatory subunit of the RNA N6-methyladenosine methyltransferase. *Cell Res.* 24, 177–189. doi:10.1038/cr.2014.3.

Pinto, L. H., Holsinger, L. J., and Lamb, R. A. (1992). Influenza virus M2 protein has ion channel activity. *Cell* 69, 517–528. doi:10.1016/0092-8674(92)90452-I.

Pleschka, S. (2013). Overview of Influenza Viruses. *Curr. Top. Microbiol. Immunol.* 370, 1–20. doi:10.1007/82.

Poole, E., Elton, D., Medcalf, L., and Digard, P. (2004). Functional domains of the influenza A virus PB2 protein: Identification of NP- and PB1-binding sites. *Virology* 321, 120–133. doi:10.1016/j.virol.2003.12.022.

Price, A. M., Hayer, K. E., Mcintyre, A. B. R., Gokhale, N. S., Abebe, J. S., Fera, A. N. Della, et al. (2020). Direct RNA sequencing reveals m6A modifications on adenovirus RNA are necessary for efficient splicing. *Nat. Commun.* 11, 1–17. doi:10.1038/s41467-020-19787-6.

Qin, P., Park, M., Alfson, K. J., Tamhankar, M., Carrion, R., Patterson, J. L., et al. (2019). Rapid and Fully Microfluidic Ebola Virus Detection with CRISPR-Cas13a. *ACS Sensors* 4, 1048–1054. doi:10.1021/acssensors.9b00239.

Qiu, W., Zhang, Q., Zhang, R., Lu, Y., Wang, X., Tian, H., et al. (2021). N 6-methyladenosine RNA modification suppresses antiviral innate sensing pathways via reshaping double-stranded RNA. *Nat. Commun.* 12, 1–16. doi:10.1038/s41467-021-21904-y.

Qiu, Y., Nemeroff, M., and Krug, R. (1995). The influenza virus NS1 protein binds to a specific region in human U6 snRNA and inhibits U6-U2 and U6-U4 snRNA interactions during splicing. *RNA* 1, 304–316.

Qu, L., Yi, Z., Zhu, S., Wang, C., Cao, Z., Zhou, Z., et al. (2019). Programmable RNA editing by recruiting endogenous ADAR using engineered RNAs. *Nat. Biotechnol.* 37, 1059–1069. doi:10.1038/s41587-019-0178-z.

Rajecka, V., Skalicky, T., and Vanacova, S. (2019). The role of RNA adenosine demethylases in the control of gene expression. *Biochim. Biophys. Acta - Gene*

Regul. Mech. 1862, 343–355. doi:10.1016/j.bbagrm.2018.12.001.

Rekart, M., Rupnik, K., Cesario, T. C., and Tilles, J. G. (1982). Prevalence of hemagglutination inhibition antibody to current strains of the H3N2 and H1N1 subtypes of influenza A virus in sera collected from the elderly in 1976. *Am. J. Epidemiol.* 115, 587–597.

Robb, N. C., Smith, M., Vreede, F. T., and Fodor, E. (2009). NS2/NEP protein regulates transcription and replication of the influenza virus RNA genome. *J. Gen. Virol.* 90, 1398–1407. doi:10.1099/vir.0.009639-0.

Roberts, B., Haupt, A., Tucker, A., Grancharova, T., Arakaki, J., Fuqua, M. A., et al. (2017). Systematic gene tagging using CRISPR/Cas9 in human stem cells to illuminate cell organization. *Mol. Biol. Cell* 28, 2854–2874. doi:10.1091/mbc.E17-03-0209.

Robinson, J. T., Thorvaldsdóttir, H., Winckler, W., Guttman, M., Lander, E. S., Getz, G., et al. (2011). Integrative genomics viewer. *Nat. Biotechnol.* 29, 24–26. doi:10.1038/nbt.1754.

Roth, M. G., Compans, R. W., Giusti, L., Davis, A. R., Nayak, D. P., Gething, M. J., et al. (1983). Influenza virus hemagglutinin expression is polarized in cells infected with recombinant SV40 viruses carrying cloned hemagglutinin DNA. *Cell* 33, 435–443. doi:10.1016/0092-8674(83)90425-7.

Rothberg, M. B., Haessler, S. D., and Brown, R. B. (2008). Complications of Viral Influenza. *Am. J. Med.* 121, 258–264. doi:10.1016/j.amjmed.2007.10.040.

Rottman, F. M., Bokar, J. A., Narayan, P., Shambaugh, M. E., and Ludwiczak, R. (1994). N6-Adenosine methylation in mRNA: Substrate specificity and enzyme complexity. *Biochimie* 76, 1109–1114. doi:10.1016/0300-9084(94)90038-8.

Roundtree, I. A., Evans, M. E., Pan, T., and He, C. (2017). Dynamic RNA Modifications in Gene Expression Regulation. *Cell* 169, 1187–1200. doi:10.1016/j.cell.2017.05.045.

Rubio, R. M., Depledge, D. P., Bianco, C., Thompson, L., and Mohr, I. (2018). RNA m 6 A modification enzymes shape innate responses to DNA by regulating interferon β. *Genes Dev.* 32, 1472–1484. doi:10.1101/gad.319475.118.

Ruigrok, R. W. H., Barge, A., Durrer, P., Brunner, J., Ma, K., and Whittaker, G. R. (2000). Membrane interaction of influenza virus M1 protein. *Virology* 267, 289–298. doi:10.1006/viro.1999.0134.

Ruigrok, R. W. H., and Baudin, F. (1995). Structure of influenza virus ribonucleoprotein particles . II . Purified RNA-free influenza virus ribonucleoprotein forms structures that are indistinguishable from the intact influe ... Structure of influenza virus ribonucleoprotein particles . II . Puri. *J. Gen. Virol.* 76, 1009–1014. doi:10.1099/0022-1317-76-4-1009.

Ryvkin, P., Leung, Y. Y., Silverman, I. M., Childress, M., Valladares, O., Dragomir, I., et al. (2013). HAMR: High-throughput annotation of modified ribonucleotides. *RNA* 19, 1684–1692. doi:10.1007/978-1-4939-8808-2_4.

Santhakumar, D., Rohaim, M. A. M. S., Hussein, H. A., Hawes, P., Ferreira, H. L., Behboudi, S., et al. (2018). Chicken Interferon-induced Protein with

Tetratricopeptide Repeats 5 Antagonizes Replication of RNA Viruses. *Sci. Rep.* 8, 1–20. doi:10.1038/s41598-018-24905-y.

Santhakumar, D., Rubbenstroth, D., Martinez-Sobrido, L., and Munir, M. (2017). Avian interferons and their antiviral effectors. *Front. Immunol.* 8. doi:10.3389/fimmu.2017.00049.

Sanz-Ezquerro, J. J., Santaren, J. F., Sierra, T., Aragon, T., Ortega, J., Ortın, J., et al. (1998). The PA influenza virus polymerase subunit is a phosphorylated protein. *J. Gen. Virol.* 79, 471–478.

Schaefer, M. (2015). *RNA 5-Methylcytosine Analysis by Bisulfite Sequencing*. 1st ed. Elsevier Inc. doi:10.1016/bs.mie.2015.03.007.

Schnell, M. J., Mebatsion, T., and Conzelmann, K. K. (1994). Infectious rabies viruses from cloned cDNA. *EMBO J.* 13, 4195–4203. doi:10.1002/j.1460-2075.1994.tb06739.x.

Schoggins, J. W., Wilson, S. J., Panis, M., Murphy, M. Y., Jones, C. T., Bieniasz, P., et al. (2011). A diverse array of gene products are effectors of the type I interferon Antiviral Response. *Nature* 472, 481–485. doi:10.1038/nature09907.A.

Schöller, E., Weichmann, F., Treiber, T., Ringle, S., Treiber, N., Flatley, A., et al. (2018). Interactions, localization, and phosphorylation of the m6A generating METTL3–METTL14–WTAP complex. *RNA* 24, 499–512.

Scholtissek, C., Bürger, H., Kistner, O., and Shortridge, K. F. (1985). The nucleoprotein as a possible major factor in determining host specificity of

influenza H3N2 viruses. *Virology* 147, 287–294. doi:10.1016/0042-6822(85)90131-X.

Schwartz, S., Bernstein, D. A., Mumbach, M. R., Jovanovic, M., Herbst, R. H., León-Ricardo, B. X., et al. (2014a). Transcriptome-wide mapping reveals widespread dynamic-regulated pseudouridylation of ncRNA and mRNA. *Cell* 159, 148–162. doi:10.1016/j.cell.2014.08.028.

Schwartz, S., Mumbach, M. R., Jovanovic, M., Wang, T., Maciag, K., Bushkin, G. G., et al. (2014b). Perturbation of m6A writers reveals two distinct classes of mRNA methylation at internal and 5' sites. *Cell Rep.* 8, 284–296. doi:10.1016/j.celrep.2014.05.048.

Selman, M., Dankar, S. K., Forbes, N. E., Jia, J. J., and Brown, E. G. (2012). Adaptive mutation in influenza A virus non-structural gene is linked to host switching and induces a novel protein by alternative splicing. *Emerg. Microbes Infect.* 1, 0. doi:10.1038/emi.2012.38.

Semenova, E., Jore, M. M., Datsenko, K. A., Semenova, A., Westra, E. R., Wanner, B., et al. (2011). Interference by clustered regularly interspaced short palindromic repeat (CRISPR) RNA is governed by a seed sequence. *Proc. Natl. Acad. Sci. U. S. A.* 108, 10098–10103. doi:10.1073/pnas.1104144108.

Sendinc, E., Valle-garcia, D., Dhall, A., Gygi, S. P., Sendinc, E., Valle-garcia, D., et al. (2019). PCIF1 Catalyzes m6Am mRNA Methylation to Regulate Gene Expression. *Mol. Cell* 75, 620-630.e9. doi:10.1016/j.molcel.2019.05.030.

Shi, H., Wang, X., Lu, Z., Zhao, B. S., Ma, H., Hsu, P. J., et al. (2017). YTHDF3

facilitates translation and decay of N 6-methyladenosine-modified RNA. *Cell Res.* 27, 315–328. doi:10.1038/cr.2017.15.

Shi, H., Wei, J., and He, C. (2019). Where, When,andHow: Context-Dependent Functions of RNA Methylation Writers, Readers, and Erasers. *Mol. Cell* 74, 640–650. doi:10.1016/j.molcel.2019.04.025.

Shima, H., Matsumoto, M., Ishigami, Y., Ebina, M., Muto, A., Sato, Y., et al. (2017). S-Adenosylmethionine Synthesis Is Regulated by Selective N6-Adenosine Methylation and mRNA Degradation Involving METTL16 and YTHDC1. *Cell Rep.* 21, 3354–3363. doi:10.1016/j.celrep.2017.11.092.

Shriwas, O., Priyadarshini, M., Samal, S. K., Rath, R., Panda, S., Das Majumdar, S. K., et al. (2020). DDX3 modulates cisplatin resistance in OSCC through ALKBH5-mediated m6A-demethylation of FOXM1 and NANOG. *Apoptosis*. doi:10.1007/s10495-020-01591-8.

Skehel, J. J., and Wiley, D. C. (2000). Receptor Binding and Membrane Fusion In Virus Entry: The Influenza Hemagglutinin. *Annu. Rev. Biochem.* 69, 531–569. Available at: http://arjournals.annualreviews.org/doi/abs/10.1146/annurev.biochem.68.1.863%5Cnpapers3://publication/uuid/37777FFE-E284-4B0C-9648-9DF205012ADD.

Skorko, R., Summers, D. F., and Galarza, J. M. (1991). Influenza A Virus in Vitro Transcription : Roles of NS , and NP Proteins in Regulating RNA Synthesis. *Virology* 180, 668–677.

Śledź, P., and Jinek, M. (2016). Structural insights into the molecular mechanism of

the m6A writer complex. *Elife* 5, 1–16. doi:10.7554/eLife.18434.

Smemo, S., Tena, J. J., Kim, K. H., Gamazon, E. R., Sakabe, N. J., Gómez-Marín, C., et al. (2014). Obesity-associated variants within FTO form long-range functional connections with IRX3. *Nature* 507, 371–375. doi:10.1038/nature13138.

Smith, G. J. D., and Donis, R. O. (2015). Nomenclature updates resulting from the evolution of avian influenza A(H5) virus clades 2.1.3.2a, 2.2.1, and 2.3.4 during 2013-2014. *Influenza Other Respi. Viruses* 9, 271–276. doi:10.1111/irv.12324.

Song, H., Feng, X., Zhang, H., Luo, Y., Huang, J., Lin, M., et al. (2019). METTL3 and ALKBH5 oppositely regulate m6A modification of TFEB mRNA, which dictates the fate of hypoxia/reoxygenation-treated cardiomyocytes. *Autophagy* 15, 1419–1437. doi:10.1080/15548627.2019.1586246.

Soppe, J. A., and Lebbink, R. J. (2017). Antiviral Goes Viral: Harnessing CRISPR/Cas9 to Combat Viruses in Humans. *Trends Microbiol.* 25, 833–850. doi:10.1016/j.tim.2017.04.005.

Squires, R. B., Noronha, J., Hunt, V., García-Sastre, A., Macken, C., Baumgarth, N., et al. (2012). Influenza Research Database: An integrated bioinformatics resource for influenza research and surveillance. *Influenza Other Respi. Viruses* 6, 404–416. doi:10.1111/j.1750-2659.2011.00331.x.

Sriwilaijaroen, N., and Suzuki, Y. (2012). Molecular basis of the structure and function of H1 hemagglutinin of influenza virus. *Proc. Japan Acad. Ser. B Phys. Biol. Sci.* 88, 226–249. doi:10.2183/pjab.88.226.

Stevens, J., Corper, A. L., Basler, C. F., Taubenberger, J. K., Palese, P., and Wilson, I. A. (2004). Structure of the Uncleaved Human H1 Hemagglutinin from the Extinct 1918 Influenza Virus. *Science (80-.).* 303, 1866–1870. doi:10.1126/science.1093373.

Stewart, C. R., Keyburn, A. L., Deffrasnes, C., and Tompkins, S. M. (2013). Potential directions for chicken immunology research. *Dev. Comp. Immunol.* 41, 463–468. doi:10.1016/j.dci.2013.05.011.

Stoilov, P., Rafalska, I., and Stamm, S. (2002). YTH: A new domain in nuclear proteins. *Trends Biochem. Sci.* 27, 495–497. doi:10.1016/S0968-0004(02)02189-8.

Stumpf, M. P. H., Thorne, T., De Silva, E., Stewart, R., Hyeong, J. A., Lappe, M., et al. (2008). Estimating the size of the human interactome. *Proc. Natl. Acad. Sci. U. S. A.* 105, 6959–6964. doi:10.1073/pnas.0708078105.

Subbarao, K., Klimov, A., Katz, J., Regnery, H., Lim, W., Hall, H., et al. (1998). Characterization of an avian influenza A (H5N1) virus isolated from a child with a fatal respiratory illness. *Science (80-.).* 279, 393–396. doi:10.1126/science.279.5349.393.

Suzuki, K., Tsunekawa, Y., Hernandez-Benitez, R., Wu, J., Zhu, J., Kim, E. J., et al. (2016). In vivo genome editing via CRISPR/Cas9 mediated homology-independent targeted integration. *Nature* 540, 144–149. doi:10.1038/nature20565.

Swayne, D. E., and Suarez, D. L. (2000). Review: Highly pathogenic avian influenza. *Rev. sci. tech. Off. int. Epiz.,* 2014, 463–482. Available at:

http://www.oie.int/wahis_2/public/wahid.php/Reviewreport/Review/viewsummary?fupser=&dothis=&reportid=14249.

Takashita, E., Meijer, A., Lackenby, A., Gubareva, L., Rebelo-De-Andrade, H., Besselaar, T., et al. (2015). Global update on the susceptibility of human influenza viruses to neuraminidase inhibitors, 2013-2014. *Antiviral Res.* 117, 27–38. doi:10.1016/j.antiviral.2015.02.003.

Takeda, M., Leser, G. P., Russell, C. J., and Lamb, R. A. (2003). Influenza virus hemagglutinin concentrates in lipid raft microdomains for efficient viral fusion. *Proc. Natl. Acad. Sci. U. S. A.* 100, 14610–14617. doi:10.1073/pnas.2235620100.

Tamura, K., Stecher, G., Peterson, D., Filipski, A., and Kumar, S. (2013). MEGA6: Molecular evolutionary genetics analysis version 6.0. *Mol. Biol. Evol.* 30, 2725–2729. doi:10.1093/molbev/mst197.

Tan, B., Liu, H., Zhang, S., Da Silva, S. R., Zhang, L., Meng, J., et al. (2017). Viral and cellular N6-methyladenosine and N6,2′-O-dimethyladenosine epitranscriptomes in the KSHV life cycle. *Nat. Microbiol.* 3, 108–120. doi:10.1038/s41564-017-0056-8.

Tan, B., Liu, H., Zhang, S., Zhang, L., Cui, X., Yuan, H., et al. (2018). Viral and Cellular N6 -Methyladenosine (m6 A) and N6 , 2′-O- Dimethyladenosine (m6 Am) Epitranscriptomes in KSHV Life Cycle. *Nat. Microbiol.* 3, 108–120. doi:10.1038/s41564-017-0056-8.Viral.

Tang, B., Yang, Y., Kang, M., Wang, Y., Wang, Y., Bi, Y., et al. (2020). M6A demethylase ALKBH5 inhibits pancreatic cancer tumorigenesis by decreasing

WIF-1 RNA methylation and mediating Wnt signaling. *Mol. Cancer* 19, 1–15. doi:10.1186/s12943-019-1128-6.

Tang, C., Klukovich, R., Peng, H., Wang, Z., Yu, T., Zhang, Y., et al. (2017). ALKBH5-dependent m6A demethylation controls splicing and stability of long 3'-UTR mRNAs in male germ cells. *Proc. Natl. Acad. Sci. U. S. A.* 115, E325–E333. doi:10.1073/pnas.1717794115.

Tang, Y. S., Xu, S., Chen, Y. W., Wang, J. H., and Shaw, P. C. (2021). Crystal structures of influenza nucleoprotein complexed with nucleic acid provide insights into the mechanism of RNA interaction. *Nucleic Acids Res.* 49, 4144–4154. doi:10.1093/nar/gkab203.

Tauber, S., Ligertwood, Y., Quigg-Nicol, M., Dutia, B. M., and Elliott, R. M. (2012). Behaviour of influenza A viruses differentially expressing segment 2 gene products in vitro and in vivo. *J. Gen. Virol.* 93, 840–849. doi:10.1099/vir.0.039966-0.

Te Velthuis, A. J. W., and Fodor, E. (2016). Influenza virus RNA polymerase: Insights into the mechanisms of viral RNA synthesis. *Nat. Rev. Microbiol.* 14, 479–493. doi:10.1038/nrmicro.2016.87.

Tellier, R. (2006). Review of aerosol transmission of influenza A virus. *Emerg. Infect. Dis.* 12, 1657–1662. doi:10.3201/eid1211.060426.

Theler, D., Dominguez, C., Blatter, M., Boudet, J., and Allain, F. H. T. (2014). Solution structure of the YTH domain in complex with N6-methyladenosine RNA: A reader of methylated RNA. *Nucleic Acids Res.* 42, 13911–13919.

doi:10.1093/nar/gku1116.

Tirumuru, N., Zhao, B. S., Lu, W., Lu, Z., He, C., and Wu, L. (2016). N6-
methyladenosine of HIV-1 RNA regulates viral infection and HIV-1 Gag protein
expression. *Elife* 5, 1–20. doi:10.7554/eLife.15528.

Titeca, K., Lemmens, I., Tavernier, J., and Eyckerman, S. (2019). Discovering cellular
protein-protein interactions Technological strategies and opportunities. *Mass
Spectrom. Rev.* 38, 79–111.

Tong, S., Zhu, X., Li, Y., Shi, M., Zhang, J., Bourgeois, M., et al. (2013). New World
Bats Harbor Diverse Influenza A Viruses. *PLoS Pathog.* 9, 1–12.
doi:10.1371/journal.ppat.1003657.

Toots, M., and Plemper, R. K. (2020). Next-generation direct-acting influenza
therapeutics. *Transl. Res.* 220, 33–42. doi:10.1016/j.trsl.2020.01.005.

Towbin, H., and Gordon, J. (1984). Immunoblotting and dot immunobinding - Current
status and outlook. *J. Immunol. Methods* 72, 313–340. doi:10.1016/0022-
1759(84)90001-2.

Toyoda, T., Adyshev, D. M., Kobayashi, M., Iwata, A., and Ishihama, A. (1996).
Molecular assembly of the influenza virus RNA polymerase: Determination of
the subunit-subunit contact sites. *J. Gen. Virol.* 77, 2149–2157.
doi:10.1099/0022-1317-77-9-2149.

Tsai, K., Courtney, D. G., and Cullen, B. R. (2018). Addition of m6A to SV40 late
mRNAs enhances viral structural gene expression and replication. *PLoS Pathog.*

14, 1–23. doi:10.1371/journal.ppat.1006919.

Tsai, K., and Cullen, B. R. (2020). Epigenetic and epitranscriptomic regulation of viral replication. *Nat. Rev. Microbiol.* 18, 559–570. doi:10.1038/s41579-020-0382-3.

Uemura, T., Mori, T., Kurihara, T., Kawase, S., Koike, R., Satoga, M., et al. (2016). Fluorescent protein tagging of endogenous protein in brain neurons using CRISPR/Cas9-mediated knock-in and in utero electroporation techniques. *Sci. Rep.* 6, 1–13. doi:10.1038/srep35861.

Urbaniak, K., and Markowska-Daniel, I. (2014). In vivo reassortment of influenza viruses. *Acta Biochim. Pol.* 61, 427–431. doi:10.1080/07391102.1997.10508144.

Vainio, O., and Imhof, B. A. (1995). The immunology and developmental biology of the chicken. *Immunol. Today* 16, 365–370. doi:10.1016/0167-5699(95)80002-6.

Valkenburg, S. A., Mallajosyula, V. V. A., Li, O. T. W., Chin, A. W. H., Carnell, G., Temperton, N., et al. (2016). Stalking influenza by vaccination with pre-fusion headless HA mini-stem. *Sci. Rep.* 6, 1–11. doi:10.1038/srep22666.

Van Der Oost, J., Westra, E. R., Jackson, R. N., and Wiedenheft, B. (2014). Unravelling the structural and mechanistic basis of CRISPR-Cas systems. *Nat. Rev. Microbiol.* 12, 479–492. doi:10.1038/nrmicro3279.

Vandemoortele, G., Eyckerman, S., and Gevaert, K. (2019). Pick a Tag and Explore the Functions of Your Pet Protein. *Trends Biotechnol.* 37, 1078–1090. doi:10.1016/j.tibtech.2019.03.016.

Varga, Z. T., Ramos, I., Hai, R., Schmolke, M., García-Sastre, A., Fernandez-Sesma, A., et al. (2011). The influenza virus protein PB1-F2 inhibits the induction of type i interferon at the level of the MAVS adaptor protein. *PLoS Pathog.* 7. doi:10.1371/journal.ppat.1002067.

Varghese, J. N., and Colman, P. M. (1991). Three-dimensional structure of the neuraminidase of influenza virus A/Tokyo/3/67 at 2·2 Å resolution. *J. Mol. Biol.* 221, 473–486. doi:10.1016/0022-2836(91)80068-6.

Varghese, J. N., Laver, W. G., and Colman, P. M. (1983). Structure of the influenza virus glycoprotein antigen neuraminidase at 2.9 Å resolution. *Nature* 303, 35–40. doi:10.1038/303035a0.

Vercoe, R. B., Chang, J. T., Dy, R. L., Taylor, C., Gristwood, T., Clulow, J. S., et al. (2013). Cytotoxic Chromosomal Targeting by CRISPR/Cas Systems Can Reshape Bacterial Genomes and Expel or Remodel Pathogenicity Islands. *PLoS Genet.* 9. doi:10.1371/journal.pgen.1003454.

Viehweger, A., Krautwurst, S., Lamkiewicz, K., Madhugiri, R., Ziebuhr, J., Hölzer, M., et al. (2019). Direct RNA nanopore sequencing of full-length coronavirus genomes provides novel insights into structural variants and enables modification analysis. *Genome Res.* 29, 1545–1554. doi:10.1101/gr.247064.118.

Vu, L. P., Pickering, B. F., Cheng, Y., Zaccara, S., Nguyen, D., Minuesa, G., et al. (2017). The N 6 -methyladenosine (m 6 A)-forming enzyme METTL3 controls myeloid differentiation of normal hematopoietic and leukemia cells. *Nat. Med.* 23, 1369–1376. doi:10.1038/nm.4416.

Wang, A., Tao, W., Tong, J., Gao, J., Wang, J., Hou, G., et al. (2022). m6A modifications regulate intestinal immunity and rotavirus infection. *Elife* 11, 1–19. doi:10.7554/eLife.73628.

Wang, G., He, Q., Feng, C., Liu, Y., Deng, Z., Qi, X., et al. (2014a). The atomic resolution structure of human alkb homolog 7 (ALKBH7), a key protein for programmed necrosis and fat metabolism. *J. Biol. Chem.* 289, 27924–27936. doi:10.1074/jbc.M114.590505.

Wang, P., Doxtader, K. A., and Nam, Y. (2016a). Structural Basis for Cooperative Function of Mettl3 and Mettl14 Methyltransferases. *Mol. Cell* 63, 306–317. doi:10.1016/j.molcel.2016.05.041.

Wang, P., Xu, J., Wang, Y., and Cao, X. (2017a). An interferon-independent lncRNA promotes viral replication by modulating cellular metabolism. *Science (80-.).* 1055, 1051–1055.

Wang, Q., Li, Q., Liu, T., Chang, G., Sun, Z., Gao, Z., et al. (2018). Host interaction analysis of PA-N155 and PA-N182 in chicken cells reveals an essential role of UBA52 for replication of H5N1 Avian influenza virus. *Front. Microbiol.* 9, 1–11. doi:10.3389/fmicb.2018.00936.

Wang, X., Feng, J., Xue, Y., Guan, Z., Zhang, D., Liu, Z., et al. (2016b). Structural basis of N6-adenosine methylation by the METTL3-METTL14 complex. *Nature* 534, 575–578. doi:10.1038/nature18298.

Wang, X., Huang, J., Zou, T., and Yin, P. (2017b). Human m6A writers: Two subunits, 2 roles. *RNA Biol.* 14, 300–304. doi:10.1080/15476286.2017.1282025.

Wang, X., Lu, Z., Gomez, A., Hon, G. C., Yue, Y., Han, D., et al. (2014b). N 6-methyladenosine-dependent regulation of messenger RNA stability. *Nature* 505, 117–120. doi:10.1038/nature12730.

Wang, X., Zhao, B. S., Roundtree, I. A., Lu, Z., Han, D., Ma, H., et al. (2015). N6-methyladenosine modulates messenger RNA translation efficiency. *Cell* 161, 1388–1399. doi:10.1016/j.cell.2015.05.014.

Wang, Y., Li, Y., Toth, J. I., Petroski, M. D., Zhang, Z., and Zhao, J. C. (2014c). N6 - methyladenosine modification destabilizes developmental regulators in embryonic stem cells. *Nat. Cell Biol.* 16, 191–198. doi:10.1038/ncb2902.

Wang, Y., Xiao, Y., Dong, S., Yu, Q., and Jia, G. (2020). Antibody-free enzyme-assisted chemical approach for detection of N 6-methyladenosine. *Nat. Chem. Biol.* 16, 896–903. doi:10.1038/s41589-020-0525-x.

Watanabe, K., Handa, H., Mizumoto, K., and Nagata, K. (1996). Mechanism for inhibition of influenza virus RNA polymerase activity by matrix protein. *J. Virol.* 70, 241–247. doi:10.1128/jvi.70.1.241-247.1996.

Waterston, R. H., Lindblad-Toh, K., Birney, E., Rogers, J., Abril, J. F., Agarwal, P., et al. (2002). Initial sequencing and comparative analysis of the mouse genome. *Nature* 420, 520–562. Available at: http://www.nature.com/nature/journal/v420/n6915/full/nature01262.html.

Webby, R. J., Perez, D. R., Coleman, J. S., Guan, Y., Knight, J. H., Govorkova, E. A., et al. (2004). Responsiveness to a pandemic alert: Use of reverse genetics for rapid development of influenza vaccines. *Lancet* 363, 1099–1103.

doi:10.1016/S0140-6736(04)15892-3.

Weber, M., Sediri, H., Felgenhauer, U., Binzen, I., Bänfer, S., Jacob, R., et al. (2015).
Influenza virus adaptation PB2-627K modulates nucleocapsid inhibition by the
pathogen sensor RIG-I. *Cell Host Microbe* 17, 309–319.
doi:10.1016/j.chom.2015.01.005.

Webster, R. G., Bean, W. J., Gorman, O. T., Chambers, T. M., and Kawaoka, Y.
(1992). Evolution and ecology of influenza a viruses. *Microbiol. Mol. Biol. Rev.*
56, 152–179. doi:10.1007/82_2014_396.

Wei, C. M., and Moss, B. (1977). Nucleotide Sequences at the N6-Methyladenosine
Sites of HeLa Cell Messenger Ribonucleic Acid. *Biochemistry* 16, 1672–1676.
doi:10.1021/bi00627a023.

Wei, J., Liu, F., Lu, Z., Fei, Q., Ai, Y., He, P. C., et al. (2018). Differential m 6 A, m 6
A m , and m 1 A Demethylation Mediated by FTO in the Cell Nucleus and
Cytoplasm. *Mol. Cell* 71, 973-985.e5. doi:10.1016/j.molcel.2018.08.011.

Wen, J., Lv, R., Ma, H., Shen, H., He, C., Wang, J., et al. (2018). Zc3h13 Regulates
Nuclear RNA m6A Methylation and Mouse Embryonic Stem Cell Self-Renewal.
Mol. Cell 69, 1028–1038. doi:10.1016/j.molcel.2018.02.015.

Weng, H., Huang, H., and Chen, J. (2019). RNA N 6-Methyladenosine Modification
in Normal and Malignant Hematopoiesis. *Adv. Exp. Med. Biol.* 1143, 75–93.
doi:10.1007/978-981-13-7342-8_4.

Wheeler, E. C., Nostrand, E. L. Van, and Yeo, G. W. (2018). Advances and

challenges in the detection of transcriptome-wide protein RNA interactions.pdf.
WIREs RNA 9, 1–11.

White, J. M. (1992). Membrane Fusion. *Science (80-.).* 258, 917–924.

White, J. M., and Wilson, I. A. (1987). Anti-peptide antibodies detect steps in a
protein conformational change: Low-pH activation of the influenza virus
hemagglutinin. *J. Cell Biol.* 105, 2887–2896. doi:10.1083/jcb.105.6.2887.

Wiedenheft, B., Lander, G. C., Zhou, K., Jore, M. M., Brouns, S. J. J., Van Der Oost,
J., et al. (2011). Structures of the RNA-guided surveillance complex from a
bacterial immune system. *Nature* 477, 486–489. doi:10.1038/nature10402.

Wiley, D. C., Wilson, I. A., and Skehel, J. J. (1981). Structural identification of the
antibody-binding sites of Hong Kong influenza haemagglutinin and their
involvement in antigenic variation. *Nature* 289, 373–378. doi:10.1038/289373a0.

Wilson, C., Chen, P. J., Miao, Z., and Liu, D. R. (2020). Programmable m6 A
modification of cellular RNAs with a Cas13-directed methyltransferase. *Nat.
Biotechnol.* doi:10.1038/s41587-020-0572-6.

Winkler, R., Gillis, E., Lasman, L., Safra, M., Geula, S., Soyris, C., et al. (2019). m6A
modification controls the innate immune response to infection by targeting type I
interferons. *Nat. Immunol.* 20, 173–182. doi:10.1038/s41590-018-0275-z.

Wise, H. M., Hutchinson, E. C., Jagger, B. W., Stuart, A. D., Kang, Z. H., Robb, N., et
al. (2012). Identification of a Novel Splice Variant Form of the Influenza A Virus
M2 Ion Channel with an Antigenically Distinct Ectodomain. *PLoS Pathog.* 8.

doi:10.1371/journal.ppat.1002998.

Wojtas, M. N., Pandey, R. R., Mendel, M., Homolka, D., Sachidanandam, R., and

Pillai, R. S. (2017). Regulation of m6A Transcripts by the 3′→5′ RNA Helicase

YTHDC2 Is Essential for a Successful Meiotic Program in the Mammalian

Germline. *Mol. Cell* 68, 374-387.e12. doi:10.1016/j.molcel.2017.09.021.

Woolhouse, M. E. J., and Brierley, L. (2018). Epidemiological characteristics of

human-infective RNA viruses. *Sci. Data* 5, 1–6. doi:10.1038/sdata.2018.17.

Woolhouse, M., Scott, F., Hudson, Z., Howey, R., and Chase-Topping, M. (2012).

Human viruses: Discovery and emeraence. *Philos. Trans. R. Soc. B Biol. Sci.* 367,

2864–2871. doi:10.1098/rstb.2011.0354.

Wu, F., Zhao, S., Yu, B., Chen, Y. M., Wang, W., Song, Z. G., et al. (2020). A new

coronavirus associated with human respiratory disease in China. *Nature* 579,

265–269. doi:10.1038/s41586-020-2008-3.

Wu, R., Li, A., Sun, B., Sun, J. G., Zhang, J., Zhang, T., et al. (2019). A novel m6A

reader Prrc2a controls oligodendroglial specification and myelination. *Cell Res.*

29, 23–41. doi:10.1038/s41422-018-0113-8.

Xia, T.-L., Li, X., Wang, X., Zhu, Y.-J., Zhang, H., Cheng, W., et al. (2021a). N6-

methyladenosine-binding protein YTHDF1 suppresses EBV replication and

promotes EBV RNA. *EMBO Rep.* 22.

Xia, Z., Tang, M., Ma, J., Zhang, H., Gimple, R. C., Prager, B. C., et al. (2021b).

Epitranscriptomic editing of the RNA N6-methyladenosine modification by

dCasRx conjugated methyltransferase and demethylase. *Nucleic Acids Res.* 49, 7361–7374. doi:10.1093/nar/gkab517.

Xiao, W., Adhikari, S., Dahal, U., Chen, Y. S., Hao, Y. J., Sun, B. F., et al. (2016). Nuclear m6A Reader YTHDC1 Regulates mRNA Splicing. *Mol. Cell* 61, 507–519. doi:10.1016/j.molcel.2016.01.012.

Xu, C., Liu, K., Ahmed, H., Loppnau, P., Schapira, M., and Min, J. (2015). Structural basis for the discriminative recognition of N6-Methyladenosine RNA by the human YT521-B homology domain family of proteins. *J. Biol. Chem.* 290, 24902–24913. doi:10.1074/jbc.M115.680389.

Xu, C., Liu, K., Tempel, W., Demetriades, M., Aik, W., Schofield, C. J., et al. (2014a). Structures of human ALKBH5 demethylase reveal a unique binding mode for specific single-stranded N6-methyladenosine RNA demethylation. *J. Biol. Chem.* 289, 17299–17311. doi:10.1074/jbc.M114.550350.

Xu, C., Wang, X., Liu, K., Roundtree, I. A., Tempel, W., Li, Y., et al. (2014b). Structural basis for selective binding of m6A RNA by the YTHDC1 YTH domain. *Nat. Chem. Biol.* 10, 927–929. doi:10.1038/nchembio.1654.

Xu, D., Shao, W., Jiang, Y., Wang, X., Liu, Y., and Liu, X. (2017). FTO expression is associated with the occurrence of gastric cancer and prognosis. *Oncol. Rep.* 38, 2285–2292. doi:10.3892/or.2017.5904.

Xu, L., and Seki, M. (2020). Recent advances in the detection of base modifications using the Nanopore sequencer. *J. Hum. Genet.* 65, 25–33. doi:10.1038/s10038-019-0679-0.

Xue, M., Zhang, Y., Wang, H., Kairis, E. L., Lu, M., Ahmad, S., et al. (2021). *Viral RNA N6-methyladenosine modification modulates both innate and adaptive immune responses of human respiratory syncytial virus*. doi:10.1371/journal.ppat.1010142.

Xue, M., Zhao, B. S., Zhang, Z., Lu, M., Harder, O., Chen, P., et al. (2019). Viral N 6-methyladenosine upregulates replication and pathogenesis of human respiratory syncytial virus. *Nat. Commun.* 10. doi:10.1038/s41467-019-12504-y.

Yamada, S., Suzuki, Y., Suzuki, T., Le, M. Q., Nidom, C. A., Sakai-Tagawa, Y., et al. (2006). Haemagglutinin mutations responsible for the binding of H5N1 influenza A viruses to human-type receptor. *Nature* 444, 378–382.

Yamayoshi, S., Watanabe, M., Goto, H., and Kawaoka, Y. (2016). Identification of a Novel Viral Protein Expressed from the PB2 Segment of Influenza A Virus. *J. Virol.* 90, 444–456. doi:10.1128/jvi.02175-15.

Yang, C. G., Yi, C., Duguid, E. M., Sullivan, C. T., Jian, X., Rice, P. A., et al. (2008). Crystal structures of DNA/RNA repair enzymes AlkB and ABH2 bound to dsDNA. *Nature* 452, 961–965. doi:10.1038/nature06889.

Yang, F., Lei, X., Rodriguez-Palacios, A., Tang, C., and Yue, H. (2013). Selection of reference genes for quantitative real-time PCR analysis in chicken embryo fibroblasts infected with avian leukosis virus subgroup J. *BMC Res. Notes* 6. doi:10.1186/1756-0500-6-402.

Yang, J., Yan, R., Roy, A., Xu, D., Poisson, J., and Zhang, Y. (2015). The I-TASSER suite: Protein structure and function prediction. *Nat. Methods* 12, 7–8.

doi:10.1038/nmeth.3213.

Yang, P., Wang, Q., Liu, A., Zhu, J., and Feng, J. (2019a). ALKBH5 Holds Prognostic Values and Inhibits the Metastasis of Colon Cancer. *Pathol. Oncol. Res.* doi:10.1007/s12253-019-00737-7.

Yang, S., Wei, J., Cui, Y. H., Park, G., Shah, P., Deng, Y., et al. (2019b). m6A mRNA demethylase FTO regulates melanoma tumorigenicity and response to anti-PD-1 blockade. *Nat. Commun.* 10. doi:10.1038/s41467-019-10669-0.

Yao, R. W., Xu, G., Wang, Y., Shan, L., Luan, P. F., Wang, Y., et al. (2019). Nascent Pre-rRNA Sorting via Phase Separation Drives the Assembly of Dense Fibrillar Components in the Human Nucleolus. *Mol. Cell* 76, 767-783.e11. doi:10.1016/j.molcel.2019.08.014.

Yasuda, J., Nakada, S., Kato, A., Toyoda, T., and Ishihama, A. (1993). Molecular assembly of influenza virus: Association of the ns2 protein with virion matrix. *Virology* 196, 249–255. doi:10.1006/viro.1993.1473.

Ye, F., Chen, E. R., and Nilsen, T. W. (2017). Kaposi's Sarcoma-Associated Herpesvirus Utilizes and Manipulates RNA N6- Adenosine Methylation To Promote Lytic Replication. *J. Virol.* 91, 1–21.

Ye, Q., Krug, R. M., and Tao, Y. J. (2006). The mechanism by which influenza A virus nucleoprotein forms oligomers and binds RNA. *Nature* 444, 1078–1082. doi:10.1038/nature05379.

Yehia, N., Naguib, M. M., Li, R., Hagag, N., El-Husseiny, M., Mosaad, Z., et al.

(2018). Multiple introductions of reassorted highly pathogenic avian influenza viruses (H5N8) clade 2.3.4.4b causing outbreaks in wild birds and poultry in Egypt. *Infect. Genet. Evol.* 58, 56–65. doi:10.1016/j.meegid.2017.12.011.

Yosef, I., Goren, M. G., and Qimron, U. (2012). Proteins and DNA elements essential for the CRISPR adaptation process in Escherichia coli. *Nucleic Acids Res.* 40, 5569–5576. doi:10.1093/nar/gks216.

Yu, J., Shen, L., Liu, Y., Ming, H., Zhu, X., Chu, M., et al. (2020). The m6A methyltransferase METTL3 cooperates with demethylase ALKBH5 to regulate osteogenic differentiation through NF-κB signaling. *Mol. Cell. Biochem.* 463, 203–210. doi:10.1007/s11010-019-03641-5.

Yue, H., Nie, X., Yan, Z., and Weining, S. (2019). N6-methyladenosine regulatory machinery in plants: composition, function and evolution. *Plant Biotechnol. J.* 17, 1194–1208. doi:10.1111/pbi.13149.

Yue, Y., Liu, J., Cui, X., Cao, J., Luo, G., Zhang, Z., et al. (2018). VIRMA mediates preferential m6A mRNA methylation in 3′UTR and near stop codon and associates with alternative polyadenylation. *Cell Discov.* 4. doi:10.1038/s41421-018-0019-0.

Zamarin, D., Ortigoza, M. B., and Palese, P. (2006). Influenza A Virus PB1-F2 Protein Contributes to Viral Pathogenesis in Mice. *J. Virol.* 80, 7976–7983. doi:10.1128/jvi.00415-06.

Zhan, X., Zhang, F., Zhong, Z., Chen, R., Wang, Y., Chang, L., et al. (2019). Generation of virus-resistant potato plants by RNA genome targeting. *Plant*

Biotechnol. J. 17, 1814–1822. doi:10.1111/pbi.13102.

Zhang, C., Samanta, D., Lu, H., Bullen, J. W., Zhang, H., Chen, I., et al. (2016a). Hypoxia induces the breast cancer stem cell phenotype by HIF-dependent and ALKBH5-mediated m6A-demethylation of NANOG mRNA. *Proc. Natl. Acad. Sci. U. S. A.* 113, E2047–E2056. doi:10.1073/pnas.1602883113.

Zhang, C., Zhang, M., Ge, S., Huang, W., Lin, X., Gao, J., et al. (2019a). Reduced m6A modification predicts malignant phenotypes and augmented Wnt/PI3K-Akt signaling in gastric cancer. *Cancer Med.* 8, 4766–4781. doi:10.1002/cam4.2360.

Zhang, C., Zhi, W. I., Lu, H., Samanta, D., Chen, I., Gabrielson, E., et al. (2016b). Hypoxia-inducible factors regulate pluripotency factor expression by ZNF217- and ALKBH5-mediated modulation of RNA methylation in breast cancer cells. *Oncotarget* 7, 64527–64542. doi:10.18632/oncotarget.11743.

Zhang, J., Guo, S., Piao, H. yan, Wang, Y., Wu, Y., Meng, X. yu, et al. (2019b). ALKBH5 promotes invasion and metastasis of gastric cancer by decreasing methylation of the lncRNA NEAT1. *J. Physiol. Biochem.* 75, 379–389. doi:10.1007/s13105-019-00690-8.

Zhang, S., Zhao, B. S., Zhou, A., Lin, K., Zheng, S., Lu, Z., et al. (2017). m6A Demethylase ALKBH5 Maintains Tumorigenicity of Glioblastoma Stem-like Cells by Sustaining FOXM1 Expression and Cell Proliferation Program. *Cancer Cell* 31, 591-606.e6. doi:10.1016/j.ccell.2017.02.013.

Zhang, T., Zhao, Y., Ye, J., Cao, X., Xu, C., Chen, B., et al. (2019c). Establishing CRISPR/Cas13a immune system conferring RNA virus resistance in both dicot

and monocot plants. *Plant Biotechnol. J.* 17, 1185–1187. doi:10.1111/pbi.13095.

Zhang, X., and Curtiss, R. (2015). Efficient generation of influenza virus with a mouse RNA polymerase I-driven all-in-one plasmid. *Virol. J.* 12, 1–10. doi:10.1186/s12985-015-0321-5.

Zhang, X., Kong, W., Ashraf, S., and Curtiss, R. (2009). A One-Plasmid System To Generate Influenza Virus in Cultured Chicken Cells for Potential Use in Influenza Vaccine. *J. Virol.* 83, 9296–9303. doi:10.1128/jvi.00781-09.

Zhang, X., Wei, L. H., Wang, Y., Xiao, Y., Liu, J., Zhang, W., et al. (2019d). Structural insights into FTO's catalytic mechanism for the demethylation of multiple RNA substrates. *Proc. Natl. Acad. Sci. U. S. A.* 116, 2919–2924. doi:10.1073/pnas.1820574116.

Zhang, Y., Liu, T., Meyer, C. A., Eeckhoute, J., Johnson, D. S., Bernstein, B. E., et al. (2008). Model-based analysis of ChIP-Seq (MACS). *Genome Biol.* 9. doi:10.1186/gb-2008-9-9-r137.

Zhang, Y., Wang, X., Zhang, X., Wang, J., Ma, Y., Zhang, L., et al. (2019e). RNA-binding protein YTHDF3 suppresses interferon-dependent antiviral responses by promoting FOXO3 translation. *Proc. Natl. Acad. Sci. U. S. A.* 116, 976–981. doi:10.1073/pnas.1812536116.

Zhang, Z., Theler, D., Kaminska, K. H., Hiller, M., De La Grange, P., Pudimat, R., et al. (2010). The YTH domain is a novel RNA binding domain. *J. Biol. Chem.* 285, 14701–14710. doi:10.1074/jbc.M110.104711.

Zhao, B. S., Roundtree, I. A., and He, C. (2016). Post-transcriptional gene regulation by mRNA modifications. *Nat. Rev. Mol. Cell Biol.* 18, 31–42. doi:10.1038/nrm.2016.132.

Zhao, J., Li, B., Ma, J., Jin, W., and Ma, X. (2020a). Photoactivatable RNA N6 - Methyladenosine Editing with CRISPR-Cas13. *Small* 1907301, e1907301. doi:10.1002/smll.201907301.

Zhao, W., Qi, X., Liu, L., Liu, Z., Ma, S., and Wu, J. (2020b). Epigenetic Regulation of m6A Modifications in Human Cancer. *Mol. Ther. - Nucleic Acids* 19, 405–412. doi:10.1016/j.omtn.2019.11.022.

Zhao, X., Yang, Y., Sun, B. F., Shi, Y., Yang, X., Xiao, W., et al. (2014a). FTO-dependent demethylation of N6-methyladenosine regulates mRNA splicing and is required for adipogenesis. *Cell Res.* 24, 1403–1419. doi:10.1038/cr.2014.151.

Zhao, X., Yang, Y., Sun, B. F., Zhao, Y. L., and Yang, Y. G. (2014b). FTO and obesity: Mechanisms of association. *Curr. Diab. Rep.* 14. doi:10.1007/s11892-014-0486-0.

Zheng, G., Dahl, J. A., Niu, Y., Fedorcsak, P., Huang, C. M., Li, C. J., et al. (2013). ALKBH5 Is a Mammalian RNA Demethylase that Impacts RNA Metabolism and Mouse Fertility. *Mol. Cell* 49, 18–29. doi:10.1016/j.molcel.2012.10.015.

Zheng, Q., Hou, J., Zhou, Y., Li, Z., and Cao, X. (2017). The RNA helicase DDX46 inhibits innate immunity by entrapping m 6 A-demethylated antiviral transcripts in the nucleus. *Nat. Immunol.* 18, 1094–1103. doi:10.1038/ni.3830.

Zhong, H., Ceballos, C. C., Massengill, C. I., Muniak, M. A., Ma, L., Qin, M., et al. (2021). High-fidelity, efficient, and reversible labeling of endogenous proteins using crispr-based designer exon insertion. *Elife* 10, 1–21. doi:10.7554/eLife.64911.

Zhong, S., Li, H., Bodi, Z., Button, J., Vespa, L., Herzog, M., et al. (2008). MTA is an Arabidopsis messenger RNA adenosine methylase and interacts with a homolog of a sex-specific splicing factor. *Plant Cell* 20, 1278–1288. doi:10.1105/tpc.108.058883.

Zhou, P., Yang, X. Lou, Wang, X. G., Hu, B., Zhang, L., Zhang, W., et al. (2020). A pneumonia outbreak associated with a new coronavirus of probable bat origin. *Nature* 579, 270–273. doi:10.1038/s41586-020-2012-7.

Zhou, Y., Hambly, B. D., and McLachlan, C. S. (2017). FTO associations with obesity and telomere length. *J. Biomed. Sci.* 24, 1–7. doi:10.1186/s12929-017-0372-6.

Zhou, Y., Zeng, P., Li, Y. H., Zhang, Z., and Cui, Q. (2016). SRAMP: Prediction of mammalian N6-methyladenosine (m6A) sites based on sequence-derived features. *Nucleic Acids Res.* 44. doi:10.1093/nar/gkw104.

Zhu, H., Gan, X., Jiang, X., Diao, S., Wu, H., and Hu, J. (2019). ALKBH5 inhibited autophagy of epithelial ovarian cancer through miR-7 and BCL-2. *J. Exp. Clin. Cancer Res.* 38, 1–15. doi:10.1186/s13046-019-1159-2.

Zhu, Z., Qian, Q., Zhao, X., Ma, L., and Chen, P. (2020). N6-methyladenosine ALKBH5 promotes non-small cell lung cancer progress by regulating TIMP3 stability. *Gene* 731, 144348. doi:10.1016/j.gene.2020.144348.

Zou, S., Toh, J. D. W., Wong, K. H. Q., Gao, Y. G., Hong, W., and Woon, E. C. Y. (2016). N 6 -Methyladenosine: A conformational marker that regulates the substrate specificity of human demethylases FTO and ALKBH5. *Sci. Rep.* 6, 1– 12. doi:10.1038/srep25677.

Zurcher, T., Luna, D., Sanz-ezquerro, J. J., Nieto, A., and Ort, J. (1996). Mutational analysis of the influenza virus A/Victoria/3/75 PA protein: studies of interaction with PB1 protein and identification of a dominant negative mutant. *J. Gen. Virol.* 77, 1745–1749.